NOTE TO USERS

This reproduction is the best copy available.

Abstract

Towards a measurement of parity nonconservation in diatomic molecules

David Rahmlow

2010

Certain aspects of electroweak parity violation can be explored in atoms and molecules using techniques common in atomic and molecular physics. Parity-nonconserving interactions between an s-state electron and the nucleus can mix electronic states of opposite parity; precise measurement of the electronic wavefunction provides information about the underlying physics. The experiment described here is intended to study nuclear spin-dependent parity-nonconserving (NSD-PNC) interactions, which are related to the Standard Model constants describing the coupling of the Z^0 boson to the proton and neutron (C_{2p} and C_{2n}) and to the nuclear anapole moment. The effect of these interactions is enhanced in certain atoms or molecules in which two levels of opposite parity are close to degeneracy. This condition can be most easily achieved in diatomic molecules by using the Zeeman effect to bring sublevels of the two lowest rotational energy levels close to crossing. Progress towards this goal is described, based on measurements of Stark effect-induced level crossings in barium monofluoride.

Towards a measurement of parity nonconservation in diatomic molecules

A Dissertation

Presented to the Faculty of the Graduate School

of

Yale University

in Candidacy for the Degree of

Doctor of Philosophy

by

David Rahmlow

Dissertation Director: David DeMille

May 2010

Contents

To Becky - thank you for the encouragement. So, now it is your turn to write again?

To Sid - who has been able to "just make it work", and whose advice and assistance has been invaluable. Sidney Cahn is the kindest, bravest, warmest, most wonderful human being I've ever known in my life, and his work has been crucial to the progress of this experiment.
Many thanks to Laura for allowing him to work here.

Part I

Description of the Experiment

Chapter 1

Introduction

This chapter presents an overview of the experiment, and a summary of my role in this work and a roadmap to the layout of this dissertation. The general overview which follows is intended for a general audience, with minimal assumptions of the reader's knowledge of atomic physics. A more technical introduction to the experiment is presented in chapters 2 and 3.

1.1 General Overview

Atomic physics can provide a useful way to study certain aspects of nuclear and particle physics without the use of high energy accelerators. Electrons with relativistic energies in s-type orbitals within atoms and molecules can spend a significant amount of time close to (or within) the atomic nucleus. When this occurs, the electron interacts with the nucleus (as it would in an accelerator experiment, albeit at lower energies). This results in a subtle but detectable change to the energy level structure of the atom or molecule, and this change in energy or state composition can be probed by spectroscopic means. Interpretation of the resulting measurements is often challenging, due to the

relative complexity of the atomic environment (with over 50 electrons, protons, and neutrons for a moderately heavy element), compared to the interaction of an electron with a single proton or neutron at high energies. Still, theorists proposed atomic and molecular physics experiments, sometimes dubbed non-accelerator particle physics, decades ago [1, 2]. Most of these experiments on fundamental symmetries and constants can be grouped into one of the following types:

- Measurements of the electric dipole moment of fundamental particles (e.g. the electron or neutron)
- Constraints on the time variation of fundamental constants (particularly the fine structure constant, α)
- Verification of fundamental symmetries (eg. Lorentz invariance)

And last,

- Electroweak parity violation

This experiment is concerned with this last topic. The discussion will begin with what is meant by parity in atoms or molecules.

Parity is one of the three fundmental symmetries (charge, along with parity and time) in physics. Parity describes what the universe would look like if the spatial coordinates were inverted - if left is switched for right, top for bottom, and front for back. This is similar to a mirror image (where left and right, and front and back are changed), with the additional exchange of up and down. Consider what effect this would have on various physical properties - such as mass, charge, position, and momentum. Properties which are independent of position, such as mass, time, charge, and power - or contain an even product of position-dependent variables, such as classical angular momentum - are unaffected. Properties based on position, such as velocity, acceleration,

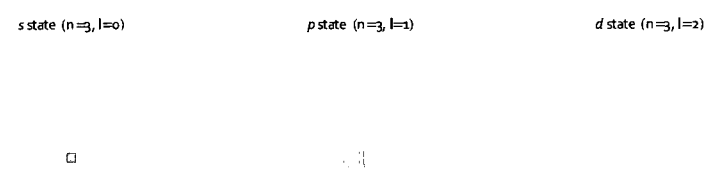

Figure 1.1: An example of the electronic wavefunction $\psi(\vec{r})$ of a few different states of the hydrogen atom (blue is positive, green is negative). The probability of finding the electron at a given point is given by taking the square of the wavefunction, $|\psi(\vec{r})|^2$. We can consider how these three states are affected by parity by thinking about what these wavefunctions would look like in a mirror. The s and d states are symmetric; the mirror image is unchanged. The p state, however, is antisymmetric; the mirror image is exactly opposite. The s and p states have *even* parity, while the p state has *odd* parity.

momentum (a function of velocity), and electric field, would be reversed. An interaction between two particles preserves parity if the energy of the interaction is unchanged when we invert spatial coordinates. Most interactions (gravity, electromagnetism, the strong force within the nucleus) preserve parity.

The idea of parity applies to the motion of the electron within the atom or molecule. One of the fundamental tenets of quantum mechanics is that the states of an atom or molecule are quantized; the energy of an electron is not continuous, but instead only takes on certain values. Each of these allowed values corresponds to a different state of the atom or molecule. The position and motion of the electron are described using a wavefunction, usually denoted by $\psi(\vec{r})$ - a map that shows how likely it is to find the electron at some particular location. As an example, figure 1.1 shows three possible states of the hydrogen atom. The probability of finding the elctron at a given point is given by taking the square of the wavefunction, $|\psi(\vec{r})|^2$. In this figure, blue areas represent places where the wavefunction is positive, and green areas where the wavefunction is negative. So, the electron is most likely to be in an area which is

strongly colored blue or green. Consider these three states to better understand the concept of parity in an atom or molecule. The parity reversal discussed in the previous paragraph (swapping left for right, up for down, and front for back) is, in two dimensions, equivalent to a 180 degree rotation. Now, look at the rotated image of each of these wavefunctions. The s and d states are symmetric; the rotated image looks the same as the original wavefunction. The rotated image of the p state, however, is the opposite of the original; the p state is antisymmetric. The s and d states are *even*, since the wavefunction satisfies $\psi(-\vec{r}) = \psi(\vec{r})$. The p state is *odd*, since the wavefunction satisfies $\psi(-\vec{r}) = -\psi(\vec{r})$. Note, however, that regardless of whether the state is even or odd, it contains one of these kinds of mirror symmetry. This is because the most important interactions within the atom or molecule - electromagnetism and the strong force - preserve parity. States that exhibit this kind of symmetry are called *parity eigenstates.*

As a consequence of the fact that most interactions preserve parity, the laws of physics should act in the same way if we were to look at the world through a mirror. Consider the process of alpha decay, in which an atom becomes a new type of element by emitting a helium nucleus ("alpha" particle):

$$ {}^{a}_{b}A \rightarrow {}^{a-4}_{b-2}B + {}^{4}_{2}\mathrm{He}^{2+} $$

This reaction changes element A into element B by removing two neutrons and two protons from the nucleus. Suppose the element A is "held" in a fixed orientation using a magnetic field, so that the nuclear spin always points in the same direction. Then, look at the direction in which the alpha particles go. The same number of alpha particles should go to the left as to the right; if left and right are swapped, nothing has changed.

However, one type of interaction does not preserve parity. The weak force is one of the four fundamental interactions, along with electromagnetism, gravity, and the strong force. Each of these interactions is related to a particle that "mediates" the interaction; electromagnetic fields are carried through space by the photon, gravity by gravitons, and the strong force by gluons. The weak interaction is carried by the $W^{\pm}$ and Z bosons. These particles behave somewhat like photons, in that photons and $W^{\pm}$ and Z bosons allow particles to exchange momentum. These particles are very different, however, since photons are massless, but the $W^{\pm}$ and Z bosons are extremely heavy, about 97 times more massive than a proton. The result is that the $W^{\pm}$ and Z only affect particles that are extremely close together. The $W^{\pm}$ and Z are also unusual in that interactions with these bosons can change the type of a particle. The existence of the weak force was first postulated in order to explain beta decay, the process by which some atomic nuclei spontaneously allow one neutron to change into a proton, emitting an electron, and electron anti-neutrino in the process, for example:

$$ {}^{a}_{b}A \rightarrow {}^{a}_{b+1}B + e^{-} + \bar{\nu}_e $$

In 1957, Wu et al. [5] looked at beta decay in ^{60}Co, in which $^{60}\mathrm{Co} \rightarrow {}^{60}\mathrm{Ni} + e^{-} + \bar{\nu}_e$. The direction of the spin of the ^{60}Co was kept pointing in the same direction by putting the atoms in a strong magnetic field. It was observed that the electrons were not emitted equally in the directions along and against the magnetic field; instead, more electrons were emitted opposite to the direction of the field. The direction that an electron takes can be written as $\vec{p}_e \cdot \vec{B}$, where $\vec{p}_e$ is the momentum of the electron and $\vec{B}$ is the magnetic field (the direction in which the nuclear spins are aligned). Under parity transformation, the momentum $\vec{p}_e$ changes sign to become $-\vec{p}_e$, while the magnetic field $\vec{B}$

remains unchanged. The sign of the expression changes; this effect is called parity violation.

Electroweak interactions violate parity within a stable atom or molecule by mixing two states of opposite parity. Considering the wavefunctions illustrated in figure 1.1, start with the s state pictured and add just a little of the p state. If you looked at the resulting wavefunction in a mirror, it would be neither the same nor reversed; the symmetry would be gone. States that look like this can be measured in atoms or molecules. The weak force is, as the name suggests, weak; the states that are allowed in the molecule are very close to being perfectly symmetric. The extent to which the weak force mixes two states of opposite parity depends on the energy difference between the two states; the smaller the energy difference, the more p state that will be mixed into the s state. This means that to measure parity violation, it can be beneficial to use atoms or molecules which have states of opposite parity that are very closely spaced. Luckily, we can use a magnetic field to change the spacing betwen energy levels, and enhance the effects of parity violation [3]. However, practical limits on the size and strength of magnets dictates the amount by which the energy levels can be shifted, so this strategy only works for levels that are naturally quite close already.

With fewer than 100 naturally occurring elements, there are few cases in which two levels of opposite parity are close enough together to be brought to degeneracy for this kind of parity violation experiment (though other experimental techniques exist to observe parity-violating effects in atoms [16, 10]). Dysprosium is the only atom known where the opposite-parity levels are close enough together to bring to degeneracy using a magnetic field [14]. Unfortunately, parity violation in Dy is suppressed for other reasons. Molecules offer more options for finding closely spaced levels with opposite parity. Molecules

have more degrees of freedom than atoms. In addition to electronic wavefunctions, the atoms within the molecule can vibrate as if they were on springs, or the molecule can rotate. This latter effect is particularly useful for diatomic molecules (molecules consisting of two atoms). As it happens, the parity (even or odd) of a molecule's wavefunction depends on an integer N that represents how fast the molecule is spinning [31]:

$$\text{parity} = (-1)^N$$

The first level, with $N = 0$, therefore has even parity; the next level, with $N = 1$, has odd parity. All diatomic molecules share this same basic property. The energy difference between these two levels is usually less than 30 GHz, and only a relatively moderate magnetic field (about 0.5 - 2 Tesla) is required to bring these levels close together. The strength of the parity-violating interactions is probed by applying an electric field that interferes with the electroweak interaction.

Now, consider the ways in which electroweak interactions can lead to parity violation in atoms or molecules. There are an infinite number of ways in which the electron can interact with the nucleus via electroweak interactions, but consider only a few of the most probable interactions. Figure 1.2 shows two Feynman diagrams, illustrating the two most likely interactions. A Feynman diagram is, in essence, a short story. Read left to right, it gives the cast of characters at the beginning of the story, what happens, and who is left at the end. Part a) shows that the electron (e) interacts with a neutron or proton (n or p, collectively called nucleons) within the nucleus by exchanging a Z boson. Afterwards, the electron and the nucleon go their separate ways. Bosons are a type of particle that allows other particles to exchange momentum; both the photon and the Z are bosons. Photons are massless, and can travel long

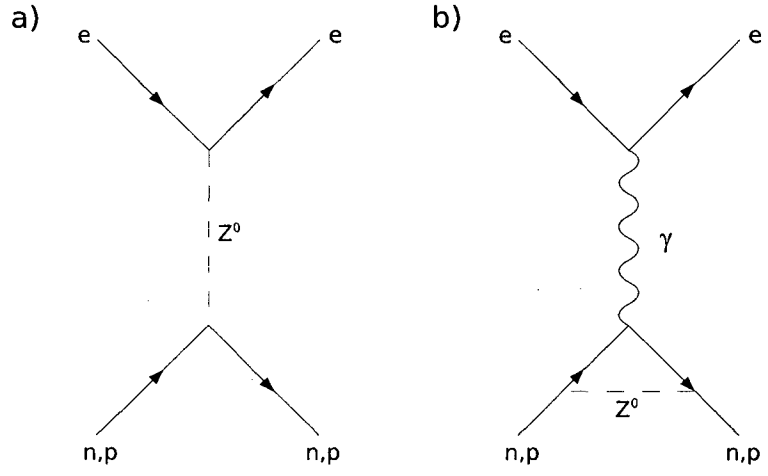

Figure 1.2: Feynman diagrams showing some possible ways for the electron to interact with the nucleus in a manner that gives rise to parity violation. These diagrams are meant to be read from left to right, telling a short and simple story. These are the most important interactions between the electron and the nucleus that contribute to spin-dependent parity violation. Part a) shows an electron interacting with the nucleus through the exchange of a Z boson. Part b) shows an electroweak interaction inside the nucleus; the electron interacts electromagnetically (by exchange of a photon) with the intermediate product.

distances between particles. However, the Z, is very massive; this means that this momentum exchange can only occur when the electron is very close to the nucleus. This diagram gives both nuclear spin-dependent and spin-independent contributions; the latter can be ignored because it does not contribute to the signals in this experiment. The nuclear spin-dependent contribution is found by counting up the contribution due to each proton or neutron in the atomic nucleus. In the nuclear ground state, each proton pairs up with another proton of equal but opposite spin if there are an even number of protons; the same holds for neutrons. Therefore, the interaction between the electron and the first proton cancels out the interaction between the electron and the second proton, the interactions with the third and fourth protons cancel, and so on. The net result is that all that matters is whether the nucleus has an even or odd number of protons, and an even or odd number of neutrons. This means that it will be important to measure this effect in isotopes with an odd number of protons and even number of neutrons, and in other isotopes with an odd number of neutrons but an even number of protons. This effect will not be seen in isotopes with even numbers of protons and neutrons. Part b) shows a process in which the electron interacts with the nucleon electromagnetically, but that there are electroweak interactions within the nucleus mediated by Z boson exchange.

The parity-violating effects with the most relevance to particle physics are shown by part a) in figure 1.2. Parameters called coupling constants describe the strength of the observed parity violation by saying how strongly two particles interact. The relevant constants, $C_{2,p}$ and $C_{2,n}$, describe the strength of the interaction between the Z boson and the proton or neutron, respectively. These coupling constants for the proton and neutron can be related to the underlying coupling constants $C_{2,u}$ and $C_{2,d}$ between the Z boson and the up and down quarks by considering the proton and neutron as a combination of up and down

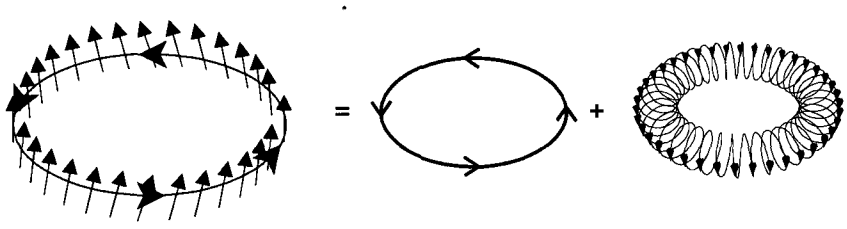

Figure 1.3: Electrical currents associated with the anapole moment. In the shell model of the nucleus, without electroweak parity violation, the valence nucleon would travel in an orbit around the nuclear core, with its spin (black arrow) held vertically (eg. in a $p_{3/2}$ valence state). The combination of the orbital angular momentum and the nuclear spin is equivalent to a single current loop (blue circle on left). Mixing with a state of opposite parity causes the spin to tilt in the direction of motion; the portion of the nuclear spin that is tilted in the direction of motion creates a current distribution equivalent to a toroidal coil. This results in an overall current equivalent to that of a current loop plus a toroidal current. This toroidal current produces a magnetic field which exists only within the torus; it only affects the electron when the electron passes through this region close to the nucleus.

quarks (a proton is two up quarks and a down quark; a neutron is one up quark and two down quarks), and parity violating effects within the proton or neutron (eg. the proton's anapole moment). The best measurements of these parameters to date has been through deep inelastic scattering experiments (electron-proton or electron-deuteron collisions at high energies) at SLAC [6, 7] and the Bates SAMPLE [8] experiment. These experiments have measured the C_2 constants with uncertainties of 300% and 70%, respectively, of the predicted values. The goal of this experiment is to reduce the level of uncertainty in the measured values of $C_{2,p}$ and $C_{2,n}$ to about 10%, limited by the accuracy of theoretical interpretation. Improved measurements of $C_{2,u}$ and $C_{2,d}$ could show evidence of physics beyond the standard model [9], such as the existence of additional types of Z bosons, if the measurements deviate from standard model predictions at the 30% level.

Part b) of figure 1.2 causes parity violation within the nucleus through an effect called the *nuclear anapole moment.* This is primarily an effect related to nuclear physics. Usually, interactions between the protons and neutrons within the nucleus preserve parity. As a result, the nucleus is in a parity eigenstate, like the electron. In the shell model, the one unpaired nucleon (valence nucleon) can be considered to be in an orbit around the nuclear core, with its spin pointing up. The combined effect of the orbital angular momentum and the spin of the nucleon is to make a current distribution equivalent to that of a current loop (blue loop in figure 1.3). However, electroweak interactions inside the nucleus create a small amount of parity violation; the net result of this is to mix in a little bit of an opposite-parity state. This mixing tilts the spin of the valence nucleon in the direction of its motion (depicted on the left side of figure 1.3). The part of the spin that is tilted makes a magnetic field equivalent to that which would result from a toroidal current (right side of figure 1.3) - a field that is only present within the torus. This field pattern is called an *anapole moment*, analogous to a monopole, dipole or quadrupole moment.[1] The type of moment tells how quickly the field falls off with increasing distance. A dipole moment, for example, causes an electric potential that is proportional to $1/r^2$ at some distance r away from the dipole. The anapole moment has a dependence on the radius of $\delta(\vec{r})$ ($\delta(\vec{r})$ is the

[1]Specifically, the vector potential corresponding to a current distribution $\vec{J}(\vec{r})$ is:

$$\vec{A}(\vec{r}) = \int \frac{\vec{J}\left(\vec{r'}\right) d\vec{r'}}{\left|\vec{r} - \vec{r'}\right|}$$

This can be expanded in a series of powers of r^{-1}. Khriplovich [2] writes the term corresponding to the anapole moment as

$$\vec{A}_a(\vec{r}) = \left(-\pi \int r^2 J\left(\vec{r'}\right) d\vec{r'}\right) \delta(\vec{r})$$

and so the anapole moment depends on the mean of the square of the radius $\langle r^2 \rangle$ of the current distribution. For the nucleus, the current distribution comes from the movement of the valence nucleon within the nucleus. The value $\langle r^2 \rangle$ is approximately equivalent to the square of the nuclear radius, r_0^2; the nuclear radius r_0, in turn, scales like $r_0 \sim A^{2/3}$ with the atomic mass A.

delta function; it is infinite at $\vec{r} = 0$, but zero everywhere else). The electron spin interacts with this magnetic field, but only when the electron is within this torus. The strength of the anapole moment is estimated by considering how much time the electron will spend within this torus. The anapole moment depends on the mean of the square of the radius $\langle r^2 \rangle$ of the current distribution, which is approximately the same as the square of the nuclear radius, r_0^2. In the liquid drop model of the nucleus, the radius of the nucleus scales like $A^{1/3}$, where A is the total number of nucleons in the nucleus. Therefore, the strength of the anapole moment will scale as $A^{2/3}$. Explicit calculations of this process predict the effect of the anapole moment to be bigger than that of Z boson exchange for atomic masses $A \gtrsim 20$. Measurements of the anapole moment would primarily be of interest to the nuclear physics community, as a point of comparison to test theoretical models of how weak interactions are modified within the nuclear medium.

It is important to note that both of these parity-violating effects look the same to the electron - a small interaction that occurs only when the electron is close to the nucleus. In fact, it is impossible to distinguish these effects given a single measurement. A full experimental program must study both light and heavy nuclei, with even-odd numbers of neutrons and protons. Some of the criteria for choosing relevant molecules are:

- Even number of protons, odd number of neutrons (or odd number of protons, even number of neutrons) in at least one of the nuclei in the molecule. (Odd proton, odd neutron isotopes will also exhibit nuclear spin-dependent parity violation, but the results may be difficult to interpret.)
- Sufficient natural abundance of the relevant isotope
- An unpaired electron spin (necessary to observe spin-dependent interactions, as well as to simplify spectroscopy and interpretation of results)

- High probability to find the valence electron at the nucleus; this requires a $^2\Sigma$ state with large amplitudes in atomic s- and p-like states
- Accessible transitions for spectroscopic state detection and preparation
- Ability to shift two levels of opposite parity to degeneracy using a magnetic field

With these parameters in mind, the initial target has been to make a parity violation measurement in $^{137}_{56}\mathrm{Ba}^{19}\mathrm{F}$. The natural abundance of ^{137}BaF is about 10%; laser diodes are readily available to cover many of the electronic transitions from the X $^2\Sigma$ ground state; and ground-state rotational levels can be brought to crossing with a magnetic field of $B_0 \approx 4600$ gauss. The relevant spectroscopic constants are well known [12].

Our implementation of this measurement uses a pulsed supersonic molecular beam, as illustrated in figure 1.4. This is a common technique used in physical chemistry to perform spectroscopic measurements on molecules. The experimental apparatus consists, in effect, of a long tube kept under vacuum. A beam of molecules is prepared at one end (step 1). The drawing at the bottom depicts the two relevant (even and odd parity) energy levels of the molecule (red and blue lines, states $|a\rangle$ and $|b\rangle$). Both of these states are in the ground electronic and vibrational state of the molecule, but one is a state with $N = 0$ (even parity) and one with $N = 1$ (odd parity). The energy difference between the two levels is indicated schematically by the distance between the lines, and the population of molecules in that state is shown by the number of circles drawn. At the beginning, the number of molecules is approximately the same in both states. The molecules travel down the tube at about 600 meters/second. As they move through the apparatus, a sequence of operations is performed on the molecules. We use a spectroscopic technique called *optical pumping* to put the molecules into the proper starting state for the experiment (step 2). A laser

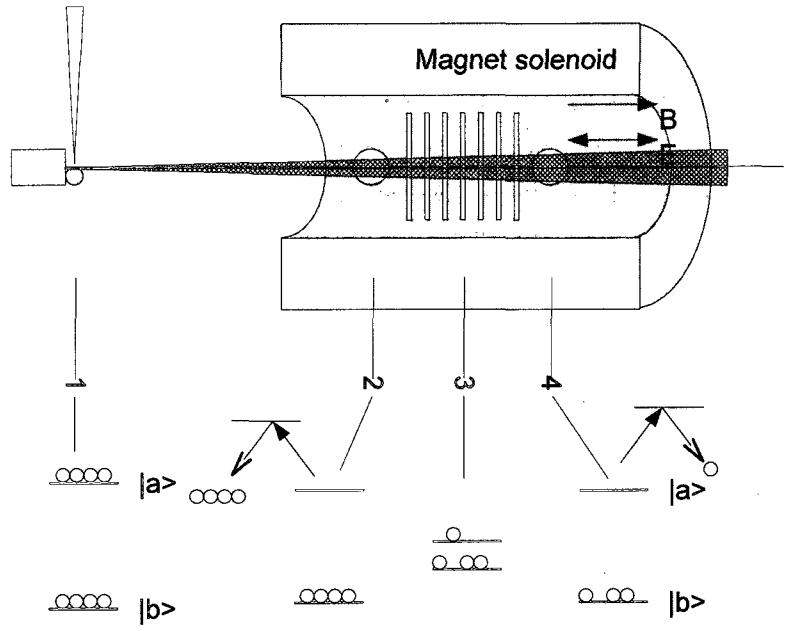

Figure 1.4: Brief description of the experiment. The top part of the drawing shows a schematic view of the apparatus, while the bottom shows the corresponding effect on two of the energy levels of the molecules. The two levels, arbitrarily labeled $|a\rangle$ and $|b\rangle$, are represented by the red and blue lines. The population of the state (probability that we find a given molecule to be in that state) is indicated by the number of blue dots shown. Molecules are created at 1; the initial state of the system is prepared at 2; a far off-resonant transition is driven at 3; the final state is detected at 4. The effect at each stage on the two energy levels we are interested in is shown at the bottom.

tuned to an optical transition drives molecules out of state $|a\rangle$ into another, unobserved state; this leaves state $|a\rangle$ depopulated. The two levels of opposite parity are brought close to degeneracy using a magnetic field, and an AC electric field is applied (step 3). This transfers some of the molecules from state $|b\rangle$ to state $|a\rangle$; the exact number depends on the nature of the electric field applied as well as the parity-violating interactions the experiment is designed to detect. Tthe population transferred into state $|a\rangle$ is then measured using laser induced fluorescence (step 4). What is important is the way in which the electric field that we applied in step 3 interacts with the parity-violating interactions. The applied electric field can be changed, and the energy difference between the states set by changing the magnetic field from the value needed to bring the levels to crossing:

$$\begin{aligned} \Delta &\equiv E_a - E_b \\ &= \mu_B \left(B - B_0\right) \end{aligned}$$

where μ_B is the Bohr magneton, and B_0 is the magnetic field required to make the energy difference between the two levels be zero. This combination of variables, $\vec{E} \cdot \left(\vec{B} - \vec{B}_0\right)$, changes sign under parity transformation; the electric field $\vec{E}$ becomes $-\vec{E}$, but the magnetic field $\vec{B}$ is invariant. In the absence of any parity-violating interactions, the sign of the applied electric field does not matter; applying a field $E = +E_0 \cos(\omega t)$ is the same as applying a field $E = -E_0 \cos(\omega t)$. The same thing is true for the energy difference between the two states $|a\rangle$ and $|b\rangle$. Having an energy difference $\Delta = E_a - E_b$ will give the same number of molecules as when we change the magnetic field to make the energy difference be $-\Delta = E_b - E_a$. This is no longer true in the presence of a parity-violating interaction; in this case, the parity-violating interaction will interfere with the electric field and we will see that the sign of the electric field,

or as well as the sign of the energy difference $\Delta = E_a - E_b$ and $-\Delta = E_b - E_a$, makes a modest but significant change in the measured signal. This is an important way to isolate the effects of parity violation, even in the presence of systematic problems (a poorly prepared electric or magnetic field, for example).

1.2 Role

My role on this experiment has been the construction of the vacuum system, beam source, laser stabilization, detection and data acquisition systems, as well as operation of the experiment and data analysis. Another graduate student, Dennis Murphree, has also played a major role in the development of the experimental apparatus, with primary responsibility for the magnetic field measurement and shimming and two-photon detection scheme. A third graduate student, Marco Ascoli, was responsible for the early development of the piezo valve beam source. We have benefitted immensely from the participation of research scientist Sidney Cahn, who has been skillful at making things "just work" despite the deficiencies in our designs. The project is operated under the direction of Prof. David DeMille in the Sloane Physics Laboratory at Yale University with funding from the National Science Foundation. A number of undergraduates have assisted with the project as part of their thesis research or summer internships. Going forward, work on the project will be continued by graduate students Jeff Ammon and Matthew Steinecker.

1.3 Roadmap

This thesis has been organized in the following manner:

- Chapter 1 has given a brief overview of the experiment and our motivation for undertaking this task.

- Chapter 2 describes the underlying theory of parity violation in more technical detail, and outline previous experiments which touch upon the measurement of nuclear spin-dependent parity non-conservation. These experiments may use either accelerator or atomic physics means to explore novel aspects of the weak interaction.

- Chapter 3 outlines the theoretical principles behind the experiment, linking the underlying constants we wish to determine to observable measurements using optical spectroscopy. There are also calculations of the expected signal in terms of the fundamental constants to be measured and the experimental parameters under our control.

- Chapter 4 gives a brief overview of the energy level structure of diatomic molecules, with a focus on the underpinnings of the methods used to calculate energy levels, level crossings, and transition energies in this experiment. The results of the calculations of relevant energy levels and simulated spectra are presented along with spectroscopic measurements.

- Chapter 5 contains a detailed discussion of the experimental apparatus, with notes on the design and operation of each major component.

- Chapter 6 shows preliminary data collected to characterize the molecular beam source and spectroscopic detection scheme.

- Chapter 7 presents data showing the mixing of levels of opposite parity when brought close to degeneracy with an external magnetic field. In addition to being of some interest in its own right, it serves as a diagnostic test of all the parts of the experiment.

- Chapter 8 summarizes the current state of the experiment and describes what needs to be done in order to continue forward and make measurements of parity violation in diatomic molecules.

- The appendices contain specific descriptions of the experimental apparatus and techniques (mechanical drawings, code) which will be of use for people working on this experiment, or who hope to implement similar devices for their own work.

I hope this will prove to be a useful introduction to the current state of this experiment.

Chapter 2

Nuclear Spin-dependent Parity Violation: Theory and Overview of Previous Experiments

This chapter will briefly discuss the fundamental origins of parity-violating interactions in atoms and molecules, and give an overview of some of the most relevant experiments. The first part of the chapter primarily follows the treatment in Khriplovich [2].

2.1 Possible Parity-Violating Interactions

One cause of parity violation in atoms and molecules is parity violation in interactions between the electron and nucleons. Khriplovich introduces the possibil-

ity of parity-violating interactions between the electron and nucleons (neutrons or protons in the atomic nucleus) in a manner which could be described as "Everything that is not forbidden is possible". The subject is introduced by suggesting all possible contact interactions between an electron (e) and nucleon (p) which

- are induced by neutral currents (no change of particle type)
- satisfy Lorentz-invariance
- are local interactions

These interactions are formed by using the Dirac γ matrices[1] (and their antisymmetric products, $\sigma_{\mu\nu} \equiv \frac{1}{2}(\gamma_\mu\gamma_\nu - \gamma_\nu\gamma_\mu)$) as a basis for all possible interactions between two spin-1/2 particles. The following list of interactions results:

$$\begin{aligned}\mathcal{H} =& G_s\bar{p}pe\bar{e}e + G_P\bar{p}\gamma_5 p\bar{e}\gamma_5 e + G_v\bar{p}\gamma_\mu p\bar{e}\gamma_\mu e \\ &+ G_A\bar{p}\gamma_\mu\gamma_5 p\bar{e}\gamma_\mu\gamma_5 e + G_T\bar{p}\sigma_{\mu\nu}p\bar{e}\sigma_{\mu\nu}e \\ &+ G'_v\bar{p}\gamma_\mu p\bar{e}\gamma_\mu\gamma_5 e + G'_A\bar{p}\gamma_\mu\gamma_5 p\bar{e}\gamma_\mu e \\ &+ iG'_s\bar{p}pe\bar{e}\gamma_5 e + iG'_P\bar{p}\gamma_5 pe\bar{e}e + G'_T\varepsilon_{\chi\lambda\mu\nu}\bar{p}\sigma_{\chi\lambda}pe\bar{\sigma}_{\mu\nu}e\end{aligned} \tag{2.1}$$

where the G'_T term results from using the identity $\gamma_5\sigma_{\mu\nu} = -\frac{i}{2}\varepsilon_{\chi\lambda\mu\nu}\sigma_{\chi\lambda}$. Terms which contain γ_5 in one (but not both) terms will be odd under parity transformations[2]; so, the first five terms (G_s, G_P, G_v, G_A, and G_T) are even under

[1] Here, the Dirac γ matrices are defined as

$$\gamma_0 = \begin{pmatrix} I & 0 \\ 0 & -I \end{pmatrix}, \quad \gamma_m = \begin{pmatrix} 0 & \sigma_m \\ -\sigma_m & 0 \end{pmatrix} \text{ for } m = 1,2,3, \quad \gamma_5 = -i\gamma_0\gamma_1\gamma_2\gamma_3$$

where the Pauli matrices σ_m are

$$\sigma_1 = \begin{pmatrix} 0 & 1 \\ 1 & 0 \end{pmatrix}, \quad \sigma_2 = \begin{pmatrix} 0 & -i \\ i & 0 \end{pmatrix}, \quad \sigma_3 = \begin{pmatrix} 1 & 0 \\ 0 & -1 \end{pmatrix}$$

[2] Following the derivation on p. 22 of Holstein[13], we note that the effect of a parity transformation on a solution of the Dirac equation $\psi(x,t)$ is

$$\psi(x,t) \rightarrow \gamma_0\psi(-x,t), \; \bar{\psi}(x,t) \rightarrow \bar{\psi}(-x,t)\gamma_0$$

parity. The remaining five terms (G'_s, G'_P, G'_v, G'_A, and G'_T) are odd under parity. Khriplovich points out that the last three terms (G'_s, G'_P, and G'_T) are also odd under time reversal, and we will not consider these here. The remaining two terms (G'_v and G'_A) are parity-odd but time-reversal invariant. These two terms in the Hamiltonian are written with a common notation:

$$\mathcal{H}_{pv} = \frac{G}{\sqrt{2}} \left(-C_1 \bar{p}\gamma_\mu p \bar{e}\gamma_\mu\gamma_5 e - C_2 \bar{e}\gamma_\mu e \bar{p}\gamma_\mu\gamma_5 p\right) \tag{2.2}$$

where the constants C_1 and C_2 have been chosen to satisfy $C_1 \equiv -\sqrt{2}G'_v/G$ and $C_2 \equiv -\sqrt{2}G'_A/G$ and G is the Fermi coupling constant, $G = \frac{10^{-5}}{m_p^2}$, which describes the strength of the interaction leading to beta decay. The Glashow, Weinberg, Salam unified theory of electroweak interactions predicts values for these constants for protons (C_{1p}, C_{2p}) and neutrons (C_{1n}, C_{2n}), based on the Standard Model [19, 2]:

$$C_{1p} = \frac{1}{2}\left(1 - 4\sin^2\theta\right) \tag{2.3}$$

$$C_{1n} = -\frac{1}{2} \tag{2.4}$$

$$C_{2p} = \frac{1}{2}\left(1 - 4\sin^2\theta\right)\lambda \tag{2.5}$$

$$C_{2n} = -\frac{1}{2}\left(1 - 4\sin^2\theta\right)\lambda \tag{2.6}$$

---

so that a term of the form

$$\bar{\psi}\gamma_\mu\psi \to \bar{\psi}\gamma_0\gamma_\mu\gamma_0\psi = \begin{cases} \bar{\psi}\gamma_0\psi & \mu = 0 \\ -\bar{\psi}\gamma_\mu\psi & \mu = 1,2,3 \end{cases}$$

behaves like a polar vector (sign changes under parity transformation), but

$$\bar{\psi}\gamma_\mu\gamma_5\psi \to \bar{\psi}\gamma_0\gamma_\mu\gamma_5\gamma_0\psi = \begin{cases} -\bar{\psi}\gamma_0\gamma_5\psi & \mu = 0 \\ \bar{\psi}\gamma_\mu\gamma_5\psi & \mu = 1,2,3 \end{cases}$$

which behaves like an axial vector (sign unchanged under parity transformation). So, γ_μ is even under parity, but $\gamma_\mu\gamma_5$ is odd under parity.

where $\lambda = 1.25$ and θ is the Weinberg angle, experimentally found to be $\sin^2\theta \approx 0.23$. Based on this, the Standard Model values for these constants are

$$C_{1p} = 0.04,\ C_{1n} = -0.5,\ C_{2p} = 0.05,\ C_{2n} = -0.05 \tag{2.7}$$

Khriplovich then states that in the limit of an infinitely heavy nucleon, the nucleon portion of the interaction can be written

$$\bar{p}\gamma_0 p = \delta(\vec{r}) \tag{2.8}$$

$$\bar{p}\gamma_{\mu\neq 0} p = 0 \tag{2.9}$$

$$\bar{p}\gamma_0\gamma_5 p = 0 \tag{2.10}$$

$$\bar{p}\gamma_{\mu\neq 0}\gamma_5 p = -\vec{\sigma_p}\delta(\vec{r}) \tag{2.11}$$

where $\vec{r}$ is the distance from the nucleon and $\vec{\sigma_p}$ are the Pauli matrices, applied to the proton wavefunction. Making these changes to eq. 2.2 gives an effective interaction Hamiltonian for an atomic electron

$$\mathcal{H}_{pv,e} = \frac{G}{\sqrt{2}}\left(C_1 e^\dagger\gamma_5 e + C_2\vec{\sigma_p}e^\dagger\gamma_0\gamma_{\mu\neq 0}e\right)\delta(\vec{r}) \tag{2.12}$$

This demonstrates two important features:

- The $\delta(\vec{r})$ component emphasizes the contact nature of the interaction.
- The term containing the C_1 constant is not dependent on the nuclear spin, but the term containing C_2 is.

The total interaction between an electron and a nucleus with Z protons and N neutrons will be the sum of the interaction between the electron and each

individual nucleon

$$\mathcal{H}_{pv,e} = \frac{G}{\sqrt{2}}\left(\left(ZC_{1p}+NC_{1n}\right)e^{\dagger}\gamma_5 e + \left(C_{2p}\sum_{i=1}^{Z}\vec{\sigma_{p,i}} + C_{2n}\sum_{i=1}^{N}\vec{\sigma_{n,i}}\right)e^{\dagger}\gamma_0\gamma_{\mu\neq 0}e\right)\delta\left(r\right)$$

In a simple shell-model description of the ground state of nuclei with an even number of protons, pairs of protons will have opposite spin and the sum $\sum_{i=1}^{Z}\vec{\sigma_{p,i}}$ is zero. The same argument holds based on the number of neutrons, for the sum $\sum_{i=1}^{N}\vec{\sigma_{n,i}}$. So, in even-odd nuclei (with even Z and odd N, or odd Z and even N), the contribution from the terms proportional to C_{2p} and C_{2n} will depend only on the last unpaired nucleon. Because of this cancellation (and the small numerical values of C_{2p} and C_{2n} compared to C_{1n}), the spin-dependent contribution is generally much smaller than the spin-independent parity violation arising from the terms containing C_{1p} and C_{1n}, for any nucleus except ^{1}H.

2.2 Nuclear Anapole Moments: Another Source of Parity Violation

Parity-violating interactions between the electron and the nucleus are not the only source of NSD-PV effects. If the nuclear wavefunction is not a parity eigenstate, interactions between the electron and the nucleus can cause the electron wavefunction to violate parity symmetry even if the interactions themselves preserve parity. Strong and electromagnetic interactions conserve parity, so the wavefunction of the nucleus is a parity eigenstate if weak interactions are neglected. Khriplovich [2] observed that electroweak interactions inside the nucleus can mix two nuclear states of opposite parity. The electron interacts electromagnetically with the magnetic field due to the finite electric current

distribution $\vec{j}(\vec{r})$ within the nucleus.

The physics within the nucleus is complicated, but the electromagnetic interaction with the electron can be summarized by finding the moments of the current distribution[3]. The lowest-order parity-violating moment is the anapole moment. The derivation of the anapole moment from the current distribution (which can be found in ref. [72]) is tedious; in summary, part of the second derivative in the Talyor series expansion includes terms which are parity-odd but time-reversal invariant (eq. 1.316-1.318 in [72], and [18]):

$$\begin{aligned} \vec{A}^{(2)}_{i,\text{Anapole}}\left(\vec{R}\right) &= -\frac{1}{4\pi c}\left(\nabla_k \nabla_l \frac{1}{R}\right)\left(\delta_{kl} a_i - \delta_{il} a_k\right) \\ &= \frac{1}{4\pi c}\left(4\pi\delta\left(\vec{R}\right)\vec{a} + \nabla\left(\vec{a}\cdot\vec{\nabla}\frac{1}{R}\right)\right) \\ &= \frac{1}{4\pi c}\left(4\pi\delta\left(\vec{R}\right)\vec{a}\right) \text{ if } \vec{\nabla}\cdot\vec{A}=0 \end{aligned}$$

[3]As a short reminder, the vector potential $\vec{A}\left(\vec{R}\right)$ from a finite electric current distribution $\vec{j}(\vec{r})$ is

$$\vec{A}\left(\vec{R}\right) = \frac{1}{c}\int \frac{\vec{j}(\vec{r})}{\left|\vec{R}-\vec{r}\right|} d^3r$$

where $\vec{R}$ and $\vec{r}$ are defined as the position relative to the nucleus, and the magnetic field is found using $\vec{B} = \vec{\nabla}\times\vec{A}$. The vector potential is rewritten in terms of moments of the current distribution, which come from substituting $\frac{1}{|\vec{R}-\vec{r}|}$ with the Taylor series expansion

$$\frac{1}{\left|\vec{R}-\vec{r}\right|} = \frac{1}{R} - \left(\nabla_k \frac{1}{R}\right) r_k + \frac{1}{2}\left(\nabla_k \nabla_l \frac{1}{R}\right) r_k r_l + \ldots$$

where, in the vector Taylor series expansion,

$$\nabla_k \frac{1}{R} = \frac{\partial}{\partial k}\frac{1}{\sqrt{R_i^2+R_j^2+R_k^2}} = -\frac{1}{2}\frac{2R_k}{\left(\sqrt{R_i^2+R_j^2+R_k^2}\right)^3} = -\frac{R_k}{R^3}$$

and

$$\nabla_k \nabla_l \frac{1}{R} = \frac{\partial}{\partial k}\frac{\partial}{\partial l}\frac{1}{\sqrt{R_i^2+R_j^2+R_k^2}} = \frac{3R_k R_{l\neq k}}{R^5} + \nabla^2\frac{1}{R}$$

The last term $\nabla^2\frac{1}{R} \propto \delta\left(\vec{R}\right)$ is nonzero only at the origin of the coordinate system (in this case, at the nucleus).

in the gauge where $\vec{\nabla} \cdot \vec{A}$ is set to 0, and the moment $\vec{a}$ is defined as

$$\vec{a} = -\pi \int \vec{j}\,(\vec{r})\, r^2 d^3 r$$

For parity-violating nucleon-nucleon interactions within the nucleus, Khriplovich derives the following expression for the anapole moment (using a simple shell-model description for an even-odd nucleus, eq. 8.25 in [2])

$$\vec{a} = \frac{G}{\sqrt{2}} \frac{9}{10} g \frac{|e|\,\mu_N}{m_p \tilde{r}_0} A^{2/3} \frac{(I+1/2)\,(-1)^{I+1/2-\ell}\,\vec{I}}{I\,(I+1)} \tag{2.13}$$

where $\tilde{r}_0 = 1.2 \times 10^{-13}$ cm is the characteristic scale for the charge radius of the nucleons, e is the electron charge, μ_N is the nuclear magneton, m_p is the nucleon mass, A is the atomic mass, and I is the total nuclear spin. Here, ℓ is the angular momentum of the nucleon within the nucleus; the value affects the sign (but not the magnitude) of $\vec{a}$. The dimensionless coupling constant g is g_p for even-odd nuclei with an odd number of protons and g_n for nuclei with an odd number of neutrons. Two analyses of experimental data from a variety of measurements of PV nucleon-nucleon interactions give $g_p = 6 \pm 1$ or $g_p = 7.3 \pm 1.2$ (expt.) ± 1.5 (theor.) and $g_n = -0.9 \pm 0.7$ (expt.) or $g_n = -1.7 \pm 0.8$ (expt.) ± 1.3 (theor.) [18].

The interaction of the electron with the anapole moment is described by the Hamiltonian

$$\mathcal{H}_a = |e|\,\vec{\alpha} \cdot \vec{a}\delta\,(\vec{r}) \tag{2.14}$$

$$= |e|\,\vec{a} \cdot e^{\dagger}\gamma_0\gamma_{\vec{\mu}} e \delta\,(\vec{r}) \tag{2.15}$$

where α are the Dirac matrices $\alpha_\mu \equiv \gamma_0\gamma_\mu$. We see that this interaction

- increases with the nuclear mass since $|\vec{a}| \propto A^{2/3}$

- only interacts with the electron wavefunction when it overlaps with the nucleus (due to the $\delta(r)$ component)
- has exactly the same functional form as the NSD-PV Hamiltonian due to Z^0 exchange (equation 2.12) since $\vec{a} \propto \vec{I}$ (represented using the Pauli matrices $\vec{\sigma}_p$)

The anapole moment turns out to be the largest source of nuclear spin-dependent parity violation in heavy atoms (with $A \gtrsim 20$).

2.3 Previous Measurements of the C_2 Constants

The electron-proton and electron-deutron deep inelastic electron scattering measurements at SLAC[6, 7] were the first measurements of the C_2 constants for the up and down quarks (and by calculation from these, for the proton and the neutron). These measurements were made by colliding a spin-polarized electron beam with energies in the range of 16 to 22 GeV on an unpolarized hydrogen or deuterium target, and observing the scattering angle of electrons. The experiment measured an asymmetry in the distribution of outgoing electrons, depending on the helicity[4] of the incoming electron beam.

The SAMPLE experiment [8] was carried out at the MIT Bates Laboratory. This experiment observed the angular distribution of elastic electron scattering from a liquid hydrogen or deuterium target at energies of 125 and 200 MeV, with the primary goal of studying the strange quark contribution to the proton. However, the experiment was also sensitive to C_{2u} and C_{2d}, the C_2 constants related to the up and down quarks, through the measurement of the nucleon axial form factors. The experiment is sensitive to linear combinations of the form $C_{2u} - C_{2d}$, based on measurements made on the deuterium target (with

[4]Helicity $h = \vec{S} \cdot \frac{\vec{p}}{|p|}$ is the projection of the spin $\vec{S}$ in the direction of momentum $\vec{p}$.

equal numbers of up and down quarks).

The experiment described in this dissertation is expected to be sensitive to the C_2 constants for the proton and neutron (C_{2p} and C_{2n} respectively) for measurements on nuclei with an odd number of protons or neutrons (respectively). Based on calculations by Marciano and Sirlin [20], these can be related to the $C_{2u,d}$ constants via the relations

$$C_{2p} = 0.935C_{2u} + 0.360C_{2d} \tag{2.16}$$

(based on eq. 11a in [20]), and

$$C_{2n} = -0.44C_{2u} + 0.765C_{2d} \tag{2.17}$$

Marciano points out that these linear combinations are significantly modified from the naive expectations of a simple quark model due to the strong interaction.

2.4 Measurement of the Nuclear Anapole Moment

The only non-null measurement of a nuclear anapole moment was made by Wieman et al. in ^{133}Cs [15, 16]. This experiment measured the strength of an electric dipole transition between the $6S$ and $7S$ states of cesium. In the absence of parity violating electroweak effects or an external electric field, this transition is forbidden by parity selection rules. However, electroweak interactions mix these states with nearby P states so that the relevant atomic states are of the form

$$|\Psi\rangle = |S\rangle + \imath A_{pv} |P\rangle$$

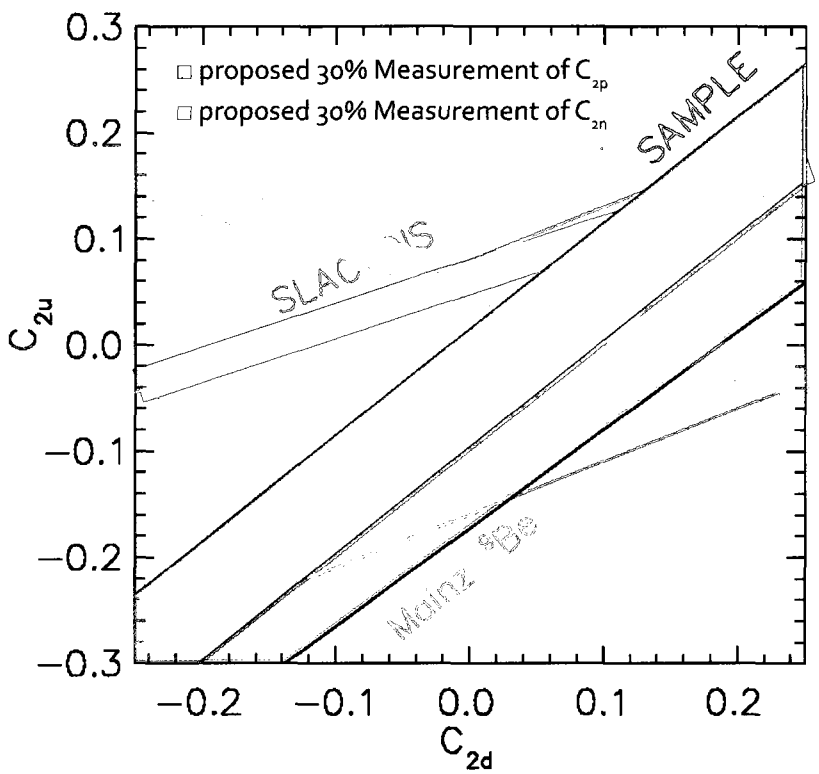

Figure 2.1: Parameter space of C_{2u} and C_{2d}. Regions allowed by the SLAC, SAMPLE, and Mainz experiment results are shown by the light green, grey, and magenta shaded region. Additional regions (with arbitrary positions) showing the expected range of our experimental sensitivity are superimposed. The underlying plot is from ref. [8], p. 41.

where $A_{pv} \sim 10^{-11}$; the coefficient fixing the relative phase between the two states is imaginary because the interaction is odd under parity inversion but invariant under time-reversal. The states are additionally mixed with an external DC electric field, which makes a real mixture of S and P states

$$|\Psi_E\rangle = |S\rangle + (A_E + \imath A_{pv})\,|P\rangle$$

where the Stark mixing $A_E \sim 10^5 A_{pv}$. In a crossed magnetic and electric field, the phase difference between the two interactions creates an interference effect which makes the transition rate for a forbidden transition depend on the polarization of the incident light. A circularly polarized dye laser tuned to the $6S - 7S$ line drives a transition between these two levels, and the resulting population transfer is measured. The beam from this laser is set up perpendicular to the direction of the atomic beam, as two counterpropagating laser beams. The transition rate depends on the interference between the Stark-induced, magnetic dipole (M1), and the weak interaction-induced transition amplitudes:

$$\begin{aligned} R &= |A_E + A_{M1} + A_{pv}|^2 \\ &\approx \left[\beta^2 E_x^2 \varepsilon_z^2 \mp 2\beta p E_x \varepsilon_x \varepsilon_z \mathrm{Im}\,(E1_{pv}) \pm 2\beta E_x M \left(\left|\varepsilon_z^{k+}\right|^2 - \left|\varepsilon_z^{k-}\right|^2\right)\right] \\ &\quad \times \left(C_{Fm}^{F'm'}\right)^2 \delta_{m,m'\pm 1} \end{aligned} \tag{2.18}$$

where

- β is the polarizability
- $\vec{E} = E_x \hat{x}$ is the applied DC electric field
- $\vec{\varepsilon} = \varepsilon_z \hat{z} + ip\varepsilon_x \hat{x}$ is the laser's electric field, where p is the handedness of the laser polarization ($p = \pm 1$)
- $E1_{pv}$ is the strength of the pv-induced transition amplitude

- $M = \langle 7S\,|\mu_z/c|\,6S\rangle$ is the highly forbidden magnetic dipole (M1) matrix element
- ε_z^{k+} and ε_z^{k-} are the amplitudes of the forward- $(+\hat{y})$ and backward- $(-\hat{y})$ propagating laser beams; e.g. the counterpropagating beams may have differing intensities
- $C_{Fm}^{F'm'}$ is the Clebsch-Gordan coefficient specific to the initial and final states involved in the transition.

The second term is sensitive to the pv-induced transition amplitude $E1_{pv}$, and is dependent on p. The third term (the interference between A_E and A_{M1}) is small if the laser field is a standing wave, but introduces a systematic effect. Neglecting this last term, the contribution to the transition rate from parity violation can be extracted by reversing E_x or p and subtracting the two results, as $E1_{pv}$ only appears in the term which is linear in E_x. The fraction of the signal (asymmetry) which changes under sign reversal is

$$\begin{aligned}\mathcal{A}_{pv} &\equiv \frac{R[+E_x] - R[-E_x]}{R[+E_x] + R[-E_x]} \\ &= \frac{2}{\beta E_x}\frac{\varepsilon_x}{\varepsilon_z}\mathrm{Im}\,(E1_{pv})\end{aligned}$$

This measurement can be made using two different hyperfine lines in the $6S - 7S$ transition, which exhibit different dependence on the underlying physics. Specifically, one particular linear combination of $E1_{pv}$ from the two hyperfine lines has no nuclear spin-dependent contribution. This combination is sensitive to the weak charge Q_w, and can be related to the C_1 constants discussed at the beginning of this chapter. The orthogonal linear combination of signals from the two lines is sensitive only to the NSD-PV effect. Because ^{133}Cs is fairly heavy, here the majority of the observed NSD-PV signal arises from the nuclear anapole moment.

Another experiment to measure parity violation in an atomic system was undertaken in dysprosium by Budker, DeMille, et al. [14]. By chance, there is a nearly degenerate pair of levels of opposite parity (the $4f^{10}5d6s$ and $4f^{9}5d^{2}6s$ states, labeled A and B respectively), which are separated by as little as 3.1 MHz for one of the isotopes. Electroweak interactions mix the levels; this mixing is enhanced by bringing the levels even closer to degeneracy in an external magnetic field. Initially state A was populated, then an AC electric field was applied to induce population transfer to level B; the resulting population of level B, P_B, could be written

$$P_B \propto \left(\frac{dE_0}{\omega}\right)^2 \sin^2(\omega t) - \frac{2dE_0H_w}{\omega}\left(\frac{\Delta}{\Delta^2+\Gamma_A^2/4}\right)\sin(\omega t) \qquad (2.19)$$

where d is the dipole matrix element of the transition, E_0 is the amplitude of the applied electric field, ω is the frequency of the applied field, Δ is the energy splitting of the two levels, Γ_A is the natural linewidth of state A, and H_w is the matrix element of the parity-violating electroweak interaction between these two levels. This experiment gave a null result for the measurement of H_w.

This NSD-PV experiment is fundamentally similar to the dysprosium experiment, but relies on searching for parity violation in molecules instead of atoms. It is unusual to find nearly-degenerate levels of opposite parity in heavy atoms, due to the strength of the electrostatic interaction that separates S and P energy levels. However, as noted before, the rotational level structure of diatomic molecules makes it easy to find closely spaced levels of opposite parity in these systems.

Chapter 3

Principle of the Experiment

The goal of this chapter is to explain the technique by which it is expected to observe parity violation in diatomic molecules. The discussion will begin with what makes for a suitable level structure for the observation and enhancement of parity violation signals in atoms and molecules. It will then describe an effective Hamiltonian for parity-violating interactions in diatomic molecules, and outline an experimental scheme to measure the strength of these interactions. Calculations of the expected signal given realistic experimental parameters are presented with the effects of these parameters on the determination of the interaction strength from experimental data. Finally, there is a general overview of our experimental implementation of this scheme.

3.1 Introduction

Suppose the state of a quantum mechanical system is perturbed slightly from its eigenstate by the addition of a perturbation V

$$H = H_0 + V$$

where the strength of V is small compared to the unperturbed Hamiltonian H_0. First order nondegenerate perturbation theory gives the expression for the perturbed states of the system as

$$|i'\rangle = |i\rangle + \sum_{j \neq i} \frac{V_{ij}}{E_i - E_j} |j\rangle \tag{3.1}$$

where E_i is the energy of state $|i\rangle$ in the unperturbed basis, V_{ij} is the matrix element $\langle i | V | j \rangle$, and $|i'\rangle$ is the new state once the effect of the perturbation is taken into account. Consider a parity-violating Hamiltonian V_{pv} which has nonzero matrix elements mixing two states $|i\rangle$ and $|j\rangle$ of opposite parity. The above result from perturbation theory shows that the amplitude of state $|j\rangle$ mixed into the perturbed state $|i'\rangle$ is

$$\langle j | i' \rangle = \frac{V_{ij}}{E_i - E_j}$$

which is enhanced when the energy difference $E_j - E_i$ between the two levels is close to zero. We will have the best chance to observe parity violation in a system where we can bring these two levels close to degeneracy. The Zeeman effect [1] is a convenient mechanism for shifting energy levels in atomic and molecular systems with an unpaired electron spin; the Zeeman Hamiltonian describes the interaction of the electron's spin and orbital angular momentum with an external magnetic field. The spacing between the unperturbed levels of the atom or molecule determines the strength of the magnetic field that needed to bring the two levels to degeneracy.

For atoms, the parity of a given energy level depends on the orbital angular momentum of the electrons. For a multi-electron atom, this generally depends on the angular momentum $\vec{\ell}$ of each electron, but for atoms with a single valence electron, the total angular momentum $\vec{L} = \vec{\ell}$ just depends on the valence

electron and the parity is

$$p = (-1)^L$$

In simple atoms, splitting between levels of opposite parity (due to electrostatic interactions) are generally on the scale of electron volts[1]. This makes it impractical to use the Zeeman effect to bring the two levels to degeneracy, since the magnetic field required would be impossible to achieve in any meaningful experimental design. The only known atom with two levels of opposite parity sufficiently close that they can be brought to degeneracy by Zeeman tuning is dysprosium, in which the $4f^{10}5d6s$ and $4f^{9}5d^{2}6s$ configurations happen to be about 0.007 to 1.4 GHz apart in the absence of an external field [14]. Unforunately, this experiment produced a null result, apparently because these electron configurations are essentially unmixed by the electroweak interaction.

For diatomic molecules in a $^2\Sigma^+$ state, the parity of a given energy level depends on the rotational quantum number N:

$$p = (-1)^N$$

so that alternate rotational levels have opposite parity. For Hund's case (b) molecules in a state with N units of angular rotational momentum, the rotational energy is [11]

$$E(N) \approx B\,N\,(N+1)$$

where the rotational constant $B \equiv 1/\left(2\mu r_e^2\right)$ depends on the reduced mass μ and the mean internuclear spacing r_0. The energy level spacing between two

[1]Rydberg atoms have been suggested as having closely spaced levels of opposite parity. However, these highly excited states have a diffuse electron wavefunction which will have a low overlap with the nucleus. This makes Rydberg atoms unsuitable for this type of experiment.

consecutive rotational levels N and $N' = N+1$, which are of opposite parity, is

$$\begin{aligned}\Delta_N &= E[N+1] - E[N] \\ &= B\left((N+2)(N+1) - (N+1)N\right) \\ &= 2B\,(N+1)\end{aligned}$$

This spacing is smallest for the lowest rotational levels, $N = 0$ and $N = 1$. Most molecules other than hydrides (which have unusually small reduced masses μ, and hence large rotational constants B) have modest rotational constants (e.g. the value for BaF is about $B \approx 0.22$ cm$^{-1} \approx 6600$ MHz). An interaction that does not mix states of opposite parity is required in order to bring these molecular states close to crossing. (The Stark interaction, for example, is unsuitable as it mixes states of opposite parity; the levels will repel, rather than be brought to crossing.) The Zeeman effect shifts the $m_S = +\frac{1}{2}$ sublevels up by about 1.4 MHz/gauss (for a molecule with $\vec{S} = \frac{1}{2}$ and $\Lambda = 0$), and one of the $N = 1$ sublevels down by the same amount. So, the magnetic field B_0 necessary to bring these sublevels close to degeneracy is roughly

$$B_0 \approx \frac{\Delta_0}{2\mu_B} = \frac{B}{\mu_B}$$

which is $B_0 \approx 4700$ gauss for BaF. Many other relevant fluorides (HgF, YbF), oxides, and nitrides require similar magnetic fields. This is the fundamental reason for searching for parity violation in diatomic molecules; there is a wide range of nuclei available which are suitable for study, and for which Zeeman tuning of the opposite-parity levels to near degeneracy should be possible.

3.2 Parity-Violating Hamiltonian

As mentioned in chapters 1 and 2, the nuclear spin-dependent part of the parity violating Hamiltonian can be written in the nonrelativistic limit as (sec. 1.3 in [2], [17]):

$$H_{PV} \propto (\kappa_Z + \kappa_a + \kappa_Q) \left(\vec{I} \cdot \vec{\sigma}\right) (\vec{\sigma} \cdot \vec{p}) \, \delta^3 (\vec{r}) \tag{3.2}$$

where κ_Z corresponds to the contribution from Z-boson exchange between the electron and the nucleon, κ_a is from the anapole moment, and κ_Q comes from higher order contributions. For this spin-dependent part of the electroweak Hamiltonian (in a simple shell-model description of a nucleus as a single valence nucleon orbiting a spin-paired core), only the interaction between the electron and the unpaired valence nucleon matters [2]. The coefficient κ_Z is, for a proton (κ_{ZP}) or a neutron (κ_{ZN})

$$\kappa_{ZP} = -\kappa_{ZN} = -\left(1 - 4\sin^2\theta_W\right) \frac{g_A}{2} \approx -0.05 \tag{3.3}$$

and is independent of the atomic mass A. The anapole contribution κ_a, however, is dependent on the atomic mass A since the strength of the moment as well as the interaction between the electron and the nucleus increases with the size of the nucleus. This contribution scales like [2]:

$$\kappa_a \approx 0.9 g_{\text{eff}} \frac{\alpha \mu_N}{m \tilde{r}_0} A^{2/3} \approx 0.08 g_{\text{eff}} \left(\frac{A}{100}\right)^{2/3} \tag{3.4}$$

where the effective coupling $g_{\text{eff},P} \approx 4$ for the proton and $g_{\text{eff},N} \lessapprox 1$ for the neutron, $\tilde{r}_0 = 1.2 \times 10^{-13}$ cm is the scale size for the nuclear liquid drop model, and μ_N is the nuclear magneton. The remaining contribution from higher-order terms, κ_Q, is also expected to scale like $A^{2/3}$. However, it is smaller in magnitude than κ_a by at least a factor of four. It also can be calculated with

good accuracy, since it depends on well-known physics. For the purposes of evaluating experimental parameters, this term can be neglected.

The discussion above considered the scaling of these parity-violating effects due to nuclear mass. There is also a scaling with the total charge Z as the electronic wavefunction is bound more strongly to the nucleus; Khriplovich [2] gives the nonrelativistic radial electron wavefunctions R_s and R_p near the nucleus for s and p states:

$$\begin{aligned} \lim_{r\to 0} R_s &= 2\left(\frac{Z}{a_0^2\nu_s^3}\right)^{1/2} \\ \lim_{r\to 0} \frac{R_p}{r} &= \frac{2}{3}\left(\frac{Z}{a_0^3\nu_p^3}\right)^{1/2}\frac{Z}{a_0} \end{aligned}$$

where a_0 is the Bohr radius and $\nu_{s,p} = n_r + \ell + 1 - \sigma_1$ is an effective quantum number for the s- or p-state (n_r and ℓ are radial and orbital quantum numbers, and σ_1 is a quantum defect which is weakly dependent on n_r). The net result is that the observed effect (which depends on the electron wavefunction overlap with the nucleus) scales like Z^2 for Z-boson exchange and $Z^2A^{2/3} \sim Z^{8/3}$ for the anapole moment. Given these scaling properties with the atomic mass, the anapole moment dominates over the contribution from Z-bosons for $A \gtrapprox 10$ (for protons) or $A \gtrapprox 100$ (for neutrons). Previous atomic experiments (such as the Wieman Cs measurement) have up to now really focused on the weak charge rather than the anapole moment. This effect scales even faster with Z (like Z^3), so these experiments looked at large Z. It happens that in this regime

1. these experiments could also look for the nuclear spin-dependent part
2. the anapole effect dominates

There have been atomic experiments (e.g. in dysprosium [14]) which have focused on measurements of the anapole moment and C_2 constants. These experiments, however, have yielded null results as the parity-violating interaction was

very small between the electronic configurations involved in the levels brought to crossing.

3.3 Available molecules

The experimental concept requires the ablity to choose both light and heavy nuclei to study, to separate the effects of the nuclear anapole moment from those of the weak interaction between the electron and nucleus. Some of the restrictions in choosing appropriate molecules are:

- *small rotational constant* - As mentioned in the previous section, the requirement to have a reasonable magnetic field limits us to non-hydride molecules.

- *single unpaired electron spin* - The interaction between the electron and nuclear spin vanishes to first order unless there is an unpaired electron spin.

- *nonzero nuclear spin* - An observation of nuclear spin-dependent parity violation requires a nucleus with nonzero nuclear spin, e.g. even-odd nuclei, in which the total proton or total neutron spin is zero. Then, in the shell model approximation, the spin-dependent interaction can be considered to belong to the single unpaired proton or neutron. Odd-odd nuclei could also be studied, but the effects here would be harder to interpret.

- *natural abundance* - Choosing abundant isotopes is necessary to produce an intense molecular beam without resorting to prohibitively expensive isotopically enriched sources.

- *states with good overlap at the nucleus* - The parity-violating interaction is short-range; the electron only feels the interaction at the nucleus.

Molecules in which the valence electron acts like an s-state valence electron are good, since in these states the electron spends a significant amount of time at the nucleus. Use of $^2\Sigma$ ground state molecules is a necessary, but not sufficient condition to ensure a sizeable contribution from atomic s-orbitals with large amplitude at the relevant nucleus. For example, $^{138}Ba^{19}F$ was considered, which has $I = \frac{1}{2}$ for the fluorine nucleus. However, the wavefunction of the valence electron is minimal at the fluorine nucleus, and any parity-violating effect would be extremely small.

- *laser-accessible transitions* - It is desirable to choose molecules with laser-accessible electronic transitions for state preparation and detection. Transitions at diode laser wavelengths are preferable.

Generally, many of the suitable choices for molecules happen to have $^2\Sigma$, Hund's case (b) electronic ground states, in which N is a good quantum number and there is a significant contribution from atomic s-orbitals. A list of some of the possible molecules was prepared by DeMille [23] and is shown in table 3.1. The table includes nuclei with unpaired protons as well as nuclei with unpaired neutrons. The ratio of the expected contribution from the anapole moment to the contribution from Z exchange is given as κ_a/κ_Z. This depends on the atomic mass and on whether the relevant nuclei are odd-neutron or odd-proton, as given by equations 3.3 and 3.4.

3.4 Parity-Violation in Diatomic Molecules

3.4.1 Effective Hamiltonian for Parity Violation in Diatomic Molecules

From the point of view of atomic physics, the effect of parity violation in molecules can be understood without having to know the details of the un-

Molecule	Z	Unpaired	$100\kappa_a$	$100\kappa_2$	κ_a/κ_2	W (Hz)	T (to 10%)
^{87}SrF	38	neutron	-3.6	-5.0	0.72	2.2	1.3×10^5 sec
^{91}ZrN	40	neutron	-3.5	-5.0	0.7	3.4	5.5×10^4 sec
^{137}BaF	56	neutron	+4.2	+3.0	1.4	-5.2	2.4×10^4 sec
^{171}YbF	70	neutron	+4.1	+1.7	2.4	-22	1.3×10^3 sec
^{27}AlS	13	proton	-11.2	+5.0	-2.2	0.3	7.1×10^6 sec
^{69}GaO	31	proton	-19.6	+5.0	-3.9	3.8	4.4×10^4 sec
Mg^{81}Br	35	proton	-21.8	+5.0	-4.4	1.3	3.8×10^5 sec
^{139}LaO	57	proton	+34.7	-3.9	-8.9	-29	7.6×10^2 sec

Table 3.1: List of some possible molecules for parity violation measurements. Whether the relevant isotope has an unpaired proton or neutron is listed, as well as the expected ratio of the anapole moment to the Z^0-boson contribution to parity violation (κ_a/κ_Z), the expected strength of the parity-violating Hamiltonian W (effective constant as defined in eq. 3.8), and the integration time required to achieve a measurement of W to 10% accuracy, where $T \sim (80 \text{ Hz}/\delta W)^2$. This assumes the beam flux is $N \approx 50$ molecules/sec detected in the proper hyperfine state and the time spent in the interaction region is 160 μs (a velocity of $\bar{v} = 500$ m/s and length of 5 cm). (from [23])

derlying physics. Khriplovich [2], for example, describes the mixing of states that results from a parity violating Hamiltonian. He considers the mixing of two hydrogen-like states ψ_0 (an $s_{1/2}$ state) and ψ_1 (a $p_{1/2}$ state) of opposite parity:

$$\psi_0 = \frac{1}{\sqrt{4\pi}} R_0(r)\,\chi \tag{3.5}$$

$$\psi_1 = \frac{1}{\sqrt{4\pi}} R_1(r)\,(-\vec{\sigma}\vec{n})\,\chi \tag{3.6}$$

where $R_0(r)$ is the radial function of the s state, $R_1(r)$ is the radial function of the p state, $\vec{\sigma}$ is the vector of Pauli matrices, $\vec{n} \equiv \vec{r}/r$ is the unit radius vector, and χ is the two-component spinor representing the electron spin. These states correspond to spherical wavefunctions. Khriplovich notes that under time inversion, the Pauli matrices go from $\vec{\sigma}$ to $-\vec{\sigma}$, and the initial and final states in the wavefunction are interchanged (corresponding to taking the Hermitian conjugate of the state). So, a mixed parity admixture of states ψ_0 and ψ_1 which

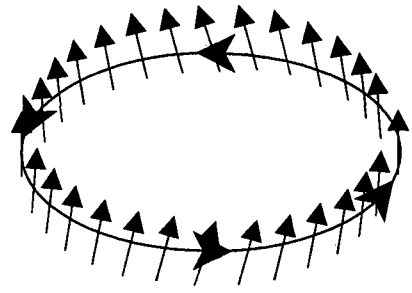

Figure 3.1: A "spin helix", resulting from the complex admixture of two states, $\psi = \frac{1}{\sqrt{4\pi}}\left(R_0\left(r\right) - \imath\eta R_1\left(r\right)\vec{\sigma}\cdot\vec{n}\right)\chi$. Khriplovich [2] points out that if this is written in the form $\psi = \frac{1}{\sqrt{4\pi}}R_0\left(r\right)\left(1 - \imath\theta\vec{\sigma}\cdot\vec{n}/2\right)\chi$, with $\theta \equiv 2\eta R_1\left(r\right)/R_0\left(r\right)$, then this mixing is analogous to a rotation of the spinor around the axis $\vec{n} \equiv \vec{r}/\left|r\right|$. This is the basis of our graphical interpretation of a spin helix.

is even under time reversal (as is relevant to our experiment) will be of the form

$$\psi = \frac{1}{\sqrt{4\pi}}\left(R_0\left(r\right) - \imath\eta R_1\left(r\right)\vec{\sigma}\cdot\vec{n}\right)\chi \tag{3.7}$$

Khriplovich notes that the effect of the former (complex admixture) is to make a "spin helix", in which the electron spin is tilted in the direction of orbital motion (figure 3.1). The imaginary coefficient in the mixture is important in that other parity-odd interactions, such as external electric fields, will result in real mixtures of states. This allows for an experiment in which interference between the weak and electromagnetic interactions is observed.

An effective Hamiltonian can be constructed with the desired properties using the quantum numbers available in the molecule. Table 3.2 lists operators that are relevant, with the given symmetries under charge, parity, and time inversion. From these, we want to find the simplest Hamiltonian which violates parity but preserves time-reversal invariance.

The direction vector along the internuclear axis $\hat{n}$ must be part of the ef-

Operator		C	P	T
Spins				
$\vec{S}$	electron spin	+	+	-
$\vec{I}$	nuclear spin	+	+	-
Angular momenta				
$\vec{N}$	molecular rotation	+	+	-
$\vec{J}_e$	electronic angular momentum	+	+	-
$\vec{J}$	electronic & molecular angular momentum	+	+	-
$\vec{F}$	total angular momentum	+	+	-
Molecular orientation				
$\hat{n}$	internuclear axis	-	-	+

Table 3.2: Operators relevant to the state of the molecule, with their transformation properties under charge-, parity-, and time-inversion.

fective Hamiltonian, since it is the only operator available which is odd under parity inversion. The Hamiltonian must include the nuclear spin $\vec{I}$ since we are interested in looking for nuclear spin-dependent parity violation. This leaves an expression that is odd under time inversion unless another angular momentum is involved. It seems natural to include the electron spin $\vec{S}$ to restore time invariance, since the fundamental nuclear spin-dependent parity violating Hamiltonian (eq. 3.2) depends explicitly on $\vec{S}\cdot\vec{I}$. We can combine three vectors into a scalar product by dotting one vector into the cross product of the other two, producing an expression of the form

$$H_{\text{eff}} \propto \left(\vec{a}\times\vec{b}\right)\cdot\vec{c}$$

It is easy to see by calculation that for three vectors $\vec{a}$,$\vec{b}$, $\vec{c}$, that the order of the cross product and dot product doesn't matter:

$$\left(\vec{a}\times\vec{b}\right)\cdot\vec{c} = \left(\vec{b}\times\vec{c}\right)\cdot\vec{a} = \left(\vec{c}\times\vec{a}\right)\cdot\vec{b}$$

and so the simplest form for an effective Hamiltonian which is parity-odd and depends on the nuclear spin $\vec{I}$ is

$$H_{pnc} = W\left(\vec{S} \times \hat{n}\right) \cdot \vec{I} \tag{3.8}$$

Here the exact relationship between the parameter W and the fundamental physics behind parity violation must be determined by a full derivation of the nonrelativistic limit of the relativistic Hamiltonian. This is beyond the scope of this thesis. However, calculations of the relevant quantities have been performed by our collaborator M. Kozlov. The results are reflected in the quantities W reported in table 3.1.

3.4.2 Evaluating $(\vec{S} \times \hat{n}) \cdot \vec{I}$ in Diatomic Molecules

The simplest parity-odd, time reversal-even nuclear spin-dependent Hamiltonian is of the form $(\vec{S} \times \hat{n}) \cdot \vec{I}$. The electronic and nuclear spins $\vec{S}$ and $\vec{I}$ are axial vectors; they do not change sign under parity but do under time reversal. The internuclear vector $\hat{n}$ is a polar vector, and does change sign under parity. We can choose a basis of the form $|N\, m_N\rangle\, |S\, m_S\rangle\, |I\, m_I\rangle$ (which we can convert to or from our usual $|N\, J\, I\, F\, m_F\rangle$ basis) in which it is easy to evaluate the relevant operators. The projections m_N (of rotational angular momentum), m_S, and m_I are taken in the lab frame, and will be good quantum numbers in the presence of a sufficiently strong external field.

The vector operators are expanded in Cartesian coordinates:

$$\left(\vec{S} \times \hat{n}\right) \cdot \vec{I} = \left(S_y n_z - S_z n_y\right) I_x + \left(S_z n_x - S_x n_z\right) I_y + \left(S_x n_y - S_y n_x\right) I_z \tag{3.9}$$

And then, using the relations $S_x = \frac{1}{2}\left(S_+ + S_-\right)$ and $S_y = -\frac{i}{2}\left(S_+ - S_-\right)$ (e.g. Sakurai 189) convert the x and y components to raising and lowering operators:

$$\begin{aligned}\left(\vec{S}\times\hat{n}\right)\cdot\vec{I} =& \frac{\imath}{4}\left(S_z\left(n_+ - n_-\right) - \left(S_+ - S_-\right)n_z\right)\left(I_+ + I_-\right) \\ &+ \frac{\imath}{4}\left(\left(S_+ + S_-\right)n_z - S_z\left(n_+ + n_-\right)\right)\left(I_+ - I_-\right) \\ &+ \frac{\imath}{4}\left(\left(S_+ - S_-\right)\left(n_+ + n_-\right) - \left(S_+ + S_-\right)\left(n_+ - n_-\right)\right)I_z\end{aligned} \tag{3.10}$$

which, after expanding, simplifies to:

$$\left(\vec{S}\times\hat{n}\right)\cdot\vec{I} = \frac{\imath}{2}\left(S_+ n_- I_z - S_- n_+ I_z + S_- n_z I_+ - S_+ n_z I_- - S_z n_- I_+ + S_z n_+ I_-\right) \tag{3.11}$$

The spin components can be evaluated using the usual relations (e.g. Sakurai p. 192):

$$\begin{aligned}S_\pm\left|S\,m_S\right\rangle &= \sqrt{(S\mp m_S)(S\pm m_S+1)}\left|S\,m_S\pm 1\right\rangle \\ S_z\left|S\,m_S\right\rangle &= m_S\left|S\,m_S\right\rangle \\ I_\pm\left|I\,m_I\right\rangle &= \sqrt{(I\mp m_I)(I\pm m_I+1)}\left|I\,m_I\pm 1\right\rangle \\ I_z\left|I\,m_I\right\rangle &= m_I\left|I\,m_I\right\rangle\end{aligned} \tag{3.12}$$

The $|N\,m_N\rangle$ part of the basis describes the rotational angular momentum of the molecule, N, and its projection in the lab frame. The rotational wavefunction is:

$$\begin{aligned}\left|N\,m_N\right\rangle &= Y_N^{m_N}(\theta,\phi) \\ \left\langle N\,m_N\right| &= \overline{Y_N^{m_N}(\theta,\phi)} = (-1)^{m_N}Y_N^{-m_N}(\theta,\phi)\end{aligned} \tag{3.13}$$

and the $\hat{n}$ operator describing the intermolecular axis is:

$$\begin{aligned}
\hat{n} &= \sin\theta\cos\phi\,\hat{x} + \sin\theta\sin\phi\,\hat{y} + \cos\theta\,\hat{z} \\
n_z &= \cos\theta = 2\sqrt{\frac{\pi}{3}}Y_1^0(\theta,\phi) \\
n_+ &= n_x + \imath n_y = \sin\theta e^{\imath\phi} = -2\sqrt{\frac{2\pi}{3}}Y_1^1(\theta,\phi) \\
n_- &= n_x - \imath n_y = \sin\theta e^{-\imath\phi} = 2\sqrt{\frac{2\pi}{3}}Y_1^{-1}(\theta,\phi)
\end{aligned} \tag{3.14}$$

So, the matrix elements for $\langle N'\, m'_N|n_{\pm,z}|N\, m_N\rangle$ as an integral over the product of three spherical harmonics are:

$$\langle N'\, m'|n_{\pm,z}|N\, m\rangle = a\int_0^{2\pi}\int_0^{\pi}\overline{Y_{N'}^{m'}}(\theta,\phi)\,Y_1^b(\theta,\phi)\,Y_N^m(\theta,\phi)\sin\theta d\theta d\phi \tag{3.15}$$

where

$$a = \begin{cases} -2\sqrt{\frac{2\pi}{3}} & \text{for } n_+ \\ 2\sqrt{\frac{\pi}{3}} & \text{for } n_z \\ 2\sqrt{\frac{2\pi}{3}} & \text{for } n_- \end{cases}$$

and

$$b = \begin{cases} 1 & \text{for } n_+ \\ 0 & \text{for } n_z \\ -1 & \text{for } n_- \end{cases}$$

This integral has the solution (Arfken 700):

$$\int_0^{2\pi}\int_0^{\pi} Y_{l_1}^{m_1} Y_{l_2}^{m_2} Y_{l_3}^{m_3} \sin\theta d\theta d\phi = \sqrt{\frac{(2l_1+1)(2l_2+1)(2l_3+1)}{4\pi}} \begin{pmatrix} l_1 & l_2 & l_3 \\ 0 & 0 & 0 \end{pmatrix} \begin{pmatrix} l_1 & l_2 & l_3 \\ m_1 & m_2 & m_3 \end{pmatrix} \tag{3.16}$$

With $l_2 = 1$, $m_2 = \pm 1, 0$, the only nonzero integrals are

$$\int_0^{2\pi}\int_0^{\pi} \overline{Y_{N+1}^{m_N+1}} Y_1^1 Y_N^{m_N} \sin\theta d\theta d\phi = \sqrt{\frac{3}{8\pi}} \sqrt{\frac{(N+m_N+1)(N+m_N+2)}{(2N+1)(2N+3)}}$$

$$\int_0^{2\pi}\int_0^{\pi} \overline{Y_{N+1}^{m_N}} Y_1^0 Y_N^{m_N} \sin\theta d\theta d\phi = \sqrt{\frac{3}{4\pi}} \sqrt{\frac{(N+m_N+1)(N-m_N+1)}{(2N+1)(2N+3)}}$$

$$\int_0^{2\pi}\int_0^{\pi} \overline{Y_{N+1}^{m_N-1}} Y_1^{-1} Y_N^{m_N} \sin\theta d\theta d\phi = \sqrt{\frac{3}{8\pi}} \sqrt{\frac{(N-m_N+2)(N-m_N+1)}{(2N+1)(2N+3)}}$$

$$\int_0^{2\pi}\int_0^{\pi} \overline{Y_{N-1}^{m_N+1}} Y_1^1 Y_N^{m_N} \sin\theta d\theta d\phi = -\sqrt{\frac{3}{8\pi}} \sqrt{\frac{(N-m_N)(N-m_N-1)}{(2N-1)(2N+1)}}$$

$$\int_0^{2\pi}\int_0^{\pi} \overline{Y_{N-1}^{-m_N}} Y_1^0 Y_N^{m_N} \sin\theta d\theta d\phi = \sqrt{\frac{3}{4\pi}} \sqrt{\frac{(N+m_N)(N-m_N)}{(2N-1)(2N+1)}}$$

$$\int_0^{2\pi}\int_0^{\pi} \overline{Y_{N-1}^{m_N-1}} Y_1^{-1} Y_N^{m_N} \sin\theta d\theta d\phi = -\sqrt{\frac{3}{8\pi}} \sqrt{\frac{(N+m_N-1)(N+m_N)}{(2N-1)(2N+1)}} \tag{3.17}$$

This experiment depends on the cases where the first and second rotational levels are mixed, i.e. N=0 and N'=1. Then the relevant matric elements are

	n_-	n_z	n_+
$\langle N'=1, m'_N=-1\|n_{...}\|N=0, m_N=0\rangle$	$\sqrt{\frac{2}{3}}$	0	0
$\langle N'=1, m'_N=0\|n_{...}\|N=0, m_N=0\rangle$	0	$\frac{1}{\sqrt{3}}$	0
$\langle N'=1, m'_N=1\|n_{...}\|N=0, m_N=0\rangle$	0	0	$-\sqrt{\frac{2}{3}}$

All of these pieces are put together in the Mathematica code on page 367. As an example, the nonzero matrix elements for a system with electronic and nuclear spin 1/2 are below:

$\langle 1\,-1\,-1/2\,1/2\|H_{pnc}\|0\,0\,-1/2\,-1/2\rangle = -\frac{iW}{2\sqrt{6}}$	$\langle 1\,0\,1/2\,-1/2\|H_{pnc}\|0\,0\,-1/2\,1/2\rangle = \frac{iW}{2\sqrt{3}}$
$\langle 1\,-1\,1/2\,-1/2\|H_{pnc}\|0\,0\,-1/2\,-1/2\rangle = \frac{iW}{2\sqrt{6}}$	$\langle 1\,1\,-1/2\,-1/2\|H_{pnc}\|0\,0\,-1/2\,1/2\rangle = -\frac{iW}{2\sqrt{6}}$
$\langle 1\,-1\,1/2\,1/2\|H_{pnc}\|0\,0\,-1/2\,1/2\rangle = -\frac{iW}{2\sqrt{6}}$	$\langle 1\,1\,-1/2\,-1/2\|H_{pnc}\|0\,0\,1/2\,-1/2\rangle = \frac{iW}{2\sqrt{6}}$
$\langle 1\,-1\,1/2\,1/2\|H_{pnc}\|0\,0\,1/2\,-1/2\rangle = \frac{iW}{2\sqrt{6}}$	$\langle 1\,1\,-1/2\,1/2\|H_{pnc}\|0\,0\,1/2\,1/2\rangle = -\frac{iW}{2\sqrt{6}}$
$\langle 1\,0\,-1/2\,1/2\|H_{pnc}\|0\,0\,1/2\,-1/2\rangle = -\frac{iW}{2\sqrt{3}}$	$\langle 1\,1\,1/2\,-1/2\|H_{pnc}\|0\,0\,1/2\,1/2\rangle = \frac{iW}{2\sqrt{6}}$

The net result of this is that the parity-violating Hamiltonian mixes particular molecular states in this spin-decoupled basis. These calculations will be used later, in chapter 4, to evaluate the strength of this mixing at particular level crossings.

3.5 Two-level Hamiltonian with Parity-Violating Term

3.5.1 Population Transfer and Expected Signal

Assume that two states of opposite parity have been brought close to crossing, so that the molecule can be considered to be a two-level system with the levels

separated by Δ and dipole matrix element d. An AC electric field of amplitude E and frequency ω is applied. The system evolves in time according to the Hamiltonian:

$$\mathcal{H} = \begin{pmatrix} 0 & dE\cos(\omega t) + \imath W \\ dE\cos(\omega t) - \imath W & \Delta \end{pmatrix} \tag{3.18}$$

where all of the underlying parity-violating effects are summarized by the parameter W, as described in eq. 3.8. The solution will be of the form

$$\Psi(t) = a(t) \mid 1\rangle + e^{-\frac{i\Delta t}{\hbar}} b(t) \mid 2\rangle \tag{3.19}$$

With this functional form, $\frac{db(t)}{dt} \rightarrow 0$ as $dE, W \rightarrow 0$ under the application of the time-dependent Schrödinger equation $\frac{d\Psi}{dt} = -\frac{i}{\hbar}\Psi$:

$$\begin{aligned} \dot{a}(t) &= -\frac{i}{\hbar} e^{-i\Delta t/\hbar}(dE\sin(\omega t) + iW) b(t) \\ \dot{b}(t) &= -\frac{i}{\hbar} e^{i\Delta t/\hbar}(dE\sin(\omega t) - iW) a(t) \end{aligned} \tag{3.20}$$

If $a(0) = 0$ and $b(t) \approx 1$ over the time that we are interested in (e.g. that we start by completely depopulating the $\mid 1\rangle$ state and that the perturbations are small enough that $a(t)$ remains small), then first-order perturbation theory gives:

$$\begin{aligned} a(t) &\approx -i\int_0^t (dE\cos(\omega t') + iW)\, e^{-i\Delta t'/\hbar} dt' \\ &\approx -ie^{-\frac{i\Delta t}{2\hbar}} \left(\frac{dE}{\omega^2\hbar^2 - \Delta^2} \left(e^{\frac{i\Delta t}{2\hbar}} \omega\hbar - e^{-\frac{i\Delta t}{2\hbar}} \omega\hbar\cos(\omega t) \right.\right. \\ &\quad \left.\left. -i\Delta e^{-\frac{i\Delta t}{2\hbar}} \sin(\omega t) \right) + \left(e^{\frac{i\Delta t}{2\hbar}} - e^{-\frac{i\Delta t}{2\hbar}} \right) \frac{W}{\Delta} \right) \end{aligned} \tag{3.21}$$

The half-angle identities are useful in cleaning this up a bit:

$$\begin{aligned}\sin(x) &= 2\sin\left(\frac{x}{2}\right)\\ \cos(x) &= 1-2\sin^2\left(\frac{x}{2}\right) = 2\cos^2\left(\frac{x}{2}\right)-1\end{aligned} \tag{3.22}$$

$$\begin{aligned}
a(t) &\approx -ie^{-\frac{i\Delta t}{2\hbar}}\left(\frac{dE}{\omega^2\hbar^2-\Delta^2}\left(e^{\frac{i\Delta t}{2\hbar}}\omega\hbar - e^{-\frac{i\Delta t}{2\hbar}}\omega\hbar\left(2\cos^2\left(\tfrac{\omega t}{2}\right)-1\right)\right.\right.\\
&\qquad \left.\left.-2i\Delta e^{-\frac{i\Delta t}{2\hbar}}\sin\left(\tfrac{\omega t}{2}\right)\cos\left(\tfrac{\omega t}{2}\right)\right)+2i\sin\left(\tfrac{\Delta t}{2\hbar}\right)\frac{W}{\Delta}\right)\\
&\approx -ie^{-\frac{i\Delta t}{2\hbar}}\left(\frac{dE}{\omega^2\hbar^2-\Delta^2}\left(\left(e^{\frac{i\Delta t}{2\hbar}}+e^{-\frac{i\Delta t}{2\hbar}}\right)\omega\hbar - 2e^{-\frac{i\Delta t}{2\hbar}}\omega\hbar\cos^2\left(\tfrac{\omega t}{2}\right)\right.\right.\\
&\qquad \left.\left.-2i\Delta e^{-\frac{i\Delta t}{2\hbar}}\sin\left(\tfrac{\omega t}{2}\right)\cos\left(\tfrac{\omega t}{2}\right)\right)+2i\sin\left(\tfrac{\Delta t}{2\hbar}\right)\frac{W}{\Delta}\right)\\
&\approx -2ie^{-\frac{i\Delta t}{2\hbar}}\left(\frac{dE}{\omega^2\hbar^2-\Delta^2}\left(\omega\hbar\cos\left(\tfrac{\Delta t}{2\hbar}\right)-\omega\hbar\cos^2\left(\tfrac{\omega t}{2}\right)\left(\cos\left(\tfrac{\Delta t}{2\hbar}\right)-i\sin\left(\tfrac{\Delta t}{2\hbar}\right)\right)\right.\right.\\
&\qquad \left.\left.-i\Delta e^{-\frac{i\Delta t}{2\hbar}}\sin\left(\tfrac{\omega t}{2}\right)\cos\left(\tfrac{\omega t}{2}\right)\right)+i\sin\left(\tfrac{\Delta t}{2\hbar}\right)\frac{W}{\Delta}\right)\\
&\approx -2ie^{-\frac{i\Delta t}{2\hbar}}\left(\frac{dE}{\omega^2\hbar^2-\Delta^2}\left(\omega\hbar\cos\left(\tfrac{\Delta t}{2\hbar}\right)\sin^2\left(\tfrac{\omega t}{2}\right)+i\omega\hbar\sin\left(\tfrac{\Delta t}{2\hbar}\right)\cos^2\left(\tfrac{\omega t}{2}\right)\right.\right.\\
&\qquad \left.\left.-i\Delta e^{-\frac{i\Delta t}{2\hbar}}\sin\left(\tfrac{\omega t}{2}\right)\cos\left(\tfrac{\omega t}{2}\right)\right)+i\sin\left(\tfrac{\Delta t}{2\hbar}\right)\frac{W}{\Delta}\right)
\end{aligned} \tag{3.23}$$

Experimental conditions allow us to change Δ and ω. It is convenient, both experimentally and theoretically, to work in a regime where $\Delta \ll \omega\hbar$, in which case $\omega^2\hbar^2 - \Delta^2 \approx \omega^2\hbar^2$. The interaction region used in this experiment is designed so that molecules feel only an integer number of oscillations of the electric field; so $\omega t \to 2\pi N$. This eliminates the $\frac{\Delta}{\omega^2\hbar^2}\sin\left(\frac{\omega t}{2}\right)\cos\left(\frac{\omega t}{2}\right)$ term:

$$a(t) \approx 2e^{-\frac{i\Delta t}{2\hbar}}\left(\sin\left(\tfrac{\Delta t}{2\hbar}\right)\left(\frac{dE}{\omega\hbar}+\frac{W}{\Delta}\right)\right) \tag{3.24}$$

The total time t_f spent in the interaction region depends on the length L of the interaction region and the molecule velocity v. The effective frequency $\omega_v \equiv \frac{2\pi N}{t_f} = 2\pi N\frac{v}{L}$ applied to the molecules is now a function of L and v. With

this, the final amplitude after the interaction region is

$$\begin{aligned} a_f &\equiv a(t_f) \\ &= 2e^{-\frac{i\Delta t}{2\hbar}} \sin\left(\frac{\Delta t_f}{2\hbar}\right)\left(\frac{dE}{\omega_v\hbar}+\frac{W}{\Delta}\right) \\ &= 2e^{-\frac{i\Delta t}{2\hbar}} \sin\left(\frac{\Delta L}{2\hbar v}\right)\left(\frac{dEL}{2\pi Nv\hbar}+\frac{W}{\Delta}\right) \end{aligned} \tag{3.25}$$

and the final population of the $\mid 1\rangle$ state, $p_{1f} = |a_f|^2$, is

$$\begin{aligned} p_{1f} &= 4\sin^2\left(\frac{\Delta L}{2\hbar v}\right)\left(\left(\frac{dEL}{2\pi Nv\hbar}\right)^2 + 2\frac{W}{\Delta}\frac{dEL}{2\pi Nv\hbar} + \left(\frac{W}{\Delta}\right)^2\right) \\ &\approx 4\sin^2\left(\frac{\Delta L}{2\hbar v}\right)\left(\left(\frac{dEL}{2\pi Nv\hbar}\right)^2 + 2\frac{W}{\Delta}\frac{dEL}{2\pi Nv\hbar}\right) \\ &\approx 4\sin^2\left(\frac{\Delta L}{2\hbar v}\right)\left(\left(\frac{dE}{\omega_v\hbar}\right)^2 + 2\frac{W}{\Delta}\frac{dE}{\omega_v\hbar}\right) \end{aligned} \tag{3.26}$$

if $W \ll \Delta$. Note that this expression has one term which is even in E, Δ and one term (proportional to W) which is odd in these quantities. So, it is useful to record a measurement of the population transfer with some choice of electric and magnetic fields, then change the sign of one or both of these fields to make a second measurement. This allows the cancellation of systematic errors in E and Δ, and extraction of the value of W. This asymmetry is defined as

$$\begin{aligned} \mathcal{A} &\equiv \frac{p_{1f}[+E] - p_{1f}[-E]}{p_{1f}[+E] + p_{1f}[-E]} \\ &= 4\pi\frac{W}{\Delta}\frac{\Delta^2 dELNv\hbar}{d^2E^2\Delta^2L^2 + 4\pi^2N^2v^2\hbar^2W^2} \\ &= 2\frac{W}{\Delta}\frac{\Delta^2 dE\omega_v\hbar}{d^2E^2\Delta^2 + \omega_v^2\hbar^2W^2} \\ &\approx 4\pi\frac{W}{\Delta}\frac{Nv\hbar}{dEL} \\ &= 2\frac{W}{\Delta}\frac{\omega_v\hbar}{dE} \end{aligned} \tag{3.27}$$

Note that the third form of this expression, derived under the assumption that $W \ll \Delta$ and hence $\left(\frac{W}{\Delta}\right)^2$ can be neglected, appears to diverge as $\Delta \to 0$. Including the higher order term prevents this; but in practice it is not possible to bring the levels exactly to crossing (because of experimental imperfections) and the problem is irrelevant.

The asymmetry is maximal when

$$\Delta = \pm\frac{2\pi W N v \hbar}{dEL} \tag{3.28}$$

3.5.2 Effect of Inhomogeneous Magnetic Fields or Velocities

The derivation above for the expected signal assumes that the magnetic field is homogeneous and all the molecules have the same velocity. In practice, the magnetic field homogenity is known to be limited to about 0.1 ppm (0.0005 Gauss for a 4630 Gauss field), and the velocity spread is about $\pm 5\%$ of a 600 m/s average transverse velocity. First, the analysis will consider the effect of a Gaussian spread in the magnetic field (suitable for finding an analytic solution for the effect of the magnetic field spread). Neglecting the $\left(\frac{W}{\Delta}\right)^2$ term, the population transfer (eq. 3.26) averaged over the spread in detuning Δ, $\langle p_{1f}\rangle_\Delta$, is given by

$$\langle p_{1f}\rangle_\Delta = \int_{-\infty}^{\infty} 4\sin^2\left(\frac{\Delta L}{2\hbar v}\right)\left(\left(\frac{dEL}{2\pi N v\hbar}\right)^2 + 2\frac{W}{\Delta}\frac{dEL}{2\pi N v\hbar}\right)\frac{e^{-\left(\frac{\Delta-\Delta_0}{\sqrt{2}\sigma_\Delta}\right)^2}}{\sqrt{2\pi}\sigma_\Delta}d\Delta$$

It is possible to find an analytic solution if $\frac{\Delta L}{2\hbar v} \lesssim 0.1$. For L =6 cm, v=600 m/s, this condition is satisfied when $\Delta \lesssim 2\pi \cdot 2$ kHz. This solution will be most useful when dE and Δ are small (magnetic field tuned close to resonance). The solution is then

$$\begin{aligned}\langle p_{1f}\rangle_\Delta &\approx \int_{-\infty}^{\infty} 4\left(\frac{\Delta L}{2\hbar v}\right)^2\left(\left(\frac{dEL}{2\pi N v\hbar}\right)^2+2\frac{W}{\Delta}\frac{dEL}{2\pi N v\hbar}\right)\frac{e^{-\left(\frac{\Delta-\Delta_0}{\sqrt{2}\sigma_\Delta}\right)^2}}{\sqrt{2\pi}\sigma_\Delta}d\Delta \\ &\approx dEL^3\frac{\left(\sigma_\Delta^2+\Delta_0^2\right)dEL+4\pi W\Delta_0 N v\hbar}{4\pi^2N^2v^4\hbar^4}\end{aligned} \tag{3.29}$$

which will give an asymmetry

$$\langle\mathcal{A}\rangle_\Delta = 4\pi\frac{W}{\Delta_0}\frac{Nv\hbar}{dEL}\frac{\Delta_0^2}{\sigma_\Delta^2+\Delta_0^2} \tag{3.30}$$

which is equivalent to the results in equation 3.27 when $\Delta_0 \gg \sigma_\Delta$. Inclusion of the higher-order $\left(\frac{W}{\Delta}\right)^2$ term in this calculation produces the same form of asymmetry, with a slightly broader lineshape; the change is negligible under reasonable experimental conditions.

To look at the effect of a finite spread of velocities, the expression for population transfer $\langle p_{1f}\rangle_\Delta$ (equation 3.29) is convolved with a Gaussian velocity distribution with spread σ_v:

$$\begin{aligned}\langle p_{1f}\rangle_{\Delta,v} &= \int_{-\infty}^{\infty}\langle p_{1f}\rangle_\Delta\frac{e^{-\frac{1}{2}\left(\frac{v-v_0}{\sigma_v}\right)^2}}{\sqrt{2\pi}\sigma_v}dv \\ &= \frac{dEL^3}{\sqrt{2\pi}\sigma_v N\hbar^3}\left(\frac{dEL\left(\sigma_B^2+\Delta_0^2\right)}{4\pi^2N\hbar}\int_{-\infty}^{\infty}\frac{e^{-\frac{1}{2}\left(\frac{v-v_0}{\sigma_v}\right)^2}}{v^4}dv+\frac{W\Delta_0}{\pi}\int_{-\infty}^{\infty}\frac{e^{-\frac{1}{2}\left(\frac{v-v_0}{\sigma_v}\right)^2}}{v^3}dv\right)\end{aligned} \tag{3.31}$$

The integrals are found using the convolution theorem $\mathcal{F}[f\star g]=k\mathcal{F}[f]\mathcal{F}[g]$:

$$\begin{aligned}\mathcal{F}\left[\frac{1}{v^2}\right] &= -\sqrt{\frac{\pi}{2}}\omega\mathrm{sgn}(\omega) \\ \mathcal{F}\left[\frac{1}{v^3}\right] &= -\frac{i}{2}\sqrt{\frac{\pi}{2}}\omega^2\mathrm{sgn}(\omega) \\ \mathcal{F}\left[\frac{1}{v^4}\right] &= \frac{1}{6}\sqrt{\frac{\pi}{2}}\omega^3\mathrm{sgn}(\omega) \\ \mathcal{F}\left[e^{-(x/c)^2}\right] &= \frac{c}{\sqrt{2}}e^{-c^2\omega^2/4}\end{aligned} \tag{3.32}$$

$$\begin{aligned}
\int_{-\infty}^{\infty} \frac{1}{v^2} e^{-\left(\frac{v-v_0}{c}\right)^2} dv &= \sqrt{2\pi}\mathcal{F}^{-1}\left[\mathcal{F}\left[\frac{1}{v^2}\right]\mathcal{F}\left[e^{-(x/c)^2}\right]\right] \\
&= -\frac{2\sqrt{\pi}}{c^2}\left(c - \sqrt{\pi} v_0 e^{-\left(\frac{v_0}{c}\right)^2} \mathrm{Erfi}\left(\frac{v_0}{c}\right)\right) \\
\int_{-\infty}^{\infty} \frac{1}{v^3} e^{-\left(\frac{v-v_0}{c}\right)^2} dv &= \sqrt{2\pi}\mathcal{F}^{-1}\left[\mathcal{F}\left[\frac{1}{v^3}\right]\mathcal{F}\left[e^{-(x/c)^2}\right]\right] \\
&= -\frac{\sqrt{\pi}}{c^4}\left(2cv_0 + \sqrt{\pi}\left(c^2 - 2v_0^2\right) e^{-\left(\frac{v_0}{c}\right)^2} \mathrm{Erfi}\left(\frac{v_0}{c}\right)\right) \\
\int_{-\infty}^{\infty} \frac{1}{v^4} e^{-\left(\frac{v-v_0}{c}\right)^2} dv &= \sqrt{2\pi}\mathcal{F}^{-1}\left[\mathcal{F}\left[\frac{1}{v^4}\right]\mathcal{F}\left[e^{-(x/c)^2}\right]\right] \\
&= \frac{2\sqrt{\pi}}{3c^6}\left(2c^3 - 2cv_0^2 + \sqrt{\pi}\left(2v_0^3 - 3c^2 v_0\right) e^{-\left(\frac{v_0}{c}\right)^2} \mathrm{Erfi}\left(\frac{v_0}{c}\right)\right)
\end{aligned} \tag{3.33}$$

so that the population transfer is:

$$\begin{aligned}
\langle p_{1f}\rangle_{\Delta,v} = &- \frac{d^2E^2L^4\left(\sigma_B^2+\Delta_0^2\right)}{8\sqrt{2}\pi^2N^2\hbar^4\sigma_v^3}\left(2\frac{v_0}{\sqrt{2}\sigma_v} - \sqrt{\pi}\left(2\left(\frac{v_0}{\sqrt{2}\sigma_v}\right)^2 - 1\right)e^{-\left(\frac{v_0}{c}\right)^2}\mathrm{Erfi}\left(\frac{v_0}{\sqrt{2}\sigma_v}\right)\right) \\
&- \frac{2dEL^3W\Delta_0}{\pi N\hbar^3c^2}\left(1 - \sqrt{\frac{\pi}{2}}\frac{v_0}{\sigma_v}e^{-\left(\frac{v_0}{c}\right)^2}\mathrm{Erfi}\left(\frac{v_0}{\sqrt{2}\sigma_v}\right)\right)
\end{aligned} \tag{3.34}$$

As before, all terms that are even in powers of E are also even in powers of Δ_0, so that changing the sign of $E \to -E$ is equivalent to changing the detuning from $\Delta_0 \to -\Delta_0$. The resulting asymmetry is:

$$\begin{aligned}
\langle \mathcal{A}\rangle_{\Delta,v} &= 4\pi\frac{W}{\Delta_0}\frac{N\hbar v_0}{dEL}\frac{\Delta_0^2}{\sigma_\Delta^2+\Delta_0^2} \\
&\quad\times\frac{2\sqrt{2}}{\frac{v_0}{\sigma_v}}\frac{1 - \sqrt{\frac{\pi}{2}}\frac{v_0}{\sigma_v}e^{-\frac{1}{2}\left(\frac{v_0}{\sigma_v}\right)^2}\mathrm{Erfi}\left(\frac{v_0}{\sqrt{2}\sigma_v}\right)}{\frac{v_0}{\sigma_v} - \sqrt{\pi}\left(\left(\frac{v_0}{\sigma_v}\right)^2 - 1\right)e^{-\frac{1}{2}\left(\frac{v_0}{\sigma_v}\right)^2}\mathrm{Erfi}\left(\frac{v_0}{\sqrt{2}\sigma_v}\right)} \\
&= 2\sqrt{2}\pi\frac{W}{\Delta_0}\frac{N\hbar v_0}{dEL}V_{\mathrm{sp}}\left(\frac{v_0}{\sigma_v}\right)\frac{\Delta_0^2}{\sigma_\Delta^2+\Delta_0^2}
\end{aligned} \tag{3.35}$$

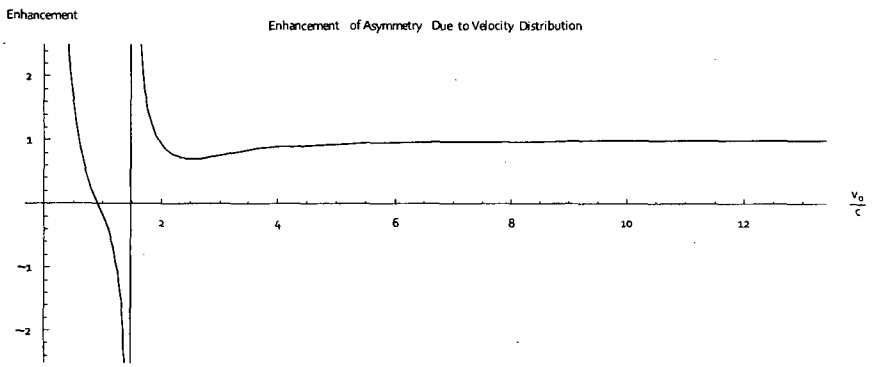

Figure 3.2: The enhancement or attenuation of the asymmetry (equation 3.35) as a function of the spread in the velocity distribution $e^{-(v_0/c)^2}$, parameterized as $\frac{v_0}{c}$. As long as the velocity distribution is narrower than $\frac{v_0}{c} \gtrsim 6$, the effect of the velocity spread is negligible.

where the coefficient $V_{\rm sp}\left(\frac{v_0}{\sigma_v}\right)$

$$V_{\rm sp}\left(\frac{v_0}{\sigma_v}\right) \equiv \frac{2}{\frac{v_0}{\sigma_v}} \frac{1 - \sqrt{\frac{\pi}{2}}\frac{v_0}{\sigma_v} e^{-\frac{1}{2}\left(\frac{v_0}{\sigma_v}\right)^2} \mathrm{Erfi}\left(\frac{v_0}{\sigma_v}\right)}{\sqrt{2}\frac{v_0}{\sigma_v} - \sqrt{\pi}\left(\left(\frac{v_0}{\sigma_v}\right)^2 - 1\right) e^{-\frac{1}{2}\left(\frac{v_0}{\sigma_v}\right)^2} \mathrm{Erfi}\left(\frac{v_0}{\sigma_v}\right)}$$

depends only on the ratio of the center velocity v_0 to the width parameter σ_v. So, the effect of the velocity distribution is similar to the expression with only the spread in magnetic fields (equation 3.30) but with an additional coefficient describing the effect of the Gaussian velocity spread. The easiest way to find the behavior of this expression is to plot it (figure 3.2). For values of $v_0/\sigma_v \gtrsim 8$, we see that the effect on the size of the observed asymmetry is negligible. For example, with $v_0 \sim 10\sigma_v$ (which is what we observe), $V_{\rm sp}(10) = 0.98$.

3.5.3 Effects of Improper State Preparation

The calculations of the population transfer in the above sections assumes that the molecules are initially prepared in a parity eigenstate. This is, of course,

generally not going to be the case. If the state preparation process does not completely deplete one of the states, the initial state will not be the desired state $\Psi(t=0) = |2\rangle$. Consider the resulting population in state $|1\rangle$ as an incoherent combination of the population transferred from a perfect preparation of state $|2\rangle$, plus an equal mix of states $|1\rangle$ and $|2\rangle$. Define η as the population depletion achieved by the state preparation process (η=1 being perfect preparation in state $|2\rangle$); the resulting population measured to be in state $|1\rangle$ would be

$$p = \eta p_{1f} + (1 - \eta) \tag{3.36}$$

where p_{1f} is the population transfer based on the perfect preparation in state $|2\rangle$ given in equation 3.26, and η is close to 1. (For an equal mix of states in a two-level system, population transfer from $|1\rangle$ to $|2\rangle$ is exactly balanced by transfer from $|2\rangle$ to $|1\rangle$).

The resulting asymmetry would be

$$\mathcal{A} = \frac{p_{1f}[+E] - p_{1f}[-E]}{p_{1f}[+E] + p_{1f}[-E] + 2\left(\frac{1-\eta}{\eta}\right)} \tag{3.37}$$

For values of η sufficiently close to 1, this modification has only a small effect. However, as will be shown in chapter 6, typically $p_{1f} \lesssim 0.1$. Under these conditions, poor optical pumping will significantly attenuate the observed asymmetry if $\eta \lesssim 0.9$. It is possible to measure η experimentally by chopping the state preparation laser beam when the magnetic field is set far from resonance.

3.5.4 Error Analysis

3.5.4.1 Statistical Errors

It is necessary to understand the amount of uncertainty in our determination of W, based on measured signals. Eq. 3.26 showed the population of state $|1\rangle$ is a function of W. However, direct measurement of the population of the state is full of systematic errors due to various experimental factors (poor state preparation, scattered light, etc.). Instead, the experimental apparatus measures

- S_+ as the measurement of the population p_{1f} with an electric field $+E$, with an energy difference Δ between states $|1\rangle$ and $|2\rangle$
- S_- as the measurement of the population p_{1f} with an electric field $-E$, with an energy difference Δ between states $|1\rangle$ and $|2\rangle$

and determine the asymmetry $\mathcal{A}(\Delta)$ by finding

$$\mathcal{A}(\Delta) = \frac{S_+ - S_-}{S_+ + S_-} \tag{3.38}$$

so that the asymmetry is a function of Δ. The value of Δ is varied by changing the magnetic field B around the field B_0 that is needed to bring states $|1\rangle$ and $|2\rangle$ to crossing, so that

$$\Delta \approx 2\pi \cdot 2\mu_B (B - B_0)$$

where the rate at which $|1\rangle$ and $|2\rangle$ change in energy with change in the magnetic field is approximately given by Bohr magneton, μ_B ≈1.4 MHz/Gauss. From this, eq. 3.30 gives

$$\langle \mathcal{A} \rangle_\Delta = 2\frac{W}{\Delta_0}\frac{\omega_v \hbar}{dE}\frac{\Delta_0^2}{\sigma_\Delta^2 + \Delta_0^2}$$

and find that W is proportional to the asymmetry. The dominant source of uncertainty is expected to be statistical uncertainty $\sigma_\mathcal{A}$ in the determination of

$\mathcal{A}$; the other variables (ω_v, d, E, and Δ_0) are comparatively well known. Under these conditions,

$$\frac{\sigma_{\mathcal{A}}}{\mathcal{A}} \approx \frac{\sigma_W}{W}$$

and a good determination of $\mathcal{A}$ leads to a good determination of W. The goal for the remainder of this section is to optimize the experimental conditions to mimimize the integration time, subject to the constraints $p_{1f} \lesssim 0.1$ (based on the assumptions made in deriving eq. 3.21), $W \ll \Delta_0$, $\Delta_0 \ll \omega_v$, and $\Delta_0 \gg \sigma_\Delta$ that were made in the derivation of the population transfer and asymmetry.

Using the formula for the uncertainty σ_f of a function $f(x_1 \pm \sigma_1, \ldots, x_i \pm \sigma_i)$ of uncorrelated parameters,

$$\sigma_f = \sqrt{\sum_i \left(\sigma_i \frac{\partial f}{\partial x_i}\right)^2} \tag{3.39}$$

the uncertainty $\sigma_{\mathcal{A}}$ in our determination of $\mathcal{A}$ based on our experimental measurements, assuming that S_+ and S_- are governed by Poisson statistics ($\sigma_S = \sqrt{S}$), is

$$\sigma_{\mathcal{A}} = 2\sqrt{\frac{S_+ S_-}{(S_+ + S_-)^3}} \tag{3.40}$$

The imact of the experimental parameters on the data we collect is seen by substituting $S_\pm = S(1 \pm \mathcal{A})$ and $\sigma_{S_\pm} = \sqrt{S_\pm}$ to write the fractional error in the asymmetry as

$$\begin{aligned} \frac{\sigma_{\mathcal{A}}}{\mathcal{A}} &= \frac{1}{\mathcal{A}}\sqrt{\frac{1-\mathcal{A}^2}{2S}} \\ &\approx \frac{1}{\sqrt{2S}\mathcal{A}} \end{aligned} \tag{3.41}$$

for small values of $\mathcal{A}$, where the signal S depends on the detection efficiency d_{eff}, beam flux R, and integration time T:

$$\begin{aligned} S &= \frac{1}{2} d_{\text{eff}} RT \left(p_{1f}\left[+E\right] + p_{1f}\left[-E\right] \right) \\ &\approx d_{\text{eff}} RT \cdot 4\sin^2\left(\frac{\pi N \Delta_0}{\hbar\omega_v}\right)\left(\frac{dE}{\omega_v \hbar}\right)^2 \end{aligned}$$

so that the relative uncertainty is

$$\begin{aligned} \frac{\sigma_{\mathcal{A}}}{\mathcal{A}} &\approx \frac{1}{4\sqrt{2 d_{\text{eff}} RT}\sin\left(\frac{\pi N|\Delta_0|}{\hbar\omega_v}\right)\left(\frac{|dE|}{\omega_v\hbar}\right)\frac{W}{|\Delta_0|}\frac{\omega_v\hbar}{|dE|}\frac{\Delta_0^2}{\sigma_\Delta^2+\Delta_0^2}} \\ &\approx \frac{\hbar\left(\omega_v/|\Delta_0|\right)}{4\pi\sqrt{2 d_{\text{eff}} RT}N\frac{W}{|\Delta_0|}\frac{\Delta_0^2}{\sigma_\Delta^2+\Delta_0^2}} \\ &= \frac{\hbar}{2\sqrt{2 d_{\text{eff}} RT}\frac{\Delta_0^2}{\sigma_\Delta^2+\Delta_0^2}}\frac{v}{L} \end{aligned}$$

under the conditions that $\Delta_0 \ll \omega_v$ and $dE \ll \sqrt{\frac{\hbar^3\omega_v^3}{\pi\Delta_0 N}}$ (eg. that $p_{1f} \ll 1$). In practical terms, this does not leave many free parameters to optimize. The statistical uncertainty for a given integration time will be improved by reducing the combination of experimental parameters $\frac{\omega_v}{N} = 2\pi v/L$, which is inversely proportional to the time the molecular beam spends within the interaction region. Our ability to do this is limited by the maximum length L over which it is possible to generate a uniform magnetic field, and by the beam velocity v. The relative uncertainty is only weakly dependent on Δ_0 as long as $\omega_v \gg \Delta_0 \gtrsim 2\sigma_\Delta$. As laid out in chapter 5, our experimental apparatus has the following typical parameters:

- $\omega_v = 2\pi\left(10^4 \text{ Hz}\right)$, based on v = 600 m/s and L=6 cm with N=1 for our pulsed supersonic source
- $\sigma_\Delta \approx 10^{-7} \times 2\pi\left(1.3 \times 10^{10} \text{ Hz}\right) = 2\pi\left(1300 \text{ Hz}\right)$ corresponds to a magnetic

field uniformity of 0.1 ppm, comparable to the best we have achieved

- W is expected to be on the order of 2π (4 Hz)
- the detected beam flux $d_{\text{eff}}R \approx 14$ counts/second for ^{137}BaF, based on a flux of 400 counts/second for ^{138}BaF (at a 10 Hz repetition rate)
- a buffer gas source (considered in chapter 8) would produce a slower beam ($v \sim 200$ m/s), which would increase the time spent within the interaction region

Under these conditions for a pulsed supersonic source, the required integration time is about $T \sim 2 \times 10^5$ seconds (2.5 days) of continuous running time. As noted in eq. 3.37, the integration time will be longer if there is a large background signal due to poor optical pumping. Under these conditions, the measured asymmetry will be reduced (using eq. 3.37) by a factor that depends on the optical pumping efficiency:

$$\mathcal{A}_\eta = \mathcal{A}\frac{p_{1f}}{p_{1f} + \frac{1-\eta}{\eta}}$$

so that the integration time T increases:

$$T \propto 1/\mathcal{A}_\eta^2 \sim \left(\frac{p_{1f} + \frac{1}{\eta}(1-\eta)}{p_{1f}}\right)^2 \tag{3.42}$$

For $p_{1f} \approx 0.1$ (to preserve the assumptions made in deriving eq. 3.21), the integration time required to achieve the same relative uncertainty in the determination of $\mathcal{A}$ is quadrupled if $\eta = 0.9$ instead of perfect optical pumping.

3.5.4.2 Systematic Errors

The discussion now turns to the possible effects of systematic errors. By design, this experiment allows reversal of the electric fields and level spacings in order to

determine the asymmetry with respect to these reversals. The most significant source of systematic errors are expected to arise from:

- Inability to properly reverse the elctric field
- Inability to properly reverse the detuning ($+\Delta$ to $-\Delta$) or to reverse the magnetic field
- Incomplete optical pumping (as calculated in equation 3.37); in addition to the added time required to overcome statistical noise, it is necessary to calculate and apply a correction to $\mathcal{A}$

First, consider the formula for population transfer in the absence of any field inhomogenities and neglecting $(W/\Delta)^2$ (eq. 3.26):

$$p_{1f} = 4\sin^2\left(\frac{\Delta L}{2\hbar v}\right)\left(\left(\frac{dEL}{2\pi N v\hbar}\right)^2 + 2\frac{W}{\Delta}\frac{dEL}{2\pi N v\hbar}\right)$$

Now, suppose there is some offset δE that prevents us from reversing the electric field properly. The experimentally observed asymmetry $\mathcal{A}_a$ will have the form:

$$\begin{aligned}\mathcal{A}_a &\equiv \frac{p_{1f}[\delta E + E] - p_{1f}[\delta E - E]}{p_{1f}[\delta E + E] + p_{1f}[\delta E - E]} \\ &= 4\pi\frac{W}{\Delta}\frac{Nv\hbar}{dEL}\frac{1 + \frac{L\Delta\delta E}{2\pi Nv\hbar W}}{1 + \frac{\delta E^2}{d^2E^2} + 4\pi\frac{WNv\hbar\delta E}{\Delta d^2E^2L}} \\ &\approx \mathcal{A}\left(1 + \frac{L\Delta}{2\pi Nv\hbar W}\delta E\right)\end{aligned} \tag{3.43}$$

For reasonable values ($v = 600$ m/s, $L = 0.06$ m, $\Delta = 2\pi\cdot 2000$ Hz, $dE = 2\pi\cdot 2000$ Hz) this corresponds to an error in the asymmetry of about $0.8\% \times a$ in Hertz. In order to keep this source of error small compared to $\mathcal{A}$, stray fields need to be controlled at a level of about $\delta E = 10$ Hz$/d \approx 10$ mV/cm. The effects of a stray electric field and a parity-violating signal can also be distinguished by measuring the asymmetry as a function of Δ. The asymmetry is odd in Δ; a stray field will lead to an asymmetry which is even in Δ.

The effect of improper optical pumping can be removed using equation 3.36:

$$p_{\pm} = \eta p_{1f,\pm} + (1 - \eta) \tag{3.44}$$

where $p_{1f,\pm}$ is the population transfer we expect if the optical pumping were completely effective, and $p_{\pm}$ is the observed population transfer. Assuming that S_+ and S_- are the experimentally measured signals with $+E$ and $-E$, respectively, and are proportional to p_+ and p_-, it is possible to experimentally determine the optical pumping effectiveness η, and use this to correct $S_{\pm}$ as long as η is close to 1:

$$S_{\pm,\text{meas}} = \eta S_{\pm,\text{actual}} + (1 - \eta) \frac{S_{\pm,\text{actual}}}{p_{1f,\pm}} \tag{3.45}$$

The last term accounts for the number of molecules that have not been depleted, and remain in the $|1\rangle$ state throughout the experiment. Inverting this to solve for $S_{\pm,\text{actual}}$,

$$S_{\pm,\text{actual}} = \frac{S_{\pm,\text{meas}}}{\eta + (1 - \eta)/p_{1f,\pm}} \tag{3.46}$$

Chapter 4

Relevant Aspects of the Structure of BaF

This chapter will outline the techniques used to calculate the energy levels of BaF and list the effective constants used. Calculations of the transitions relevant to optical pumping and detection are presented with selected measured spectra for comparison.

4.1 Information Required for This Experiment

The most important part of our experimental apparatus is also the smallest - diatomic molecules of barium monofluoride. Interactions with laser light are used to manipulate and detect the state of the molecule; it is necessary to know where to tune the lasers, and how the spectra change in a magnetic field. The experimental design also requires precise control over how the two levels of opposite parity are brought close to crossing and understanding of the properties of these states near crossing. The electronic, vibrational and rotational energy

levels of BaF in the absence of an external field are well documented in many sources, including Herzberg[11]. More recent references which more thoroughly describe the excited electronic states include Effantin *et al.* [12]. The dipole moment of the ground state is required in order to calculate the dipole matrix elements between states near crossing and the dipole matrix element is needed for transition intensities. The literature also contains measured values for the dipole moment of the A-X transition[24] and of the ground state[27, 26]. Information on the Franck-Condon factors suggest that the probability of changing vibrational states during an electronic transition tends to be low[24, 25]. It is harder to find information on the behavior of BaF in the presence of a magnetic field. Prof. Steimle at Arizona State University assisted us in measuring the Zeeman shift of the A-X transition[56] and in doing field-free spectroscopy of BaF during my visit.

4.2 Level Scheme

The electronic energy levels of BaF (figure 4.1) result from $Ba^+(6s^1)+F^-$ (closed shell); at larger internuclear spacings, the states would resemble hydrogen-like wavefunctions of one electron around the barium nucleus. Drawing from the level structure of Ba^+, there is a $6s$ ground state, followed by a $5d$ excited state, then a $6p$, etc. The tightly bound electronic states follow from this structure; the $6s$ ground state has no angular momentum, so there is a $X^2\Sigma_{1/2}$ molecular ground state (in which the Σ denotes that the projection of electronic angular momentum along the internuclear axis, $\Lambda \equiv L \cdot \hat{n}$, is 0). The first manifold of electronic excited states are derived primarily from the $5d$ configuration; with $L = 2$, the projection $|\Lambda|$ can be 0 ($B^2\Sigma$ state), 1 ($A^2\Pi$ states), or 2 ($A'^2\Delta$ states). The next manifold of states, coming from a $6p$ configuration with $L = 1$, produces the $D^2\Sigma$ and $C^2\Pi$ states. These atomic orbital configurations

are only approximations of the true wavefunction in the molecule. Ernst et al. [33] inferred the $X^2\Sigma$ state to be a mixing of 76% $6s$, 21.5% $6p$, and 2.5% $5d$ (Ba^+); that is,

$$\left|\Psi\left(X^2\Sigma^+\right)\right\rangle = 0.873\left|\Psi_{6s}\right\rangle - 0.463\left|\Psi_{6p}\right\rangle - 0.155\left|\Psi_{5d}\right\rangle \tag{4.1}$$

In each case, since there is only one valence electron, the spin $S = 1/2$ and all the states are doublets. The quantum number $\Sigma = -S \ldots S$ is defined to be the projection of the spin onto the internuclear axis: $\Sigma \equiv \vec{S} \cdot \hat{n}$. Additionally, spin-orbit interactions split each of the states that have $\Lambda > 0$ into two groups of levels, identified by the quantum number $|\Omega| \equiv \left|\vec{J} \cdot \hat{n}\right| = |\Sigma + \Lambda|$. For example, the $A^2\Pi$ electronic level is split into the $A^2\Pi_{1/2}$ and $A^2\Pi_{3/2}$ states; however, the ground state $X^2\Sigma$ only has $X^2\Sigma_{1/2}$.

The ground $X^2\Sigma$ state and the excited $D^2\Sigma$ states of barium fluoride are well described by Hund's case (b) (as are most states with $\Lambda = 0$ [30]), in which the electron spin $\vec{S}$ is not strongly coupled to the internuclear axis. The $A^2\Pi$ states may be described by Hund's case (a), particularly for low rotational levels. In case (a), the total electronic angular momentum $\vec{J}_e = \vec{L} + \vec{S}$ couples strongly to the internuclear axis; as a result, $|\Omega| = |\Lambda + \Sigma|$ is a good quantum number. The total angular momentum $\vec{J}$ is then the sum of the electronic angular momentum and the molecular rotation $\vec{N}$: $\vec{J} \equiv \vec{J}_e + \vec{N}$.

A schematic view of the rotational energy level structure of the X-A band is shown in figure 4.2. Generally, the transitions within the band are classified based on the change in angular momentum from the ground state (J) to the upper state (J'). R-branch lines consist of transitions with $J' = J+1$. Similarly, Q-branch lines have $J' = J$, and P-branch lines have $J' = J - 1$. Consider, for a moment, just the R-branch transitions to the $J' = 3/2$ level of the $^2\Pi_{1/2}$ state. There are two transitions to this level with $J = 1/2$; one originates from

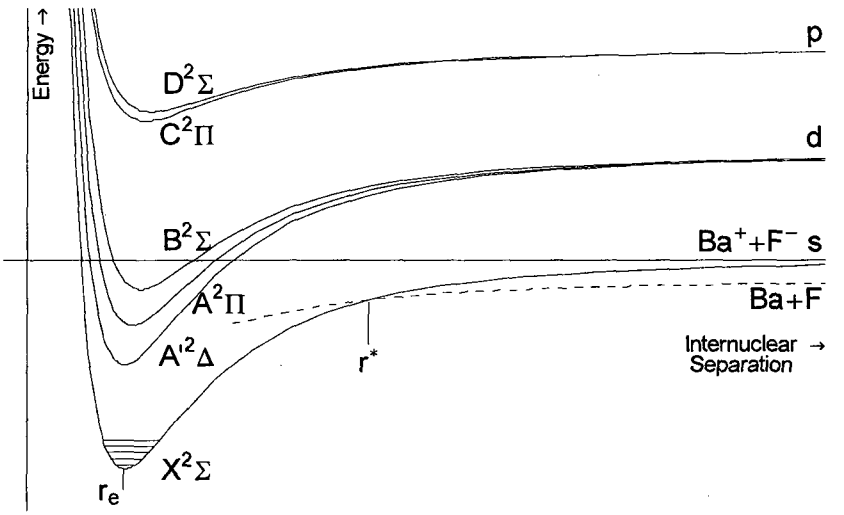

Figure 4.1: The energy of the electronic energy levels of the BaF molecule are a function of the intermolecular distance. At infinite distances, the lowest energy state is Ba $(6s^2)$+F $(2p^5)$. At closer distances, it is more favorable to make $Ba^+ + F^-$, and the levels act as single-electron orbitals of Ba^+ polarized by the electric field due to the closed-shell F^- orbitals. In this case, the F^- has a closed shell, and the Ba^+ has a single valence electron. The internuclear separation at which the ionic molecule Ba^+F^- is equal in energy to BaF is marked as r^* (=7.8 Å for BaF [12]). The equilibrium separation r_e (=2.2 Å) is the deepest part of the potential well. In this case, Herzberg's criterion for an ionic state is satisfied ($r^* > 2r_e$). At shorter distances ($r \approx r_e$), there are bound molecular states. A multitude of vibrational states (depicted by the horizontal levels residing in the potential well) reside in each of these bound states; as the vibrational energy increases, the molecule resides at a shallower depth within this potential well. Each vibrational level also has rotational structure (not pictured). Bernard et al. [12] note that the X $^2\Sigma$ state is no more than 76% $6s\sigma$ (due to hybridization), and that the $A^2\Pi$ state has 42% p, 55% d, and 2% f atomic orbital character.

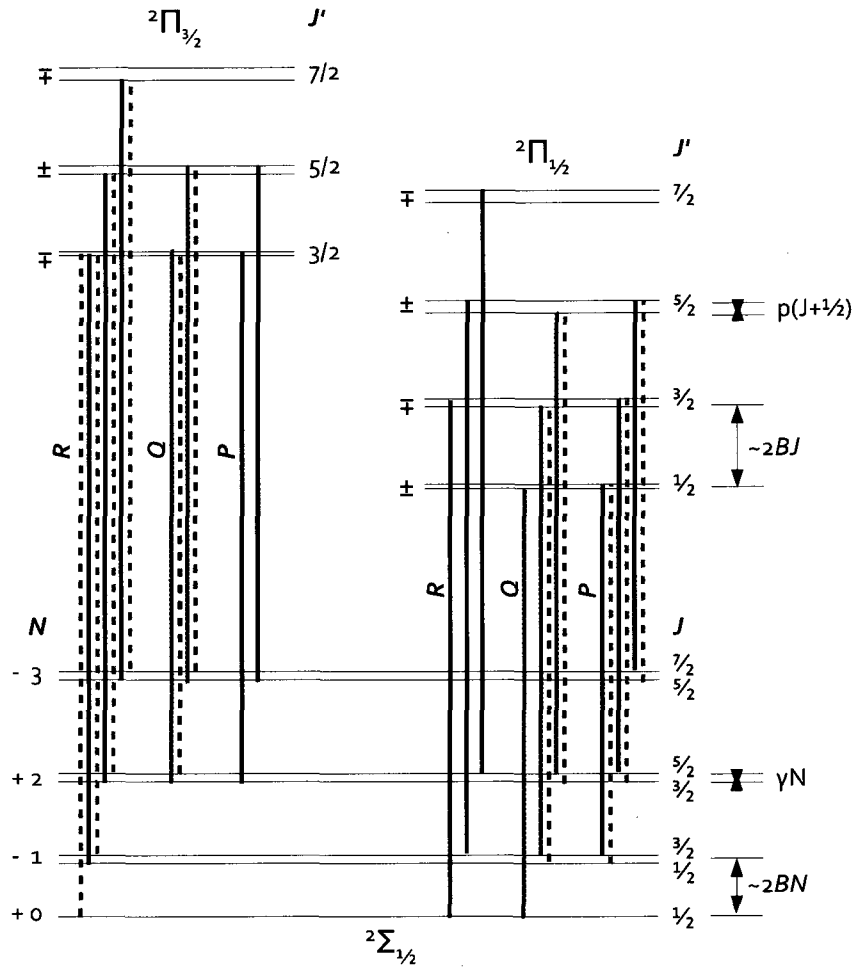

Figure 4.2: Energy level diagram for the first few lines of a $^2\Pi(a) - ^2\Sigma$ band (simplified from fig. 123 in Herzberg [11]). The type of branch is indicated by color, and satellite branches are indicated by dashed lines. The spin-doublet splitting between the $^2\Pi_{1/2}$ and $^2\Pi_{3/2}$ states is much larger than shown. Spin-doubling in the lower state separates states with the same N but of different J, and Λ-doubling in the upper state splits states with the same value of J. The parity of the level is indicated by $+$ or $-$. We can see that we need to use either the first R or Q-branch line if we want to access the $N = 0$ level of the ground state; only the R-branch line happens to be in a region that is far from other lines. The scaling of the splitting between energy levels is indicated; the rotational line spacing, spin-orbit splitting, and Λ-doubling all increase at larger N (or J).

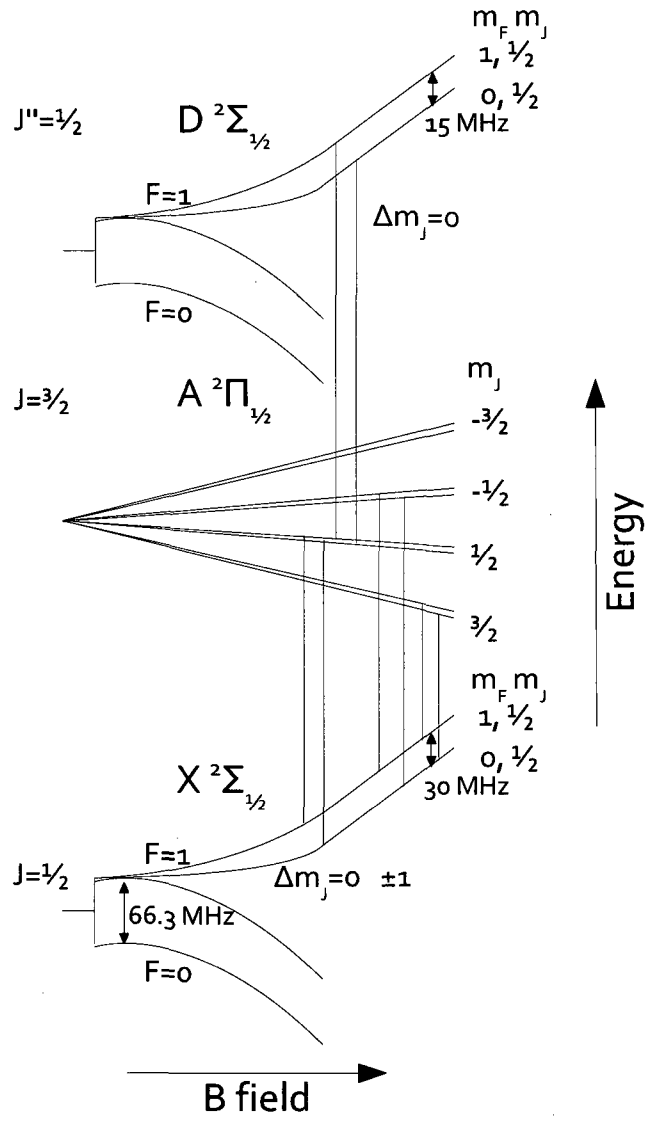

Figure 4.3: Diagram of hyperfine structure of the energy levels of ^{138}BaF involved in the X-A and A-D transitions from the $N = 0$ state in the presence of a magnetic field (not to scale). The transitions marked in blue and orange ($\Delta m_J = 0$) are for incident light polarized parallel to the magnetic field; the transitions in red ($\Delta m_J = \pm 1$) are for light polarized perpendicular to the field. The blue and red transitions are at 860 nm; the orange transition is at 797 nm. The hyperfine levels in the A state are separated by $\sim$ 450 kHz (calculation based on measurements from figure 4.9), much smaller than the separation in the X or D states. The levels are well decoupled into m_J, m_I at fields greater than 30 Gauss.

the $N = 0$ level of the ground state, the other from the $N = 1$ level. The latter will be very close in energy to the second Q branch line, which also originates from $N = 1$ but begins in $J = 3/2$. In general, this subset of R-branch lines (with $J' = N - 1/2$) will be similar to the Q-branch; therefore, it is called a satellite branch (Q-form R branch, or in Herzberg notation, R_{21}). In figure 4.2, we indicate the type of branch (R, Q, P) by color, and satellite branches are drawn with dashed lines.

From figure 4.2, we see that there are three possible lines that we can use to access the ground rotational state of the molecule using the X-A transition. The first R- and Q-branch lines to the $^2\Pi_{1/2}$ are suitable, as well as the first satellite R-branch line to the $^2\Pi_{3/2}$ state. We have chosen to use the first R-branch line from the X $^2\Sigma$ to the A $^2\Pi_{1/2}$ state; this transition at 859 nm (11631.275 cm^{-1}) is a slightly more convenient choice for laser diodes (due to the cesium transition at 852 nm), and unlike the Q branch, the line is far from any other spectral features.

The hyperfine structure of the X $N = 0$, $J = 1/2$ and A $J = 3/2^-$ states of ^{138}BaF is illustrated in figure 4.3. The spin of the ^{19}F nucleus ($I = 1/2$) splits the $J = 1/2$ ground state into two levels with a total angular momentum $F = 0$ and $F = 1$, separated by 66.3 MHz, while the hyperfine structure of the A $J = 3/2^-$ state is unresolvably small as the A$^2\Pi$ electronic wavefunction has little overlap with the atomic nuclei.

4.3 Approximate Energy Levels of a Diatomic Molecule and Spectroscopic Constants

Table 4.1, from Effantin *et al.* [12], gives the effective field-free constants for the energy levels relevant to this experiment. These constants are written with

respect to an effective Hamiltonian, which presents a simplified picture of the interactions within the molecule in terms of rotational angular momentum, electron and nuclear spins, and their projections. A useful presentation of the effective Hamiltonian in the Hund's case ($a_{\beta s}$) basis is given in Brown and Kopp [29] and will be summarized in section 4.4.1. This basis uses Hund's case (a) states to represent the electronic component of the molecular wavefunction; the angular momentum $\vec{J}$ is then coupled to the nuclear spin $\vec{I}_1$ to produce an intermediate sum $\vec{F}_1$, and $\vec{F}_1 + \vec{I}_2$ to produce the total angular momentum $\vec{F}$ with projection $m_F \equiv F_z$ in the laboratory frame.

Hund's case (b) states

	T_e	ω_e	$\omega_e\chi_e$	B	α_e	γ
$X\,^2\Sigma$	0	469.416	1.83727	0.215951	0.00116358	0.0027246
$B\,^2\Sigma$	14062.502	424.732	1.8283	0.207823	0.0012236	-0.26268
$D\,^2\Sigma$	24157.149	508.4	1.88	0.2274137	0	0.007130

Hund's case (a) states

	T_e	ω_e	$\omega_e\chi_e$	A	α_A	B	$10^3\alpha_e$	p	$10^6 q$
$A\,^2\Pi$	11962.174	437.899	1.854	632.409	-0.5068	0.212416	1.2563	-0.257039	-84
$A'\,^2\Omega$	11158.538	437.41	1.833	206.171	0.966	0.210082	1.2052	-2×10^{-8}	
$C\,^2\Pi$	20325.72	459.180	1.6584	195.098	4.4365	0.214560	1.097	-0.013605	-39

Lifetimes & transition moments

	$A^2\Pi_{1/2}$	$A^2\Pi_{3/2}$	$B^2\Sigma$	$C^2\Pi_{1/2}$	$C^2\Pi_{3/2}$
Lifetime (ns)	56.0	46.1	41.7	23.8	23.5
R_e^2 (Debye^2)	37.5	43.9	28.4	16.8	16.8

Table 4.1: Effective electronic, vibrational, and rotational constants for selected states of ^{138}BaF[12] in cm^{-1}. Table 1 in Ref. [12] has a typographic error, and listed values of T_{00} incorrectly as T_e; the values listed here have been corrected appropriately. The state lifetimes are from [24, 25]; in Berg et al., R_e^2 is defined as the square of the electronic transition moment to the ground state.

Hund's cases are defined based on the relative strength of certain interactions inside the molecule. In these cases, certain quantum numbers are assumed to be valid, and it is possible to write an explicit expression for the energy levels without having to diagonalize the full Hamiltonian. This is useful if the state of interest is not strongly mixed with other nearby states, and conforms to one

of the Hund's cases. Herzberg [11] provides an approximate formula for the vibrational and rotational energy levels of a Hund's case (a) state, which often describes low-J states within a $^2\Pi$ band (and holds very well for the A $^2\Pi$ state of BaF):

$$\begin{aligned} E(v,J,P) &= T_e + \omega_e\left(v+\tfrac{1}{2}\right) - \omega_e\chi_e\left(v+\tfrac{1}{2}\right)^2 + (A-\alpha_A v)\,\Lambda\Sigma \qquad (4.2)\\ &\quad + \left(B-\alpha_e\left(v+\tfrac{1}{2}\right)\right) J(J+1) - P(-1)^{J-\frac{1}{2}}\frac{p+2q}{2}\left(J+\tfrac{1}{2}\right) \qquad (4.3)\end{aligned}$$

where

- T_e denotes the electronic energy level spacing
- ω_e and the higher order correction $\omega_e\chi_e$ give the spacing of vibrational levels
- A gives the spin-orbit splitting
- B is the rotational constant that determines the spacing between rotational levels
- α_A and α_e are corrections to A and B for higher vibrational levels
- P is the parity of the state; Λ-doubling leads to two states, one of each parity, for each value of J in states with $\Lambda \geq 1$
- p, q are the Λ-doubling parameters [31]

This formula does not include any parameters for hyperfine structure. A typical case (a) band is shown as the upper state in figure 4.2. The band is split into two bands; in BaF these are separated by hundreds of cm^{-1} by the spin-orbit splitting. Within each of these bands in BaF, the rotational levels (characterized by J) are split into two levels of opposite parity by Λ-doubling.

Herzberg also gives an approximate formula for Hund's case (b) states, when there is little mixing with nearby states (as is valid for the X and D states of BaF):

$$E(v,J,N) = T_e + \omega_e\left(v+\tfrac{1}{2}\right) - \omega_e\chi_e\left(v+\tfrac{1}{2}\right)^2 \quad (4.4)$$

$$+\left(B-\alpha_e\left(v+\tfrac{1}{2}\right)\right)N(N+1)+\frac{\gamma}{2}\text{sign}(J-N)N \quad (4.5)$$

where

- N is the rotational angular momentum of the molecule (such that $\vec{J} = \vec{S}+\vec{N}$)
- γ, the spin-rotation constant, parameterizes the interaction between the spin and rotational angular momentum ($\mathcal{H}_{sr} = \gamma\vec{S}\cdot\vec{N}$)
- the parity P of a Hund's case (b) state is $P = (-1)^N$

The lower state in figure 4.2 shows a typical case (b) band. The rotational levels, characterized by N, are split into two levels of the same parity but different J by spin-rotation interactions. It is worth noting (for the purpose of calculations) that Brown and Carrington [31] provides a formula relating case (a) and (b) states.

The spectral data reported in the literature is primarily for ^{138}BaF. However, we are ultimately interested in the odd-N isotope ^{137}BaF. Hence, we need to know how to use the reported constants to calculate the position of ^{137}BaF levels. There are well-known formulas to modify the effective constants for use

with a different isotope [11]. The most important corrections are:

$$\omega_e' = \rho\omega_e \tag{4.6}$$

$$\omega_e x_e' = \rho^2 \omega_e x_e \tag{4.7}$$

$$B' = \rho^2 B \tag{4.8}$$

$$\alpha' = \rho^3 \alpha \tag{4.9}$$

where $\rho \equiv \sqrt{\mu/\mu'}$, $\mu \equiv \frac{m_1 m_2}{m_1+m_2}$, m_1, m_2 are the masses of the isotopes of the initial set of constants, and m_1', m_2' are the masses of the desired isotopes. This is a necessary, but not sufficient, step to understand the spectra of different isotopes; for example, these formulas predict the first R branch line of ^{137}BaF to be at an energy 0.0063 cm^{-1} (188 MHz) below the line for ^{138}BaF, and the line for ^{136}BaF to be 0.0126 cm^{-1} (378 MHz) below the ^{138}BaF line. The ^{138}BaF and ^{136}BaF isotopes have only weak hyperfine structure from the ^{19}F nucleus, and so their spectra will look similar. However, the ^{137}BaF isotope has a hyperfine splitting of about 0.14 cm^{-1} (4.3 GHz), which is much larger than the size of the isotope shift. There is also a purely electronic isotope shift, typically of order 1 GHz for change in mass by 1 amu, for transitions of this type in heavy molecules [36]. This electronic shift arises from the change in nuclear volume, along with the finite overlap of the electron wavefunction with the nucleus and is not included in these formulas.

Based on equations 4.3, 4.5, and 4.7, the approximate transition frequencies can be calculated for the P ($J' = J-1$)[1], Q ($J' = J$) and R ($J' = J+1$) branch lines - that is, frequencies to which the laser should be tuned to excite BaF. These results have been found to be correct to within our experimental accuracy (about 0.02 cm^{-1}) for low values of J. A table of the estimated positions for the $X-A$, $X-D$, and $A-D$ transitions of ^{138}BaF and for the $X-A$ transition

[1] J' in the upper state, J in the lower state

State	Isotope	b_F, Ba	c, Ba	b_F, F	c, F	q_0Q
X	138	0	0	63.5	8.2	0
X	137	2400	48	63.5	8.2	-117
$A^2\Pi_{1/2}$	138,137	0	0	0	0	0
D	138	0	0	38	8.2	0

All values in MHz.

State	g_S^e	g_L	$g_\parallel$	$g_\perp$	g_N, Ba (μ_N)	g_N, F (μ_N)
X, ^{138}BaF	1.98		1.998	1.992	0	4.55
X, ^{137}BaF	1.98		1.998	1.992	1.21	4.55
A, ^{138}BaF	1.864	1.05	-0.24	-0.48	0	4.55
D, ^{138}BaF	1.98		1.98	1.974	0	4.55

For the $^2\Sigma$ states, $g_\parallel = g_S^e$ and $g_\perp = g_S^e + g_l^e$. The g_S^e, g_L are given in terms of Bohr magnetons (μ_B).
For the A $^2\Pi_{1/2}$ state, $g_\parallel = g_S^e - 2g_L$ and $g_\perp = g_{l'}$.

Table 4.2: Hyperfine and Zeeman constants for selected states of BaF; hyperfine data is based on Ref. [33], the Zeeman constants g_S, g_L are from Steimle [56]. The nuclear Zeeman constants g are from [34]. The values for $g_\perp$ in the A state and b_F,F in the D state are calculated from our spectroscopic measurements.

of ^{137}BaF is given in appendix E.

The hyperfine and Zeeman constants used are shown in table 4.2 [33]. The effective Hamiltonian for the hyperfine interaction looks like [29]

$$\mathcal{H}_{\text{hfs}} = aI_zL_z + b_F\vec{I}\cdot\vec{S} + \frac{1}{3}c\left(3I_zS_z - \vec{I}\cdot\vec{S}\right) - \frac{1}{2}d\left(S_+I_+ + S_-I_-\right) \qquad (4.10)$$

so, in general, we expect the hyperfine constants to be nonzero only for isotopes with a nonzero nuclear spin (eg. ^{137}Ba, ^{19}F). In addition, since the strength of the hyperfine interaction depends on the overlap of the electron wavefunction with the nucleus, we expect it to be largest for states with significant s-orbital character, i.e. Σ states.

The Zeeman Hamiltonian accounts for the interaction between the electron spin, electron angular momentum, and the external magnetic field [35]. The

largest contributions are:

$$\mathcal{H}_z = -\mu_B \left(g_S \vec{S} \cdot \vec{B} + g_L \vec{L} \cdot \vec{B} \right) \tag{4.11}$$

In general, the constants g_S and g_L must be measured for the molecule in question, but are often expected to be close in value to $g_S \approx 2.002$ and $g_L \approx 1$. However, for an ideal $^2\Pi_{1/2}$ state, the projection of the spin along the internuclear axis $\Sigma = \pm 1/2$ and, to keep $\Omega = |\Sigma + \Lambda| = 1/2$, then $\Lambda = \mp 1$. Therefore, $\vec{L}$ and $\vec{S}$ point in opposite directions, and $\left(g_S \vec{S} + g_L \vec{L} \right) \approx \left(2.002 \cdot \frac{1}{2} - 1 \cdot 1 \right) = 0.001$ [35]. So, in this case, the Zeeman effect is almost completely cancelled out. In practice, spin-orbit interactions can cause the effective coefficient of the spin-field interaction $g_S^e \vec{S} \cdot \vec{B}$ to deviate from g_S by a significant amount. This is discussed in more detail in section 4.4.4.

4.4 Empirical Hamiltonian for Energy Levels

For better accuracy, and for predicting energy levels in a strong external field, it is useful to diagonalize the effective Hamiltonian that was used to produce the constants provided in the literature. The Hamiltonian includes terms that describe interactions within the molecule (rotation, spin-rotation interaction, hyperfine, etc.), and interactions between the molecule and external electric or magnetic fields. The general procedure is:

1. Choose a set of basis states.
2. Use the molecular constants to calculate the matrix elements of the effective Hamiltonian in the chosen basis.
3. Diagonalize the Hamiltonian matrix to find the energy levels in the system.

There are two sets of codes used to calculate the states of the molecule for this experiment. The first was provided by Steimle [56]; the code is based on a calculation in the Hund's case ($a_{\beta s}$) basis[2] described by Brown and Kopp [29] with some modifications based on Brown and Carrington [31] to accommodate calculations on molecules with two nuclear spins. This code is designed to calculate $^2\Sigma$ and $^2\Pi$ states, as well as transition strengths and simulated spectra, including the effects of finite temperature. However, our version of the code only calculates field-free spectra. As a result, this code is particularly useful for identifying spectral features but not for calculating the structure of the levels in the field. More detailed information on this program can be found in appendix H, with a description of the procedure below.

The second program was written by Kozlov, based on his calculations in the Hund's case (c) basis [3]. This code is designed to calculate the energy levels in the presence of an external magnetic and electric field, locate level crossings, and calculate the dipole matrix element between sublevels near the crossing. It has been extended to calculate the transition strength and simulate spectra. The original code has also been modified to add a nuclear Zeeman effect term to the Hamiltonian ($\mathcal{H}_{z,nuc} = -\vec{\mu}_I \cdot \vec{B}$), display state content of a given level, and to run within Mathematica for easier manipulation and display of the output data. A detailed description of the usage and structure of the program is given in appendix H.1.

[2]The case ($a_{\beta s}$) basis is an extension of the Hund's case (a) basis to include a coupling scheme for nuclear spins.

4.4.1 General Form of the Effective Hamiltonian

Within a given electronic and vibrational state, a suitable effective Hamiltonian will include the terms [29]:

$$\mathcal{H} = \mathcal{H}_{SO} + \mathcal{H}_{SS} + \mathcal{H}_{SR} + \mathcal{H}_{rot} + \mathcal{H}_{cd} + \mathcal{H}_{LD} + \mathcal{H}_{hfs} + \mathcal{H}_{Q} \tag{4.12}$$

where (in the molecule-fixed frame)

- $\mathcal{H}_{SO} = AL_zS_z$ is the spin-orbit interaction
- $\mathcal{H}_{SS} = \frac{2}{3}\lambda\left(3S_z^2 - \vec{S}^2\right)$ is the spin-spin interaction; for a doublet state, $\vec{S}^2 = \frac{1}{2}\left(\frac{1}{2}+1\right)$ and $3S_z^2 = 3\left(\frac{1}{2}\right)^2$ so that this term is zero and λ is undefined
- $\mathcal{H}_{SR} = \gamma\vec{S}\cdot\vec{N}$ is the spin-rotation interaction
- $\mathcal{H}_{rot} = B\vec{R}^2$ is the rotational kinetic energy, where $\vec{R} \equiv \vec{J} - \vec{L} - \vec{S} = \vec{N}$ in a Hund's case (a) or (c) coupling scheme
- $\mathcal{H}_{cd} = -D\vec{R}^2\vec{R}^2$ is the centrifugal distortion energy; this term is typically much smaller than the rotational kinetic energy ($D \approx 10^{-6}B$) and is negligible at small $\vec{J}$. For the purposes of this experiment, this term can be neglected (though values are available in [12])
- $\mathcal{H}_{LD} = \frac{1}{2}o\left(S_+^2 + S_-^2\right) - \frac{1}{2}p\left(N_+S_+ + N_-S_-\right) + \frac{1}{2}q\left(N_+^2 + N_-^2\right)$ is the Λ-doubling Hamiltonian (links states with $\Delta\Lambda = \pm1, \pm2$). For doublet states, the operators S_+^2 and S_-^2 (which connect states with $\Delta S{=}\pm2$) will be zero and o is undefined
- $\mathcal{H}_{hfs} = aI_zL_z + b_F\vec{I}\cdot\vec{S} + \frac{1}{3}c\left(3I_zS_z - \vec{I}\cdot\vec{S}\right) - \frac{1}{2}d(S_+I_+ + S_-I_-)$ is the magnetic hyperfine interaction (this will apply to each nonzero nuclear spin in the molecule). a and d will be zero for ^{138}BaF, a is zero for the

ground state of ^{137}BaF ($L_z = 0$), and d is assumed to be negligbly small for ^{137}BaF. b_F is sometimes referred to as A_{iso}, or the Fermi contact term; c is equivalent to A_{dip}

- $\mathcal{H}_Q = \frac{eq_0Q}{4I(2I+1)}\left(3I_z^2 - \vec{I}^2\right) - \frac{eq_2Q}{8I(2I-1)}\left(I_+^2 + I_-^2\right)$ is the electric quadrupole hyperfine interaction; q_2Q is zero for ^{138}BaF, and is asssumed to be negligibly small for ^{137}BaF.

Some of these interactions are relatively straightforward; for example, $\mathcal{H}_{rot}$ is analogous to the classic rotational kinetic energy of a dumbbell spinning about its center of mass. The rotational angular momentum is

$$I\dot{\theta} = \hbar\vec{R}$$

and so the rotational kinetic energy is:

$$E_{rot} = \frac{1}{2}I\dot{\theta}^2 = \frac{\hbar\vec{R}^2}{2I}$$

The moment of inertia of a dumbbell is [3]

$$I = \mu r_0^2$$

[3]For a dumbbell with weights m_1 at a distance r_1 and m_2 at a distance r_2 from the center of mass, separated by a total distance r_0,

$$\begin{aligned} r_1 m_1 &= r_2 m_2 \\ r_0 &= r_1 + r_2 = r_1\frac{m_1+m_2}{m_2} = r_2\frac{m_1+m_2}{m_1} \end{aligned}$$

the moment of inertia is

$$\begin{aligned} I &= m_1 r_1^2 + m_2 r_2^2 \\ &= \frac{r_0^2}{(m_1+m_2)^2}\left(m_1 m_2^2 + m_1^2 m_2\right) \\ &= \mu r_0^2 \end{aligned}$$

where $\mu \equiv \frac{m_1 m_2}{m_1+m_2}$ is the reduced mass.

and so the rotational kinetic energy is

$$E_{rot} = \frac{\hbar \vec{R}^2}{2\mu r_0^2} \equiv B\vec{R}^2$$

This can be used as a way to calculate the equilibrium internuclear distance r_0, given the rotational constant B.

The spin-orbit interaction AL_zS_z is present in the $^2\Pi$ state. Its diagonal matrix element evaluates to $A\Lambda\Sigma$, and is (for the A state of BaF) the largest term; it separates the $^2\Pi_{1/2}$ and $^2\Pi_{3/2}$ states. If it is only necessary to consider the $^2\Pi_{1/2}$ state, it can be assumed there is no mixing between these and work with just the $\Omega = 1/2$ states.

The arrangement of some of the other terms in the Hamiltonian is less straightforward. The arrangement of constants in the hyperfine interaction, for example, uses $\vec{I} \cdot \vec{S}$ as part of two separate terms. Taken this way, b_F can be interpreted as related to the overlap of the electron wavefunction at the nucleus $|\Psi(0)|^2$ [31] and the constant c is related to $\left\langle \left(3\cos^2\theta - 1\right)/r^3 \right\rangle$. This relationship is important to note, since the strength of a possible parity-violating interaction depends, like b_F, on the value of $|\Psi(0)|^2$. The hyperfine constants can be rewritten in the form

$$\begin{aligned} A_\parallel &\equiv b_F + \frac{2}{3}c \\ A_\perp &\equiv b_F - \frac{c}{3} \end{aligned}$$

which serves the purpose of putting $\mathcal{H}_{\rm hfs}$ in the form

$$\mathcal{H}_{\rm hfs} = A_\parallel S_z I_z + A_\perp \left(S_x I_x + S_y I_y\right)$$

4.4.2 Calculation in the Hund's Case ($a_{\beta s}$) Basis

The Hund's case ($a_{\beta s}$) basis uses the quantum numbers

$$|S\,\Sigma;\ \Lambda\,\Omega\,J;\ I_1\,F_1\,I_2\,F\,m_F\rangle \tag{4.13}$$

to generate a complete basis set for a single electronic and vibrational state with two nuclear spins $\vec{I}_1$ and $\vec{I}_2$. The projections of the orbital angular momentum ($\Lambda \equiv \vec{L}\cdot\hat{n}$) and spin ($\Sigma \equiv \vec{S}\cdot\hat{n}$) to the intermolecular axis are presumed to be good quantum numbers, through moderately strong spin-orbit interactions coupling $\vec{L}$ and $\vec{S}$, and strong electrostatic forces coupling $\vec{L}$ to the internuclear axis $\hat{n}$ [31]. $\Omega \equiv \Lambda + \Sigma$ is therefore also a good quantum number. The angular momentum of the molecule $\vec{J}$ is the sum of the electron spin, electron orbital angular momentum, and the rotation of the molecule: $\vec{J} = \vec{S} + \vec{L} + \vec{N}$. In this scheme, the angular momentum $\vec{J}$ is coupled with the first nuclear spin $\vec{I}_1$ to form the intermediate sum $\vec{F}_1 = \vec{J} + \vec{I}_1$, and this is taken to form the total angular momentum $\vec{F} = \vec{F}_1 + \vec{I}_2$. In order to more easily compare to Brown and Kopp [29] which was written with one nuclear spin in mind, the second nuclear spin can be separated:

$$|S\Sigma\Lambda\Omega J I_1 F_1 I_2 F m_F\rangle = \sum_{m_{I_2}=-I_2}^{I_2} \langle F_1 m_{F_1}; I_2 m_{I_2}|F m_F\rangle |S\Sigma\Lambda\Omega J I_1 F_1 m_{F_1}\rangle |I_2 m_{I_2}\rangle \tag{4.14}$$

where $m_{F_1} = m_F - m_{I_2}$ in order to have a nonzero Clebsch-Gordan symbol. With the second nuclear spin decoupled, the remaining wavefunction can be used to treat any interaction that does not act upon $|I_2 m_{I_2}\rangle$. In the same way, $|I_1 m_{I_1}\rangle$ is decoupled to make states of the form $|S\Sigma\Lambda\Omega J m_J\rangle\ |I_1 m_{I_1}\rangle\ |I_2 m_{I_2}\rangle$, and $\vec{J} + \vec{I}_2$ can be recombined to study hyperfine for the second nuclear spin using the formulas given. It is also worth noting that a Hund's case (a) state can be

written in terms of parity eigenstates (eg. Brown and Carrington 10.116):

$$\begin{aligned} |J\, m_J +\rangle &= \frac{1}{\sqrt{2}}\left(|\Lambda, S, +\Sigma, J, m_J, \Omega\rangle + (-1)^{J-S}\,|-\Lambda, S, -\Sigma, J, m_J, -\Omega\rangle\right) \\ |J\, m_J -\rangle &= \frac{1}{\sqrt{2}}\left(|\Lambda, S, +\Sigma, J, m_J, \Omega\rangle - (-1)^{J-S}\,|-\Lambda, S, -\Sigma, J, m_J, -\Omega\rangle\right) \end{aligned}$$

or, by inverting this to solve for the case (a) state,

$$\begin{aligned} |\Lambda, S, +\Sigma, J, m_J, \Omega\rangle &= \frac{1}{\sqrt{2}}\left(|J\, m_J +\rangle + |J\, m_J -\rangle\right) \\ |-\Lambda, S, -\Sigma, J, m_J, -\Omega\rangle &= \frac{(-1)^{J-S}}{\sqrt{2}}\left(|J\, m_J +\rangle - |J\, m_J -\rangle\right) \end{aligned}$$

where $+\Sigma$ denotes a state with positive Σ and $-\Sigma$ with negative Σ. When it is possible to neglect electronic angular momentum (e.g. some $^2\Sigma$ states), these parity eigenstates can be rewritten in terms of $|N\, m_N\rangle|S\, m_S\rangle$:

$$\begin{aligned} |J\, m_J +\rangle &= \sum_{m_S=-S}^{S} \langle N,\, m_N;\, S,\, m_S|\, J,\, m_J\rangle\, |N,\, m_N;\, S,\, m_S\rangle\,, \; N \text{ even} \\ |J\, m_J -\rangle &= \sum_{m_S=-S}^{S} \langle N,\, m_N;\, S,\, m_S|\, J,\, m_J\rangle\, |N,\, m_N;\, S,\, m_S\rangle\,, \; N \text{ odd} \end{aligned}$$

where $m_N = m_J - m_S$ and N is chosen to be an even (+) or odd (-) integer from $J - S \leq N \leq J + S$. This is useful for analyzing the parity and projection of the spin m_S of a given eigenstate calculated in the case (a) basis.

4.4.3 Calculation in the Hund's Case (c) Basis

The Hund's case (c) basis uses the quantum numbers

$$|S\, \Omega\, J_e\, J; I_1\, F_1\, I_2\, F\, m_F\rangle$$

to generate a complete basis set for a single electronic and vibrational state with two nuclear spins $\vec{I}_1$ and $\vec{I}_2$. This case arises when the spin-orbit coupling is larger than the coupling to the internuclear axis; the projections $\Lambda \equiv \vec{L} \cdot \hat{n}$ and $\Sigma \equiv \vec{S} \cdot \hat{n}$ are no longer good quantum numbers. However, the total electronic angular momentum's projection onto the intermolecular axis ($\Omega \equiv \vec{J}_e \cdot \hat{n}$) is considered to be a good quantum number. In general, it is not possible to explicitly relate case (c) states to case (a) or (b). However, in the case of doublet molecules in $^2\Sigma$ or $^2\Pi$ states, such a transformation is possible. Here, each value of $\Omega = \pm\frac{1}{2}, \pm\frac{3}{2}$ corresponds to a unique combination of Σ and Λ. This relationship is valid to the extent that a given electronic state (eg. A $^2\Pi$) can be considered "pure"; the presence of strong interactions between nearby states (eg. A $^2\Pi$ and A' $^2\Delta$) would require the use of a true case (c) basis in which Λ is not assumed to be a good quantum number.

4.4.4 Zeeman Hamiltonian

An external magnetic field shifts the energy levels of the molecules and lifts the degeneracy of the magnetic sublevels m_F. The largest effects come from the interaction of the electron spin or orbital angular momentum with the magnetic field, but there are also non-negligible effects from the interaction of the nuclear spin and molecular rotation with the field. The Zeeman Hamiltonian for a $^2\Sigma$ state is [35, 31][4]

$$\begin{aligned} {}^2\Sigma: \mathcal{H}_Z &= \mu_B \left((g_S^e + g_l^e)\, \vec{S} \cdot \vec{B} - g_l^e\, (\vec{S}\cdot\hat{n})\, (\vec{B}\cdot\hat{n}) - g_r \vec{N} \cdot \vec{B} \right) + \mu_N g_N \vec{I} \cdot \vec{B} \\ &= \mu_B \left(g_\perp \vec{S}\cdot\vec{B} + (g_\parallel - g_\perp)\, (\vec{S}\cdot\hat{n})\, (\vec{B}\cdot\hat{n}) - g_r \vec{N}\cdot\vec{B} \right) + \mu_N g_N \vec{I} \cdot \vec{B} \end{aligned} \quad (4.15)$$

[4]For quick reference, a summary of the notation used for the hyperfine and Zeeman Hamiltonians is given in section 4.7.

where, to second order,

$$g_{\|} = g_S - 2\xi \sum_n \frac{\langle 0 | L_z | n \rangle \langle n | L_z | 0 \rangle}{E_n - E_0} - 2\xi^2 \sum_n \frac{|\langle n | L_x | 0 \rangle|^2}{(E_n - E_0)^2}$$

and

$$g_{\perp} = g_S - 2\xi \sum_n \frac{\langle 0 | L_x | n \rangle \langle n | L_x | 0 \rangle}{E_n - E_0}$$

where ξ is the molecular constant defined by the spin-orbit Hamiltonian[5], $\mathcal{H}_{SO} = \xi \vec{L} \cdot \vec{S}$, and n numbers the excited states. For a $^2\Sigma$ state, $\langle n | L_z | 0 \rangle = 0$ and so $g_{\|} \equiv g_S^e$ differs from $g_S = 2.002$ by a small amount related to the second-order term. This leads to the definition

$$\Delta g_{\perp} \equiv \frac{2\xi}{E_{\Pi} - E_{\Sigma}} \langle \Pi | L_x | \Sigma \rangle \langle \Sigma | L_x | \Pi \rangle$$

for a Σ state interacting with an excited Π state. In the notation above, $g_{\perp} \equiv g_S^e + g_l^e$. The Curl equation

$$\gamma = -2B\Delta g_{\perp} \tag{4.16}$$

relates g_l^e (which is approximately $\Delta g_{\perp}$) to the spin-rotation coupling γ and rotational constant B:

$$g_l^e \approx -\frac{\gamma}{2B} \tag{4.17}$$

which, for BaF, is about 0.0063.

The third term $(g_r \vec{N} \cdot \vec{B})$ is the rotational magnetic moment. $g_r \equiv g_r^n - g_r^e$ receives contributions from the nuclear rotation (g_r^n) and the rotation of the

[5]Weltner uses ξ as the spin-orbit constant for the molecular wavefunction, and ζ as the spin-orbit constant for an atom (expected to be similar to the molecular constant). For example, in the $A^2\Pi$ state of BaF, ξ would refer to the spin-orbit constant A, and ζ would be the spin-orbit constant in a $5d$ state of Ba^+. In some parts of the book, the two symbols are used interchangeably.

electron wavefunction (g_r^e). Weltner suggests that

$$g_r^n \approx \frac{1}{2}\mu_N = \frac{1}{2}\frac{m_e}{m_p}\mu_B \tag{4.18}$$

for diatomic molecules other than hydrides; that is $g_r^n \approx 2.7\times10^{-4}$. An alternate derivation (connecting the calculation of g_r to the dipole moment) is presented in reference [37]. The electron component g_r^e is related to the spin-rotation and spin-orbit interaction ξ through the Curl equation:

$$g_r^e \approx \frac{|\gamma|}{\xi} \tag{4.19}$$

For a heavy element like Ba, ξ would be large enough to suppress g_r^e to a level negligible for our experiment. An initial estimate of ξ for the $X^2\Sigma$ state can be made using the decomposition of the state into atomic orbitals (eq. 4.1). The atomic spin-orbit splitting for ^{55}Cs ($6p$ orbital) is 554 cm^{-1} and the state makeup of $X^2\Sigma$ is 76% $6s$; we would expect to find $\xi \approx 0.24 \cdot 554$ cm^{-1} = 133 cm^{-1} and that g_r^e will be on the order of 10^{-5} for the X state. Bernard et al. [12] note that (at least in the A, A′, and B states) mixing with orbitals with smaller spin-orbit coupling constants substantially reduces the observed value of ξ.

The last term ($\mu_N g_N \vec{I}\cdot\vec{B}$) involves the interaction between the nuclear spin (^{19}F for ^{138}BaF) with the magnetic field. g_N is of order unity (≈ 4.55 for ^{19}F), but this term is overall suppressed by the ratio of $\mu_N/\mu_B = m_e/m_p \approx 5.4\times10^{-4}$ relative to $g_\parallel$.

Figure 4.4 shows the effect of the various terms of the Zeeman Hamiltonian on the crossings of $m_F = 0$ states ($N = 0, 1$) near $B_z = 4630$ Gauss. We measure the population transfer between the two states due to an applied DC electric field as a function of magnetic field, as outlined in chapter 7, and observe a resonance

when the levels cross (shown on the plot inset). The coefficients of the various terms ($g_\perp$ and g_r) are then adjusted to match the observed resonances.

- The most significant contribution to the level energy is from the interaction of the electron spin ($g_\parallel$) with the magnetic field; this shifts the levels by nearly 6500 MHz, to bring one $N = 0$ state and two $N = 1$ states together. However, the two $N = 1$ states are left nearly degenerate. In the absence of additional interactions, the two crossings with the $N = 0$ state would occur at nearly the same magnetic field.

- Introduction of the nuclear magnetic moment g_N and the rotational Zeeman term g_r splits the two $N = 1$, m_F=0 levels and increases the separation between their two crossings with the N=0, m_F=0 level.

In figure 4.4, the energy of each of the three $m_F = 0$ states is shown as a function of the magnetic field and the g-factors in the first table. The second table shows the magnetic field B_z of the two crossings as a function of the g-factors. This is used to find g_r given the magnetic field at which the resonance is observed. This measurement can be remarkably precise, as a shift in the energy of the $N = 1$ levels by 1 MHz corresponds to a 0.71 Gauss shift in the magnetic field at crossing (and the magnetic field is controlled to an accuracy of about 1 milliGauss). However, these terms (g_N, g_r) have a similar effect for the two $m_F = 0$ levels and cannot be distinguished from a measurement of these two crossings[6]. Accurate determinations of the nuclear Zeeman effect ($g_N = 5.2578$ for ^{19}F) based on NMR studies are available for ^{19}F and ^{137}BaF in the literature [34], and so we choose to adjust g_r instead to match the measured splitting of the crossings. The value of $g_\parallel \equiv g_S^e$ was then adjusted to match the position

[6]The nuclear Zeeman term gives a matrix element proportional to $m_I \delta_{I,I'} \delta_{J,J'} \delta_{\Omega,\Omega'}$, while the rotational term is proportional to $m_J \delta_{I,I'} \delta_{J,J'} \delta_{\Omega,\Omega'}$. For $m_F = 0$, $m_J = -m_I$ and these terms will have similar effects. Observations at additional values of m_F would allow unique determination of g_r and g_N.

and the values $g_r = -(1.47 \pm 0.01) \times 10^{-3}$ and g_S^e=1.998±0.001 (deviation of -0.003 from g_S=2.001) were observed. Using

$$g_r \approx \frac{1}{2}\frac{m_e}{m_p} - \frac{|\gamma|}{\xi} \tag{4.20}$$

(eqs. 4.18, 4.19) suggests a value of $\xi \approx 1.6$ cm^{-1} for the spin-orbit coupling. As mentioned before, this is much smaller than the anticipated value. However, given the possibility of other corrections at a similar level, this interpretation of the value of g_r remains to be confirmed by observing other crossings in BaF. The crossing of the two m_F=1 levels at approximately 4600 Gauss would be an ideal place to look for confirmation of these values.

The Zeeman Hamiltonian for the $^2\Pi$ state includes contributions related to the electronic orbital angular momentum:

$$\begin{aligned} {}^2\Pi: \quad \mathcal{H}_Z &= \mu_B \Big(g_S^e \vec{S}\cdot\vec{B} + (g_L' + g_r)\,\vec{L}\cdot\vec{B} - g_r \vec{N}\cdot\vec{B} + g_l\,(S_x B_x + S_y B_y) \\ &\quad - g_r^{e\prime}\left(e^{-2i\phi}N_+ B_+ + e^{2i\phi}N_- B_-\right) \\ &\quad + g_l'\left(e^{-2i\phi}S_+ B_+ + e^{2i\phi}S_- B_-\right)\Big) + \mu_N g_N \vec{I}\cdot\vec{B} \end{aligned}$$

Our interest in the $^2\Pi$ state is for the prediction of spectra (transition frequencies and strengths) in a magnetic field. In this case, smaller contributions that result in shifts smaller than the linewidth can be neglected ($\sim$ 5 MHz; i.e. effects at a level $\sim$1000 times less precise than needed for the X state level crossings). The largest values are g_S^e and g_L', which are usually close to the values expected outside of a molecule ($g_S = 2.002$ and $g_L = 1$, respectively). Steimle [28] reports values of $g_S^e = 1.86$ and $g_L' = 1.05$. The spin-rotation constant γ is not defined for the $^2\Pi$ state, but it is assumed that g_l will be small. The rotational Zeeman term g_r is also expected to be small (order of 10^{-3}, as in the $^2\Sigma$ state). The two remaining new terms, $g_r^{e\prime}$ and g_l', contain raising and lowering operators that

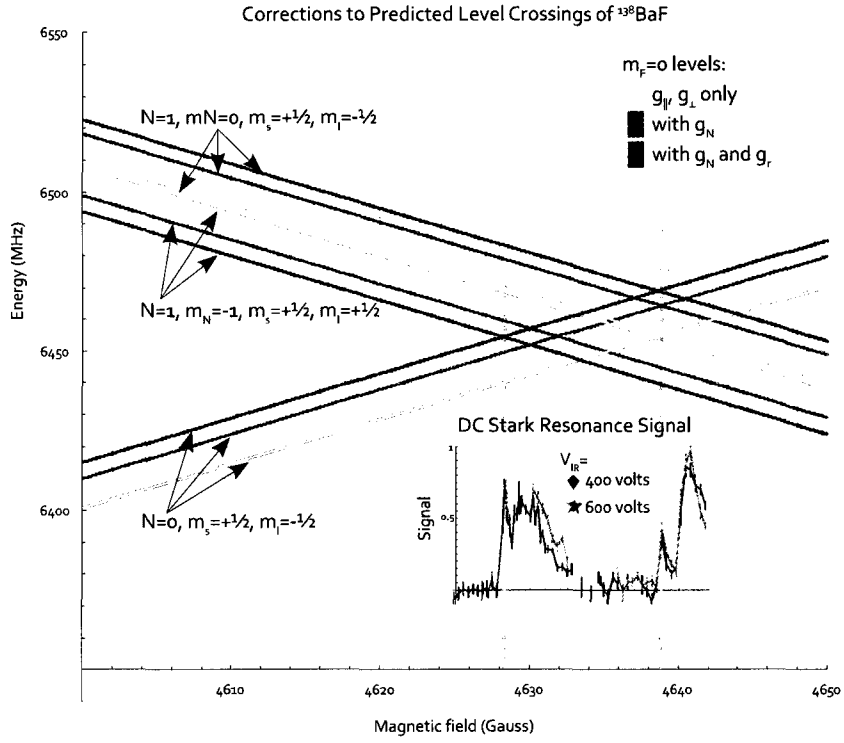

a)

b)

State	Energy (MHz) at B_z (in Gauss)
$N=0$	$-24.27+1.3967B_z+1.764g_N-3469.6g_r$
$N=1$	$12937.4-1.3977B_z-1.729g_N+3467.3g_r$
$N=1$	$12916.2-1.3928B_z+1.729g_N-2993.0g_r$

c)

Crossing	Resonance at B_z (Gauss)
1	$0.35786\,(12961.7-3.49g_N+6936.88g_r)$
2	$0.35848\,(12940.5-0.03547g_N+476.55g_r)$

Figure 4.4: The nuclear ($\mu_N g_N \vec{I}\cdot\vec{B}$) and rotational ($\mu_B g_r \vec{N}\cdot\vec{B}$) Zeeman terms make small but important contributions to the energy shift in a strong magnetic field. Since the magnetic field is controlled to an accuracy of $\approx$1 milliGauss, measurements of the level crossings (shown on inset graph) give significant information about the strength of these effects (part a). The parameters g_N and g_r are much smaller than g_s, but are necessary to lift the near-degeneracy of the two N=1 levels. If it is assumed that the energy levels vary linearly in the limit of small values of g_N and g_r, (e.g. first order perturbation theory), the energies of each of the states can be written as a linear combination of these constants (part b). Solving for the crossings of two levels (part c) relates the observed position of the resonance with the g-factors.

connect states with different N and L; the states connected by these operators are mixed by the Λ-doubling Hamiltonian:

$$\mathcal{H}_{LD} = -\frac{1}{2}p\left(N_+S_+ + N_-S_-\right) + \frac{1}{2}q\left(N_+^2 + N_-^2\right)$$

So, typically $g_r^{e\prime} \approx -\frac{q}{B}$ and $g_l' \approx \frac{p}{2B}$. The value of $g_r^{e\prime} \approx -4 \times 10^{-4}$ is small enough to ignore, but $g_l' \approx -0.6$ is of order unity. Figure 4.12 shows how a value of $g_l' = -0.48 \pm -0.05$ was observed using the spectra under $\hat{x}, \hat{y}$-polarized light.

It is easiest to see how $g_\parallel$ and $g_\perp$ are defined in the $^2\Pi$ state by examining the calculation of the Zeeman Hamiltonian for a $^2\Sigma$ or $^2\Pi_{1/2}$ state in a Hund's case (a) or (c) basis. Brown and Carrington [31] gives an explicit form for the matrix elements in a case (a) basis (eq. 9.71, neglecting $g_r^{e\prime}$)[7]:

$$\begin{aligned}
&\langle \Lambda; S, \Sigma; J, \Omega; m_J; I, m_I \,|\mathcal{H}_Z|\, \Lambda'; S, \Sigma'; J', \Omega'; m_J; I, m_I\rangle \\
&= \mu_B B_z \left(-1\right)^{J-m_J+J-\Omega} \sqrt{\left(2J+1\right)\left(2J'+1\right)} \begin{pmatrix} J & 1 & J' \\ -m_J & 0 & m_J \end{pmatrix} \\
&\quad \times \left[\sum_q \delta_{\Lambda,\Lambda'} \begin{pmatrix} J & 1 & J' \\ -\Omega & q & \Omega' \end{pmatrix} \left\{\left(g_L' + g_r\right)\Lambda\delta_{\Sigma,\Sigma'} - g_l\Sigma\delta_{\Sigma,\Sigma'}\right.\right. \\
&\quad \left.\left. + \left(g_S^e + g_r + g_l\right)\left(-1\right)^{S-\Sigma}\sqrt{S\left(S+1\right)\left(2S+1\right)} \begin{pmatrix} S & 1 & S \\ -\Sigma & q & \Sigma' \end{pmatrix}\right\}\right. \\
&\quad \left. - \sum_{q=\pm 1} \delta_{\Lambda,\Lambda\pm 2} g_l' \begin{pmatrix} J & 1 & J' \\ -\Omega & -q & \Omega' \end{pmatrix} \left(-1\right)^{S-\Sigma} \sqrt{S\left(S+1\right)\left(2S+1\right)} \begin{pmatrix} S & 1 & S \\ -\Sigma & q & \Sigma' \end{pmatrix}\right] \\
&\quad - \left(g_r\mu_B B_z m_J + g_N\mu_N B_z m_I\right)\delta_{J,J'}\delta_{\Sigma,\Sigma'}\delta_{\Lambda,\Lambda'}
\end{aligned}$$

For the $^2\Sigma$ state, $\Lambda = 0$ and $\Omega = \Sigma$ so the above expression can be written

[7] $\begin{pmatrix} a & b & c \\ m_a & m_b & -m_c \end{pmatrix} = (-1)^{m_c+a-b}\sqrt{2c+1}\,\langle a, m_a, b, m_b | c, m_c\rangle$ are the Wigner 3-j symbols, which serve a similar purpose as the Clebsch-Gordan coefficients in problems involving the sum of two angular momenta.

as:

$$
\begin{aligned}
{}^2\Sigma: \quad \langle \mathcal{H}_z \rangle &= \mu_B B_z (-1)^{J-m_J+J-\Omega} \sqrt{(2J+1)(2J'+1)} \begin{pmatrix} J & 1 & J' \\ -m_J & 0 & m_J \end{pmatrix} \\
&\quad \times \begin{pmatrix} J & 1 & J' \\ -\Omega & \Omega-\Omega' & \Omega' \end{pmatrix} \left[\{ \delta_{\Omega,\Omega'} (g_S^e + g_r) + \delta_{\Omega,\Omega'\pm 1} (g_S^e + g_r + g_l) \} \right. \\
&\quad \left. \times (-1)^{S-\Omega} \sqrt{S(S+1)(2S+1)} \begin{pmatrix} S & 1 & S \\ -\Omega & \Omega-\Omega' & \Omega' \end{pmatrix} \right] \\
&\quad - (g_r \mu_B B_z m_J + g_N \mu_N B_z m_I) \delta_{J,J'} \delta_{\Omega,\Omega'}
\end{aligned}
$$

Note that this expression for the ${}^2\Sigma$ state matrix element is valid in the Hund's case (a) basis, rather than the case (b) basis that describes the energy eigenstates. The value $g_\parallel \equiv g_S^e + g_r \approx g_S^e$ is defined as the coefficient for matrix elements with $\Omega = \Omega'$, and $g_\perp \equiv g_S^e + g_r + g_l$ to be the coefficient for matrix elements with $\Omega = \Omega' \pm 1$. But for the ${}^2\Pi_{1/2}$ state, $\Lambda = \pm 1$ and $\Sigma = \mp\frac{1}{2}$ are opposite in sign in order to make $\Omega = \pm\frac{1}{2}$:

$$
\begin{aligned}
{}^2\Pi_{1/2}: \quad \langle \mathcal{H}_z \rangle &= \mu_B B_z (-1)^{J-m_J+J-\Omega} \sqrt{(2J+1)(2J'+1)} \begin{pmatrix} J & 1 & J' \\ -m_J & 0 & m_J \end{pmatrix} \\
&\quad \times \begin{pmatrix} J & 1 & J' \\ -\Omega & \Omega-\Omega' & \Omega' \end{pmatrix} \left[\{ \delta_{\Omega,\Omega'} (g_S^e - 2g_L' - g_r) + \delta_{\Omega,\Omega'\pm 1} g_l' \} \right. \\
&\quad \left. \times (-1)^{S-\Omega} \sqrt{S(S+1)(2S+1)} \begin{pmatrix} S & 1 & S \\ -\Omega & \Omega-\Omega' & \Omega' \end{pmatrix} \right] \\
&\quad - (g_r \mu_B B_z m_J + g_N \mu_N B_z m_I) \delta_{J,J'} \delta_{\Omega,\Omega'}
\end{aligned}
$$

In this case, using $g_\parallel \equiv g_S^e - 2g_L' - g_r$ as the coefficient for matrix elements with

$\Omega = \Omega'$ and $g_\perp \equiv g'_l$ for $\Omega = \Omega' \pm 1$ brings the equation to the same functional form. Experimentally determined values for the A $^2\Pi_{1/2}$ state of BaF were found to be $g_\parallel = -0.24 \pm 0.01$ and $g_\perp = -0.48 \pm 0.05$.

4.4.5 Dipole Moment and PNC

The proposed parity violation experiment requires an effective Hamiltonian as a proxy to predict the strength of the parity nonconservation effect between particular combinations of molecular states. The implementation of the parity violation Hamiltonian in chapter 3 that is used in Kozlov's program is[8]:

$$\begin{aligned}
&\left\langle \left(\vec{S} \times \hat{n}\right) \cdot \frac{\vec{I}}{|I|} \right\rangle \\
&= \frac{i}{I_1} \delta_{F_1,F_1'} \delta_{F,F'} \delta_{m_F,m_F'} \delta_{J,J'\pm 1,0} \delta_{\Omega,\Omega'\pm 1} \\
&\quad \times \sqrt{2}\Omega' \left(\Omega - \Omega'\right) (-1)^{F_1'+J+J'+I_1-\Omega} \\
&\quad \times \sqrt{I_1 \left(I_1+1\right) \left(2I_1+1\right) \left(2J+1\right) \left(2J'+1\right)} \\
&\quad \times \left\{ \begin{array}{ccc} F_1' & I_1 & J \\ 1 & J' & I_1 \end{array} \right\} \left(\begin{array}{ccc} J & 1 & J' \\ -\Omega & \Omega - \Omega' & \Omega' \end{array} \right)
\end{aligned}$$

This Hamiltonian will give a matrix element as large as $\frac{1}{2}$ (spin of $S = \frac{1}{2}$ multiplied by two unit vectors) between two states of opposite parity.

It is also necessary to find the dipole matrix element between two levels of the same electronic state; this determines the width of the resonance when the levels are brought to crossing in a laboratory frame electric field $E\hat{z}$:

---

[8] $\left\{ \begin{array}{ccc} a & b & c \\ d & e & f \end{array} \right\}$ are the Wigner 6-j symbols, which are used in problems where interactions work in two separate subsystems, e.g. $\langle a'\, m_a'\, b'\, m_b'\, J'\, m' \left| T^{(k)} \cdot U^{(k)} \right| a\, m_a\, b\, m_b\, J\, m \rangle = \delta_{J,J'} \delta_{m,m'} (-1)^{m_a+m_b'+J} \left\{ \begin{array}{ccc} J & m_a' & m_b' \\ k & m_a & m_b \end{array} \right\} \langle a'\, m_a' \left| T^{(k)} \right| a\, m_a \rangle \langle b'\, m_b' \left| U^{(k)} \right| b\, m_b \rangle$

$$\mathcal{H}_{\text{Stark}} = \left\langle \vec{d} \cdot (E\hat{z}) \right\rangle$$

$$= \langle \eta' \Lambda'; S, \Sigma'; J', \Omega'; I_1, F_1', I_2; F', m_F' \left| \mathcal{H}_{\text{Stark}} \right| \eta\Lambda; S, \Sigma; J, \Omega; I_1, F_1, I_2; F, m_F \rangle$$

$$= D\delta_{\Omega,\Omega'}\delta_{J,J'\pm1,0}\delta_{\Omega,\Omega'\pm1,0}\delta_{F,F'}\delta_{F_1,F_1'}\delta_{m_F,m_F'\pm1,0}\,(-1)^{F+F'+F_1+F_1'+I_1+I_2+\Omega-m_F}$$

$$\times\sqrt{(2F_1+1)\,(2F_1'+1)\,(2F+1)\,(2F'+1)\,(2J+1)\,(2J'+1)}\begin{Bmatrix} F_1 & F & I_2 \\ F' & F_1' & 1 \end{Bmatrix}$$

$$\times\begin{Bmatrix} J & F_1 & I_1 \\ F_1' & J' & 1 \end{Bmatrix}\begin{pmatrix} F & 1 & F' \\ -m_F & m_F - m_F' & m_F' \end{pmatrix}\begin{pmatrix} J & 1 & J' \\ -\Omega & \Omega - \Omega' & \Omega' \end{pmatrix}$$

The overall constant D is the body-fixed dipole moment of the electronic state (D=3 Debye for the X state of BaF [27]). As will be shown later, this results in matrix elements on the order of 0.1-3 kHz/(V/cm) for most of the level crossings.

4.4.6 Electronic Transitions and Predicted Laser Excitation Spectra

Electronic transitions are allowed for states of opposite parity with the same projections of electronic and nuclear spin, and $\Delta J = 0, \pm 1$. Transition strengths are calculated based on the case (a) matrix element of the electric dipole operator μ given in Brown and Kopp [29], extended for use in molecules with two nonzero

nuclear spins:

$$\begin{aligned}
\mu \equiv & \left\langle \eta' \Lambda' S \Sigma' J' \Omega' I_1 F_1' I_2 F' m_F' \left| T_p^1(\mu) \right| \eta \Lambda S \Sigma J \Omega I_1 F_1 I_2 F m_F \right\rangle \\
= & \sum_{m_{I_2}} \delta_{\Sigma,\Sigma'} \delta_{m_F, m_F'+p} \left\langle F_1, m_{F_1}; I_2, m_{I_2} \right| F, m_F \rangle \left\langle F_1', m_{F_1}'; I_2, m_{I_2} \right| F', m_F' \rangle \\
& \times (-1)^{F_1+F_1'-m_{F_1}'+2J'+I_1+1-\Omega'} \begin{pmatrix} F_1' & 1 & F_1 \\ -m_{F_1}' & p & m_{F_1} \end{pmatrix} \begin{Bmatrix} I_1 & J' & F_1' \\ 1 & F_1 & J \end{Bmatrix} \\
& \times \sqrt{(2J'+1)(2J+1)} \sqrt{(2F_1'+1)(2F_1+1)} \\
& \times \begin{pmatrix} J' & 1 & J \\ -\Omega' & \Omega'-\Omega & \Omega \end{pmatrix} \sum_q \left\langle \eta' \Lambda' \left| T_q^1(\mu) \right| \eta \Lambda \right\rangle
\end{aligned}$$

where $T_p^1(\mu)$ is the spherical tensor decomposition of the electric dipole operator $\vec{\mu}$ in terms of polarization states (p=0 for linear $\hat{z}$ polarization, ± 1 for circular polarization) and $T_q^1(\mu)$ is the molecule-frame decomposition of $\vec{\mu}$.

A list of allowed transitions with dipole matrix element μ_n and energy E_n is prepared . The simulated spectrum is

$$S(E) = \sum_n \mu_n^2 \frac{(\Gamma/2)^2}{(\Gamma/2)^2 + (E - E_n)^2}$$

where the FWHM Γ is chosen to match the observed linewidth (6-10 MHz in most measurements).

4.5 Temperature

The temperature of the molecular beam will affect the initial population distribution and, hence, the strength of lines in the observed spectrum. There is more than one possible temperature distribution related to the molecular beam; a temperature can be defined relative to the population distribution among

vibrational or rotational states, or by velocity spread (translational temperature). Typically in a supersonic beam like the one used in this experiment the translational and rotational temperatures are very similar, but the vibrational temperature is typically higher in supersonic expansions, because the number of collisions needed to quench vibrationally excited states is larger than the actual number of collisions during the expansion. Hence the vibrational degree of freedom does not have sufficient time to equilibrate with the otherwise cold expansion of argon. The translational temperature will be discussed later (in equation 5.3), as it does not affect the spectroscopic measurements. The population distribution over vibrational states will be

$$P_{\text{vib}}(v) = \frac{e^{-\frac{E_v}{kT}}}{\sum_{u=0}^{\infty} e^{-\frac{E_u}{kT}}} \tag{4.21}$$

where $P_{\text{vib}}(v)$ is the probability to be found in vibrational level v, E_v is the energy of vibrational level v (approximately $\omega_e(v + 1/2)$), k is the Boltzmann constant, and T is the vibrational temperature. While the vibrational temperature was not measured, a qualitative understanding of the population distribution is useful for estimating the fraction of molecules prepared in the ground state (figure 4.6). In this case, almost all of the molecules will be found in the vibrational ground state as long as the temperature is below $T_{vib} \lesssim 200$ K.

The population distribution among rotational levels in a particular vibrational state will be approximately [11]

$$P(n) = \frac{(2J_n + 1)e^{-\frac{E_n}{kT}}}{\sum_{m=0}^{\infty}(2J_m + 1)e^{-\frac{E_m}{kT}}} \tag{4.22}$$

where $P(n)$ is the probability to be found in state n, J_n is the total angular momentum in state n, $(2J_n + 1)$ is the multiplicity of levels in this state, E_n is the energy of the state and T is the rotational temperature. Figure 4.5 shows

a simulated spectrum of the R branch of the X-$A^2\Pi_{1/2}$ transition of BaF for a few different rotational temperatures. This simulation can be compared against the absorption spectra in chapter 6 to estimate the rotational temperature. Estimates of the rotational temperature were made in a room temperature buffer gas and using fluorescence spectroscopy. It is possible to find the temperature through the population ratio of two different rotational lines:

$$R(J', J) \equiv \frac{2J'+1}{2J+1} e^{-\frac{E_{J'}-E_J}{kT}} \tag{4.23}$$

where J and J' are from the ground states of the two lines chosen for comparison. However, for a given choice of lines, the usable temperature range is limited. Figure 4.7, shows the sensitivity $\frac{dR}{dT}$ of the ratio $R(N' + 1/2, N + 1/2)$ for population measurements based on two R-branch lines. The temperature range over which the measurement of R is useful depends on the rotational temperature. While most of this work has been with the $N = 0$ state, there is some data on the population of higher rotational states. Section 6.3 discusses absorption measurements in a room temperature buffer gas, and laser-induced fluorescence measurements of higher rotational states are described in section 6.4.2. Room-temperature buffer gas measurements were (by comparison with figure 4.5) consistent with a temperature on the order of 1000 K, and the temperature deduced from the LIF measurements was $T_{\rm rot} = 30 \pm 12$ K. However, the rotational levels chosen were not particularly sensitive to the temperatures we expected; as a result, the suitability of this data for determining the rotational temperature is limited.

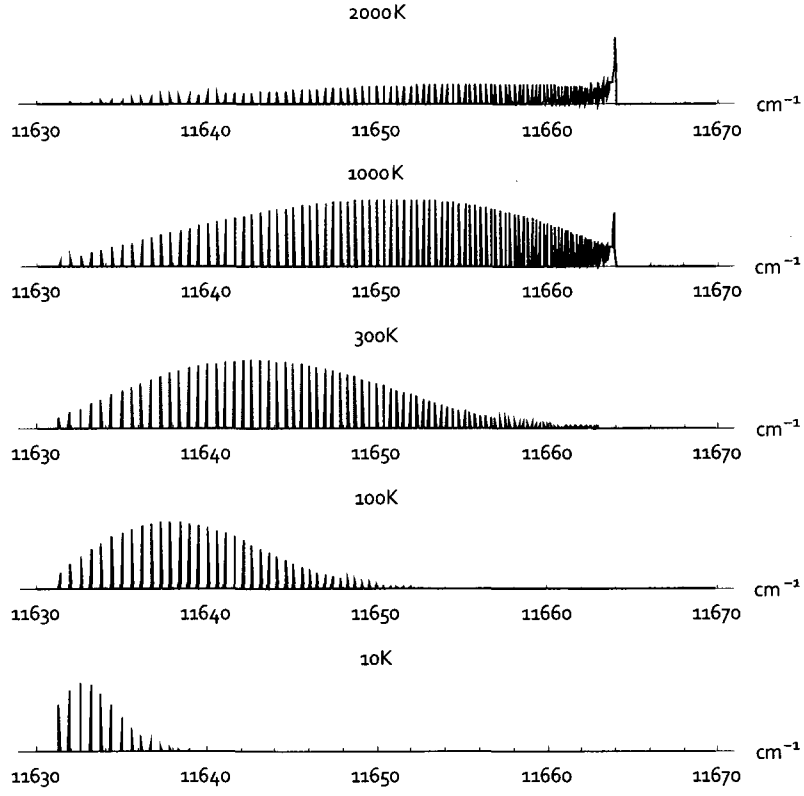

Figure 4.5: Simulated spectra of the R-branch of the $A^2\Pi_{1/2}$-X, $v\,(0 \rightarrow 0)$ transition of BaF showing the effect of different temperature distributions. The line strength is assumed to be proportional to the ground state population, $S\left(\vec{J}\right) \propto (2J+1)\exp\left(-\frac{E_J}{kT}\right)$

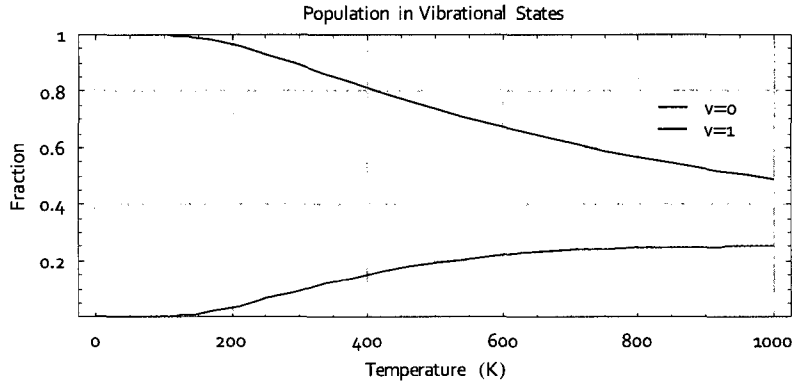

Figure 4.6: Fraction of the population in the vibrational ground state (v=0) and the first vibrational excited state (v=1), depending on the vibrational temperature, for BaF (ω_e=469 cm^{-1}). The X-A transitions of the first vibrational state (v=1→1) will be shifted about 16 cm^{-1} lower in energy than for the 0 → 0 lines. Unless the vibrational temperature of the beam is particularly high, almost all of the molecules will be found in the ground state.

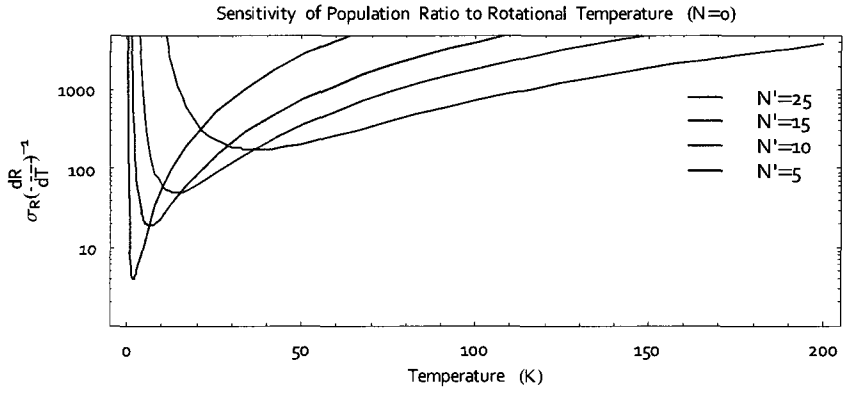

Figure 4.7: Sensitivity of the ratio of two rotational level populations to changes in temperature. Here, we are looking at the uncertainty $\sigma_T \sim \sigma_R \left(\frac{dR}{dT}\right)^{-1}$ if we take the ratio of the population of a state with N' to the population of the ground state, $N = 0$ ($R \equiv \frac{P(N')}{P(0)}$). Comparing against states with low N' is useful if the rotational temperature is low, but yields a measurement insensitive to temperature if the rotational temperature is too high. Conversely, measurements with larger N' are insensitive to temperature if the temperature is too low.

4.6 Levels and Transitions for State Preparation and Detection

The proposed parity violation experiment and the DC Stark interference experiment discussed in the next chapter involve the level crossings between an $N = 0$ and an $N = 1$ level from the X state. Our LIF measurements of the BaF beam have concentrated on the first R-branch line of the $A^2\Pi_{1/2}$-$X^2\Sigma$ $(v = 0, 0)$ transition, with $N = 0$ $(J = 1/2)$ in the ground state and $J' = 3/2$ (- parity) in the excited state as a means of state preparation and detection (figure 4.3). This line is far from other rotational transitions, which aids in identification and use for state detection. We also use the $D^2\Sigma$-$A^2\Pi_{1/2}$ $(v = 0, 0)$ transition with $J' = 3/2$ (- parity) in the A state and $N = 0, 2$ in the D state. This A-X, D-A two-photon transition is used in the state detection region after the magnet as, for various technical reasons outlined in section 5.4, it is more efficient to detect the resulting emission at 413 nm rather than the single photon emission at 860 nm.

Figure 4.9 illustrates the spectrum of the A-X transition in the absence of an external magnetic field. The $J = \frac{1}{2}$, $J' = \frac{3}{2}$ transition for ^{138}BaF is prominently centered at 11631.275 cm^{-1}; the 63 MHz splitting due to the ^{19}F hyperfine is not visible given the Doppler-broadened linewidth (a large skimmer diameter was used to optimize the signal size). The first two R branch lines (figure 4.8) show the hyperfine structure and isotope shifts for the naturally occurring barium isotopes. There are two peaks for each of ^{137}BaF and ^{135}BaF, split by about 4010 MHz due to the hyperfine strucutre of the barium nucleus. The experimental predictions using Steimle's modeling code are superimposed, and the parameter $T_0 \equiv T_e + \omega_e/2 - \omega_e x_e/4$ is adjusted for each isotope to match the observed spectra. The values found for T are in table 4.3.

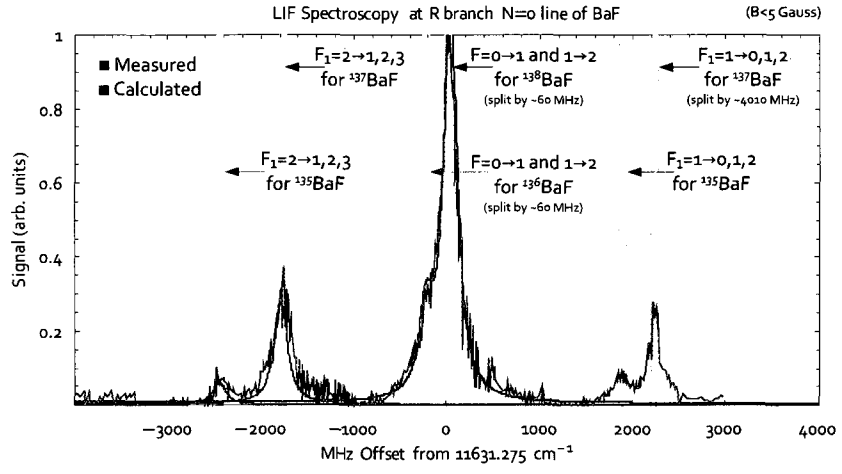

a)

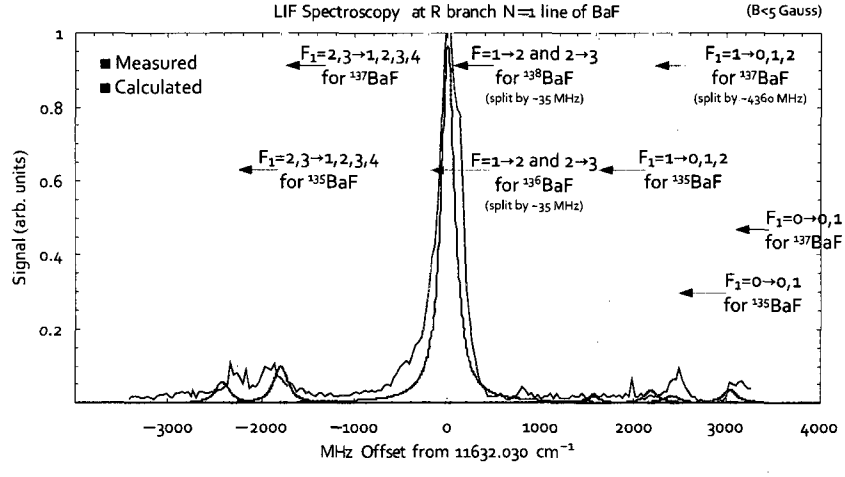

b)

Figure 4.8: a) Measured LIF spectrum of the first R branch line of the A-X $v = 0, 0$ transition. This data was taken in collaboration with Prof. Steimle using a beam apparatus at Arizona State University). The broad linewidth precludes observation of the hyperfine structure in ^{138}BaF and the clear observation of ^{136}BaF, for which the predicted location is indicated by the grey marker. The constant T for each isotope is adjusted so that the calculated spectra matches the measurements. b) Measured LIF spectrum of the second R branch line of the A-X $v = 0, 0$ transition. There is a third peak in the hyperfine spectrum of the odd isotopes of BaF. The magnetic field was < 1 Gauss. Note that for the odd isotopes, there are only two peaks for the $N = 0$ line, but three for higher rotational levels. This is due to the sum of the angular momentum J with $I_1 = \frac{3}{2}$; for $N = 0$, $J = \frac{1}{2}$ and $F_1 = |J - I_1| \ldots J + I_1 = 1, 2$. Larger values of N and J allow a full range of $F_1 = J - I_1 \ldots J + I_1$.

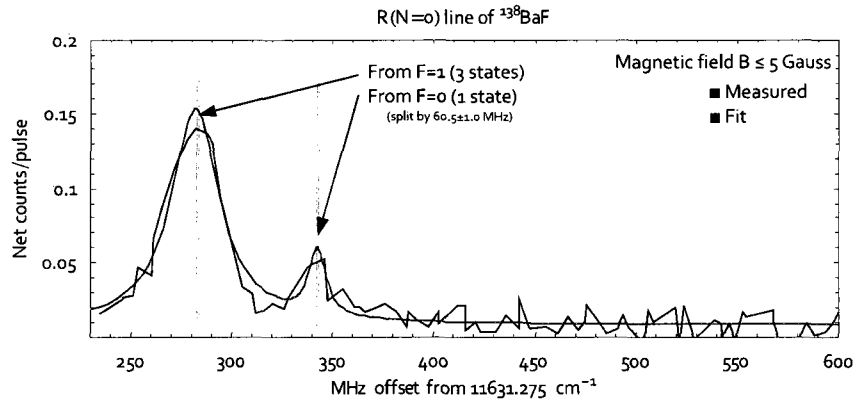

Figure 4.9: Measured LIF spectrum of the first R branch line of the A-X $v = 0, 0$ transition. The splitting between the $F = 1$ and $F = 0$ peaks is due to the difference in hyperfine constants between the X and A states; for the given hyperfine constants in the X state and no hyperfine structure in the A state, we expect a splitting of 66.3 MHz. (A second data set had a splitting of 63.5 ± 1.0 MHz; this suggests that b_F for ^{19}F in the A state is $\lesssim 4$ MHz, compared to 63.5 MHz in the ground state.) The linewidth of the $F = 1$ state is about 30 MHz FWHM, while the width of the $F = 0$ state is about 5 MHz. The broadening of the $F = 1$ state is consistent with an applied magnetic field of $B \lesssim 5$ Gauss, which would separate the magnetic sublevels $m_F = 1$ and $m_F = -1$ by 14 MHz.

Isotope	T (based on eq. 4.7)	T(obs.)-T(calc)	Observed T
^{135}BaF	11946.351 cm^{-1}	-3660 MHz	11946.229 cm^{-1}
^{136}BaF	11946.375 cm^{-1}	-3970 MHz	11946.243 cm^{-1}
^{137}BaF	11946.389 cm^{-1}	-4110 MHz	11946.252 cm^{-1}
^{138}BaF	11946.403 cm^{-1}	-4510 MHz	11946.253 cm^{-1}

Table 4.3: The parameter $T_0 \equiv T_e + \omega_e/2 + \omega_e x_e/4$ giving the spacing between the X $^2\Sigma$ ($v = 0$) and A $^2\Pi$ ($v = 0$) electronic and vibrational states; the parameter can be calculated using the isotope shift formulas for vibrational and rotational structure given in equation 4.7 (calculated value in this table). The observed value that matches spectroscopic observations of the first two R-branch lines is also given. For example, the ^{136}BaF line R($J = 1/2$) lies 255 MHz lower in energy than the same line for ^{138}BaF.

4.6.1 Spectroscopy and Calculations for ^{138}BaF and ^{136}BaF

In the parity violation apparatus, the LIF measurements on ^{138}BaF will be made in a magnetic field for two reasons: first, it is possible to resolve particular magnetic sublevels and address only the one of interest; second, it allows a reduction in the length of the molecular beam (and improved signal size) by performing state preparation and detection close to the magnet. For practical reasons, a field of 115 Gauss at the position where the laser beams interact with the molecules was chosen. For this experimental configuration, this gives a change in magnetic field with position of $\sim$ 5 Gauss/cm, which will result in a shift of less than the natural linewidth ($\sim$5 MHz) in the transition frequency for a 3 mm positioning error. This allows the use of the same laser to excite the A-X transition in both the state preparation and state detection regions.

Figure 4.10 shows the structure of the X state $N = 0$ and A state $N' = 1$ rotational levels in a magnetic field. In the X state, the angular momenta quickly decouple so that $|S, m_S\rangle\,|I, m_I\rangle$ becomes a good basis at fields above 30 Gauss. The A state decouples $|I, m_I\rangle$, but most of the states retain a mixture of $m_S = \pm\frac{1}{2}$. Therefore, for incident $\hat{z}$-polarized light, the selection rules ($\Delta m_F = 0$, $\Delta m_S = 0$, $\Delta m_I = 0$) allow four possible transitions out of the X $m_S = +\frac{1}{2}$ ground state. The transitions labeled a and b will be much stronger than c and d. There also are two strong transitions from the X $m_S = -\frac{1}{2}$ states; figure 4.11 shows the observed LIF spectra. Two small peaks associated with ^{136}BaF are observed; these are from the X $m_S = -\frac{1}{2}$ states. Transitions for ^{136}BaF are similar in structure to ^{138}BaF, but (for this pair of rotational levels) are shifted down in energy by 255 MHz. Since the spectra in the state preparation and detection regions are simultaneously recorded, the positions of the peaks can be compared to find the difference in magnetic fields between the two regions. Using the splitting between the $m_S = +\frac{1}{2}$ and $m_S = -\frac{1}{2}$ transitions, it is observed that

the magnetic field is 1.2 Gauss lower in the state detection region (a difference of 3.2 MHz in the splitting, or 1.6 MHz in transition frequency). Since the shift in transition frequency is small compared to the natural linewidth, this is acceptable. Table 4.4 summarizes the fit to each of the observed lines in figure 4.11. Additional measurements (figure 4.13) confirm the position and spacing of the ^{136}BaF peaks.

The polarization of the incident light determines which transitions are allowed, as seen in figure 4.12. There are two important points to make about the spectra observed under $\hat{x}, \hat{y}$-polarized light; first, that the $\hat{x}, \hat{y}$-polarized spectrum can be used to find g_l' for the A state. Of the eight lines visible in the $\hat{x}, \hat{y}$-polarized spectrum, the most obvious structure is the separation into two groups of four peaks each (due to the value of m_S in the ground state). Each group of four peaks is divided into two groups of two, depending on the ground state hyperfine splitting. The separation of these two pairs depends on g_l'. The second point is that there are strong transitions close to the transition used to probe the X state. This will interfere with optical pumping and state detection if the laser is not properly polarized in $\hat{z}$; a line which overlaps with the desired transition can lead to large background signals.

It is possible to specifically look at the overlap of other transitions on top of the one used to probe the $\left|m_S = \frac{1}{2}, m_I = -\frac{1}{2}\right\rangle$ state. Figure 4.14 shows the simulated $\hat{z}$-polarized spectrum for the X-A transition, broken down by the originating ground state. If the laser intensity is not large enough to saturate the transition, the contribution from other nearby, unwanted lines will depend on the overlap of the broadened line with the laser tuned to the desired transition. The lineshape is approximated as a Lorentzian $L(x) = \frac{(\Gamma/2)^2}{(\Gamma/2)^2+(x-x_0)^2}$, and note that fraction of a Lorentzian which falls within a band $\pm\frac{b}{2}$ of the laser frequency x_1 is $\frac{1}{\pi}\left(\arctan\left(\frac{b+2(x_0-x_1)}{\Gamma}\right) + \arctan\left(\frac{b-2(x_0-x_1)}{\Gamma}\right)\right)$. For the two $m_S = +\frac{1}{2}$

transitions (separated by 30.6 MHz), the overlap of the $m_F = 1$ transition on top (eg. within 5 MHz) of the $m_F = 0$ line is 1.7% if the FWHM is 10 MHz, and 3.1% if the FWHM is 20 MHz. For the two-photon transition to $N'' = 0$, the separation of the peaks is only 15 MHz, and the overlap is 7% (figure 4.18).

The last calculation presented here regarding the A-X transition is the spectrum at a magnetic field near 4630 Gauss (figure 4.15). As discussed in chapter 3, it will be necessary to perform state preparation inside of the magnetic field. Since the ground-state energy levels are already decoupled into m_S, m_I at 115 Gauss, the primary effect is to separate the pairs of lines with $m_S = \pm\frac{1}{2}$ by about 14 GHz. The position of each of these lines (relative to the field-free ^{138}BaF transition) is given in figure 4.15).

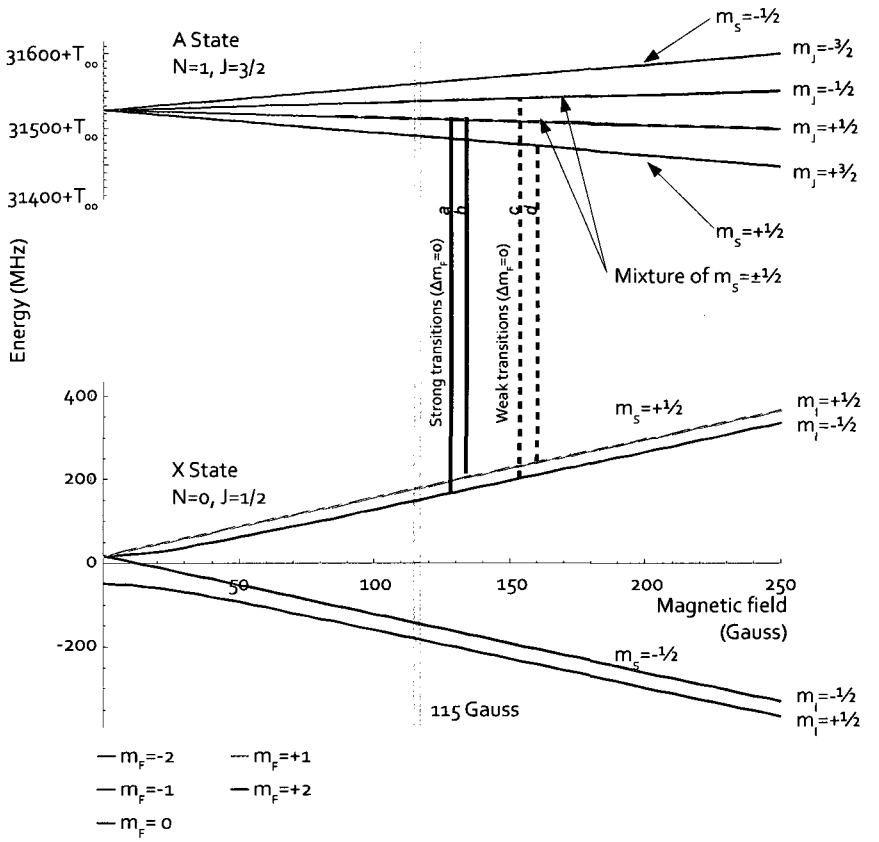

Figure 4.10: Calculated energy levels for the $N = 0$ and $J' = \frac{3}{2}^-$ states of ^{138}BaF. The transitions are color-coded by m_F, and the $\Delta m_F = 0$ transitions (excitable with $\hat{z}$-polarized light) from the $N = 0$, $m_S = +\frac{1}{2}$ level are noted. The letters indicated on each transition match the labels shown in figure 4.11. At 115 Gauss, the ground state levels are well-defined combinations of m_S and m_I, but the excited states can be a mixture of both values of m_S.

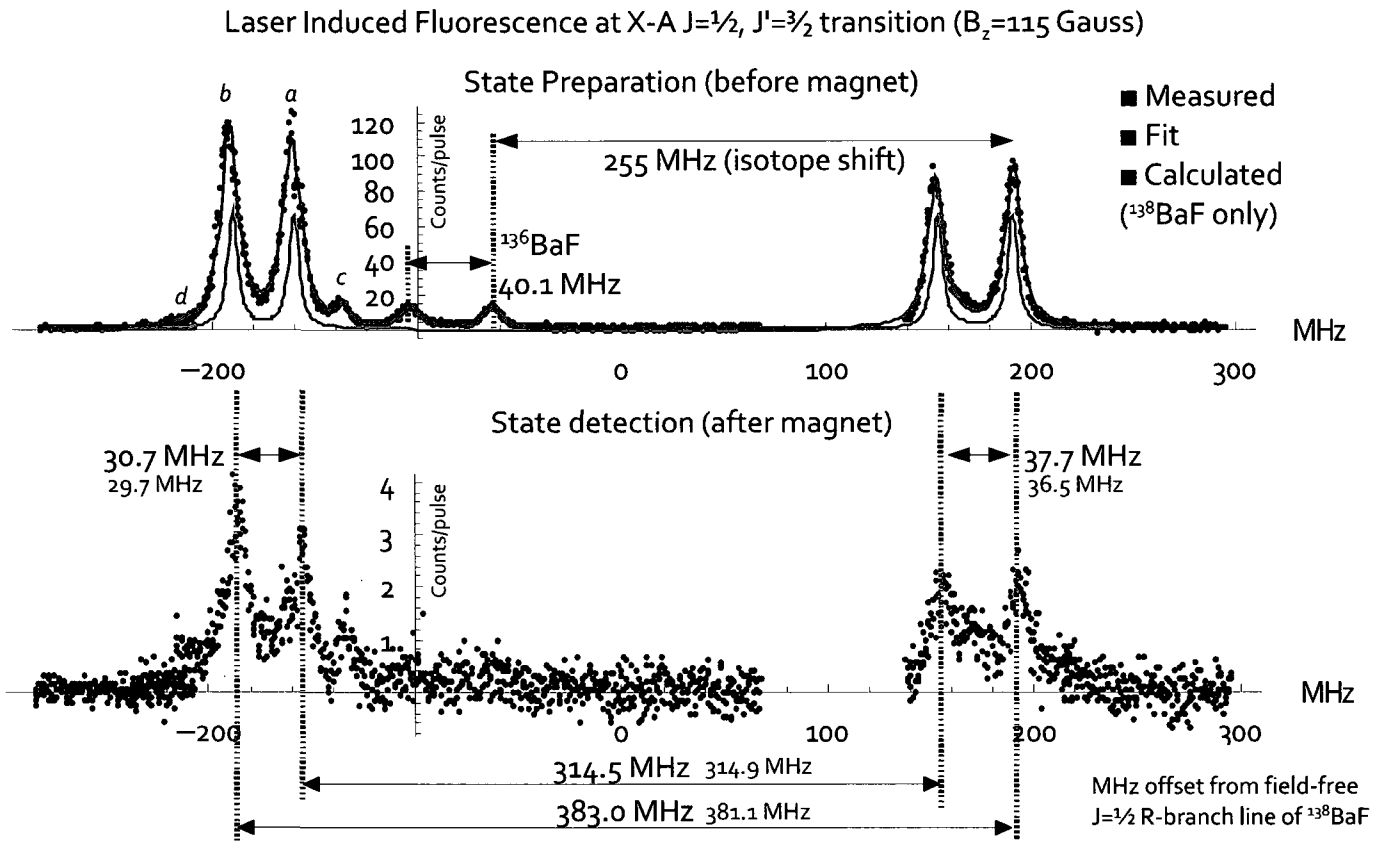

Figure 4.11: Measured LIF spectra for the X-A transition near 11631.28 cm^{-1}, with $\hat{z}$-polarized light and a magnetic field of B=115 Gauss (along $\hat{z}$). The measured spectra are shown for the state preparation region (top) and the state detection region (bottom). The indicated intervals show the difference between measured (black) and predicted (red) separation between the peaks. In addition to the expected ^{138}BaF spectrum, there is evidence of the ^{136}BaF isotope. The transitions noted here correspond to transitions from the X $\left|m_S = -\frac{1}{2}\right\rangle$ states, but about 255 MHz below the corresponding peaks in ^{138}BaF due to the isotope shift. The observed height of the ^{136}BaF peaks is 11 $\pm$ 1% of the ^{138}BaF peaks, similar to the ratio of isotopic abundance (6% ^{136}BaF:70% ^{138}BaF). The fit is to a sum of seven Lorentzian lineshapes; the calculated spectra shows the peak heights as proportional to the square of the dipole matrix element between the lower and upper states. The frequency is calibrated by means of offset locking using an AOM.

	State preparation			State detection		
Peak	Height	FWHM	Position	Height	FWHM	Position
^{138}BaF $m_F = 1$	117 ± 1	9.9 ± 0.1	-191.51 ± 0.04	3.19 ± 0.08	13.8 ± 0.6	-185.7 ± 0.2
^{138}BaF $m_F = 0$	107 ± 1	10.5 ± 0.1	-160.81 ± 0.14	2.19 ± 0.07	17 ± 1	-154.5 ± 0.3
^{138}BaF $m_F = -1$	86 ± 1	10.0 ± 0.2	153.73 ± 0.06	1.72 ± 0.07	21 ± 1	157.5 ± 0.4
^{138}BaF $m_F = 0$	93 ± 1	9.2 ± 0.1	191.47 ± 0.05	1.82 ± 0.08	16 ± 1	193.3 ± 0.3
^{138}BaF $m_F = 0$	11 ± 1	5.2 ± 1.0	-136.2 ± 0.3			
^{136}BaF $m_F = -1$	12 ± 1	10.4 ± 1.2	-103.2 ± 0.4			
^{136}BaF $m_F = 0$	12 ± 1	9.8 ± 1.1	-63.1 ± 0.4			

Table 4.4: Fit parameters for measured LIF spectra for the A-X transition near **11631.28** cm^{-1} at $B_z = 115$ Gauss with $\hat{z}$-polarized incident light (figure 4.11). The fit for each line is of the form $\frac{a(\Gamma/2)^2}{(x-x_0)^2+(\Gamma/2)^2}$. The separation of the two pairs of lines ($m_S = \pm\frac{1}{2}$) is 3.2 MHz smaller in the state detection region than in the state preparation region; this corresponds to a difference in the magnetic field of 1.2 Gauss. The transitions are shifted less than the observed linewidth, and so light from the same laser is used to excite both the state preparation and detection regions. This confirms our understanding of the spectroscopy of the $N = 0$ level.

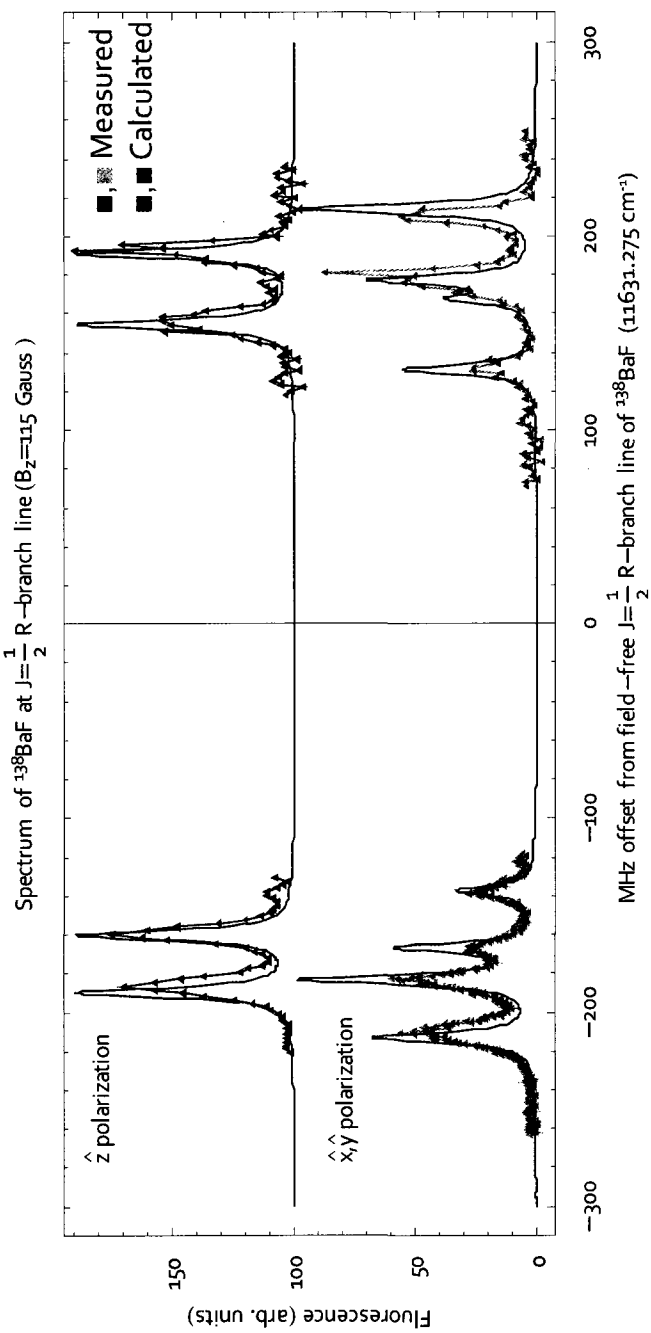

Figure 4.12: The LIF spectra for the X-A transition near 11631.28 cm^{-1} was recorded with both $\hat{z}$- and $\hat{x}, \hat{y}$-polarized light (to show $\Delta m_J = 0$ and $\Delta m_J = \pm 1$ transitions) at a magnetic field B_z=115 Gauss. The spacing between the pairs of $\hat{z}$-polarized peaks is primarily due to g_s in the X state; the value of $g_{||} \rightarrow -0.24$, $g_{\perp} \rightarrow -0.48$ in the A state was chosen to match the features observed with $\hat{x}, \hat{y}$-polarized light. Steimle's measurement of $g_S = 1.86(4)$ and $g_L = 1.05(2)$ is consistent with this value of $g_{||} = g_S - 2g_L$. The linewidth was found to be $\approx$ 10 MHz FWHM. These constants are necessary to understand the spectra of ^{137}BaF in a magnetic field. The calculated peak heights are taken as proportional to the square of the dipole matrix element connecting the initial and final states.

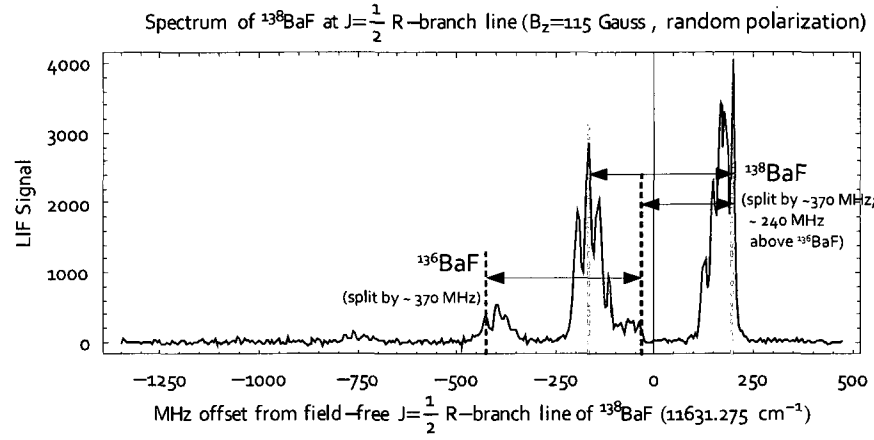

Figure 4.13: Unpolarized spectrum of the first R-branch line in the spectrum of BaF, showing features from ^{138}BaF and ^{136}BaF. The frequency calibration on this scan is based on the FSR of the Fabry-Perot, rather than an AOM frequency offset as in figure 4.11. Consequently, the measured line spacings here are about 5% smaller than in the other figure. However, we see that ^{138}BaF and ^{136}BaF have the same spacing between $m_S = \pm\frac{1}{2}$ peaks (and hence the same values of g_S, g_L, and $g_{l'}$). Unlike the previous plots, all the transitions related to ^{136}BaF are observed. The transitions of ^{137}BaF are outside the range of this scan.

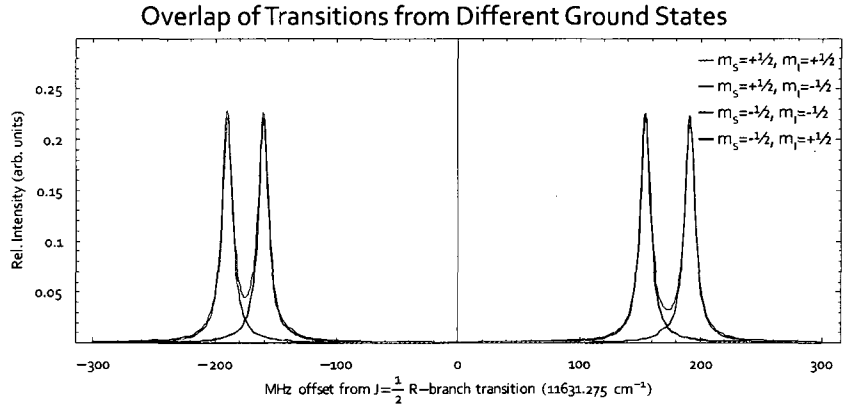

Figure 4.14: Each of the four hyperfine levels from the $J = \frac{1}{2}$ ground state contributes one strong $\Delta m_J = 0$ transition to the observed spectrum from $\hat{z}$-polarized light. This simulated spectrum of the $J = \frac{1}{2}$ R-branch transition at $B_z = 115$ Gauss shows that there is very little overlap between the transition used to pump or probe the population of the $\left|m_S = +\frac{1}{2}, m_I = -\frac{1}{2}\right\rangle$ state and the other nearby transitions.

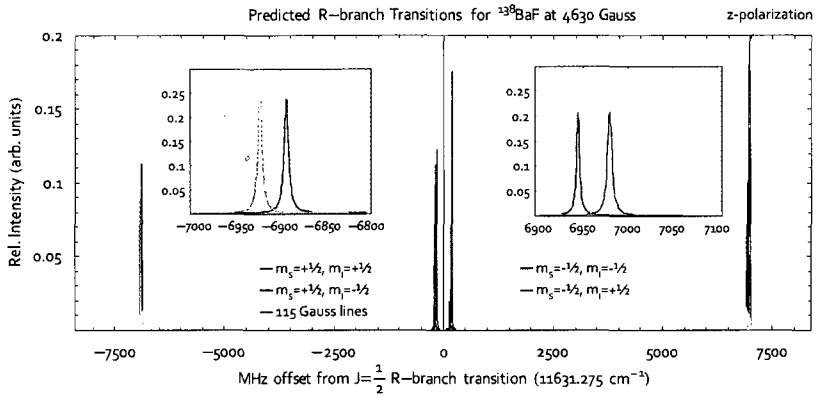

m_S	m_I	Frequency offset (MHz) near 4630 Gauss
$+\frac{1}{2}$	$+\frac{1}{2}$	$-6924 - 1.485\,(B_z - 4630\ \text{Gauss})$
$+\frac{1}{2}$	$-\frac{1}{2}$	$-6893 - 1.485\,(B_z - 4630\ \text{Gauss})$
$-\frac{1}{2}$	$-\frac{1}{2}$	$6944 + 1.509\,(B_z - 4630\ \text{Gauss})$
$-\frac{1}{2}$	$+\frac{1}{2}$	$6979 + 1.509\,(B_z - 4630\ \text{Gauss})$

Figure 4.15: Simulated spectra for the $J = \frac{1}{2}$ R-branch transition of ^{138}BaF at $B_z = 4630$ Gauss with $\hat{z}$-polarized incident light, for use in depopulation of the ground state within the magnet. The positions of the transitions change by about 1.5 MHz/Gauss, as indicated. The splitting of the pair with $m_S = +\frac{1}{2}$ is 31 MHz, and with $m_S = -\frac{1}{2}$ is 35 MHz. For reference, the transitions at $B_z = 115$ Gauss are shown in gray. The transition to access the $m_S = +\frac{1}{2}$, $m_I = -\frac{1}{2}$ state has shifted down in energy by 6732 MHz compared to the transition in the state detection region (at $B_z = 115$ Gauss). The state composition of the A state is effectively the same at 115 and 4630 Gauss, so the transition intensities will be unchanged.

For various technical reasons, a scheme using a two-photon transition to probe the contents of the X state was also investigated. The current implementation uses the A-X transition at 860 nm, followed by the D-A transition at 797 nm and detection of the resulting emission at 413 nm. Either $N'' = 0$ (figure 4.16) or $N'' = 2$ (figure 4.17) can be used as the final level in the D state. The $J' = \frac{3}{2}^-$ level is used as the intermediate A state, as for the single photon transition. In practice, the single photon transition is used for state preparation, and the two photon transition for state detection. The scattered photons from the single photon transition are used to verify that the laser is on resonance with the A-X portion of the two photon transition; only the D-A laser needs to be scanned to address the desired X-A-D line.

A naive implementation of the two-photon transition will theoretically be less efficient than a single transition scheme. Consider the process involved in a single photon transition from the ground X state to the excited A state:

1. Stimulated absorption transfers population out of the desired level of the X state into the A state

2. Stimulated emission can drive molecules out of the A state back to the original X state; the molecule gets another chance at stimulated absorption, but the photon from stimulated emission is correlated with the direction of the laser beam and cannot be detected

3. Spontaneous emission from the A state emits a photon which may be detected; the molecule decays to one of the levels of the X state (most likely not the initial level; the molecule is therefore "lost" from the process)

4. Given sufficient time and/or incident laser power, the entire population of the desired level of the X state will be depleted through this process. The only loss process is through spontaneous emission from the A state, which

is detectable

The two-photon scheme has

1. Stimulated absorption transfers population out of the desired level of the X state into the A state

2. Stimulated emission can drive molecules from the A state back to the original X state (lossless), or

   (a) Stimulated absorption transfers population out of A to the D state, or

   (b) Spontaneous emission from the A state emits a near-infrared photon (loss process)

3. Spontaneous emission from the D state emits a higher energy photon (a loss process, but a detectable photon is emitted)

At best, the process places an equal population of molecules in both the A and D states. The probability that a molecule undergoes spontaneous emission from the D state (instead of the A state) then depends on the natural lifetimes of the A and D states. If the states have roughly equal lifetimes (as they do for these states in BaF), then only half the molecules will emit a visible photon; the rest will be lost through spontaneous emission from the A state. In practice, however, the gains in detection efficiency far outweigh this loss.

In addition, a process called "stimulated rapid adiabatic passage" (STIRAP) [38] can be used to recover this loss in detection efficiency. In STIRAP, population is transferred from the initial to the final state without populating the intermediate state. More details of this process can be found in [62].

The predicted and observed spectra for the two photon transition (figures 4.18 and 4.19) show that the separation between the desired $m_F = 0$ (used to

probe the X $|m_S = +\frac{1}{2}, m_I = -\frac{1}{2}\rangle$) and nearby $m_F = 1$ transitions is smaller than for the X-A transition. The observed peak separation is fit to conclude that the ^{19}F hyperfine constant $b_F \approx$37 MHz in the D state. This is about 60% of the value of b_F in the X state. Neither the $N'' = 2$ nor the $N'' = 0$ levels in the D state are ideal; the line separation is only 15 MHz in the $N'' = 0$ state, which leads to a 7% overlap between the two transitions. The $N'' = 2$ level exhibits a weaker $m_F = 1$ transition that directly overlaps with the $m_F = 0$ line. However, by tuning the 860 nm X-A laser slightly to the blue (figure 4.20), the contribution from the $m_F = 1$ level in the $N'' = 0$ transition is reduced. This is important because signals from other levels create a background which would obscure the desired parity violation signal. It is also possible to add a sideband to the state preparation laser, in order to deplete population from the nearby ground-state sublevel and hence eliminate this source of background entirely.

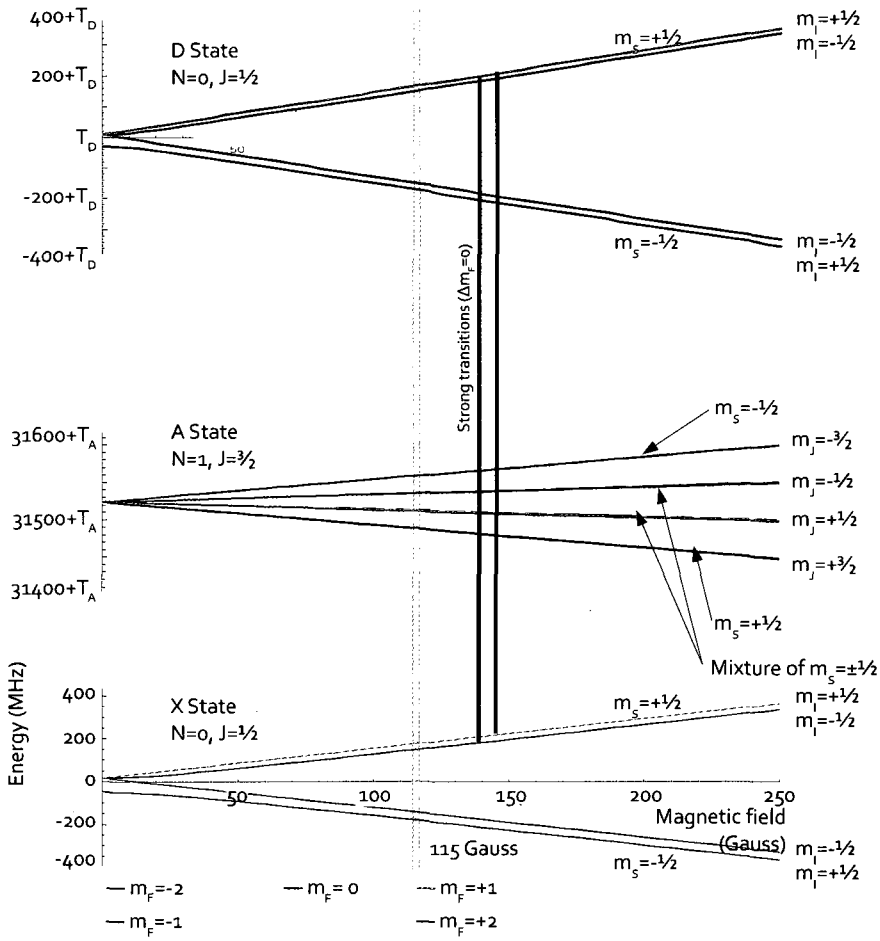

Figure 4.16: Magnetic field dependence of relevant lines for the X-A-D N"=0 transition.

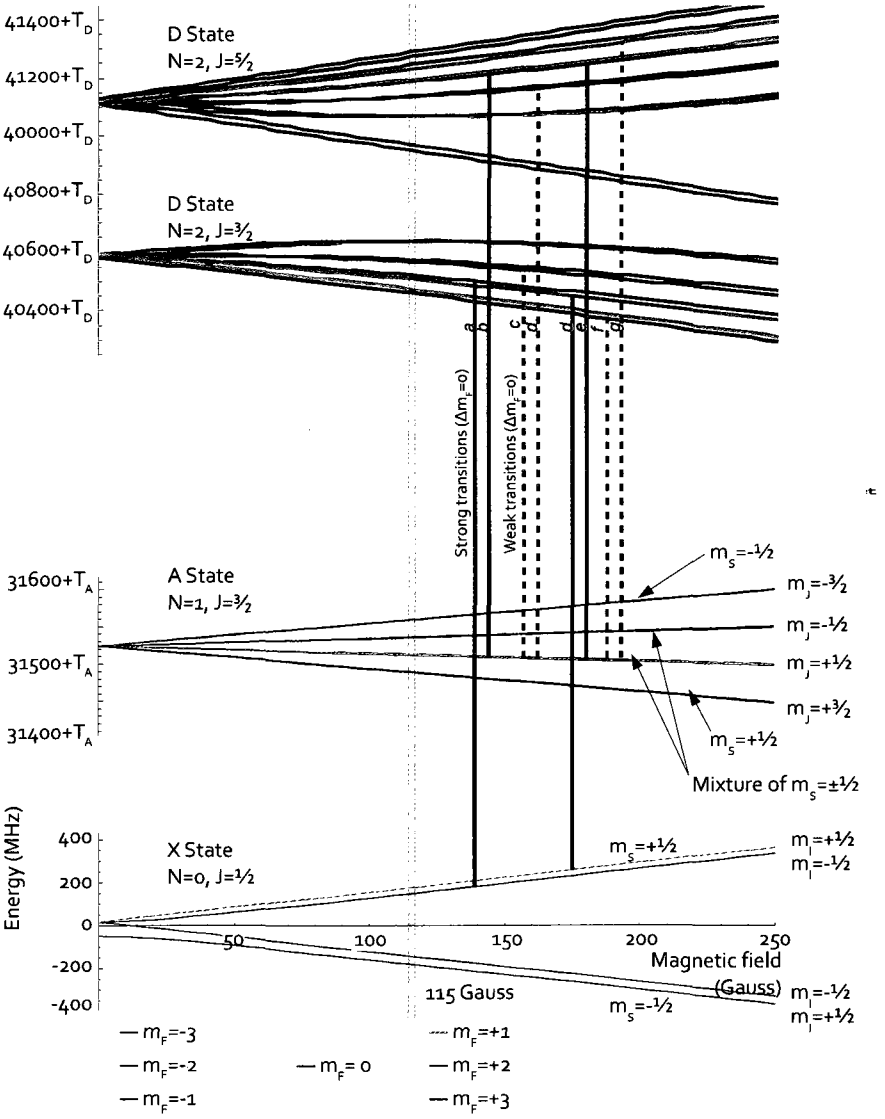

Figure 4.17: Magnetic field dependence of relevant lines for the X-A-D $N'' = 2$ transition

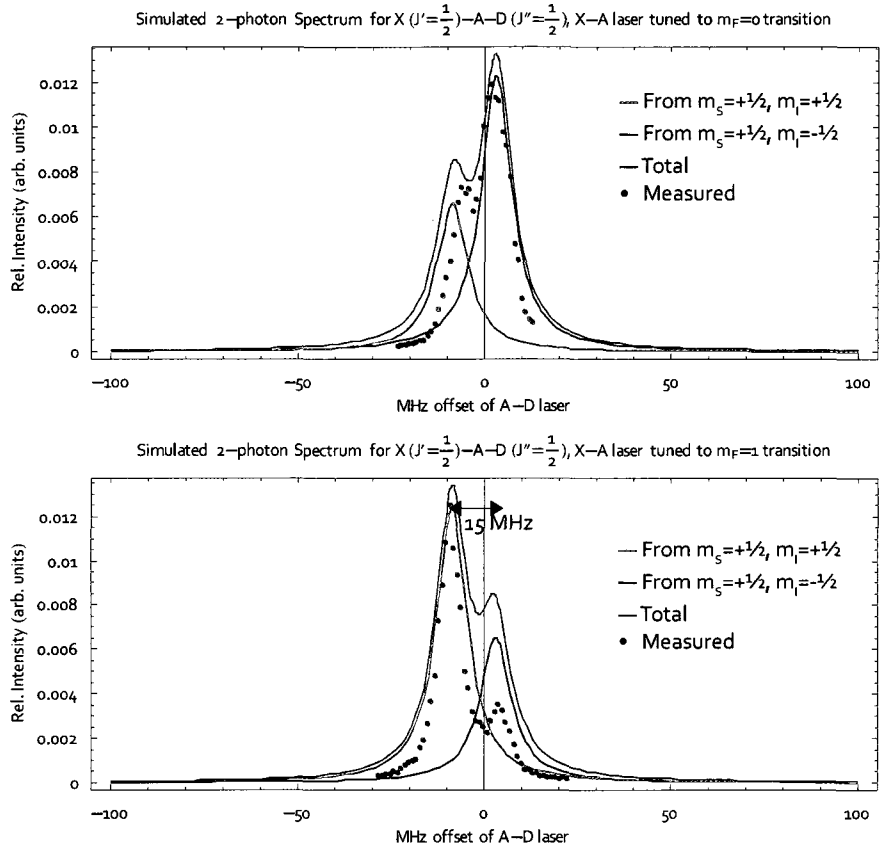

Figure 4.18: Simulation and observed LIF fluorescence for a two-photon transition from X ($N = 0$) - A ($J' = \frac{3}{2}$)- D ($N'' = 0$). The simulated spectra are color-coded based on the ground state of the transition. The D state hyperfine constants are adjusted to produce the best match to both of the observed spectra. The relative heights of the two peaks depends on which transition the laser exciting the X-A transition is tuned to. In the top figure, the X-A laser is tuned to the $m_F = 0$, $m_S = +1/2$, $m_I = -1/2$ transition; however, the $m_F = 0$ and $m_F = 1$ transitions are not clearly resolved. This limits the effectiveness of optical pumping using this transition, unless both of the $|m_S = +\frac{1}{2}\rangle$ states are depleted during state preparation. In the bottom figure, the X-A laser is tuned to the $m_F = 0$, $m_S = +1/2$, $m_I = +1/2$ transition. The calculated spectrum shown shows the peak heights as proportional to the square of the dipole matrix elements connecting the upper, intermediate, and lower states.

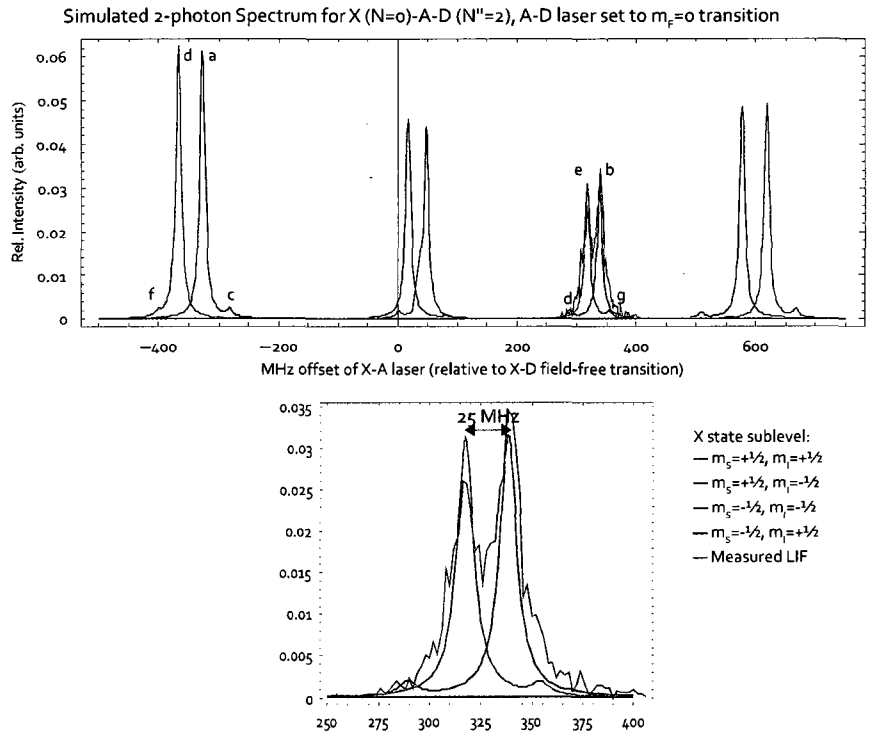

Figure 4.19: Simulation and observed LIF fluorescence for a two-photon transition from X ($N = 0$) - A ($J' = \frac{3}{2}$)- D ($N'' = 2$). In the measured LIF spectrum presented here (transitions to the $N'' = 2$, $J'' = \frac{5}{2}$ state), the D-A laser is kept tuned to the $m_F = 0$ transition frequency, and the A-X laser is scanned. The simulated spectra are color-coded based on the ground state of the transition and show the square of the dipole matrix element connecting the initial, intermediate, and final states as the relative height of each peak. The spacing of the peaks was used to determine the fluorine hyperfine $b_F \approx 37$ MHz in the D state. The observed spectra suggest that the transition at point (a) (to D $N'' = 2$, $J'' = \frac{3}{2}$, at -350 MHz) may be the best choice for detection of the X $\left|m_S = +\frac{1}{2}, m_I = -\frac{1}{2}\right\rangle$ state due to the minimal contamination with transitions from the $m_F = 1$ state (point (d)). The transitions (a) and (d) are further separated than the relevant transitions in the D ($N'' = 0$) state (figure 4.18), and avoid overlapping with the smaller peaks (c) and (f), unlike the $J'' = \frac{5}{2}$ state (b, d, e, and g).

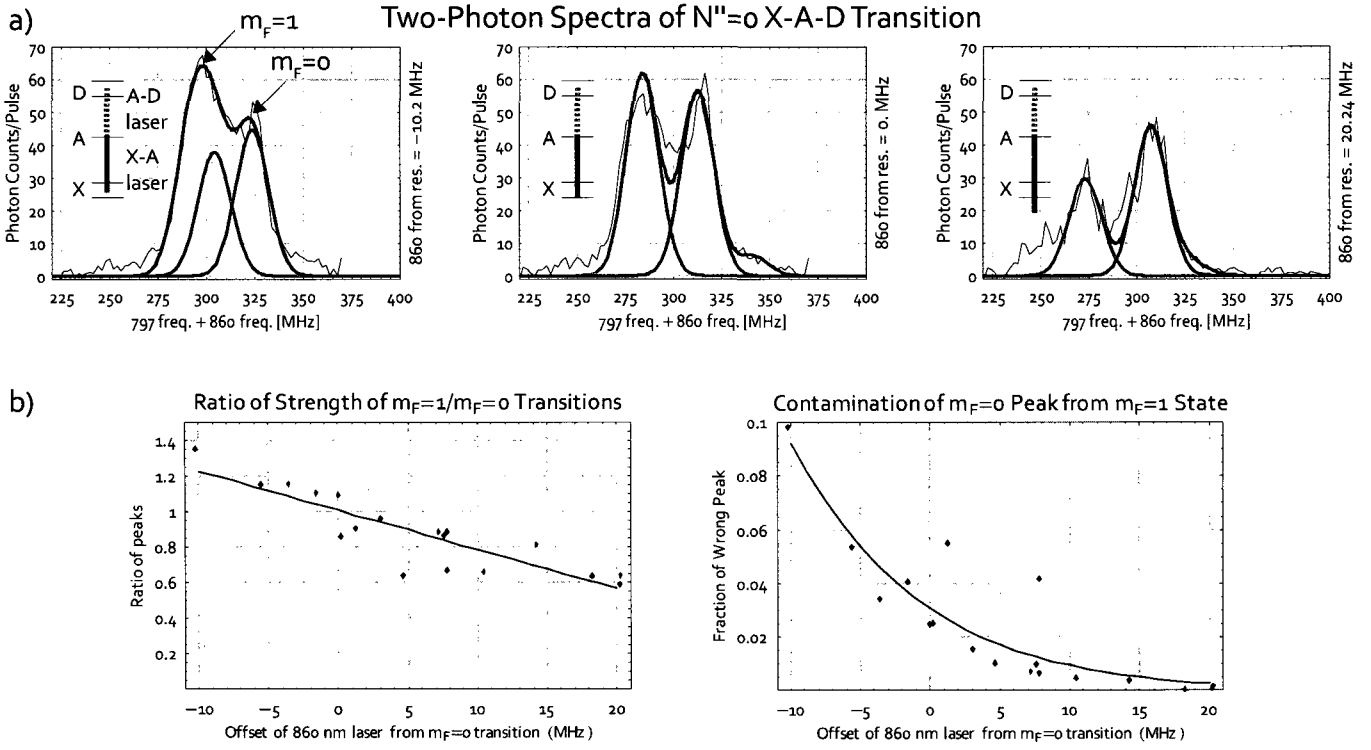

Figure 4.20: The position of the peaks in the observed two-photon spectra for the X-A-D transition depends on the total energy of the two lasers; the sum of the energies must match the D-X energy separation in order to drive the transition. The relative height of the peaks depends on the tuning of the A-X (860 nm) laser. The spectra in part a) show the number of molecules counted using $\hat{z}$-polarized light as the D-A laser is tuned through the two $N'' = 0$ transitions, for three tunings of the A-X laser. In the first case, the A-X laser is tuned 10 MHz to the red of the desired $m_F = 0$ transition; the $m_F = 1$ transition is larger than the $m_F = 0$ line. As the laser is shifted to resonance with (and then to the blue of) the A-X transition, the amplitude of the $m_F = 1$ transition decreases. Choosing the offset of the A-X transition properly can reduce the contribution of the $m_F = 1$ line when measuring the population of the X $\left|m_S = \frac{1}{2},\, m_I = -\frac{1}{2}\right\rangle$ state. The curve through each peak in part a) is a fit to the observed spectra.

4.6.2 Calculations for ^{137}BaF

The experiment to measure parity violation requires the use of a molecule with nonzero nuclear spin on the nucleus which interacts strongly with the electron wavefunction. For barium, ^{137}BaF (natural abundance of 11%) and ^{135}BaF (6.6%) are suitable; both have a nuclear spin of $I = 3/2$ for the barium nucleus. The intent is to first investigate ^{137}BaF since it has a larger abundance. Most of the spectroscopic constants can be adapted from those known for ^{138}BaF, as noted in the previous sections. Hyperfine data on the ^{137}BaF ground (X $^2\Sigma$) state is available[33], and the A $^2\Pi$ hyperfine splittings are expected to be small. Magnetic constants ($g_\parallel$ and $g_\perp$) are expected to be close to those of ^{138}BaF.

Like the level crossing experiment with ^{138}BaF, the parity violation experiment requires knowledge of the crossing of $N = 0$ and $N = 1$ levels of the ground state (X), and of the transitions to the A and D states for state preparation and detection. The level crossings will be discussed first. At each level crossing, it is useful to know:

- the state involved
- which transitions can be used to probe the state
- the magnetic field required to bring the levels to degeneracy
- the dipole matrix element between the crossing levels
- and strength of the parity-violation interaction

The strength of the parity-violating interaction depends on the specific levels involved in each crossing. The relative strength is based on a calculation of $\langle PNC \rangle = \left(\vec{S} \times \hat{n}\right) \cdot \vec{I}/|I|$ (eq. 3.8) as an effective Hamiltonian to represent parity-odd interactions. Note that the magnitude of this term can be at most $\frac{1}{2}$ for a system with one unpaired electron. Figure 4.21 shows the crossings

related to the $N = 0, 1$ states. There are 11 crossings that exhibit a value of $\langle PNC \rangle$ of order unity; these are indicated on the right. The dipole matrix elements between the levels at the crossing are given in terms of kHz/$^{V}/_{cm}$. The dipole matrix element determines the width of the resonance, and the rate of population transfer for a given electric field, as in eq. 3.27. Figures 4.22 through 4.26 show all of the level crossings available. Nearby crossings with small values of $\langle PNC \rangle$ are useful for verifying that the observed asymmetry is related to the PNC effect.

The second important point (figure 4.27) is the expected laser spectra for ^{137}BaF. The ground state levels are colored by m_F, to demonstrate which transitions can be used to probe the levels involved in particular crossings.

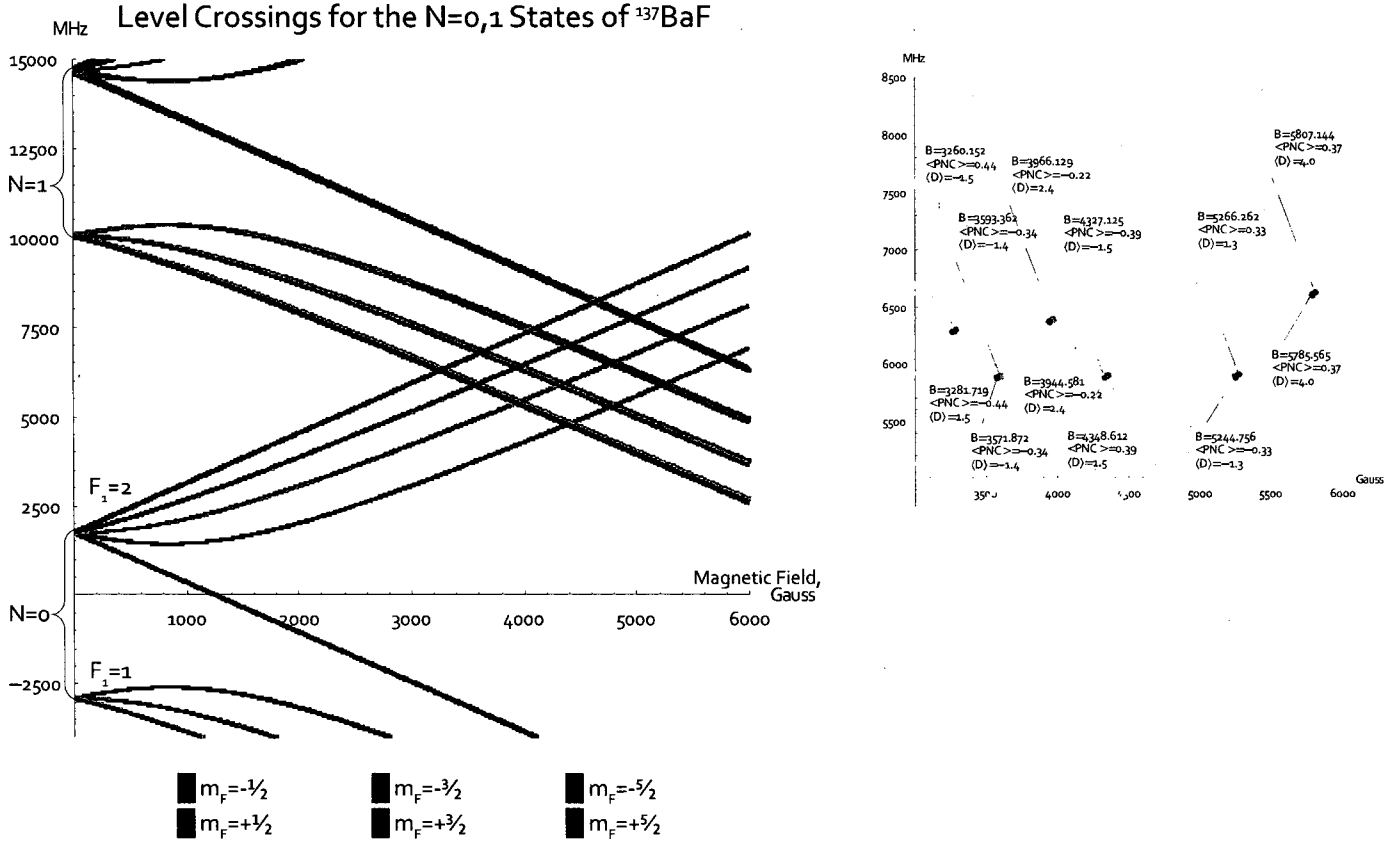

Figure 4.21: The energy level diagram for the $N = 0, 1$ rotational levels of the $X^2\Sigma_{1/2}$ state of ^{137}BaF show the Zeeman shift associated with the external magnetic field. The level crossings with the strongest parity-violating effects are shown at the right. The predicted magnetic field of the crossing B is written in Gauss. The expectation values $\langle PNC \rangle = \left\langle \left(\vec{S} \times \hat{n} \right) \cdot \vec{I} \right\rangle / |I|$ show the relative strength of the expected parity violation signal at each transition. The dipole matrix elements $\langle D \rangle$ are given in kHz/$^{V}/_{cm}$.

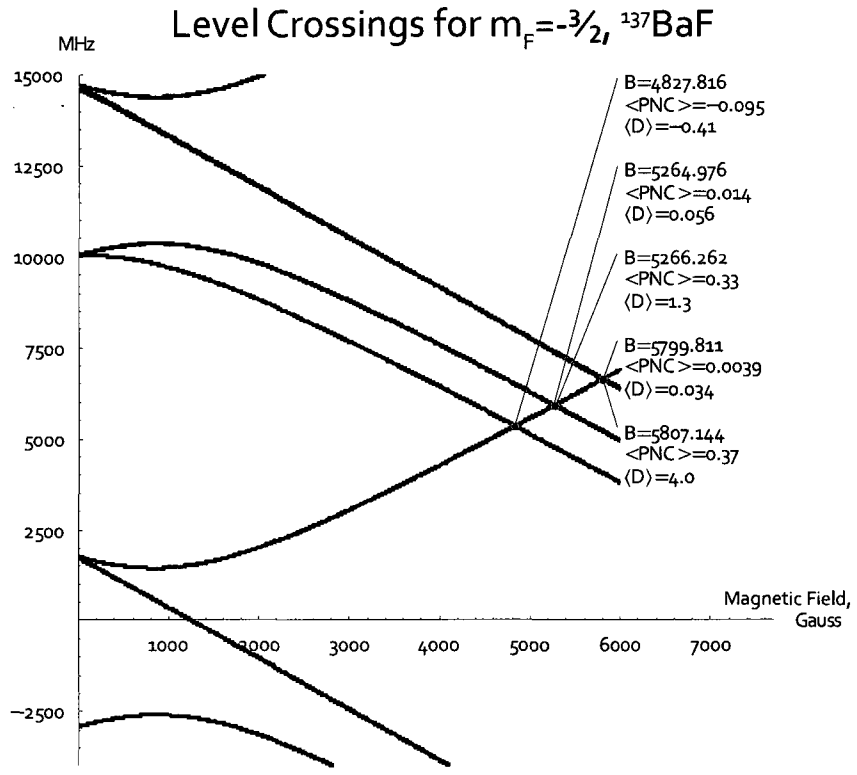

Figure 4.22: The level crossings associated with $\Delta m_F = 0$ transitions within the $m_F = -\frac{3}{2}$ level are illustrated. Five level crossings are available between even ($N = 0$) and odd ($N = 1$) parity states. Some of these crossings are very close together, separated due to the ^{19}F hyperfine contribution. The predicted magnetic field of the crossing B is written in Gauss. The expectation values $\langle PNC \rangle = \left\langle \left(\vec{S} \times \hat{n} \right) \cdot \vec{I} \right\rangle / |I|$ show the relative strength of the expected parity violation signal at each transition. The dipole matrix elements $\langle D \rangle$ are given in kHz/$^{\text{V}}$/$_{\text{cm}}$ in the figure, and in MHz/$^{\text{V}}$/$_{\text{cm}}$ in the table. The numbers refer to the transitions (figures 4.28 and 4.29) that can be used to probe the $N = 0$ level involved in the crossing.

B Gauss	Energy MHz	<PNC>	Dipole kHz/V/cm	Composition (N=0 state)	(N=1 state)
4827.82	5329.42	-0.095	-0.41	1 $-0.98\left\{N=0, m_N=0, m_S=\frac{1}{2}, m_{I1}=-\frac{3}{2}, m_{I2}=-\frac{1}{2}\right\}$	$-0.99\left\{N=1, m_N=-1, m_S=-\frac{1}{2}, m_{I1}=\frac{1}{2}, m_{I2}=-\frac{1}{2}\right\}$
5264.98	5905.92	0.014	0.056	1 $-0.99\left\{N=0, m_N=0, m_S=\frac{1}{2}, m_{I1}=-\frac{3}{2}, m_{I2}=-\frac{1}{2}\right\}$	$-0.99\left\{N=1, m_N=-1, m_S=-\frac{1}{2}, m_{I1}=-\frac{1}{2}, m_{I2}=\frac{1}{2}\right\}$
5266.26	5907.63	0.33	1.3	1 $0.99\left\{N=0, m_N=0, m_S=\frac{1}{2}, m_{I1}=-\frac{3}{2}, m_{I2}=-\frac{1}{2}\right\}$	$-0.93\left\{N=1, m_N=-1, m_s=\frac{1}{2}, m_{I1}=-\frac{1}{2}, m_{I2}=-\frac{1}{2}\right\}$ $-0.33\left\{N=1, m_N=0, m_s=-\frac{1}{2}, m_{I1}=-\frac{1}{2}, m_{I2}=-\frac{1}{2}\right\}$
5799.81	6618.69	0.0039	0.034	1 $0.99\left\{N=0, m_N=0, m_S=\frac{1}{2}, m_{I1}=-\frac{3}{2}, m_{I2}=-\frac{1}{2}\right\}$	$-0.94\left\{N=1, m_N=-1, m_s=\frac{1}{2}, m_{I1}=-\frac{3}{2}, m_{I2}=\frac{1}{2}\right\}$ $-0.33\left\{N=1, m_N=0, m_s=-\frac{1}{2}, m_{I1}=-\frac{3}{2}, m_{I2}=\frac{1}{2}\right\}$
5807.14	6628.51	0.37	4.0	1 $0.99\left\{N=0, m_N=0, m_S=\frac{1}{2}, m_{I1}=-\frac{3}{2}, m_{I2}=-\frac{1}{2}\right\}$	$0.94\left\{N=1, m_N=0, m_s=\frac{1}{2}, m_{I1}=-\frac{3}{2}, m_{I2}=-\frac{1}{2}\right\}$ $-0.34\left\{N=1, m_N=1, m_s=-\frac{1}{2}, m_{I1}=-\frac{3}{2}, m_{I2}=-\frac{1}{2}\right\}$

Table 4.5: The level crossings associated with $\Delta m_F = 0$ transitions within the $m_F{=}-\frac{3}{2}$ level are given, with the composition of the states involved in the crossing. This information can be used to find an appropriate transition for state preparation and detection appropriate for a particular crossing. The numbers refer to the transitions (figures 4.28 and 4.29) that can be used to probe the $N = 0$ level involved in the crossing.

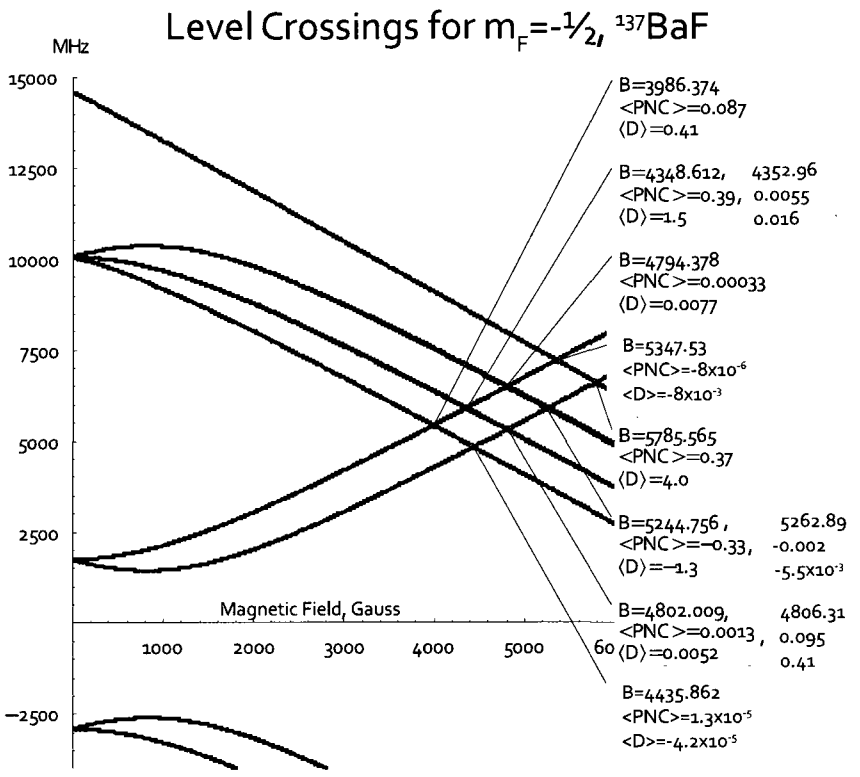

Figure 4.23: The level crossings associated with $\Delta m_F = 0$ transitions within the $m_F = -\frac{1}{2}$ level are illustrated. Some of these crossings are very close together, separated due to the ^{19}F hyperfine contribution. The predicted magnetic field of the crossing B is written in Gauss. The expectation values $\langle PNC \rangle = \left\langle \left(\vec{S} \times \hat{n} \right) \cdot \vec{I} \right\rangle / |I|$ show the relative strength of the expected parity violation signal at each transition. The dipole matrix elements $\langle D \rangle$ are given in kHz/$^{V}/_{cm}$.

B Gauss	Energy MHz	<PNC>	Dipole kHz/V/cm		Composition (N=0 state)	(N=1 state)
3986.37	5429.27	0.087	0.41	2	$0.98\left\{N=0, m_N=0, m_S=\frac{1}{2}, m_{I1}=-\frac{1}{2}, m_{I2}=-\frac{1}{2}\right\}$	$0.99\left\{N=1, m_N=-1, m_S=-\frac{1}{2}, m_{I1}=\frac{3}{2}, m_{I2}=-\frac{1}{2}\right\}$
4348.61	5897.75	0.39	1.5	2	$-0.98\left\{N=0, m_N=0, m_S=\frac{1}{2}, m_{I1}=-\frac{1}{2}, m_{I2}=-\frac{1}{2}\right\}$	$-0.93\left\{N=1, m_N=-1, m_S=\frac{1}{2}, m_{I1}=\frac{1}{2}, m_{I2}=-\frac{1}{2}\right\}$ $-0.32\left\{N=1, m_N=0, m_S=-\frac{1}{2}, m_{I1}=\frac{1}{2}, m_{I2}=-\frac{1}{2}\right\}$
4352.96	5903.41	0.0055	0.016	2	$-0.98\left\{N=0, m_N=0, m_S=\frac{1}{2}, m_{I1}=-\frac{1}{2}, m_{I2}=-\frac{1}{2}\right\}$	$-0.98\left\{N=1, m_N=-1, m_S=-\frac{1}{2}, m_{I1}=\frac{1}{2}, m_{I2}=\frac{1}{2}\right\}$
4435.86	4828.65	0.000013	-42e-6	3	$-0.98\left\{N=0, m_N=0, m_S=\frac{1}{2}, m_{I1}=-\frac{3}{2}, m_{I2}=\frac{1}{2}\right\}$	$0.99\left\{N=1, m_N=-1, m_S=-\frac{1}{2}, m_{I1}=\frac{3}{2}, m_{I2}=-\frac{1}{2}\right\}$
4794.38	6481.16	0.00033	0.0077	2	$-0.99\left\{N=0, m_N=0, m_S=\frac{1}{2}, m_{I1}=-\frac{1}{2}, m_{I2}=-\frac{1}{2}\right\}$	$0.93\left\{N=1, m_N=-1, m_S=\frac{1}{2}, m_{I1}=-\frac{1}{2}, m_{I2}=\frac{1}{2}\right\}$ $+0.33\left\{N=1, m_N=0, m_S=-\frac{1}{2}, m_{I1}=-\frac{1}{2}, m_{I2}=\frac{1}{2}\right\}$
4802.01	5304.39	0.0013	0.0052	3	$0.98\left\{N=0, m_N=0, m_S=\frac{1}{2}, m_{I1}=-\frac{3}{2}, m_{I2}=\frac{1}{2}\right\}$	$0.93\left\{N=1, m_N=-1, m_S=\frac{1}{2}, m_{I1}=\frac{1}{2}, m_{I2}=-\frac{1}{2}\right\}$ $+0.33\left\{N=1, m_N=0, m_S=-\frac{1}{2}, m_{I1}=\frac{1}{2}, m_{I2}=-\frac{1}{2}\right\}$
4806.31	5310.01	0.095	0.41	3	$-0.98\left\{N=0, m_N=0, m_S=\frac{1}{2}, m_{I1}=-\frac{3}{2}, m_{I2}=\frac{1}{2}\right\}$	$-0.99\left\{N=1, m_N=-1, m_S=-\frac{1}{2}, m_{I1}=\frac{1}{2}, m_{I2}=\frac{1}{2}\right\}$
5244.76	5886.46	-0.33	-1.3	3	$-0.99\left\{N=0, m_N=0, m_S=\frac{1}{2}, m_{I1}=-\frac{3}{2}, m_{I2}=\frac{1}{2}\right\}$	$0.93\left\{N=1, m_N=-1, m_S=\frac{1}{2}, m_{I1}=-\frac{1}{2}, m_{I2}=\frac{1}{2}\right\}$ $+0.33\left\{N=1, m_N=0, m_S=-\frac{1}{2}, m_{I1}=-\frac{1}{2}, m_{I2}=\frac{1}{2}\right\}$
5260.15	5906.82	0.0017	0.0048	3	$-0.99\left\{N=0, m_N=0, m_S=\frac{1}{2}, m_{I1}=-\frac{3}{2}, m_{I2}=\frac{1}{2}\right\}$	$0.93\left\{N=1, m_N=-1, m_S=\frac{1}{2}, m_{I1}=-\frac{1}{2}, m_{I2}=\frac{1}{2}\right\}$ $+0.33\left\{N=1, m_N=0, m_S=-\frac{1}{2}, m_{I1}=-\frac{1}{2}, m_{I2}=\frac{1}{2}\right\}$
5262.89	5906.83	-0.0020	-0.0055	3	$-0.99\left\{N=0, m_N=0, m_S=\frac{1}{2}, m_{I1}=-\frac{3}{2}, m_{I2}=\frac{1}{2}\right\}$	$-0.93\left\{N=1, m_N=0, m_S=\frac{1}{2}, m_{I1}=-\frac{1}{2}, m_{I2}=-\frac{1}{2}\right\}$ $+0.33\left\{N=1, m_N=1, m_S=-\frac{1}{2}, m_{I1}=-\frac{1}{2}, m_{I2}=-\frac{1}{2}\right\}$
5347.53	7213.26	-7.9e-6	0.0080	2	$-0.99\left\{N=0, m_N=0, m_S=\frac{1}{2}, m_{I1}=-\frac{1}{2}, m_{I2}=-\frac{1}{2}\right\}$	$0.94\left\{N=1, m_N=0, m_S=\frac{1}{2}, m_{I1}=-\frac{3}{2}, m_{I2}=\frac{1}{2}\right\}$ $-0.34\left\{N=1, m_N=1, m_S=-\frac{1}{2}, m_{I1}=-\frac{3}{2}, m_{I2}=\frac{1}{2}\right\}$
5785.57	6605.09	0.37	4.0	3	$-0.99\left\{N=0, m_N=0, m_S=\frac{1}{2}, m_{I1}=-\frac{3}{2}, m_{I2}=\frac{1}{2}\right\}$	$-0.94\left\{N=1, m_N=0, m_S=\frac{1}{2}, m_{I1}=-\frac{3}{2}, m_{I2}=\frac{1}{2}\right\}$ $+0.34\left\{N=1, m_N=1, m_S=-\frac{1}{2}, m_{I1}=-\frac{3}{2}, m_{I2}=\frac{1}{2}\right\}$

Table 4.6: The level crossings associated with $\Delta m_F = 0$ transitions within the $m_F = -\frac{1}{2}$ level are given, with the composition of the states involved in the crossing. This information can be used to find an appropriate transition for state preparation and detection appropriate for a particular crossing. The numbers refer to the transitions (figures 4.28 and 4.29) that can be used to probe the $N = 0$ level involved in the crossing.

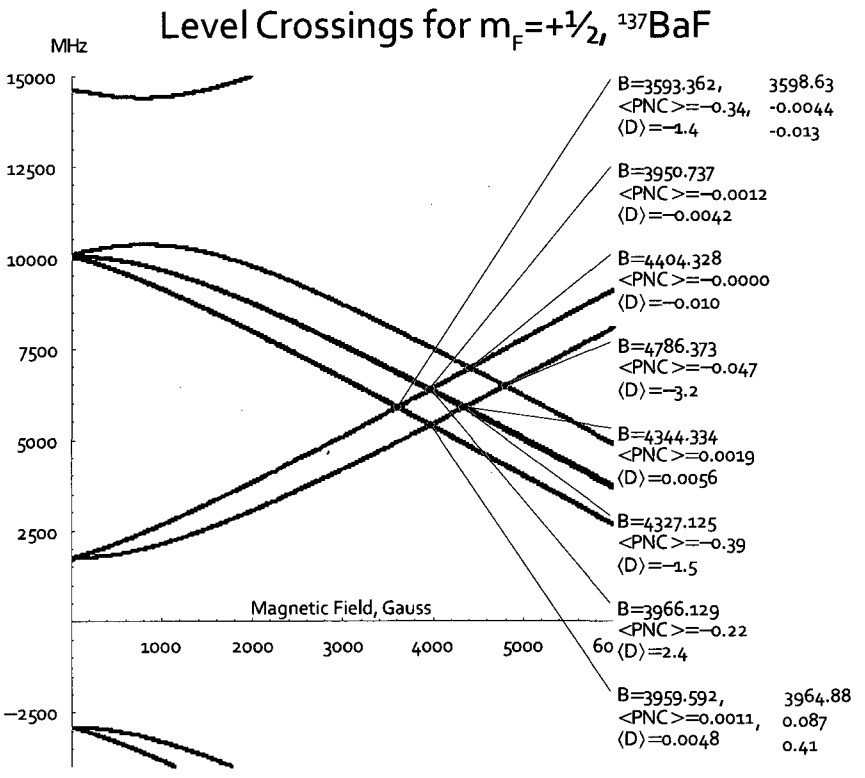

Figure 4.24: The level crossings associated with $\Delta m_F = 0$ transitions within the $m_F = +\frac{1}{2}$ level are illustrated. Some of these crossings are very close together, separated due to the ^{19}F hyperfine contribution. The predicted magnetic field of the crossing B is written in Gauss. The expectation values $\langle PNC \rangle = \left\langle \left(\vec{S} \times \hat{n} \right) \cdot \vec{I} \right\rangle / |I|$ show the relative strength of the expected parity violation signal at each transition. The dipole matrix elements $\langle D \rangle$ are given in kHz/$^{V}/_{cm}$.

B Gauss	Energy MHz	<PNC>	Dipole kHz/V/cm		Composition (N=0 state)	(N=1 state)
3593.36	5893.63	-0.34	-1.4	4	$-0.99\left\{N==0, m_N==0, m_S==\frac{1}{2}, m_{I1}==\frac{1}{2}, m_{I2}==-\frac{1}{2}\right\}$	$0.93\left\{N==1, m_N==-1, m_s==\frac{1}{2}, m_{I1}==\frac{3}{2}, m_{I2}==-\frac{1}{2}\right\}$
3598.63	5900.6	-0.0044	-0.013	4	$-0.99\left\{N==0, m_N==0, m_S==\frac{1}{2}, m_{I1}==\frac{1}{2}, m_{I2}==-\frac{1}{2}\right\}$	$-0.99\left\{N==1, m_N==-1, m_s==-\frac{1}{2}, m_{I1}==\frac{3}{2}, m_{I2}==\frac{1}{2}\right\}$
3950.74	6368.45	-0.0012	-0.0042	4	$-0.99\left\{N==0, m_N==0, m_S==\frac{1}{2}, m_{I1}==\frac{1}{2}, m_{I2}==-\frac{1}{2}\right\}$	$-0.93\left\{N==1, m_N==-1, m_s==\frac{1}{2}, m_{I1}==\frac{1}{2}, m_{I2}==\frac{1}{2}\right\}$
3959.59	5406.46	0.0011	0.0048	5	$0.98\left\{N==0, m_N==0, m_S==\frac{1}{2}, m_{I1}==-\frac{1}{2}, m_{I2}==\frac{1}{2}\right\}$	$0.93\left\{N==1, m_N==-1, m_s==\frac{1}{2}, m_{I1}==\frac{3}{2}, m_{I2}==-\frac{1}{2}\right\}$
3964.88	5413.23	0.087	0.41	5	$0.98\left\{N==0, m_N==0, m_S==\frac{1}{2}, m_{I1}==-\frac{1}{2}, m_{I2}==\frac{1}{2}\right\}$	$0.99\left\{N==1, m_N==-1, m_s==-\frac{1}{2}, m_{I1}==\frac{3}{2}, m_{I2}==\frac{1}{2}\right\}$
3966.13	6388.97	-0.22	2.4	4	$-0.99\left\{N==0, m_N==0, m_S==\frac{1}{2}, m_{I1}==\frac{1}{2}, m_{I2}==-\frac{1}{2}\right\}$	$0.92\left\{N==1, m_N==0, m_s==\frac{1}{2}, m_{I1}==\frac{1}{2}, m_{I2}==-\frac{1}{2}\right\}$
4327.12	5880.29	-0.39	-1.5	5	$-0.98\left\{N==0, m_N==0, m_S==\frac{1}{2}, m_{I1}==-\frac{1}{2}, m_{I2}==\frac{1}{2}\right\}$	$-0.93\left\{N==1, m_N==-1, m_s==\frac{1}{2}, m_{I1}==\frac{1}{2}, m_{I2}==\frac{1}{2}\right\}$
4344.33	5902.61	0.0019	-0.0056	5	$-0.98\left\{N==0, m_N==0, m_S==\frac{1}{2}, m_{I1}==-\frac{1}{2}, m_{I2}==\frac{1}{2}\right\}$	$0.93\left\{N==1, m_N==0, m_s==\frac{1}{2}, m_{I1}==\frac{1}{2}, m_{I2}==-\frac{1}{2}\right\}$
4404.33	6975.37	-42e-6	-0.010	4	$-0.99\left\{N==0, m_N==0, m_S==\frac{1}{2}, m_{I1}==\frac{1}{2}, m_{I2}==-\frac{1}{2}\right\}$	$-0.92\left\{N==1, m_N==0, m_s==\frac{1}{2}, m_{I1}==-\frac{1}{2}, m_{I2}==\frac{1}{2}\right\}$
4786.37	6479.61	-0.047	-3.2	5	$0.99\left\{N==0, m_N==0, m_S==\frac{1}{2}, m_{I1}==-\frac{1}{2}, m_{I2}==\frac{1}{2}\right\}$	$0.93\left\{N==1, m_N==0, m_s==\frac{1}{2}, m_{I1}==-\frac{1}{2}, m_{I2}==\frac{1}{2}\right\}$

Table 4.7: The level crossings associated with $\Delta m_F = 0$ transitions within the $m_F{=}+\frac{1}{2}$ level are given, with the composition of the states involved in the crossing. This information can be used to find an appropriate transition for state preparation and detection appropriate for a particular crossing. The numbers refer to the transitions (figures 4.28 and 4.29) that can be used to probe the $N = 0$ level involved in the crossing.

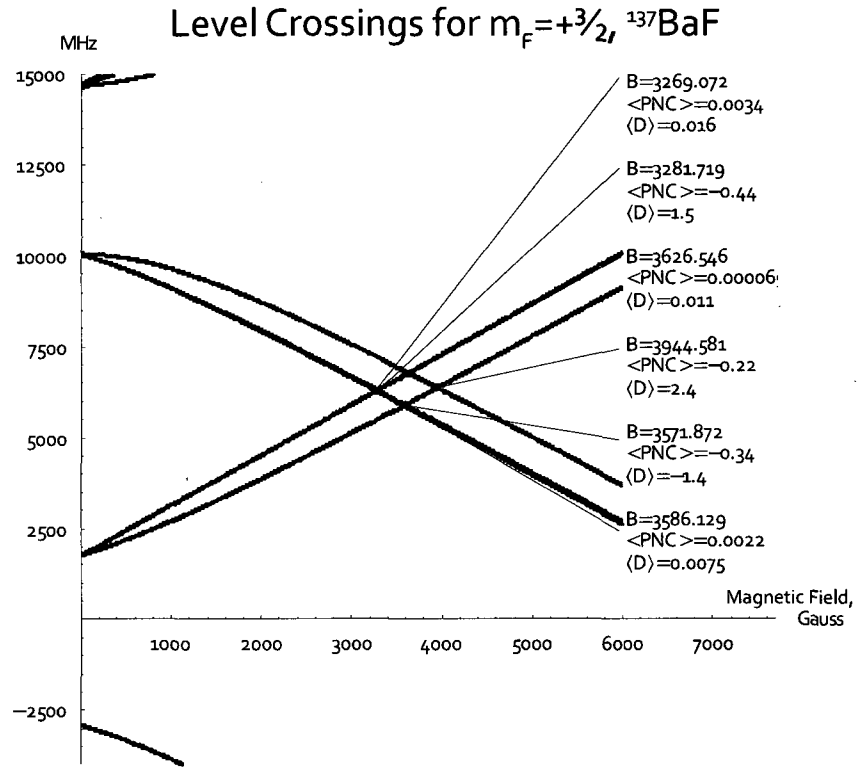

Figure 4.25: The level crossings associated with $\Delta m_F = 0$ transitions within the $m_F = +\frac{3}{2}$ level are illustrated. Six level crossings are available between even ($N = 0$) and odd ($N = 1$) parity states, of which three are expected to exhibit strong signs of parity violation. Some of these crossings are very close together, separated due to the ^{19}F hyperfine contribution. The predicted magnetic field of the crossing B is written in Gauss. The expectation values $\langle PNC \rangle = \left\langle \left(\vec{S} \times \hat{n} \right) \cdot \vec{I} \right\rangle / |I|$ show the relative strength of the expected parity violation signal at each transition. The dipole matrix elements $\langle D \rangle$ are given in $\mathrm{kHz}/^{V}/_{cm}$.

B Gauss	Energy MHz	<PNC>	Dipole kHz/V/cm	Composition (N=0 state)		(N=1 state)	
3269.07	6280.32	0.0034	0.016	6	$1.0\left\{N==0, m_N==0, m_S==\frac{1}{2}, m_{I1}==\frac{3}{2}, m_{I2}==-\frac{1}{2}\right\}$		$0.93\left\{N==1, m_N==-1, m_S==\frac{1}{2}, m_{I1}==\frac{3}{2}, m_{I2}==\frac{1}{2}\right\}$
3281.72	6297.92	-0.44	1.5	6	$1.0\left\{N==0, m_N==0, m_S==\frac{1}{2}, m_{I1}==\frac{3}{2}, m_{I2}==-\frac{1}{2}\right\}$		$0.93\left\{N==1, m_N==0, m_S==\frac{1}{2}, m_{I1}==\frac{3}{2}, m_{I2}==-\frac{1}{2}\right\}$
3571.87	5879.20	-0.34	-1.4	7	$-0.99\left\{N==0, m_N==0, m_S==\frac{1}{2}, m_{I1}==\frac{1}{2}, m_{I2}==\frac{1}{2}\right\}$		$0.93\left\{N==1, m_N==-1, m_S==\frac{1}{2}, m_{I1}==\frac{3}{2}, m_{I2}==\frac{1}{2}\right\}$
3586.13	5898.02	0.0022	0.0075	7	$0.99\left\{N==0, m_N==0, m_S==\frac{1}{2}, m_{I1}==\frac{1}{2}, m_{I2}==\frac{1}{2}\right\}$		$0.93\left\{N==1, m_N==0, m_S==\frac{1}{2}, m_{I1}==\frac{3}{2}, m_{I2}==-\frac{1}{2}\right\}$
3626.55	6777.93	69×10^{-6}	0.011	6	$-1.0\left\{N==0, m_N==0, m_S==\frac{1}{2}, m_{I1}==\frac{3}{2}, m_{I2}==-\frac{1}{2}\right\}$		$-0.92\left\{N==1, m_N==0, m_S==\frac{1}{2}, m_{I1}==\frac{1}{2}, m_{I2}==\frac{1}{2}\right\}$
3944.58	6372.99	-0.22	2.4	7	$0.99\left\{N==0, m_N==0, m_S==\frac{1}{2}, m_{I1}==\frac{1}{2}, m_{I2}==\frac{1}{2}\right\}$		$-0.92\left\{N==1, m_N==0, m_S==\frac{1}{2}, m_{I1}==\frac{1}{2}, m_{I2}==\frac{1}{2}\right\}$

Table 4.8: The level crossings associated with $\Delta m_F = 0$ transitions within the $m_F{=}+\frac{3}{2}$ level are given, with the composition of the states involved in the crossing. This information can be used to find an appropriate transition for state preparation and detection appropriate for a particular crossing. The numbers refer to the transitions (figures 4.28 and 4.29) that can be used to probe the $N = 0$ level involved in the crossing.

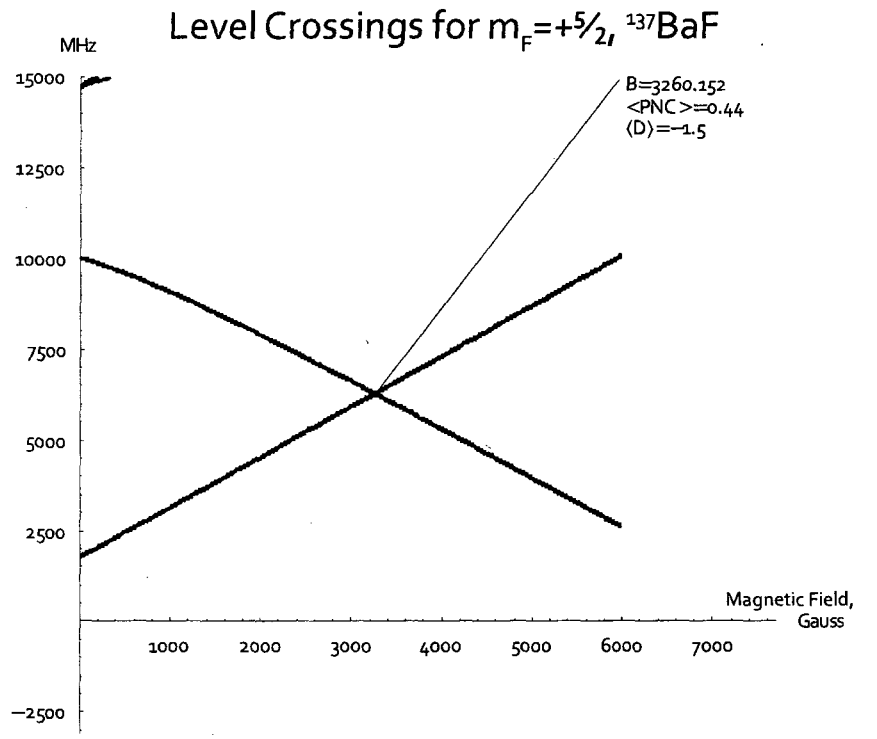

B Gauss	Energy MHz	<PNC>	Dipole kHz/V/cm	Composition (N=0 state)	(N=1 state)
3260.15	6284.7	0.44	-1.5	8 $1.0\left\{N=0, m_N=0, m_S=\frac{1}{2}, m_{I1}=\frac{3}{2}, m_{I2}=\frac{1}{2}\right\}$	$0.93\left\{N=1, m_N=0, m_S=\frac{1}{2}, m_{I1}=\frac{3}{2}, m_{I2}=\frac{1}{2}\right\}$

Figure 4.26: The sole level crossing associated with $\Delta m_F = 0$ transitions within the $m_F = +\frac{5}{2}$ level is illustrated. The predicted magnetic field of the crossing B is written in Gauss. The expectation values $\langle PNC \rangle = \left\langle \left(\vec{S} \times \hat{n} \right) \cdot \vec{I} \right\rangle / |I|$ show the relative strength of the expected parity violation signal at each transition. The dipole matrix elements $\langle D \rangle$ are given in kHz/V/cm. The numbers refer to the transitions (figures 4.28 and 4.29) that can be used to probe the $N = 0$ level involved in the crossing.

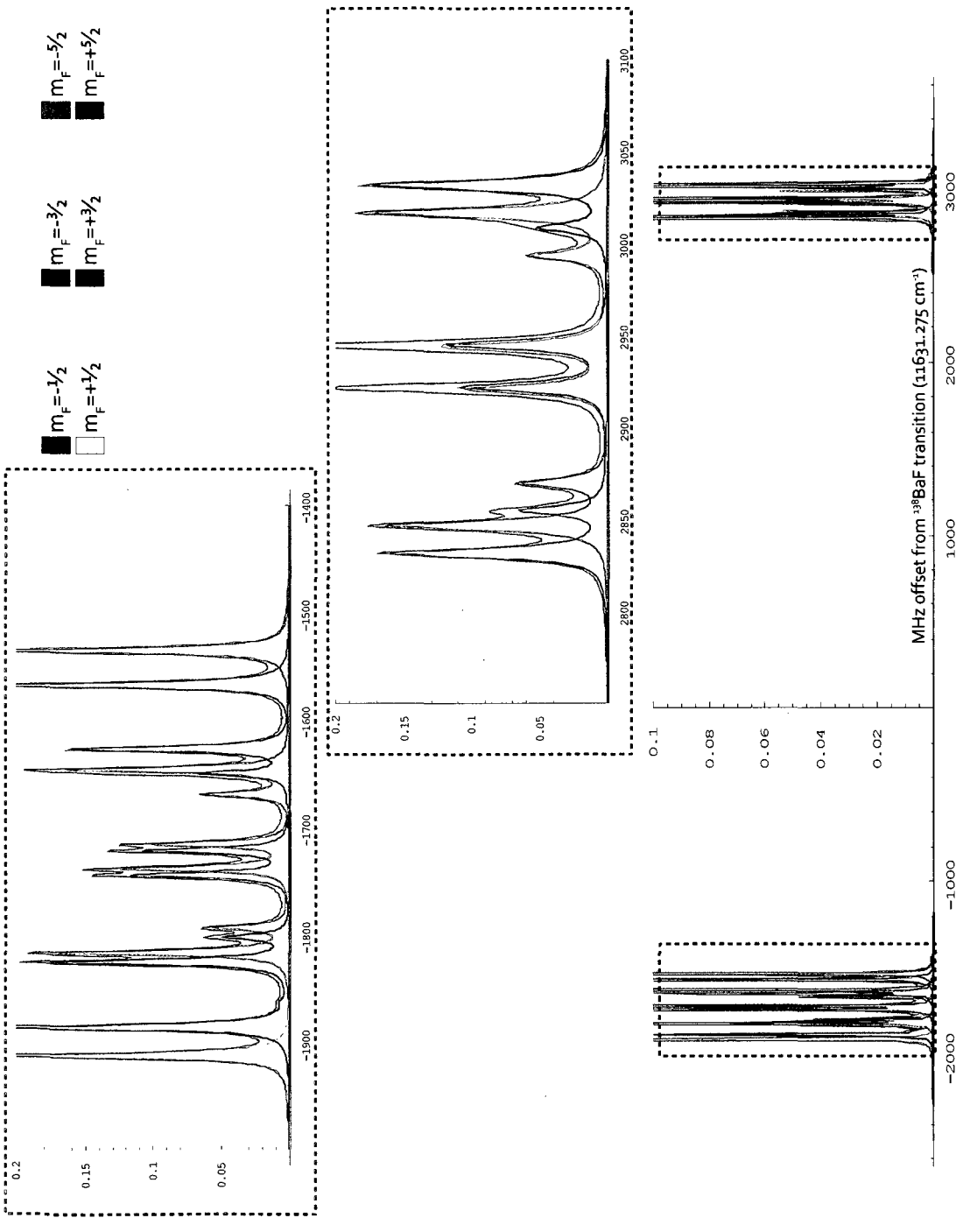

Figure 4.27: Simulated R-branch $J = \frac{1}{2}$, $J' = \frac{3}{2}$ X-A transitions of ^{137}BaF at 115 Gauss, with $\hat{z}$-polarized light. The frequency axis is offset from the center of the ^{138}BaF transitions at 11631.275 cm^{-1}. The simulated specta is colored by the value of m_F in the ground state, with height determined by the square of the dipole matrix element between the upper and lower states in the transition. The lower group of lines (between -2000 and -1000 MHz) are from states involved in level crossings. The state content of the lower level of these transitions is detailed in figures 4.28 and 4.29.

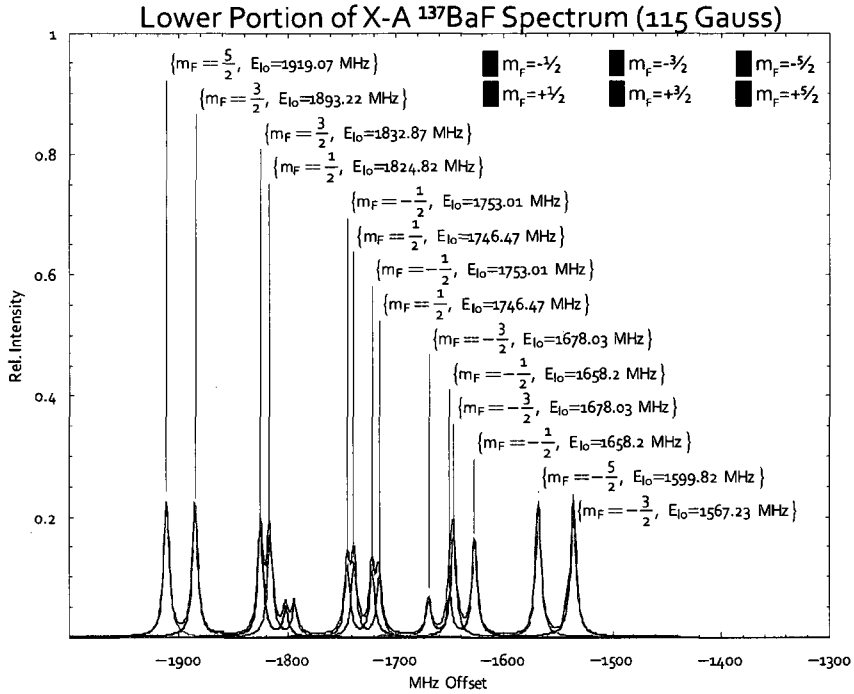

m_F	E_{lo} (MHz)		Composition
$-\frac{5}{2}$	1599.82		$0.999999\,\{N=0, m_N=0, m_S=-\frac{1}{2}, m_{I1}=-\frac{1}{2}, m_{I2}=-\frac{1}{2}\}$
$-\frac{3}{2}$	1567.23		$-0.849103\,\{N=0, m_N=0, m_S=-\frac{1}{2}, m_{I1}=-\frac{3}{2}, m_{I2}=\frac{1}{2}\} + 0.367672\,\{N=0, m_I=0, m_S=-\frac{1}{2}, m_{I1}=-\frac{1}{2}, m_{I2}=-\frac{1}{2}\}$
$-\frac{3}{2}$	1678.03	1	$0.424374\,\{N=0, m_N=0, m_S=-\frac{1}{2}, m_{I1}=-\frac{3}{2}, m_{I2}=\frac{1}{2}\} + 0.735037\,\{N=0, m_I=0, m_S=-\frac{1}{2}, m_{I1}=-\frac{1}{2}, m_{I2}=-\frac{1}{2}\} - 0.424374\,\{N=0, m_I=0, m_S=\frac{1}{2}, m_{I1}=-\frac{3}{2}, m_{I2}=-\frac{1}{2}\}$
$-\frac{1}{2}$	1658.2	3	$-0.84807\,\{N=0, m_N=0, m_S=-\frac{1}{2}, m_{I1}=-\frac{1}{2}, m_{I2}=\frac{1}{2}\} - 0.489634\,\{N=0, m_N=0, m_S=\frac{1}{2}, m_{I1}=-\frac{3}{2}, m_{I2}=\frac{1}{2}\}$
$-\frac{1}{2}$	1753.01	2	$0.692505\,\{N=0, m_N=0, m_S=-\frac{1}{2}, m_{I1}=\frac{1}{2}, m_{I2}=-\frac{1}{2}\} + 0.692505\,\{N=0, m_N=0, m_S=\frac{1}{2}, m_{I1}=-\frac{1}{2}, m_{I2}=-\frac{1}{2}\}$
$\frac{1}{2}$	1746.47		$-0.686712\,\{N=0, m_I=0, m_S=-\frac{1}{2}, m_{I1}=\frac{1}{2}, m_{I2}=\frac{1}{2}\} - 0.686712\,\{N=0, m_N=0, m_S=\frac{1}{2}, m_{I1}=-\frac{1}{2}, m_{I2}=\frac{1}{2}\}$
$\frac{1}{2}$	1824.82		$0.485764\,\{N=0, m_N=0, m_S=-\frac{1}{2}, m_{I1}=\frac{3}{2}, m_{I2}=-\frac{1}{2}\} + 0.841369\,\{N=0, m_N=0, m_S=\frac{1}{2}, m_{I1}=\frac{1}{2}, m_{I2}=-\frac{1}{2}\}$
$\frac{3}{2}$	1832.87	7	$0.484864\,\{N=0, m_N=0, m_S=-\frac{1}{2}, m_{I1}=\frac{3}{2}, m_{I2}=\frac{1}{2}\} + 0.839808\,\{N=0, m_N=0, m_S=\frac{1}{2}, m_{I1}=\frac{1}{2}, m_{I2}=\frac{1}{2}\}$
$\frac{3}{2}$	1893.22	6	$0.970232\,\{N=0, m_N=0, m_S=\frac{1}{2}, m_{I1}=\frac{3}{2}, m_{I2}=-\frac{1}{2}\}$
$\frac{5}{2}$	1919.07	8	$0.999999\,\{N=0, m_N=0, m_S=\frac{1}{2}, m_{I1}=\frac{3}{2}, m_{I2}=\frac{1}{2}\}$

Figure 4.28: The value of m_F, the lower state energy, and its composition are marked for the strongest of the R-branch $N = 0$, $\Delta m_F = 0$ X-A transitions of ^{137}BaF. The portion of the spectrum shown is the lower group of lines from figure 4.27. The frequency axis is offset from the center of the ^{138}BaF transitions at 11631.275 cm^{-1}, and heights are proportional to the square of the dipole matrix element between the upper and lower states. The spectral lines are color-coded by the value of m_F. The numbers refer to the crossings (figures 4.22 through 4.26) that can be used to probe the $N = 0$ level involved in the transition.

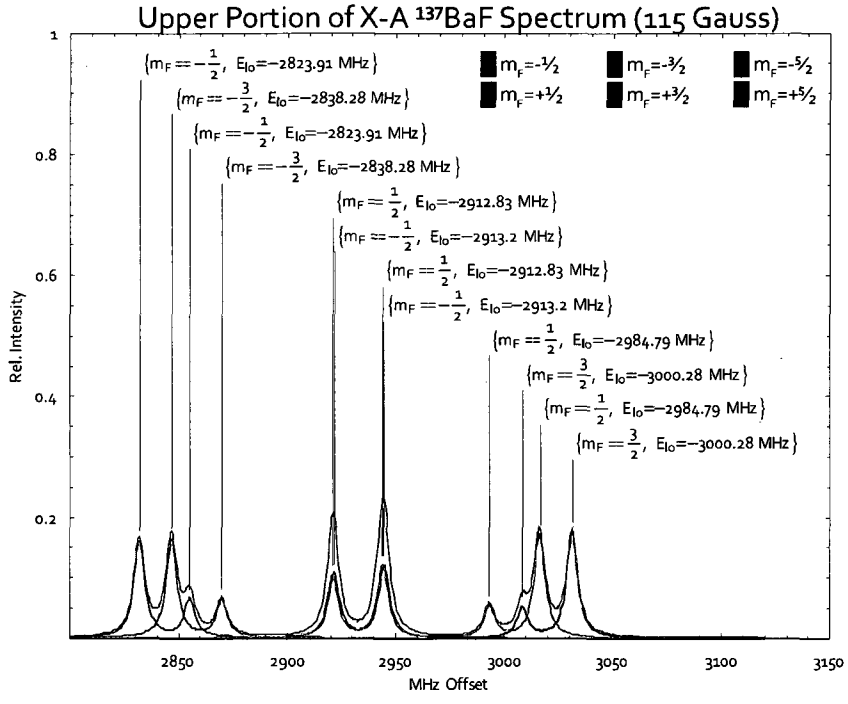

m_F	E_{lo} (MHz)		Composition
$-\frac{3}{2}$	-2838.28	1	$-0.499798\left\{N=0, m_N=0, m_S=-\frac{1}{2}, m_{I1}=-\frac{1}{2}, m_{I2}=-\frac{1}{2}\right\}+0.865676\left\{N=0, m_N=0, m_S=\frac{1}{2}, m_{I1}=-\frac{3}{2}, m_{I2}=-\frac{1}{2}\right\}$
$-\frac{1}{2}$	-2913.2	2	$-0.701432\left\{N=0, m_N=0, m_S=-\frac{1}{2}, m_{I1}=\frac{1}{2}, m_{I2}=-\frac{1}{2}\right\}+0.701432\left\{N=0, m_N=0, m_S=\frac{1}{2}, m_{I1}=-\frac{1}{2}, m_{I2}=-\frac{1}{2}\right\}$
$-\frac{1}{2}$	-2823.91	3	$-0.495949\left\{N=0, m_N=0, m_S=-\frac{1}{2}, m_{I1}=-\frac{1}{2}, m_{I2}=\frac{1}{2}\right\}+0.859009\left\{N=0, m_N=0, m_S=\frac{1}{2}, m_{I1}=-\frac{3}{2}, m_{I2}=\frac{1}{2}\right\}$
$\frac{1}{2}$	-2984.79	5	$0.856276\left\{N=0, m_N=0, m_S=-\frac{1}{2}, m_{I1}=\frac{3}{2}, m_{I2}=-\frac{1}{2}\right\}-0.494371\left\{N=0, m_N=0, m_S=\frac{1}{2}, m_{I1}=\frac{1}{2}, m_{I2}=-\frac{1}{2}\right\}$
$\frac{1}{2}$	-2912.83	6	$-0.698885\left\{N=0, m_N=0, m_S=-\frac{1}{2}, m_{I1}=\frac{1}{2}, m_{I2}=\frac{1}{2}\right\}+0.698885\left\{N=0, m_N=0, m_S=\frac{1}{2}, m_{I1}=-\frac{1}{2}, m_{I2}=\frac{1}{2}\right\}$
$\frac{3}{2}$	-3000.28	7	$-0.865586\left\{N=0, m_N=0, m_S=-\frac{1}{2}, m_{I1}=\frac{3}{2}, m_{I2}=\frac{1}{2}\right\}+0.499746\left\{N=0, m_I=0, m_S=\frac{1}{2}, m_{I1}=\frac{1}{2}, m_{I2}=\frac{1}{2}\right\}$

Figure 4.29: The value of m_F, the lower state energy, and its composition are marked for the strongest of the R-branch $N = 0$, $\Delta m_F = 0$ X-A transitions of ^{137}BaF. The portion of the spectrum shown is the upper group of lines from figure 4.27. The frequency axis is offset from the center of the ^{138}BaF transitions at 11631.275 cm^{-1}, and heights are proportional to the square of the dipole matrix element between the upper and lower states. The spectral lines are color-coded by the value of m_F. The numbers refer to the crossings (figures 4.22 through 4.26) that can be used to probe the $N = 0$ level involved in the transition.

4.7 Summary of Effective Constants

Hyperfine Hamiltonian and common alternate formulations

$$\mathcal{H}_{hfs} = b_F \vec{I}\cdot\vec{S} + \frac{1}{3}c\left(3I_zS_z - \vec{I}\cdot\vec{S}\right)$$

$$\begin{aligned} A_{iso} &= b_F \\ A_{dip} &= c \end{aligned}$$

$$\begin{aligned} A_{\parallel} &\equiv b = b_F + \frac{2}{3}c \\ A_{\perp} &\equiv b_F - \frac{c}{3} \end{aligned}$$

$^2\Sigma$ Zeeman Hamiltonian

$$\begin{aligned} {}^2\Sigma: \quad \mathcal{H}_Z &= \mu_B\left(\left(g_S^e + g_l^e\right)\vec{S}\cdot\vec{B} - g_l^e\left(\vec{S}\cdot\hat{n}\right)\left(\vec{B}\cdot\hat{n}\right) - g_r\vec{N}\cdot\vec{B}\right) + \mu_N g_N \vec{I}\cdot\vec{B} \\ &= \mu_B\left(g_\perp\vec{S}\cdot\vec{B} + \left(g_\parallel - g_\perp\right)\left(\vec{S}\cdot\hat{n}\right)\left(\vec{B}\cdot\hat{n}\right) - g_r\vec{N}\cdot\vec{B}\right) + \mu_N g_N\vec{I}\cdot\vec{B} \end{aligned}$$

$$g_S = 2.002\ldots, \qquad g_L = 1$$

$$g_S^e \approx g_S \qquad g_l^e \cong 0$$

$$g_\parallel = g_z \cong g_S \qquad g_\perp = g_S^e + g_l^e \ (\Sigma\text{state only})$$

$^2\Pi$ Zeeman Hamiltonian

$$
\begin{aligned}
^2\Pi: \quad \mathcal{H}_Z &= \mu_B \Big(g_S^e \vec{S}\cdot\vec{B} + (g_L' + g_r)\,\vec{L}\cdot\vec{B} - g_r \vec{N}\cdot\vec{B} + g_l\,(S_x B_x + S_y B_y) \\
&\quad - g_r^{e\prime}\left(e^{-2i\phi} N_+ B_+ + e^{2i\phi} N_- B_-\right) \\
&\quad + g_l'\left(e^{-2i\phi} S_+ B_+ + e^{2i\phi} S_- B_-\right)\Big) + \mu_N g_N \vec{I}\cdot\vec{B}
\end{aligned}
$$

$$
g_S^e \cong g_S \qquad g_L' \cong 1 \qquad g_l \cong -\frac{\gamma}{2B}
$$

$$
g_l' \simeq \frac{p}{2B} \qquad g_r^{e\prime} \simeq -\frac{q}{B}
$$

Part II

Details of Experimental Setup

Chapter 5

Experimental Apparatus

5.1 Overview

The experimental apparatus can be divided into four main parts:

1. The molecular beam
2. Magnet and interaction region
3. Lasers
4. Light collection, data acquisition & control

The molecular beamline consists of three vacuum chambers (containing the beam source and regions for state preparation and detection) and the superconducting magnet (figure 5.1). The vacuum chamber containing the beam source (left) allows the molecular beam to pass to the rest of the beamline through a small aperture (skimmer). This allows the apparatus to maintain a high vacuum in the rest of the system despite having a high gas load in the first chamber, so that the molecular beam is not scattered due to collisions with the background gas. The second vacuum chamber has windows to allow a laser beam to enter

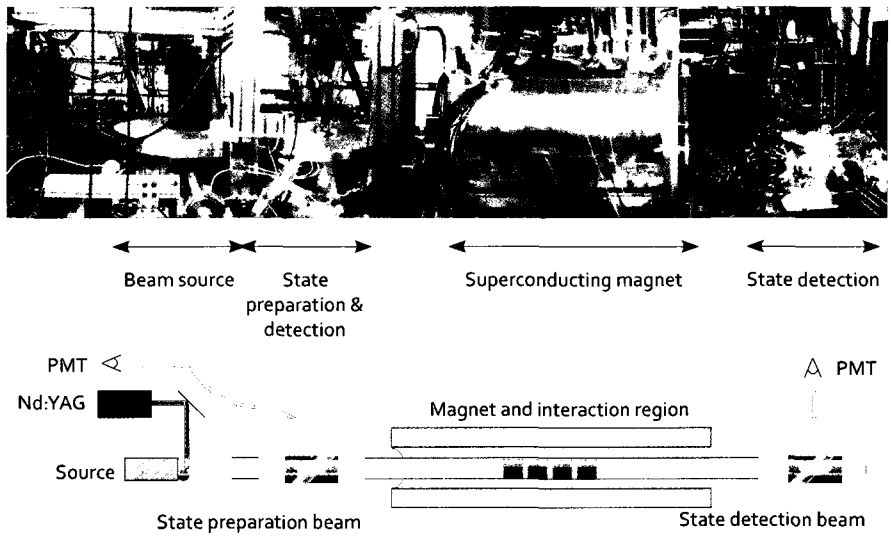

Figure 5.1: Photograph of the molecular beam path (merged from three images due to the size of the experiment), with the function of each part illustrated in the schematic view at the bottom. The beam is prepared on the left, and travels to the right. The total length of the molecular beam is about 260 cm.

and exit, and contains optics and a photomultiplier tube to collect light from laser induced fluorescence. This is used to conduct laser induced fluorescence spectroscopy, or to prepare the state of the molecules. A long glass tube carries the beam through the magnet from chamber 2 to chamber 3. Chamber 3 also has windows for laser access, and contains light collection optics and a second PMT. These are used to measure the final state of the molecules.

The lasers and frequency stabilization hardware are mounted on a separate optical table, with the laser outputs fiber coupled to the state preparation and detection regions on the molecular beamline (figure 5.2). We currently use a Littman-Metcalf external cavity diode laser in the near infrared for driving the A-X transition, a near-infrared Littrow external cavity diode laser for the D-A transition, and a frequency stabilized helium-neon laser for stabilizing the frequency of the diode lasers.

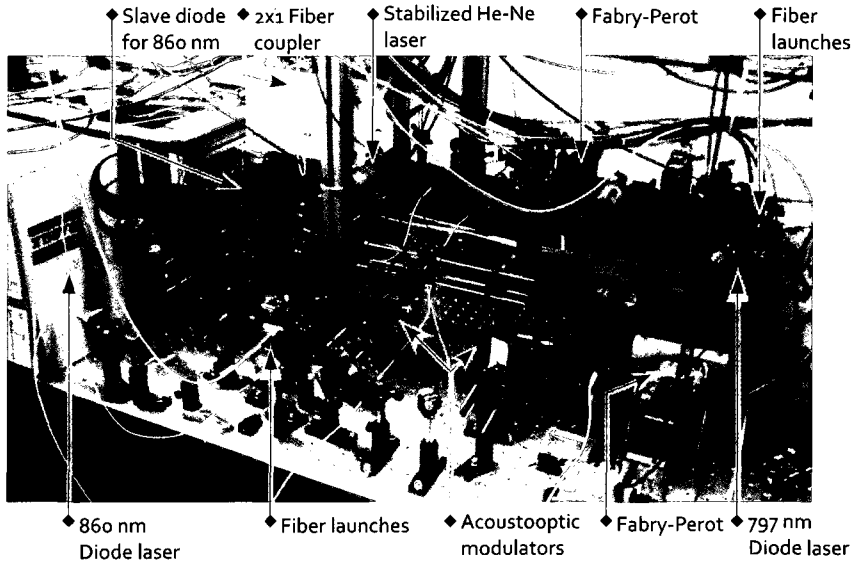

Figure 5.2: Photograph of the lasers and frequency stabilization hardware. Optical paths are marked for clarity in blue for 860 nm, yellow for 797 nm, and red for 632 nm.

Operation of the system is controlled by a computer-based data acquisition system. In addition to synchronizing the ablation and gas pulse, it controls the magnetic field, logs system status, and records and analyzes data from the PMTs. In this chapter, details of the operation of each of these subsystems are given.

5.2 Beam source

5.2.1 Introduction

This experiment uses a pulsed molecular beam which is similar in design to those commonly used in physical chemistry research. The principle is to use the rapid expansion of a carrier gas into vacuum to cool and entrain some warm source of molecules which you wish to study. The carrier gas is released from a

nozzle on a high-pressure reservoir into vacuum. Many experiments of this type, including this one, use argon as the carrier gas, since it is cheap, non-reactive, and fairly heavy (leading to lower velocities at a given temperature). Some experiments may use helium or xenon to achieve higher or lower beam velocities (and possibly greater rotational cooling). A small amount of other gases may be mixed in with the carrier gas if a chemical reaction is necessary to produce the desired molecule. There are alternate techniques for producing molecular beams (eg. ovens, cryogenic buffer gas sources [52], and RF plasma [53]); this source type was chosen since it is widely used as a source of molecules in low rotational states.

The principles of an atomic or molecular beam source using the expansion of gas through a nozzle are outlined in a number of references, including Scoles[43], Arnó and Bevan[44], and Van Wylen[45], but the most up-to-date source is Pauly[46]. Historically, supersonic expansions were first characterized by looking at gas flow through a converging-diverging (Laval) nozzle, as shown in part a) of figure 5.3. The nozzle is fed on the left side from a reservoir with constant pressure P_0 and a mean gas velocity close to zero. A pressure differential drives a flow through the nozzle into a region with pressure $P_B \ll P_0$. It is assumed that the flow is isentropic; that is, that the gas does not exchange heat with its surroundings and therefore entropy is held constant through the process. If the pressure differential is sufficiently large, the flow will reach sonic velocities (the Mach number $M_a = 1$) at the narrowest part of the nozzle, where $dA = 0$. As the gas expands in the diverging part of the nozzle, the flow becomes supersonic. However, supersonic expansion in the context of a molecular beam source does not require a precisely shaped Laval nozzle. Most experiments of this type, including this one, choose to use a free jet expansion instead. In this design, the nozzle need only be a hole or slit, with no particular shape to control the

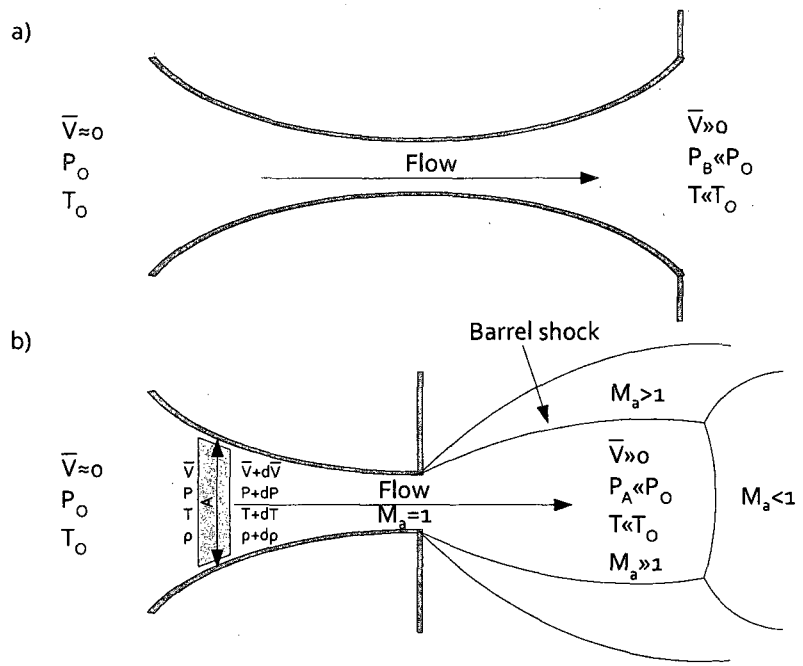

Figure 5.3: Examples of isentropic nozzles, which channel the gas flow from a stagnant reservoir (with velocity $\bar{V}$=0, pressure P_0, and temperature T_0) into a low pressure region with background pressure $P_B \ll P_0$. The Mach number M_a (ratio of gas velocity to the local speed of sound) is an important factor in determining the behavior of the gas flow. Part a) shows a converging-diverging supersonic nozzle, which controls both the compression and supersonic expansion of the gas. Part b) shows a "free" jet, in which the diverging part of the nozzle is eliminated. The shock wave from interactions with background gas defines the size of the expanding region.

supersonic expansion.

Two easily measured properties of the beam are the mean velocity and the translational temperature. Time-of-flight data from a pulsed beam source can be used to characterize both of these properties. Anderson and Fenn[49] give an expression for the velocity profile of the gas intensity from a pulsed source, $S(v)$, as:

$$S(v) \propto \frac{1}{L^2}\left(\frac{m}{2\pi k_B T_s}\right)^{3/2} v^3 \exp\left(-\frac{m}{2k_B T_s}(v-v_s)^2\right) dv \tag{5.1}$$

where v is the beam velocity, v_s is the center velocity, T_s is the translational temperature, m is the molecular weight, L is the distance from the source to the detector, and $S(v)$ gives the pressure as a function of beam velocity. By changing $v \rightarrow \frac{L}{t}$, $dv \rightarrow -\frac{L}{t^2}dt$, the gas pulse time-of-flight signal (pressure observed as a function of time t) is (as mentioned by Hinds et al. [51])

$$S(L,t) \propto \left(\frac{m}{2\pi k T_s}\right)^{3/2} \frac{L^2}{t^5} \exp\left(-\frac{mL^2}{2k_B T_s}\left(\frac{t-t_s}{t\,t_s}\right)^2\right) dt \tag{5.2}$$

If we fit the experimental data to a Gaussian ($S(t) = S_0 \exp\left(-\frac{1}{2}\left(\frac{t-t_s}{\sigma_t}\right)^2\right)$) and assume $t \approx t_s$, then

$$T_s = \frac{m\,L^2\sigma_t^2}{k_B\,t^2\,t_s^2} \approx \frac{m\,\bar{v}^2\sigma_t^2}{k_B t_s^2} \tag{5.3}$$

This will be useful later to find the translational temperature by fitting the measurement of gas pulse pressure as a function of time to a Gaussian.

5.2.2 Pulsed valve

There are several types of pulsed valve designs in common use for molecular beam experiments. In conjunction with the choice of valve, there is a decision

about whether to use a shaped diverging nozzle to control the supersonic expansion or to allow it to emerge as a free jet. Like Hinds et al. [51], the latter was chosen for this experiment. Each valve was characterized by a fast ionization gauge (Beam Dynamics FIG-1), which has a bare emitter/collector that can be placed in the beam path, and by LIF spectroscopy of the BaF beam source. The fast ionization gauge measurements presented here, are the only measurements of the valve performance that are independent of the rest of the system.

Two of these pulsed valve designs (piezo valve, solenoid valve) have been used in this experiment. The first was a piezo valve based on a design by Proch and Trickl[54]. This implementation of the design is shown in figure 5.4, with full drawings provided in the Appendix. The plunger is adjusted so that it rests against the surface of the o-ring, sealing the nozzle. When the piezo disc is actuated by an applied voltage of -1000 volts, the plunger moves a maximum distance of 100 microns and gas can flow through the nozzle. The valve body can be pressurized up to at least 10 atmospheres without any significant leakage into the vacuum system while closed. The piezo is driven by a Instrument Research Corporation pulse power supply, capable of supplying pulses of up to -1000 volts for 10 μs or longer. The power supply design is capable of driving (but not sinking) a load. A resistor/diode network (figure 5.6) is attached between the power supply and piezo in order to charge and discharge the piezo element with the appropriate time constant.

Here, the gas pulse is shown as a function of backing pressure (figure 5.7) and distance downstream from the nozzle (figure 5.8). Close to the source, the gas pulse appears clean and approximately Gaussian in shape. This is used to measure the translational temperature of the beam by using equation 5.3, and to choose the optimal operating conditions for the pulsed valve. Generally, a short but intense pulse will maximize the gas flow during ablation (to entrain and cool

as much material as possible), while limiting the total gas load on the vacuum system. After optimizing the operating conditions, the source was redesigned to use a solenoid valve in the hope that the solenoid valve would produce better results. In practice, there was not a significant difference in beam flux between the two designs. The solenoid valve was used for the remainder of the experiment since there would be no advantage to reinstalling the piezo valve.

Most of our work has been conducted with a solenoid valve design, based on a variant of the Parker Series 99 General valve (figure 5.9). This type of valve is frequently used in pulsed molecular beam experiments, including those of Steimle[55] and Hinds[51]. The valve is designed to be opened for a period of about 5 ms with a 24 volt control signal, but can be opened for times as short as 100 μs if the solenoid is overdriven to 200-300 volts. The model used here is designed with a conflat flange, which is convenient for ablation experiments. The valve is not used in conjunction with any antechamber or expanding nozzle; as with the piezo valve,there is a free supersonic expansion of the argon carrier gas. There are five adjustable parameters:

1. Pulse width (figure 5.10)
2. Pulse voltage (figure 5.11)
3. Stagnation pressure (figure 5.11)
4. Repetition rate (figure 5.11)
5. Spring tension

Adjusting the pulse width qualitatively changes the characteristics of the gas pulse. Figure 5.10 shows how the gas pulse changes as the pulse width to the valve is increased. Short pulses produce a single, small, fast peak. Longer pulses introduce a second and (eventually) third peak which can be much larger. Each of these peaks is approximately Gaussian and appears at the same time

regardless of backing pressure, but the height of the peak saturates as the pulse width becomes large. That is, long pulse widths still produce the initial small, fast peak; but it cannot be cleanly separated from the additional slower peaks that appear. In addition, it is observed that long pulse widths produce an "echo" a few milliseconds after the primary peak. This is probably a mechanical bounce of the valve poppet when it closes rapidly. In practice, it has no effect on the experiment. Each of the peaks is fit to the form $S(t) \propto \exp\left(-\frac{1}{2}\left(\frac{t-t_0}{\sigma_t}\right)^2\right)$ and equation 5.3 is used to estimate a translational temperature for the argon beam. The first peak is consistently colder than the second peak, though there is considerable uncertainty due to the difficulty in resolving the different velocity peaks.

Changing the pulse voltage has a similar effect as changing the pulse width (part c of 5.11). Lower voltages produce a single, clean peak; higher voltages produce additional slower velocity distributions and "echoes". The effect of changing the stagnation pressure (part a) is slightly different. The gas pulse grows in height as the pressure is increased, but the shape does not change as significantly. The effect of repetition rate on the characteristics of the argon gas pulse is minimal up to 100 Hz. (A decrease in the LIF signal is observed at higher repetition rates.)

The spring tension can be adjusted by rotating the valve body relative to the flange base, though the performance changes seen mimic those of adjusting the pulse width or voltage. The poppet was replaced after 6-12 months of operation; while it showed some signs of wear, the new poppet did not produce noticeably different results.

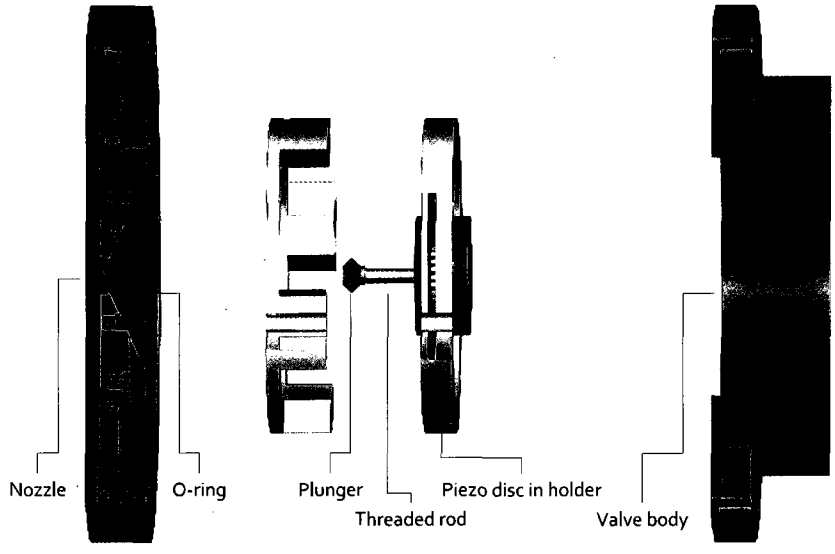

Figure 5.4: Exploded view of piezo valve based on Proch & Trickl design. The nozzle (0.5 mm diameter) is sealed when the brass plunger is pushed up against the o-ring. The threaded rod length can be adjusted using a lock nut against the piezo disc holder, so that the plunger seals against the o-ring when the piezo is discharged, but opens when the piezo is charged to -1000 volts ($\approx$100 μm displacement). The interior of the valve body can be pressurized up to at least 10 atmospheres; electrical and gas feedthroughs are placed on the rear of the valve body.

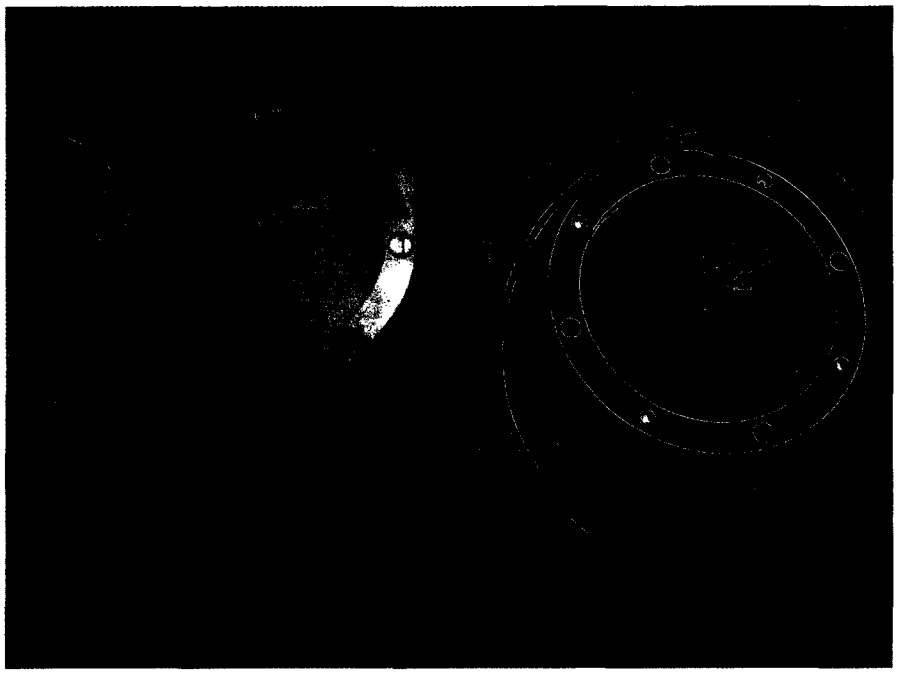

Figure 5.5: The piezo actuator used in the valve. The part on the left is the Physik Instrumente P-286.20, with a tapped hole and metal supports on both sides of the disc; this part was successfully used in the valve for years of operation. The initial design used the part on the right (P-286.23), which lacks the added support. This failed after a few weeks of operation due to cracking of the piezo ceramic.

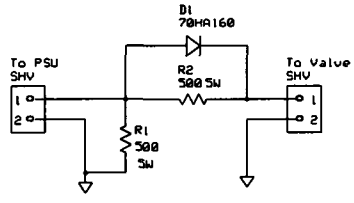

Figure 5.6: Drive network for piezo element in pulse valve to control the rise and fall times of the voltage pulse that the power supply (PSU) delivers to the piezo. The piezo is effectively a capacitive load with C=13 nF; the 500Ω resistors set the time constant to be about 7 μs.

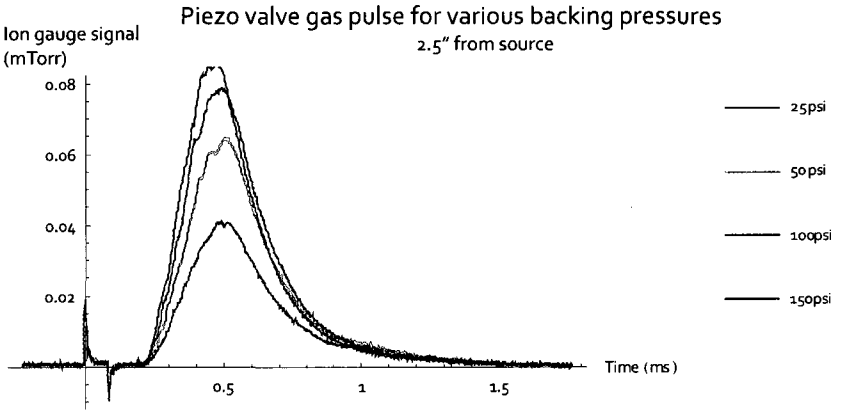

Figure 5.7: Gas pulse from the piezo valve as a function of backing pressure (with 80 μs width, -900 volts electronic drive pulse parameters), measured 2.5" from the source.

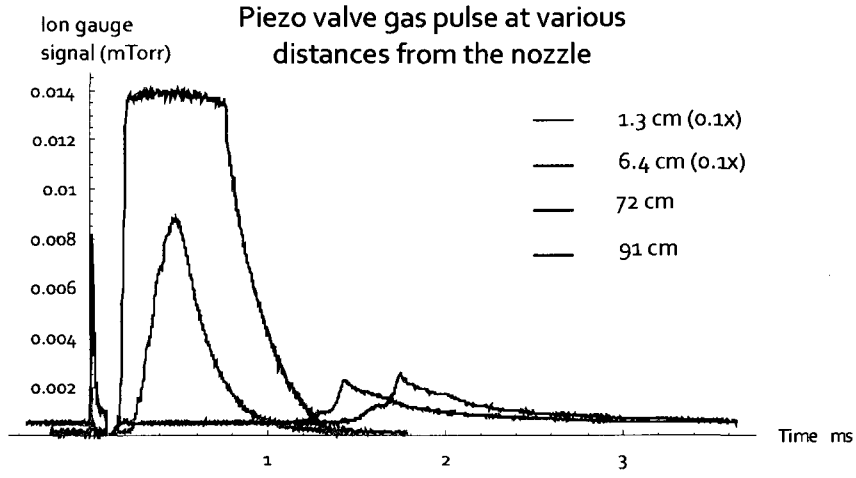

a)

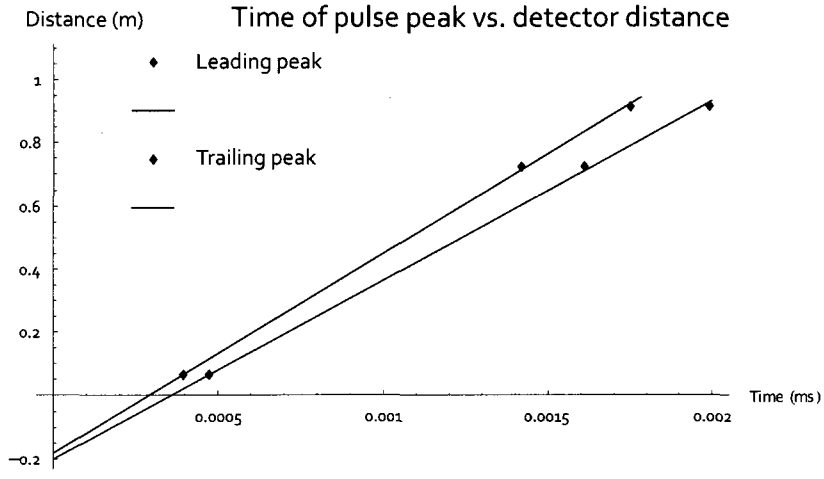

b)

Figure 5.8: The gas pulse from the piezo valve (80 μs width, -900 volts electronic drive pulse) is shown at various distances from the nozzle in part a). The pulses (particularly at larger distances) show some structure suggesting that different parts are traveling at different velocities. The time-of-flight signal in part a) is fit to a sum of two Gaussian peaks; the arrival time is used in part b), to show that the early and later peaks have different velocities. The leading part suggests a velocity of 630 m/s, with a broader second velocity distribution centered around 565 m/s. The difference in offsets (corresponding to $\approx$ 67 μs) is close to the width of the gas pulse.

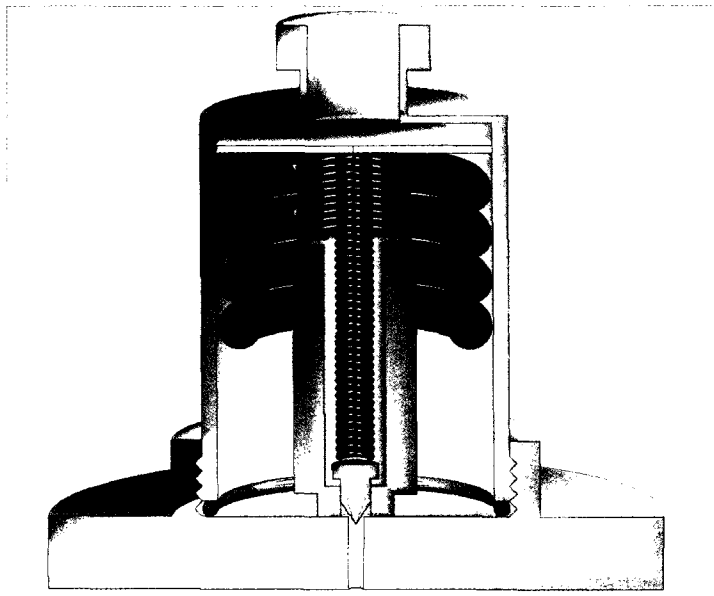

Figure 5.9: Cross-sectional view of Series 9/99 solenoid valve with conflat front flange, which is the type of solenoid valve used in this experiment. Gas enters through the fitting on the top, and leaves through a 1 mm aperture on the bottom which is sealed with a Teflon poppet (gold). The poppet is actuated by pulling the hollow iron cylinder (dark grey) into the solenoid coils (dark red). Springs provide restoring force to the iron cylinder and the poppet separately, minimizing the time to close the valve.

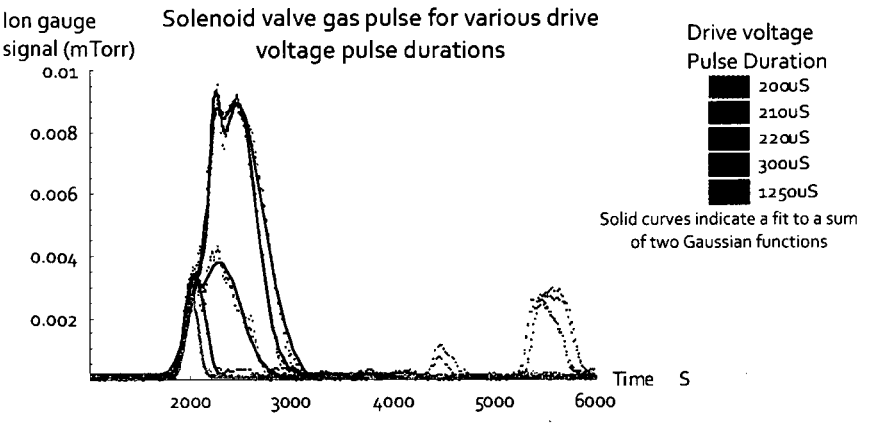

a)

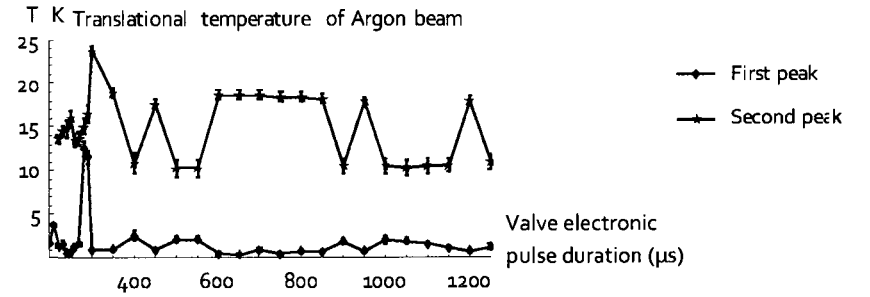

b)

Figure 5.10: The gas pulse from the solenoid valve (plot (a)) strongly depends on the drive voltage pulse duration. Longer pulses exhibit peaks showing multiple Gaussian velocity distributions and "echoes" believed to be due to bouncing the poppet. A translational temperature is estimated based on the peak width, shown in plot b), using eq. 5.3; the faster and slower velocity distributions have different temperatures. (Measurements are at 225V drive pulse amplitude, 10 Hz repetition rate, skimmer 4" from source, 70 psig stagnation pressure)

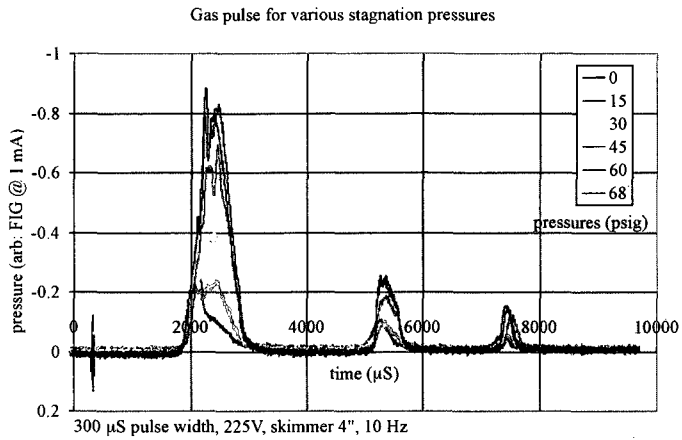

a) 300 μS pulse width, 225V, skimmer 4", 10 Hz

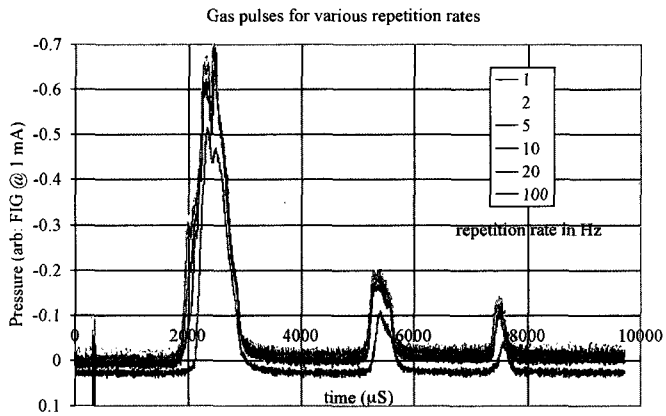

b) 300 μS pulse width, 225V, skimmer 4", 45 psig

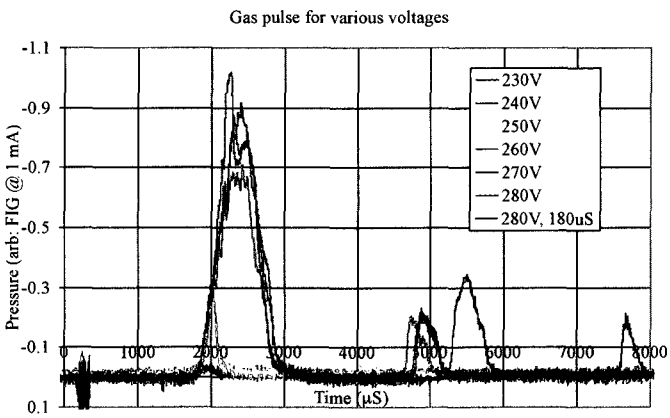

c) 200 μS pulse width (unless noted), 70 psig, skimmer @ 4"

Figure 5.11: Solenoid valve gas pulses and their dependence on a) stagnation pressure, b) repetition rate, and c) applied voltage. The valve itself shows minimal performance degradation up to 100 Hz (though we will see later that less fluorescence is observed from BaF at high repetition rates). Voltage acts similarly to pulse width in terms of the characteristics of the gas pulse produced.

5.2.3 Target

The molecules we are interested in, e.g. BaF, are radicals; unlike experiments with gaseous precursors, eg., ammonia or nitrogen, they must be produced within the apparatus. Two approaches to producing BaF were used during this experiment: using a precursor that contains BaF (BaF_2), or ablating barium metal in the presence of a fluorine-bearing compound (SF_6). Various methods exist to produce a beam of radicals, including oven and RF plasma sources. Laser ablation was chosen because of its ability to produce an intense pulse of atoms or molecules from a wide range of materials. We use a Big Sky CFR200 pulsed Nd:YAG laser for ablation, which produces up to 18 mJ pulses at up to 100 Hz. A frequency-doubling crystal is installed that allows production of both 532 nm and 1064 nm light with variable relative intensities (the laser power is nominally specified as 30 mJ/pulse without the doubling crystal). Laser light is directed on to the target with one fold mirror and a lens. The laser beam has about a 3 mm diameter coming out of the laser head; the choice of lens position and focal length determines the spot size on the target. One axis of the fold mirror is controlled by a motorized micrometer, so that the laser can be rastered over the target surface if necessary. The ablated material mixes with the expanding free gas jet (part a in figure 5.12); some experiments (eg. Steimle [56]) instead ablate the material into an extended nozzle where the material can mix with the carrier gas before the free jet expansion. Based on comparisons with Steimle's results, our experience is that the expanding free jet works better for the production of BaF molecules (table 6.2).

The initial target design was based around a crystalline BaF_2 source (a 1-2" diameter, 3 mm thick disc sold as an infrared window). The disc was held flat against the nozzle, with one edge of the disc about 3-6 mm (adjustable) below the nozzle. The disc could be rotated during operation, and the ablation laser

was rastered over the edge of the disc below the nozzle. This produced a useful flux of BaF molecules, but the target lifetime was extremely short (significant damage after 2-8 hours of operation at 10 Hz). The disc would crack, and large pieces would break off. An example of the laser damage (after less than 1 second of operation) is shown in 5.13. The best explanation is that the laser power is poorly absorbed by the surface of the material (which is transparent over the visibile and near infrared parts of the spectrum). In order to achieve a useful yield of molecules with laser ablation, Nd:YAG beam needs to be tightly focused. This power is not completely absorbed at the surface (as with a metal target), but most likely adds heat and stress within the material. Attempts were made to improve the strength of the target by sandwiching it with metal shim stock, but that did not noticeably prevent damage.

The second target tested was a pressed powder BaF_2 target from Sophisticated Alloys, Inc. Ablation produced noticeable laser damage to the target surface, but the pressed powder did not suffer the same sort of stress damage that the crystalline target suffered from. Due to the awkward shape, this target was tested in a room temperature buffer gas instead of using LIF in a molecular beam. The largest flux of molecules (for the purposes of this test, in the $N = 14$ state) was produced when the spot size on the target was about 0.78 mm for about 15 mJ of incident power (figure 5.14), or a fluence (laser energy per area) of 3.1 $\frac{\text{J}}{\text{cm}^2}$. This type of target is also difficult to integrate into a supersonic beam source, but might be ideal for a cryogenic buffer gas experiment (where a gaseous precursor like SF_6 would freeze out on the cell walls).

The current version of the experiment uses a barium metal rod target and SF_6 added as a reactant to the beam carrier gas. A 1/4" diameter barium rod, between 1" and 4" long, is machined on a lathe from a $\approx$ 1/2" diameter piece of material (Sigma-Aldrich); the small diameter allows the laser ablation

to be located near the nozzle. The rod is continuously brushed with mineral oil during machining to prevent oxidation. (A flame can result if material is removed too quickly and not lubricated with oil.) A hole is drilled in the center to accommodate a $\#6-32$ threaded rod, which is used to hold the barium rod to a 1/4" steel shaft (figure 5.15). This rod fits snugly within a teflon block (figure 5.16) mounted on the front of the valve nozzle. (Earlier designs allowed the rod to move up and down by 3 mm relative to the nozzle, with a resulting 50% modulation in the number of molecules observed.) The block securely holds both sides of the rod, so that the distance from the ablation point to the nozzle does not vary as the rod is rotated. Teflon has low friction, and the parts do not bind in air or vacuum. The steel rod on the side is long enough ($\approx$4 inches) that the entire length of the barium part can be pushed up to the nozzle. The end of the steel shaft is attached to a 1/4" $-$ 80 threaded rod (eg. Thorlabs F25SS300 & F25SSN2) so that the assembly is translated as it is rotated. The threaded rod is driven by a motor outside the chamber, connected through a rotation feedthrough and a telescoping universal joint (eg. Small Parts TDS-4/4). Infrared reflective sensors can detect the end of travel so we can reverse the direction of motion.

Unlike the BaF_2 target, the metal target produces a higher flux of molecules when the ablation laser is somewhat defocused (15 mJ/pulse in a $\approx$ 1.5 mm diameter spot, figure 5.17, measured in a room temperature buffer gas). This corresponds to a fluence (energy per pulse on the target surface) of 0.85 $\frac{J}{cm^2}$. The specific reasons for the difference between the two materials are unclear and the target design is ultimately an empirical process. The Ba metal rod target has given the best performance so far and is currently in use. However, we have also implemented or designed several other types of barium metal targets. These include:

- Forming a barium rod by melting barium metal pieces: Barium has a relatively low melting point (727°C), so the initial attempts used here to form a 1/4" rod were to melt small pieces of barium metal inside a quartz tube under vacuum. These attempts, though, produced a brittle rod with a tendency to crumble (possibly due to traces of mineral oil contaminating the sample).

- Fixed target: Given the malleability of barium, it is possible to fill a small hole in a wedged aluminum block with barium metal. This is easy to prepare, but has a limited lifetime since the target cannot be moved relative to the nozzle. It is fine for quick tests.

- Wheel target: We have prepared a target on which a ribbon of barium metal (prepared by ESPI Metals) is glued to the rim of a thin aluminum disc, about 6" in diameter. The disc can be rotated, and the position adjusted relative to the nozzle, using motorized actuators within the vacuum system. This mechanism has been assembled (but not tested) in the experiment.

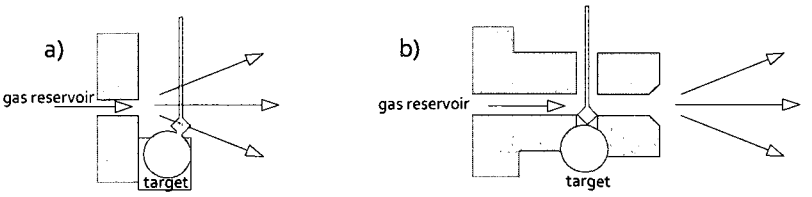

Figure 5.12: Two ways to introduce ablated material into the gas expansion. In a), the rod of material is placed close in front of and slightly below the nozzle, taking care to avoid disturbing the supersonic flow. (The material may be partially embedded in a solid block for both support and to minimize disturbances.) The ablation laser (green) creates a plume of hot material synchronized with the pulsed supersonic jet. Alternatively, in b), the ablated material mixes with the gas jet in an antechamber before the expansion begins. Based on comparisons with the measured beam flux in Steimle's experiment[56] (table 6.2), the free expansion in a) appears to produce a better flux of molecules for BaF.

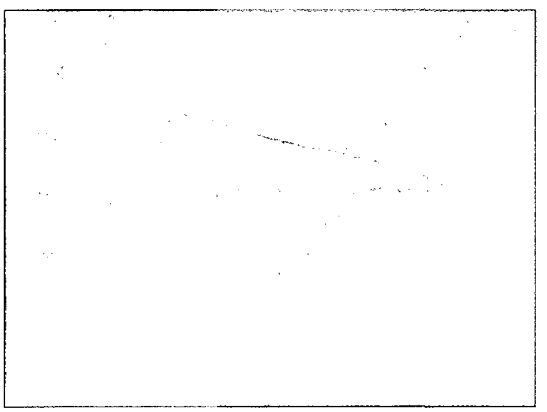

Figure 5.13: Ablation damage to a crystalline BaF_2 target.

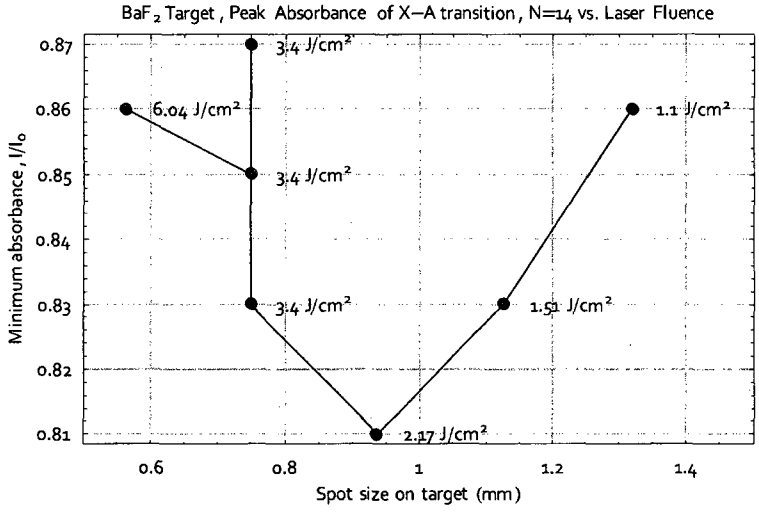

Figure 5.14: Absorption signals from BaF molecules produced by ablation of the BaF_2 pressed powder target showing the effect of changing the spot size (and hence the laser fluence, or energy per unit area) of the ablation laser. This suggests that the optimal spot size on the target is a diameter of about 0.78 mm, given 15 mJ of available ablation laser power.

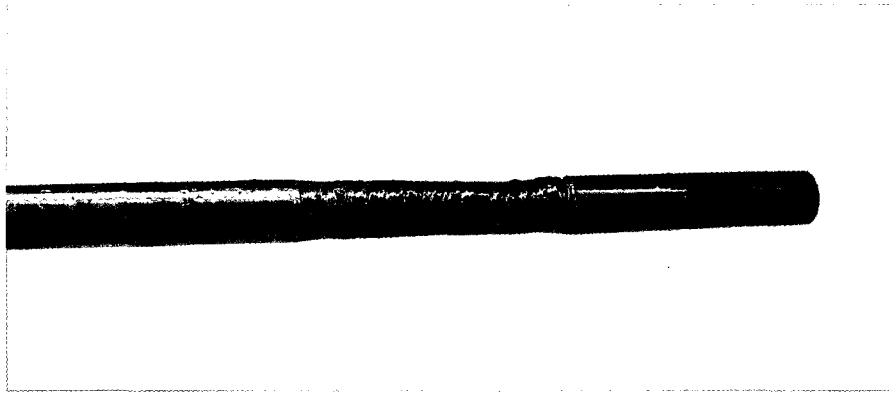

Figure 5.15: Barium metal rod assembly. A barium metal rod (center) is cut on the lathe to an outer diameter just under 1/4" (to avoid jamming in the rod holder) and center drilled to accommodate a $\#6-32$ threaded rod. The 1/4"-diameter steel rods on the left and right are drilled and tapped to thread on to the threaded rod, which holds the assembly together. When handled in air, the barium metal is coated with mineral oil to prevent oxidation.

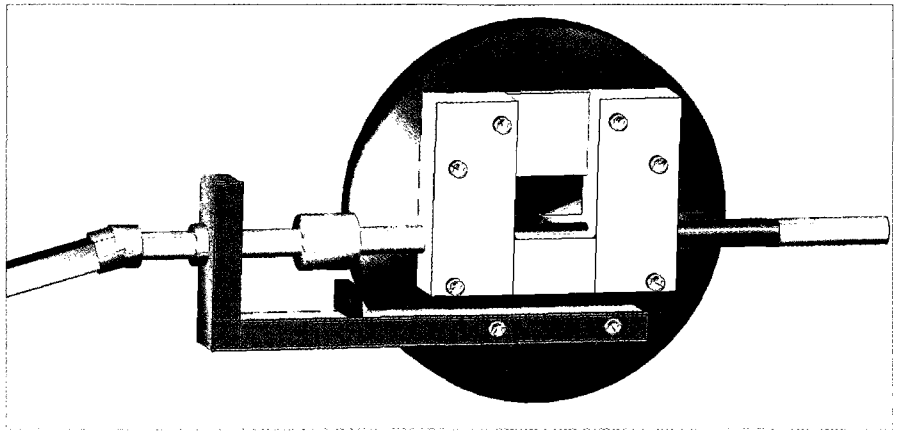

Figure 5.16: Target assembly for barium metal rod target. A teflon block (white) is mounted on the front of the nozzle; the rod assembly is held firmly in place in a closely spaced hole in this block. Different blocks were machined with different rod-nozzle spacings. An arm underneath the block holds a $1/4-80$ threaded rod (in collar, gold) used to advance the block, and one or more infrared reflective sensors (dark green) to indicate end of travel. A telescoping universal joint (orange) allows the rod to be turned from an external rotation feedthrough. The ablation laser hits the top of the rod close to the nozzle; the position can be adjusted closer to the front or back edge of the rod to optimize BaF production.

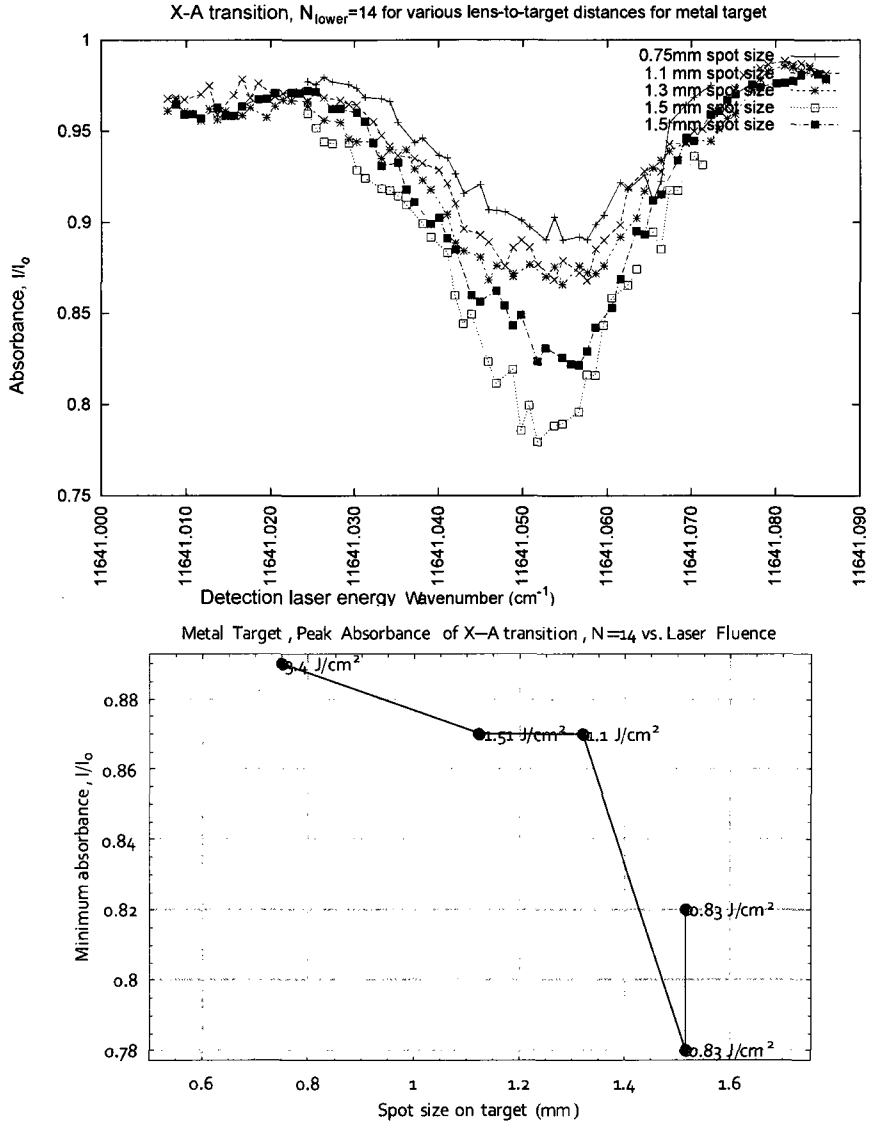

Figure 5.17: Absorption signals from BaF molecules produced using the metal target in a room temperature buffer gas. Individual spectra are taken across the $N = 14$ R-branch line of the X-A transition of ^{138}BaF (top) for various choices of ablation laser spot size on the target, with a total power of 15 mJ/pulse in the ablation laser beam. The maximum absorbance is taken as indicative of the amount of BaF produced in this state (bottom). The amount of BaF produced increases as the laser is defocused (the total power remains constant; the area ablated increases). The spot size is related to the focal length of the lens used: $d = (3\text{ mm})\left(1 - \frac{f.l.}{400\text{ mm}}\right)$. The optimal operating conditions within a room temperature buffer gas are suggestive (but not conclusive) about the ideal parameters for a molecular beam.

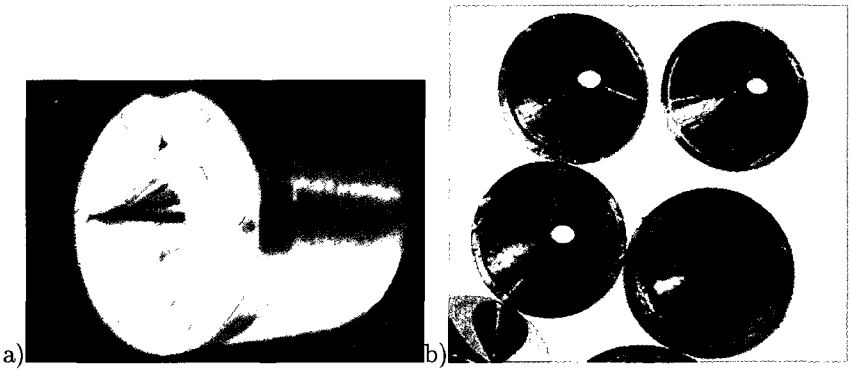

Figure 5.18: Molecular beam skimmers. Part a) shows a skimmer purchased from Beam Dynamics; b) shows examples of skimmers fabricated here.

5.2.4 Skimmer

The purpose of the skimmer is to allow for differential pumping of the vacuum system by isolating the high pressure region near the beam source so that high vacuum can be achieved on the beamline. Under some conditions, this can be achieved with an iris or other small aperture being the only opening between two separately pumped vacuum chambers. However, there is often concern about the reflection of the supersonic gas jet from the sides of the aperture. Typical molecular beam skimmers are designed with razor-sharp forward edges and a curved conical shape to mitigate this problem. The skimmer walls are steeply sloped near the aperture to prevent the gas jet from being scattered back into the beam path. The walls widen to prevent the beam entering the skimmer from interacting with the skimmer walls.

Three types of beam skimmers have been used in this experiment. An iris was used to control the aperture size, and this usually produces acceptable results under the conditions in our system. The Beam Dynamics skimmers (figure 5.18) have been hard to use because of their small aperture size. A skimmer model from R. A. Chilton (now called ICPMS Cones Ltd) with a larger aperture.

Alternately, this experiment has also used skimmers fabricated here (initially designed as baffles for stray light reduction) by electroforming copper on to a stainless steel mandrel; this is the type currently used in the experiment. The procedure was devised by one of the undergraduates working in the lab, George Burkhard [65], and is described in appendix F. The skimmer is mounted so that the skimmer aperture is the only significant vacuum conductance between the source chamber and the rest of the beamline. In this experiment, under the conditions in the vacuum system, there was no advantage to using the Chilton skimmer over the homemade copper skimmer; and the the iris was almost as good as using a proper skimmer. (In face, Steimle uses a simple iris in his molecular beam apparatus.)

There are two scenarios to consider when deciding where to place the skimmer. If the density of gas in the jet and in the surrounding area is high enough, then the jet expands supersonically for a time, before (at a point termed the Mach disc) the expansion collapses and the gas jet proceeds subsonically. However, if the background pressure is low enough (which is the case here), the collision rate in the expanding gas pulse will drop below the rate needed to keep the gas jet in thermal equilibrium. The properties of the gas are said to "freeze out"; this is the free molecular flow regime. In this case, the skimmer can be placed anywhere after the transition to free molecular flow. In either case, the skimmer should be placed far enough away from the gas jet source to prevent reflections from the skimmer face from interfering with the supersonic expansion. The skimmer has been placed at a few distances betwen 2" and 6" from the source, without any apparant change in the number of molecules observed in a particular rotational state. This experiment takes place in the free molecular flow regime.

The skimmers fabricated here have a 1/4" diameter aperture. This is a rel-

atively large aperture size to use compared to most skimmers sold for use in molecular beams, but it makes alignment easy and gives a large flux of molecules. (A usable signal wasnot observed using the smaller skimmers tried.) Another consideration regarding the skimmer diameter and position is that these parameters can determine the apparant linewidth during spectroscopy. This was the case during initial measurements with laser-induced fluorescence. (In later stages of the experiment, collection optics were installed that effectively limited the size of the beam that is detected. The discussion of the Doppler width still applies, but depends on the aperture determined by the size and position of the collection optics instead of the skimmer.) The aperture size determines the maximum transverse velocity of the molecular beam (and by extension the Doppler width). The maximum transverse velocity $|v_\perp|$ will be

$$|v_\perp| = \frac{d}{2x_s}\bar{v} \tag{5.4}$$

where d is the aperture diameter, x_s is the distance from the nozzle to the skimmer, and $\bar{v}$ is the average translational velocity. The Doppler shift due to the transverse velocity will be

$$f_D = \frac{v_\perp}{c}\nu * 30000\frac{\text{MHz}}{\text{cm}^{-1}} \tag{5.5}$$

For a 6 mm diameter skimmer, this would result in a transverse velocity of 18 m/s and a Doppler shift of 21 MHz. In practice, when there are smaller apertures in the beam (eg. the diameter of the sensitive region of the light collection optics or probe laser), the effective aperture size will be smaller and the Doppler broadening will be less. For example, the Doppler broadening at the collection optics in the state preparation region will be $f_D \sim 2$ MHz, which is less than the natural linewidth. It is important to ensure that the transitions

are narrow, since there are often unrelated transitions near the lines used to pump (or probe) the ground state; exciting these transitions could create a large background signal.

5.3 Vacuum System

The requirements of each part of the system determine many aspects of the overall mechanical and vacuum system design. The first issues to consider are the number and spacing of vacuum chambers along the beamline. The supersonic jet source creates a significant gas load on the vacuum system. So, a pump with high throughput is required in this part of the system. The gas load is lower after the skimmer, but both ends of the tube that passes through the magnet need to be pumped. Given the limited size of the magnet bore ($\approx$ 30 cm), this tube was made to be 2" in diameter.

The length of the vacuum apparatus was chosen based on the following considerations. The intensity of the molecular beam is proportional to e^{-ar}/r^2, where the exponential part of the decay depends on the background gas in the vacuum system and the r^2 falloff is purely geometric. It is desirable to make the distance to the detector as short as possible; however, we want to make sure that the magnetic field is the same when we do state preparation and state detection so that we can use the same laser in both regions. Figure 5.20 shows the decay of the fringe fields outside of the magnet, along the magnet axis. The closest location where $\frac{dB}{dz}$ is sufficiently small (eg. the Zeeman shift of the optical A-X transition, $\approx$ 1.4 MHz/Gauss, is sufficiently small that the conceivable irreproducability in position (eg. 3 mm) leads to transition shifts less than the transition linewidth, $\approx$ 5 MHz[1]) is when we are about 46 cm

[1]The natural linewidth is the dominant factor in determining the linewidth, and is about 5 MHz.

from the front face of the magnet, and 60 cm from the back. At this point, $\left|\frac{dB}{dz}\right| \approx 3.5$ gauss/cm and $B \approx 116$ gauss. This makes the minimum possible length of the beamline about 2 meters. The additional distance between the beam source and the state preparation region adds an additional 57 cm, for a total length (from source to detector) of 260 cm (figure 5.19). For air at 300K, the mean free path length is about 7 meters at 10^{-6} Torr [66] . Hence 10^{-6} Torr is an adequate pressure, and is not particularly challenging to achieve. (O-ring sealed components such as QF or ISO flanged systems are fine, and bakeout is unneeded.)

There is a choice of vacuum pump technologies. The following issues apply:

- Turbopumps are clean and effective, but expensive. A turbopump capable of handling the gas load at the beam source would be in excess of $12,000. Most turbopumps are specified to run at external magnetic fields less than 50 Gauss, which presents installation problems.

- Cryopumps are also clean and effective, and relatively cheap to acquire on the used market. Cryopumps are questionable for any high gas load application, and are ineffective at pumping helium under any conditions. They are a plausible candidate for the state preparation and detection regions with an argon carrier gas, but would be inappropriate for a cryogenic helium buffer gas source, as we are likely to use in the future.

- Diffusion pumps are relatively dirty (due to oil backstreaming), but extremely cheap. Diffusion pumps are able to pump helium reasonably well, and can handle high gas loads with ease.

Diffusion pumps were chosen for each of the three chambers in the system. The state preparation and detection chambers have 6" diffusion pumps (a Varian VHS-6 and CVC PMC-6 pump, respectively) with water baffles (a Varian model

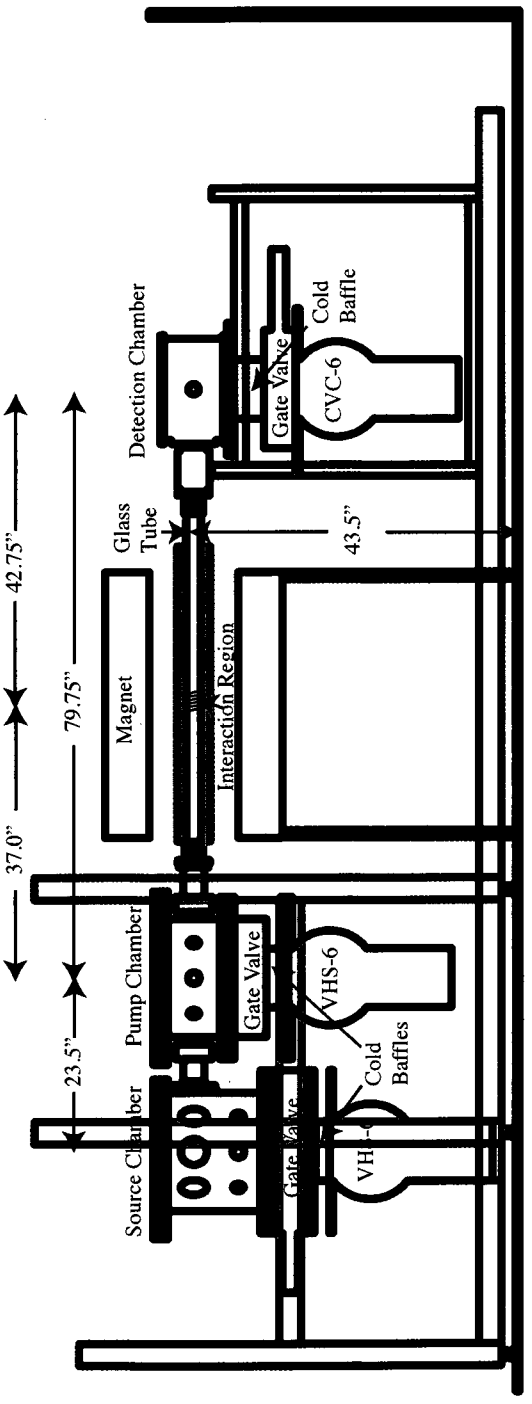

Figure 5.19: Scale drawing of the beamline, showing distance between components. Structural components are outlined in blue; the region of the beamline inside the magnet is highlighted in green.

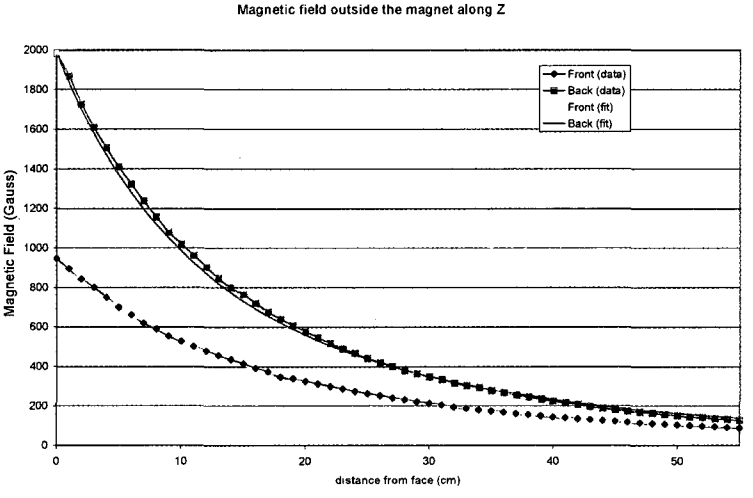

Figure 5.20: Magnetic field outside of the magnet, along the $\hat{z}$ axis. The field is fit to the form $B(z) = B_0 \left(\frac{z_0}{z-z_0}\right)^3$, with B_0=957.6 Gauss, z_0=-45.3 cm for the front face of the magnet and B_0=1982.3 Gauss, z_0=-37.9 cm for the back face. In effect, the same field is reached (50 or 100 Gauss) 15 cm farther from the back face than from the front. The functional form was chosen to have a $1/z^3$ falloff, like a current loop or bar magnet, with a scale factor z_0 to account for the finite diameter of the magnet.

336 and CVC BC-61 multi-coolant baffle). Initially, an Edwards HS-16 16" diffusion pump was installed on the beam source, but performance was only minimally degraded when it was replaced by a 6" VHS-6. (The 16" pump was replaced in order to lower the height of the beamline to match the height of the magnet.) A Model 336 water baffle was also added to the beam source chamber to prevent significant oil backstreaming. While it halves the nominal pumping speed, it does not harm system performance at higher repetition rates (figure 5.21).

Later, the hypothesis that patch potentials could be causing problematic stray electric fields within the interaction region will be explored in more detail. One possible cause of these patch potentials is that a thin film of oil (backstreaming from the diffusion pump) could build up on the surface of electrodes within the interaction region. Under vacuum, large potentials could build up on the surface of this insulator without any way to dissipate the charge. Our proposed solution to this is to cool the baffles to $-40°$C. Baffles are often cooled to liquid nitrogen temperatures to prevent oil backstreaming and improve the pumping of water vapor. The options of exchanging the water baffles for LN_2 traps or closed-loop chilled baffles (eg. Polycold systems) were considered. However, Chambreau et al. [60] have demonstrated that the types of water baffles used here (Varian model 336) can be used with a closed-loop chiller at $-40°$C to eliminate oil backstreaming (although water vapor is not significantly affected). This requires minimal changes to our apparatus, and an FTS Systems RC302ZDL chiller was set up to implement this.

The vacuum system as described has three independently pumped regions, and can be isolated by means of the two gate valves along the beamline. Each chamber is equipped with an ion gauge and a Pirani gauge for pressure measurement. The valves (roughing, foreline, vent, and gate valves) are controlled

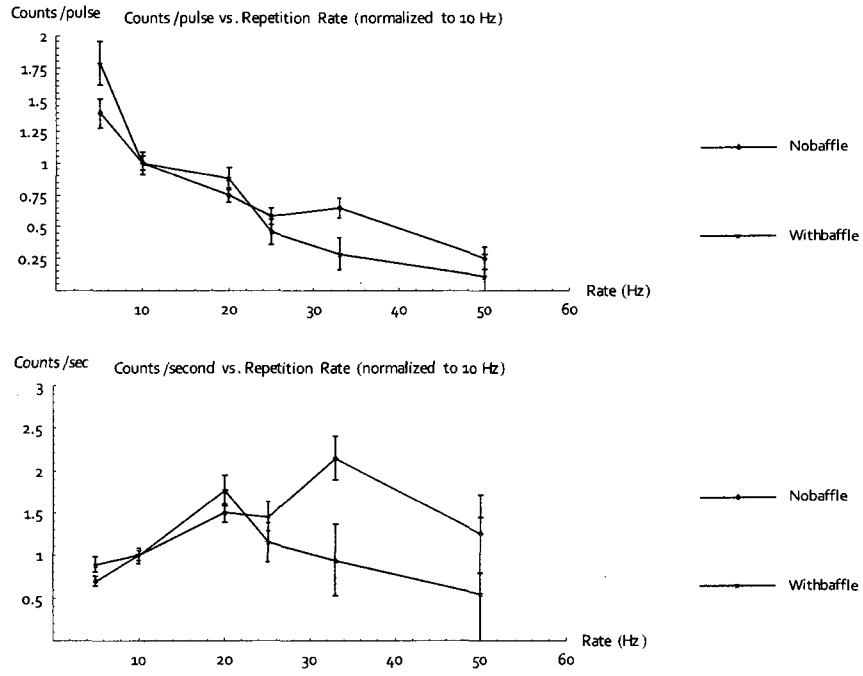

Figure 5.21: Detection rate as a function of repetition rate, with and without a water baffle on the beam source vacuum chamber. The detection rate is normalized to performance at 10 Hz, with different normalizations for conditions "with" and "without" the baffle. If the addition of the water baffle harms the system performance, the number of molecules observed will scale differently with repetition rate. At low repetition rates, the gas load will be small; even though the pumping speed is reduced, the system still has time to recover before the next gas pulse. So, it should not matter whether the baffle is installed. As the repetition rate is increased, the background pressure will rise faster in the system with the water baffle (due to its decreased pumping speed) than without the baffle. If that is the case, the beam intensity will be lower with the water baffle than without the baffle at high repetition rates. However, a significant decrease in performance at high repetition rates after installing the baffle is not observed.

by a Trilogi Logic T100MD2424+ PLC interfaced to the pressure gauge controller. More details of the operation and programming of the PLC are in the Appendix.

In planning the vacuum system, it is useful to calculate what the pressure is expected to be so that pumps and components can be chosen to meet requirements. It is important to make sure that the pressure along the molecular beam path (eg. in the middle of the magnet) does not exceed the levels we would expect. It is possible to calculate what the pressure should be in each part of the vacuum system if the conductance between each part of the system is known and the sources of gas (eg. outgassing, leaks, or the gas jet) at each point can be estimated. The vacuum system can be described as a set of nodes (eg. each vacuum chamber) and conductances (how freely gas can flow between two directly connected nodes)(5.22). Conservation of mass and the definition of conductance let us say that, at any given point (node) of the vacuum system,

$$I_{\text{source},n} + \sum_{m \neq n} C_{mn} \left(P_m - P_n \right) = 0 \tag{5.6}$$

where P_n is the pressure at node n, $I_{\text{source},n}$ is the gas load generated at node n (eg. outgassing, leaks, etc), and $C_{mn} = 1/R_{mn}$ is the conductance between the nodes m and n. This can be written as a matrix equation describing all the interconnected parts of the system:

$$\mathbf{S} \cdot \vec{P} = -\vec{I}_{\text{source}} + \vec{P}_{\text{fixed}} \tag{5.7}$$

where $S_{n,m} = \begin{cases} C_{n,m} & n \neq m \\ -\sum_{m \neq n} C_{n,m} & n = m \end{cases}$ if node n is to be solved for and $S_{n,m} = -\delta_{n,m}$ if node n is maintained at a constant pressure. For example, the vacuum system pictured in (5.22) would have

$$\mathbf{C} = \begin{pmatrix} -1 & 0 & 0 & 0 & 0 \\ C_{skimmer} & 0 & C_{tube} & 0 & C_{pump} \\ 0 & C_{tube} & 0 & C_{tube} & 0 \\ 0 & 0 & C_{tube} & 0 & C_{pump} \\ 0 & 0 & 0 & 0 & -1 \end{pmatrix}, \vec{P} = \begin{pmatrix} P_{source} \\ 0 \\ 0 \\ 0 \\ 0 \end{pmatrix} \quad (5.8)$$

The individual conductance of a given tube or aperture can be found using Dushman's table[61]. C_{pump} is usually specified on the pump data sheet. Conductances are divided by 2 for every right-angle bend or optically dense baffle inserted in the path. Eq. (5.7) can then be used to find the pressure given an estimated leak rate (or vice versa if the pressures are known). This is particularly useful for estimating what the pressure might be at parts of the system where it is not practical to place a gauge, such as the middle of the glass tube (node 3).

For our system, the estimate is that $C_{skimmer} \approx 3$ Torr·ℓ/s, $C_{tube} \approx 12$ Torr·ℓ/s, $C_{pump} \approx 1200$ Torr·ℓ/s (including the effects of an installed optically opaque water baffle), and the diffusion pump ultimate pressure is 10^{-7} Torr. Using these estimates, the calculations can be compared to the measured pressures:

Location	Calculated	Measured (at 10 Hz)
Source chamber	1×10^{-4} Torr	1×10^{-4} Torr
State preparation region	3×10^{-7} Torr	1×10^{-7} Torr
Interaction region	2×10^{-7} Torr	—
State detection region	1×10^{-7} Torr	1×10^{-7} Torr

The vacuum system, then, exceeds requirements for background gas pressure throughout the system. Based on these measurements, the pressure within the interaction region is sufficiently low that it will not significantly attenuate the

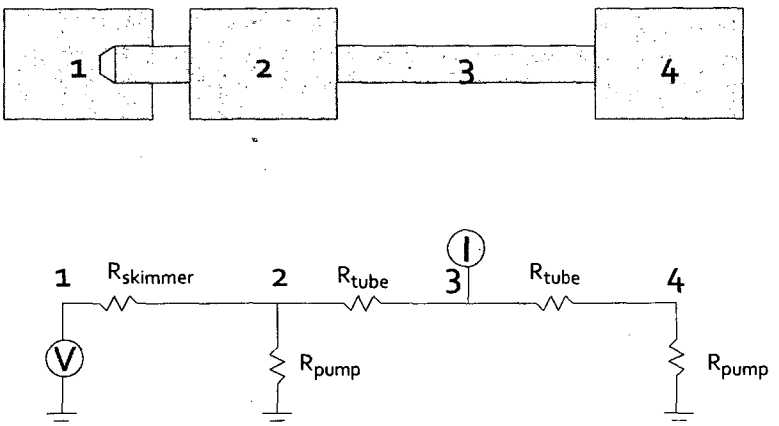

Figure 5.22: Finding the pressure in the vacuum system is analogous to measuring the voltage in an electric circuit. The pressure at each numbered point in the system is equivalent to the voltage at the corresponding node of the circuit on the bottom. The resistances are the reciprocal of the vacuum conductance of the links between each of the chambers; a constant voltage source is a constant pressure source; a constant current source represents a constant mass flow (eg. outgassing off a wall). A vacuum pump is represented by a limited conductance to ground (zero pressure).

molecular beam.

5.4 LIF Measurement

The primary means used for state preparation and detection is laser-induced fluorescence. The molecular beam is illuminated perpendicular to the beam direction with laser light tuned to an optical transition, driving molecules from the ground state to an electronic excited state. Molecules can spontaneously decay from the excited state, emitting a photon in a random direction.

Light collection optics inside the vacuum system surrond the intersection of the detection laser with the molecular beam. The collection optics are designed to direct as much of the isotropically emitted fluorescence light into a lightguide, which carries the light out of the vacuum system to the detector. Generally

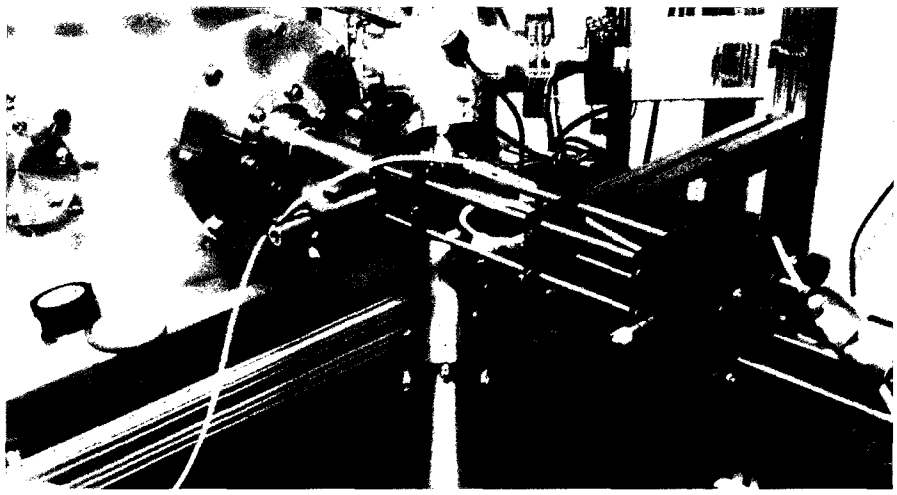

Figure 5.23: Optics to bring laser light into the vacuum system. Light is brought in on a polarization-preserving single-mode fiber (yellow) to an aspheric lens fiber launch (in the optics mount on the right side of the picture). Tilt and position can be adjusted using the stage and kinematic mounts. Apertures can be mounted along the optical rails, which are attached to Brewster-angle vacuum windows. The windows are epoxied with Torr-seal to the 1" brass tube, which is brazed to a QF40 flange. The inside of the flange has a Thorlabs lens tube thread, so that optical components (such as additional apertures to block scattered light) can be mounted inside the brass tube.

speaking, the following constraints apply:

- Light is emitted from the end of the lightguide at large angles, determined by the numerical aperture of the lightguide or - for a straight lightguide - the angular spread of the input light. The lightguide can only be coupled to the detector efficiently if the detector is similar in size or larger than the lightguide (figure 5.26).

- The detector size is extremely limited for single photon detectors with high quantum efficiency in the near infrared (860 nm). The available detectors include microchannel plate-based PMTs with crystalline GaAs photocathodes ($\approx \$20,000$) and smaller, amorphous GaAs-photocathode photomultiplier tubes with discrete dynodes ($\approx \$3000$). The latter, which has a 5 mm diameter photocathode and about 12% quantum efficiency at 860 nm, is used in this experiment. Larger, cheaper PMTs are available for use at shorter wavelengths (eg. the Hamamatsu R7600U-200, which has $>$ 40% quantum efficiency at 400 nm and a 18mm x 18mm photocathode).

- Small diameter lightguides tend to have large losses, due to the large number of reflections and poor manufacturing tolerances when the diameter is small.

Initial measurements were made by inserting a 1/2" lucite lightguide into the vacuum system through a compression seal, so that the end of the lightguide was about 1/2" – 1" from the point where the molecular beam was illuminated by the laser. In this configuration, all fluorescence light entering the face of the lightguide could, in principle, exit at the other face. The small GaAs PMT was placed on top of the other end of the lightguide. The optical efficiency is estimated as the following:

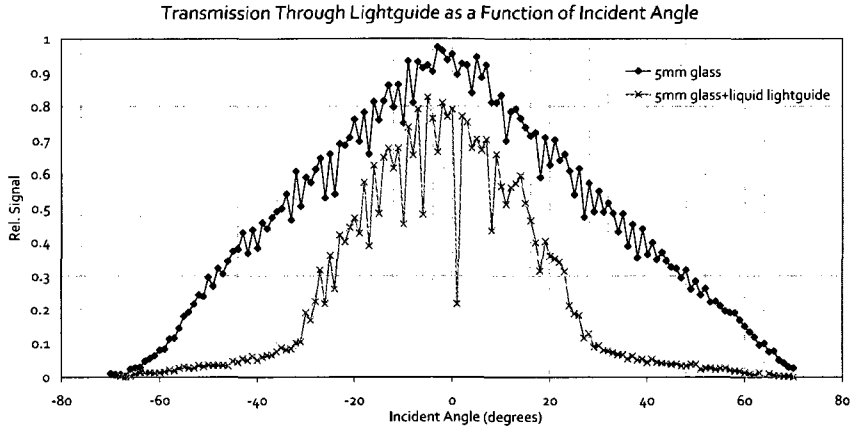

Figure 5.24: Lightguide transmission as a function of angle of incident light (vertical axis in arbitrary units) for the 5 mm glass lightguide alone, and for the glass lightguide coupled to the liquid lightguide. This demonstrates the cumulative effect of the optical components to transfer light from the collection optics to the detector. The vertical axis is normalized to 100% transmittance.

Component	Efficiency
Fraction of light entering lightguide[2]	0.03
Transmission through lightguide[3]	0.8
Fraction of light entering PMT[4]	0.05
PMT quantum efficiency[5]	0.12
Total	1.5×10^{-4}

This setup positioned the PMT directly on top of the lightguide, and cannot be used with the magnetic field at the current PMT location. This was used for the measurement of laser-induced fluorescence before the system was integrated with the magnet.

A better scheme uses a combination of mirrors to collect photons emitted at all angles and redirect them on to a lightguide (figure 5.25). This system uses a combination of an ellipsoidal and a spherical mirror. The molecular beam and detection laser light intersect at one of the focal points of the ellipsoidal

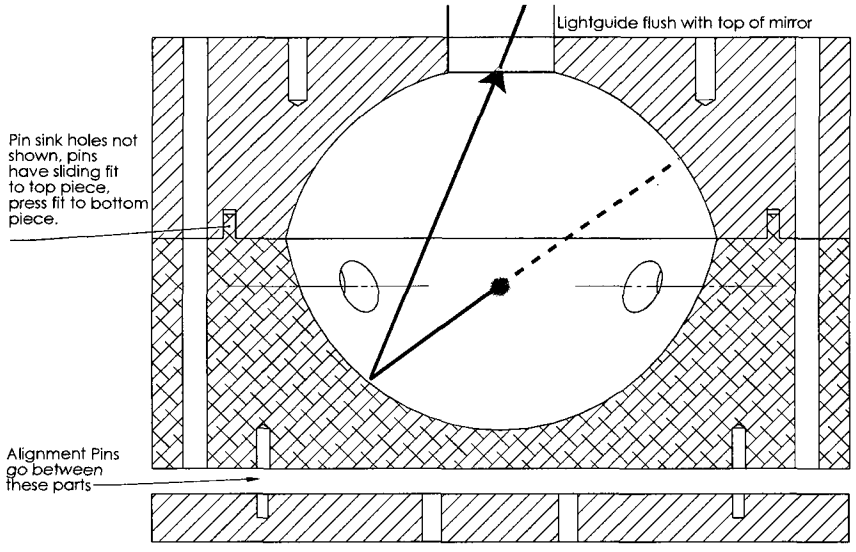

Figure 5.25: The light collection optics combine a spherical mirror (top) with an ellipsoidal mirror (bottom). Laser light and molecules pass through the four ports on the sides of the mirror assembly, and a light guide fits in to the opening at the top. The position at which the laser and molecular beams cross (blue circle) is at the center of the spherical mirror and the lower focal point of the ellipse. The upper focal point of the ellipsoidal mirror is at the end of the lightguide. Photons which are emitted downwards reflect off the ellipsoidal mirror, and are reimaged on to the end of the lightguide (solid red ray). Photons which are emitted upwards reflect off the spherical mirror, back through the point at which they were emitted (dashed red ray), and reflect off the ellipsoidal mirror into the lightguide. With proper design and a large-area detector, over 80% of the emitted photons can be collected. However, the efficiency is reduced if the lightguide is narrow compared to the fluorescence to be collected. The optics for collecting light into a 5 mm lightguide have an efficiency of about 30%.

mirror. Photons which are emitted downward are reflected towards the other focal point of the ellipse, where the lightguide is located. A spherical mirror is placed on top, such that the intersection of the molecular beam and detection laser light is at the center of the sphere. Photons emitted upwards reflect off the spherical mirror, back through the center, and then off the ellipsoidal mirror into the lightguide. A mirror assembly, designed as an undergraduate project by David Price, for detection of 860 nm light is described now.

The efficiency of collecting fluorescence light using the mirror system together with the 860 nm detector is estimated in the state preparation/detection region. First, consider the solid angle covered by the mirror assembly. Ray-tracing calculations and measurements (using a ruby sphere illuminated by a doubled YAG laser as a quasi-isotropic emitter) indicate that the collection efficiency is about 0.3 (eg. about 30% of the photons emitted by the molecular beam are collected and transferred to the lightguide). This is probably due to the small size of the collection optics and of the lightguide, compared to the size of the light source.

Next, look at the efficiency of the lightguides that transfer light from the collection optics to the PMT. For this setup, we use a 5 mm diameter quartz lightguide to bring the light out of the vacuum system, and then use a flexible 5 mm diameter liquid lightguide to bring the light to the PMT (placed outside of the magnetic field, about 1 meter away). Figure 5.24 shows the transmittance through the lightguide as a function of angle. This assembly of two lightguides has a strong falloff in transmittance as the incident angle of light increases. Geometrically,an isotropic point-like source will produce an angular distribution of light that looks like $I(\theta) \propto \sin(\theta)$, so that the efficiency ε is

$$\varepsilon = \frac{\int_0^{\theta_{max}} E(\theta) \sin(\theta)\, d\theta}{\int_0^{\theta_{max}} \sin(\theta)\, d\theta} \tag{5.9}$$

where $E(\theta)$ is the lightguide transmittance at an incident angle θ, and the maximum angle of incidence $\theta_{\max} \approx 45°$ depends on the geometry of the light collection optics. Based on the measured data, the efficiency ε of the lightguide (averaged over all incident angles) is about 18%.

Finally, the efficiency of transferring light from the lightguide into the photomultiplier tube is considered. The design of the H7422P-50 PMT module (figure 5.26) is somewhat problematic, in that the photocathode is recessed far behind the entrance window. The light divergence angle coming out of the lightguide is too high to effectively use transfer lenses to reimage the light on to the photocathode. The coupling efficiency is calculated by comparing the ratio of the photocathode area to the spot size out of the lightguide:

$$\varepsilon_{\text{cpl}} = \left(\frac{d}{2l \tan(\theta) + w} \right)^2 \tag{5.10}$$

where d is the diameter of the photocathode (5 mm), l is the distance from the end of the lightguide to the photocathode, θ is the half-angle correspoding to the numerical aperture $NA = n \sin(\theta)$ describing the spread of light coming out of the lightguide, and w is the diameter of the lightguide. For $\theta = 15°$, $l = 19.7$ mm, and $w = 6.35$ mm (dimensions on fig. 5.26), the total efficiency of coupling from lightguide to PMT is about 9%. Taking all effects into account, the total efficiency of detecting molecules in this geometry is about 0.2% (see table below).

Component	Efficiency
Collection optics	0.30
Lightguides	0.18
PMT coupling	0.09
PMT quantum efficiency	0.12
Total	2×10^{-3}

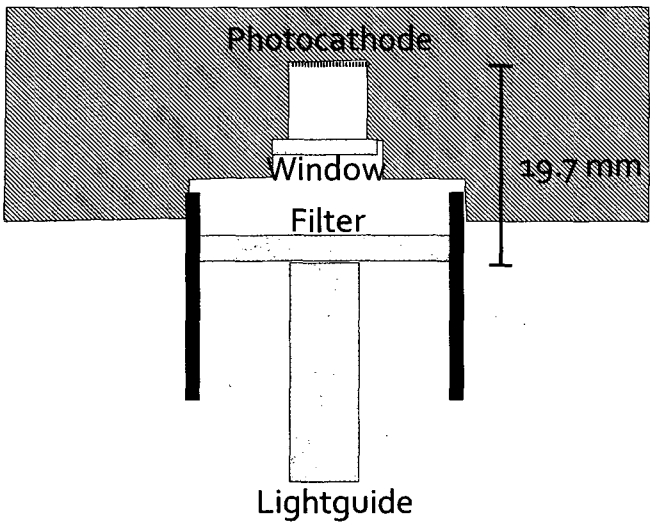

Figure 5.26: Coupling of lightguide to the Hamamatsu H7422P-50. Efficiency is low because the photocathode is set far back inside the PMT module housing and light diverges rapidly from the lightguide.

The previous section describes the fluorescence collection optics used in the pump region, as well as an older version of the probe region. More recently, a two-photon detection scheme was implemented in the probe chamber, with the goal to improve the overall detection efficiency. The goal was to shift the fluorescence to the blue, where large area ($\approx 17 \times 17$ mm), high quantum efficiency (40%) photomultiplier tubes are available. The new collection optics efficiency, as calculated by simulation, is 80%. Here, it is assumed that the 1" diameter lightguides have a 90% transmittance, with losses primarily due to reflectivity of the front and back surfaces. A geometric loss comes about from coupling a 1" diameter lightguide directly against the 17x17 mm PMT. The expected optical performance is improved by a factor of 85:

Component	Efficiency
Collection optics	0.80
Lightguides	0.9
PMT coupling	0.59
PMT quantum efficiency	0.4
Total	0.17

While the actual performance gains are on the order of 40x compared to the single photon detection system initially used in the probe region, the new detection system is still a welcome improvement. The details of this setup are presented in [62].

It has been considered whether there would be any benefit to using avalanche photodiodes (APDs) instead of PMTs for signal detection. The best APDs are available with large active areas, and have a quantum efficiency of $\sim 80\%$ at the wavelengths of interest. However, the gain mechanism inside the APD makes the device as "noisy" as a PMT with half the quantum efficiency. If the APD (using the single-photon excitation scheme on the A-X transition) is compared with the two-photon scheme (on the A-X, D-A transition with emission from D-X), there are only two potential advantages to using an APD:

- the APD may be operated at higher magnetic fields, and could be installed inside the chamber without a lightguide (higher efficiency in getting fluorescence to the detector)
- operation using the single-photon scheme bypasses losses from the intermediate A state (if STIRAP is not in use), and near-infrared emissions from the D state (D-C, D-B, D-A)

These factors would only be small improvements, while the two-photon scheme allows for the complete rejection of scattered light and is the lowest noise option

for very small signals. As such, we don't believe we would benefit significantly from using an APD over the two-photon detection scheme.

5.5 Interaction Region

5.5.1 DC Response of the Interaction Region

The desired asymmetry measurement requires the application of an electric field $\vec{E} = E(t)\hat{z}$ to the molecules within a uniform portion of the magnetic field along the beamline, in order to drive a far-off-resonance transition with $\Delta m_F = 0$. In practice, the parity violation measurement is sensitive to the phase and number of cycles of the applied field, but not particularly sensitive to the absolute frequency. Therefore, this experiment uses an interaction region design that allow the application of an electric field that is constant in time but varying in space, $E(z) = E_0 \cos\left(2\pi f \frac{z}{\bar{v}}\right)$, which relies on the velocity $\bar{v}$ of the molecules to generate an effective AC field with $f \approx 100$ kHz, $\bar{v} \approx 600$ m/s, and E_0 on the order of a few volts/cm. Other electric field patterns (eg. a constant field $E(z) = E_0$) are used to perform diagnostic tests of the apparatus. The minimum possible length of the interaction region is determined by the beam velocity and the desired frequency and number of cycles of the electric field. For a full-cycle at 100 kHz, this is 6 cm. There are the following additional design parameters:

- The electrodes should not disrupt the magnetic field or block the molecular beam.
- Optical access is needed to perform state preparation immediately before the interaction region.
- The electrodes must control the electric field over any regions where the

magnetic field is such that the energy levels used in the asymmetry measurement are close to crossing.

The interaction region has been fabricated as a flexible circuit board(5.27) which is rolled up and inserted into either a clear lucite or a Teflon tube. When the board is rolled up, only the series of ring electrodes is visible inside the assembly. It contains two flat planes of copper on either side, with thirty strip electrodes in the middle. The spacing of the strip electrodes is 2 mm, with a 0.13 mm gap between electrodes. A conductor from each electrode leads out to a 40-pin flex cable connector on the edge of the board (FCI p/n 62684-401100ALF, available from Digi-Key). A cable from this connector goes to a flex cable feedthrough (PAVE Technologies). The electrodes can be driven by either a voltage divider (a single high-voltage connection sets up a linear voltage gradient across the electrode array) or individually from a 32-channel analog output board from National Instruments. Optical access is available through the twelve slits cut into the board. The reverse side of the flex board has a solid ground plane with an insulating polyimide coverlay.

The electric field within the interaction region can be determined from the applied voltages on the ring electrodes, either analytically or numerically. Here the analytic relationship is derived. Beginning with the Laplace equation for the potential φ in cylindrical coordinates (r, θ, z):

$$\frac{\partial^2 \varphi}{\partial r^2} + \frac{1}{r}\frac{\partial \varphi}{\partial r} + \frac{1}{r^2}\frac{\partial^2 \varphi}{\partial \theta^2} + \frac{\partial^2 \varphi}{\partial z^2} = 0 \tag{5.11}$$

To model the interaction region, the potential is specified on the surface of the cylinder as $\varphi(r_0, z) = V(z)$. The z and r coordinates are separated by assuming a solution of the form $\varphi = R(r)\cos\left((2k+1)\pi\frac{z}{L}\right)$ or $R(r)\sin\left((2k)\pi\frac{z}{L}\right)$, which satisfies the boundary conditions $\varphi = 0$ at $z = \pm\frac{L}{2}$. (This condition corresponds to grounding both of the large outer electodes in our assembly. This is a natural

a)

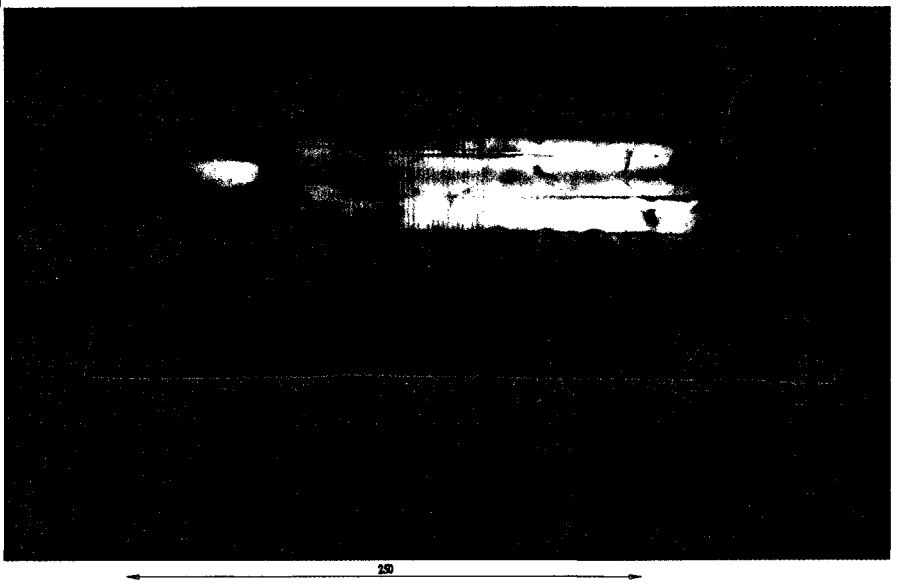

b)

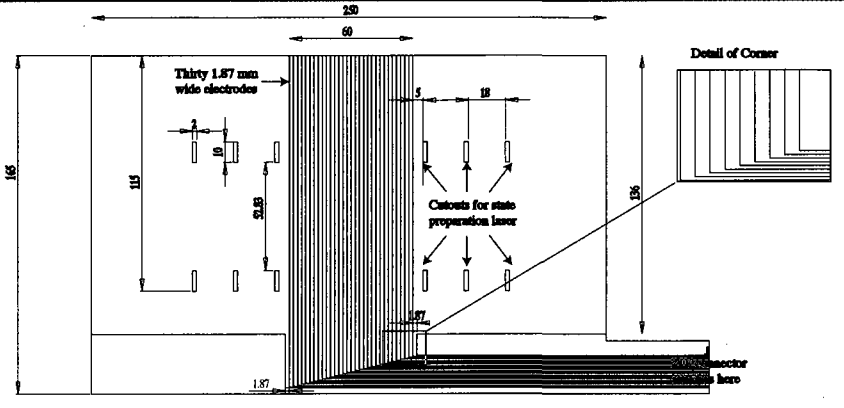

Figure 5.27: Interaction region flexible circuit board and holder (a), and schematic (b). The flex board is rolled up so that the electrode pattern is on the inside of the tube, and that the two rows of slits are opposite each other. The roll is then put into the clear plastic tube (bottom of the photo). The slits allow a laser to illuminate the molecular beam immediately before or after the interaction region. An electrical connection is made to the 32 electrodes using the miniature ribbon cable connector on the right. The rear of the board has a solid copper plane covered with a polyimide insulator. A dimensioned schematic of the flex board is in the Appendix.

choice for the parity violation experiment, where it is necessary to apply a full cycle of a sinusoidal electric field. It is a less natural choice for the linear potential used in the level crossing experiment described in chapter 7; however, the potential does return to ground after the end of the interaction region and so the boundary value conditions are fulfilled.) For the former ($\cos(\ldots)$), neglecting θ (cylindrical symmetry),

$$\frac{\partial^2 R}{\partial r^2} + \frac{1}{r}\frac{\partial R}{\partial r} - \left((2k+1)\frac{\pi}{L}\right)^2 R(r) = 0 \tag{5.12}$$

The solution is the modified Bessel function of the first kind, $I_n(x)$, which satisfies $x^2y'' + xy' - (x^2+n^2)y = 0$. So we let $R(r) = aI_0(br)$ and, using $I_n'(z) = I_{n-1}(z) - \frac{n}{z}I_n(z)$ (Abramowitz 9.6.26), find

$$R'(r) = ab\,I_1(br)$$

$$R''(r) = ab^2\left(I_0(br) - \frac{1}{br}I_1(br)\right)$$

$$b^2 I_0(br) - \left((2k+1)\frac{\pi}{L}\right)^2 I_0(br) = 0$$

so that $a = \frac{1}{I_0(br_0)}$ is chosen to make $R(r_0) = 1$, and $b = (2k+1)\frac{\pi}{L}$. This is used to construct an analytic series solution

$$\varphi = \sum_{k=0}^{\infty} A_k \cos\left((2k+1)\pi\frac{z}{L}\right)\frac{I_0\left((2k+1)\pi\frac{r}{L}\right)}{I_0\left((2k+1)\pi\frac{r_0}{L}\right)} + B_k \sin\left((2k)\pi\frac{z}{L}\right)\frac{I_0\left((2k)\pi\frac{r}{L}\right)}{I_0\left((2k)\pi\frac{r_0}{L}\right)} \tag{5.13}$$

where

$$A_k = \frac{\int_{-L/2}^{L/2} V(z) \cos\left((2k+1)\pi\frac{z}{L}\right) dz}{\int_{-L/2}^{L/2} \cos^2\left((2k+1)\pi\frac{z}{L}\right)} = \frac{2}{L}\int_{-L/2}^{L/2} V(z) \cos\left((2k+1)\pi\frac{z}{L}\right) dz$$

and

$$B_k = \frac{\int_{-L/2}^{L/2} V(z) \sin\left((2k)\pi\frac{z}{L}\right) dz}{\int_{-L/2}^{L/2} \sin^2\left((2k)\pi\frac{z}{L}\right)} = \frac{2}{L}\int_{-L/2}^{L/2} V(z) \sin\left((2k)\pi\frac{z}{L}\right) dz$$

The electric field $\vec{E} = E_z\hat{z}$ is found by differentiating eq. 5.13 term-by-term with respect to z. This solution converges fairly quickly when $r/r_0 \ll 1$, since distance tends to smooth out high order harmonics and the ratio $\frac{I_0((2k)\pi r/L)}{I_0((2k)\pi r_0/L)}$ rapidly decreases with increasing k as long as $r \lesssim 1/2r_0$. This relationship can be inverted to find the necessary electrode potentials, given a desired electric field along the axis. Let's start by differentiating eq. 5.13 with respect to z to find the electric field and setting it equal to the desired field $f(z)$ with $r = 0$ ($I_0(0) = 1$). Both sides are multiplied by $\sin((2m+1)\pi z/L)$ or $\cos(2m\pi z/L)$ and integrated over $-L/2$ to $L/2$:

$$\begin{aligned}
&\int_{-L/2}^{L/2} f(z) \sin\left((2m+1)\pi\tfrac{z}{L}\right) dz \\
&\quad = -\sum_k A_k \frac{(2k+1)\pi/L}{I_0\left((2k+1)\frac{\pi r_0}{L}\right)} \int_{-L/2}^{L/2} \sin\left(\tfrac{(2k+1)\pi z}{L}\right) \sin\left(\tfrac{(2m+1)\pi z}{L}\right) dz \\
&\int_{-L/2}^{L/2} f(z) \cos\left(2m\pi\tfrac{z}{L}\right) dz \\
&\quad = \sum_k B_k \frac{2k\pi/L}{I_0\left(2k\frac{\pi r_0}{L}\right)} \int_{-L/2}^{L/2} \cos\left(2k\pi\tfrac{z}{L}\right) \cos\left(2m\pi\tfrac{z}{L}\right) dz
\end{aligned} \tag{5.14}$$

The integral of the product of two sine or cosine functions over this interval will be 0 unless $k = m$, in which case the integral is $L/2$. So

$$\begin{aligned}
&\int_{-L/2}^{L/2} f(z) \sin\left((2k+1)\pi \tfrac{z}{L}\right) dz \\
&\quad = -\frac{(2k+1)\pi/L}{I_0\left((2k+1)\pi r_0/L\right)} \int_{-L/2}^{L/2} V(z') \cos\left((2k+1)\pi \tfrac{z'}{L}\right) dz' \\
&\int_{-L/2}^{L/2} f(z) \cos\left(2k\pi \tfrac{z}{L}\right) dz = \frac{2k\pi/L}{I_0\left(2k\pi r_0/L\right)} \int_{-L/2}^{L/2} V(z') \sin\left(2k\pi \tfrac{z'}{L}\right) dz' \quad (5.15)
\end{aligned}$$

This effectively relates the field on axis to the discrete cosine (or sine) transform of the electrode potentials.

Alternatively, relaxation techniques can be used to calculate the solution to $\nabla^2\varphi = 0$ numerically in cylindrical coordinates. Start with Laplace's equation in cylindrical coordinates(5.11) and, neglecting θ (cylindrical symmetry), make a difference equation by substituting:

$$\begin{aligned}
\frac{\partial\varphi}{\partial r} &= \frac{\varphi(r+dr,z) - \varphi(r-dr,z)}{2\,dr} \\
\frac{\partial^2\varphi}{\partial r^2} &= \frac{1}{dr}\left(\frac{\partial\varphi(r,z)}{\partial r} - \frac{\partial\varphi(r-dr,z)}{\partial r}\right) \\
&= \frac{\varphi(r+dr,z) + \varphi(r-dr,z) - 2\varphi(r,z)}{dr^2} \\
\frac{\partial^2\varphi}{\partial z^2} &= \frac{\varphi(r,z+dz) + \varphi(r,z-dz) - 2\varphi(r,z)}{dz^2}
\end{aligned}$$

and so if (for convenience) $d \equiv dz = dr$,

$$\begin{aligned}
\varphi(r,z) &= \frac{1}{4}\left(\varphi(r+d,z) + \varphi(r-d,z) + \varphi(r,z+d) + \varphi(r,z-d)\right) \\
&\quad + \frac{d}{8r}\left(\varphi(r+d,z) - \varphi(r-d,z)\right) \qquad (5.16)
\end{aligned}$$

except at $r = 0$, where the conditions are symmetric at $r + d$ and $r - d$:

$$\varphi(r,z) = \frac{1}{4}\left(\varphi(r+d,z) + \varphi(r-d,z) + \varphi(r,z+d) + \varphi(r,z-d)\right)$$

Space is divided into a 2-dimensional grid with resolution $dr = dz$, and fix the potential at the grid points corresponding to the edges of the electrodes. We repeatedly apply the equation above to calculate a new value of $\varphi(r,z)$ for each point based on the current value of its neighbors. This solution converges in a reasonable number of iterations, dependent on the size of the object and the choice of dr. It is easy to implement this as a spreadsheet, so that different electrode potentials can be explored interactively, or (for high resolution) as a C++ program (RELAX.CPP).

The results of the relaxation calculation in cylindrical coordinates are shown in figure 5.28. This simulation models the linear potential applied to the interaction region electrodes used for the single-photon level crossing data in chapter 7. In this configuration, the left side of the interaction region is grounded, and the right side is held at a potential $V{=}V_{\mathrm{max}}$. The intermediate electrodes are set to give a linear potential gradient from $V{=}0$ to $V{=}V_{\mathrm{max}}$. The region after the interaction region ($z{>}250$ mm) is assumed to be at ground[6]. The model is calculated on a 0.1 mm grid and includes a 0.1 mm gap between adjacent electrode segments. In practice, calculations on a 1 mm grid which neglect this gap produce nearly identical results ($\approx$1% mean difference on-axis) since this gap is significantly smaller than the electrode size. The field is uniform to within a mean difference of $\approx$3.5% within a radius of $r{<}10$ mm; this shows that the electric field uniformity is good across the entire molecular beam. However, the limited length of the interaction region creates a large negative electric field at $z \approx 250$ mm. The level-crossing experiment described in chapter 7 requires an

[6]The surface is insulating, and the actual potential on the surface is unknown. The surface is assumed to be grounded for the purpose of this model.

electric field profile similar to the step function shown in part c); this unintended field can cause a false signal.

To mitigate this problem, an additional electrode to extend the potential $V=V_{\max}$ further along the beamline was added before collecting the two-photon level crossing data described in chapter 7. However, there was a modest gap between the interaction region and the added electrode. Figure 5.29 shows the electric potential and field profile with a 3 mm gap between the interaction region and extended electrode[7]. Part c) shows that this configuration reduces the magnitude of the unwanted field, but that the remaining field is still significant. The correct way to handle this problem is to seamlessly extend the electrode so that there is no gap. The next iteration of the interaction region design is to be fabricated on a longer piece of flexible circuit board, so that it will not be necessary to install extra electrodes.

The interaction region is usually operated at up to $V_{\max} = 600$ volts (linear potential gradient), after taking care to ensure that no copper remains near the edges of the board (to prevent shorts between the electrodes and the ground plane on the back of the board). Some of the interaction regions have been run at up to $V_{\max} = 1000$ volts, but were eventually damaged by arcs that created a conductive path through the board substrate. In practice, it is not necessary to run at more than about $V \approx 150$ volts ($E_z \approx 30$ V/cm) for the DC Stark effect diagnostic measurements or for the parity violation measurement.

5.5.2 AC Response of the Interaction Region

The DC Stark and the parity violation experiment depend only on DC behavior of the voltage divider, as any effective AC field is generated by the motion of the molecules through the spatially varying field inside the interaction region.

[7]For this model, the interaction region and extended electrode are assumed to be held inside a larger, coaxial electrode at ground. This corresponds to the ground plane on the back side of the interaction region circuit board.

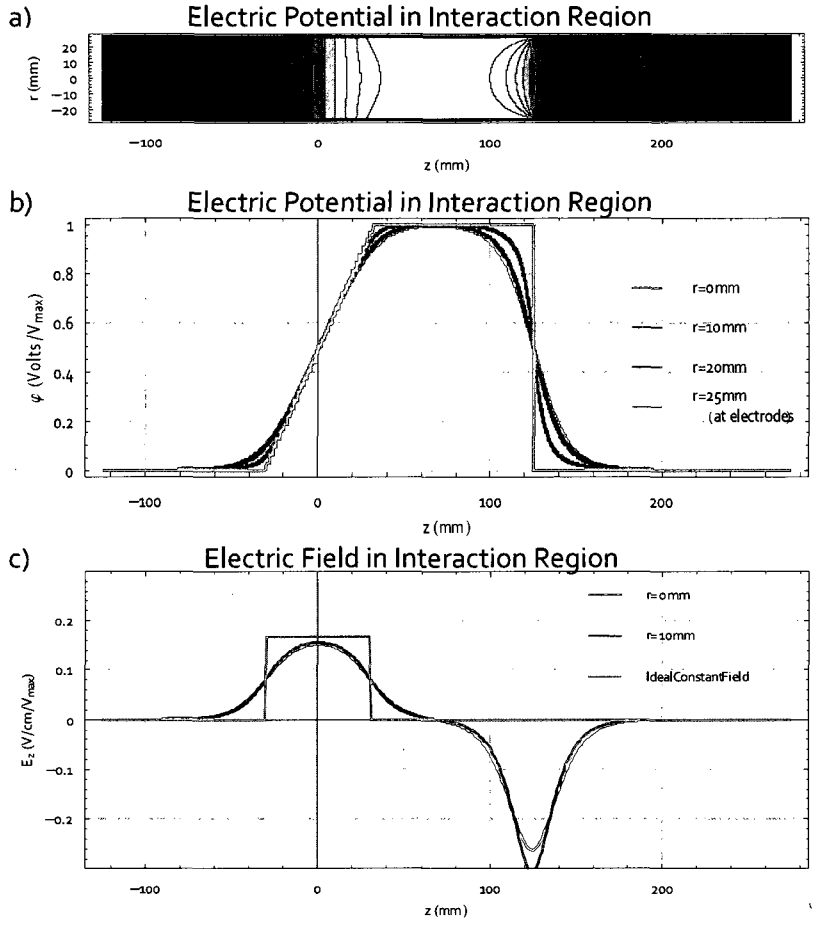

Figure 5.28: Numerical simulation for a linear potential applied to the interaction region electrodes using a relaxation technique, calculated on a 0.1 mm grid spacing. The left side of the interaction region is grounded; the voltage on each electrode increases linearly to $V = V_{\max}$ across the electrode segments (95 mm$< z <$155 mm), and is kept at $V_{\max}$ until the end of the interaction region (at z =250 mm). The model includes a 0.1 mm gap between adjacent electrode segments. Part a) shows the electric potential as a function of position within the interaction region, with part b) showing the potential in more detail at selected values of r. In our experiment, the limited aperture size of the state dectection optics limits the useful diameter of the molecular beam to about $r \approx 5$ mm. Out to a radius of r=10 mm, the mean deviation of the potential from the value on axis is less than 3.5%. This shows that this geometry achieves good electric field uniformity for all of the molecules in the molecular beam, regardless of position, as long as the beam radius is less than 1 cm. Part c) shows the electric field produced by the interaction region under these conditions. The electric field on axis is only an approximation of the desired constant field; instead, it reaches a maximum of $\vec{E} \approx \frac{V_{\max}}{L}\hat{z}$ (L=interaction region length) only in the center of the interaction region.

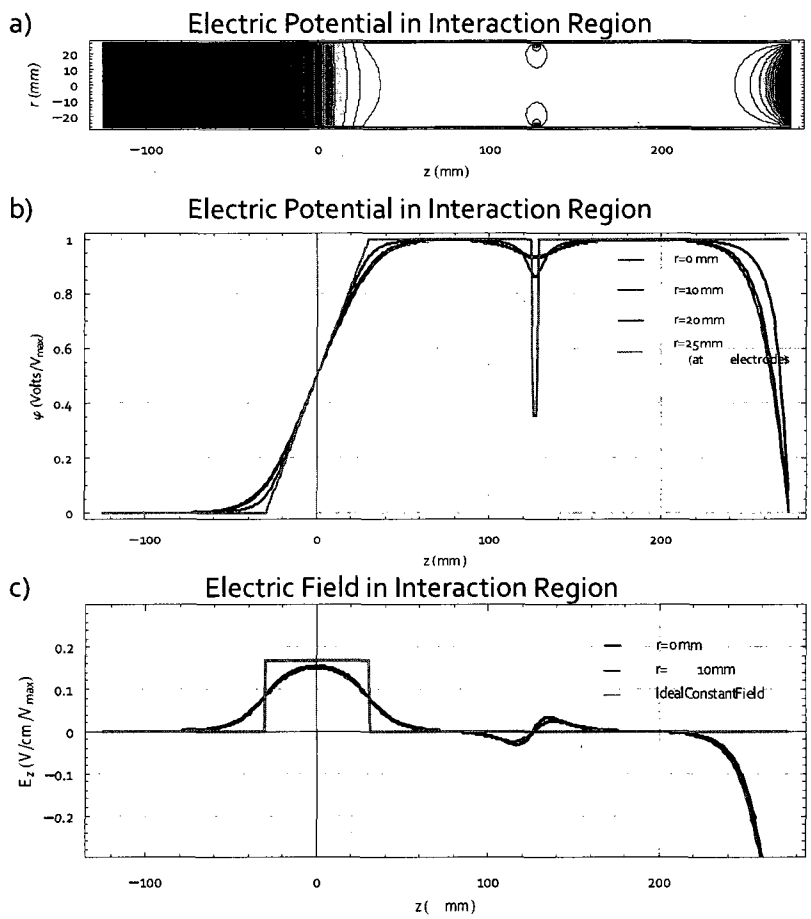

Figure 5.29: Numerical simulation for a linear potential applied to the interaction region electrodes using a relaxation technique. The electrode configuration is similar to that in fig. 5.28, except that (after a 3 mm break) there is an additional electrode kept at $V{=}V_{\max}$. This models the electrode configuration used for the later experimental measurements of level crossings described in chapter 7, in which an extension to the interaction region was installed in an attempt to prevent the unwanted negative electric field at $z \approx 250$ mm. However, the added component does not seamlessly connect to the interaction region; part c) shows that in the presence of such a gap (and assuming ground potential within the gap) the extension reduces the magnitude of the unwanted field, but does not eliminate it.

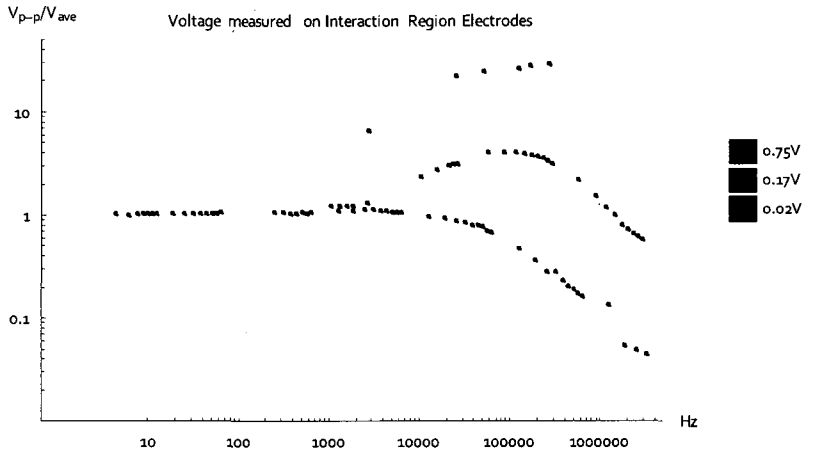

Figure 5.30: Interaction region electrode response as a function of frequency applied to the input of the voltage divider box. At low frequencies, the AC potential scales linearly with position on the voltage divider, like the DC voltage. Some electrodes have a resonance that enhances the AC field above $\approx$ 10 kHz; other electrodes see an attenuated response.

However, other experiments in which we use an AC field to drive a transition when the molecules are close to (but not on) resonance with the magnetic field could be considered, or in which we apply an AC field to individual electrodes to look at spatial variations of the magnetic field. To investigate the possibility of such auxiliary experiments, the response of the interaction region to applied AC voltages was measured. 5.30 shows the frequency response of the interaction region, when connected to the voltage divider and flex circuit cables. The frequency response differs for different electrodes; those at the high end of the voltage divider show a cutoff frequency of about 100 kHz; electrodes further down the voltage divider show an enhanced resonant response above 10 kHz. This non-ideal behavior likely precludes the use of this interaction region for any meaningful experiments with AC electric fields.

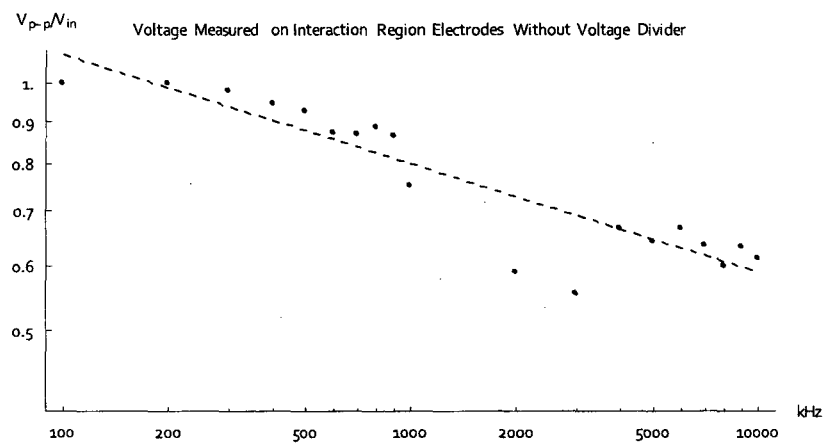

Figure 5.31: Interaction region electrode response as a function of frequency applied directly to the ribbon cable, without use of the voltage divider box. This tests the response at the electrode if a single electrode is driven with adjacent electrodes kept at ground. The falloff starts at about 200 kHz (similar to the response of the high end of the linear voltage divider), but falls off more slowly.

5.6 Magnet

This experiment uses an Oxford 2.0 Tesla horizontal bore superconducting magnet to generate the magnetic field necessary to bring two rotational sublevels close to crossing. The desired uniformity of the magnetic field is determined by the need to carefully control the energy splitting of these two levels. The splitting has a sensitivity of about 2.8 MHz/gauss; controlling the splitting to within 10 kHz corresponds to controlling the magnetic field at a level of 3 milligauss. For a 5000 gauss magnetic field (roughly the size of field needed to achieve level crossings in BaF), this level of control corresponds to about 0.6 ppm. This is achieved by a custom-designed system that reads the magnetic field at 32 positions around the interaction region using nuclear magnetic resonance in a water sample; the resonance frequency f is

$$f = \gamma_p B$$

where the proton gyromagnetic ratio in water is γ_p=42.576375 MHz/T [63], and B is the magnetic field. Any inhomogenieties in this field are corrected by changing the currents flowing through the room temperature shim coil array, a device containing 15 coils designed to produce magnetic fields corresponding to an orthogonal set of spatial functions. Details are provided in [62]. The magnet can reliably be shimmed to better than 0.2 ppm, which is expected to be adequate for the planned parity violation experiment.

In addition to the NMR probe array, a Hall effect probe was used to measure the field along the axis of the magnet (fig. 5.33). The Hall probe has a very low accuracy; but, unlike the NMR probe, it can measure the magnetic field at any value and is not sensitive to local field inhomogenieties. This makes it a useful tool for measuring the magnetic field along the molecular beam from the detection region through the center of the magnet. Figure 5.33 shows that

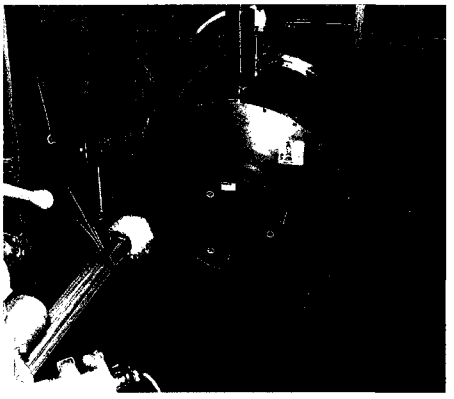

Figure 5.32: Oxford 2.0 tesla horizontal-bore magnet. The magnet contains a solenoidal superconducting coil carrying a persistent current of up to 86 amps, and seven additional superconducting coils ("shim coils") designed to mimic various spherical harmonics (Z_1, X, Y, ZX, ZY, XY, and $X^2 - Y^2$). The coils are buried in a liquid helium cryostat to maintain superconductivity. An additional room temperature shim coil array (hollow black cylinder in the magnet bore) contains 15 additional computer-controlled shim coils that can be used to adjust the uniformity of the magnetic field. The bore diameter is about 30 cm; the magnet length is 36"; the usable region inside the magnet over which the field is highly uniform is about 10 cm.

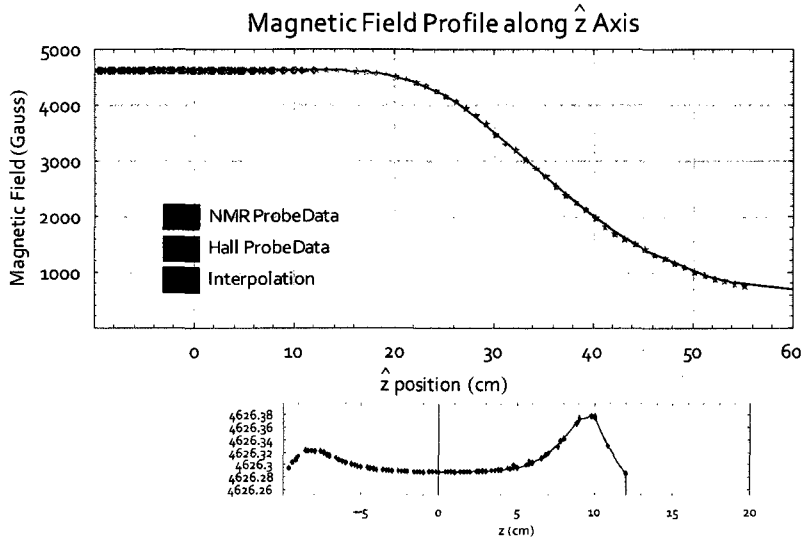

Figure 5.33: Measurement of the magnetic field along the magnet bore, from outside the magnet to the center, using a Hall Effect probe (~3 Gauss precision) and, when possible, a NMR probe ($\sim 5 \times 10^{-4}$ Gauss precision). This shows, to within the precision of the Hall probe measurements, that the magnetic field monotonically increases going into the magnet. The high-precision measurements from the NMR probes (inset) show that the field does overshoot the maximum value by a small amount.

the magnetic field increases smoothly and monotonically; there are no sudden changes in the magnetic field, or unexpected field crossings far from the center of the magnet.

5.7 Laser Stabilization

Locking the laser to a desired wavelength is still something that every atomic or molecular physics experiment seems to reimplement for themselves. Most experiments require much more precision in wavelength than commerecially available wavemeters usually provide. Atomic experiments often use a vapor cell to lock the laser directly to an absorption line of the atom they are working with. In

general, however, it is difficult to maintain a vapor of molecules (particularly free radicals such as are required for this experiment). Some groups use an iodine cell to provide wavelength markers for comparison, but these lines rarely coincide exactly with the spectral line you are interested in locking to.

In our experiment, we use a commercially produced wavemeter (Agilent 86120B) for coarse tuning in conjunction with a homebuilt Fabry-Perot interferometer for fine tuning and laser stabilization. The wavemeter accuracy is 300 MHz, and the free spectral range (FSR) of the Fabry-Perot cavity can be set from 75 to 750 MHz.

5.7.1 Fabry-Perot cavity

The scheme we use relies on a Fabry-Perot cavity to stabilize the laser frequency. A Fabry-Perot cavity can provide precise information on the wavelength of the laser, modulo the free spectral range of the cavity. When used in conjunction with a wavemeter for a coarse determination of the wavelength, we can easily scan the laser over a broad range of frequencies. However, we the length of the Fabry-Perot cavity must be stabilized to prevent it from drifting over time. For this, we use a Spectra-Physics frequency stabilized HeNe laser as a frequency reference. This scheme does have some complications. Operation over a very wide wavelength range is required, from 632.8 nm (for the HeNe reference) through 860 nm (for the BaF A-X transition). Furthermore, some applications (such as Pound-Drever-Hall locking) place upper limits on the required free spectral range; here, the FSR must be smaller than the tuning range of an available acousto-optic modulator (AOM) in order to implement offset locking. A few commercial devices are available with a wide wavelength range, such as the Toptica FPI100, and others are available with a small (300 MHz) FSR. However, a commercial product with both characteristics could not be found.

An undergraduate (Matt Nicholas) designed and assembled a homebuilt Fabry-Perot cavity for us [64] using one curved and one flat mirror. In this cavity, the free spectral range can be set to one of a number of values by changing the distance between the two mirrors [67, 68, 69]. The cavity will have resonances at various axial and transverse nodes, but if the ratio of the cavity length d to the mirror curvature R is set to

$$\frac{2d}{R} = 1 - \cos\left(\frac{l\pi}{N}\right)$$

where l and N are mutually prime integers describing the cavity modes, then the free spectral range (FSR) is given by

$$\text{FSR} = \frac{c}{4dN} \tag{5.17}$$

For example, the largest FSR of $\frac{c}{8d} \sim$ 1500MHz (using a mirror with R =10 cm radius of curvature in a half-confocal configuration with a flat mirror) is set by placing the mirrors at a distance of $d = R/4 = 2.5$ cm apart, with light bouncing 8 times before repeating its path. However, other modes are possible. For N=13 and l=6, a spacing of $d = 2.20$ cm will give a FSR $\approx$ 262 MHz. It has been difficult to find suitable mirrors. The flat mirror is a Semrock MaxMirror, a dielectric mirror designed to have high reflectance throughout the visible and near-infrared spectrum. The curved mirror was custom-coated by Semrock with the same coating. While these mirrors do seem to have the specified reflectivity ($\gtrsim$ 99.0%), the light that is not reflected appears to be primarily scattered or absorbed. This isn't a problem for normal mirror applications, but it significantly decreases the total amount of light transmitted through the Fabry-Perot cavity when it is tuned to resonance.

The simplest method to stabilize the diode laser relative to the HeNe is

to put both beams into the Fabry-Perot cavity, and sweep the cavity length over a range where both resonances are visible. A program can read the peak positions, and produce feedback to adjust the laser wavelength to maintain a fixed distance between the peaks. It is difficult, however, to make this method robust in many situations. For example, if multiple signals must be recorded on one detector, care must be taken to ensure that each peak is correctly identified with its own laser source. In this setup, small signal sizes make it challenging (but not impossible) to measure the transmitted light on separate detectors.

5.7.2 Fourier-Transform locking with the Fabry-Perot cavity

It is possible to take advantage of the fact that the HeNe and diode lasers are at different frequencies, and that therefore the Fabry-Perot cavity must be scanned different distances to go one FSR of the diode or HeNe lasers. The output signal is shown as a function of the distance between the two mirrors in the Fabry-Perot cavity in figure 5.34. The detector signal is the sum of the expected output for the HeNe and the diode lasers alone. The number of peaks seen is dependent on how far the piezo element in the Fabry-Perot cavity is ramped (here aligned in a half-confocal configuration so that FSR $= c/8dN$). Each laser should result in a signal transmitted through the cavity that looks like $S_i(\lambda, d)$:

$$S_i(\lambda, d) \propto \frac{(1-R)^2}{1+R^2-2R\cos[8d\frac{2\pi}{\lambda}]} \approx 1 + b\cos[8d\frac{2\pi}{\lambda}] + b'\cos[2(8d\frac{2\pi}{\lambda})] + \ldots \tag{5.18}$$

where R is the reflectivity coefficient of the mirrors, b is the amplitude of the fundamental frequency (with respect to change in mirror spacing d), and b'

of the first harmonic. The Fourier transform of the signal is taken and higher frequency harmonics are neglected. Looking at transmittance through the cavity with two lasers (and consider just the two fundamental frequencies as we ramp the mirror spacing), the signal is:

$$S(\delta) = b_1 \cos(a_1(\delta + d_0)) + b_2 \cos(a_2(\delta + d_0))$$

where δ is the distance that we are ramping the piezo element, d_0 is an arbitrary offset from which we start ramping the piezo (typically $d_0 \approx 5$ cm $\gg \delta \approx 100$ μm), and the constants a_1, a_2 incorporate the cavity free spectral range and the laser wavelength (eg.

$$a_i = \frac{16\pi}{\lambda}$$

Considering small changes in frequency $\Delta\nu$ from a center wavelength λ_0,

$$\lambda = c(\frac{c}{\lambda_o} + \Delta\nu)^{-1}$$

so that a_{diode} for the diode laser (to be stabilized) is defined as

$$a_1(\lambda_1) \approx 8\frac{2\pi}{\lambda_1} + 8\frac{2\pi}{c}\Delta\nu + \ldots \approx a_{\text{diode}}(1 + \frac{\lambda\Delta\nu}{c})$$

where $\frac{\Delta\nu}{c} \ll \frac{1}{\lambda_1}$, and

$$a_2(\lambda_2) = \approx a_{\text{HeNe}}$$

for the reference helium-neon laser. So, the signal looks like:

$$\begin{aligned} S(d, \Delta\nu) &= b_1 \cos[a_{\text{diode}}(1 + \frac{\lambda\Delta\nu}{c})(\delta + d_0)] + b_2 \cos[a_{\text{HeNe}}(\delta + d_0)] \\ &= b_1 \cos[a_{\text{diode}}(\delta + (1 + \frac{\lambda\Delta\nu}{c})d_0)] + b_2 \cos[a_{\text{HeNe}}(\delta + d_0)] \end{aligned}$$

where a_{diode} and a_{HeNe} can be considered as fixed values, experimentally determined from the recorded signal, and higher order terms have been dropped. The signal $S(d)$ is recorded as the spacing between the two mirrors is ramped, and the phase information from the Fourier transform is taken at the frequencies corresponding to a_1, a_2 to find the values

$$\varphi_{\text{diode}} = a_{\text{diode}}(1 + \frac{\lambda\Delta\nu}{c})d_0 \bmod 2\pi$$

and

$$\varphi_{\text{HeNe}} = a_{\text{HeNe}} d_0 \bmod 2\pi$$

(On a computer, the easiest way to do this is with an FFT, but it could be implemented on a microcontroller or DSP by finding the value only at the points needed.) From these two phases, we can find (within a value of 2π):

$$\Delta\nu = \frac{c}{\lambda}\left(\frac{\varphi_{\text{diode}}}{a_{\text{diode}}} - \frac{\varphi_{\text{HeNe}}}{a_{\text{HeNe}}}\right)$$

This value is invariant under drifts of the length of the Fabry-Perot cavity[8] up to corrections of order $d\frac{\Delta\nu}{c}$, which are negligible. This is used as the basis of a PID loop to control the laser frequency shifts $\Delta\nu$. The loop can be used to stabilize the frequency, or to scan the laser over a broad range. The algorithm can be implemented in software as follows:

1. Determine a_{diode}, a_{HeNe} by looking at the number of points acquired per free spectral range (only need to do this once); this is the periodicity of the photodiode signal as the applied voltage is increased
2. Ramp the mirror spacing in the Fabry-Perot cavity over many (at least 10) peaks
3. Record the light intensity on the detector
4. Take the Fourier transform of the signal as a function of applied voltage
5. Find the phases φ_{diode}, φ_{HeNe} at the frequencies corresponding to a_{diode}, a_{HeNe}
6. Track the total number of fringes we have passed through
   (a) If the last value of φ was $> 0.9(2\pi)$ and the current value of φ is $< 0.1(2\pi)$, increment N
   (b) If the last value of φ was $< 0.1(2\pi)$ and the current value of φ is $> 0.9(2\pi)$, decrement N

[8] There is some concern that the piezo used to drive the Fabry-Perot cavity may not be linear over the range that the cavity is scanned. Indeed, the Thorlabs FP used to stabilize the 797 nm laser has a nonlinearity on the order of a few percent over two FSR (1.5 GHz/FSR), which is corrected for by modifying the piezo voltage profile. This homebuilt cavity for nonlinearity has not been characterized, but it is mitigated by two factors:

1. The cavity is operated in a higher-order mode, so that it is possible to scan over many FSRs with a shorter distance of travel
2. The phase extracted from the Fourier transform is effectively an average over all the FSRs scanned over; only the nonlinearity over one FSR needs to be considered, not over the entire scan.

7. Find $error = \frac{N_{\text{diode}}+\varphi_{\text{diode}}}{a_{\text{diode}}} - \frac{N_{\text{HeNe}}+\varphi_{\text{HeNe}}}{a_{\text{HeNe}}} - setpoint$ and $sumerror = sumerror + error$

8. Find the new control voltage out: $G_P \cdot error + G_I \cdot sumerror + G_D(error - lasterror)$

9. Repeat from step 2

The laser diode controller primarily controls the wavelength by using a piezo element to change the position of the grating (Littman-Metcalf laser) but also changes the diode current slightly. With a control loop written in C on a 2 GHz Pentium 4 computer, the limiting factor is the maximum rate at which we can ramp the cavity spacing. At a 200 Hz scan repetition rate over about 10 peaks (peak spacing $\sim$ 266 MHz FSR using a higher order mode of the cavity), CPU usage is about 50%. Our program is set up to communicate with LabView (or other user programs) by means of a TCP/IP port, so it can be run on either the main data acquistion computer or be remotely controlled.

Some advantages of this method include:

- Easier and cheaper hardware setup (relative to Pound-Drever-Hall scheme)
  - Doesn't require AOMs, and needs only a small amount of diode laser light compared to schemes using AOMs.
- Ability to scan over wide frequency bands, far from reference spectra

Some drawbacks are:

- Modest repetition rate
  - The 200 Hz loop time is enough to cancel out most drifts, but sharp vibrations or modehops will be problematic.
- Lasers must be separated in wavelength

  - This scheme relies on the periodicity of the diode laser and HeNe peaks being different. Two closely spaced lasers would be indistinguishable with only 10 peaks available.

- No absolute frequency information
  - This only controls position relative to some arbitrary offset
  - Needs a wavementer or absorption cell for an absolute reference
- Still requires some expensive equipment (Fabry-Perot cavity, frequency stabilized HeNe laser)

Some of the drawbacks could be minimized by setting the Fabry-Perot cavity to have a small FSR, so that ramping the mirrors by a given distance covers more repetitions of the peaks. Ideally, the FSR could be made comperable to the linewidth of the cavity, and the detector output will appear nearly sinusoidal. This would improve the ability to distinguish between two lasers of similar wavelength. With additional hardware complexity, we could also modulate one of the lasers at a higher frequency (eg. by modulating the diode current) and use lock-in detection to isolate the part of the detector signal due to that laser.

There has not been an attempt to analyze systematic errors in this method arising from e.g. nonlinearity in the piezo scan distance vs. applied volage; distorted lineshapes due to imperfect mode-matching; etc. Rather, this was implemented directly on the experiment, and in the course of this work some crude attempts at characterization of its performance were made. Ultimately, for a variety of reasons a different locking scheme (described in the next section) was chosen.

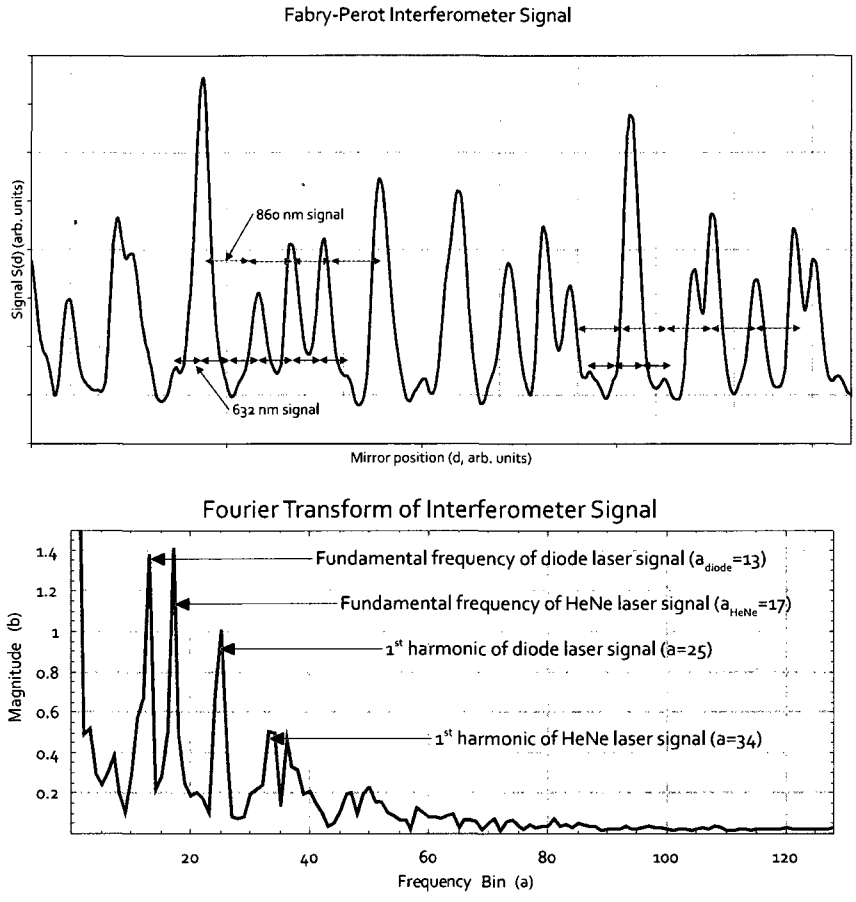

Figure 5.34: The transmitted light signal from the Fabry-Perot interferometer vs. scanning mirror position (part a), with two lasers (an 860-nm external cavity diode laser and a frequency-stabilized 632 nm HeNe), over ~12 free spectral ranges. The transmitted signal is the sum of the signals from the two lasers. The periodicity of each laser signal is proportional to the wavelength of the laser, so that even though the signals overlap, the two signals can be separated. Taking the Fourier transform of the signal (part b) shows this periodicity. The frequency bins (a) are dependent on experimental parameters (voltage ramp, piezo response, sampling rate). The values a_{diode} and a_{HeNe} are chosen to correspond to the fundamental frequencies of the periodic diode laser and HeNe laser signals. We use the phase shift at each of these frequencies to calculate the laser drift.

5.7.3 Analog Locking

A laser locking scheme mirroring an implementation developed by other projects in the DeMille group[71] was set up. The length of the Fabry-Perot cavity is first stabilized by locking it to a frequency-stabilized HeNe laser. The HeNe laser's frequency is internally modulated at ≈ 5 kHz; the detector output is mixed with this 5 kHz reference. The mixed signal goes to 0 when the cavity mirror spacing is in resonance with the HeNe laser, and the integral of this signal is used to control the mirror spacing.

To lock the diode laser to the stabilized cavity, some fraction of the diode laser light is given a tunable offset using a double-pass high-frequency (220 MHz) AOM (here, an IntraAction ATM-2201A2-1) and also modulated by using a single pass through a low-frequency (110 MHz) AOM (NEOS 23110). This scheme (using separate devices for offset locking and modulation) prevents residual amplitude modulation of the laser intensity synchronous with the lock-in detection frequency. The low-frequency modulator is driven with a time-varying frequency $f_m = \cos\left((\omega_1 + \cos(\omega_2 t))\, t\right)$, with $\omega_1 \approx 80$ MHz and $\omega_2 \approx 100$ kHz. This provides a 100 kHz modulation of the diode laser signal after the Fabry-Perot cavity, and a similar mix-and-integrate circuit provides feedback to stabilize the laser diode. The high-frequency AOM provides a tunable offset between the actual diode laser frequency and the resonance of the Fabry-Perot cavity. So, the drive frequency of the AOM can be changed slowly (shifting the frequency of the light from the diode laser going into the cavity), and the integrator circuit compensates by shifting the laser diode frequency in the opposite direction. A clever trick developed by Petreka, Glenn, and DeMille allows the laser tuning to be extended beyond the range of the AOM without losing laser lock. When the laser frequency has been shifted by exactly one FSR of the cavity, the signal will look the same if we suddenly shift the AOM by one FSR. So, this makes

available a "rachet-lock" mechanism:

1. Shift the AOM frequency to near the bottom (or top) of its range
2. Suddenly increase (or decrease) the shift of the high-frequency AOM by one FSR
3. Repeat step 1

The lock-in and integrator circuits should see exactly the same conditions as before, but the laser will have been shifted by one FSR. Multiple lasers can be used with the same Fabry-Perot interferometer by modulating them at different frequencies. The lock bandwidth is about 1-2 kHz, limited by the response time of the piezo element in the diode laser. This could be extended by also including servo feedback to the diode laser current, but this has not been implemented in our setup.

The experiment would benefit from better performance of both the 860nm Littman-Metcalf and the 797nm Littrow lasers. The primary flaw of the Sacher TEC-50 design is an extreme sensitivity to mechanical vibrations at audio frequencies. This has been observed by analyzing the light from this laser on a scanning Fabry-Perot cavity. A modest audio-frequency noise will cause a significant (> 20 MHz) dithering in the output laser frequency. As a rule of thumb, preventing this would require a servo loop with a bandwidth at least 10 times higher than the highest audio frequency we want to compensate for. The output power of the Sacher laser is also less than might be desired, primarily because the laser is based on an anti-reflection coated diode in a Littman-Metcalf configuration. AR-coated diodes tend to output less power than an uncoated diode, but offer much better resilience against mode-hopping or multi-mode operation. The Toptica Littrow design used in the 797nm laser is mechanically sturdy, and we easily achieve an adequate amount of output power. However, the use

of a diode without an AR coating means that this laser is extremely sensitive to modehopping; proper operation during a long data collection run requires careful tweaking beforehand to optimize the current and temperature settings.

5.7.4 797 nm Laser Lock

The Toptica DL100 797 nm Littrow external cavity diode laser maintains a relatively stable output frequency, and under most conditions only requires a slow servo loop to keep it locked. To this end, some of the light from this laser is combined with 860 nm light from the stabilized Sacher laser using a polarizing beamsplitter and sent through a scanning Fabry-Perot cavity. The cavity output is separated by means of a second polarizing beamsplitter, and measured on separate photodiodes for the two lasers. A software program running under LabVIEW tracks the position of the peaks, and adjusts the feedback voltage to the laser piezo to maintain the desired peak position. Scanning across multiple spectral ranges can be accomplished by "jumping" from one peak to the next as a given laser peak reaches the edge of the scan range.

5.8 Data acquisition & control

The data acquisition and control tasks are divided as follows:

1. Control of system state and interlocks
2. Control of the beam source
3. Control of the magnet
4. Control of the lasers
5. Acquiring the laser-induced-fluorescence signals
6. Monitoring system state

Control of the state of the vacuum system and interlocks is accomplished by a PLC. A Trilogi Logic T100MD2424+ PLC[9] controls the pneumatically-actuated vacuum valves and is connected to the motor that advances the barium metal rod ablation target. It is controlled by an LCD and pushbutton interface panel, and receives input from the vacuum gauge controller. It can communicate with the data logging computer via an RS232 link. The PLC prevents inappropriate combinations of valves from being opened, and automatically shuts down the vacuum system in the event of a leak. Details about operation of the PLC can be found in the Appendix.

The molecular beam source requires signals to synchronize the firing of the pulsed Nd:YAG ablation laser with the gas pulse from the pulsed valve and with the data acquisition system. Figure 5.35 shows the sequence of timing signals. The main data acquisition computer downloads the configuration via GPIB before each run.

Control of the magnetic field is handled by a separate computer, due to the high computational load of the curve-fitting algorithms used. This system performs the NMR readings of the magnetic field on the probe array, and adjusts the currents going to each of the room-temperature shim coils. The main data acquisition computer can request that the magnetic field be changed via a network connection. More information on the probe measurement and control procedure can be found in [62].

The 860 nm laser was for some time controlled directly through a program running on the data acquisition computer, but more recently through the analog circuit-based locking scheme as outlined in the previous section. The 797 nm laser is controlled by a separate computer which scans a Fabry-Perot cavity and uses a peak-finding routine to adjust the control voltage of the laser, as mentioned in the previous section. This system can receive commands to scan

[9]Programmable logic controller; this is an embedded CPU designed for machine control.

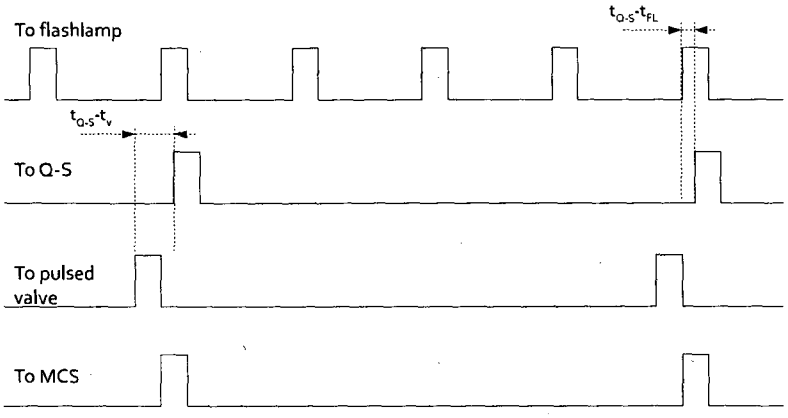

Ch	Connection	Delay	Width	Mode	Wait	Pol.	Ampl.
T1	YAG Flashlamp	T0+5000 μs	100 μs	normal	0	H	5V
T2	Pulsed valve	T0+4760 μs	360 μs	duty cycle on 1, off n	100	H	5V
T3	YAG Q-switch	T1+5155 μs	100 μs	duty cycle on 1, off n	100	H	5V
T4	DAQ "start" trigger	T0+5155 μs	100 μs	duty cycle on 1, off n	100	H	5V

Mode continuous, period 0.01 sec.

Figure 5.35: Timing signals for sequencing the beam source. The Nd:YAG flashlamp must fire at 100 Hz when the laser is on; this 100 Hz timebase is generated by a clock within a digital pulse and delay generator (Quantum Composer). All other pulses are offset by $\approx$ 5000 μs so that the pulsed valve can be triggered before the start of the laser. The "duty cycle" mode allows the pulsed valve and Q-switch to be fired at a lower repetition rate than the flashlamp, to reduce gas load on the system and wear on the target. For 10 Hz, operation, for example, $n = 9$. The configuration is programmed into the Quantum Composer by the computer before each data collection run.

the laser from the data acquisition computer.

The main data acquisition computer undertakes the following tasks:

- Setting up the system parameters (beam source configuration, magnetic field, laser wavelength)
- Acquiring time-of-flight resolved counts of the number of photons detected using a multichannel scaler
- Recording status information about the system

The photomultiplier tubes used to detect laser induced fluorescence are operated in photon-counting mode. Each incident photon that is converted to an electric signal produces a pulse with a height of 5-15 mV and a duration of about 5 ns. Instataneous count rates typically do not exceed 4 MHz (400 counts in a 100 μs window), so pile-up is not a concern. This signal is amplified (by a Minicircuits ZHL-32A, gain of 25 db, on the H7422P PMT, or a SRS SR445A preamplifier, 5x voltage gain, on the R7600U-200 PMT) and converted to TTL using the discriminators on a Fast-Comtec P7882 multichannel scaler board and a NIM-to-TTL logic level translator. The TTL signals are counted by a dual input multichannel scaler implemented using the buffered counter mode on a National Instruments PCI-6259 M-series data acquisition board. The buffered counting mode is set up to record the total number of photon counts registered at 10 μs intervals (for a total of 600 intervals). The details of configuring the National Instruments board for buffered counting mode can be found in the Appendix. Subtracting the difference in total counts between each interval gives the number of photons observed in that time bin. The discriminator threshold can be scanned over a voltage range to determine the optimal discriminator setting (figure 5.36). The computer automatically controls the photomultiplier drive voltage and state of the H7422P PMT module to turn the module off

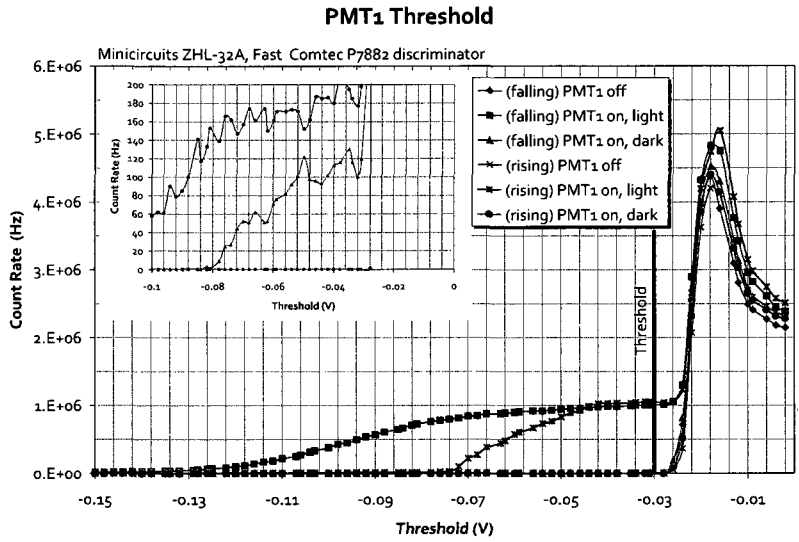

Figure 5.36: Counts recorded as a function of discriminator threshold. This shows the dark counts of the PMT, and the effect of triggering a count on a rising vs. falling edge. While the PMT signal is a negative-voltage pulse, it is worth checking triggering on both edges in case there is a significant asymmetry in the behavior of the electronics; the discriminator appears to behave in a complementary fashion if the threshold is set to "rising" rather than falling, but perhaps the counting electronics require a long "0" pulse before triggering on an edge. Choosing a threshold larger than -30 millivolts eliminates electronic noise; however, dark counts (zoomed in on inset plot) cannot be distinguished from photoelectrons. The threshold is typically set at about -30 mV.

at the end of a measurement run, but does not yet automatically control the R7600U-200 PMT.

The operation of the main system diagnostic and monitoring programs, *monitor.vi* and *mcs_and_laser.vi*, as well as the data acquisition routine *scanb.vi* is described in appendix G.

Chapter 6

Molecular Beam Performance

A series of experiments were performed during the construction of the molecular beam source to characterize and optimize the beam intensity. The experimental methods are summarized in table 6.1. The first diagnostic tool used was a fast ion gauge; this measures the instantaneous pressure at a fixed location as the pulsed beam travels by. The gauge is also sensitive to the background pressure level, and records the rise in pressure due to the release of the carrier gas, and the recovery time of the vacuum system. The second diagnostic test is to perform absorption spectroscopy in the beam, close to the target. Unlike the first test, this test is only sensitive to the desired species of molecule. The third set of experiments involved measuring the number of BaF molecules ablated from the target through absorption spectroscopy in a room temperature buffer gas. Beam performance was then measured using laser-induced fluorescence (LIF). This tested the detection optics, laser stabilization, and our understanding of the level structure of BaF. Finally, laser-induced fluorescence was used to measure the beam performance after the magnet and interaction region.

For the fast ionization gauge, absorbance, and earlier LIF experiments, the

Diagnostic tool	Requires	Tests
Fast Ion Gauge	vacuum system	pulsed valve and carrier gas dynamics
Absorption spectroscopy in beam	vacuum system, pulsed valve, target design	target design, ablation timing, tunable laser, beam yield
Buffer gas absorption spectroscopy	vacuum system	target design, tunable laser, ablation yield
Laser-induced fluorescence	vacuum system, pulsed valve, target design, ablation timing, tunable laser	optics & electronics, spectroscopic calculations, laser stabilization, beam yield and attenuation

Table 6.1: List of experiments performed to characterize the molecular beam and experimental apparatus. Successive experiments build upon each other; later experiments use the subsystems tested in the earlier experiments.

apparatus was configured as shown in figure 6.1. The fast ionization gauge could be moved if it was necessary to measure the gas pulse at a different position in the system.

6.1 Pulsed Beam Source (Fast ionization gauge)

The first test is to characterize the carrier gas pulse from the pulsed valve by looking at the gas pulse using a fast ion gauge (Beam Dynamics, FIG-1). The fast ion gauge is a bare ionization gauge which is optimized for fast response times by incorporating the amplifier circuitry into the gauge head. First, the presence of the gas pulse indicates the proper performance of the pulsed valve. The fast ion gauge can also be useful in determining the proper timing and positioning of the ablation laser pulse. Jony Hudson of Imperial College pointed out their empirical observation (in a similar system) that when molecules are being produced the ablation plume appears to displace carrier gas from the pulse, making a "notch" corresponding to the presence of the entrained molecules (figure 6.2). The same behavior was observed in our apparatus. Part a) shows

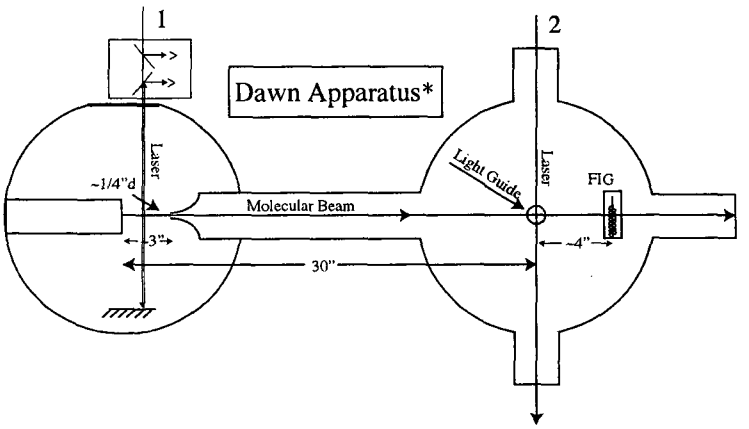

Figure 6.1: Configuration of the experiment for fast ion gauge, fluorescence, and absorption measurements. The absorption measurements were made at location 1 near the beam source, while laser-induced fluorescence was observed at 2 on the right. The fast ionization gauge could be moved as necessary, but was usually placed after the region for observing fluorescence to avoid interfering with the molecular beam. The vacuum system was later reconfigured and attached to the magnet to allow passage of the molecules through the superconducting magnet.

* The "dawn horse", eohippus, is the predecessor to the modern-day horse. Both may be found on Science Hill at Yale University.

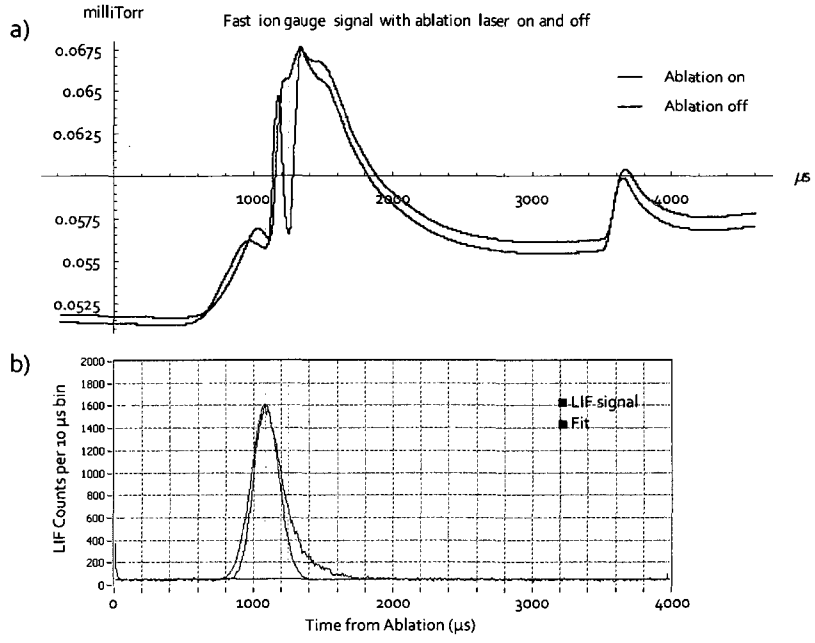

Figure 6.2: Fast ion gauge signal with and without the ablation laser on (top), and the resulting time-of-flight recording of the laser-induced fluorescence (bottom, with time axis in 10 μs increments). The plume of ablated material removes a substantial amount of argon gas from the gas jet, resulting in a significant dip in the observed pressure coincident with the fluorescence signal from the ablated material. This can be used to roughly set the time delay between the ablation laser pulse and the gas valve trigger, without having to rely on spectroscopic measurements.

the shape of the gas pulse, with the ablation laser turned on (blue) and off (orange). If the ablation laser is properly timed, it will make a notch in the middle of the gas pulse. In figure 6.2, this is indicated by the dip in the pressure signal with laser ablation on (visible at 1250 μs). It is seen in part b) that molecules are detected in fluorescence at about the same time (at 1100 μs; the LIF signal precedes the gas signal since the detector is closer to the source - at 600 m/s, the 150 μs difference corresponds to 9 cm).

6.2 Absorption Spectroscopy in the Molecular Beam

After verifying the performance of the gas valve and vacuum system, absorption spectroscopy was used to test the molecular beam performance. There were two separate experiments based on absorption spectroscopy; the beam was measured close to the source and then by ablation in a room temperature buffer gas. Spectroscopy in the beam was useful for developing the beam source; it allowed investigation of the properties of the molecular beam close to the beam source, where the flux of molecules is high, before switching to laser-induced fluorescence measurements.

Absorption spectroscopy in the molecular beam allowed exploration of the spectral features of BaF without having to set up apparatus for laser-induced fluorescence. The measurement scheme is outlined in figure 6.3. Light from a detection laser (Sacher TEC500 AR-coated Littman-Metcalf external cavity diode laser tuned to the 860 nm X ($v = 0$)-A ($v = 0$) transition) is split; some of the power is sent to a detector, and the remainder is sent through a cloud of molecules. This light is retroreflected back through the cloud, and measured on a second photodiode. The detector output is amplified and subtracted from the signal from the first photodiode; the gain is chosen so that (in the absence of absorption) the difference in signal between the two detectors is zero. If absorption increases, the two detector signals will become unbalanced, and the output of the differencer will differ from zero. This way, noise that is common to both detectors, such as fluctuations in the laser power, is cancelled out.

Absorption spectroscopy can be significantly easier to implement than laser-induced fluorescence, if the situation allows for it. Measurements were made on an intense part of the molecular beam, close to the source. As a result of the

wide transverse velocity spread (Doppler broadening), the linewidths tend to be very broad. Typical spectral lines may be more than 200 MHz wide; hyperfine features cannot be resolved, but it is very easy to find rotational lines in the spectrum. Light is plentiful in most situations; cheap silicon photodiodes are ideal for use as detectors. High efficiency light collection optics were not needed, as they are for laser-induced fluorescence, because the measurement is of the transmitted power. The main drawback is that sensitivity is limited to about 1 part in 1000 (uncertainty in transmittance $\sigma_T = 0.001$), due to fluctuations in the power of the light source and noise in the detector. This makes absorption spectroscopy inappropriate for measuring the number of molecules in the state preparation or state detection regions of the apparatus, where the density of molecules is too low to get an absorption signal larger than the sensitivity.

The spectrum in figure 6.4 was recorded using absorption spectroscopy in the absence of an external magnetic field. This allowed identification of the known spectral features of BaF, as well as adjustment of experimental parameters to maximize the beam intensity. Some important features include the Q-branch bandhead at 11630.6 cm^{-1}, the R-branch bandhead at 11663 cm^{-1}, and the isolated first line in the R-branch at 11631.28 cm^{-1}. The P-branch begins at 11630.07 cm^{-1}, and proceeds downward. The R-branch line was chosen for state preparation and detection because it is the only isolated spectral line associated with the ground state; the P- and Q-branch lines are in a congested region of the spectrum.

Note that the presence of absorption lines through and beyond the R-branch bandhead indicates significant population up through rotational number $N \sim 100$. There has not been an attempt to rigorously characterize the temperature of this beam; but, by comparing against simulated spectra (figure 4.5), the rotational temperature is estimated - as observed under these conditions - to be

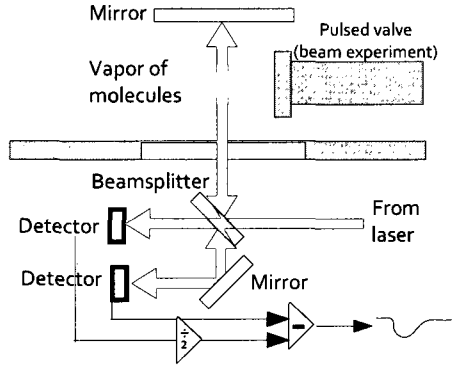

Figure 6.3: Absorption spectroscopy setup. Laser light is split on a beamsplitter; half the light is sent to a detector; the remainder is sent through the cloud of molecules and retro-reflected. The returning beam is sent to a second detector. One of the detectors is amplified and subtracted from the other, so that (when no molecules are in the beam) the output of the subtraction is zero. When there is absorption in the path of the detection laser, the detector output becomes unbalanced, and we register a signal. The optics and detector are placed on a moveable stage (which can be translated left and right), so that the beam can be studied at different distances from the source (beam experiment). For the buffer gas experiment, the beam is centered over the ablation point on the target.

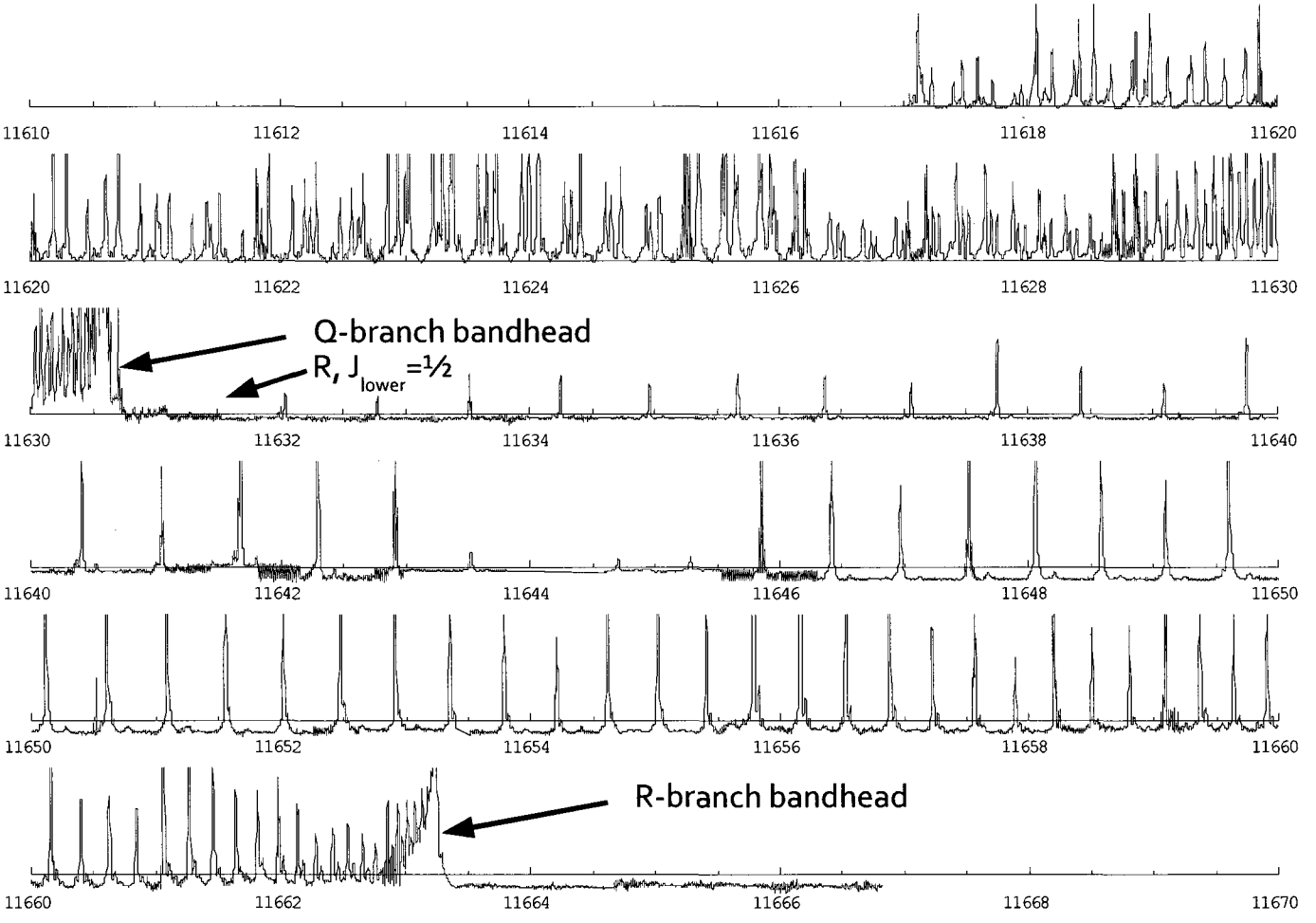

Figure 6.4: Measured absorption spectrum of the $X - A^2\Pi_{1/2}, v\,(0,0)$ band of BaF, with selected spectral features marked. The first R-branch line is the transition chosen to probe or prepare the ground state population. The vertical axis is arbitrary; the horizontal axis is in cm^{-1}.

1000K-2000K.

6.3 Absorption Spectroscopy in a Buffer Gas

Laser ablation is often a finicky process; some materials produce an unusually large or small number of molecules when ablated. Spectroscopy in a buffer gas was primarily used to study the properties of ablation targets; the high background gas density slowed the motion of the molecules in the ablation plume so that we could measure the ablation yield of the target under various conditions. In order to evaluate the suitability of target materials, room temperature buffer gas spectroscopy was performed to measure the number of molecules ablated per shot of the pulsed YAG laser. For this purpose, the same optical setup was used as in the previous section (figure 6.3), with the detection beam positioned over the target. In addition, the vacuum chamber was backfilled with about 1 to 10 milliTorr of argon+SF_6 gas by throttling the pumpdown of the vacuum chamber and triggering the pulsed valve in the system to open until the pressure gauges read the desired level. Models[71] suggest that under these conditions, the ablated material will come into thermal equilibrium with the buffer gas and form a plume about 1 cm in diameter at a distance of 1 cm above the target surface.

The total number of molecules produced in the process of laser ablation can be found by measuring the peak absorption through this point and making some simple assumptions about the geometry involved. The absorption A through the cloud is [71]

$$A = 1 - \frac{I}{I_0} = nl\sigma_{\text{abs}} f \tag{6.1}$$

where I/I_0 is the ratio of transmitted to incident light, n is the average number density of molecules in the detection volume, l is the length over which the

detection laser beam interacts with the molecules, σ_{abs} is the absorption cross-section, and f is the fraction of molecules are in the state to which the laser is tuned. The cross-section σ_{abs} depends on the transition being used to make the measurement; f depends only on the initial state in the transition.

The value of f depends on the multiplicity of states and the Boltzmann factor [11]:

$$f(N,J,T) = \frac{(2J+1)\, e^{-\frac{\omega_e}{2k_BT}} e^{-\frac{E(N,J)}{k_BT}}}{\sum_{v=0}^{\infty} e^{-\frac{\omega_e(v+1/2)}{k_BT}} \sum_{M=0}^{\infty} \left((2M)\, e^{-\frac{E\left(M,M-\frac{1}{2}\right)}{k_BT}} + (2M+2)\, e^{-\frac{E\left(M,M+\frac{1}{2}\right)}{k_BT}} \right)} \tag{6.2}$$

where $E(N,J) \approx BN(N+1) + \frac{\gamma}{2}\text{sign}(J-N)\,N$ is the rotational part of the energy of the state with quantum numbers N and J, and the initial state is taken to have vibrational quantun number $v = 0$.

The cross-section σ_{abs} is the ratio of the transition rate W_{eg} between the excited and ground states to the incident photon flux Φ [72]:

$$\sigma_{\text{abs}} = \frac{W_{eg}}{\Phi} \tag{6.3}$$

where (eq. 3.138 in [72])

$$W_{eg} = \frac{\varepsilon_0^2}{\gamma_{\text{tot}}\hbar^2} \frac{|\langle g, J \,\|d\|\, e, J'\rangle|^2}{(2J+1)(2J'+1)} \sum_{m_J, m_{J'}} |\langle J, m_J\ 1, 0|\ J', m_{J'}\rangle|^2 \tag{6.4}$$

with electric field amplitude ε_0 and total linewidth γ_{tot}. The sum over the Clebsch-Gordan coefficients is

$$\sum_{m_J, m_{J'}} |\langle J, m_J\ 1, 0|\ J', m_{J'}\rangle|^2 = \frac{(2J'+1)}{3}$$

(eq. 3.139 in [72]), and the reduced matrix element for the dipole moment is

$$|\langle g, J \| d \| e, J' \rangle|^2 = \frac{3}{4} (2J' + 1) \hbar \gamma_p \frac{c^3}{\omega_0^3}$$

(eq. 3.143 in [72], γ_p is the partial linewidth of the transition); so

$$W_{eg} = \frac{\varepsilon_0^2}{\gamma_{\text{tot}} \hbar^2} \frac{3}{4} (2J' + 1) \hbar \gamma_p \frac{c^3}{\omega_0^3} \frac{1}{(2J + 1)(2J' + 1)} \frac{(2J' + 1)}{3} \tag{6.5}$$

$$= \frac{\varepsilon_0^2}{4\hbar} \frac{\gamma_p}{\gamma_{\text{tot}}} \frac{c^3}{\omega_0^3} \frac{2J' + 1}{2J + 1} \tag{6.6}$$

The photon flux Φ is

$$\Phi = \frac{\varepsilon_0^2}{8\pi\hbar} \frac{c}{\omega_0} \tag{6.7}$$

so

$$\sigma_{\text{abs}} = 2\pi \frac{c^2}{\omega_0^2} \frac{2J' + 1}{2J + 1} \frac{\gamma_p}{\gamma_{\text{tot}}} \tag{6.8}$$

$$= \frac{\lambda^2}{2\pi} \frac{2J' + 1}{2J + 1} \frac{\gamma_p}{\gamma_{\text{tot}}} \tag{6.9}$$

The total linewidth of the transition is the sum (in quadrature) of the natural linewidth and Doppler broadening. γ_{tot} is defined as the FWHM (in radians/sec) of the absorption line with a Gaussian half-width Γ:

$$\frac{1}{2} = \exp\left(-\frac{\gamma_{\text{tot}}}{2\Gamma}\right) \tag{6.10}$$

For our absorption measurements, the dominiant contribution to Γ comes from Doppler broadening [72]:

$$\Gamma_{\text{Doppler}} = \frac{2\pi}{\lambda} \sqrt{\frac{2k_B T}{m}} \tag{6.11}$$

So, γ_{tot} is

$$\gamma_{\rm tot} = \frac{2\pi}{\lambda}\sqrt{\frac{8k_BT\log 2}{m}} \tag{6.12}$$

The partial linewidth γ_p is the linewidth of the transition from the excited state to the given ground state; the partial linewidth from an excited state e to decay into the ground state g is

$$\gamma_{p,e\to g} \equiv \xi_{e\to g}\gamma \tag{6.13}$$

where γ is the natural linewidth () and $\xi_{e\to g}$ is the branching ratio. The branching ratio will be

$$\xi = F_{v(0,0)}\frac{H_{e\to g}}{\sum_i H_{e\to i}} \tag{6.14}$$

where $F_{v(0,0)}$ is the Franck-Condon factor for the X-A $v = 0$ to $v' = 0$ transition and $H_{e\to i}$ is the Hönl-London factor for the $e \to i$ transition. Herzberg [11] gives the Hönl-London factors for a transition between a Π excited state and a Σ ground state as

$$R\text{-branch}: \qquad H_{J\to J+1} = \frac{J+2}{4} \tag{6.15}$$

$$Q\text{-branch}: \qquad H_{J\to J} = \frac{2J+1}{4} \tag{6.16}$$

$$P\text{-branch}: \qquad H_{J\to J-1} = \frac{J-1}{4} \tag{6.17}$$

$$\text{Total}: \qquad \sum_{J'} H_{J\to J'} = \frac{1}{2}(2J+1) \tag{6.18}$$

With these terms, the cross-section (for an R-branch transition, $J' = J+1$, as used in our measurements) is

$$\sigma_{\rm abs} = \frac{\lambda^3}{2(2\pi)^2}\frac{2J+3}{2J+1}\frac{J+2}{2J+1}\sqrt{\frac{m}{8k_BT\log 2}}\frac{F_{v(0,0)}}{\tau} \tag{6.19}$$

The Franck-Condon factors for BaF were derived by Berg and Olsson [25][1] and, for the X-A transition, found to be 0.93 for the $v = 0 \rightarrow 0$ transition and 0.07 for the $v = 0 \rightarrow 1$ transition. The lifetime of the $A^2\Pi$ state is $\tau = 56.0 \pm 0.9$ ns [24]. The transition is at λ =860 nm, and the room temperature buffer gas is at T =300K; with these values, for $N = 7, J = {}^{15}/_{2}$,

$$\gamma_p = 6.0 \times 10^6 \frac{\text{rad}}{\text{s}} = 2\pi \cdot 0.95 \text{ MHz} \quad (6.20)$$

$$\gamma_{\text{tot}} = 2.16 \times 10^9 \frac{\text{rad}}{\text{s}} = 2\pi \cdot 344 \text{ MHz} \quad (6.21)$$

$$\sigma_{\text{abs}} = 3.6 \times 10^{-12} \text{ cm}^2 \quad (6.22)$$

$$f = 0.0070 \quad (6.23)$$

Now return to the equation relating the number density to the observed absorption signal (eq. 6.1):

$$A = 1 - \frac{I}{I_0} = nl\sigma_{\text{abs}} f$$

Since the detection laser was positioned 1 cm above the surface, assume $l \approx 1$ cm. It was observed that absorption was $A = 6\%$ at the $J = {}^{15}/_{2}$ line, so

$$n_v \approx 2 \times 10^{12}/\text{cm}^3$$

It was further assumed that the cloud of molecules fills a spherical volume of diameter $d \approx 1$ cm, with volume $V \approx 0.5$ cm^3, so that the total number of molecules N ablated per pulse (among all rotational and vibrational states) is

$$N = n_v V \approx 1 \times 10^{12} \quad (6.24)$$

[1] Berg and Olsson [25] relate the lifetime of a vibrational state τ_v to the transition frequency $\nu_{v,v'}$, Franck-Condon factor $F_{v,v'}$, and electronic transition moment R_e through the Einstein spontaneous emission coefficient

$$\frac{1}{\tau_v} = \sum_{v'} A_{v,v'} = \frac{64\pi^4}{3h} \sum_{v'} \nu^3_{v,v'} F_{v,v'} R^2_{e,v,v'}$$

A significant difference in ablation yield among the targets we tested (crystalline BaF_2, pressed powder BaF_2, or barium metal ablated in the presence of SF_6) was not observed. The only significant difference between the targets was in the amount of laser damage done to the target. As noted in the previous chapter, the laser damage quickly rendered the crystalline target unusable, but the pressed and metal targets were fine. The number of BaF molecules produced by laser ablation from these targets is similar to the amount of YbF produced by laser ablation [51], so there is no reason to believe that BaF is a poor candidate for this technique. In fact, as shown in section 6.5, the pulsed supersonic molecular beam of BaF exhibits ~70% of the flux of the Hinds group YbF beam. However, the amount of material entrained into the pulsed supersonic beam appears to be only a small fraction of the BaF produced in the buffer gas. Other techniques, such as cryogenic buffer gas sources, couple almost all of the material into the beam, and the yield will be close to the total number of molecules presented here. This will be discussed more at the end of the chapter.

6.4 Laser-induced Fluorescence Spectroscopy

The main advantage of laser-induced fluorescence (LIF) spectroscopy is its sensitive detection of small signals. In LIF, the laser is tuned to an electronic transition and used to transversely illuminate the molecular beam. The molecules absorb light, and reemit photons isotropically through spontaneous emission. Some amount of this light is collected and detected, usually using a photomultiplier tube. Depending on the size of the skimmer and the distance from the source, the observed linewidth may be limited by Doppler broadening from the transverse velocity spread of the beam, or by the natural linewidth of the transition being studied. The hardware setup was detailed in the previous chapter; measurements were made with LIF both in a field-free environment and in a

$\sim$ 100 Gauss external magnetic field. In this system, LIF spectroscopy serves the dual purposes of state preparation and detection.

The proposed parity violation experiment and the DC Stark interference experiment discussed in the next chapter involve the level crossings between an $N = 0$ and an $N = 1$ level from the X state. Our LIF measurements of the BaF beam have concentrated on the first R-branch line of the $X^2\Sigma$-$A^2\Pi_{1/2}$ ($v = 0, 0$) transition, with $N = 0$ ($J = 1/2$) in the ground state and $J' = 3/2$ (- parity) in the excited state. This line is far from other rotational transitions, which aids in identification and use for state detection.

Most of the calculations and results from LIF which are related to spectroscopy have been presented in section 4.6. The topics which remain to be discussed cover the properties of the LIF technique:

- background from other sources of emission
- time-of-flight measurement of the LIF signal
- the relationship between detection laser power and optical pumping efficiency
- statistical variation of the LIF signal

6.4.1 Beam Forward Velocity

The LIF signal is digitized using a multichannel scaler, and so it is practical to look at the time at which molecules in the molecular beam arrive at the detector regions (figure 6.5). The timing of the laser ablation relative to the argon expansion has a distinct effect on these time-of-flight signals. In general, the electrical signal to open the valve should precede the laser ablation by about 250-350 μs to entrain the ablated material into the gas flow. However, the mean velocity of the molecular beam appears to depend on the exact time at which

ablation occurs. By changing the timing, either a "fast" or a "slow" velocity distribution can be chosen. In this case, the "fast" peak has a velocity of v=625 m/s, and the "slow" peak is v=500 m/s. The magnitude of the LIF signal does not appear to depend on which velocity we choose; we consistently choose to set the timing for the "fast" peak.

By fitting the time-of-flight signal to a sum of two Gaussians and using equation 5.3

$$T_{tr} \approx \frac{m\,\bar{v}^2\sigma^2}{2\,k_B t_{1,2}^2}$$

we can find a translational temperature T_{tr} for the molecular beam. The fit parameters, for $T_{Q\text{-}S}$-T_{valve}=305 μs in figure 6.5b, are

$$S = S_1 e^{-\left(\frac{t-t_1}{\sigma_1}\right)^2} + S_2 e^{-\left(\frac{t-t_2}{\sigma_2}\right)^2} + c$$

S_1	t_1	σ_1	S_2	t_2	σ_2	c
400 ± 2	959.6 ± 0.6	144 ± 1	462 ± 3	1213.4 ± 0.3	62.4 ± 0.5	392.7 ± 0.5

from which we find T_{tr}=84 K for the "fast" peak, and T_{tr}=6 K for the "slow" peak. It may be of interest in the future to look at other beam properties, e.g. rotational temperature, optical pumping efficiency, etc. when the timing is set for the "slow" peak, since in principle a slower beam gives better sensitivity to the PNC effect.

6.4.2 Rotational Temperature

The LIF signal was measured at higher rotational lines in the R branch (figure 6.6), with lower-state rotational numbers N=0, 2, 7, 11 and 15, without an external magnetic field. The main feature visible (for N>0) is the hyperfine interaction, which gives two spectral lines for ^{138}BaF separated by about 35 MHz (1.2×10^{-3} cm^{-1}). A fit to two Lorentzian components gives coefficients

for the heights, widths, and positions of the lines. [2] The peak heights are used to estimate the rotational temperature (figure 6.7), on the presumption that the peak height is proportional to the population of level N in the Boltzmann distribution:

$$p(N) \propto (2N+1)e^{-E_N/(kT_{\rm rot})}$$

where E_N is the energy of the state with ground state rotational quantum number N, $T_{\rm rot}$ is the rotational temperature, and $(2N+1)$ is the multiplicity of degenerate states. As discussed in chapter 4, the sensitivity of this technique is limited by the choices made for N. Based on the available data, $T_{\rm rot} = 30 \pm 12$ K in the beam.

6.4.3 Repetition Rate

To improve signal rates for the PNC measurement, it is desirable to operate at the highest possible repetition rate of the molecular beam. However, increasing the repetition rate can decrease the amount of LIF observed per pulse if the background pressure in the vacuum system rises enough to shorten the mean free path of the molecular beam, or if the target has a finite recovery time after an ablation pulse for any reason. Figure 6.8 shows the observed LIF signal at repetition rates of 10, 25, 33, and 50 Hz in both the state preparation and state detection regions (using the single-photon transition for detection). Operation at 25 Hz does not limit performance, though operation at higher rates is degraded. A similar measurement of the effect of repetition rate on LIF signal size was shown in figure 5.21 as a means of evaluating the performance of the vacuum system.

[2] For $N<15$, the predicted transition frequencies (given by the polynomial formulas in section 4.3) are consistent with the measured values to within the precision of the wavemeter (0.03 $\rm cm^{-1}$). The calculated values overestimate the transition frequency at high J.

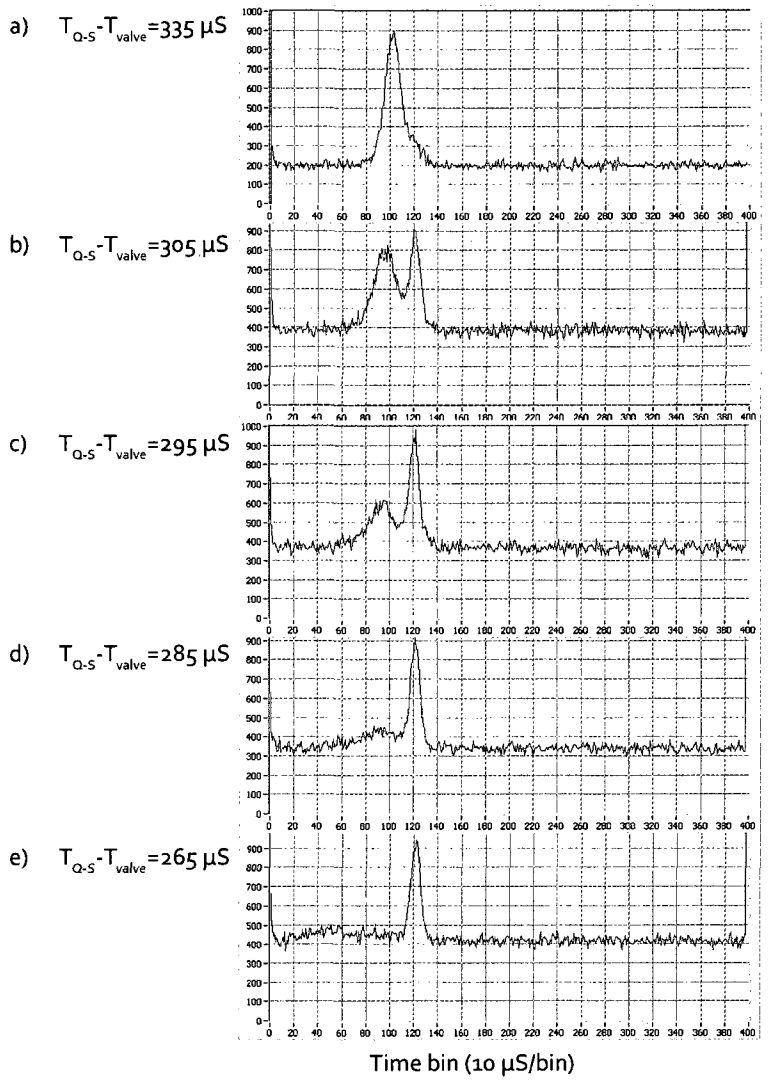

Figure 6.5: The shape of the time-of-flight signal during LIF spectroscopy depends on the time at which the laser ablation injects material in to the argon gas expansion. The early and late peaks are separated by 300 μs; but the time between the ablation laser and the gas pulse has changed by only 70 μs. In normal operation, we set the timing to optimize the earlier peak. The two peaks correspond to velocities of 640 and 500 m/s. The measurement in part a) was integrated for less time than the other measurements; the observed background is smaller as a result.

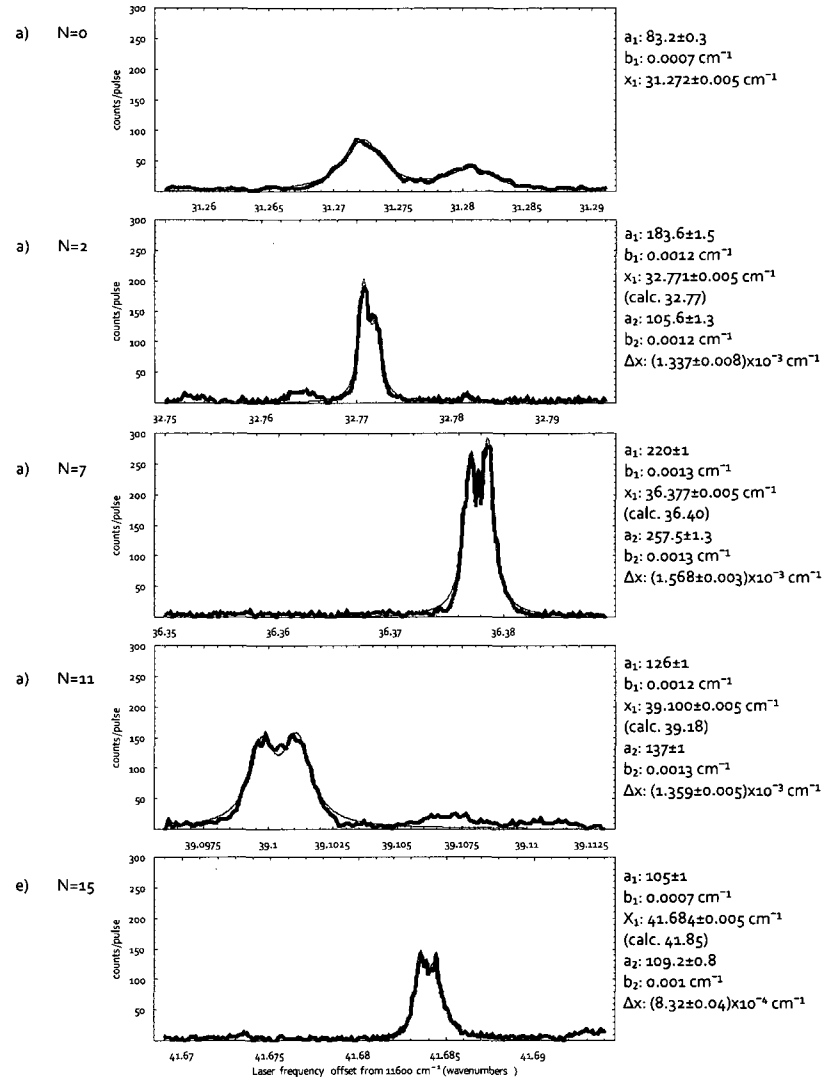

Figure 6.6: LIF signals from several different rotational lines. Higher rotational lines are still highly populated (selected measurements on R-branch transitions up to $N = 15$ are shown). The primary feature visible in the field-free spectra is the effect of the hyperfine interaction. The fit shown is to the two-line profile $s(\nu) = \frac{s_1}{1+(\gamma_1/2)^{-2}(\nu-\nu_1)^2} + \frac{s_2}{1+(\gamma_2/2)^{-2}(\nu-\nu_1-\Delta\nu)^2}$ so that the heights and separation of the two peaks are resolved. The calculated line positions given are from the simplest calculation of the energy levels (section 4.3), which allows unambiguous assignment of the quantum numbers relevant to each observed line. The relative rotational population p(N) is inferred from the fitted peak heights from these data.

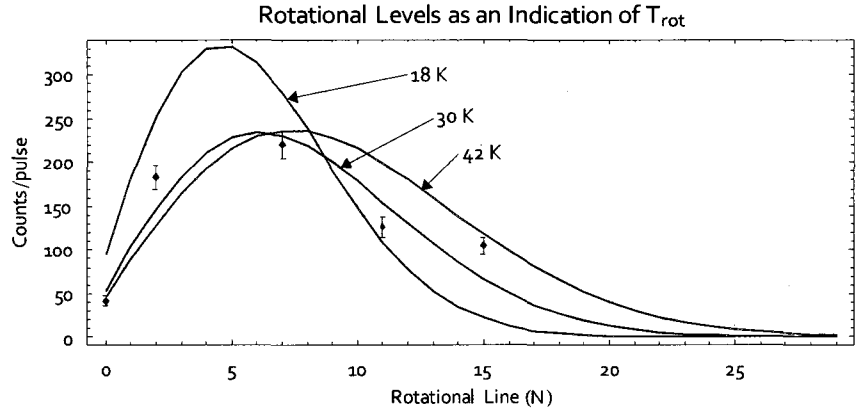

Figure 6.7: The measured heights of the rotational lines from figure 6.6 are used to estimate the rotational temperature T_{rot} of the molecular beam. The number of counts is considered to be proportional to the ground state population $p(N) \propto (2J+1)e^{-E_n/kT_{rot}}$. However, as mentioned in chapter 4, these measurements do not extend to large enough N to be highly sensitive to T_{rot}; the fit from this plot gives $T_{rot} = 30 \pm 12$ Kelvin.

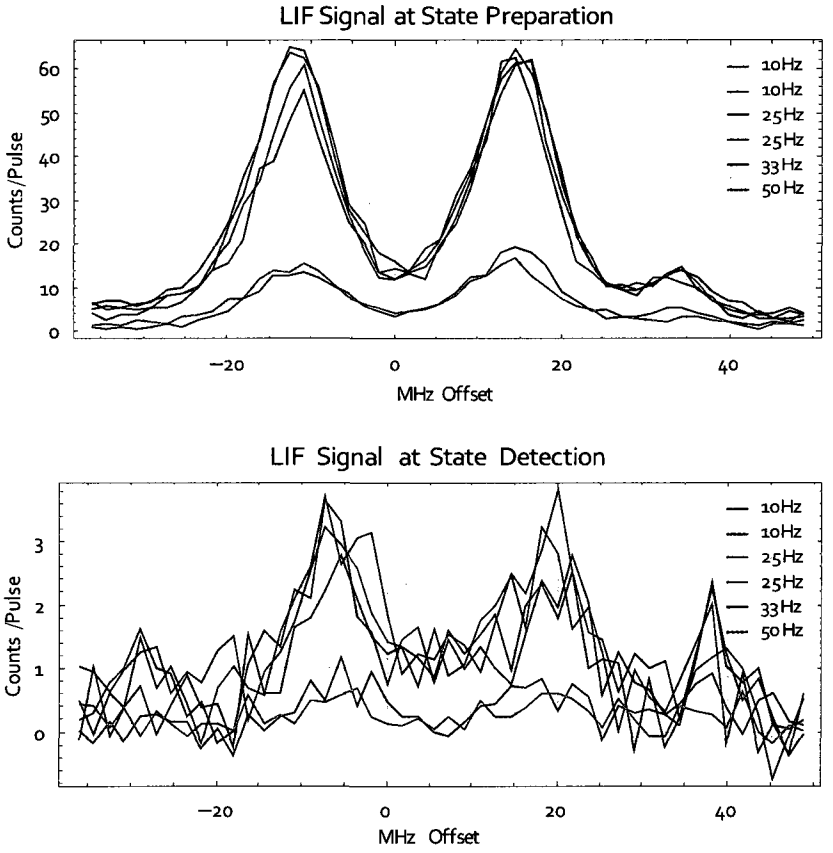

Figure 6.8: The signal intensity may diminish if the repetition rate of the beam source is too high. The LIF signal in the state preparation and state detection regions (1-photon transition) are compared to see what rate can be sustained. Rates up to 25 Hz do not appear to reduce the peak height in either region; however, measurements above 33 Hz show decreased signal sizes. It is peculiar that the signal size declines so dramatically for the 33 Hz and 50 Hz measurements; it may be useful to repeat this measurement.

6.4.4 Time Stability

The time stability of the fluorescence signal was also investigated. Over short timescales, the uncertainty in our measurement of the signal will be dominated by Poisson statistics (number of photons detected by the photomultiplier tube). Integrating over longer times T should improve the measurement $\propto 1/\sqrt{T}$. However, other experimental issues can cause long-term drift; this will not necessarily average out over repeated observations. If lock-in type detection is used (synchronously switching experimental conditions, such as optical pumping to deplete the initial state, or the applied electric field), it is desirable to do so at time scales faster than those associated with drift.

To quantitatively determine this time scale, it is useful to measure the Allen deviation of the LIF signal. The Allan deviation $\sigma(\tau)$ is a measure of the variation of the signal over various timescales, defined as

$$\sigma(\tau) \equiv \sqrt{\frac{1}{2(L-2)}\sum_i (x_{i+1} - x_i)^2}$$

where x_i is the mean of the data points taken from time $(i-1)\tau$ to $i\tau$ and L is the number of blocks of data (total time $T = L\tau$). The measured Allan deviation of the LIF signal is shown in figure 6.10. The time dependence of the Allan deviation gives us some information about the statistical distribution of our measurements and indicates the time scales over which averaging without lock-in modulation continues to increase the sensitivity. The integrated net signal from LIF per unit time (figure 6.9) is

$$\dot{N}_s = \dot{N} - \dot{N}_b$$

where $\dot{N}$ is the number of photons detected (per unit time) as the molecular beam goes through the detector, $\dot{N}_b$ is the number of background counts in a

similar time interval (eg. due to scattered light), and $\dot{N}_s$ is the number of counts due to molecules (net difference). If $\dot{N}_s$ and $\dot{N}_b$ are purely Poisson processes, then, integrated over a time τ, a total number of counts $N = \left(\dot{N}_s + \dot{N}_b\right)\tau$ and background counts $N_b = \dot{N}_b\tau$ are measured, with uncertainties $\sigma_N = \sqrt{N}$ and $\sigma_b = \sqrt{N_b/w}$. The uncertainty in the average net signal per shot is

$$\sigma_s(\tau) = \frac{\sqrt{\sigma_N^2 + \sigma_b^2}}{\tau} = \frac{\sqrt{N + N_b/w}}{\tau} = \frac{\sqrt{N_s + (1 + 1/w)\, N_b}}{\sqrt{\tau}}$$

Suppose, however, that N in fact drifts about some initial value $\bar{N}$ (random walk) with step size δ, possibly because of changes in the source intensity or laser frequency.[3] Any given measurement of N will exhibit the same Poisson statistics, but there is now an additional source of fluctuations $\sigma_r = \sqrt{2\delta^2\tau}\tau$:

$$\begin{aligned}
\sigma_s(\tau) &= \frac{\sqrt{\sigma_N^2 + \sigma_b^2 + \sigma_r^2}}{\tau} \\
&= \frac{\sqrt{N + N_b + 2\delta\tau^3}}{\tau} \\
&= \frac{\sqrt{\dot{N}_S + (1 + 1/w)\,\dot{N}_b + 2\delta^2\tau^2}}{\sqrt{\tau}}
\end{aligned} \tag{6.25}$$

The random walk will limit the improvement in uncertainty possible by averaging over longer timescales. For the single-photon data recorded in the state detection region at beam repetition rate $R = 10$ Hz (figure 6.10), $\dot{N}_s$=50 counts/second (5.0 counts/pulse) was observed, with a background rate of 6.8

[3] After a random walk of n steps, the probability of being k steps away from the starting position is the same as the binomial distribution, with $p = 0.5$ and $(n + k)/2$ successes:

$$P(k) = 2^{-n}\begin{pmatrix} n \\ \frac{n+k}{2} \end{pmatrix}$$

The expected value of k is $\langle k\rangle = \sum_k k\,P(k) = 0$ and $\langle k^2\rangle$ asymptotically approaches $2n$ for $n \gg 1$. So, the variance between two sets of data points increases with the number of steps taken:

$$\sigma^2 = 2n\delta^2$$

where δ is the size of each step taken.

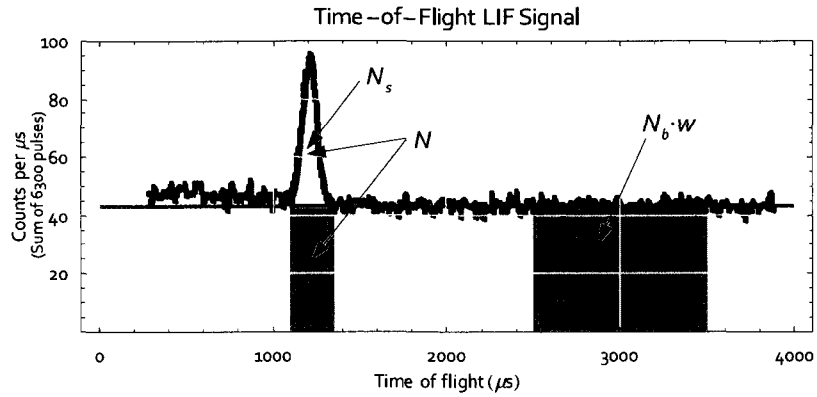

Figure 6.9: The time-of-flight signal shows a net excess of scattered photons synchronous with the passage of the molecular beam through the detector. The net signal per unit time $\dot{N}_s$ is the difference between the number of counts per unit time $\dot{N}$ in the temporal region of interest, and the number of background counts $\dot{N}_b$ in the same region. $\dot{N}_b$ is determined by looking at a background region; this region can be chosen to be longer than the region of interest to improve the determination of $\dot{N}_b$. If the background region is w times longer than the region of interest, then $\dot{N}_b \cdot w$ counts are measured, and the uncertainty σ_b in the number of background counts is given by $\sigma_b = \sqrt{\dot{N}_b/w}$. The width w is limited by fluctuations in the laser power or other noise that affects the scatter rate, and by the maximum time in the recorded time-of-flight data. Typically, $w \approx 3$ was used.

kHz ($\dot{N} + \dot{N}_b$=187 counts per second, integrating over a 400 μs region). The data for $\sigma_s(\tau)$ agrees reasonably with the functional dependence of eqn. 6.25, with the extracted value of the parameter δ being δ=9.8 $\times$ 10^{-3} counts/second. From inspection of the Allan deviation plot (figure 6.10), we see that the noise is dominated by Poisson statistics in the signal + background (i.e., is not contaminated by the "extra" noise term due to δ) as long as the signal is modulated at periods shorter than 10 seconds. The measurements made based on this modulated signal can then be combined to improve the statistical uncertainty.

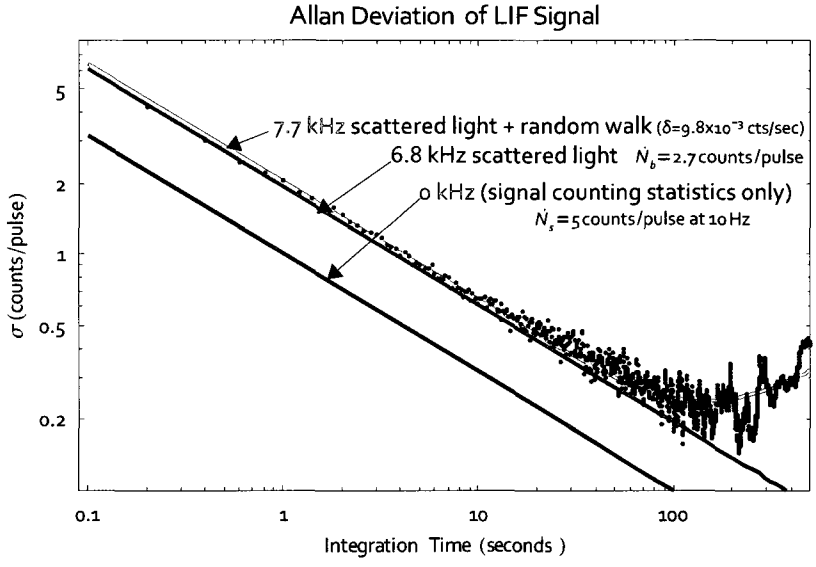

Figure 6.10: Allan deviation of the LIF signal (single-photon measurement in the state detection region). The deviation from linearity beyond τ =50 seconds is due to drift in the experimental apparatus; the statistics of a "random walk" do not improve with additional averaging time (total time measured was 8000 seconds).

6.4.5 Optical Pumping and State Preparation Efficiency

The size and intensity of the laser beam used for LIF need to be sufficient to bring population from the X state to the A state for optical pumping and detection. The spontaneous emission lifetime of the A state is about $\tau = 46$ ns. To perform optical pumping efficiently, both τ and the inverse of the Rabi frequency Ω (the rate at which stimulated emission and absorption transfer population between the X and A states) must be short compared to the time T spent interacting with the laser beam. Then, spontaneous emission from the A state will give an observable photon (and deplete the specific X state sublevel that was excited, transferring its population to some other X state subelevel). To deplete the X state sublevel to a population fraction ϵ, the interaction time with the detection laser beam must exceed $-2\tau \log_2(1-\epsilon)$. This places a requirement on the minimum diameter of the laser beam. At a molecular beam velocity of $v = 600$ m/s, this corresponds to a minimum diameter for the laser beam of 0.4 mm for $\epsilon = 0.99$ or 0.6 mm for $\epsilon = 0.999$. The necessary amount of laser power is determined by the Rabi frequency

$$\Omega = \sqrt{\left|\frac{1}{\hbar}\vec{d}_0 \cdot \vec{E}\right|^2 + \Delta^2}$$

which depends on the strength of the applied electric field $\vec{E}$ (a function of the laser intensity $I = \frac{cn\epsilon_0}{2}\left|\vec{E}\right|^2$, or $\left|\vec{E}\right|/\sqrt{I} = 0.2745\frac{\mathrm{V/cm}}{\sqrt{\mathrm{W/m^2}}}$, where the index of refraction $n = 1$), the dipole moment d_0, and the detuning of the laser from the transition (Δ). For $d_0 \approx 3$ Debye and with the laser tuned to the resonance

($\Delta = 0$), Ω is

$$\begin{aligned}\Omega &= 4.12 \times 10^5 \sqrt{\frac{I}{\mathrm{W/m^2}}}\ \mathrm{rad/s} \\ &= 2\pi \cdot 6.6 \times 10^4 \sqrt{\frac{I}{\mathrm{W/m^2}}}\ \mathrm{Hz}\end{aligned}$$

The LIF laser beam has a Gaussian profile with a $1/e$ intensity radius of $b = 1.6$ mm (described by $I = \frac{P_0}{b^2\pi} e^{-\left(\frac{z^2+y^2}{b^2}\right)}$). The total number of Rabi oscillations felt by a molecule traveling towards $+\hat{z}$ at an offset y from the z axis at velocity v is

$$N_{osc} = \int_{-\infty}^{\infty} \frac{\Omega(z)}{v}\, dz = 970 \cdot e^{-\frac{y^2}{2b^2}} \sqrt{P_0}\ (\text{in W})$$

Figure 6.11 shows the number of Rabi cycles undergone by a molecule for a 1-photon transition, under conditions typical of our experimental apparatus (detection laser power $I_0 = 1$ mW, b=1.6 mm, $v = 600$ m/s). N_{osc} scales slowly ($\propto \sqrt{I_0}$) with the total amount of power in the detection laser. If there are three possible decay paths out of the excited state ($\Delta J = \pm 1, 0$), then the remaining population in the X state sublevel will decrease like

$$\begin{aligned}P_X &= \frac{1}{3^{N_{osc}}} \\ &\equiv 1 - \eta\end{aligned}$$

with each cycle, where we have defined η as the optical pumping efficiency. The diameter of the molecular beam that is effectively depleted (where $P_X < 1\%$ and $N_{osc} \gtrsim 4$) is about 6 mm. If the state preparation and detection regions are not properly aligned, molecules may be detected in the latter (after the magnet) without having the ground state depleted in the former (before the magnet). This is one possible source of poor optical pumping ratios. One solution is to increase the diameter of the detection laser beam in the state preparation region.

The downside to this is that large beams lead to a high background rate when counting photons from spontaneous emission.

The population in the state detection region was observed to depend on the intensity of the probe laser used in the state preparation region, as shown in figure 6.12. Even with a large amount of laser power, the optical pumping does not improve quickly. In practice, we tend to find $1 - \eta$ =16-20% of the population remaining in the ground state in the detection region, even with the highest optical pumping power available. There are a few possible problems:

- Metastable states can decay and repopulate the ground state. Fluorescence from such states was observed, and rough estimates suggested that it could make up ~5% of the LIF signal. Given the large uncertainties in this estimate, it seems conceivable that this process is responsible for nearly all of the residual population seen in the detection region.

- The transition used to probe the state overlaps with another transition (eg. as in figure 4.18). The $m_F = 0$ and $m_F = 1$ transitions are close in energy, separated by less than 30 MHz. This is more relevant for the two-photon transition scheme outlined in section 4.6.1, as the $D^2\Sigma$ and $X^2\Sigma$ states have similar structure and the transitions used to address different sublevels in the X state are closer together than the A-X transition discussed here. In chapter 4, we estimated that the overlap could contribute between 2% and 7% to the LIF signal for the X-A-D transition, but it should be negligible for the A-X measurements. This therefore seems unlikely, since we observe a similar amount of optical pumping with both the single- and two-photon detection schemes. If this is a problem, eliminating this effect would require depopulating ground state sublevels near the state of interest.

- The probe laser beam is insufficiently large to cover enough of the molec-

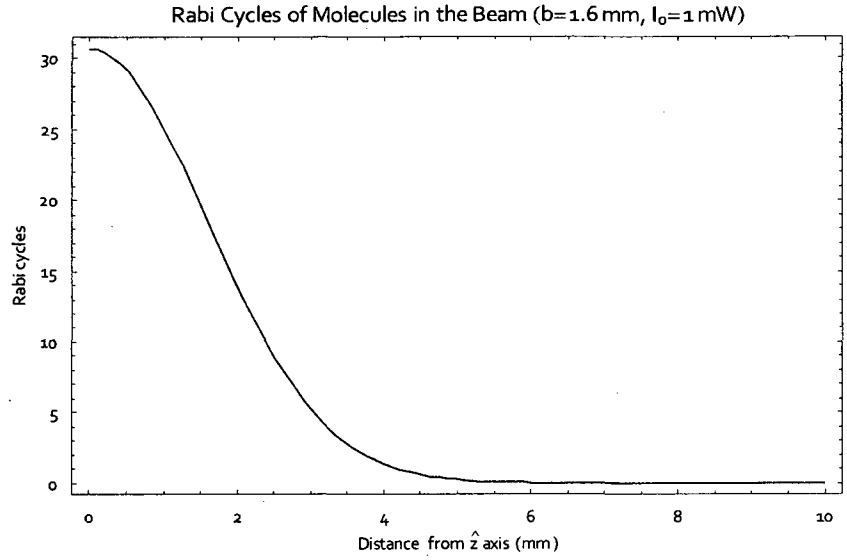

Figure 6.11: The number of Rabi cycles N_{osc} felt by molecules crossing the detection laser beam scales with the intensity of the beam as $\sqrt{I_0}$, and depends on whether the molecules pass through the center of the beam. If $N_{osc} \gg 1$, the detection laser will mix the ground and excited states, and spontaneous emission will deplete the ground state. The maximum radius for which e.g. $N_{osc} \geq 10$ is $y_{10} = b\sqrt{\frac{1940}{10}\sqrt{P_0/\text{Watts}}}$.

ular beam. This seems unlikely, as adjustment of the probe laser size and position has not been useful in fixing the problem. The molecular beam also diverges as it moves downstream, and so the area depleted by the laser will be larger by the time the beam reaches the state detection region.

6.4.6 Observations Related to Imperfect Optical Pumping

In this experiment, BaF molecules are detected by exciting an optical transition and observing laser-induced fluorescence. The PMTs used as detectors in the state preparation and detection regions are sensitive to the spontaneously emitted photon. This technique, laser-induced fluorescence, is used to optically

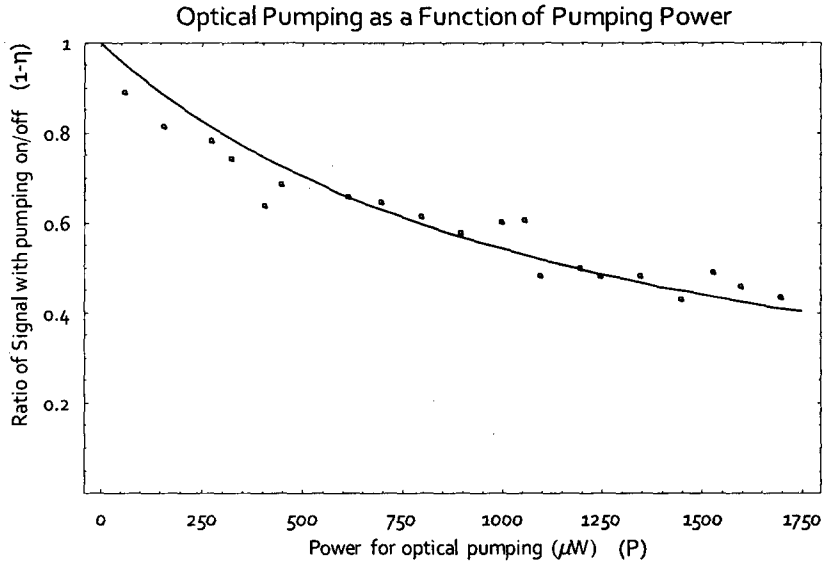

Figure 6.12: Effectiveness of optical pumping for the single-photon transition, as a function of the laser intensity used for optical pumping. The data is fit to the empirically chosen form $\frac{S_{on}}{S_{off}} \equiv 1-\eta = \frac{1}{1+P/P_{sat}}$ where $P_{sat} = 1.18 \pm 0.06$ mW. An alternate parameterization $\frac{1-S_{min}}{1+P/P_{sat}} + S_{min}$ which does not enforce the condition that $\frac{S_{on}}{S_{off}} \to 0$ as $x \to \infty$ has $P_{sat} = 620 \pm 120$ μW and $S_{min} = 0.26 \pm 0.05$.

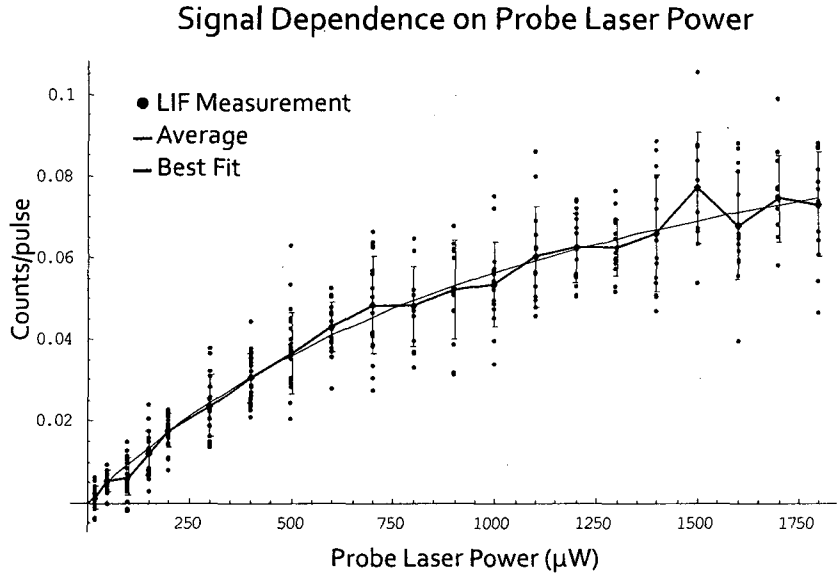

Figure 6.13: The number of counts per pulse that are measured in the state detection region (single photon transition) depends on the intensity of light. A fit to the form $C\frac{P}{P_{sat}+P}$ gives $C = 0.127 \pm 0.006$ and $P_{sat} = 1250 \pm 120$ μW. Higher probe laser intensities give diminishing returns, and increase statistical uncertainty due to scattered light.

pump out of one of the states, and to detect population transfer back into this state. Despite our best efforts to deplete the state, at most 85% of the molecules are pumped out of the state. This means that at least one of the following conditions is true:

- The ground state is not being depleted effectively.
- There are long-lived metastable excited states that can decay and repopulate the ground state.

The first condition was addressed during the discussion of optical pumping in section 6.4.5. Detection is time-resolved to measure the time-of-flight of the molecular beam. Some amount of fluorescence was observed to be is correlated with the passage of BaF molecules through the state preparation region, even when the pump laser is off (part a of figure 6.14). This effect is small compared to the LIF signal (typically 1/50 of the number of counts), but supports the hypothesis that metastable states can repopulate the ground state. This observation of spontaneous emission suggests that there is a large population of molecules in a long-lived excited state with sufficient energy to emit a near-infrared photon. Decay to the ground state may repopulate the sublevel after being depleted by optical pumping.

6.4.6.1 General Problem

The number of molecules decaying out of a long-lived level with an initial population P_e and exponential decay lifetime τ, in the time interval between t and $t + \Delta t$ (where $t = 0$ is the time of initial population of the level) is

$$S_d = P_e\, e^{-t/\tau} - P_e\, e^{-(t+\Delta t)/\tau}$$

Consider what this means for detecting the decay of such long-lived molecules in the state preparation region, where $t = d/v \approx 1.6 \times 10^{-3}$ seconds (the state preparation region is d=1 meter from the source, and v=600 m/s is the BaF beam forward velocity) and $\Delta t = 10^{-5}$ seconds is the time required to fly through the detection region (0.6 cm sensitive region in detector). The signal size is therefore highly sensitive to the state lifetime. If τ is too long, the spontaneous emission rate will be too low to create a large signal; but if τ is too short, the population is depleted by the time the molecular beam reaches the detector. Given this detector geometry, a lifetime on the order of τ=1-20 ms will produce the largest fluorescence signal (part (a) of figure 6.16), with a peak at 0.24% of the initial population at $\tau \approx 1.5$ ms.

Now, consider the connection between the fluorescence observed and the extent to which the ground state is repopulated between the state preparation and detection regions. The same formula is applicable to calculating the repopulation of the ground state due to decay out of the long-lived state between the state preparation region (where the ground state is depopulated) and the downstream detection regions. The variables are (see also figure 6.15):

- The detector geometry is determined by t_1 (the time at which the molecular beam passes through the first detector), t_2 (the time at which the molecular beam passes through the second detector), and Δt (time for the molecular beam to pass through the detector). Here, $t_1 \approx 1$ ms (60 cm at 600 m/s), $t_2 \approx 5$ ms (3 meters at 600 m/s), and $\Delta t \approx 10^{-5}$ s (6 mm).

- The only parameter intrinsic to the molecule is τ, the lifetime of the excited state. The initial population of states in the beam is determined by the technique used as a beam source; P_e is defined as the total number of molecules initially in all sublevels of the excited state, and $P_{X,\mathrm{sub}}$ as the

initial population of the particular ground-state sublevel that we are probing. $P_{X,\text{new}}$ is the number of molecules that decay from the excited state into the ground-state sublevel, between the first and second detectors.

- S_d is the number of counts measured from spontaneous decay from the excited state, as the molecular beam passes through the first detector with the excitation laser off. S_X is the number of counts measured when $P_{X,\text{sub}}$ is excited by the laser and detected using LIF as the molecular beam passes through the first detector. S_d/S_X is measured to be $\sim 1/50$.

- f is the fraction of states in P_e that decay into $P_{X,\text{sub}}$. As a rough estimate, this is approximately the fraction of the population of P_e that has the same J and m_J as $P_{X,\text{sub}}$. In order to relate the decay from P_e into $P_{X,\text{sub}}$ (repopulation of the ground state) with the observed fluorescence, ee will assume that P_e is a thermal distribution with the same T_{rot} as the X state:

$$f = \frac{e^{-\frac{E_{J=1/2}}{k_B T_{\text{rot}}}}}{\sum_J (2J+1)\, e^{-\frac{E_J}{k_B T_{\text{rot}}}}}$$

  For T_{rot}=30 K, f is $\sim$1%.

The connection between the observed fluorescence and the repopulation of the ground state depends on the population distribution within the excited state. The total initial population of the excited state (P_e) is inferred to be related to the initial population of the single ground-state sublevel (P_X) by

$$P_e = P_{X,\text{sub}} \frac{S_d}{S_X} \frac{1}{e^{t_1/\tau}\left(1 - e^{-\Delta t/\tau}\right)}$$

(This neglects changes in the QE of the photomultiplier tube; but, these changes are minimal for the PMT we are using, for wavelengths between $\approx$ 600$-$870 nm.) Using the values for this experiment, we can estimate $P_e/P_{X,\text{sub}}$ as a function

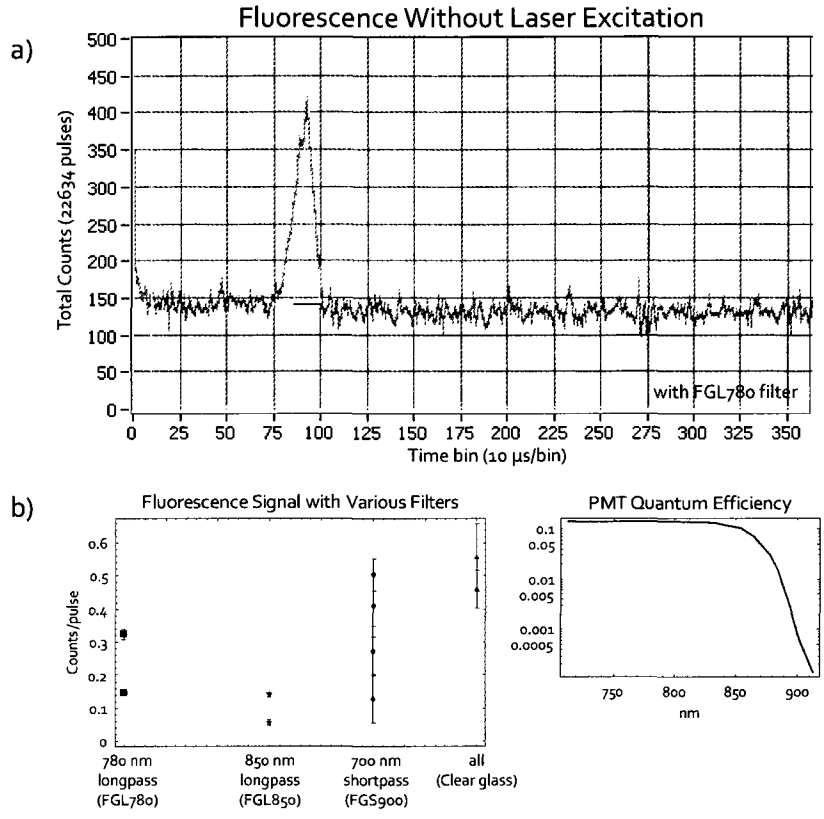

Figure 6.14: A fluorescence signal is observed in the pump region (part a), even though the laser used to excite a transition is off. This signal is about 1/50 of the amplitude of the normal LIF signal. The size of this signal is recorded using various colored glass filters (part b), to determine the wavelength of the fluorescence. The Thorlabs FGL780 and FGL850 filters are long-pass filters with cutoffs at 780 nm and 850 nm, and the FGS900 is a shortpass filter with a gradual cutoff between 700 and 900 nm. The photomultiplier tube (Hamamatsu R7400P-50) has a photocathode whose sensitivity decays rapidly at wavelengths longer than ~850 nm (plot based on specifications from manufacturer). Regardless of the filter used, the PMT is expected to have a very low sensitivity to light with wavelength longer than ~870 nm.

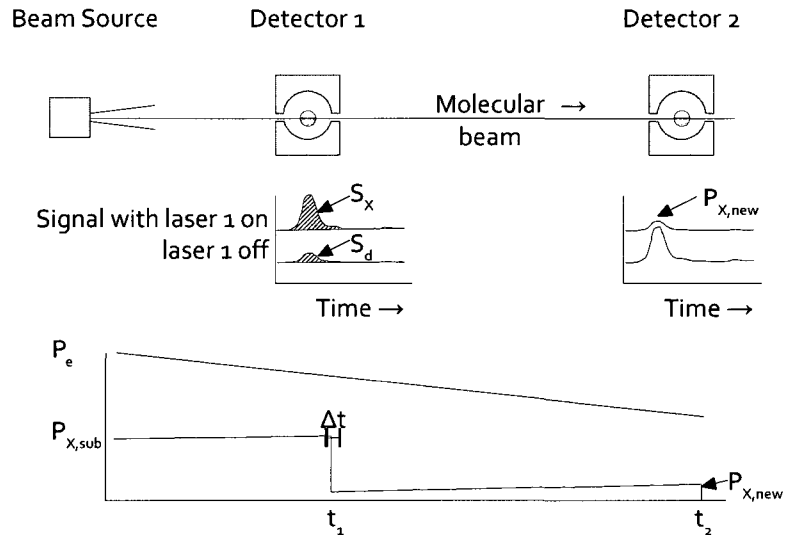

Figure 6.15: The population of the ground-state sublevel ($P_{X,\mathrm{sub}}$) is measured at two detectors along the path of the molecular beam using laser-induced fluorescence if the laser is on. The population is assumed to be completely depleted at the first detector, and the population seen at the second detector is $P_{X,\mathrm{new}}$. Without any populated metastable state, $P_{X,\mathrm{new}}$ would be 0. However, some of the decay out of a metastable state (with population P_e among all levels) can decay into $P_{X,\mathrm{sub}}$. The fraction of the decay $f \equiv \frac{P_{X,\mathrm{new}}}{P_e(t)-P_e(t_1)}$ that decays into $P_{X,\mathrm{sub}}$ is assumed to depend primarily on the population distribution among levels of P_e (eg. that if the ground state sublevel has $J = \frac{1}{2}$, then f is the fraction of P_e in a single sublevel with $J = \frac{1}{2}$).

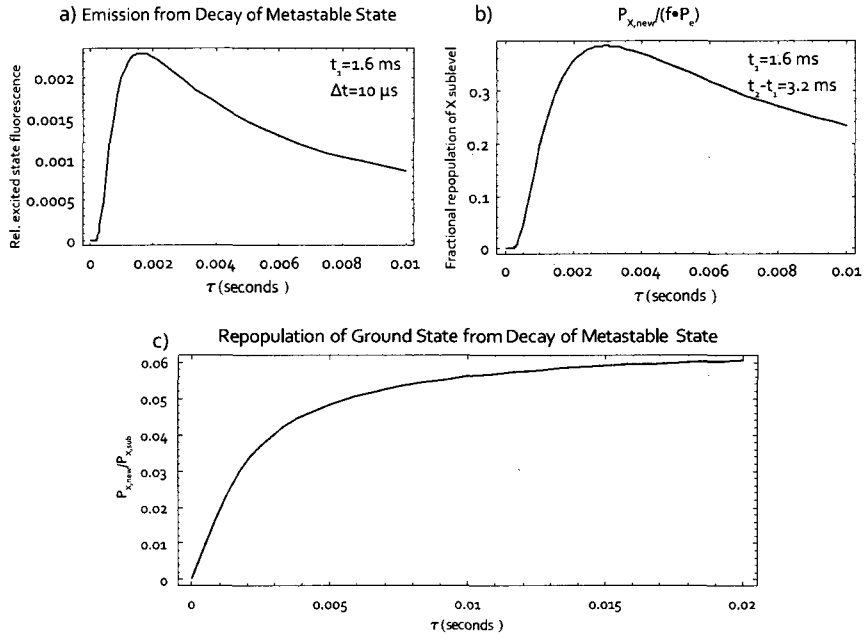

Figure 6.16: The signal from decays of a long-lived metastable state depends on the detector configuration (distance from the source and relevant transit time), and on the state lifetime. Part (a) shows how the signal from molecules decaying from the metastable state in detector 1 (state preparation region) depends on the state lifetime. This signal from spontaneous emission will be strongest if the lifetime is on the order of τ=1-20 ms. The same mechanism will also produce a significant repopulation of the ground state by the time the molecular beam reaches the state detection region; part (b) shows the population found in the ground state at detector 2 as a function of the state lifetime. Up to 40% of the initial population of the excited state may decay to the ground state between the state preparation and state detection region. Part (c) shows the repopulation of the ground state, estimated using the measured value of $S_d/S_X \approx 1/50$ (eq. 6.26), as a function of the state lifetime. The repopulation reaches a maximum value of 6% for $\tau \gtrsim 10$ ms. A practical upper limit on τ is placed by considering the implied metastable state population; a long lifetime τ suggests a high initial population of the metastable state. The lifetime of the relevant state(s) is most likely in the range of 1 ms $< \tau <$ 100 ms.

of τ. If, for example, the lifetime is about τ=8 ms, then the initial population of the excited state (summed over all rotational and vibrational levels) is about 20 times larger than the initial population of the single detected rovibrational level of X. The fraction of this population that decays and repopulates state X depends on the fraction f of the excited state population that decays to the particular sublevel X:

$$\begin{aligned} P_{X,\text{new}} &= f P_e e^{t_1/\tau}\left(1 - e^{-(t_2-t_1)/\tau}\right) \\ &= f P_{X,\text{sub}} \frac{S_d}{S_X} \frac{1 - e^{-(t_2-t_1)/\tau}}{1 - e^{-\Delta t/\tau}} \end{aligned} \tag{6.26}$$

The repopulation of the ground state, $P_{X,\text{new}}/P_{X,\text{sub}}$, does not depend on τ as long as the lifetime greatly exceeds $t_2 - t_1$. Instead, it depends on f and the observed ratio S_d/S_X. In this system, with the above values, the repopulation of the ground state sublevel ($P_{X,\text{new}}/P_{X,\text{sub}}$) is about 5-6% for any lifetime τ>5 ms (figure 6.16). In practice, we find that the optical pumping leaves at least 16% of the population remaining in the ground state at the state detection region ($1 - \eta \geq 0.16$). There is no reason to expect that this phenomena is the only plausable cause of poor optical pumping. Also, the calculations above are based on rough estimates, particularly of f. The best way to proceed is to identify specific mechanisms that could be responsible for the observed fluorescence, and to suggest ways to minimize their effect.

6.4.6.2 Specific Mechanisms

Now consider the nature of possible long-lived states in our BaF molecules that could be responsible for these effects. Laser ablation may create a molecular beam in which a substantial fraction of the molecules are initially in highly excited electronic, vibrational, and rotational states. Most of the low-lying electronic states (A, B, C, D, etc.) are known to have a short lifetime (< 50

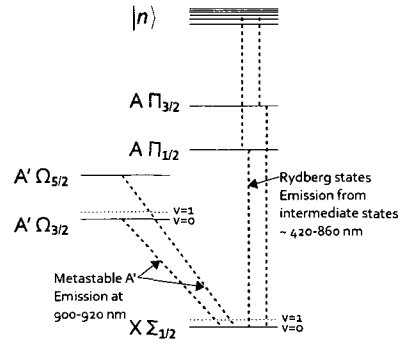

Figure 6.17: Possible mechanisms for the observation of spontaneous emission in the absence of laser excitation depend on long-lived or metastable states of BaF. E1 transitions from the A′ state are forbidden due to the selection rule $\Delta\Omega = \pm 1, 0$, so emission depends on mixing with $A^2\Pi_{3/2}$. Another possible mechanism is decay from long-lived Rydberg states. Decay from the X v=1 state will also be long-lived, but is not energetic enough to produce a near-infrared photon.

ns) and will decay to the ground state well before the molecules reach the state preparation region. A plausible candidate will have a long lifetime ($\tau \gtrapprox 5$ ms) and decay with enough energy to produce a detectable photon. A few mechanisms (fig. 6.17) can produce long-lived or metastable states:

1. Rydberg levels: Rydberg levels are states with a high effective quantum number $n^\star \equiv \sqrt{\mathrm{R}/(IP - T_0)}$ (where R = 109736.93 cm^{-1} is the Rydberg constant, and for BaF, the ionization potential is IP = 38745 cm^{-1} [73, 74]) analogous to n in the hydrogen atom. States with $n^\star$ from 4 to 14 have been reported by Jakubek et al. Data on the lifetimes of the Rydberg states is not available, but the lifetime of Rydberg states generally scales as $\tau \propto n^{3}$[4]. Based

[4]The wavefunction for high $n^\star$ keeps the electron at large distances from the nucleus, compared to the ground state. So, the dipole matrix element of the electron wavefunction with the ground state, $\langle 0, 0 \,|\mu|\, n^\star, l\rangle$, mostly depends on the portion of $|n^\star, l\rangle$ which lies close to the nucleus[75]. The normalization of the wavefunction scales as $n^{-3/2}$, so the state lifetime scales like $\tau \propto 1/\mu^2 \propto n^3$.

on the $A^2\Pi$ state (τ=46 ns, n^*=2.0), a lifetime of $\tau \gtrsim 1$ ms corresponds to $n^* \gtrsim 56$. This is much higher than the group of states documented by Jakubek. However, the large radius of Rydberg states means that the polarizability of the state increases rapidly with n^*. If this is the source of our background signals, it should be easy to eliminate. An electric field can be used to ionize any Rydberg molecules present and sweep them free of the molecular beam. However, this has not been attempted.

This hypothesis does, however, plausibly explain the observed spectrum of photons from decay. Figure 6.14 showed the signal observed through four different colored glass filters (two longpass, one shortpass, and one clear glass). The results suggest that roughly half the detected photons are between 780 and 860 nm, and the other half have a wavelength less than 780 nm. Rydberg states could decay using the excited electronic states (A, B, C, D, etc.) as intermediate states, and so we would not see emission at a single wavelength.

2. Vibrational states: Vibrationally excited states can have long lifetimes ($>$ 10 ms) in the ground electronic state, but are not energetic enough to emit a near-infrared photon. Repopulation of the ground state from the v=1 level can still lead to poor optical pumping if the vibrational temperature is hot enough to place a significant population in the v=1 level, so this cannot be a cause of the observed fluorescence but could (if the lifetime is right) contribute to repopulation of the ground state. The lifetime is calculated from the Einstein coefficient for spontaneous emission

$$\tau = \frac{1}{A} = \frac{3hc^3\epsilon_0}{16\pi^3 f^3 |\mu|^2} = \frac{3\left(6.6\times10^{-34}\frac{\text{kg}\cdot\text{m}^2}{\text{s}}\right)\left(3\times10^{8}\frac{\text{m}}{\text{s}}\right)^3\left(8.854\times10^{-12}\frac{\text{s}^4\text{A}^2}{\text{m}^3\text{kg}}\right)}{16\pi^3\left(\nu(\text{cm}^{-1})\cdot3\times10^{10}\frac{\text{cm}}{\text{s}}\right)^3|\mu|^2} \tag{6.27}$$

where the dipole matrix element $\vec{\mu}$ is the expectation value of dipole moment

$\vec{p} \cdot \vec{E}$ for the two states involved in the transition [76]:

$$\begin{aligned} &= \left| \left\langle v'l'm' \left| \vec{p} \cdot \vec{E} \right| vlm \right\rangle \right|^2 / |E|^2 \\ &= \left| \int u_{v'}(r') \left(\vec{p} \cdot \vec{E} \right) u_v(r')\, dr \cdot \int Y^*_{l'm'}(\theta, \phi) \cos\theta Y_{lm}(\theta, \phi)\, d\Omega \right|^2 \end{aligned}$$

where the vibrational wavefunction u_v and rotational wavefunctions Y_{lm} are separated. First, consider the integral over the vibrational wavefunction. The dipole moment is expanded in a Taylor series

$$\vec{p} \cdot \vec{E} = p_0 E \cos\theta + p_1 r' E \cos\theta + \ldots$$

with the first coefficient, p_0, approximately equal to the static dipole moment of the molecule, and $p_1 \equiv \frac{\partial p}{\partial r'} \approx \frac{p_0}{r_e}$. The integral over the vibrational wavefunction is

$$V \equiv \int u_{v'}(r') (p_0 + p_1 r') u_v(r')\, dr$$

The vibrational wavefunction is approximated as a simple harmonic oscillator, centered around the equilibrium intermolecular distance r_e:

$$u_v(r) \equiv \frac{1}{\sqrt{2^v v!}} \left(\frac{m\omega_e}{\pi\hbar} \right)^{1/4} e^{-\frac{m\omega_e (r-r_e)^2}{2\hbar}} H_v\left(\sqrt{\frac{m\omega_e}{\hbar}} (r - r_e) \right)$$

For a diatomic molecule, the equilibrium distance r_e can be found from the rotational constant

$$r_e = \sqrt{\frac{\hbar}{2mB_e}}$$

where $B_e = B - \alpha_e (v + 1/2)$ is the effective rotational constant, corrected for excited vibrational levels. For the X state of BaF,

B	0.215951 cm^{-1}
α_e	1.16358×10^{-3} cm^{-1}
$r_e\,(v=0)$	5.41046 Å
$r_e\,(v=1)$	5.42513 Å
$d \approx p_0$	3.14 Debye
p_1	0.58 Debye/Å

which gives the expectation values[5]

$$\begin{aligned} \langle v=1|v=0\rangle &= -0.0316 \\ \langle v=1\,|r'|\,v=0\rangle &= -0.1133 \text{ Å} \\ V &= 0.16 \text{ Debye} \end{aligned}$$

The only nonzero value of the rotational integral with $l=0$ is from the $l'=1$, $m'=0$ state:

$$\langle 1\,0\,|\cos\theta|\,0\,0\rangle = \frac{1}{\sqrt{3}}$$

so that

$$\begin{aligned} |\mu|^2 &= \sum_{m_g} |\langle e, m_e\,|\vec{r}|\,0,0\rangle|^2 = \frac{1}{3}\left(0.16 \text{ Debye} \cdot 3.336\times10^{-30}\frac{\text{C·m}}{\text{Debye}}\right)^2 \\ &= 9.5\times10^{-62}\,(\text{C·m})^2 \end{aligned}$$

[5]The vibrational wavefunctions used for this calculation are

$$\psi_v = \frac{1}{\sqrt{2^v v!}}\left(\frac{m\omega_e}{\pi\hbar}\right)^{1/4} e^{-\frac{m\omega_e}{2\hbar}(r-r_e)^2} H_v\left(\sqrt{\frac{m\omega_e}{\hbar}}\,(r-r_e)\right)$$

where v is the vibrational quantum number, m is the reduced mass, H_v is a Hermite polynomial, and r_e is the equilibrium internuclear distance (determined from B_e). These wavefunctions are nominally orthogonal, except that $B_e = B - \alpha_e\left(v+\frac{1}{2}\right)$ makes r_e a function of the vibrational level.

and

$$\tau = 3.6 \text{ seconds}$$

This is much longer than the optimal lifetime for the repopulation of the ground state, unless the population of the v=1 state is much larger than the v=0 state. The contribution to the repopulation of the ground state will be

$$\frac{P_{X,\text{new}}}{P} = \frac{e^{-\frac{\omega_e(3/2)}{k_B T_{\text{vib}}}}}{\sum_v e^{-\frac{\omega_e(v+1/2)}{k_B T_{\text{vib}}}}} e^{-t_1/\tau}\left(1 - e^{-(t_2-t_1)/\tau}\right)$$

where the initial population of the v=1 state is assumed to follow the Boltzmann distribution based on the vibrational temperature T_{vib}, and t_1 and t_2 are the arrival times at the state preparation and state detection regions. For a lifetime of τ=3.6 seconds, this suggests $P_{X,\text{new}}/P < 0.02\%$, and that this should not be a significant cause of poor optical pumping. It is possible to measure the population of the v=1 state through LIF; the v=1→1 X-A transition will be about 31.526 cm^{-1} lower in energy than the v=0→0 transition; the first R branch line should be at about 11599.75 cm^{-1}. This line will be mixed in among various P- and Q-branch lines of the v=0→0 transition, however, and may be hard to identify.

3. $A'^2\Delta$ metastable state: The $A'^2\Delta$ state lies less than 1000 cm^{-1} below the $A^2\Pi$ and $B^2\Sigma$ levels. It cannot decay directly to the ground state by an E1 transition, since $\Delta\Omega = 2$ to go from a $^2\Delta$ to a $^2\Sigma$ state. The primary mechanism for spontaneous emission will be different for the $^2\Delta_{3/2}$ and $^2\Delta_{5/2}$ levels. The $^2\Delta_{3/2}$ component is mixed with the nearby $A^2\Pi_{3/2}$ level; Bernard et al. give a value for the spin-orbit interaction responsible for the mixing:

$$\alpha_{00} = 210 \text{ cm}^{-1} \approx A = 192 \text{ cm}^{-1}$$

and with an energy difference of

$$\begin{aligned} E_{A^2\Pi_{3/2}} - E_{A'^2\Omega_{3/2}} &= (11946.4 - 632.2/2) - (10924.3 - 206.659)\ \mathrm{cm}^{-1} \\ &= 912.7\ \mathrm{cm}^{-1} \end{aligned}$$

the amplitude of the mixing of the states is

$$\eta \sim \frac{\alpha_{00}}{E_{A^2\Pi_{3/2}} - E_{A'^2\Omega_{3/2}}} = 0.23$$

and the estimate of the lifetime is

$$\begin{aligned} \tau_{A'3/2} &\sim \eta^{-2}\tau_A \\ &= 19\tau_A \\ &= 0.8\ \mu\mathrm{s} \end{aligned}$$

This is too fast to lead to the observed effect. Decay from the $^2\Delta_{5/2}$ state can be by direct E2 transitions, which are expected to be similar to the lifetime of the metastable atomic Ba^+ 5d state (32 s for the $2D_{5/2}$ level, or 89 s for $2D_{3/2}$), or by decay to the $^2\Delta_{3/2}$. The latter is estimated by using eq. 6.27, and scaling the lifetime based on the A-X transition and accounting for the spin flip needed to make a transition with $\Delta\Omega = 1$:

$$\tau_{A'5/2} \sim \frac{1}{\eta^2}\left(\frac{E_A - E_X}{E_{A'5/2} - E_{A'3/2}}\right)^3 \tau_A = 17\ \mathrm{ms}$$

This is squarely within the range of values that could create a background signal from spontaneous emission and interfere with optical pumping. However, the decay from the ground vibrational state of the A' $^2\Omega_{3/2}$ state is at ~ 930 nm, which is excluded by the glass filter data. The $v = 2$ level is close in energy

to the A $^2\Pi$ state, but it seems unlikely that it would be highly populated. Unfortunately, it is not easy to get rid of this source of background if it is indeed the root of the problem. The most obvious solution would be to transfer the $A'^2\Delta_{5/2}$ population by optical pumping to the $C^2\Pi_{3/2}$ state (9043 cm^{-1}, 1.10 μm). However, adding and maintaining an additional laser for this purpose would add significant complexity to the experiment.

Based on these considerations, population of the Rydberg states during formation of the pulsed supersonic beam is the most plausable candidate for causing the observed spontaneous emission of near-infrared fluorescence in the absence of a probe laser. If this is indeed the case, it contributes to (but may not be the sole cause of) incomplete optical pumping. As mentioned in section 3.5.3, poor optical pumping adds considerably to the statistical noise in the proposed parity violation experiment, and so proper handling of this problem will be necessary. Measurements of the optical pumping efficiency can be found in section 6.4.5.

6.5 Comparison of Beam Flux

Table 6.2 compares the performance of the molecular beam against three other reported beams of similar type. Two of these other experiments are using pulsed supersonic beams; the third is a cryogenic buffer gas source. These numbers are compiled based on the detector geometry and observed signal sizes. From these, the intensity per pulse is inferred as a detector-independent way to compare the source intensity. The procedure is as follows:

- The distance from the beam source to the detector, L, is recorded as "Distance".
- The "detected beam diameter", D, is determined by the diameter of the part of the beam that is measured at the detector. This will be the smaller

of the diameter of the probe laser, or of the molecular beam size due to apertures before the detector.

- The "fraction of fluorescence collected" f is, for LIF detection, the fraction of spontaneously emitted photons captured by the detector optics.

- The "detector efficiency" d_e is the probability that a collected photon is counted as part of the signal.

- The "repetition rate" r is the repetition rate of the beam source.

- The "counts/pulse observed", N, is the number of events seen by the detector, with the laser tuned to detect a particular sublevel. For our experiment, this refers to the X-A transition in the state detection region. The state may be different in each experiment, but in each case is a sublevel from the $N = 0$ rotational, $v = 0$ vibrational ground state.

- The "molecules/sr/pulse" I is the inferred intensity of the molecular beam in a particular sublevel, based on the above numbers. This is a detector-independent comparison of the molecular beam implementations. The intensity is calculated as

$$I = \frac{N}{f d_e} \frac{4L^2}{4\pi (D/2)^2}$$

- The "molecules/sr/sec" is $I \cdot r$, measured at what is assumed to be an optimal choice of r. Generally, a higher value for $I \cdot r$ is desirable. If the background fluctions are the dominant source of noise then the signal-to-noise ratio will improve with $\sqrt{r}$ as the pulse rate is increased, but like I as the intensity per pulse varies since background fluctuations (scattered light) are usually the same for each pulse.

- The divergence of the molecular beam is not generally measured; the detection region is far from the source and subtends a very small solid angle. Calculating the total yield of the molecular beam (over all angles) requires assumptions about the divergence of the beam; this is usually considered to be about $\pi/2$ steradian (for the supersonic sources) or 0.12 steradians (for the buffer gas source) [77]. The latter corresponds to an 11° half-angle of the source divergence. However, for the purposes of most molecular beam experiments (including this experiment) the intensity I rather than the total yield is the relevant figure of merit.

A few comments stand out:

Steimle's beam intensity per pulse is unusually low; this is probably because he uses an antechamber-based nozzle design. However, for the sort of physical chemistry experiments he performs, a flexible design is more important than one which is optimized for one species. Also, a shorter beamline compensates for the low yield.

The measured rotational temperature is unusually high for a source of this type. This is on the upper end of what we would expect, based on the calculations for temperature in a supersonic expanding jet (figure A.2). These calculations suggested cooling by a factor of $T/T_0 = 0.05 - 0.1$ before the expansion freezes out. It is warmer than Steimle's beam, and much warmer than Hinds et al. It is not clear what leads to this difference.

One of the biggest advantages of the buffer gas source is the low divergence angle of the molecular beam [77]. This gives a large number of molecules downstream, even though the source does not have a significantly higher intensity. The lower rotational temperature also contributes to the improved yield of ground-state molecules. The time distribution of molecules in the buffer gas beam is known to be longer (the pulsed beam is spread out over milliseconds) and

System	Ours (prep region)	Ours (det. region)	Hinds et al [70]	Steimle [56]	DeMille buffer gas[77]	DeMille buffer gas
Technique	supersonic	supersonic	supersonic	supersonic	cryo. buffer gas	cryo. buffer gas
Molecule	BaF	BaF	YbF	BaF	SrF	BaF
Distance (L)	0.8 m	3 m	2 m	0.4 m	0.40 m	0.025 m
Detected beam diameter (D)	1.3 cm	1 cm	1 cm	1.3 cm	0.6 cm	1 cm
Fraction of fluorescence collected (f)	0.0625	0.425	0.4	0.2	0.05	1
Detector efficiency (d_e)	0.023	0.4	0.1	0.1	50	1
Counts/pulse observed (N)	200	80	800	88	1.4×10^6	2×10^{10}
Repetition rate (r, Hz)	20	20	50	10	10	1
Molecules/sr/pulse/state	6.7×10^8	5.4×10^7	1.0×10^9	5.3×10^6	3.2×10^9	1.6×10^{11}
Molecules/sr/second/state	1.3×10^{10}	1.1×10^9	5.1×10^{10}	5.3×10^7	3.2×10^{10}	1.6×10^{11}
Temperature (T_{rot})	$\sim$ 30K	30K	3K	10 – 20K	4K	4K

Table 6.2: Comparison of beam flux for four different experiments; our molecular beam, Hinds et al, Steimle, and DeMille's buffer gas experiment. For Hinds, experimental parameters are estimated based on the description of the apparatus in published papers/posters. The DeMille cryogenic buffer gas experiment used absorption spectroscopy rather than LIF. The statistics are based on the population of a single ground-state sublevel. For our experiment, the parameters shown are for light collection with a 1/2" diameter lightguide and the counts/pulse observed reflects the population of the $N = 0$, $m_S = +\frac{1}{2}$, $m_F = 0$ sublevel of the X state.

slower ($\bar{v} \sim 200$ m/s) than the supersonic expansion. The first issue should not pose any problems for our experiment, since we do not rely on the time-of-flight data for any purpose other than background rejection (and the two-photon detection scheme can have very low backgrounds from scattered light). The slower velocity may in fact be beneficial since the PNC sensitivity scales as $1/\bar{v}$. There are other properties of the buffer gas beam which have not been studied that may be completely different from the pulsed supersonic expansion. For example, the cryogenic buffer gas technique relies on a large number of collisions between the BaF and helium atoms to cool the molecules before they leave the cell; our pulsed supersonic expansion cools the molecules through a smaller number of collisions with argon atoms. This could affect the initial population of whatever metastable state is responsible for the backgrounds described in section 6.4.6. The net result is that a cryogenic buffer gas source is a promising alternative to a pulsed supersonic beam for this experiment. While there are some differences in the beam properties, there is no clear reason to expect these to be problematic in this application.

An additional comparison to the cryogenic buffer gas experiment concerns the use of a cycling transition in SrF [78] (unrelated to the properties of the molecular beam itself). This allows for the experiment to achieve a much higher detection efficiency. A similar technique should be possible in BaF, due to the highly diagonal Franck-Condon factors that limit the rate of loss to high vibrational levels.

Chapter 7

Level Crossing Experiments

7.1 DC Stark Effect measurement

At this point, all of the parts of the experimental apparatus necessary for a measurement of parity nonconservation in diatomic molecules have been developed. As a precursor to the actual parity-violation experiment with ^{137}BaF, a measurement of the DC Stark effect using the more common ^{138}BaF isotope can be performed. This experiment has the goal of verifying the operation of the interaction region and the magnetic field uniformity necessary to bring two rotational levels close to crossing, as well as our understanding of the basic physics of our system. One level is depopulated before the magnet, and the Stark effect with a DC electric field is used in the interaction region to drive a transition between the two levels. Population transfer after the magnet is then measured. This is meant to verify:

- LIF spectroscopic detection after the magnet
- Ability to Zeeman shift two levels close to crossing (predicted field and control of magnet)

- Understanding of spectroscopic parameters related to the level crossings
- Performance of interaction region (electric field)
- Understanding of the basic physics of the system

7.1.1 Predictions for Observations

A simple model of the interaction region for the DC Stark experiment is constructed by assuming that the molecules pass through a region of varying electric field. The electric field is assumed to be $E = E_0$ for a time $0 < t < T$, and zero at all other times. The transitions between $E = 0$ and $E = E_0$ are considered to be sudden (nonadiabatic). The goal is to find the population at $t > T$, after the molecules have left the interaction region. Assume a two level system (states $|a\rangle$ and $|b\rangle$), with a Hamiltonian of the form:

$$\mathcal{H} = \begin{pmatrix} 0 & dE(t) \\ dE(t) & \Delta \end{pmatrix}$$

where Δ is the B-field dependent splitting between the two levels $|a\rangle$ and $|b\rangle$ (with no electric field present), $d \cdot E$ is the electric dipole matrix element connecting $|a\rangle$ and $|b\rangle$, and $E(t)$ is the applied electric field. The state of the system $\psi(t)$ is a linear combination of these two states, $\psi = c_a(t)|a\rangle + c_b(t)|b\rangle$. The applied magnetic field is assumed to have shifted these levels sufficiently close that no other levels need to be considered. Assuming for now that Δ is a constant, the time-dependent Schrödinger equation defines the time evolution of the state amplitudes

$$\begin{aligned} i\hbar\dot{c}_a &= dEc_b \\ i\hbar\dot{c}_b &= dEc_a + \Delta c_b \end{aligned}$$

which for $E(t) = E$ (constant) can be decoupled into two second order ODEs

$$\begin{aligned} -\hbar^2 \ddot{c_a} &= (dE)^2 c_a + i\hbar\Delta\dot{c_a} \\ -\hbar^2 \ddot{c_b} &= (dE)^2 c_b + i\hbar\Delta\dot{c_b} \end{aligned}$$

This has solutions

$$c_a(t) \rightarrow e^{\frac{i\left(-i\Delta\hbar - \sqrt{-4(dE)^2\hbar^2 - \Delta^2\hbar^2}\right)t}{2\hbar^2}} c_1 + e^{\frac{i\left(\sqrt{-4(dE)^2\hbar^2 - \Delta^2\hbar^2} - i\Delta\hbar\right)t}{2\hbar^2}} c_2$$

where c_1 and c_2 are arbitrary constants defined by the initial conditions. If the initial condition is that all population is all in state $|b\rangle$ ($c_a(0) = 0$, $c_b(0) = 1$), then the population of state $|a\rangle$ at time t is

$$P_a^{(b)}[E, \Delta] = |c_a(t)|^2 = \frac{4(dE)^2 \sin^2\left(\frac{\sqrt{4(dE)^2+\Delta^2}}{2\hbar}t\right)}{4(dE)^2 + \Delta^2}$$

and if the initial condition is that all population is in state $|a\rangle$ ($c_a(0) = 1$, $c_b(0) = 0$), then the population of state $|a\rangle$ is

$$P_a^{(a)}[E, \Delta] = |c_a(t)|^2 = \cos^2\left(\frac{\sqrt{4(dE)^2 + \Delta^2}}{2\hbar}t\right) + \frac{\Delta^2 \sin^2\left(\frac{\sqrt{4(dE)^2+\Delta^2}}{2\hbar}t\right)}{4(dE)^2 + \Delta^2}$$

for times $0 < t \leq T$. The population in each state remains constant after the electric field is turned off at time T. In practice, the initial population distribution will not be a state that is purely $|a\rangle$ or $|b\rangle$. The initial state before optical pumping will be an incoherent combination of molecules starting with equal probabilities in states $|a\rangle$ and $|b\rangle$. Define the optical pumping efficiency $\eta = 1$ to mean that the $|a\rangle$ state was initially fully depleted, and $\eta = 0$ if no optical pumping took place. Taking this distribution as the molecules enter the

electric field region, the final population of the $|a\rangle$ state will be given by a linear combination of these two solutions (equations 7.2 and 7.3) which depends on the optical pumping efficiency η with which level $|a\rangle$ is initially depopulated. The population of level $|a\rangle$ immediately after optical pumping is assumed to be

$$P_A[E, \eta, \Delta, t = 0] = \frac{1-\eta}{2}$$

and the final population of level $|a\rangle$ at $t \geq T$ is

$$P_A[E, \eta, \Delta] = \tfrac{1}{2} P_a^{(b)}[E] + \frac{1-\eta}{2} P_a^{(a)}[E] \tag{7.1}$$

Experimentally, $N\langle P_A[E, \eta, \Delta]\rangle$ is measured, where N is the number of molecules in state $|a\rangle$ with both optical pumping and E-field turned off, $E = E_0$ or 0 depending on whether the electric field is on or off, $\eta = \eta_0 \leq 1$ or 0 depending on whether optical pumping is on or off, and $\langle P_A\rangle$ is the population P_A averaged over the velocity distribution of the molecular beam. During the experiment, a form of lock-in detection is implemented by interleaving measurements with the electric field and optical pumping on and off in order to verify that the effect seen is due to the population transfer from the DC Stark effect (figure G.3), rather than simply due to fluctuations in N. The procedure is, for a value of the detuning Δ:

1. Turn the electric field off, and open the shutter (optical pumping on) and record $P_{0,\eta_0} = N\langle P_A[0, \eta_0, \Delta]\rangle = \frac{1-\eta_0}{2} N$
2. With the electric field still off, close the shutter (optical pumping off) and record $P_{0,0} = N\langle P_A[0, 0, \Delta]\rangle = \frac{1}{2} N$
3. Set the electric field to E_0, and open the shutter (optical pumping on) and record $P_{E_0,\eta_0} = N\langle P_A[E_0, \eta_0, \Delta]\rangle$

4. Keeping the electric field at E_0, close the shutter (optical pumping off) and record $P_{E_0,0} = N \langle P_A [E_0, 0, \Delta] \rangle = \frac{1}{2} N$

These measurements are used to derive a value for the population of the $|a\rangle$ state, P_A, which is independent of experimental imperfections related to imperfections in the optical pumping ratio η_0 and the velocity distribution. Assuming that the source intensity (proportional to N) and optical pumping efficiency η are constant over this cycle, the calculated signal (referred to as the optical pumping ratio, or R) is

$$\begin{aligned} R &\equiv \frac{P_{E_0,\eta_0}}{P_{E_0,0}} - \frac{P_{0,\eta_0}}{P_{0,0}} \\ &= \frac{\langle P_A [E_0, \eta_0, \Delta] \rangle}{\frac{1}{2}} - \frac{1-\eta_0}{2} \\ &= \left\langle P_a^{(b)} [E_0, \Delta] \right\rangle + (1-\eta_0) \left\langle P_a^{(a)} [E_0, \Delta] \right\rangle - \frac{1-\eta_0}{2} \end{aligned}$$

which cancels out variations in the source intensity (N).

Now the velocity distribution of the molecular beam is taken into account to find $\langle P_A \rangle$. As seen in the time-of-flight signal (figure 6.5), it is reasonable to approximate the true velocity distribution by a Gaussian distribution in time. A distribution of the form $\frac{1}{\delta T \sqrt{\pi}} e^{-\left(\frac{T-T_0}{\delta t}\right)^2}$ (defining T_0 as the center of the distribution of T) allows for an analytic solution:

$$\left\langle P_a^{(b)}[E,\Delta] \right\rangle = \frac{(dE)^2}{4(dE)^2+\Delta^2} \left(1 - e^{-\delta T^2 \frac{4(dE)^2+\Delta^2}{4\hbar^2}} \cos\left(\frac{\sqrt{4(dE)^2+\Delta^2}}{\hbar} T_0 \right) \right) \quad (7.2)$$

$$\left\langle P_a^{(a)}[E,\Delta] \right\rangle = \frac{1}{2} \left(1 + e^{-\delta T^2 \frac{4(dE)^2+\Delta^2}{4\hbar^2}} \cos\left(\frac{\sqrt{4(dE)^2+\Delta^2}}{\hbar} T_0 \right) \right) + \frac{\Delta^2}{2(4(dE)^2+\Delta^2)} \left(1 - e^{-\delta T^2 \frac{4(dE)^2+\Delta^2}{4\hbar^2}} \cos\left(\frac{\sqrt{4(dE)^2+\Delta^2}}{\hbar} T_0 \right) \right) \quad (7.3)$$

Using the velocity-averaged solutions above, the expected population in the $|a\rangle$ state is

$$\langle P_A[E,\eta,\Delta]\rangle = \frac{1}{2}(1-\eta) + \frac{(dE)^2\,\eta\left(1-e^{-\frac{4(dE)^2+\Delta^2}{4\hbar^2}\delta T^2}\cos\left(\frac{\sqrt{4(dE)^2+\Delta^2}}{\hbar}T_0\right)\right)}{4(dE)^2+\Delta^2} \tag{7.4}$$

From this, R is found to be

$$R = 2\eta_0\frac{(dE_0)^2}{4(dE_0)^2+\Delta^2}\left(1-e^{-\frac{4(dE_0)^2+\Delta^2}{4\hbar^2}\delta T^2}\cos\left(\frac{\sqrt{4(dE_0)^2+\Delta^2}}{\hbar}T_0\right)\right)$$

The normalized optical pumping ratio $\bar{R}$ can be defined to remove the effect of incomplete optical pumping ($\eta < 1$):

$$\begin{aligned}
\bar{R} &\equiv \frac{R}{1-\frac{P_{0,\eta_0}}{P_{0,0}}} \\
&= \frac{2\eta_0\frac{(dE_0)^2}{4(dE_0)^2+\Delta^2}\left(1-e^{-\frac{4(dE_0)^2+\Delta^2}{4\hbar^2}\delta T^2}\cos\left(\frac{\sqrt{4(dE_0)^2+\Delta^2}}{\hbar}T_0\right)\right)}{1-(1-\eta_0)} \\
&= \frac{1}{2}\frac{(dE_0)^2}{(dE_0)^2+(\Delta/2)^2}\left(1-e^{-\frac{4(dE_0)^2+\Delta^2}{4\hbar^2}\delta T^2}\cos\left(\frac{\sqrt{4(dE_0)^2+\Delta^2}}{\hbar}T_0\right)\right) \\
&= \frac{R}{\eta_0}
\end{aligned}$$

which is independent of the observed optical pumping efficiency, η_0. So, $\bar{R}$ is free of the most significant effects of experimental imperfections, such as poor optical pumping.

The expression for population transfer is further simplified if the velocity spread is sufficiently large. When $\sqrt{4(dE)^2+\Delta^2}\delta T/\hbar \ll 1$, the last term in equation 7.4 causes $\langle P_A\rangle$ to oscillate rapidly as a function of Δ, E, and t_0 (figure 7.1). However, as δT (or dE or Δ) becomes large (such that $\sqrt{4(dE)^2+\Delta^2}\delta T/\hbar \gtrsim 1$), the term is exponentially suppressed and the population transfer varies

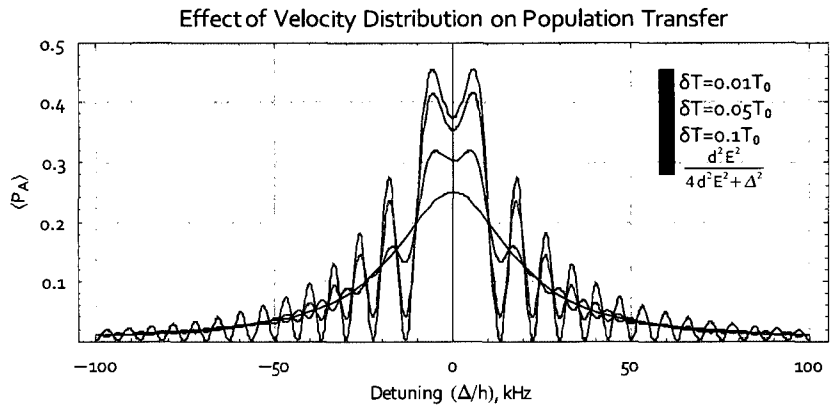

Figure 7.1: The spread of velocities in the molecular beam has the effect of smoothing out rapid variations in the population transfer P_A (second term in equation 7.4). As the velocity spread characterized by δT becomes large compared to $\hbar/\sqrt{4(dE)^2+\Delta^2}$, the oscillations are suppressed. This plot was prepared with $\eta = 1$, $T_0 = \frac{0.1\text{ m}}{600\text{ m/s}}$, and $dE/\hbar$=2π (10 kHz), corresponding to $E \sim 3$ V/cm (for the crossing with $d/\hbar \sim 2\pi$ (3 kHz/$^{\text{V}}/_{\text{cm}}$)).

smoothly as a function of the level splitting Δ:

$$\begin{aligned}\langle P_A[E,\eta]\rangle &\approx \frac{1}{2}(1-\eta)+\eta\frac{(dE)^2}{4(dE)^2+\Delta^2} \\ &\approx \frac{(dE)^2}{4(dE)^2+\Delta^2} \text{ if } \eta{=}1\end{aligned}$$

This behavior is shown in figure 7.1, where $\delta T \approx 0.05T$ describes the pulsed supersonic beam used in our experiment. Under these conditions (where dE or δT are sufficiently large to smooth out $\langle P_A\rangle$), the optical pumping ratio R becomes

$$R = \frac{1}{2}\eta_0\frac{(dE_0)^2}{(dE_0)^2+(\Delta/2)^2} \tag{7.5}$$

and like R, the normalized optical pumping ratio $\bar{R}$ simplifies to a Lorentzian if

$\delta T \gg 4\hbar/\sqrt{4\,(dE)^2 + \Delta^2}$:

$$\bar{R} \approx \frac{1}{2}\frac{(dE_0)^2}{(dE_0)^2 + (\Delta/2)^2} \tag{7.6}$$

For typical values in this experiment ($\delta T \approx 0.05 T_0$), this condition will be satisfied if $d \cdot E/\hbar \gg 2\pi \cdot (19\text{ kHz})$. For the $|1, 0, 1/2, -1/2\rangle$ crossing (table 7.1) used in this experiment, $d/\hbar \sim 2\pi\,(3\text{ kHz/V/cm})$ and this is satisfied if $E \gtrsim 6$ V/cm. The $|1, -1, 1/2, 1/2\rangle$ crossing has $d/\hbar \sim 2\pi\,(145\text{ Hz/V/cm})$, and this is satisfied if $E \gtrsim 130$ V/cm.

The population transfer $\langle P_A \rangle$ changes as the electric field applied across the interaction region is varied (figure 7.2). The effect of inhomogeniety of the electric field is examined by comparing two calculations with similar applied fields. Calculations in chapter 5 showed that the electric field homogeniety will be better than $\sim 3.5\%$ for $r < 1$ cm from the axis of the interaction region. As an example, the calculated population transfer for E=64 V/cm and E=65 V/cm (1.5% change) can be compared. The change in electric field changes the exact value of the peak on-resonance, similar to the effect of the velocity spread. It is also possible to consider the effect of an inhomogeneous magnetic field. A magnetic field inhomogeneity on the order of 0.1 ppm (the precision to which we can shim the magnetic field) would correspond to a convolution of $\langle P_A(\Delta) \rangle$ with a Gaussian function of width $\sigma_\Delta/h \sim$1.3 kHz.

The maximum electric field that can be applied is based on V_{max}=1000 volts. With V_{max} applied to make a linear electric potential gradient across the electrodes in the interaction region (with total length $L \approx 6$ cm), the maximum electric field is about $E = V/L$ =150 Volts/cm. Throughout E-fields are reported as determined in this way from the applied voltage, i.e. $E = V/(6\text{ cm})$.

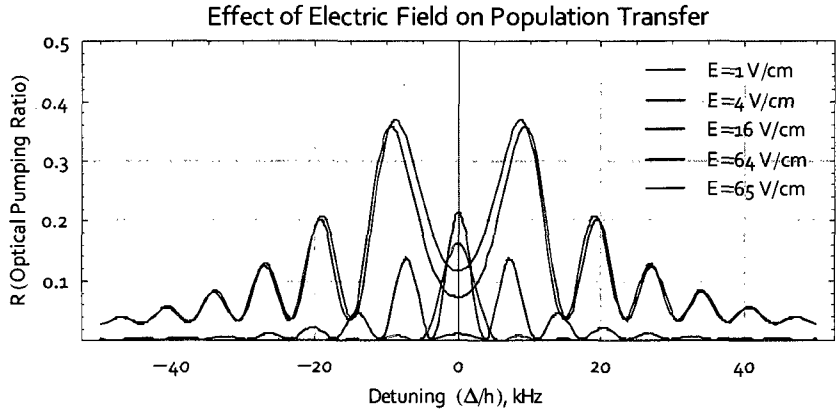

Figure 7.2: The optical pumping ratio R changes with the electric field E created by the interaction region. In this plot, $d/\hbar$=$2\pi \cdot$(145 Hz/V/cm), corresponding to the $|1, -1, 1/2, 1/2\rangle$ crossing, $\eta_0 = 1$, $T_0 = \frac{0.06\text{ m}}{600\text{ m/s}}$, and $\delta T = 0.05T$. A magnetic field inhomogeneity on the order of 0.1 ppm would correspond to a convolution of the signal with a function of the form $f(\Delta) \propto e^{-\frac{1}{2}\left(\frac{\Delta-\Delta_0}{\sigma_\Delta}\right)^2}$, with $\sigma_\Delta/h \sim 1.3$ kHz.

7.1.2 Observations

Initial measurements were made covering a range of magnetic fields from 4625 to 4645 Gauss to find the two $m_F = 0$ crossings of the $N = 0^+$ and $N = 1^-$ rotational levels of ^{138}BaF $[X\,(v = 0)]$. The data collection scheme involved tuning the magnetic field to a selected value, and measuring the laser induced fluorescence with optical pumping on or off, and the electric field on or off, as described in the previous section (fig. 7.3). The level scheme near crossing (figure 7.4) shows three crossings of levels with $\Delta m_F = 0$ which can be driven with an electric field E_z (parallel to $\vec{B}$, as our apparatus is designed to produce). The first crossing, of levels with $m_F = 1$, was not investigated (figure 7.5). Initial data was taken at low signal-to-noise using the one-photon detection scheme; the $|1, -1, 1/2, 1/2\rangle$ crossing was located at B_0 =4628.207 Gauss and subsequently was measured again at higher B-field resolution and a better signal-to-noise ratio using the two-photon detection scheme (figure 7.6). The $|1, 0, 1/2, -1/2\rangle$

m_F	B_p, Gauss	B_f, Gauss	d (Hz/V/cm)	$\|N\, m_S\, m_I\rangle$	$\|N'\, m'_N\, m'_S\, m'_I\rangle$
1	4607	-	-3400	$\|0, 1/2, 1/2\rangle$	$\|1, -1, -1/2, 1/2\rangle$
0	4623	4628.207	145	$\|0, 1/2, -1/2\rangle$	$\|1, -1, 1/2, 1/2\rangle$
0	4630.5	4638.8	-3500	$\|0, 1/2, -1/2\rangle$	$\|1, 0, 1/2, -1/2\rangle$

Table 7.1: $\Delta m_F = 0$ level crossings of ^{138}BaF. The predicted B-field values B_p given are based on prior measurements of the ground-state g-factors [28, 35] and are compared to the measured values (B_f). The predicted values of the electric dipole matrix elements d are derived in chapter 4. The levels involved in the crossings are predominantly ($\gtrsim 90\%$) composed of the states given here.

crossing was only measured using the single photon detection scheme. From these data, the value of the dipole matrix element d between the $|0, 1/2, -1/2\rangle$ and $|1, -1, 1/2, 1/2\rangle$ states was estimated (figure 7.7).

There are a few mysteries observed in the resonance data.

- There is a wide, field-dependent peak present from 1-3 Gauss above the expected narrow resonances, visible on fig. 7.5.
- There is a weak resonance observed near the $|1, -1, 1/2, 1/2\rangle$ crossing (fig. 7.6), even when the applied electric field is nominally turned off. This resonance is shifted 0.02 Gauss ($2\pi\cdot$(56 kHz)) away from the resonance observed with a field applied.
- The optical pumping was often observed to change slowly after turning off the electric field (fig. 7.3). This was noticed with the original configuration of the interaction region, and was not checked after the interaction region electrodes were extended.

A few possible explanations for these unexpected observations have been considered. One related effect of the passage of the molecular beam through a level crossing at a point outside of the constant electric field inside the interaction region. This must happen in at least two places whenever the magnetic field B exceeds the field at crossing, B_0, and may happen in additional locations if the

magnetic field does not change monotonically going into or out of the interaction region. If a stray electric field is present at the spatial location where the level crossing occurs, there may be an unintended population transfer which looks like a resonance signal. This is described by the Landau-Zener effect and is the focus of the next section.

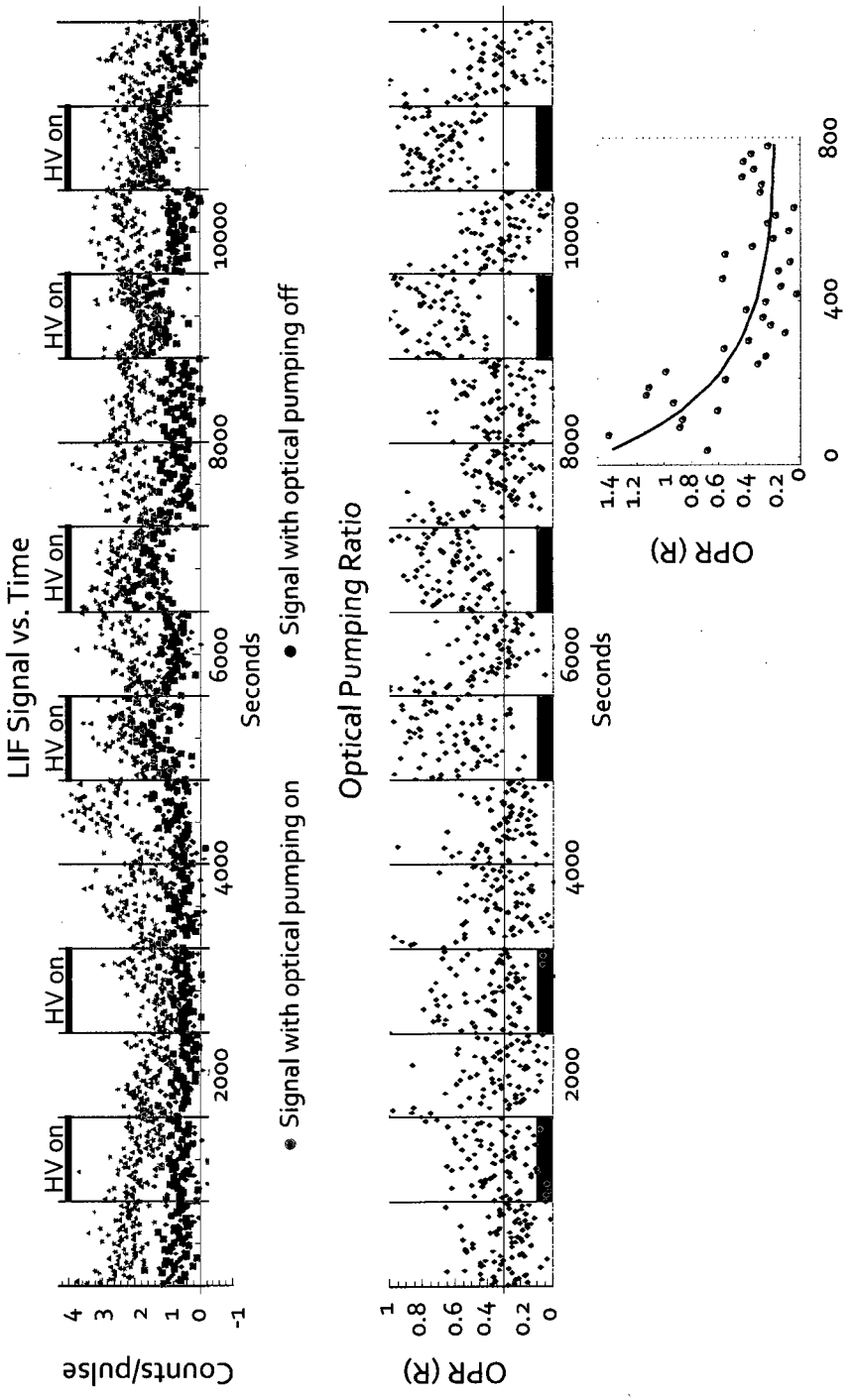

Figure 7.3: The data acquisition procedure for the level crossing data involves tuning the magnetic field to resonance, and summing the number of counts observed under a combination of experimental conditions (electric field on or off, and optical pumping on or off). A sample data collection run near resonance is shown; the optical pumping can be varied on short timescales, but the electric field cannot be switched quickly. The optical pumping ratio exhibits a slow decay (e.g. in the time block shown, the fit $R \approx 1.52 - 1.35\left(1 - e^{-t/184 \text{ seconds}}\right)$) and so the electric field cannot be switched faster than once every 6 minutes.

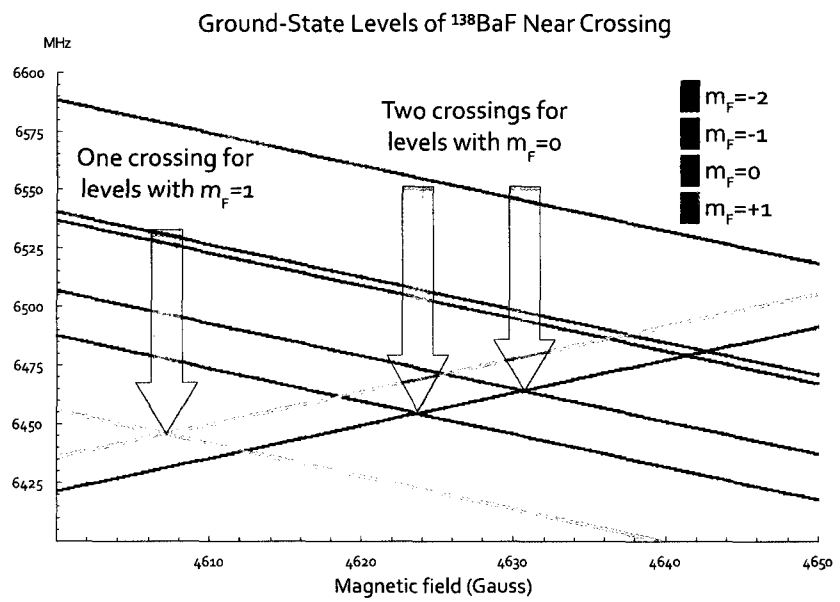

Figure 7.4: ^{138}BaF energy levels near crossing. Rising levels are from the $N = 0$ (+ parity) ground state, and descending levels are from the $N = 1$ (- parity) first rotationally excited state (both are the ground electronic and vibrational states). Molecular constants used are from Effantin (field-free) and Steimle (g-factors). Crossings with a $\Delta m_F = 0$ are accessible with an electric field E_z parallel to the magnetic field; three crossings are available here. Most of the data has been taken on the crossing at B=4628 Gauss, and some also on the crossing at B=4639 Gauss. The crossing at B=4607 Gauss has not been studied experimentally yet.

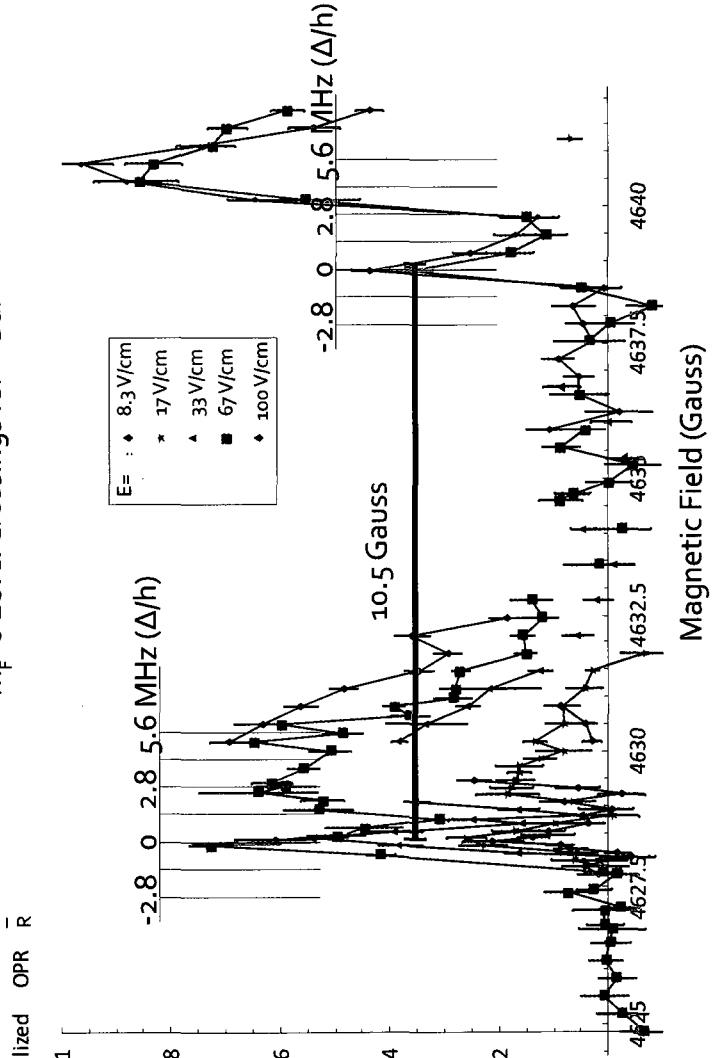

Figure 7.5: Normalized optical pumping ratio $\bar{R}$ as a function of the magnetic field for various applied DC electric fields. This data was taken using the single-photon detection scheme; although the detection scheme should not affect the behavior, it leads to fairly low signal/noise.

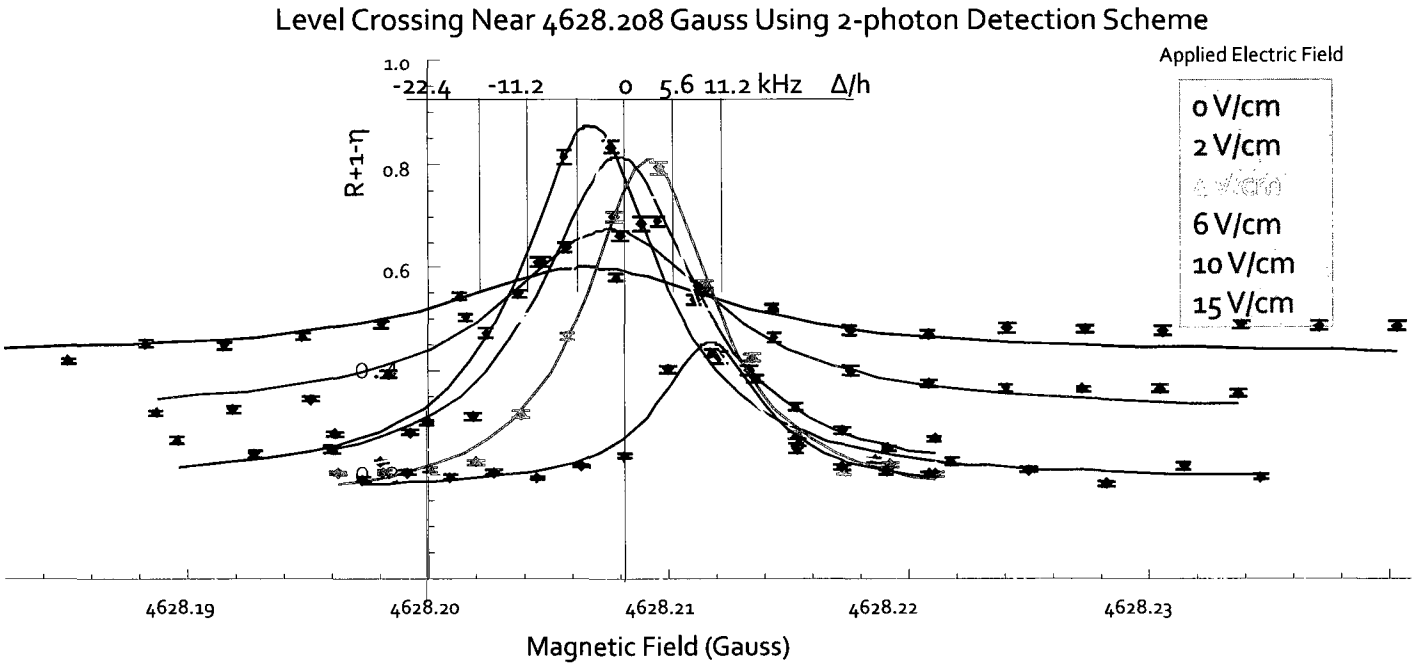

Figure 7.6: Optical pumping ratio $R+1-\eta$ as a function of the magnetic field for various applied DC electric fields. Here, the electric field was kept on for the entire scan; as a result, the signal is $S \equiv R+1-\eta$; the effect of incomplete optical pumping is not removed. For analysis, the data are fit to the form $S(\Delta) = (1-\eta) + \frac{\eta}{2}\frac{d^2E^2}{d^2E^2+\frac{1}{2}(\Delta-\Delta_0)^2} + a$. The physical interpretation of the offset a is unclear, but it is included to allow the fit to converge properly. The offset a may be due to the mechanism responsible for poor optical pumping (e.g. if the ground state is repopulated from a higher state, whether molecules decay to the ground state before or after the magnet). Another unexpected feature is the resonance observed with an applied field of E=0 Volts. This suggests the presence of a significant stray electric field within the apparatus, and is discussed further in the text.

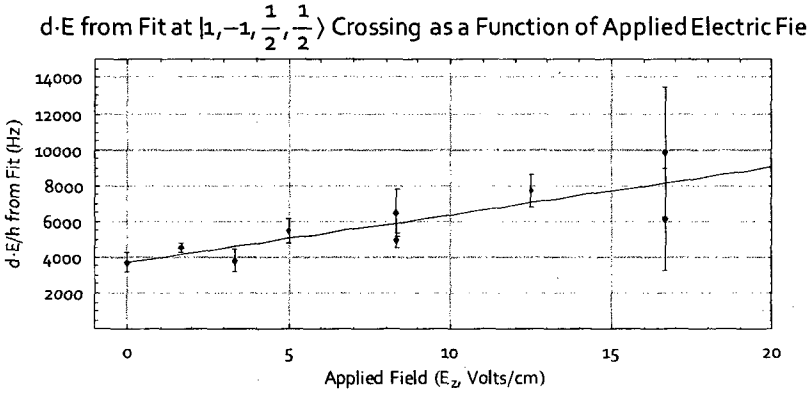

Figure 7.7: The dipole matrix element as inferred from fits to the observed resonance peaks at the values of the various DC electric fields applied, for the $|1, -1, 1/2, 1/2\rangle$ crossing. The data from fig. 7.6 are fit to the form expected from eq. 7.5 and the value of $d \cdot E/h$ is plotted as a function of the applied electric field, E. The dipole moment is then the slope of the plot, $d/\hbar = 2\pi \cdot (270 \pm 70$ Hz/V/cm), in rough agreement with the predicted value of $2\pi \cdot (145$ Hz/V/cm). An unexpected feature is that $d \cdot E/h \neq 0$ at $E = 0$ Volts; the fit to the data gives an offset of 3700 ± 700 Hz/V/cm.

7.1.3 Adiabatic passage through level crossing (Landau-Zener effect)

Some features of the level crossing data deserve more thorough investigation. For example, fig. 7.5 shows broad, noisy peaks in the normalized OPR signal at magnetic fields higher than the resonances (from 4629 to 4632 Gauss for the resonance at 4628.207 Gauss, and from 4640 to 4642 Gauss for the resonance at 4638.8 Gauss). Qualitatively understanding these features requires a more thorough understanding of the experimental apparatus.

For technical reasons, state preparation and detection both take place outside of the strong magnetic field. After state preparation, the two levels of opposite parity $|a\rangle$ and $|b\rangle$ are brought to close to crossing by the magnetic field $\vec{B} = B_z\hat{z}$ within the interaction region. The electric field is then applied to induce population transfer, as described in section 7.1.1. However, there are other situations in which the $|a\rangle$ and $|b\rangle$ levels cross. Depending on the magnetic field at which the two levels are degenerate in energy ($B_z = B_0$) and the exact profile of the magnetic field within the magnet, the following scenarios are possible:

- $B_z < B_0$ everywhere: the two levels never cross, and there will be little or no population transfer from $|b\rangle$ into $|a\rangle$
- $B_z \approx B_0$ at some point z, but $E_z(z) \cong 0$: the two levels cross, but there is no electric field present to mix $|a\rangle$ and $|b\rangle$ so there will be no population transfer
- $B_z \approx B_0$ at some point z, and $E_z(z) \neq 0$: the two levels cross, and (dependent on the magnetic field profile and E_z) there is some population transfer from $|b\rangle$ into $|a\rangle$ (avoided crossing, fig. 7.8)

This last case is different than the problem presented in section 7.1.1 in that the energy splitting between the two levels (Δ) is no longer held constant. Instead,

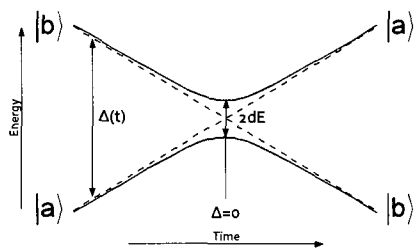

Figure 7.8: Example of an avoided crossing. The two levels are brought through a resonance by changing an external field so that their separation is $\Delta(t) = \dot{\Delta}t$. If the rate of change in energy $\dot{\Delta}$ is slow compared to the square of the coupling $(dE)^2$, population is transferred to the new state along the solid lines shown. If the change is fast, the population transfer proceeds along the dotted lines.

consider the situation where $\Delta(t)$ goes from $\Delta(t_1) < 0$ to $\Delta(t_2) > 0$ (for two times t_1 and t_2). In the apparatus, this happens wherever the magnetic field $B = B_0$; this will occur in at least two places whenever the magnetic field at the center of the magnet $B_z > B_0$. The electric field should be zero at each of these locations, and so there would be no population transfer between $|a\rangle$ and $|b\rangle$. If this is not the case, the Landau-Zener formula [79] gives the probability of finding the population transfer from $|b\rangle$ into $|a\rangle$. In the ideal case, the molecules are treated as a two-level system, subject to the Hamiltonian

$$\mathcal{H} = \begin{pmatrix} -\frac{1}{2}\Delta(t) & dE \\ dE & \frac{1}{2}\Delta(t) \end{pmatrix}$$

where the energies of the two levels $(\pm\frac{1}{2}\Delta(t))$ are functions of time, and the off-axis matrix element dE mixing the two levels is responsible for creating an avoided crossing. An exact solution can be found if the energies are chosen to be linear functions of time (eg. $\Delta(t) = \dot{\Delta}t$), in which case the probability of finding population in an initially depleted state $|a\rangle$ is

$$P_A = 1 - e^{-2\pi\Gamma} \tag{7.7}$$

where

$$\Gamma = \frac{d^2E^2/\hbar}{\left|\dot{\Delta}\right|}$$

evaluated at the point z where external fields cause $\Delta(t) = 0$. So, the final value of P_A will be small if $d^2E^2 \ll \left|\dot{\Delta}\right| \hbar$. Specifically, to keep P_A below a threshold $P_{\max} > P_A$, the electric field at crossing must be

$$|E| < \frac{1}{d}\sqrt{\frac{-\log(1-P_{\max})}{4\pi^2}\frac{d\Delta}{dB}v\frac{dB}{dz}}$$

where $\dot{\Delta} = \frac{d\Delta}{dB}v\frac{dB}{dz}$ expresses this condition in the experimentally important quantities $\frac{d\Delta}{dB}$ (shift in level spacing with change in magnetic field), v (beam velocity), and $\frac{dB}{dz}$ (change in magnetic field with position). Whether this condition is met depends on the specific electric and magnetic field profile in the system (fig. 7.9). The maximum allowed stray electric fields for the system are plotted in fig. 7.10 as a function of position. A few hypotheses can be made based on this profile:

- There is a large dip in the allowed stray field near $z = 4$ cm and 19 cm, which correspond to the points where $\frac{dB}{dz} = 0$. The population transfer will be particularly sensitive to stray fields at these points, at which the B field is 0.02 - 0.06 Gauss higher than within the interaction region. This could result in an apparant resonance even when V_{IR}=0 Volts, though it would be shifted in the opposite direction than that observed in fig. 7.6.

- Large stray fields in the region near $22<z<25$ cm could result in the wide, field-dependent peak that is observed 1-3 Gauss above each of the resonances in fig. 7.5. However, the expected size of this field from the electric field calculations in chapter 5 cannot explain the large effect observed.

- It has been suggested that the surface of a dielectric material (e.g. a thin coating of oil or other insulator on the surface of the electrodes, or part of the supporting teflon tubes) could develop and hold a large stray charge in vacuum. If this occurred in the region from $22 < z < 25$ cm, it could be responsible for the observed effect. Further experiments are underway to validate this hypothesis by replacing the interaction region with a clean, gold-plated tube that will not be susceptible to this sort of charge buildup. It is not a very satisfying hypothesis, in that we cannot at this point make any qualitative predictions about the magnitude of this effect. The motivation for considering this to be a likely cause is the observation that the optical pumping ratio takes a long time to diminish after the interaction region voltage is turned off (fig. 7.3). None of the other mechanisms proposed (such as the electrode design of the interaction region) account for this sort of behavior.

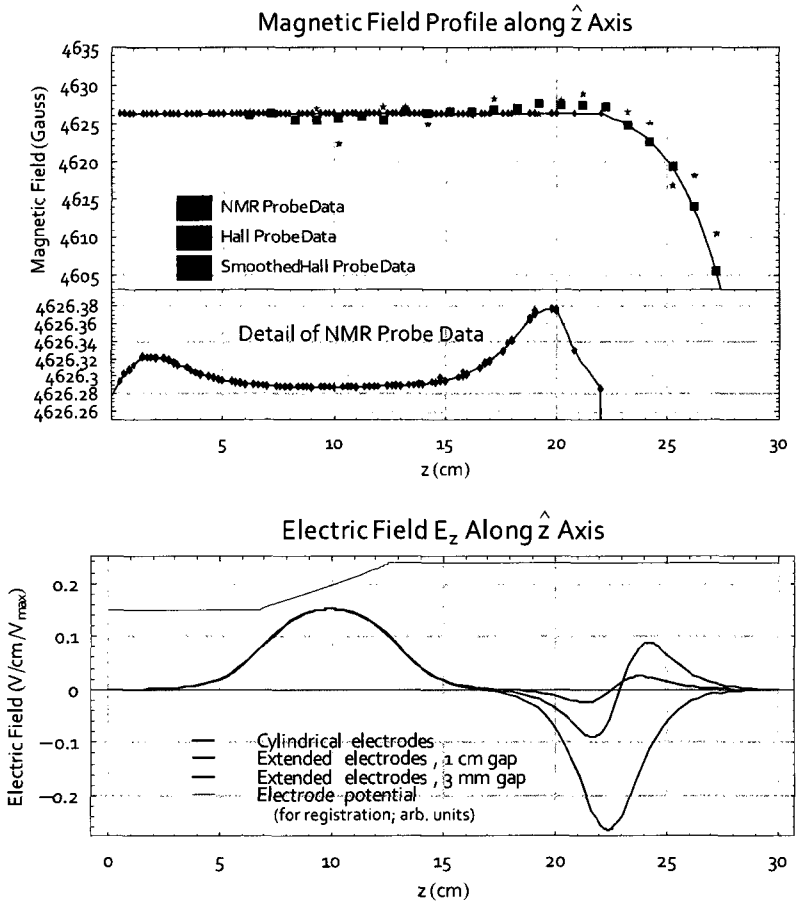

Figure 7.9: Magnetic (B_z) and electric (E_z) field profiles along the z-axis. The magnetic field is measured by sliding an NMR and a Hall probe along the axis; three different electric field profiles are simulated (the electrode configuration is discussed in more detail in chapter 5). It is difficult to measure the field outside the region of high uniformity, but these measurements suggest that the field typically changes by about 25-50 milliGauss/cm (4.2 GHz/sec) just outside of the center of the interaction region, and even faster (2.5 Gauss/cm) later.

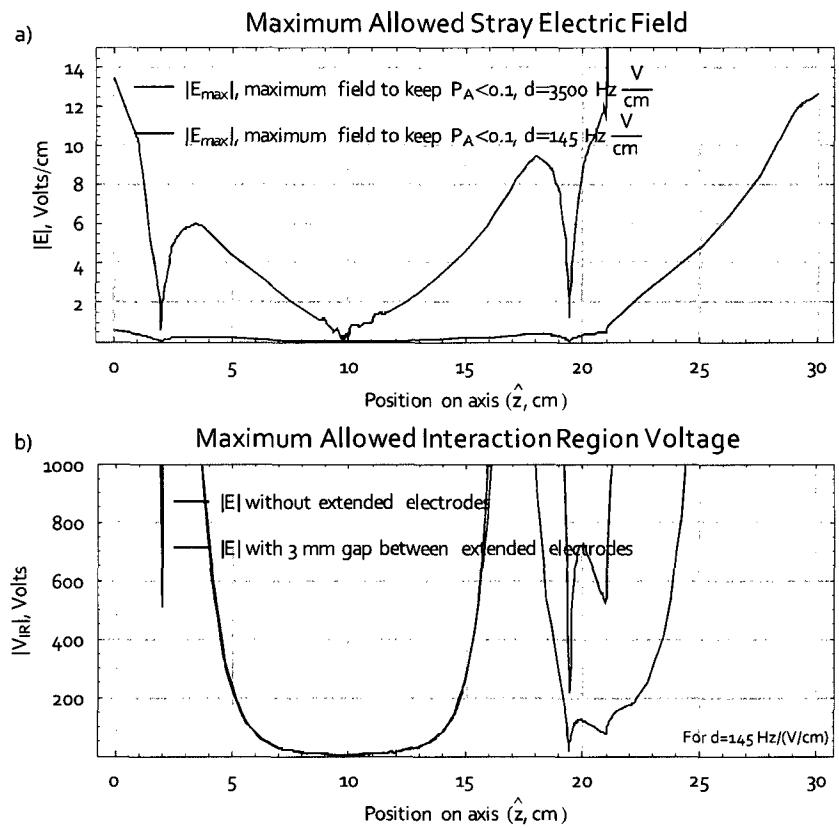

Figure 7.10: The maximum allowed stray electric field to prevent an unintended population transfer (P_A>0.1) during a Landau-Zener level crossing (part a) depends on the rate of change of the magnetic field, which is a function of position. Particular attention should be paid to the region from 22 cm$< z <$25 cm, where a stray field could cause population transfer when the magnetic field is 1-3 Gauss above resonance. Part b) shows the maximum interaction region voltage that (using the electric field models in chapter 5) would generate the maximum allowed stray field for the $|1, -1, 1/2, 1/2\rangle$ crossing.

Chapter 8

Conclusions and Outlook

8.1 Where Things Stand Now

The ability to produce a beam of BaF and to perform spectroscopic detection and state preparation of ^{138}BaF has been demonstrated. The magnetic field within the apparatus can be applied and controlled in a manner suitable for bringing levels of opposite parity to crossing, and transitions have been demonstrated at these level crossings induced by the Stark effect. These measurements suggest the need to improve the interaction region design to better control the electric field; however, the changes required should be straightforward in nature. Now, there are two major limitations preventing progress with the parity violation experiment:

- insufficient beam flux: the flux of ^{138}BaF molecules observed using the two-photon detection scheme was adequate for the DC Stark measurements made in chapter 7. Between the ratio of natural isotopic abundances (7:1 for ^{138}BaF to ^{137}BaF) and the larger number of hyperfine ground states (4:1 for the $I=\frac{3}{2}$ nuclear spin of ^{137}Ba to the $I=0$ nuclear

spin of ^{138}Ba) present, the beam flux for ^{137}BaF will be about 1/28 of the observed flux of ^{138}BaF. Under the assumptions made in section 3.5.4.1, the parity violation experiment to be run would require a long, but still conceivably viable integration time ($T \sim 2.5$ days) to make a suitable (10%) measurement using ^{137}BaF with the current beam flux. However, obviously a significant increase in flux could greatly benefit the experiment.

- poor optical pumping: possible reasons for observations of poor optical pumping were discussed in chapter 6. In chapter 3 it was noted that problems in state preparation would greatly increase the amount of data collection time needed to reach the same level of statistical uncertainty (eq. 3.42). An optical pumping efficiency of $\eta = 0.9$ would (compared to perfect optical pumping, $\eta = 1$) quadruple the amount of time required to achieve the same level of accuracy. An optical pumping efficiency of $\eta \approx 0.85$ is currently observed, as outlined in chapter 6.

There are plans to address both of these issues.

8.2 Improved Optical Pumping

Chapter 6 suggested possible causes for poor optical pumping. If the preferred explanation (decay from long-lived Rydberg states) is indeed correct, the problem can be fixed by applying a moderate electric field ($E \sim 50$ V/cm) near the beam source to ionize and sweep these molecules from the beam. This modification has not yet been tested. In any case, it will be necessary to move the state preparation laser from its current location in Chamber 2 to a location near the interaction region (see section 5.5). This will reduce the time between optical pumping and final detection of any molecule by a factor of ~ 2. If the imperfect

optical pumping is due to decays from any type of excited level, this is expected to decrease 1-η by a factor of ~ 2.

8.3 Beam Source

A few possibilities have been considered with respect to improving the flux of the molecular beam. Compared to other beam sources used by other groups for similar types of molecules (section 6.5), this beam has lower flux in the desired (rotational and vibrational) ground state [70]. Based on spectroscopy of the low-lying rotational states, the beam is warmer and hence has a lower fraction of molecules in the rotational ground state. The techniques used here (section 5.2.3) are generally similar to those of Hinds et al., but more careful attention to differences in experimental technique may be important. The current design is similar to one of the earlier designs used by the Hinds group[51]. Later work by Hinds, Tarbutt et al. suggest that it is important to arrange the target so that it is near the nozzle but does not interfere with the expansion of the argon gas. It is also unclear how sensitive the beam flux and temperature is to the position of the ablation point and target. The production of the ground state of BaF has been optimized to the extent allowed by the geometry of our target design, but a design change may yield a significant improvement in the observed flux. The newer design of Hinds et al. uses a strip of metal attached to the rim of a disk that can be placed directly against the face of the nozzle. That prevents the possibility of part of the argon pulse reflecting from the target and interfering with the flow.

To that end, progress has been made on implementing similar modifications to the beam source. A new design using a barium metal strip epoxied to the rim of a 2 mm thick, 4" diameter disk has been prepared. The disk can be positioned relative to the nozzle using vacuum compatible motorized actuators

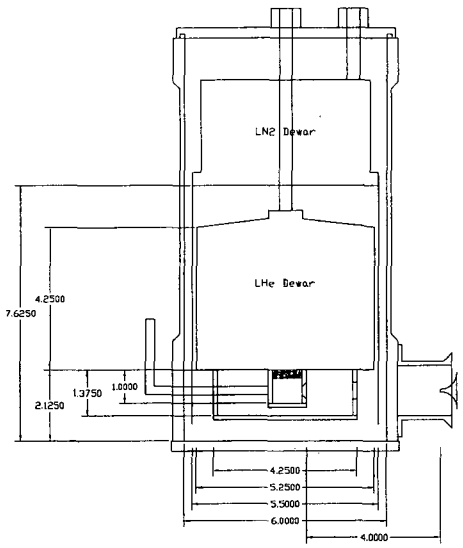

Figure 8.1: Mechanical drawing of proposed buffer gas source. The cell, located at the bottom of the liquid helium dewar, is kept at 4 Kelvin. Helium gas flows into the cell (at a rate $\approx 1-20$ sccm) and out the nozzle on the right hand side. Material which is laser ablated in the cell thermalizes with the 4 K helium gas and is carried out through the nozzle. Charcoal sheets kept between 4 and 10 K placed within the vacuum system outside of the cell effectively cryopump the helium gas flow. The molecular beam generated in the cell passes though the skimmer, at right, into the rest of the vacuum system. This design is currently under development by the DeMille group at Yale and by the Doyle group at Harvard.

that can be controlled from outside the vacuum system.

Another possibility is to switch to using a cryogenic buffer gas beam setup (fig. 8.1) similar to the type that is being developed in the DeMille group for use with microwave trapping of SrO[71] and by the Doyle group[52]. This method involves flowing cold ($\sim$ 4K) helium gas into a small cell (also cooled to $\sim$ 4K) containing the ablation target material. A nozzle in one side of the cell allows helium and ablated molecules to flow out of the cell into a vacuum system, but the helium flow is set to maintain a relatively high (few millitorr) pressure within the cell. Material ablated from the target rapidly cools to thermal equilibrium

with the helium, and is entrained in the flow out of the cell. Current experiments show this to be a reliable way to produce cold molecules. Some of the properties of the cryogenic buffer gas beam are different than the pulsed supersonic source; some of these are beneficial (eg. slower beam velocity and a higher fraction of the population in the ground rotational state). Some other properties, such as an extended distribution in time[1], are not expected to be harmful in the version of this experiment, as proposed in chapter 3. Note that the buffer gas method requires a target which can decompose into the desired compound. For example, we would have to use a BaF_2 target rather than a barium metal/SF_6 gas because the SF_6 would freeze out on the walls of the cell. There have been significant problems with the use of a crystalline BaF_2 ablation target in the pulsed supersonic beam design. However, preliminary tests using a sintered BaF_2 target in a buffer gas cell have been very promising. To this end, cryogenic buffer gas sources for BaF have been constructed by Dennis Murphree, John Barry, Matthew Steinecker, and Emil Kirilov and tested independently of the apparatus described in this thesis. Measurements on the cryogenic BaF beam source (using a BaF_2 target) demonstrated a large flux of molecules a short distance outside of the cell, and experiments with SrF have observed molecules 40 cm downstream from the source. This may soon replace the pulsed supersonic source as the beam source on the apparatus.

8.4 Detection efficiency

An alternative to improving the source flux is to increase the detection efficiency. Most of the "easy" improvements have already been made by switching from the

[1]For example, with our current beam source we observe the molecules to arrive within a 400 microsecond window, 1 meter downstream from the nozzle. The cryogenic buffer gas beam lasts in excess of 5 milliseconds, immediately outside the nozzle. This would prevent us from easily inferring the velocity of the molecules from the time-of-flight data; however, other methods can be used to determine the velocity.

single-photon to the two-photon detection scheme. This has allowed use of a larger detector, with more efficient lightguides, and to eliminate scattered laser light as a source of background count rate. No conclusive evidence of STIRAP has been observed using this setup; it is possible that further optimization could improve the detection efficiency by preventing loss from the intermediate state of the two-photon transition which occurs in stepwise (as opposed to coherent STIRAP) excitation.

John Barry, Edward Shuman, Prof. DeMille, et al. have recently observed cycling transitions using SrF [78]. They have observed tens or hundreds of scattered photons per molecule. It is not clear if a similar scheme would be suitable for improving the detection or state preparation of BaF.

8.5 Further Investigations of Level Crossings

To date, the two $m_F = 0$ level crossings available with ^{138}BaF have been investigated. As noted in chapter 4, the relevant but previously unknown spectroscopic parameters (g_r, g_s) cannot be redundantly determined from these two points alone. Measurement of the $m_F = 1$ crossing predicted to be near $B \sim$4612 Gauss would provide useful confirmation of this determination of these values. Most importantly, more detailed study of all the crossings should help confirm the nature of the level crossings before beginning to take parity violation data.

Part III

Appendices

Appendix A

Supersonic Gas Flow

A.1 Introduction

The description of the properties of a supersonic expansion from a free jet source can be studied based on the thermodynamic properties of an isentropic gas expansion and the equations governing fluid flow. We will generally follow the treatment used in Pauly[46], with the goal of calculating the temperature and velocity of the gas jet. We will also calculate the number of collisions in the gas jet, in order to see when the thermodynamic properties of the jet "freeze" out. This transition, when the number of collisions per unit length becomes small compared to the rate of change of thermodynamic properties, marks the end of the supersonic expansion and the beginning of free molecular flow. This is useful for characterizing where we can put the beam skimmer, an aperture which selects a portion of the molecular beam for use in the experiment.

A.2 Isentropic Gas Flow-Fundamental Equations

The topic of isentropic gas flow is covered in Van Wylen[45] and chapter 3 of Pauly[46]. The latter contains a particularly useful discussion in the context of free jet expansions relevant to the production of atomic or molecular beams. We will cover some of the most relevant relationships here. The notation here uses ρ as the density of the gas, $\vec{w}$ as the velocity (considered to be a vector quantity unless assuming one-dimensional flow), P as the pressure, h is the enthalpy per unit mass, M is the mass, T is temperature, R is the gas constant, M_a is the Mach number, c is the local speed of sound in the gas, κ is the specific heat ratio c_P/c_V (sometimes referred to as γ).

There are three important fundamental relationships governing steady flow, as described in chapter 3.2 of Pauly.

- The *continuity equation* states the principle of conservation of mass:

$$\nabla \cdot (\rho \vec{w}) = 0 \tag{A.1}$$

which, if we have cylindrical symmetry ($\vec{w} = w_r \hat{r} + w_z \hat{z}$), means

$$\frac{1}{r}\frac{\partial}{\partial r}(\rho w_r r) + \frac{\partial}{\partial z}(\rho w_z) = 0 \tag{A.2}$$

For one-dimensional flow ($w = w_z$) in a tube of cross-sectional area A, we neglect w_r but instead say that the flow through any cross-section of the tube is conserved:

$$\frac{\partial}{\partial z}(\rho w A) = 0 = \frac{dw}{w} + \frac{d\rho}{\rho} + \frac{dA}{A} \tag{A.3}$$

- The *conservation of momentum* relates the pressure to the acceleration of the gas using $F = ma$:

$$\rho \frac{\mathrm{D}\vec{w}}{\mathrm{D}t} = -\nabla P \tag{A.4}$$

where $\frac{\mathrm{D}\vec{w}}{\mathrm{D}t} = \frac{\partial \vec{w}}{\partial t} + (\vec{w} \cdot \nabla)\vec{w}$ is the substantial derivative. In cylindrical coordinates, $(\vec{w}\nabla)\,\vec{w} = w_r \frac{\partial \vec{w}}{\partial r} + \frac{w_\theta}{r}\frac{\partial \vec{w}}{\partial \theta} + w_z \frac{\partial \vec{w}}{\partial z}$ and the momentum equation for steady-state flow is

$$\rho\left(w_r \frac{\partial w_r}{\partial r} + w_z \frac{\partial w_r}{\partial z}\right) = -\frac{\partial P}{\partial r} \tag{A.5}$$

$$\rho\left(w_r \frac{\partial w_z}{\partial r} + w_z \frac{\partial w_z}{\partial z}\right) = -\frac{\partial P}{\partial z} \tag{A.6}$$

For one-dimensional flow, we let $w = w_z$, w_r, $\frac{\partial}{\partial r} \rightarrow 0$ and so

$$w\,dw = -\frac{dP}{\rho} \tag{A.7}$$

For isentropic flow, we can use equation A.32 to replace the dependence on pressure with a dependence on density.

- The *conservation of energy* requires that the total energy of the gas be constant, since the isentropic flow cannot exchange heat with the environment. This is written in terms of the specific enthalpy, defined as the sum of the internal energy per unit mass e and the thermal energy per unit mass:

$$h \equiv e + \frac{P}{\rho} = e + \frac{RT}{M} \tag{A.8}$$

The total energy per unit mass is the enthalpy plus the kinetic energy; which, using the dot product in cylindrical coordinates), gives:

$$\frac{\mathrm{D}}{\mathrm{D}t}\left(h + \frac{\vec{w}^2}{2}\right) = 0 \tag{A.9}$$

In cylindrical coordinates, the dot product of two vectors is

$$r_1 r_2 \left(\cos\left(\theta_1\right)\cos\left(\theta_2\right) + \sin\left(\theta_1\right)\sin\left(\theta_2\right) + z_1 z_2\right)$$

and the substantial derivative is interpreted as $\frac{D\phi}{Dt} = \frac{\partial\phi}{\partial t} + \vec{v} \cdot \nabla\phi$ (where $\vec{v}$ is the velocity of the flow):

$$\vec{w} \cdot \nabla \left(h + \frac{w_r^2 + w_z^2}{2} \right) = 0 \quad \text{(A.10)}$$

$$w_r \left(\frac{\partial h}{\partial r} + w_r \frac{\partial w_r}{\partial r} + w_z \frac{\partial w_z}{\partial r} \right) = 0 \quad \text{(A.11)}$$

$$w_z \left(\frac{\partial h}{\partial z} + w_r \frac{\partial w_r}{\partial z} + w_z \frac{\partial w_z}{\partial z} \right) = 0 \quad \text{(A.12)}$$

For one-dimensional flow, this reduces to

$$w\,(dh + w\,dw) = 0 \quad \text{(A.13)}$$

We can use equation A.17 for the change in the enthalpy h during an isentropic expansion to replace the derivatives in h with an expression in terms of ρ.

These equations governing the flow give a set of five nonlinear equations for a cylindrically symmetric system, with six spatial derivatives to be determined ($\frac{\partial w_r}{\partial r}$, $\frac{\partial w_r}{\partial z}$, $\frac{\partial w_z}{\partial r}$, $\frac{\partial w_z}{\partial z}$, $\frac{\partial \rho}{\partial r}$, $\frac{\partial \rho}{\partial z}$). This system can be solved using the method of characteristics if the flow is supersonic. In supersonic flow, sound waves cannot propagate backwards against the flow, so the properties at any point in the system are determined only by the conditions upstream of that point. This has been modeled numerically in various papers[47, 48].

A.3 Isentropic Gas Equations of State

Chapter 3.1 of Pauly[46] uses the first law of thermodynamics to describe the change in internal energy per unit mass e for an ideal gas:

$$dq = de + P\,dV = de + P\,d(1/\rho) \tag{A.14}$$

Specific enthalpy, defined as the sum of the internal energy per unit mass e and the thermal energy per unit mass, can be written in terms of the volume V of a unit mass of gas, the temperature T, or the density ρ:

$$h \equiv e + PV = e + \frac{RT}{M} = e + \frac{P}{\rho} \tag{A.15}$$

We can take the derivative:

$$dh = de + \frac{1}{\rho}dP + P\,d(1/\rho) \tag{A.16}$$

$$dq = de + P\,d(1/\rho) = dh - \frac{1}{\rho}dP \tag{A.17}$$

so that we see that $dh - \frac{1}{\rho}dP = 0$ in an isentropic process.

The specific heat is defined with respect to heating at a constant volume or at a constant pressure:

$$c_V = \left(\frac{dq}{dT}\right)_V = \left(\frac{de}{dT}\right)_V \tag{A.18}$$

$$c_P = \left(\frac{dq}{dT}\right)_P = \left(\frac{dh}{dT}\right)_P \tag{A.19}$$

The definition of specific enthalpy in terms of the temperature T ($h \equiv e + \frac{RT}{M}$, eq. A.15) can be used to find a relationship between c_V and c_P in terms of the specific heat ratio $\kappa \equiv c_P/c_V$ (sometimes referred to as γ):

$$\frac{dh}{dT} = \frac{de}{dT} + \frac{R}{M} \tag{A.20}$$

$$c_P = c_V + \frac{R}{M} \tag{A.21}$$

$$c_P = \frac{\kappa}{\kappa - 1}\frac{R}{M} \tag{A.22}$$

$$c_V = \frac{1}{\kappa - 1}\frac{R}{M} \tag{A.23}$$

The specific heat ratio κ is experimentally determined, but is about 1.7 for argon (and less than 2.1 for all gases). It is also a function of temperature, but we will consider it to be constant, as it is for an ideal gas.[1]

For an isentropic process, the gas is not able to exchange heat with its surroundings ($dS = 0$, $dq = 0$). This lets us use equation A.14 and the ideal gas law ($P = \frac{R}{M}\rho T$) to write:

$$de + P\,d\,(1/\rho) = 0 \tag{A.24}$$

$$c_V dT + \frac{R}{M}\rho T\left(-\frac{d\rho}{\rho^2}\right) = 0 \tag{A.25}$$

$$\frac{1}{\kappa - 1}\frac{dT}{T} - \frac{d\rho}{\rho} = 0 \tag{A.26}$$

and similarly with equation A.17 and the ideal gas law ($\rho = P\frac{M}{RT}$):

$$dh - \frac{1}{\rho}dP = 0 \tag{A.27}$$

$$c_P dT - \frac{RT}{PM}dP = 0 \tag{A.28}$$

$$\frac{\kappa}{\kappa - 1}\frac{dT}{T} - \frac{dP}{P} = 0 \tag{A.29}$$

[1]For diatomic gases, the specific heat is roughly constant until the temperature falls below the temperature equivalent of the rotational energy.

Combining the two equations gives

$$\kappa \frac{d\rho}{\rho} = \frac{dP}{P} \tag{A.30}$$

which, if we assume κ is constant (as it is for an ideal gas), gives the relationship between ρ and P at two points in the isentropic process:

$$\ln \frac{P_2}{P_1} = \int_{\rho_1}^{\rho_2} \kappa \frac{d\rho}{\rho} = \kappa \ln \frac{\rho_2}{\rho_1} \tag{A.31}$$

$$\frac{P_2}{P_1} = \left(\frac{\rho_2}{\rho_1}\right)^{\kappa} \tag{A.32}$$

with similar relationships for the temperature and pressure

$$\frac{P_2}{P_1} = \left(\frac{T_2}{T_1}\right)^{\frac{\kappa}{\kappa-1}} \tag{A.33}$$

and for the temperature and density

$$\frac{\rho_2}{\rho_1} = \left(\frac{T_2}{T_1}\right)^{\frac{1}{\kappa-1}} \tag{A.34}$$

The local speed of sound, as noted in Pauly chapter 3.3.1, is

$$c = \sqrt{\kappa \frac{P}{\rho}} = \sqrt{\kappa \frac{RT}{M}} \tag{A.35}$$

A.4 Isentropic Gas Flow-Thermodynamic Properties

Chapter 3.3.2 of Pauly[46]uses the one-dimensional flow equations A.3, A.7, and A.13 along with the equations of state (eqs. A.32, A.33, and A.34) and

the speed of sound (eq. A.35) to find the following useful relationships for the thermodynamic variables T, w, P, ρ in terms of the Mach number M_a of a one-dimensional isentropic flow through a nozzle:

$$\frac{T}{T_0} = \left(1+\frac{\kappa-1}{2}M_a^2\right)^{-1} \tag{A.36}$$

$$w = M_a\sqrt{\kappa\frac{RT_0}{M}/\left(1+\frac{\kappa-1}{2}M_a^2\right)} \tag{A.37}$$

$$\frac{P}{P_0} = \left(1+\frac{\kappa-1}{2}M_a^2\right)^{-\kappa/(\kappa-1)} \tag{A.38}$$

$$\frac{\rho}{\rho_0} = \left(1+\frac{\kappa-1}{2}M_a^2\right)^{-1/(\kappa-1)} \tag{A.39}$$

where T_0 is the stagnation temperature, P_0 is the stagnation pressure, and ρ_0 the density in the gas reservoir behind the nozzle in which the velocity is effectively zero.

Inverting eq. A.38 gives

$$M_a = \sqrt{\frac{2}{\kappa-1}\left(\left(\frac{P_0}{P}\right)^{(\kappa-1)/\kappa}-1\right)} \tag{A.40}$$

from which it is clear that the pressure ratio P_0/P of the stagnation pressure behind the nozzle to the background pressure in the vacuum chamber must be at least

$$\frac{P_0}{P} \geq \left(\frac{\kappa+1}{2}\right)^{\kappa/(\kappa-1)} \tag{A.41}$$

in order to reach a Mach number of 1 in the nozzle and achieve a supersonic expansion.

We will look at a few properties of the gas jet, in the limiting case that the expansion proceeds to an extremely low temperature. We can find the gas

velocity as a function of the difference in enthalpy between the gas reservoir and a point in the jet by applying conservation of energy:

$$h_0 - h = {}^1/_2\bar{v}^2 \tag{A.42}$$

The specific heat capacity at constant pressure $c_P \equiv \left(\frac{dE}{dT}\right)_P = \left(\frac{dh}{dT}\right)_P$ can be used to write the enthalpy as a function of temperature:

$$2\,(h_0 - h) = 2\int_T^{T_0} c_P\,dT = \bar{v}^2 \tag{A.43}$$

So, we find the velocity to be

$$\bar{v} = \sqrt{2\frac{\kappa}{\kappa - 1}\frac{R}{M}\,(T_0 - T)} \tag{A.44}$$

As long as we look at a part of the expansion where the gas has cooled substantially, the velocity will be close to that with $T \to 0$. For argon gas starting at room temperature (300K), the mean terminal velocity $\bar{v} = 550\,m/s$.

A.5 Supersonic Free Gas Jet Expansion

The flow of a gas jet in a free supersonic expansion can be solved by the method of characteristics, but the solution is not particularly tractable. We can make some headway in describing the nature of the jet expansion if we limit ourselves to the properties near the jet's axis of symmetry. If we are a moderate distance away from the nozzle, we can assume that the flow near the axis behaves as if it emanates from a point source at the nozzle (figure A.1). For a round nozzle, the flux of the gas flow in a unit area will fall off like ${}^1/_{x^2}$ as we look farther from the nozzle; it will fall off like ${}^1/_x$ for a slit nozzle. The flux of this gas flow at a given point is the product of the density ρ times the velocity w. This gives (as

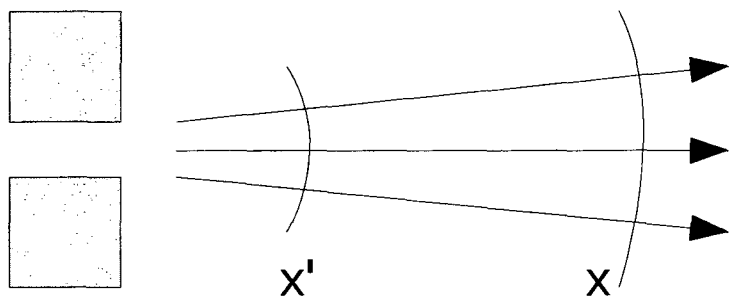

Figure A.1: Continuity condition as applied to the supersonic expansion near the center of the gas jet. Near the axis, the gas appears to expand radially from the nozzle. The gas flux will fall off like $1/x^2$ as we look farther from the nozzle

shown in Pauly 3.82) us a way to show how the gas density and velocity vary as we look farther away from the nozzle:

$$\frac{x}{x'} = \left(\frac{\rho' w'}{\rho w}\right)^{(2-\delta)/2} \tag{A.45}$$

where $\delta = 1$ represents a round nozzle and $\delta = 0$ a slit nozzle. We can use equations A.37 and A.39 to substitute for ρ and w in terms of the Mach number M_a, as in Pauly eq. 3.83:

$$M_a = \left(\frac{x}{x'}\right)^{(\kappa-1)/(2-\delta)} \left(\frac{\kappa+1}{\kappa-1}\right)^{(\kappa+1)/4} \tag{A.46}$$

The Mach number can be parametrized in this form for distances $x/d > 0.5$ (d being the nozzle diameter) from the source; details are in Pauly equation 3.84 and table 3.1[46]. The resulting calculation of Mach number, temperature, and pressure is shown in figure A.2.

These calculations for a supersonic expansion assume that the mean free path is always short enough that the gas stays in thermodynamic equilibrium. However, as seen above, the density drops sharply. Pauly (chapter 3.6.2) points

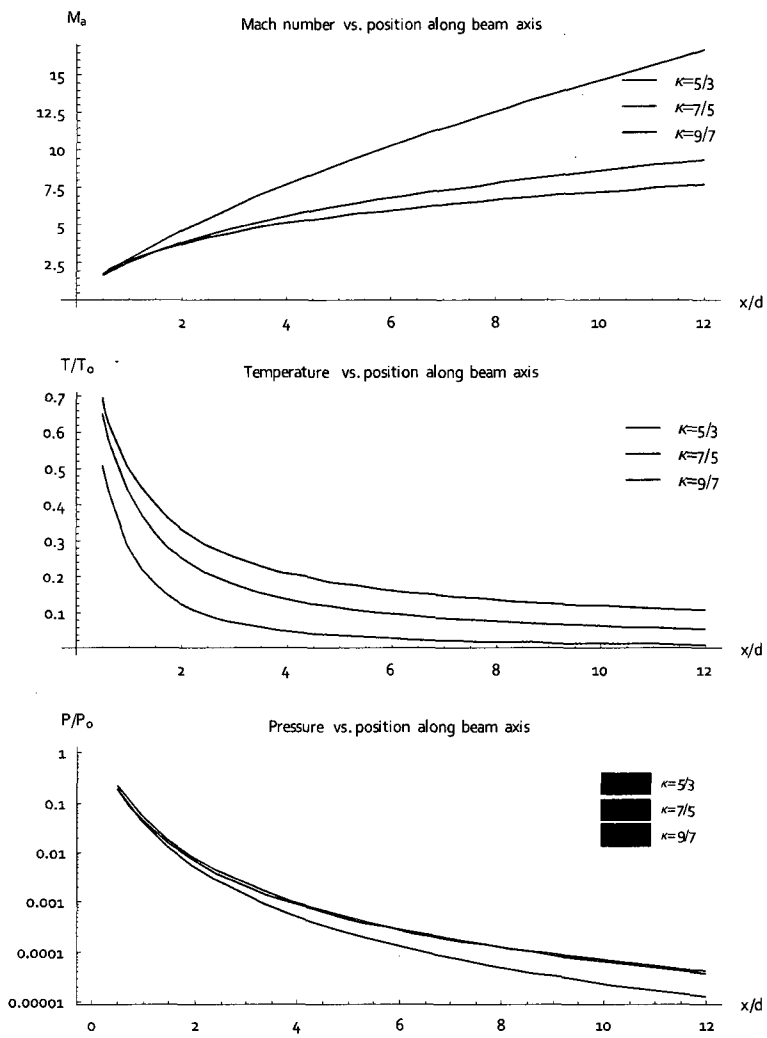

Figure A.2: Mach number, temperature, and pressure as a function of distance along the axis of the supersonic jet expansion, using the empirical form[48] shown in equation 3.84 in Pauly[46].

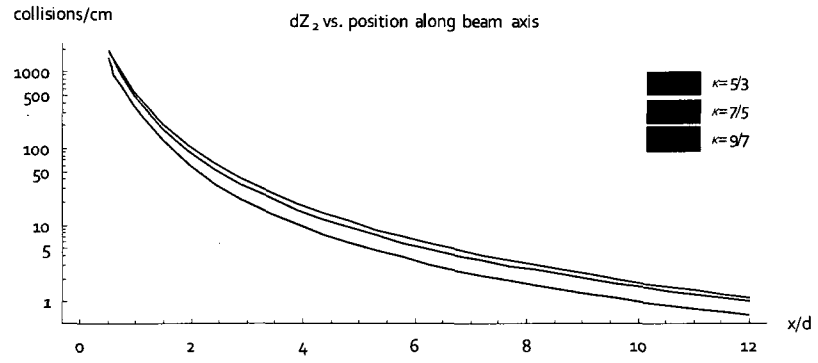

Figure A.3: Collisions per centimeter in the supersonic expansion, assuming a cross-section of $5\times10^{-17}\text{cm}^2$ at 300K, and a stagnation pressure of 1 atmosphere. Once gas conditions start to change rapidly compared to the collision rate, the beam stops acting like a supersonic expansion and enters the free molecular flow regime.

out that the two-body collision rate is

$$dZ_2 = n(x)\,\bar{\sigma_{eff}}\bar{v}(x)\,dt = n(x)\,\bar{\sigma_{eff}}\frac{\bar{v}(x)}{w(x)}dx \tag{A.47}$$

where $n(x)$ is the number density and $\bar{\sigma_{eff}} = \sigma(T_0)\left(\frac{T}{T_0}\right)^{1/3}$ is the effective collision cross-section. Figure A.3 shows the collision rate for a stagnation pressure of 1 atmosphere for a cross-section $\sigma(300K) \approx 5\times10^{-17}\text{cm}^2$ ($\approx 7\times10^{-9}$ cm radius for argon)[2]. We see that the transition to a free molecular flow happens after a fairly short distance, within 20 mm of the source (for a 1 mm nozzle diameter).

Although we are using a pulsed source, the duration of the gas pulses (100-

[2]We can measure the argon-argon scattering cross-section at room temperature by measuring the attenuation of the argon gas pulse in the presence of background gas. We find that the pulse height h decreases exponentially with background gas pressure:

$$h = a\exp(-n\sigma l) = a\exp(-Pl\sigma/kT)$$

where the number density $n = P/kT$, l=beam path length (here, 22"=55 cm), and σ is the cross-section.

For a fit coefficient $\exp(-bx)$, $b = 0.22$ mTorr$^{-1} = \sigma l/kT$, then $\sigma = 1.2\times10^{-16}cm^2$

300 μs) is sufficient that we can consider it as if it were a continuous gas jet (the pulsed gas stream quickly reaches a steady state). The gas jet approaches equilibrium conditions once the valve has been open for a time $t \gg d/\bar{v}$, where d is the nozzle diameter and $\bar{v}$ is the gas velocity. This gives a settling time of about 6 μs.

Appendix B

Mechanical Drawings

B.1 Piezo Valve

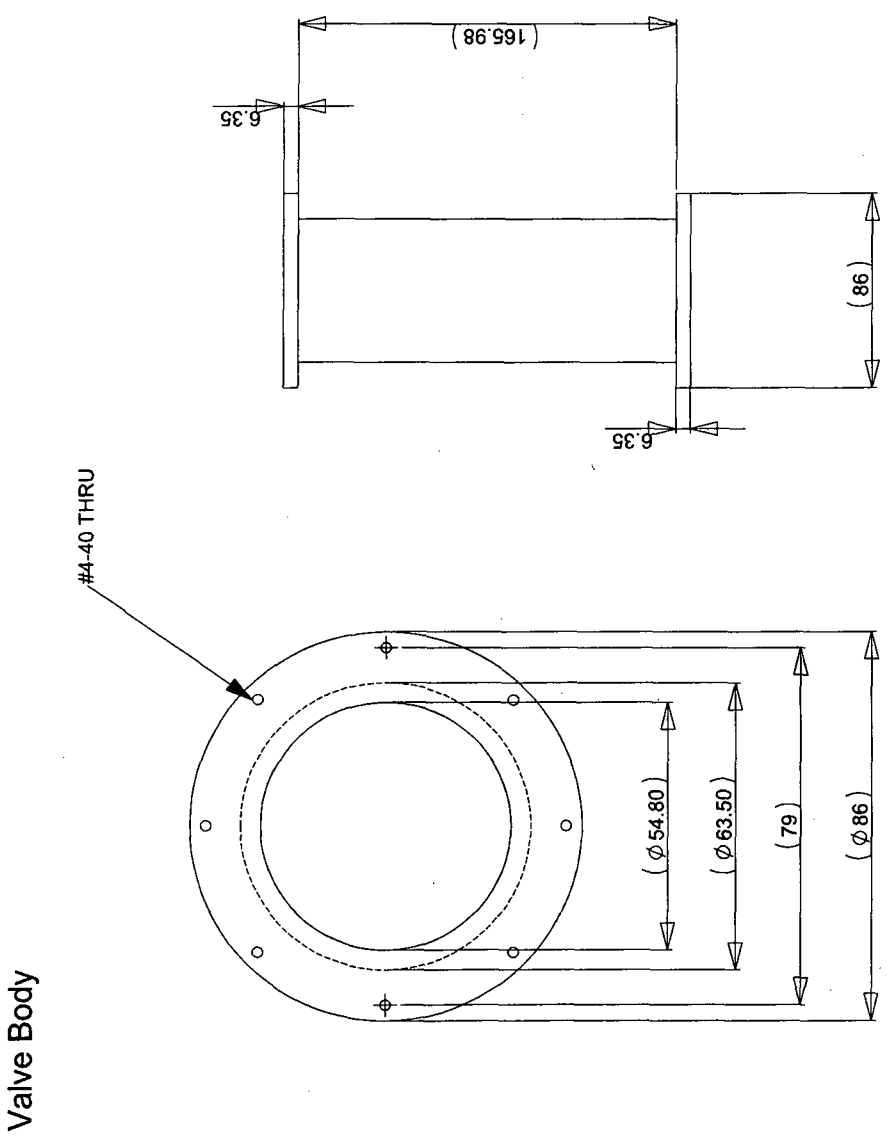

Figure B.1: Piezo valve body. The nozzle is bolted to the front, and the back is bolted to the chamber valve flange to hold the valve inside an ISO80F port.

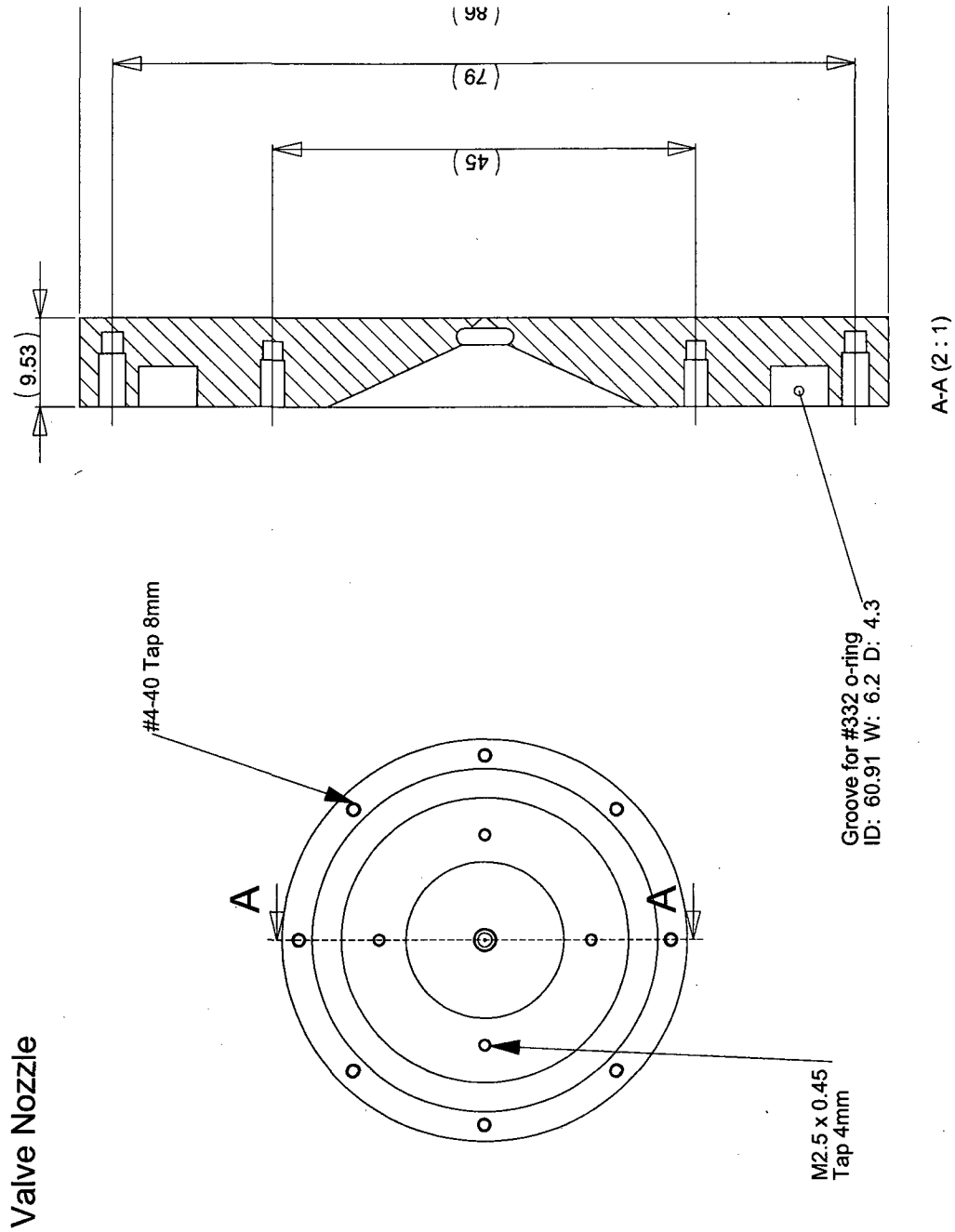

Figure B.2: Piezo valve nozzle (bolts to front of valve body). Inner bolt ring supports the piezo holder.

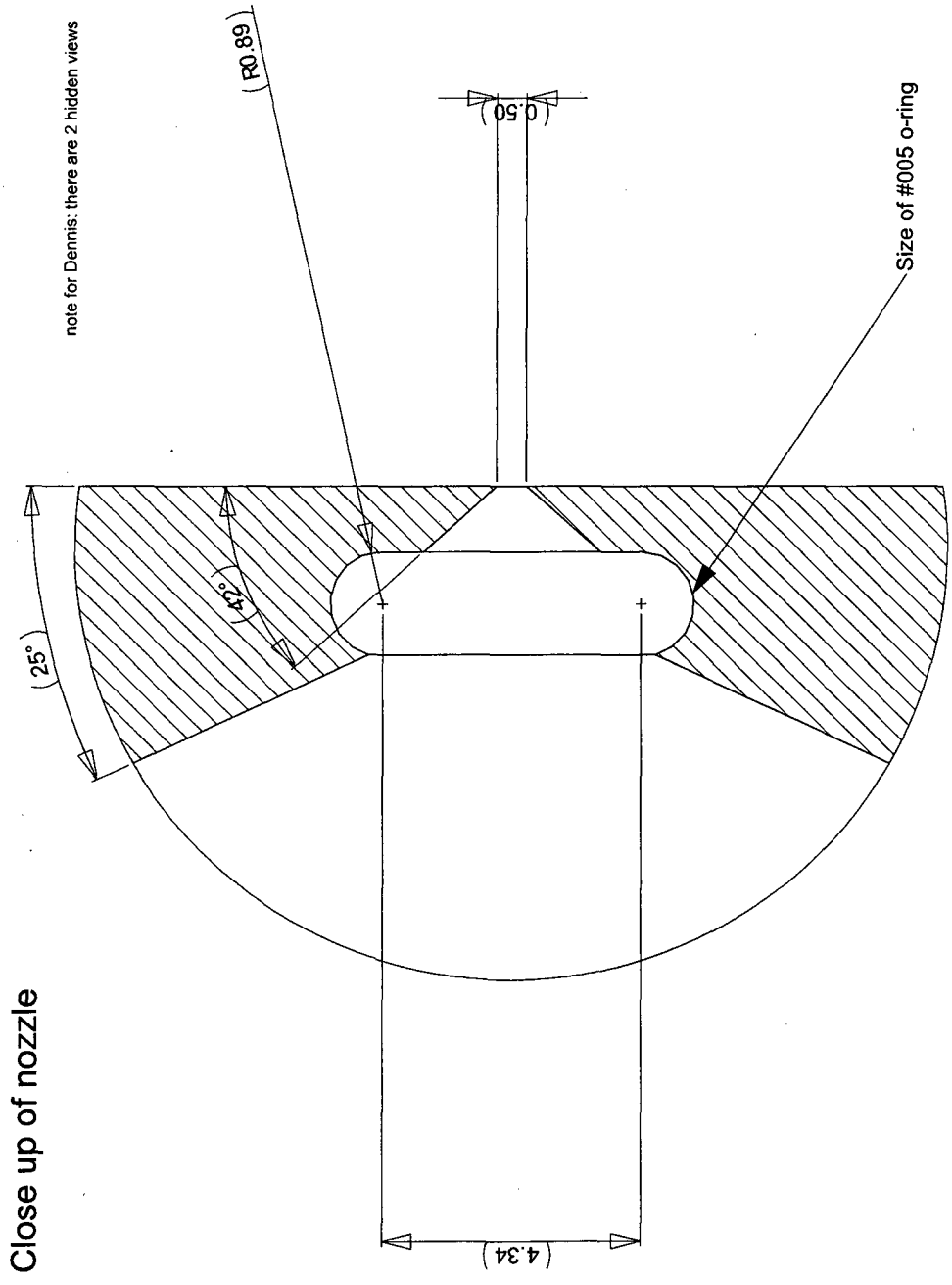
Close up of nozzle
note for Dennis: there are 2 hidden views
R0.89
0.50
Size of #005 o-ring
25°
47°
4.34

Figure B.3:

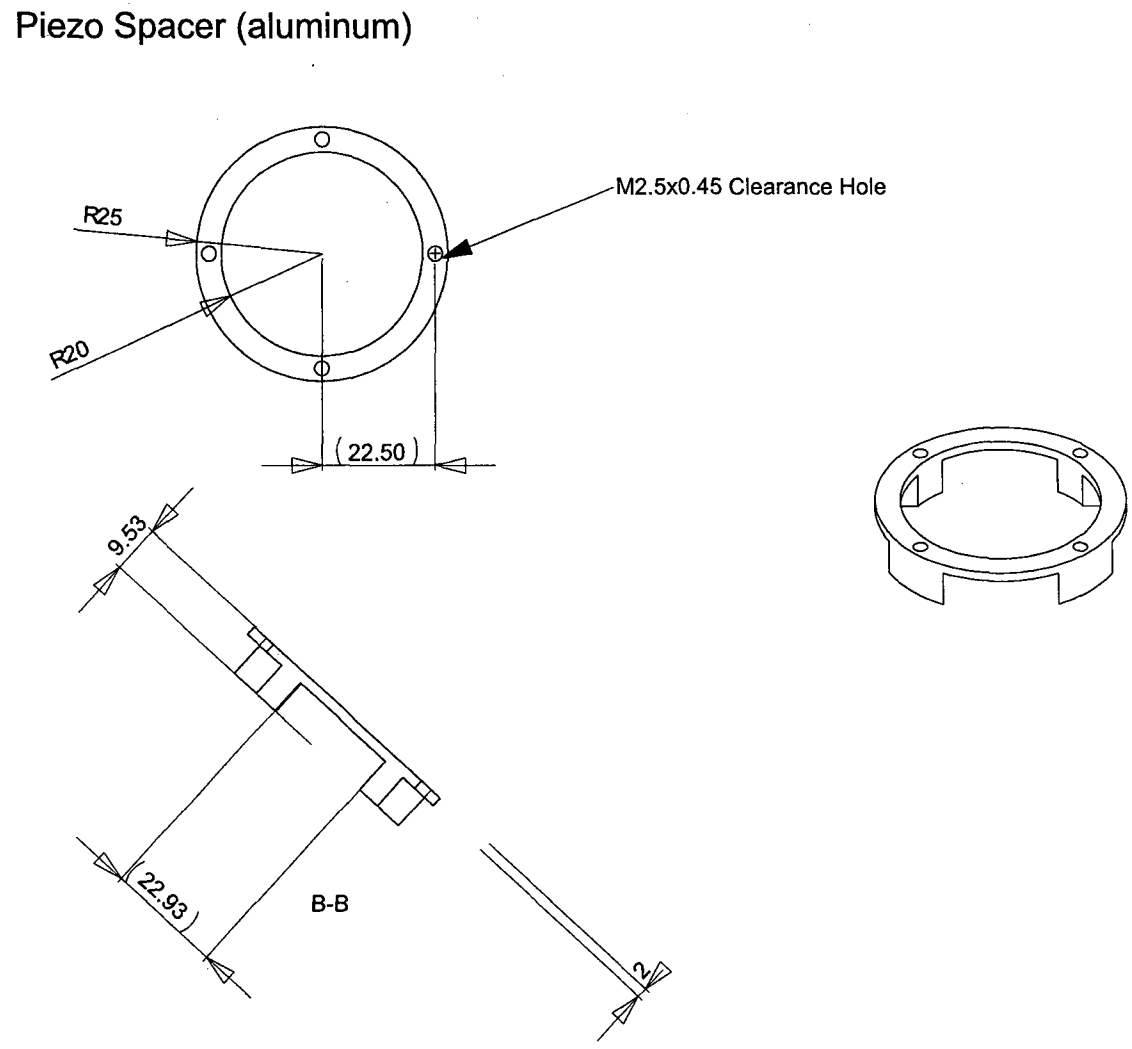

Figure B.4: The piezo spacer bolts to the nozzle, and supports the piezo element (Physik Instrumente P-286.20 disc translator).

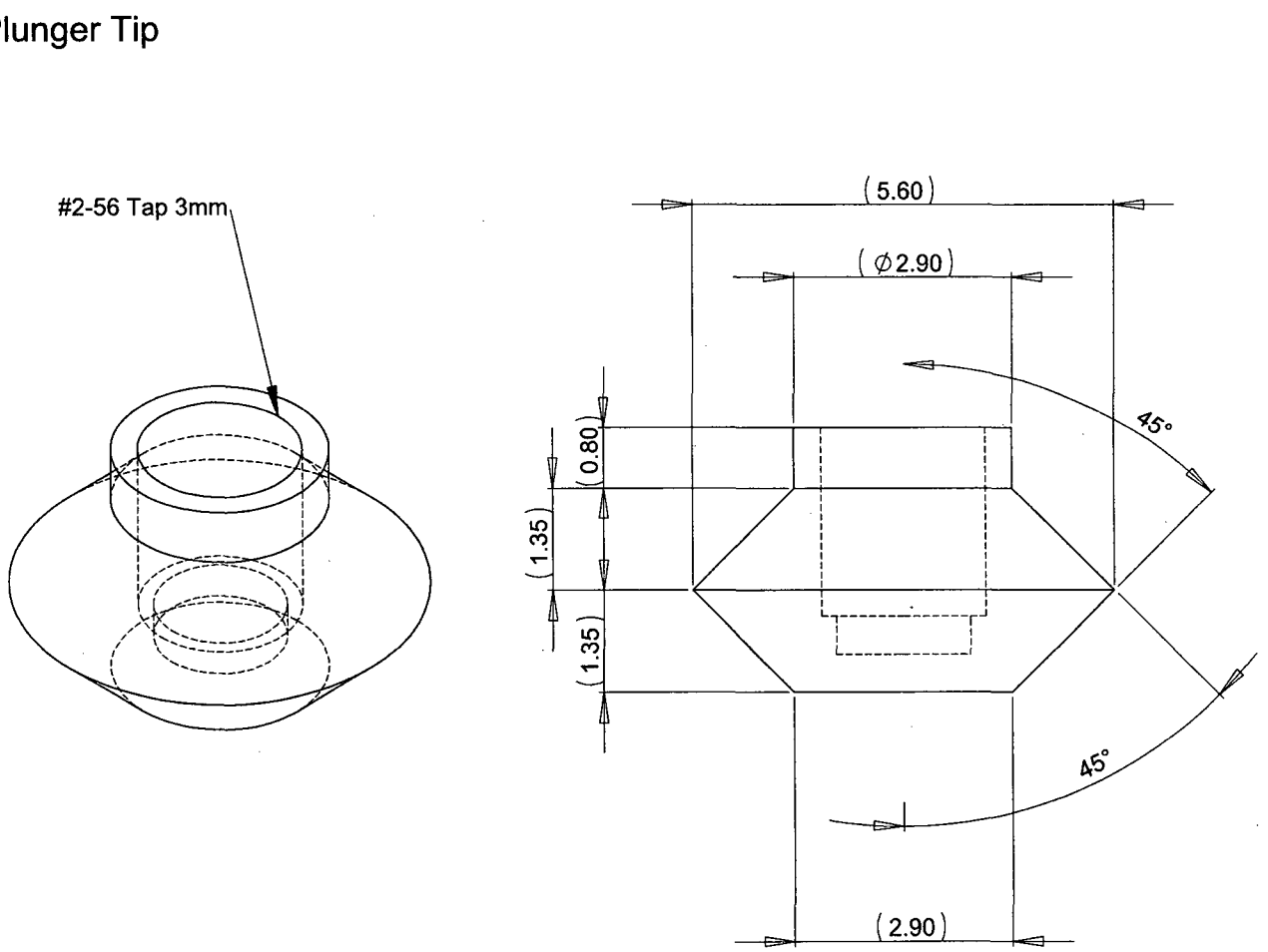

Figure B.5: The brass plunger tip is tapped for an M3 threaded rod, which connects it to the piezo element (which has a tapped M3 hole in its center).

Chamber-Valve Flange

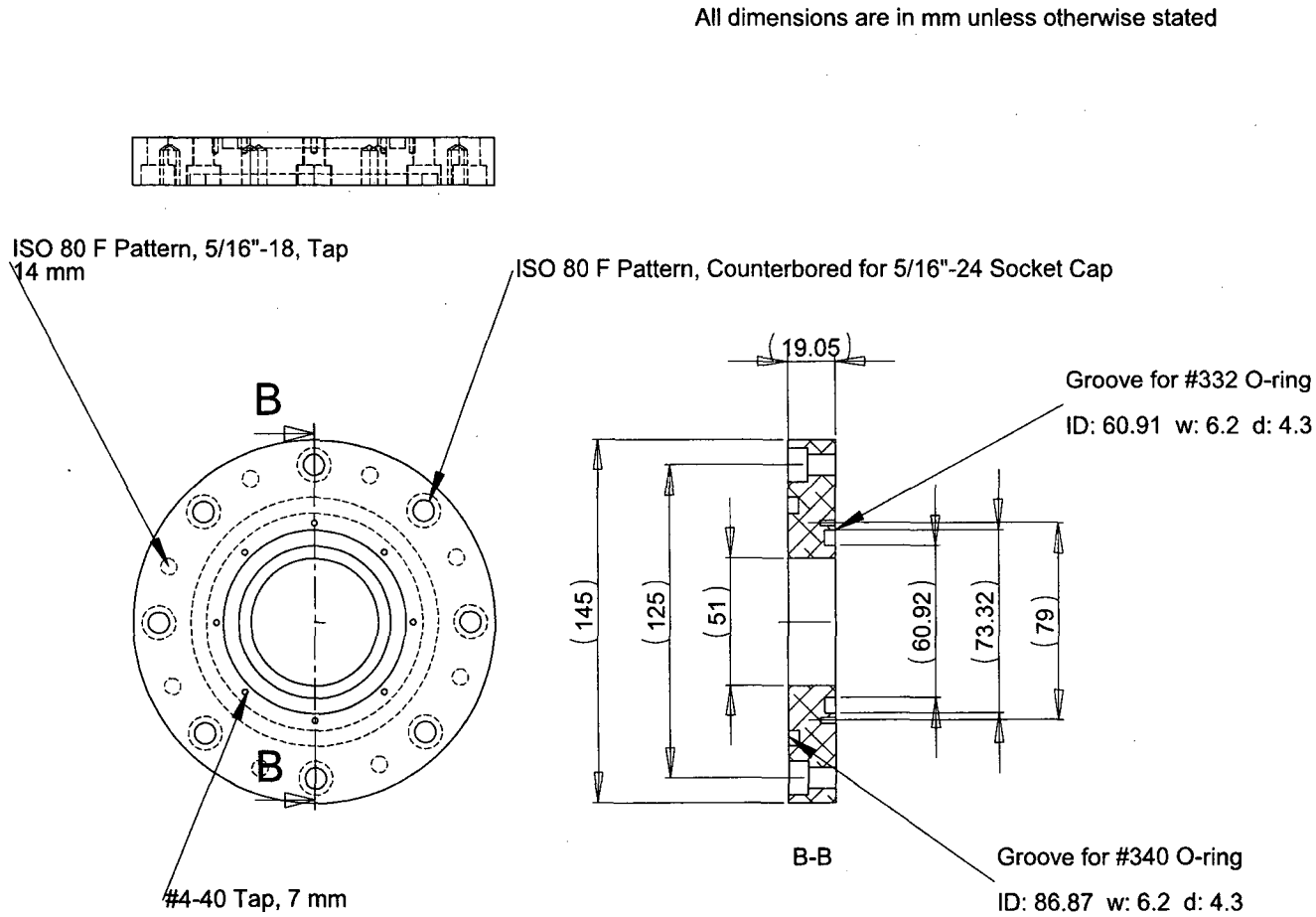

Figure B.6: The chamber valve flange mounts the valve assembly inside an ISO80F flange on the vacuum system.

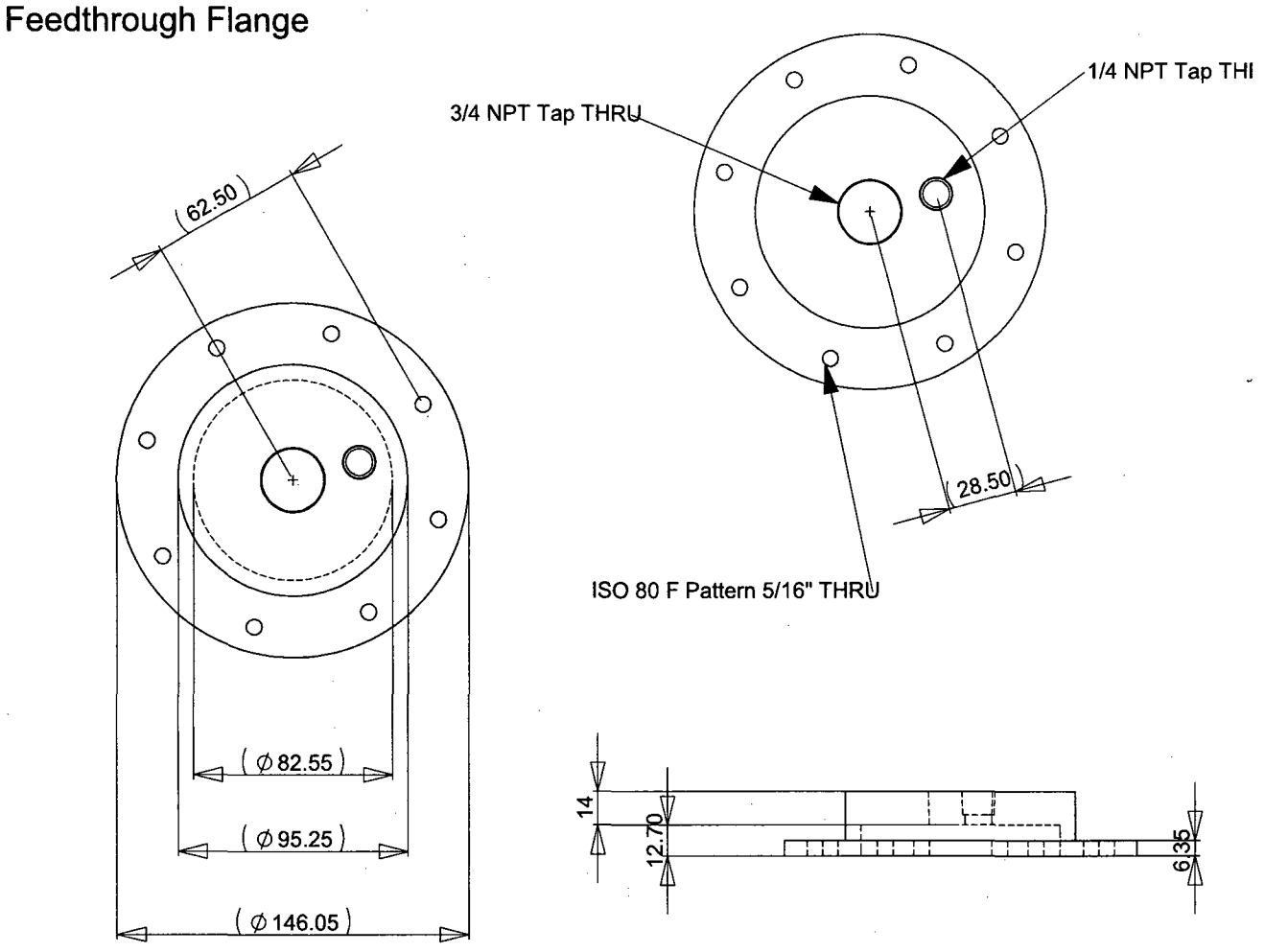

Figure B.7: The feedthrough flange mounts on the back of the chamber valve flange, and allows the electrical and gas connections to be made to the valve. The hole sizes (3/4 NPT, 1/4 NPT) may be changed to accommodate a specific choice of feedthroughs.

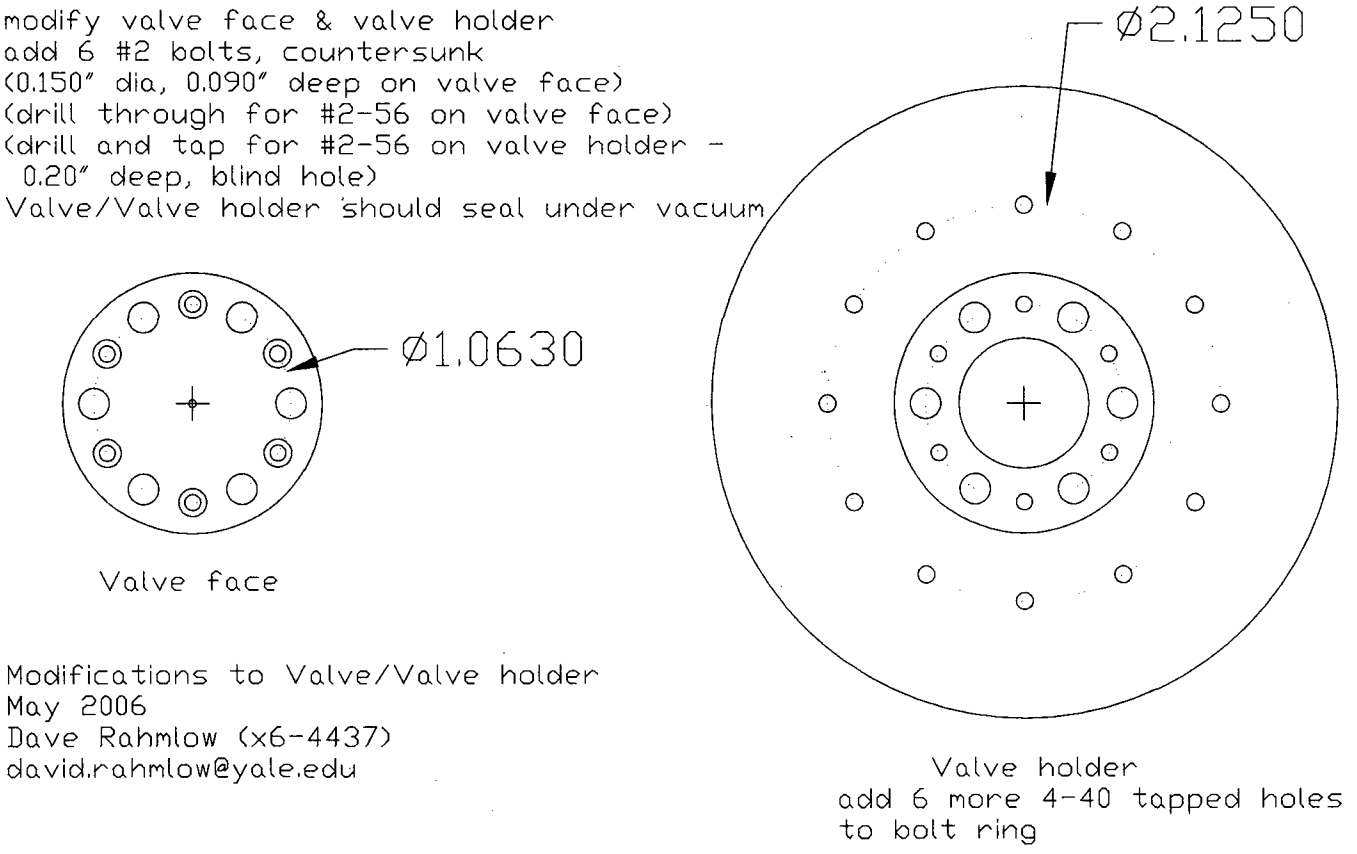

Figure B.8: Modifications to piezo valve face design that allow attachment of the Series 9/99 conflat-flanged solenoid valve to the valve body, in place of the piezo assembly.

B.2 Target

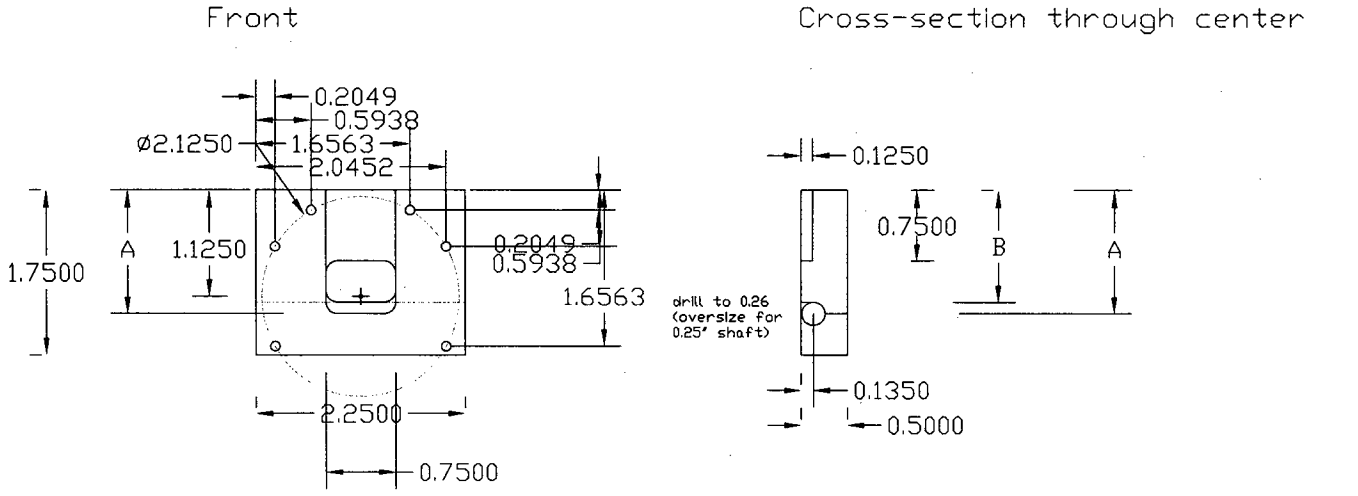

A	B
1.310	1.185
1.330	1.205
1.350	1.225
1.370	1.245
1.390	1.265

Teflon, 1/2" thick

Ba rod holder
April 2007
Dave Rahmlow
david.rahmlow@yale.edu (x6-4437)

5 parts listed on this page
make 1 ea with each choice of A,B

Fillet radius 0.125; tolerances +/- 0.010

Figure B.9: Teflon holder to support the barium rod assembly. This attaches to the front of the nozzle (nozzle position indicated by the tick mark in the center).

B.3 Vacuum System

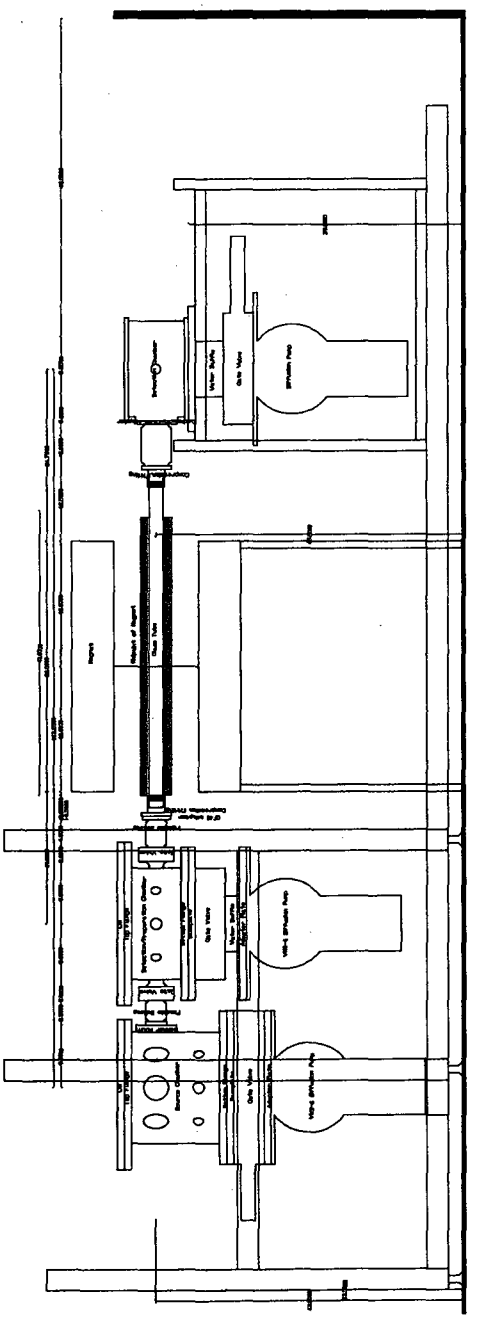

Figure B.10: Dimensions of entire system. The chambers (numbered 1 to 3, from left to right) have the following components: 1) Vacuum Research Corp. 16" ASA END-STD-16-N1 aluminum gate valve, Varian 336 water baffle, Varian VHS-6 diffusion pump, E2M125 mechanical pump; 2) Vacuum Research Corp. 6" ASA END-STD-6-N1 aluminum gate valve, Varian 336 water baffle, Varian VHS-6 diffusion pump; 3) CVC 6" aluminum gate valve, CVC BC-61 multi-coolant baffle, CVC PMC-6 diffusion pump, E2M40 mechanical pump (shared with chamber 2).

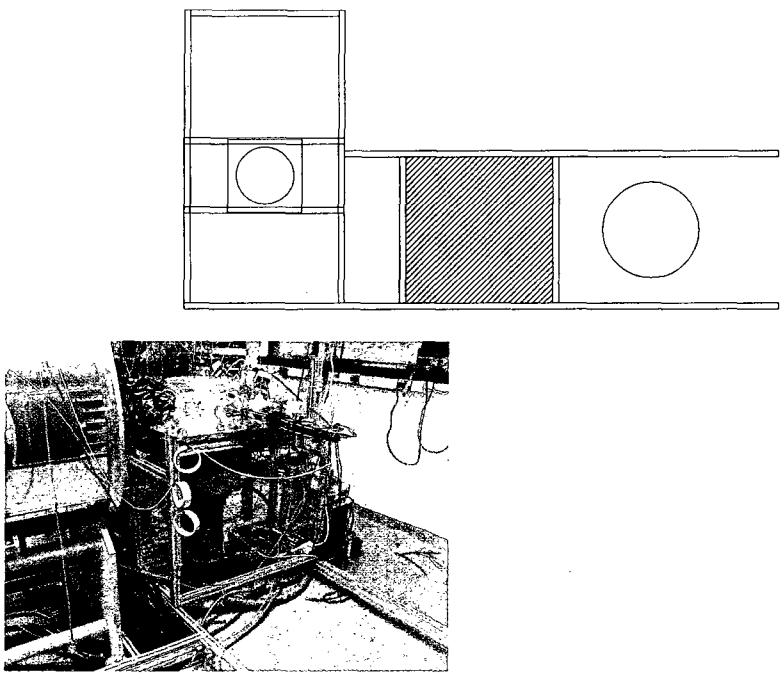

Figure B.11: Chamber 3 (state detection), mounted on cart in gray area at left, can be moved away from the magnet (hatched area) as shown for better access (eg. to remove the glass tube or the probe array).

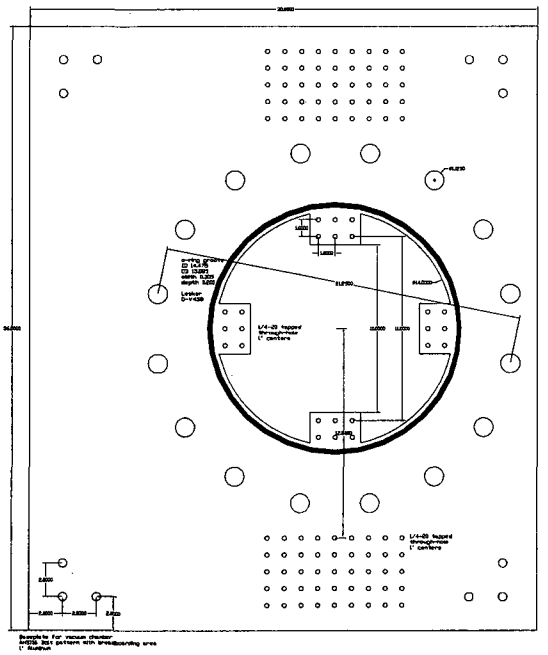

Figure B.12: Dimensioned drawing of baseplate for chamber 1 (beam source). The baseplate is designed to seal to an ASA16-flanged gate valve (mounted below the plate) and to an ASA16 flange on the bottom of the chamber body (sitting on the baseplate). Breadboard areas inside and outside the chamber allow fixtures to be mounted rigidly. Height and tilt can be adjusted by supporting the baseplate through the holes at the corners with threaded rod and hex nuts.

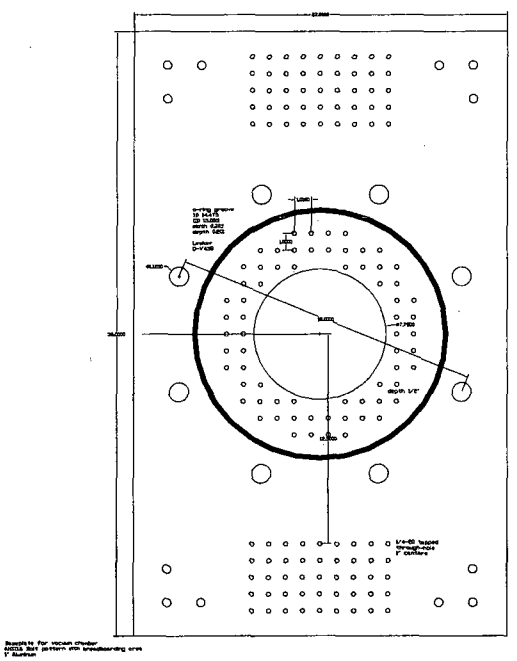

Figure B.13: Dimensioned drawing of baseplate for chamber 2 (state preparation and detection). The baseplate is designed to seal to a flange on the chamber body (sitting on the baseplate), with an aluminum plate below to press a 6" baffle against the bottom of the baseplate and support a 6" diffusion pump.

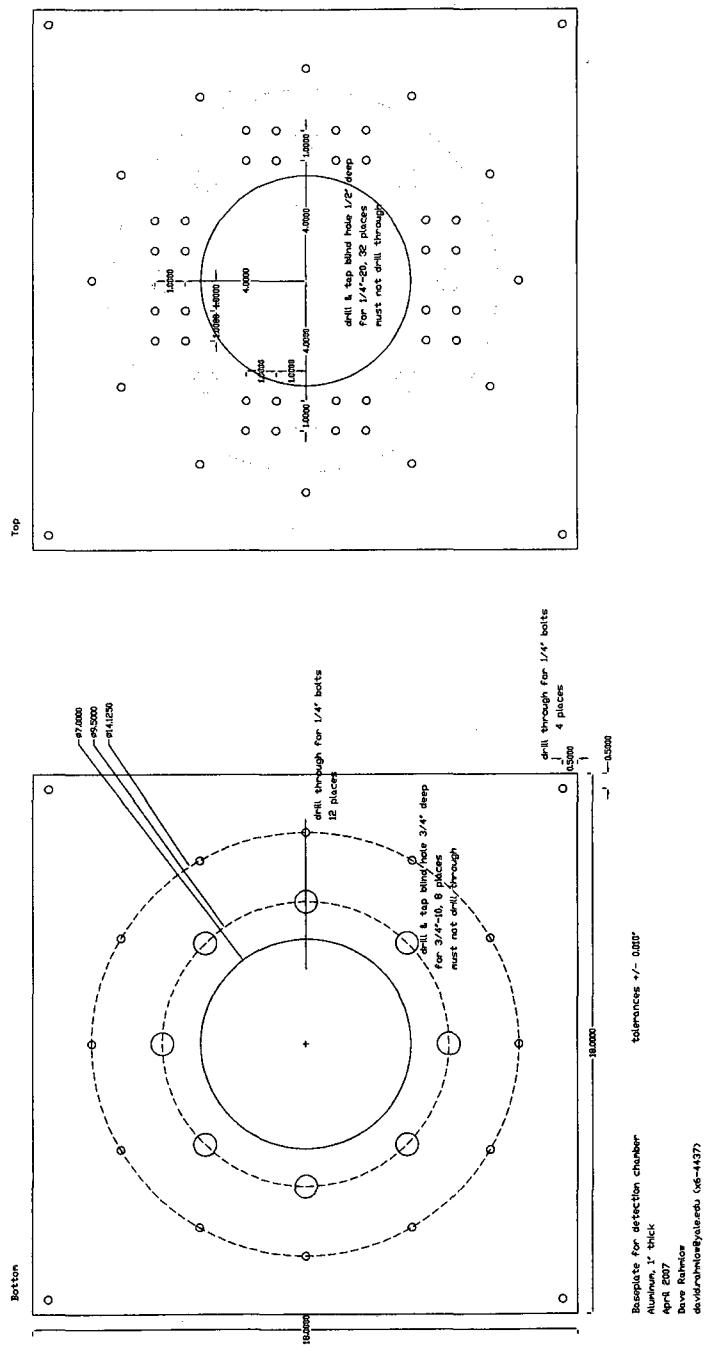

Figure B.14: Baseplate for chamber 3 (state detection).

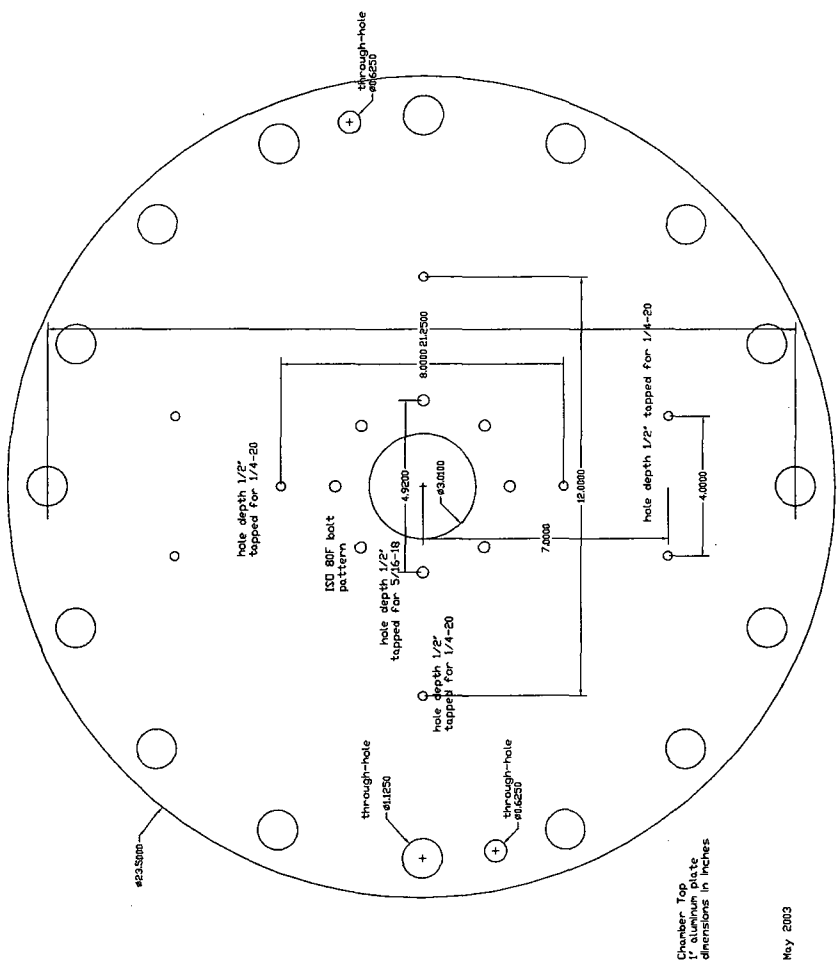

Figure B.15: Chamber lid. A vertical rod mounted through the 0.625" through hole allows the lid to be swung to the side for access to the chamber. Additional tapped holes are available to mount any necessary fixtures.

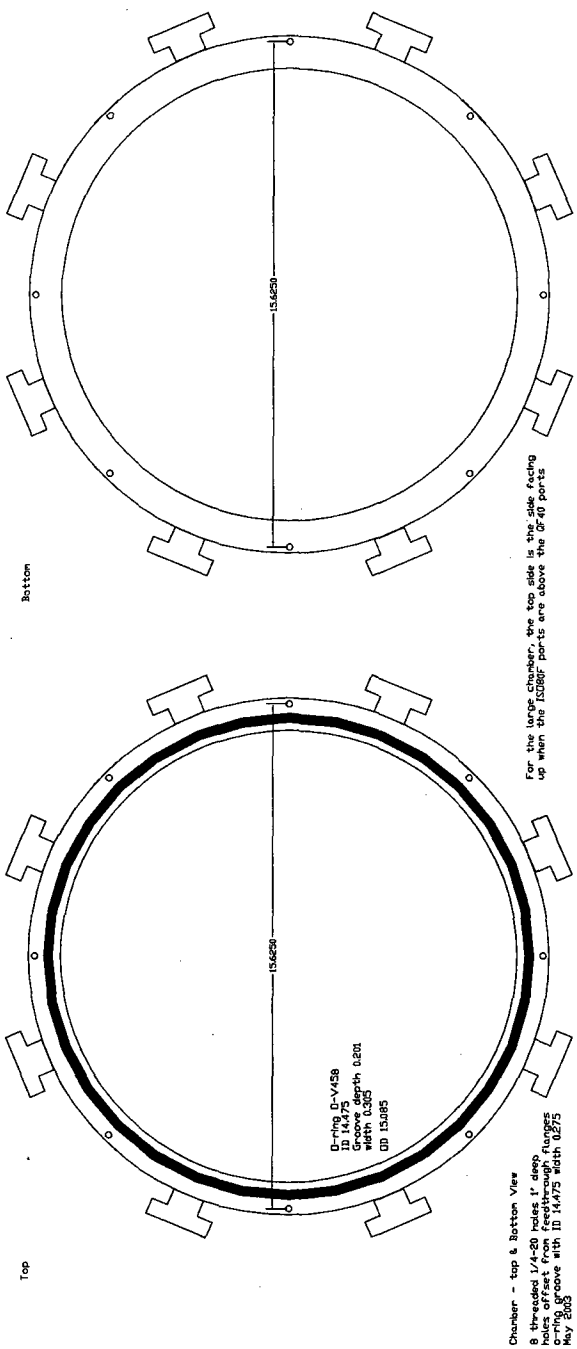

Figure B.16: Top and bottom views of the body of chambers 1 and 2. These chambers were adapted from spare parts from the PbO experiment.

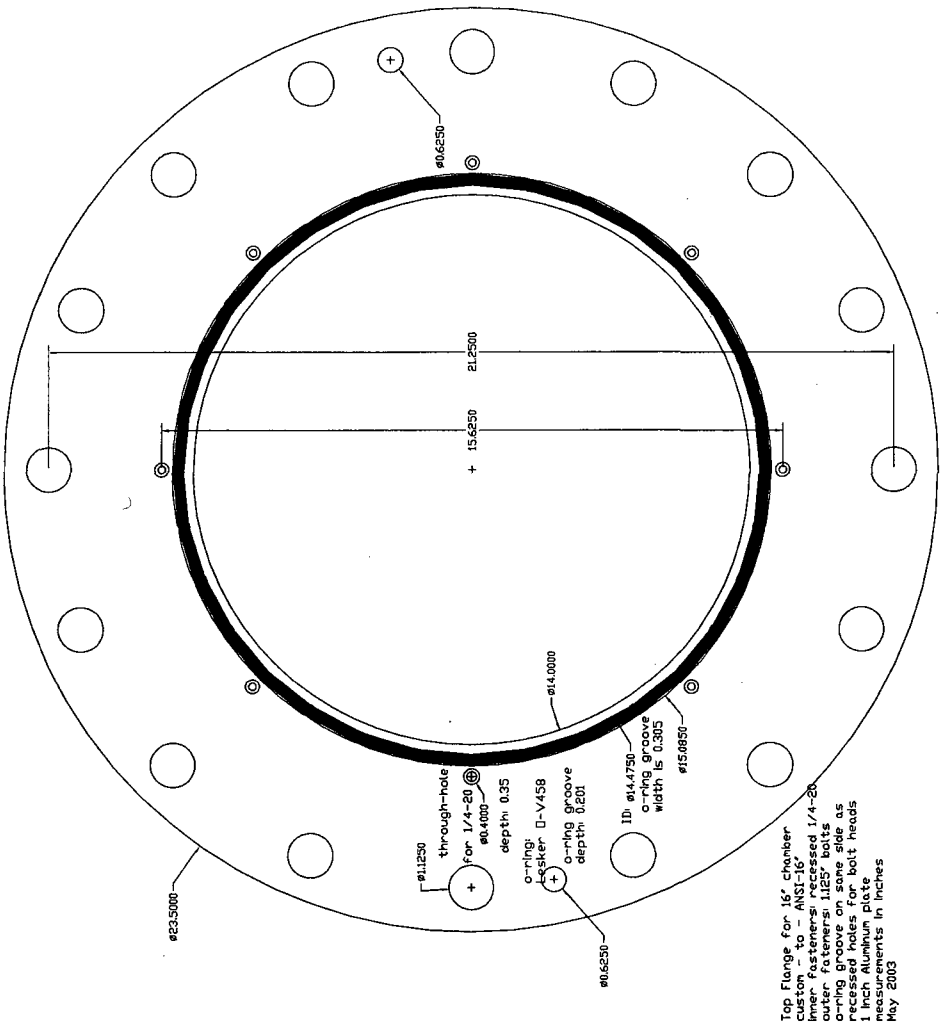

Figure B.17: Chamber top flange. Chambers 1 and 2 have a 14" inner diameter and 16" outer diameter with tapped 1/4" – 20 holes on the top and bottom. This converts the chamber to sit on an ASA16 flange.

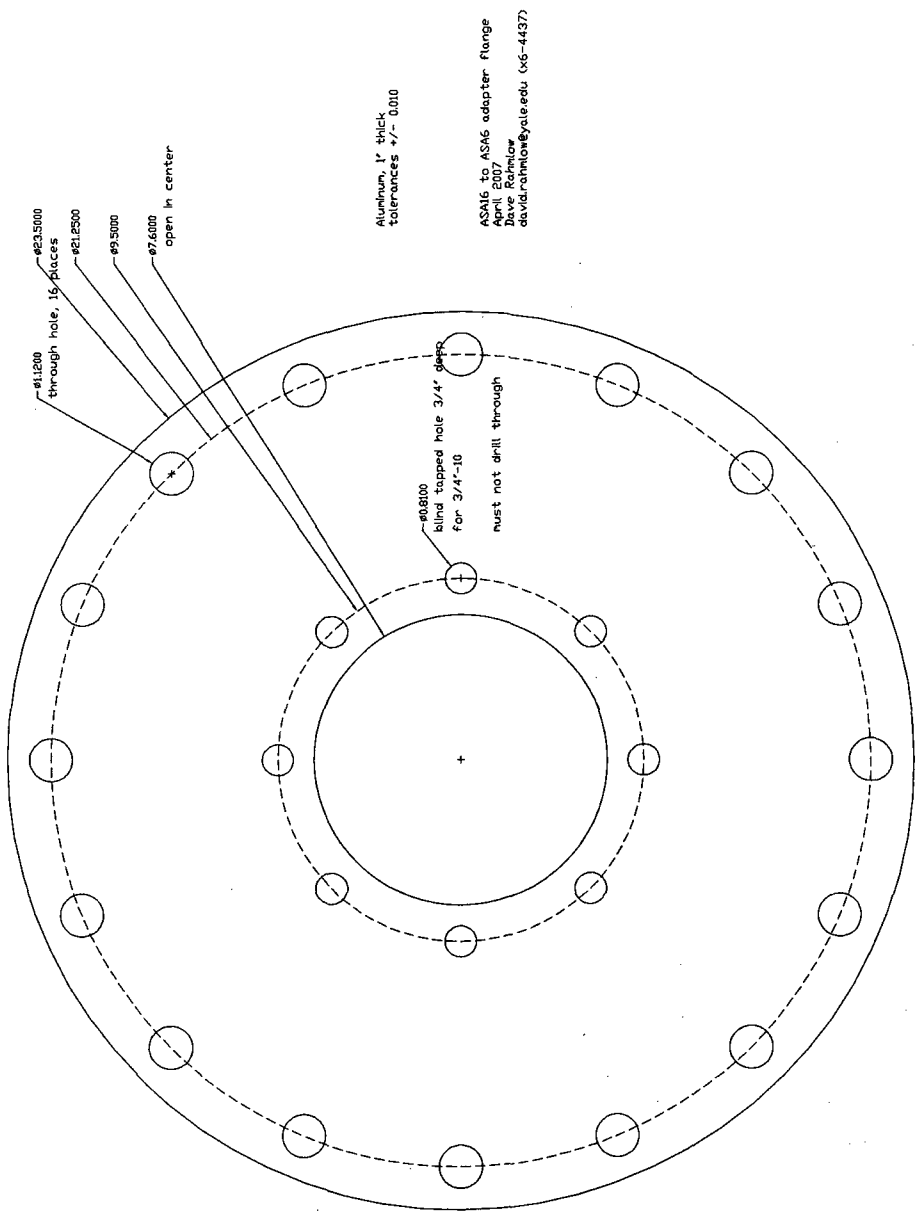

Figure B.18: ASA16 to ASA6 adapter flange, used to hold a 6" diffusion pump on the 16" gate valve on chamber 1.

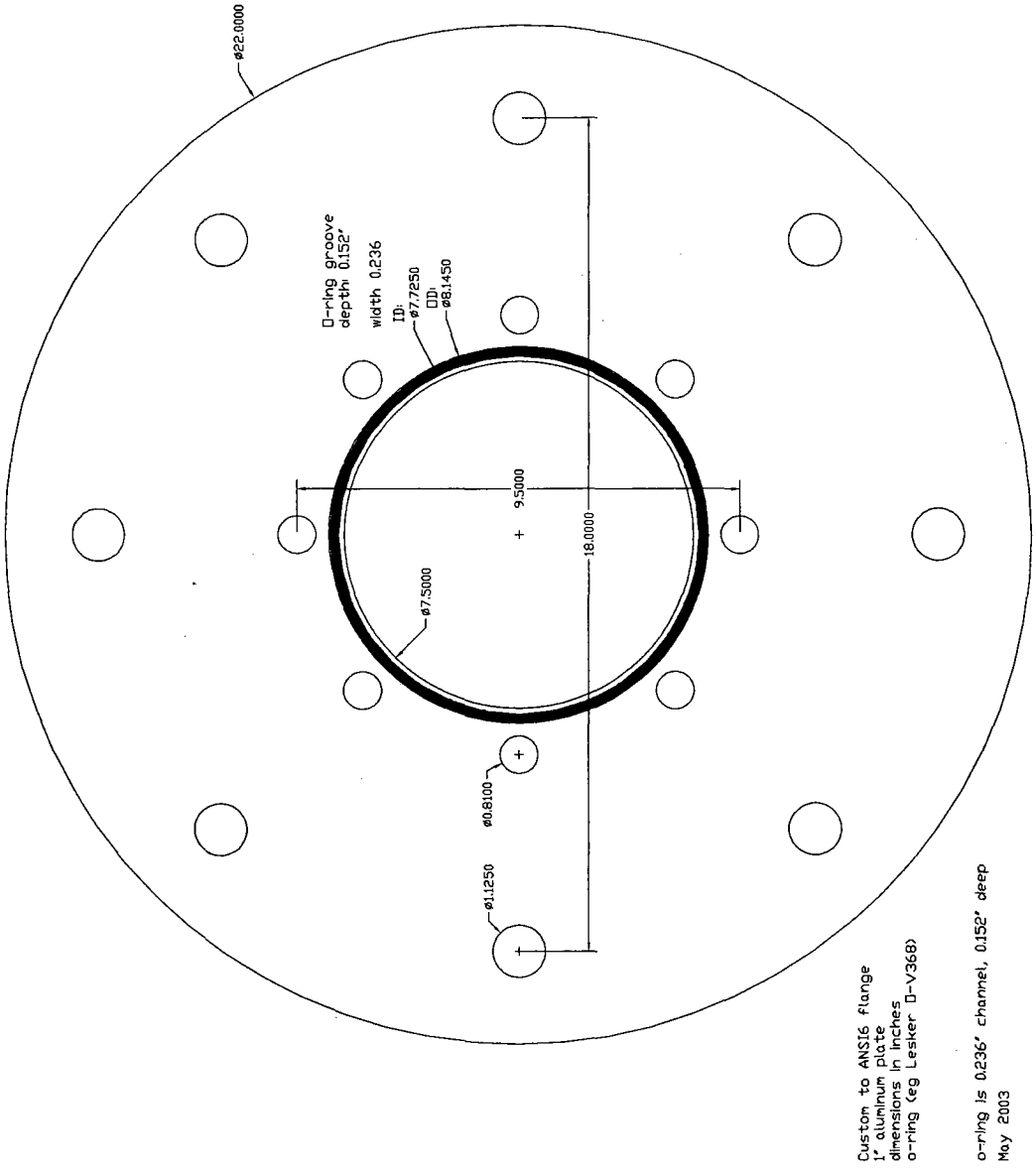

Figure B.19: ASA6 holder to attach a 6" diffusion pump and water baffle below chamber 2.

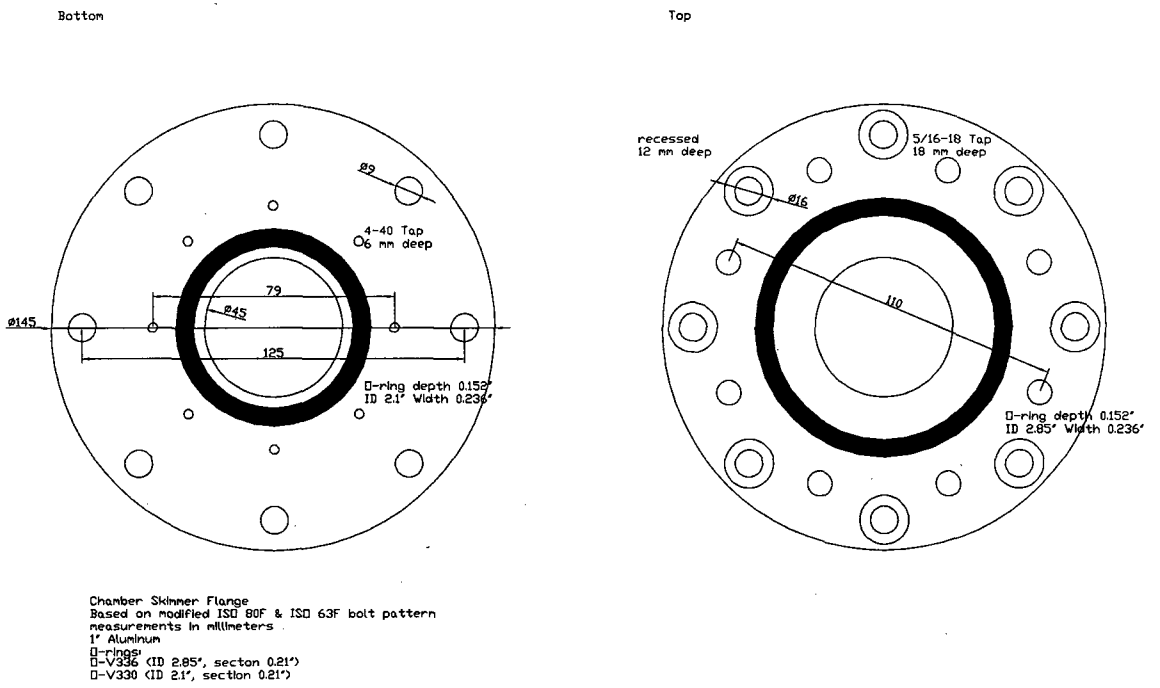

Figure B.20: The skimmer flange mounts on the ISO80 port on the back of chamber 1, opposite the nozzle. It provides a point on which to mount the skimmer holder. An ISO63 flexible bellows can be attached to the back to allow connection to chamber 2.

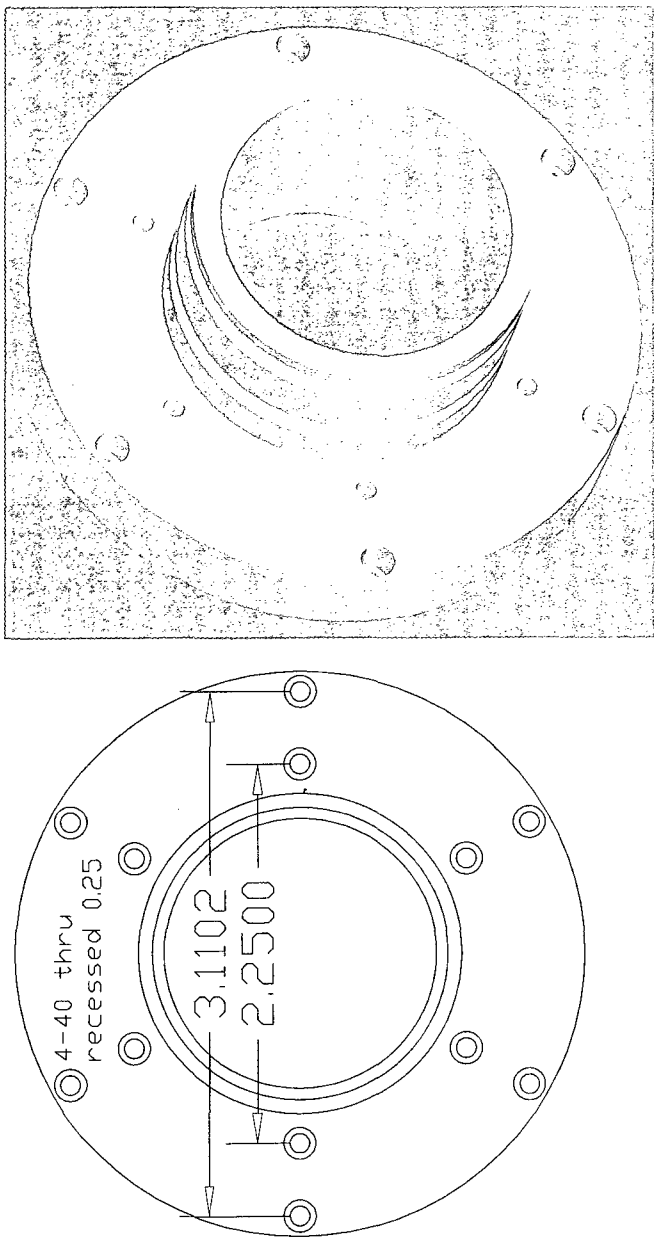

Figure B.21: The first part of the skimmer holder mounts to the inside wall of the skimmer flange mount on the back of chamber 1. This part supports a rigid tube that attaches to the second part of the skimmer holder. The length of the tube determines the distance between the source and the skimmer.

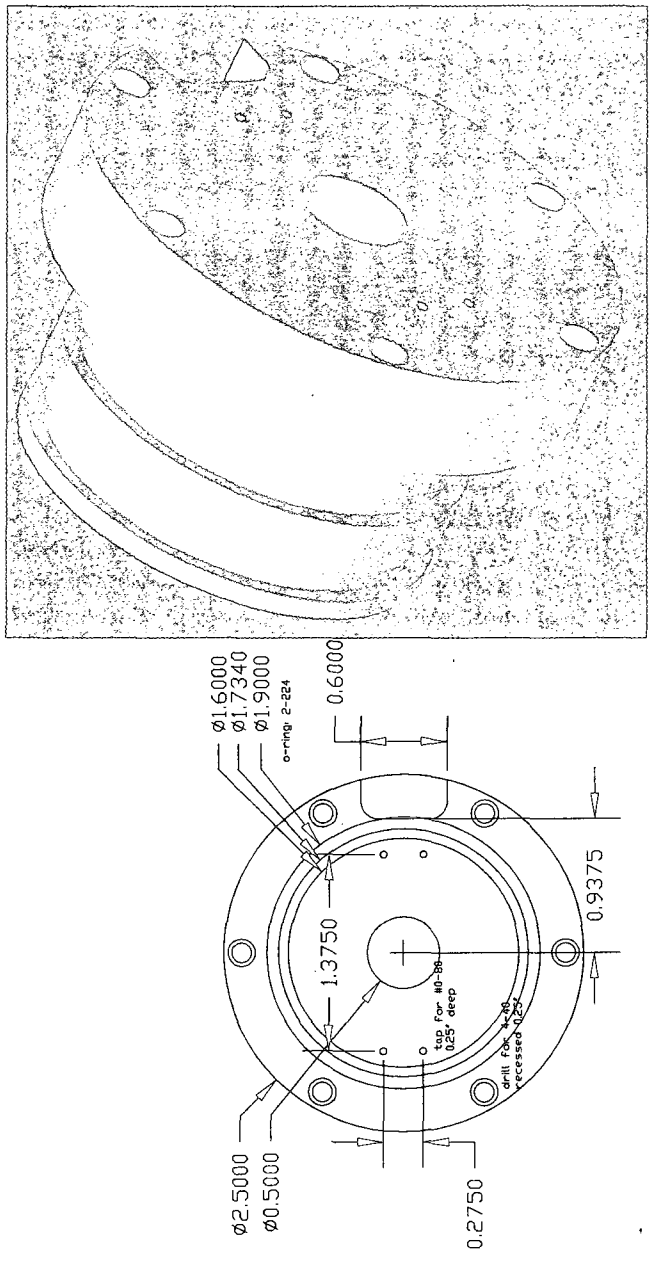

Figure B.22: The skimmer is mounted on the front of this part of the skimmer holder. The back of this holder fits inside a tube mounted on the back of the chamber; the length of the tube determines the distance between the source and the skimmer. The skimmer can either be directly mounted to the front of this holder, or attached to a stage mounted on the four small bolt holes (Edmund Optics #38-532).

B.4 Interaction Region

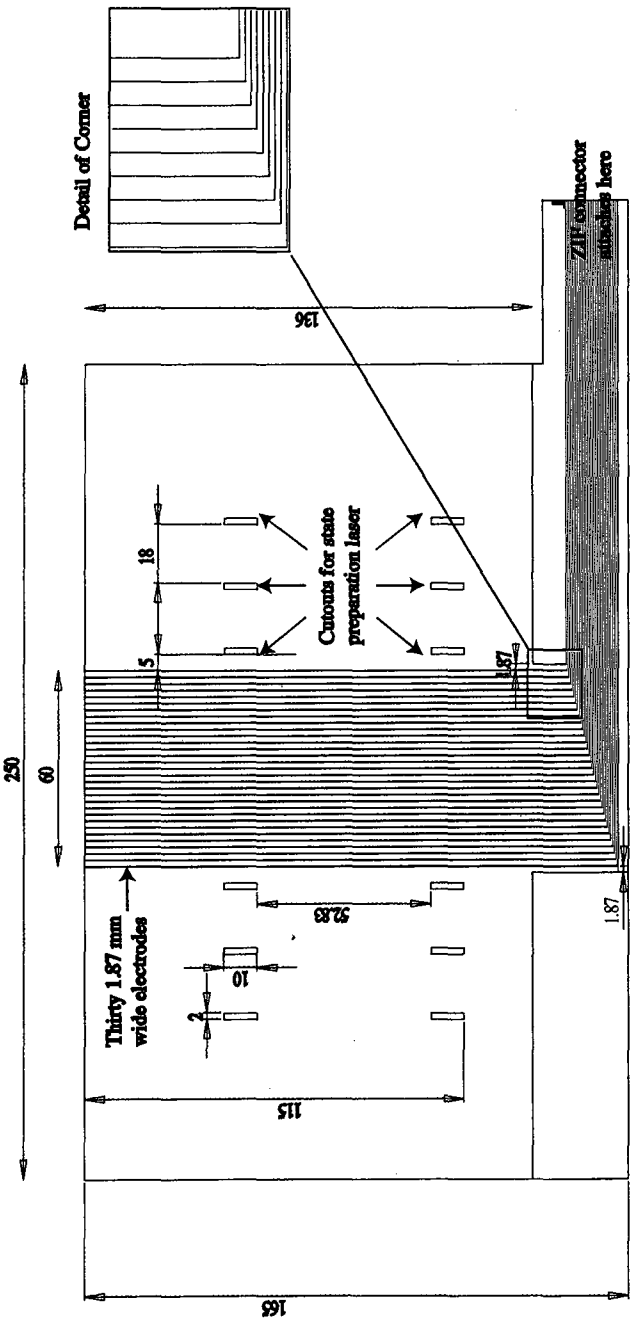

Figure B.23: Interaction region flexible circuit board

B.5 Magnet Region

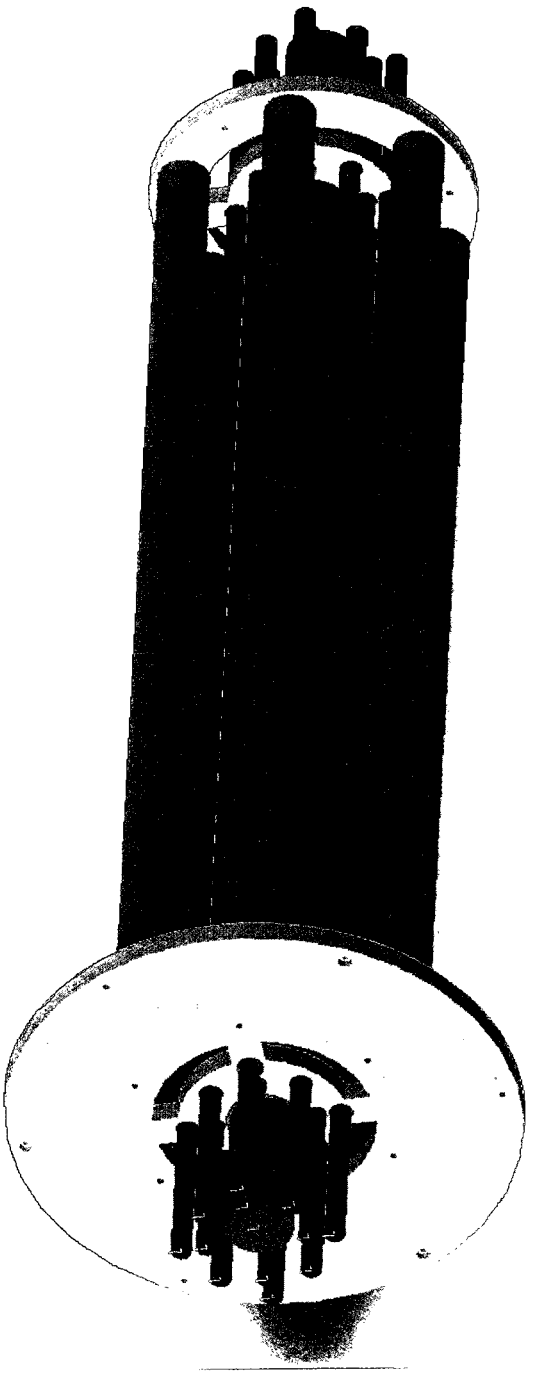

Figure B.24: 3-D view of the probe array holder inside the magnet. The green cylinders are strucutral supports (aluminum rods, 1.5" in diameter, 36.5" long, with a #10-32 tapped hole on each end). The red cylinder is the glass tube (part of the vacuum system); the blue cylinders are water-filled glass tubes which hold the individual NMR probes.

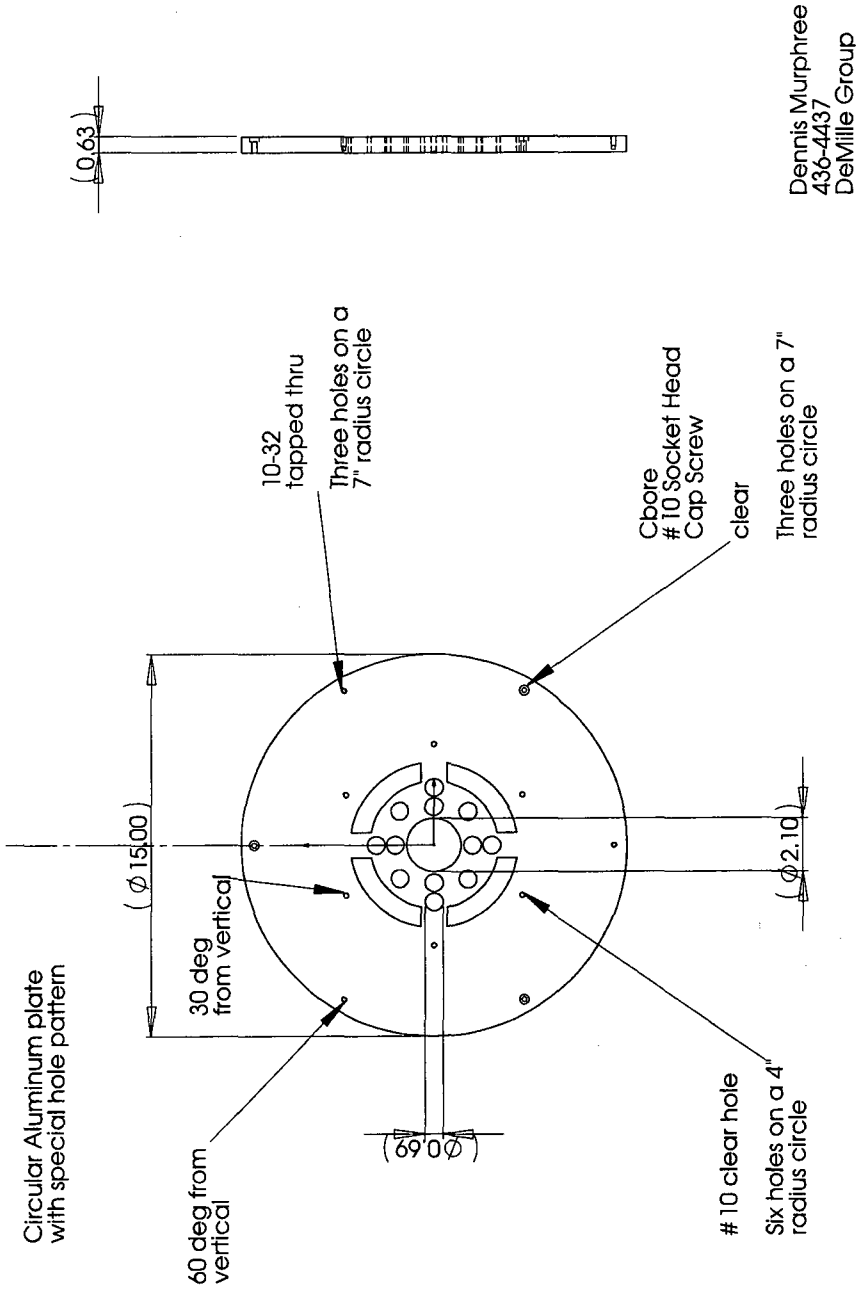

Figure B.25: End plate which supports the probe array; this plate has

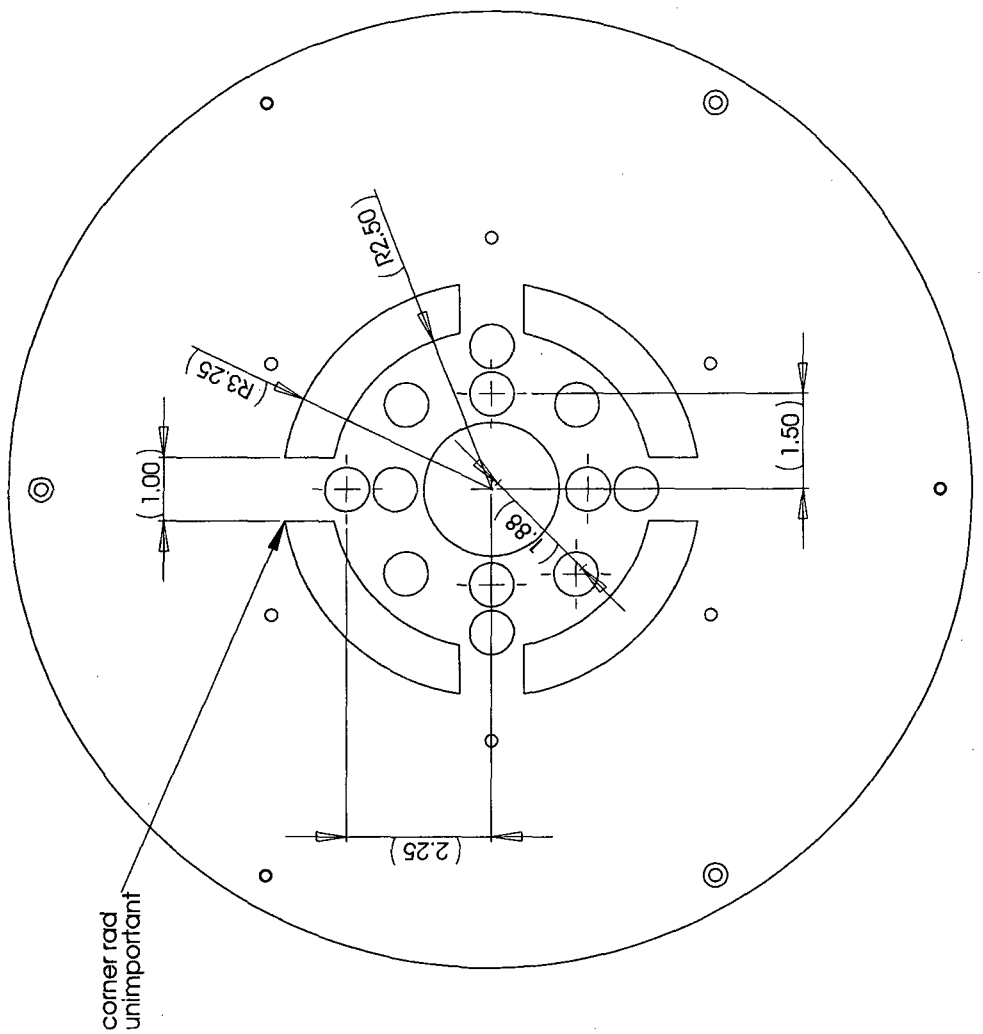

Figure B.26: Additional dimensions for first end plate

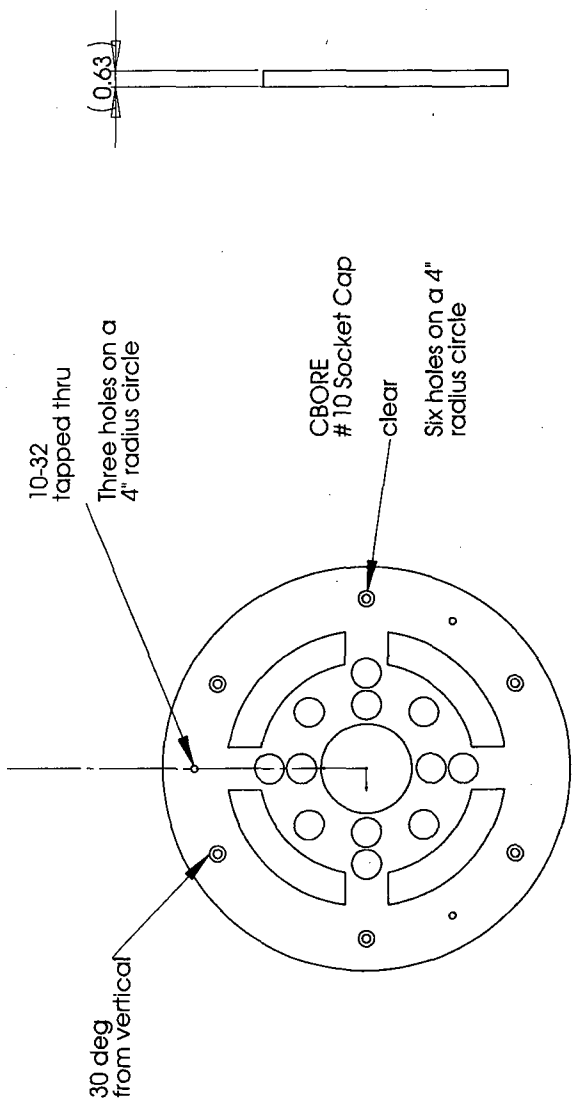

Dimensions are identical to Base Part 1 except that the OD of the entire piece is 9.50" instead of 15.00". The hole pattern differs as noted.

Figure B.27: Other end plate to support probe array; this is sized to fit inside the bore of the room temperature shim coils.

B.6 Light Collection Optics

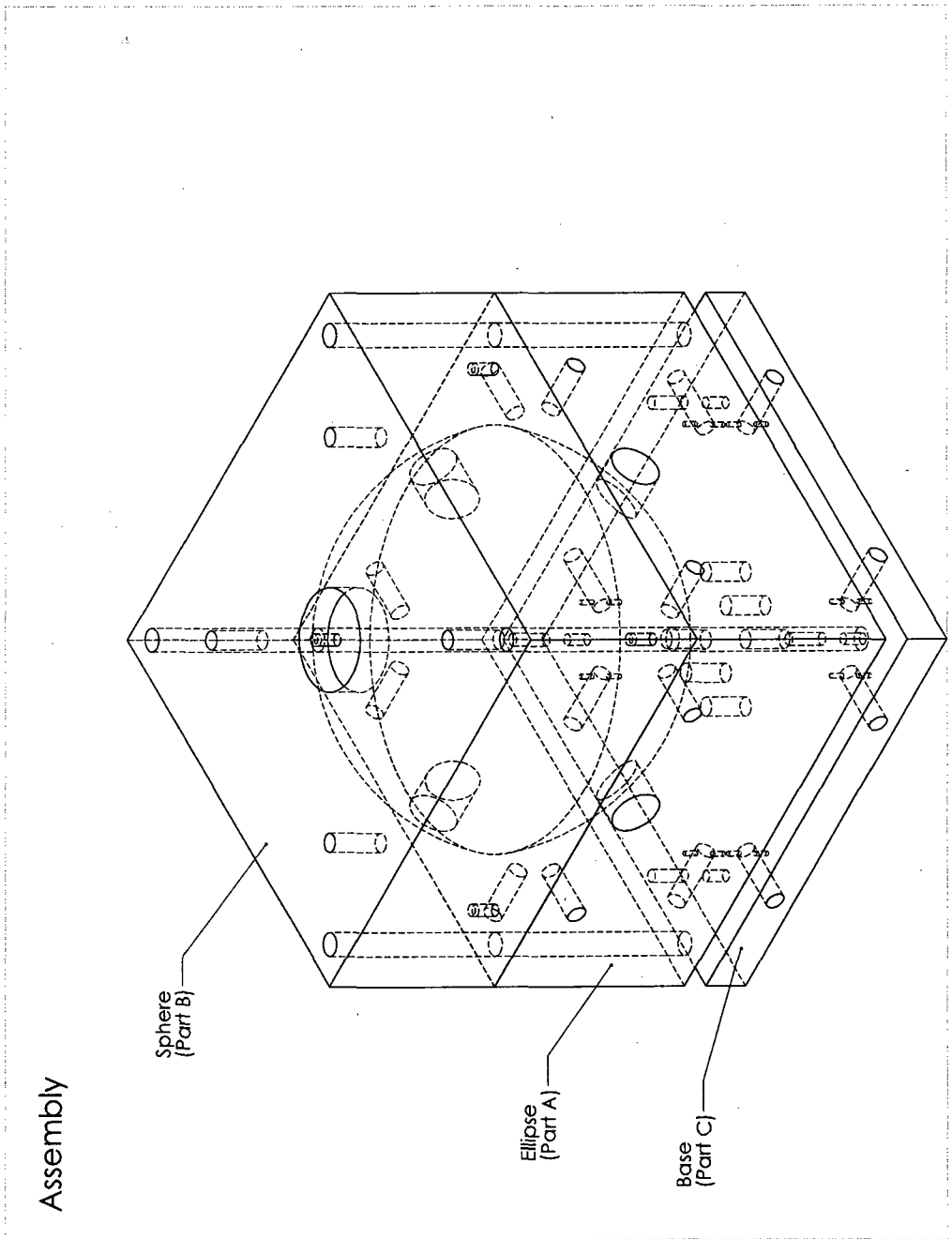

Figure B.28: Blue light collection optics assembly, 3-D view.

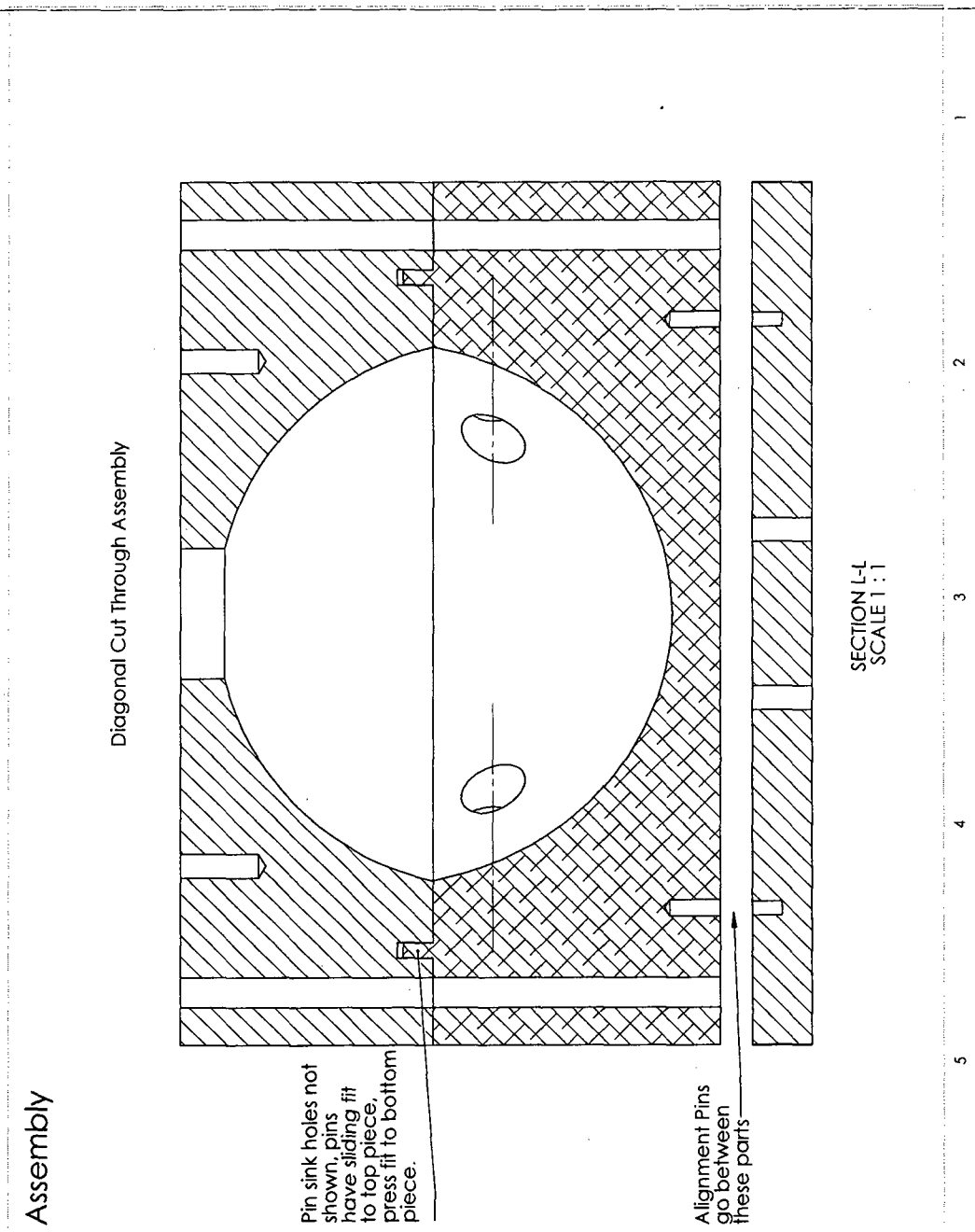

Figure B.29: Blue light collection optics assembly, cross-sectional view.

For Upper Mirror:

The blue markings are 8-32 clearance holes, drilled through and centered ~.25 inches from any side.

For Lower Mirror:

The ellipse has major axis 1.526 inches, minor axis 1.398 inches, and is centered above the center of the block, .374 inches above the top. Or: eccentricity .4, focal length 1.220 inches.

The green markings are ¼-20 tapped holes, centered ~.5 inches from the bottom and ~.7 inches from each edge, going ~.3 inches deep.

The blue markings are 8-32 tapped holes, ~.25 inches from any side and drilled through. The holes only need to be tapped to ~.3 inches.

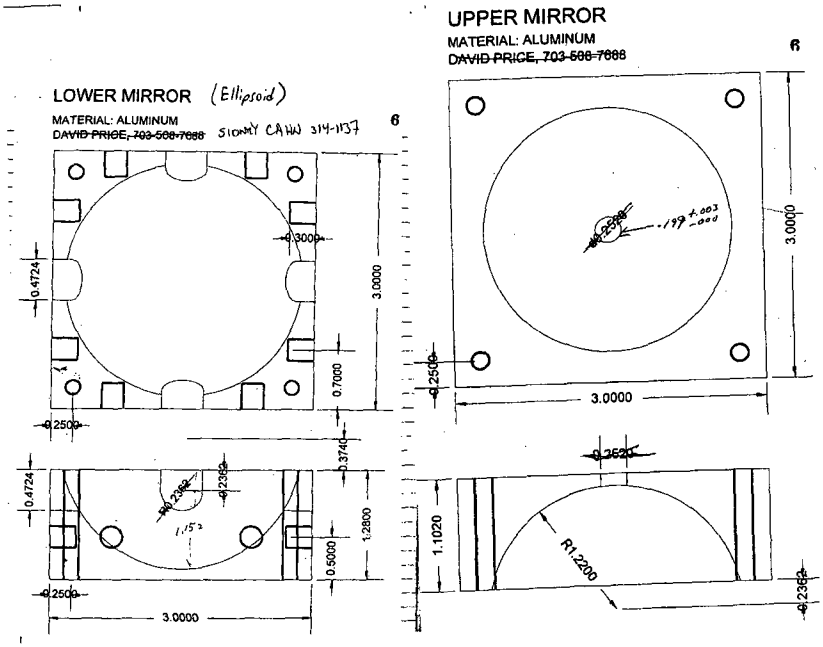

Figure B.30: Light collection optics for 860 nm (5 mm lightguide).

Appendix C

Electronics

C.1 Solenoid valve control

C.2 Micrometer driver

A simple motorized micrometer driver (designed for Thorlabs Z600 series actuators) was designed for the project. The Z600 actuator has a DC motor with isolated leads, and a four-step optical encoder and limit switches for motion feedback. While the motor is designed for 12 volt operation with low current draw (tens of milliamps), it will run on 5 volts from a digital logic output. We can design a simple microcontroller based circuit to control the actuator. The microcontroller counts the number of steps traveled to keep track of relative positions, as well as the positions of the absolute limits (if encountered). In addition to forward/backward/go-to operation, a "sweep" mode of operation repeatedly moves the actuator between two preset positions. The microcontroller supports a computer interface over RS232.

The firmware and board layout used, as well as a short operating manual,

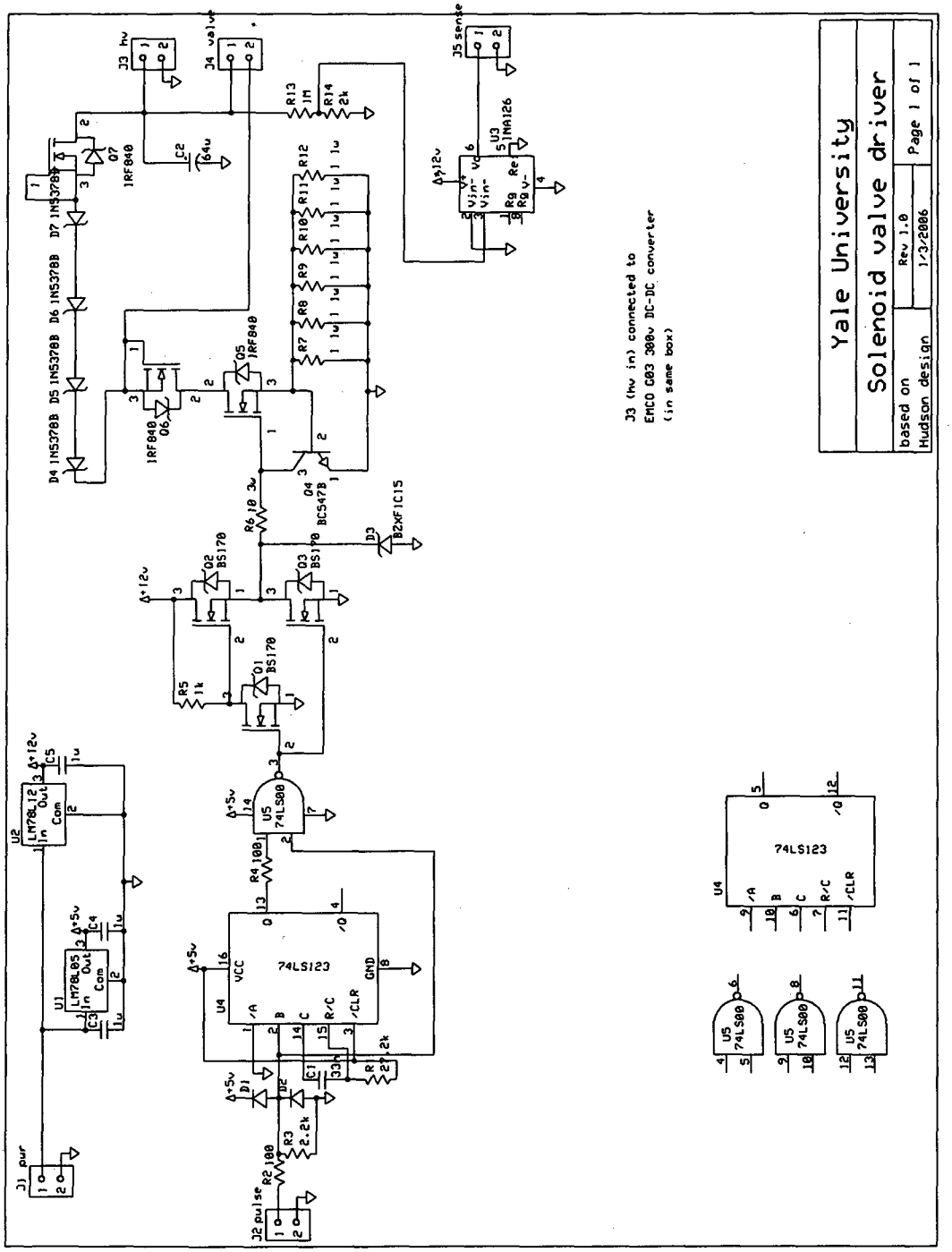

Figure C.1: Solenoid valve driver, based on Hudson design

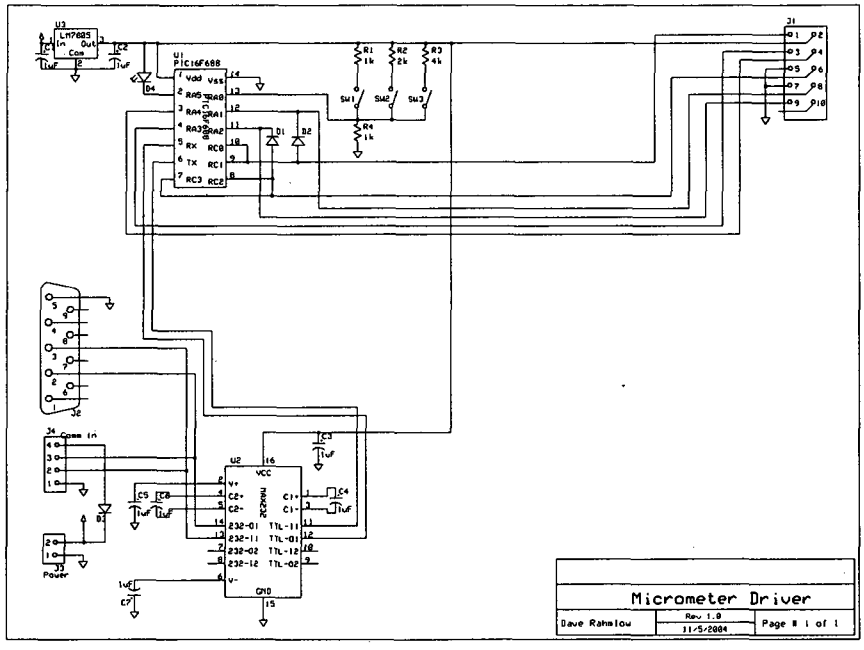

Figure C.2: Micrometer driver schematic. A sample PCB layout in ExpressPCB format is included as `micrometerdriver.pcb`

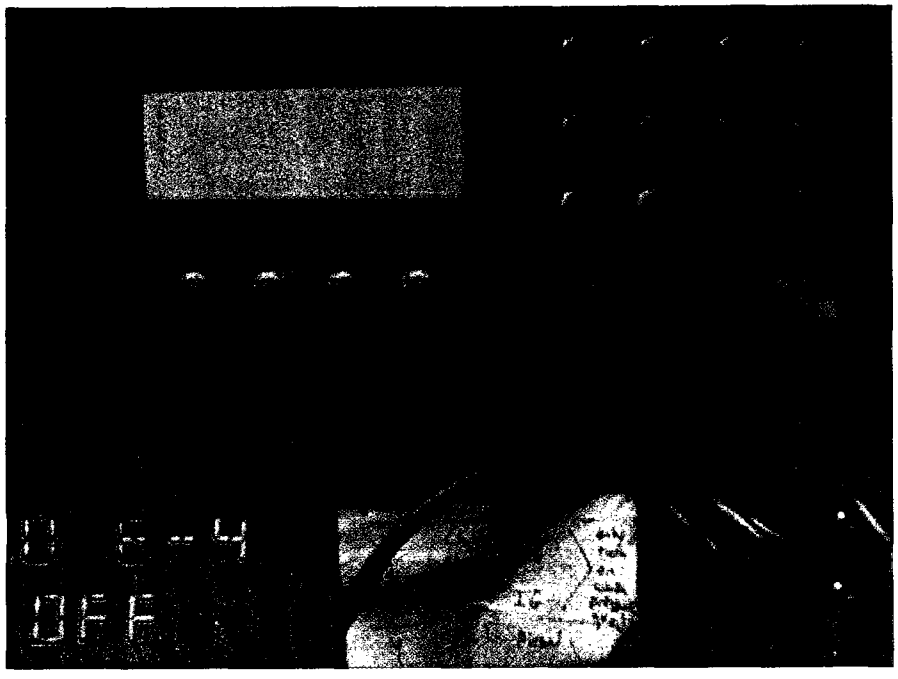

Figure C.3: The front panel of the PLC.

are included in the accompanying files in the "micrometerdriver" directory.

C.3 Ladder Logic

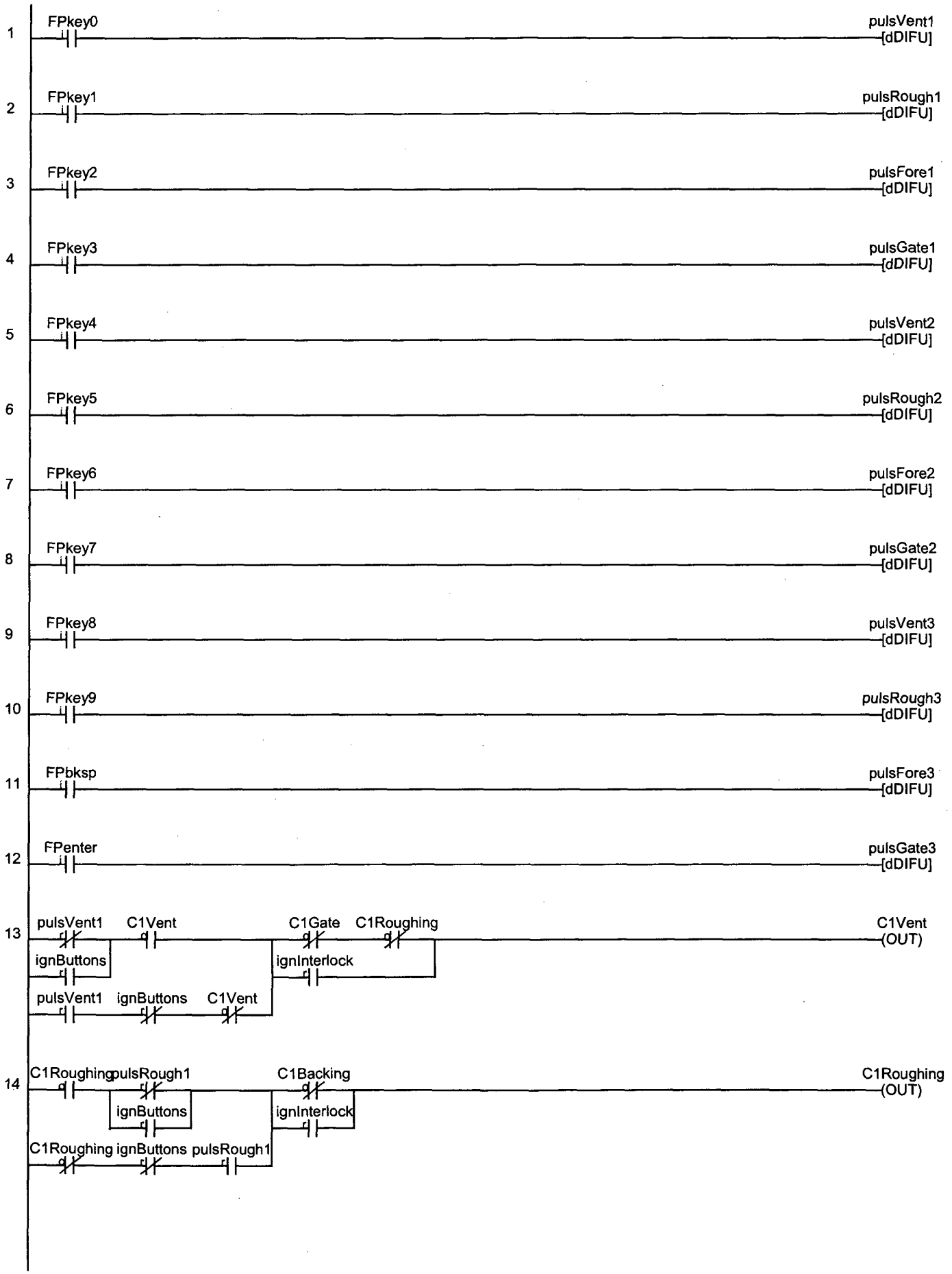
1
FPkey0
pulsVent1
[dDIFU]
2
FPkey1
pulsRough1
[dDIFU]
3
FPkey2
pulsFore1
[dDIFU]
4
FPkey3
pulsGate1
[dDIFU]
5
FPkey4
pulsVent2
[dDIFU]
6
FPkey5
pulsRough2
[dDIFU]
7
FPkey6
pulsFore2
[dDIFU]
8
FPkey7
pulsGate2
[dDIFU]
9
FPkey8
pulsVent3
[dDIFU]
10
FPkey9
pulsRough3
[dDIFU]
11
FPbksp
pulsFore3
[dDIFU]
12
FPenter
pulsGate3
[dDIFU]
13
pulsVent1
C1Vent
C1Gate
C1Roughing
C1Vent
(OUT)
ignButtons
ignInterlock
pulsVent1
ignButtons
C1Vent
14
C1Roughing
pulsRough1
C1Backing
C1Roughing
(OUT)
ignButtons
ignInterlock
C1Roughing
ignButtons
pulsRough1

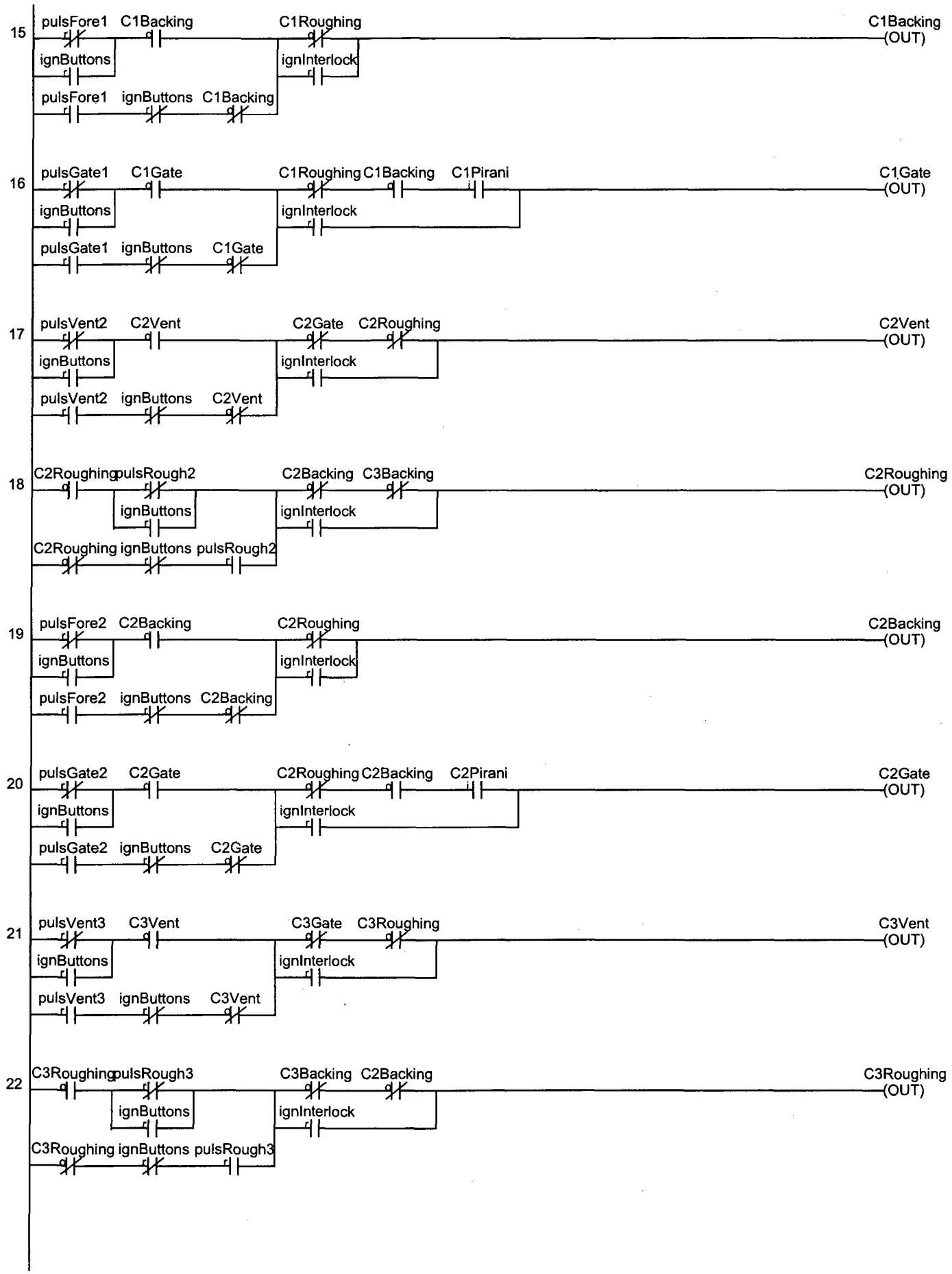
15
pulsFore1
C1Backing
C1Roughing
C1Backing
(OUT)
ignButtons
ignInterlock
pulsFore1
ignButtons
C1Backing
16
pulsGate1
C1Gate
C1Roughing
C1Backing
C1Pirani
C1Gate
(OUT)
ignButtons
ignInterlock
pulsGate1
ignButtons
C1Gate
17
pulsVent2
C2Vent
C2Gate
C2Roughing
C2Vent
(OUT)
ignButtons
ignInterlock
pulsVent2
ignButtons
C2Vent
18
C2Roughing
pulsRough2
C2Backing
C3Backing
C2Roughing
(OUT)
ignButtons
ignInterlock
C2Roughing
ignButtons
pulsRough2
19
pulsFore2
C2Backing
C2Roughing
C2Backing
(OUT)
ignButtons
ignInterlock
pulsFore2
ignButtons
C2Backing
20
pulsGate2
C2Gate
C2Roughing
C2Backing
C2Pirani
C2Gate
(OUT)
ignButtons
ignInterlock
pulsGate2
ignButtons
C2Gate
21
pulsVent3
C3Vent
C3Gate
C3Roughing
C3Vent
(OUT)
ignButtons
ignInterlock
pulsVent3
ignButtons
C3Vent
22
C3Roughing
pulsRough3
C3Backing
C2Backing
C3Roughing
(OUT)
ignButtons
ignInterlock
C3Roughing
ignButtons
pulsRough3

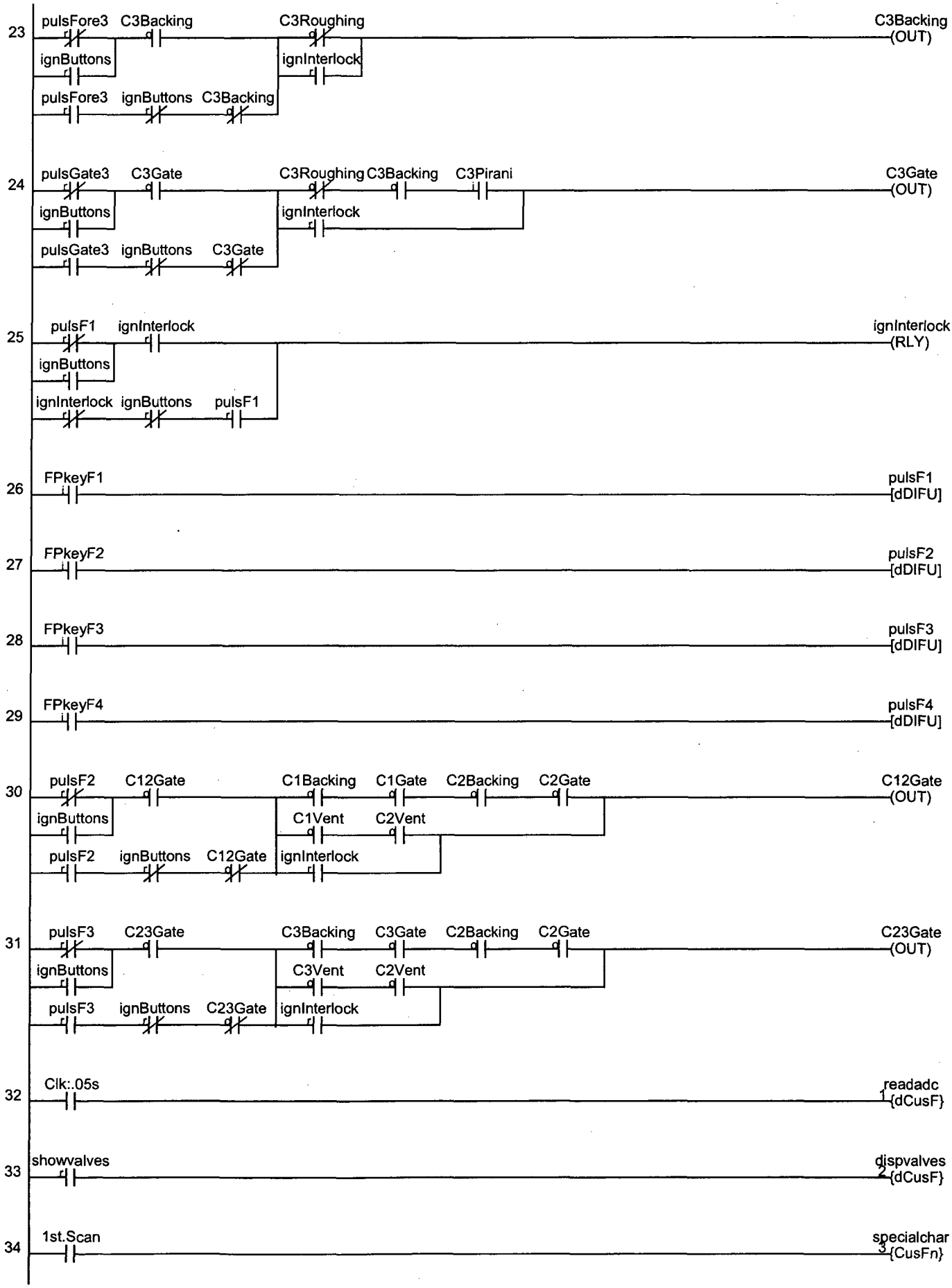
23
pulsFore3
C3Backing
C3Roughing
C3Backing
(OUT)
ignButtons
ignInterlock
pulsFore3
ignButtons
C3Backing
24
pulsGate3
C3Gate
C3Roughing
C3Backing
C3Pirani
C3Gate
(OUT)
ignButtons
ignInterlock
pulsGate3
ignButtons
C3Gate
25
pulsF1
ignInterlock
ignInterlock
(RLY)
ignButtons
ignInterlock
ignButtons
pulsF1
26
FPkeyF1
pulsF1
[dDIFU]
27
FPkeyF2
pulsF2
[dDIFU]
28
FPkeyF3
pulsF3
[dDIFU]
29
FPkeyF4
pulsF4
[dDIFU]
30
pulsF2
C12Gate
C1Backing
C1Gate
C2Backing
C2Gate
C12Gate
(OUT)
ignButtons
C1Vent
C2Vent
pulsF2
ignButtons
C12Gate
ignInterlock
31
pulsF3
C23Gate
C3Backing
C3Gate
C2Backing
C2Gate
C23Gate
(OUT)
ignButtons
C3Vent
C2Vent
pulsF3
ignButtons
C23Gate
ignInterlock
32
Clk:.05s
readadc
1
{dCusF}
33
showvalves
dispvalves
2
{dCusF}
34
1st.Scan
specialchar
3
{CusFn}

1 readadc

```
if y <> output[2] or z <> output[3] or abs(b-adc(6))>10 then
□y = output[2]
□z = output[3]
      b=adc(6)
□call dispvalves
endif
```

2 dispvalves

```
a$="[---]"+"  [---]   [---]"
setlcd 1,1,a$
a$="[   ]"
if TestIO(C12Gate) a$=a$+"=" : else : a$=a$+"X" : endif
a$=a$+"=[   ]"
if TestIO(C23Gate) a$=a$+"=" : else : a$=a$+"X" : endif
a$=a$+"==[   ]"
setlcd 2,1,a$
if TestIO(C1Roughing) a$="[!" : else : a$="[-" : endif
if TestIO(C1Gate) a$=a$+"!" : else : a$=a$+"-" : endif
if TestIO(C1Vent) a$=a$+"!" : else : a$=a$+"-" : endif
a$=a$+"]  ["
if TestIO(C2Vent) a$=a$+"!" : else : a$=a$+"-" : endif
if TestIO(C2Gate) a$=a$+"!" : else : a$=a$+"-" : endif
if TestIO(C2Roughing) a$=a$+"!" : else : a$=a$+"-" : endif
a$=a$+"]   ["
if TestIO(C3Roughing) a$=a$+"!" : else : a$=a$+"-" : endif
if TestIO(C3Gate) a$=a$+"!" : else : a$=a$+"-" : endif
if TestIO(C3Vent) a$=a$+"!]" : else : a$=a$+"-]" : endif
setlcd 3,1,a$
if TestIO(C1Backing) a$= " !" : else : a$= " -" : endif
a$=a$+"?      ?"
if TestIO(C2Backing) a$=a$+"!" : else : a$=a$+"-" : endif
a$=a$+"====="
if TestIO(C3Backing) a$=a$+"!" : else : a$=a$+"-" : endif
a$=a$+"?  "
setlcd 4,1,a$
```

3 specialchar

```
setdac 1,0
setdac 2,0
call dispvalves
```

4 display

```
setlcd 1,1,chr$(1)
if b<1024 then
   a$=" 1: "
   if TestIO(C1Vent) then : a$=a$+"vent ":endif
   if TestIO(C1Roughing) then : a$=a$+"rough ":endif
   if TestIO(C1Backing)  then : a$=a$+"fore ":endif
   if TestIO(C1Gate)     then : a$=a$+"gate ":endif
   setlcd 1,1,a$
else
if b<2048 then
   a$="1:"
   if TestIO(C1Vent) then : a$=a$+"open    ":endif
   if TestIO(C1Roughing) then : a$=a$+"roughing":endif
   if TestIO(C1Backing) and TestIO(C1Gate)=0 then : a$=a$+"---     ":endif
   if TestIO(C1Backing) and TestIO(C1Gate) then : a$=a$+"ready   ":endif
   setlcd 1,1,a$
else
if b<3192 then
   setlcd 1,1,"Page 3"
else
   setlcd 1,1,"Page 4"
endif : endif : endif
setlcd 4,1,str$(adc(6))
```

5 updateadc

```
setlcd 4,4,str$(adc(1))
setlcd 4,15,str$(adc(2))
```

I/O #	Inputs	Outputs	Relays	Relay+256	Timers	S.V.	Counters	S.V.
1	C1Pirani		pulsRough1					
2	C2Pirani		pulsVent1					
3			pulsFore1					
4			pulsGate1					
5			pulsRough2					
6			pulsVent2					
7	C3Pirani		pulsFore2					
8			pulsGate2					
9			pulsVent3					
10			pulsRough3					
11			pulsFore3					
12			pulsGate3					
13			ignButtons					
14			ignInterlock					
15			pulsF1					
16			pulsF2					
17		C1Backing	pulsF3					
18		C1Gate	pulsF4					
19		C1Roughing	showvalves					
20		C1Vent						
21		C2Backing						
22		C2Gate						
23		C2Roughing						
24		C2Vent						
25		tC3Backing						
26		tC3Gate						
27		tC3Roughin						
28		tC3Vent						
29								
30		tC23Gate						
31								
32		tC12Gate						
33		C3Backing						
34		C3Gate						
35		C3Roughing						
36		C3Vent						
37								
38		C23Gate						
39								
40		C12Gate						
41								
42								
43								
44								

I/O #	Inputs	Outputs	Relays	Relay+256	Timers	S.V.	Counters	S.V.
45								
46								
47								
48								
49								
50								
51								
52								
53								
54								
55								
56								
57	FPkey0	FPlamp1						
58	FPkey1	FPlamp2						
59	FPkey2	FPlamp3						
60	FPkey3	FPlamp4						
61	FPkey4	FPlampF1						
62	FPkey5	FPlampF2						
63	FPkey6	FPlampF3						
64	FPkey7	FPlampF4						
65	FPkey8							
66	FPkey9							
67	FPbksp							
68	FPenter							
69	FPkeyF1							
70	FPkeyF2							
71	FPkeyF3							
72	FPkeyF4							
73								
74								
75								
76								
77								
78								
79								
80								
81								
82								
83								
84								
85								
86								
87								
88								

Appendix D

Code

D.1 Data Browser

I created a web-based front end to allow interactive, collaborative access to the level crossing data saved by SCANB.VI. The program is written in a combination of PHP and Javascript; it can be accessed on the local network using an HTML5-capable browser (tested with Firefox 3.5-3.6) by accessing

`http://anapole-desk/browser.php`

The main window (figure D.1) displays the available datasets (contents of the directory C:\ANAPOLE_EXPERIMENT\DATA\FLUORESCENCE , or other directory as specified in SETTINGS.PHP, on the server computer) and allows the user to sort the datasets by certain commonly-used criteria (# of points in data file, date, the voltage applied to the interaction region during data collection, range of magnetic fields over which data was collected). The user can "rate" the file (on a scale of 1 to 5) to flag the file, e.g. as being of low or high quality. Clicking on the dot to the left of the file name will show additional details about the experimental parameters, and allow the user to tag the file with a comment for

later reference.

The "Filters" button brings up a separate dialog (fig. D.2) within the same window. Any number of parameters may be entered in the files provided to restrict the file list to datasets matching particular criteria. In the example shown, the user would be shown only datasets taken with an interaction region voltage between $30 \leq V_{IR} \leq 50$ Volts, and with at least 12 data points in the file.

The bottom of the main window shows an interactive plot area which includes the currently selected datasets. Dragging the mouse over the plot area will zoom in on the selected region; the three buttons to the right of the plot can be used to zoom out, zoom to fit all selected data, or to show the plot full-screen. Clicking a color box on the legend to the right of the plot will show details of the data set, and provide a link to download the processed data for further analysis. The processed data includes a short header containing the internal ID number of the dataset, the interaction region voltage, and the source filename. The body of the data contains the Z_0 coil control voltage, optical pumping ratio (as defined in eq. 7.5), and an uncertainty determined by the available counting statistics. The data processing script is shown below for reference.

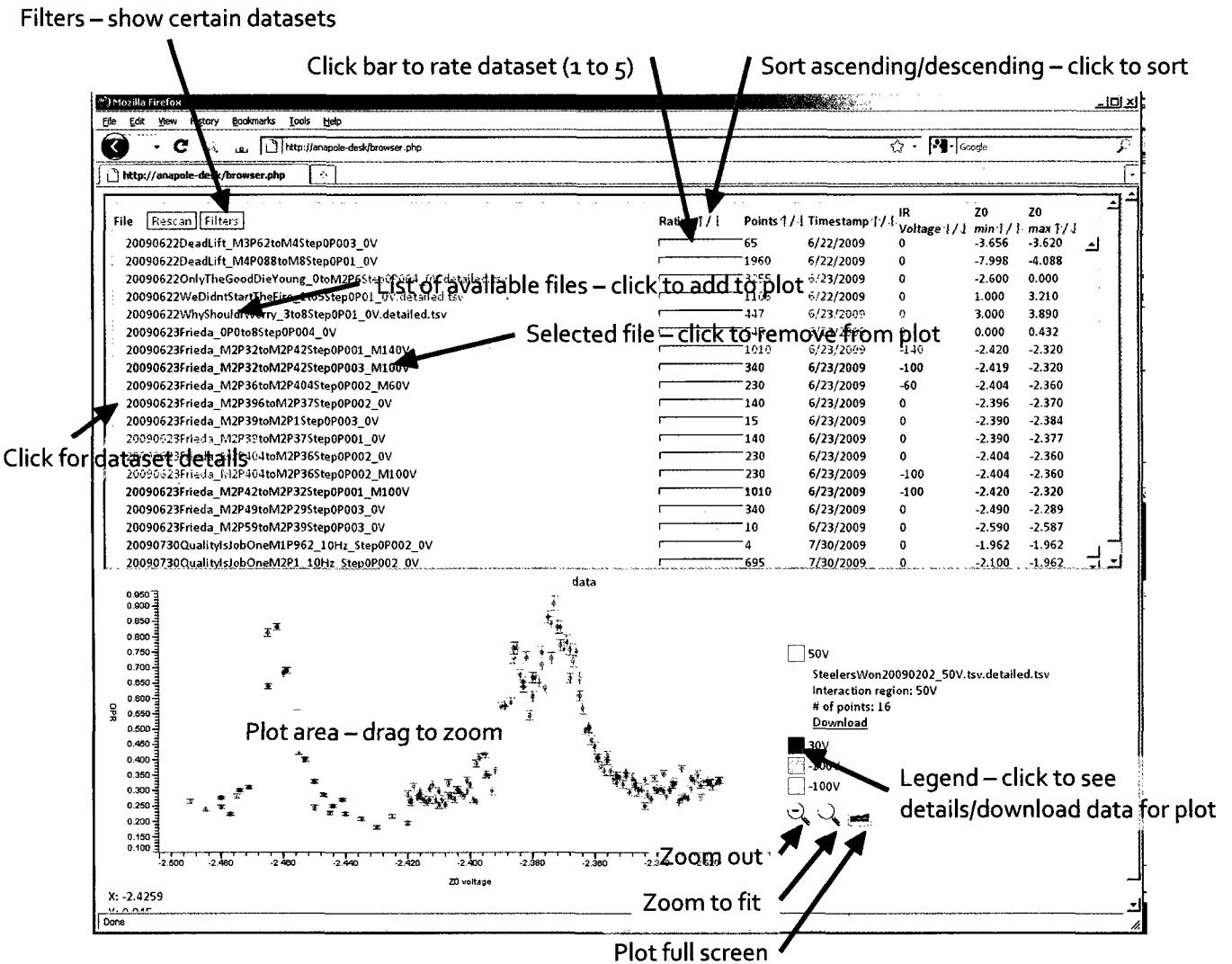

Figure D.1: The web-based data browser program can be used to find, compare, and plot data sets collected by SCANB.VI. The data sets can be sorted or filtered by the number of points in the file, date taken, interaction region voltage, magnetic field range covered, and a user-assigned "rating". The interactive plot shows the optical pumping ratio (defined as R in eq. 7.5) as a function of the voltage applied to the Z_0 shim coil. The magnetic field calibration is not stored in the same file, and so the program cannot automatically display the data directly in terms of magnetic field.

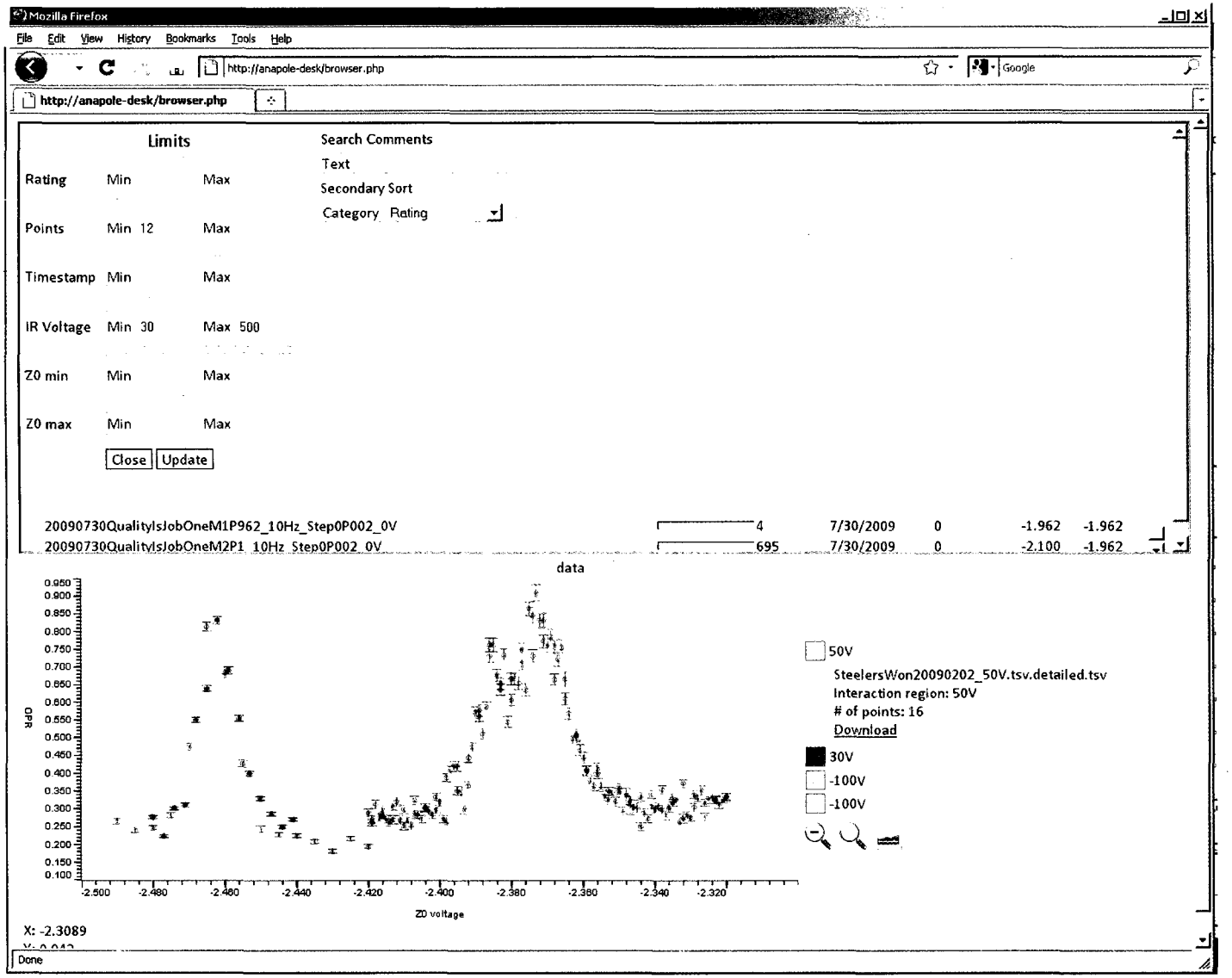

Figure D.2: Filter dialog in data browser. Any combination of the fields can be filled out to show only data sets meeting particular criteria (in the case shown, with an IR voltage between $30 \leq V_{IR} \leq 500$ Volts, and at least 12 data points in the file).

```
<?php
// getdata.php
// use as getdata.php?id=123&merge=1
//    id = identifier of data set to retrieve (key into database
    file)
//    merge = method to use for merging data points with the same B
     field
//       (0:don't merge, 1:combine opr, 2:combine opr w/stDev, 3:
    total counts)
//    sigmaCutoff = threshold to discard points with large errors,
    default 1.0

// Output (text file) is
//    first line        : id TAB IR voltage
//    second line       : data file name
//    third line to end: data points as xvalue TAB yvalue TAB
    yerror

header('Content-type: text/plain');

function sqr($x) { return $x*$x; }

//
    ////////////////////////////////////////////////////////////////////////////

// mergeopr(...)
// combines data points with the same B field
//    $errorAnalysis : method for combining points
//    $oprdata       : array of ('opr', 'sigma')
//    $open          : total # of net counts with shutter open
//    $closed        : total # of net counts with shutter closed
//    $openBkg       : total # of background counts in ROI with
    shutter open
//    $closedBkg     : total # of background counts in ROI with
    shutter closed
//  returns an array of ('opr', 'sigma')

function mergeopr($errorAnalysis, $oprdata, $open, $closed,
    $openBkg, $closedBkg) {
  // we have 3 options for combining points:
  //    1. opr is straight or weighted average, sigma from error of
       points
  //    2. opr is straight or weighted average, sigma from stdev()
  //    3. opr from sum of open vs. closed counts, sigma from sum
      of total counts

  // find weights for each point to average
  // weighted average: for Sum[c_i*(a_i +/- s_i)]/Sum[c_i],
  //   we minimize final error by choosing c_i such that
  //   c_i = Product[s_j^2, j != i]/Sum[Product[s_j^2, j != k], k]
  //   (eg. c_1 = (s_2 s_3 s_4)^2/((s_2 s_3 s_4)^2+(s_1 s_3 s_4)
      ^2+(s_1 s_2 s_4)^2+(s_1 s_2 s_3)^2)

  $totalWeight = 0.0;
  foreach ($oprdata as $key1 => $value1) {
    $w = 1.0;
    foreach ($oprdata as $key2 => $value2) {
```

```
      if ($key1 != $key2) $w *= $value2['sigma'];
    }
    $weight[$key1] = $w;
    $totalWeight += $w;
  }

  // weighted average, sigma from error of points
  // use this if selected, or if we have too few data points for a
      stDev
  if ($errorAnalysis==1 || ($errorAnalysis==2 && count($oprdata)<=
      4)) {

    $opr = 0.0; $sigmaopr = 0.0;
    foreach ($oprdata as $key => $value) {
      $opr += $weight[$key] * $value['opr'];
      $sigmaopr += sqr($weight[$key]*$value['sigma']);
    }
    $opr /= $totalWeight;
    $sigmaopr = sqrt($sigmaopr)/$totalWeight;

  // weighted average, sigma from stDev()
  } else if ($errorAnalysis==2) {

    $opr = 0.0; $sigmaopr = 0.0;
    foreach ($oprdata as $key => $value) {
      $opr += $weight[$key] * $value['opr'];
    }
    $opr /= $totalWeight;
    foreach ($oprdata as $key => $value) {
      $sigmaopr += $weight[$key]*sqr($value['opr']-$opr);
    }
    $sigmaopr = sqrt(count($oprdata)*$sigmaopr / ((count($oprdata)
        -1)*$totalWeight));

  // opr from sum of open vs. closed counts
  // eg. treat this as one big data set instead of many small data
      sets
  } else { // if ($errorAnalysis==3) {
    $opr = $open / $closed;
    $sigmaopen = sqrt($open + 2.0*$openBkg);
    $sigmaclosed = sqrt($closed + 2.0*$closdBkg);
    $sigmaopr = sqrt(sqr($sigmaopen / $closed) + sqr($sigmaclosed*
        $open/sqr($closed)));
  }

  return array('opr' => $opr, 'sigma' => $sigmaopr);
}

//
    ////////////////////////////////////////////////////////////////////////////

// begin main code here


include 'settings.php';

// load the database
```

```
$handle = fopen($dbpath . DIRECTORY_SEPARATOR . "scanb_cache.dat",
    "r");
$buff = fread($handle, filesize($dbpath . DIRECTORY_SEPARATOR . "
    scanb_cache.dat"));
$flist = unserialize($buff);
fclose($handle);

// write out the header (id, IR voltage, and file name)
$id = $_REQUEST['id'];
echo $id, "\t", $flist[$id]['IR_Voltage'], "\n";
echo $flist[$id]['File'], "\n";

// set a flag if we want to return xdata as calibrated in B field
    vs. Z0 voltage
if (isset($_REQUEST['Bcal'])) $bcal = $_REQUEST['Bcal'];
else $bcal = 'Z0';

// set a flag for the type of analysis method to use (eg. treat all
     data as
//   having the E field on, regardless of whether it is marked as
    on or off)
if (isset($_REQUEST['datatype'])) $analysis = $_REQUEST['datatype'
    ];
else $analysis = 'onlyon';

// open the data file
if ($handle = fopen($flist[$id]['Path'] . DIRECTORY_SEPARATOR .
    $flist[$id]['File'], "r")) {

// ignore the first line (header)
fgets($handle);  // dump first line

// we track the following data (in order to combine multiple values
     for same Z0)
$oprdata = array();  // store OPR data, eg. if we want to combine
    data points
$totalOpen      = 0; // # of net counts in ROI which shutter open
$totalClosed    = 0; // # of net counts in ROI which shutter closed
$totalOpenBkg   = 0; // # of background counts in ROI which shutter
     open
$totalClosedBkg = 0; // # of background counts in ROI which shutter
     closed

// set flags for whether (and how) to merge data for same Z0 values
if (isset($_REQUEST['merge'])) $combineSameB = $_REQUEST['merge'];
else $combineSameB = true;

// set threshold for whether to drop points with large errors
if (isset($_REQUEST['sigmaCutoff'])) $sigmaCutoff = (float)
    $_REQUEST['sigmaCutoff'];
else $sigmaCutoff = 1.0;

if (isset($_REQUEST['merge'])) $errorAnalysis = (int) $_REQUEST['
    merge']; else $errorAnalysis = 1;

// for each data point in the file...
while (!feof($handle)) {
```

```
// read a line, and split on tabs (tab-separated values)
$data = split("[\t]+", fgets($handle));
if (count($data) > 16) {
    // The data set columns are arranged as follows:
    // col 0      1       2       3              4
                          5                6
    //      Block WM          Z0              Off,Open,PMT1c   Off
        ,Open,PMT2c   Off,Open,PMT1b   Off,Open,PMT2b
    //
    // 7              8               9               10
                     11              12
    // Off,Clsd,PMT1c Off,Clsd,PMT2c   Off,Clsd,PMT1b   Off,Clsd,
        PMT2b   On,Open,PMT1c    On,Open,PMT2c
    //
    // 13             14              15              16
                     17              18              19
    // On,Open,PMT1b  On,Open,PMT2b    On,Clsd,PMT1c    On,Clsd,
        PMT2c    On,Clsd,PMT1b    On,Clsd,PMT2b    timestamp
  $Z0 = $data[1];
  $CtsEoffOpen= $data[4];
  $CtsEoffClsd= $data[8];
  $CtsEonOpen = $data[12];
  $CtsEonClsd = $data[16];

  $BkgEoffOpen = $data[6];
  $BkgEoffClsd = $data[10];
  $BkgEonOpen = $data[14];
  $BkgEonClsd = $data[18];

  // apply Z0 to B field conversion, if requested
  if ($bcal == 'Z0') {
    $Bfield = $Z0;
  } else if ($bcal == 'jan09') {
    $Bfield = 4629.796950362 + 0.645556721*$Z0;
  }

  // apply analysis to convert data to OPR
  if ($analysis == 'onlyon') {
    // field always on - disregard Eon vs Eoff
    $open = $CtsEoffOpen + $CtsEonOpen;
    $closed = $CtsEoffClsd + $CtsEonClsd;
    $opr = $open / $closed;
    $sigmaopen = sqrt($open + 2.0*$BkgEoffOpen + 2.0*$BkgEonOpen)
        ;
    $sigmaclosed = sqrt($closed + 2.0*$BkgEoffClsd + 2.0*
        $BkgEonClsd);
    $sigmaopr = sqrt(sqr($sigmaopen / $closed) + sqr($sigmaclosed
        *$open/sqr($closed)));

  }

  if ($sigmaopr > $sigmaCutoff) continue;

  // if we want to combine data points with the same B field
      value...
  if ($combineSameB && count($oprdata) > 0) {
    // if this data point has the same B field as the previous
```

```
        point, add it
      if (abs($Bfield - $oprdata[count($oprdata)-1]['Bfield']) < 1e
          -6) {
      } else {    // this point is different; average the points we
          have

        // calculate the average and standard deviation
        $merged = mergeopr($errorAnalysis, $oprdata, $totalOpen,
            $totalClosed, $totalOpenBkg, $totalClosedBkg);

        // print out the data point
        echo $oprdata[0]['Bfield'], "\t", $merged['opr'], "\t",
            $merged['sigma'], "\n";

        // clear the array, and add as a new point (part of the
            next B field value)
        $oprdata = array();
        $totalOpen      = 0;
        $totalClosed    = 0;
        $totalOpenBkg   = 0;
        $totalClosedBkg = 0;
      }
    } else if ($combineSameB) {
      // if we want to combine points with the same B, we don't
          need to do anything special
      //   (we'll add it to the array below)
    } else {
      // not combining data points, so just write the data out
      echo $Bfield, "\t", $opr, "\t", $sigmaopr, "\n";
    }

    // add point to the array
      $oprdata[] = array('Bfield' => $Bfield, 'opr' => $opr, 'sigma
          ' => $sigmaopr);
      $totalOpen      += $open;
      $totalClosed    += $closed;
      $totalOpenBkg   += $BkgEoffOpen + $BkgEonOpen;
      $totalClosedBkg += $BkgEoffClsd + $BkgEonClsd;
  }
}

// if we are combining opr, we need to write out the last data
    point
if ($combineSameB && count($oprdata) > 0) {
  $merged = mergeopr($errorAnalysis, $oprdata, $totalOpen,
      $totalClosed, $totalOpenBkg, $totalClosedBkg);
  echo $oprdata[0]['Bfield'], "\t", $merged['opr'], "\t", $merged['
      sigma'], "\n";
}

fclose($handle);
} else echo "Can't open file\n";

?>
```

D.2 Code for Spin-Dependent Parity Non-conserving Hamiltonian

This calculates the parity-violating part of the Hamiltonian, $\left(\vec{S} \times \hat{n}\right) \cdot \vec{I}$ in the $|N\, m_N\rangle\, |S\, m_S\rangle\, |I\, m_I\rangle$ basis for an $S = \frac{1}{2}$, $I = \frac{3}{2}$ molecule:

$$\texttt{Sval} = \frac{1}{2}; \texttt{Ival} = \frac{3}{2};$$

$$\texttt{states} = \texttt{Flatten}[\texttt{Table}[\{\texttt{N}, \texttt{mN}, \texttt{Sval}, \texttt{mS}, \texttt{Ival}, \texttt{mI}\},$$

$$\{\texttt{N}, 0, 1\}, \{\texttt{mN}, -\texttt{N}, \texttt{N}\}, \{\texttt{mS}, -\texttt{Sval}, \texttt{Sval}\}, \{\texttt{mI}, -\texttt{Ival}, \texttt{Ival}\}], 3];$$

$$\texttt{N}_{\texttt{J\_}} := \texttt{states}[\![\texttt{j}, 1]\!]$$

$$\texttt{mN}_{\texttt{J\_}} := \texttt{states}[\![\texttt{j}, 2]\!]$$

$$\texttt{S}_{\texttt{j\_}} := \texttt{states}[\![\texttt{j}, 3]\!]$$

$$\texttt{mS}_{\texttt{j\_}} := \texttt{states}[\![\texttt{j}, 4]\!]$$

$$\texttt{I}_{\texttt{j\_}} := \texttt{states}[\![\texttt{j}, 5]\!]$$

$$\texttt{mI}_{\texttt{j\_}} := \texttt{states}[\![\texttt{j}, 6]\!]$$

$$\delta_{\texttt{a\_},\texttt{b\_}} := \texttt{KroneckerDelta}[\texttt{a}, \texttt{b}]$$

$$\texttt{S}_+ := \delta_{\texttt{S}_\texttt{j},\texttt{S}_\texttt{k}} \delta_{\texttt{mS}_\texttt{j},\texttt{mS}_\texttt{k}+1} \sqrt{(\texttt{S}_\texttt{k} - \texttt{mS}_\texttt{k})(\texttt{S}_\texttt{k} + \texttt{mS}_\texttt{k} + 1)}$$

$$\texttt{S}_- := \delta_{\texttt{S}_\texttt{j},\texttt{S}_\texttt{k}} \delta_{\texttt{mS}_\texttt{j},\texttt{mS}_\texttt{k}+1} \sqrt{(\texttt{S}_\texttt{k} + \texttt{mS}_\texttt{k})(\texttt{S}_\texttt{k} - \texttt{mS}_\texttt{k} + 1)}$$

$$\texttt{Sz} := \delta_{\texttt{S}_\texttt{j},\texttt{S}_\texttt{k}} \delta_{\texttt{mS}_\texttt{j},\texttt{mS}_\texttt{k}} \texttt{mS}_\texttt{k}$$

$$\texttt{I}_+ := \delta_{\texttt{I}_\texttt{j},\texttt{I}_\texttt{k}} \delta_{\texttt{mI}_\texttt{j},\texttt{mI}_\texttt{k}+1} \sqrt{(\texttt{I}_\texttt{k} - \texttt{mI}_\texttt{k})(\texttt{I}_\texttt{k} + \texttt{mI}_\texttt{k} + 1)}$$

$$\texttt{I}_- := \delta_{\texttt{I}_\texttt{j},\texttt{I}_\texttt{k}} \delta_{\texttt{mI}_\texttt{j},\texttt{mI}_\texttt{k}-1} \sqrt{(\texttt{I}_\texttt{k} + \texttt{mI}_\texttt{k})(\texttt{I}_\texttt{k} - \texttt{mI}_\texttt{k} + 1)}$$

$$\texttt{Iz} := \delta_{\texttt{I}_\texttt{j},\texttt{I}_\texttt{k}} \delta_{\texttt{mI}_\texttt{j},\texttt{mI}_\texttt{k}} \texttt{mI}_\texttt{k}$$

$$\texttt{n}_+ := (-\sqrt{\frac{(\texttt{N}_\texttt{k} + \texttt{mN}_\texttt{k} + 1)(\texttt{N}_\texttt{k} + \texttt{mN}_\texttt{k} + 2)}{(2\texttt{N}_\texttt{k} + 1)(2\texttt{N}_\texttt{k} + 3)}} \delta_{\texttt{N}_\texttt{j},\texttt{N}_\texttt{k}+1} + \sqrt{\frac{(\texttt{N}_\texttt{k} - \texttt{mN}_\texttt{k})(\texttt{N}_\texttt{k} - \texttt{mN}_\texttt{k} - 1)}{(2\texttt{N}_\texttt{k} - 1)(2\texttt{N}_\texttt{k} + 1)}} \delta_{\texttt{N}_\texttt{j},\texttt{N}_\texttt{k}-1})$$

$$* \delta_{\texttt{mN}_\texttt{j},\texttt{mN}_\texttt{k}+1}$$

$$\texttt{n}_- := (\sqrt{\frac{(\texttt{N}_\texttt{k} - \texttt{mN}_\texttt{k} + 2)(\texttt{N}_\texttt{k} - \texttt{mN}_\texttt{k} + 1)}{(2\texttt{N}_\texttt{k} + 1)(2\texttt{N}_\texttt{k} + 3)}} \delta_{\texttt{N}_\texttt{j},\texttt{N}_\texttt{k}+1} - \sqrt{\frac{(\texttt{N}_\texttt{k} + \texttt{mN}_\texttt{k} - 1)(\texttt{N}_\texttt{k} + \texttt{mN}_\texttt{k})}{(2\texttt{N}_\texttt{k} - 1)(2\texttt{N}_\texttt{k} + 1)}} \delta_{\texttt{N}_\texttt{j},\texttt{N}_\texttt{k}-1})$$

$$* \delta_{\texttt{mN}_\texttt{j},\texttt{mN}_\texttt{k}-1}$$

$$\texttt{n}_\texttt{z} := (\sqrt{\frac{(\texttt{N}_\texttt{k} + \texttt{mN}_\texttt{k} + 1)(\texttt{N}_\texttt{k} - \texttt{mN}_\texttt{k} + 1)}{(2\texttt{N}_\texttt{k} + 1)(2\texttt{N}_\texttt{k} + 3)}} \delta_{\texttt{N}_\texttt{j},\texttt{N}_\texttt{k}+1} + \sqrt{\frac{(\texttt{N}_\texttt{k} + \texttt{mN}_\texttt{k})(\texttt{N}_\texttt{k} - \texttt{mN}_\texttt{k})}{(2\texttt{N}_\texttt{k} - 1)(2\texttt{N}_\texttt{k} + 1)}} \delta_{\texttt{N}_\texttt{j},\texttt{N}_\texttt{k}-1}) \delta_{\texttt{mN}_\texttt{j},\texttt{mN}_\texttt{k}}$$

$$(\texttt{H}_{\texttt{pnc}} = \texttt{Table}[\{\frac{i}{2}(\texttt{S}_+\texttt{n}_-\texttt{Iz} - \texttt{S}_-\texttt{n}_+\texttt{Iz} + \texttt{S}_-\texttt{I}_+\texttt{n}_\texttt{z} - \texttt{S}_+\texttt{n}_\texttt{z}\texttt{I}_- - \texttt{Sz}\,\texttt{n}_-\texttt{I}_+ + \texttt{Sz}\,\texttt{n}_+\texttt{I}_-)\},$$

$$\{\texttt{j}, \texttt{Length}[\texttt{states}]\}, \{\texttt{k}, \texttt{Length}[\texttt{states}]\}])//\texttt{MatrixForm}$$

D.2.1 Extracting a Plot from a Picture

Sometimes, a plot is saved as a bitmapped file (eg. .BMP, .GIF, or .PNG) but the source data is unavailable. It is easy to use Mathematica to digitize the trace, particularly if the trace is a unique solid color. The following function *convert* reads an image file (f), and returns an array of the data underlying the trace. In the code below, the trace is assumed to be dark blue ($\{0, 0, 128\}$), which is often used as a default color in Excel plots. The x- and y-range of the plot must be given in order to correctly scale the data.

```
convert[f_, {xmin_, xmax_}, {ymin_, ymax_}, {yminp_, ymaxp_}] :=
  Block[{plt = Import[f], pos, minmaxx, minmaxy},
    Print[Union[Flatten[plt[[1, 1]], 1]]];
    pos = Position[plt[[1, 1]]^T, {0, 0, 128}];
    minmaxx = {Min[pos[[All, 1]]], Max[pos[[All, 1]]]};
    minmaxy = {yminp, ymaxp};
    {xmin + (xmax - xmin)Rescale[#[[1]], minmaxx], ymin + (ymax - ymin)*
        Rescale[#[[2]], minmaxy]}&/@pos]
```

The first *Print[Union[...]]* statement displays a list of the colors used in the image (useful for determining the exact color of the trace). The *Position[...]* statement locates all occurences of this color. The x-values are automatically rescaled to match the given range $\{xmin, xmax\}$ on the assumption that the plot trace continues out to these values. However, we need to be told the pixel range $\{yminp, ymaxp\}$ which corresponds to the given y-axis range $\{ymin, ymax\}$. The function returns a list of $\{x, y\}$-value pairs corresponding to the trace on the plot.

The pixel range $\{yminp, ymaxp\}$ can be determined by running

`Show[Import["filename"]]`

and selecting the image. Holding the CTRL button down while moving the

mouse over the image will show the pixel location.

D.3 Relaxation Calculation

The code implementing the relaxation method calculation of the electric field inside the interaction region is below.

```
#include <stdio.h>
#include <stdlib.h>
#include <string.h>
#include <math.h>

#define max(a, b) (a > b ? a : b)

// iCartesian()
// calculates one iteration of the relaxation technique on a 2-d grid
// representing a rectangular coordinate system
//    mx, my : grid size
//    Vin    : input data (indexed like Vin[x+mx*y])
//    Vout   : output data (indexed like Vout[x+mx*y])
//    fixed  : indicates points of fixed potential (fixed[x+mx*y]==1)
// returns the maximum fractional amount by which any one grid value has
// changed from the previous to the current iteration
//
// preconditions:
//    fixed[] should be 1 for all grid boundaries (closed boundary
//      conditions)

double iCartesian(int mx, int my, double *Vin, double *Vout, int *fixed)
{
    double *Vi=Vin, *Vo=Vout;
    int l=mx*my;
    int *f=fixed;
    double maxdiff=0.0, maxchg=0.0;

    for (int i=0; i<l; i++) {
      if (*f) {
        *Vo = *Vi;
      } else {
        *Vo = 0.25*( *(Vi+1) + *(Vi-1) + *(Vi-mx) + *(Vi+mx) );
```

```
        double diff = fabs(*Vo-*Vi);
        if (diff > maxdiff) {
          maxdiff = diff;
          if (fabs(*Vo)>0.0) maxchg = diff / fabs(*Vo);
          else maxchg = diff;
        }
      }
      f++; Vo++; Vi++;
    }
    return maxchg;
}

// iCylindrical()
// calculates one iteration of the relaxation technique on a 2-d grid in
// a cylindrical coordinate system
//    mr, mz : grid size
//    Vin    : input voltage potentials (indexed like Vin[r+mr*z])
//    Vout   : output voltage potentials (indexed like Vout[r+mr*z])
//    fixed  : indicates points of fixed potential (fixed[r+mr*z]==1)
//    cenmask: precomputed grid setting the weights d/(2r)
// returns the maximum fractional amount by which any one grid value has
// changed from the previous to the current iteration
//
// preconditions:
//    fixed[] should be 1 on outer edges (r==mr-1, z==0, and z==mz-1),
//      e.g. closed boundary conditions
//    cenmask[] should be initialized to be d/(2r) for all r>0, and 1 at
//      r==0 (where d=grid spacing)

double iCylindrical(int mr, int mz, double *Vin, double *Vout, int *fixed,
                    double *cenmask)
{
    double *Vi=Vin, *Vo=Vout, *cm=cenmask;
    int l=mr*mz;
    int *f=fixed;
    double maxdiff=0.0, maxchg=0.0;

    for (int i=0; i<l; i++) {
      if (*f) {
        *Vo = *Vi;
      } else {
```

```
        *Vo = 0.25*( *(Vi+1)*(1+*cm) + *(Vi-1)*(1-*cm) + *(Vi-mr) + *(Vi+mr) );
        double diff = fabs(*Vo-*Vi);
        if (diff > maxdiff) {
          maxdiff = diff;
          if (fabs(*Vo)>0.0) maxchg = diff / fabs(*Vo);
          else maxchg = diff;
        }
      }
      f++; Vo++; Vi++; cm++;
    }
    return maxchg;
}

// calcCartesian()
// iterates the relaxation technique on the given potential
// distribution V until a maximum number of iterations is reached,
// or the change is smaller than a preset amount
//    mx, my : grid size
//    V      : voltage potential (as V[x+mx*y]; overwritten by output)
//    fixed  : indicates points of fixed potential (fixed[r+mr*z]==1)
// fixed[] will be set for closed boundary conditions
// status (# iterations, change this iteration, change last iteration)
//   will be written to stderr
// the maximum number of iterations is 200*max. dimension of array

void calcCartesian(int mx, int my, double *V, int *fixed)
{
    int l = mx*my;
    double *Vin = V, *Vout = (double *) malloc(sizeof(double)*l);
    double chglast=0.0, chgthis;

    for (int i=0; i<mx; i++) { fixed[i] = fixed[i+(my-1)*mx] = 1; }
    for (int i=0; i<my; i++) { fixed[i*mx] = fixed[i*mx+mx-1] = 1; }

    // limit max. # of iterations to 200*max. dim. of array

    for (int iter=0;iter<200*max(mx,my);iter++) {
      chgthis = iCartesian(mx, my, Vin, Vout, fixed);

      if (iter % 20 == 0)
        fprintf(stderr, "␣%d,␣%lg,␣%lg\n", iter, chgthis, chglast);
```

```
      // when the change is small enough, break; change this number to
      // change the threshold!

      if (chgthis < 1e-7) {
        fprintf(stderr, "␣break␣on␣%d\n", iter);
        break;
      }

      double *t = Vin; Vin=Vout; Vout = t;
      chglast = chgthis;
    }

    if (V==Vin) {
      memcpy(V, Vout, sizeof(double)*l);
      free(Vout);
    } else free(Vin);
}

// calcCylindrical()
// iterates the relaxation technique on the given potential
// distribution V until a maximum number of iterations is reached,
// or the change is smaller than a preset amount
//    mx, my : grid size
//    V      : voltage potential (as V[x+mx*y]; overwritten by output)
//    fixed  : indicates points of fixed potential (fixed[r+mr*z]==1)
//    minchange: threshold for breaking out of the loop (typ. 1e-7)
// fixed[] will be set for closed boundary conditions
// status (# iterations, change this iteration, change last iteration)
//   will be written to stderr
// the maximum number of iterations is 200*max. dimension of array


void calcCylindrical(int mr, int mz, double *V, int *fixed, double minchange)
{
    int l = mr*mz;
    double *Vin = V, *Vout = (double *) malloc(sizeof(double)*l);
    double *cenmask = (double *) malloc(sizeof(double)*l);
    double chglast=0.0, chgthis;

    for (int i=0; i<mr; i++) { fixed[i] = fixed[i+(mz-1)*mr] = 1; }
```

```
    for (int i=0; i<mz; i++) { fixed[i*mr+mr-1] = 1; }

    // generate cenmask; weights points by distance from center, d/(2r)
    for (int r=0; r<mr; r++) for (int z=0; z<mz; z++) {
      if (r>0) cenmask[r+z*mr] = 0.5/r;
      else cenmask[r+z*mr] = 1.0;
    }

    // iterate at most 200*max. dim. of array times
    for (int iter=0;iter<200*max(mr,mz);iter++) {
      chgthis = iCylindrical(mr, mz, Vin, Vout, fixed, cenmask);

      if (iter % 20 == 0)
        fprintf(stderr, "␣%d,␣%lg,␣%lg\n", iter, chgthis, chglast);

      // break out of loop if change was very small
      if (chgthis < minchange) {
        fprintf(stderr, "␣break␣on␣%d\n", iter);
        break;
      }

      double *t = Vin; Vin=Vout; Vout = t;
      chglast = chgthis;
    }

    if (V==Vin) {
      memcpy(V, Vout, sizeof(double)*l);
      free(Vout);
    } else free(Vin);
    free(cenmask);
}


double clip(double x, double low, double high)
{
  return ( x < low ? low : (x > high ? high : x));
}

// printCSV
// prints an array to a file handle in CSV format
//    f       : file handle (eg. stdout)
```

```
//    mx, my : size of array
//    V      : array to print (indexed as V[x+mx*y])

void printCSV(FILE *f, int mx, int my, double *V)
{
    for (int y=0; y<my; y++) {
      fprintf(f, "%lf", V[y*mx]);
      for (int x=0; x<mx; x++) {
        fprintf(f, ", %lf", V[y*mx+x]);
      }
      fprintf(f, "\n");
    }
}

// printgnuplot()
// prints an array in a form that gnuplot can use to make a surfaceplot
//    mx, my : size of array
//    V      : array to print (index as V[x+mx*y])

void printgnuplot(int mx, int my, double *V)
{
    for (int y=0; y<my; y++) {
      for (int x=0; x<mx; x++) {
        printf("%lf\n", V[y*mx+x]);
      }
      printf("\n");
    }
}

void doCartesianTest()
// simulate electrode configuration in rectangular coordinates
{
    // array size will be 54 mm x 400 mm
    int mx=54, my=400;
    // fixed[] sets which points are electrodes (fixed potential)
    int *fixed = (int *) malloc(sizeof(int)*mx*my);
    // V[] sets electrode potentials, and stores results
    double *V = (double *) malloc(sizeof(double)*mx*my);

    // initialize electrode configuration:
    //    electrodes at x=+/- 25 mm, ground at ends
```

```
    //      V=0 from 0<z<95 mm, V=1 from 155<=z<250 mm, V=0 for 250<=z<400 mm
    //      linear potential ramp from 95<=z<155 mm
    //    this is meant to simulate the non-extended interaction region

    for (int x=0; x<mx; x++) for (int y=0; y<my; y++) {
      fixed[x+y*mx] = (x==2 || x== 52 ? 1 : 0);
      V[x+y*mx] = ((x==2 || x==52) && y<250 ? clip((y-95.0)/60.0,0,1) : 0.0);
    }

    // do the calculation
    calcCartesian(mx, my, V, fixed);

    // print the results
    printCSV(stdout, mx, my, V);
}

void doCylindricalTest()
// simulate electrode configuration in cylindrical coordinates
{
    // array size will be 27 mm radius, 400 mm length
    //    (mm units are "arbitrary"; technique is scale-invariant)
    int mr=27, mz=400;
    // fixed[] sets which points are electrodes (fixed potential)
    int *fixed = (int *) malloc(sizeof(int)*mr*mz);
    // V[] sets electrode potentials, and stores results
    double *V = (double *) malloc(sizeof(double)*mr*mz);

    // initialize electrode configuration:
    //    electrodes at r=25 mm,
    //      V=0 from 0<z<95 mm, V=1 from 155<=z<250 mm, V=0 for 250<=z<400 mm
    //      linear potential ramp from 95<=z<155 mm
    //    this is meant to simulate the non-extended interaction region
    for (int r=0; r<mr; r++) for (int z=0; z<mz; z++) {
      fixed[r+z*mr] = (r==25 ? 1 : 0);
      V[r+z*mr] = ((r==25) && z<250 ? clip((z-95.0)/60.0,0,1) : 0.0);
    }

    // do the calculation (stopping when fractional change dV/V < 1e-7)
    calcCylindrical(mr, mz, V, fixed, 1e-7);

    // print the results
```

```
    printCSV(stdout, mr, mz, V);
}

void doCylindricalTest2()
// simulate electrodes with gaps between (high resolution)
{
    // start with a small grid (27 mm x 400 mm, 1 mm spacing)
    int mr=27, mz=400;
    // fixed[] sets which points are electrodes (fixed potential)
    int *fixed = (int *) malloc(sizeof(int)*mr*mz);
    // V[] sets electrode potentials, and stores results
    double *V = (double *) malloc(sizeof(double)*mr*mz);

    // initialize electrode configuration:
    //    electrodes at r=25 mm,
    //      V=0 from 0<z<95 mm, V=1 from 155<=z<250 mm, V=0 for 250<=z<400 mm
    //      linear potential ramp from 95<=z<155 mm
    //    this is meant to simulate the non-extended interaction region

    for (int r=0; r<mr; r++) for (int z=0; z<mz; z++) {
      fixed[r+z*mr] = (r==25 ? 1 : 0);
      V[r+z*mr] = ((r==25) && z<250 ? clip((z-95.0)/60.0,0,1) : 0.0);
    }

    // do the calculation (stopping when fractional change dV/V < 1e-7)
    calcCylindrical(mr, mz, V, fixed, 1e-7);

    // save the results of this "small" calculation
    int mrsm=mr, mzsm=mz;
    int *fixedsm=fixed;
    double *Vsm=V;

    // now, kick the resolution up by a factor of 10 (0.1mm grid spacing)
    // in order to simulate the 0.1 mm gaps between electrodes
    mr=270; mz=4000;
    fixed = (int *) malloc(sizeof(int)*mr*mz);
    V = (double *) malloc(sizeof(double)*mr*mz);

    // initialize electrode configuration:
    //    electrodes at r=25 mm,
    //      V=0 from 0<z<95 mm, V=1 from 155<=z<250 mm, V=0 for 250<=z<400 mm
```

```
    //       linear potential ramp from 95<=z<155 mm
    //     this is meant to simulate the non-extended interaction region
    // to speed convergence, we use the solution from the small grid as
    // the initial solution for the potentials

    for (int r=0; r<mr; r++) for (int z=0; z<mz; z++) {
      if (r != 250) fixed[r+z*mr] = 0;
      else if (z < 950 || z > 950+30*20) fixed[r+z*mr] = 1;
      else fixed[r+z*mr] = ((z-930) % 20 ? 1 : 0);

      V[r+z*mr] = ( (r==250) && z<2500 ?
          clip( ((z-930)/20)*0.03125,0,1) : Vsm[r/10 + z/10*mrsm]);
    }

    // do the calculation (stopping when fractional change dV/V < 1e-5)
    calcCylindrical(mr, mz, V, fixed, 1e-5);
    // print the resulsts
    printCSV(stdout, mr, mz, V);
}


void doCylindricalTest3()
// simulate a high-potential electrode, but with a gap between the
// interaction region and the extension
{
    // array size will be a 27 mm radius, 400 mm length
    int mr=27, mz=400;
    // fixed[] sets which points are electrodes (fixed potential)
    int *fixed = (int *) malloc(sizeof(int)*mr*mz);
    // V[] sets electrode potentials, and stores results
    double *V = (double *) malloc(sizeof(double)*mr*mz);

    // initialize electrode configuration:
    //     electrodes at r=25 mm,
    //       V=0 from 0<z<95 mm, V=1 from 155<=z<250 mm, V=0 for 250<=z<253 mm
    //       V=1 from 253<z<400 mm; linear potential ramp from 95<=z<155 mm
    //     this is meant to simulate the extended interaction region with
    //     a small gap between the interaction region and the extension

    for (int r=0; r<mr; r++) for (int z=0; z<mz; z++) {
      fixed[r+z*mr] = (r==25 && (z<250 || z>253) ? 1 : 0);
```

```
      V[r+z*mr] = ((r==25) ? clip((z-95.0)/60.0,0,1) : 0.0);
    }

    // do the calculation (stopping when fractional change dV/V < 1e-7)
    calcCylindrical(mr, mz, V, fixed, 1e-7);
    // print the results
    printCSV(stdout, mr, mz, V);
}


int main()
{
    doCylindricalTest3();
}
```

D.4 LabVIEW Code

D.4.1 Multichannel Scaler Implemented in LabVIEW

ctr_mcs2_continuous.vi
C:\anapole_experiment\vi\general\ctr_mcs2_continuous.vi
Last modified on 6/5/2008 at 11:20 AM
Printed on 9/1/2009 at 1:04 PM

Connector Pane

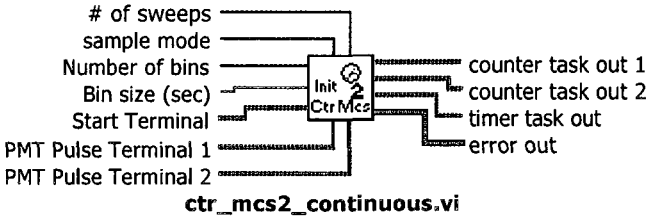

Front Panel

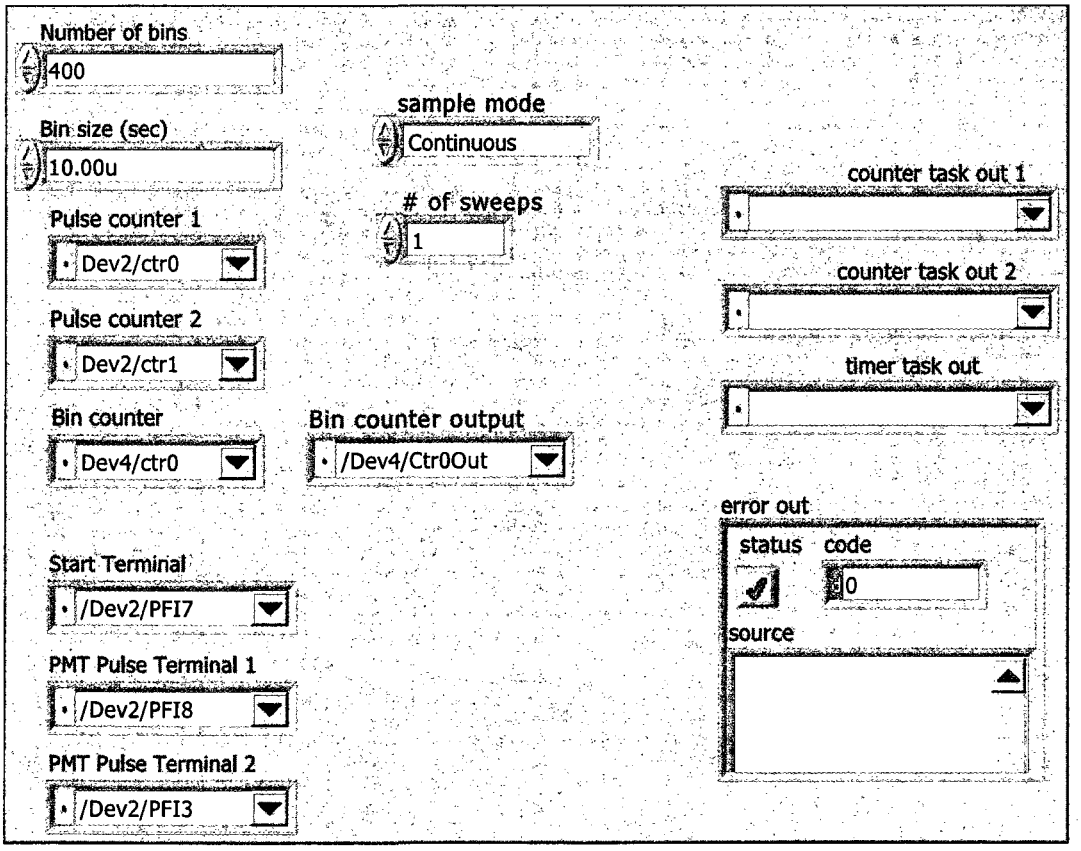

ctr_mcs2_continuous.vi
C:\anapole_experiment\vi\general\ctr_mcs2_continuous.vi
Last modified on 6/5/2008 at 11:20 AM
Printed on 9/1/2009 at 1:04 PM

Block Diagram

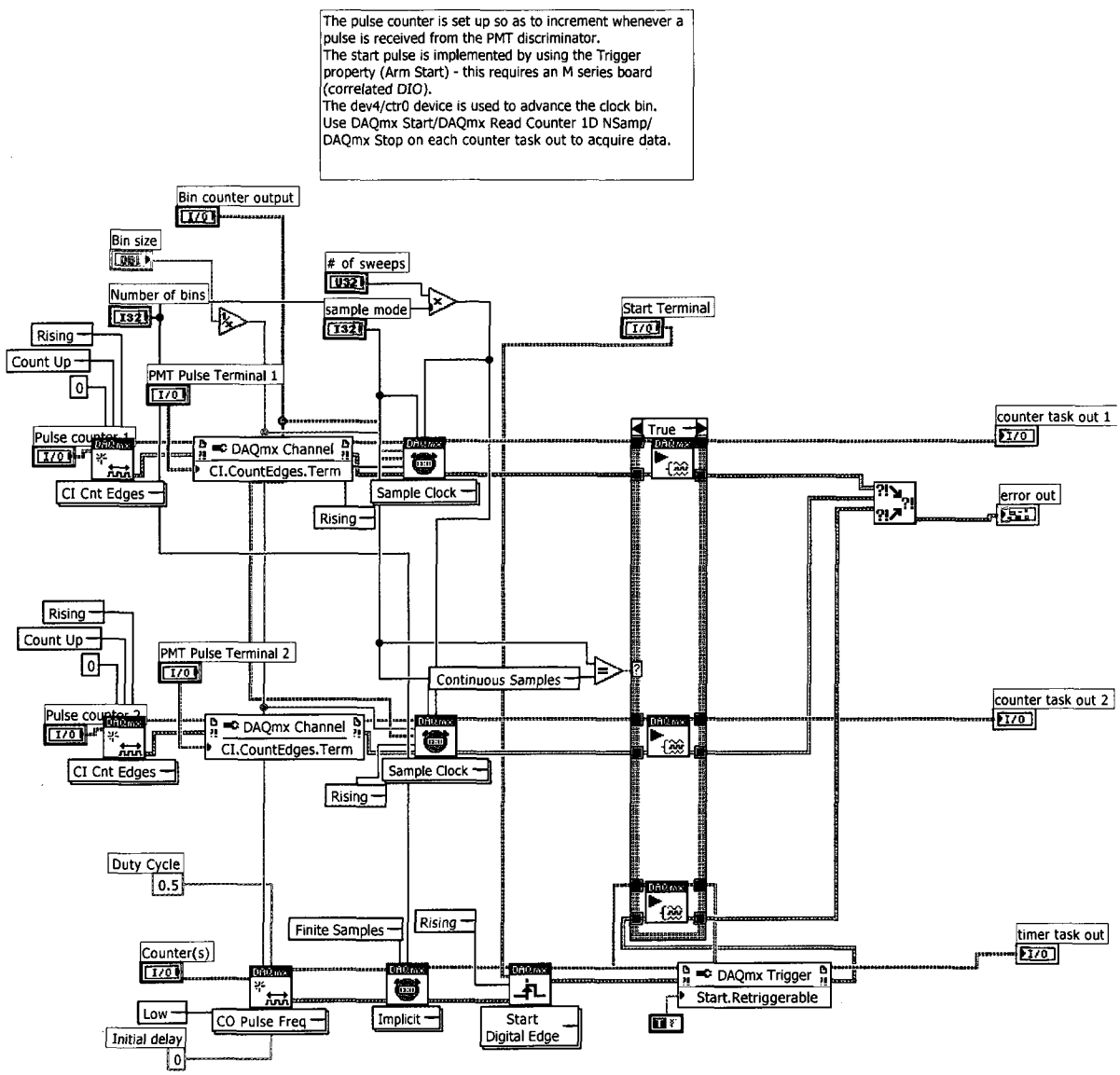

Appendix E

Transitions of BaF

E.1 ^{138}BaF

$A^2\Pi\ (v = 0) \leftrightarrow X^2\Sigma\ (v = 0)$

	P_1	Q_1	R_1	P_2	Q_2	R_2
N_{lower}	$1+i$	i	i	$3+i$	$2+i$	$1+i$
J_{lower}	$\frac{3}{2}+i$	$\frac{1}{2}+i$	$\frac{1}{2}+i$	$\frac{1}{2}+i$	$\frac{3}{2}+i$	$\frac{1}{2}+i$
J_{upper}	$\frac{1}{2}+i$	$\frac{1}{2}+i$	$\frac{3}{2}+i$	$\frac{3}{2}+i$	$\frac{3}{2}+i$	$\frac{3}{2}+i$

i	P_1	Q_1	R_1	P_2	Q_2	R_2
0	11630.07	11630.25	11631.27	12260.58	12262.39	12262.73
1	11629.97	11630.32	11632.02	12259.79	12262.28	12262.80
2	11629.87	11630.39	11632.77	12258.99	12262.17	12262.86
3	11629.75	11630.45	11633.51	12258.19	12262.05	12262.92
4	11629.63	11630.50	11634.25	12257.37	12261.93	12262.97
5	11629.50	11630.55	11634.97	12256.55	12261.80	12263.01
6	11629.37	11630.59	11635.69	12255.73	12261.66	12263.05
7	11629.23	11630.62	11636.40	12254.89	12261.51	12263.07
8	11629.08	11630.64	11637.11	12254.05	12261.36	12263.09
9	11628.92	11630.66	11637.81	12253.20	12261.20	12263.11
10	11628.76	11630.67	11638.50	12252.35	12261.03	12263.11
11	11628.59	11630.67	11639.18	12251.48	12260.86	12263.11
12	11628.41	11630.67	11639.86	12250.61	12260.67	12263.10
13	11628.23	11630.66	11640.53	12249.74	12260.48	12263.09
14	11628.03	11630.64	11641.19	12248.85	12260.29	12263.06
15	11627.84	11630.61	11641.85	12247.96	12260.08	12263.03
16	11627.63	11630.58	11642.49	12247.06	12259.87	12263.00
17	11627.42	11630.54	11643.13	12246.16	12259.66	12262.95
18	11627.19	11630.49	11643.77	12245.24	12259.43	12262.90
19	11626.97	11630.44	11644.39	12244.32	12259.20	12262.84
20	11626.73	11630.38	11645.01	12243.39	12258.96	12262.78

$D^2\Sigma\ (v = 0) \leftrightarrow A^2\Pi\ (v = 0)$

	P_1	Q_1	R_1	Q_{12}
J_{lower}	$\frac{3}{2} + i$	$\frac{1}{2} + i$	$\frac{1}{2} + i$	$\frac{1}{2} + i$
N_{upper}	i	i	$1 + i$	$1 + i$
J_{upper}	$\frac{1}{2} + i$	$\frac{1}{2} + i$	$\frac{3}{2} + i$	$\frac{1}{2} + i$

i	P_1	Q_1	R_1	Q_{12}
0	12545.36	12546.38	12546.59	12546.58
1	12544.63	12546.34	12546.73	12546.72
2	12543.94	12546.32	12546.92	12546.89
3	12543.27	12546.33	12547.13	12547.10
4	12542.63	12546.38	12547.37	12547.33
5	12542.03	12546.45	12547.64	12547.60
6	12541.46	12546.56	12547.95	12547.90
7	12540.92	12546.70	12548.29	12548.23
8	12540.40	12546.87	12548.65	12548.59
9	12539.93	12547.07	12549.05	12548.98
10	12539.48	12547.31	12549.48	12549.41
11	12539.06	12547.57	12549.95	12549.86
12	12538.68	12547.87	12550.44	12550.35
13	12538.32	12548.19	12550.96	12550.86
14	12538.00	12548.55	12551.52	12551.41
15	12537.71	12548.94	12552.11	12551.99
16	12537.45	12549.36	12552.72	12552.60
17	12537.22	12549.81	12553.37	12553.24
18	12537.02	12550.30	12554.05	12553.92
19	12536.85	12550.81	12554.77	12554.62
20	12536.72	12551.35	12555.51	12555.36

$D^2\Sigma\ (v = 0) \leftrightarrow X^2\Sigma\ (v = 0)$

	P_1	P_2	R_1	R_2
N_{lower}	$1 + i$	$2 + i$	i	$1 + i$
J_{lower}	$\frac{3}{2} + i$	$\frac{3}{2} + i$	$\frac{1}{2} + i$	$\frac{1}{2} + i$
N_{upper}	i	$1 + i$	$1 + i$	$2 + i$
J_{upper}	$\frac{1}{2} + i$	$\frac{1}{2} + i$	$\frac{3}{2} + i$	$\frac{3}{2} + i$

i	P_1	P_2	R_1	R_2
0	24176.20	24175.79	24177.09	24177.56
1	24175.79	24175.41	24177.57	24178.06
2	24175.41	24175.05	24178.07	24178.58
3	24175.06	24174.71	24178.60	24179.13
4	24174.72	24174.40	24179.16	24179.71
5	24174.42	24174.11	24179.73	24180.30
6	24174.13	24173.84	24180.34	24180.92
7	24173.87	24173.60	24180.96	24181.57
8	24173.64	24173.39	24181.61	24182.24
9	24173.42	24173.20	24182.29	24182.93
10	24173.24	24173.03	24182.98	24183.65
11	24173.07	24172.88	24183.70	24184.39
12	24172.93	24172.76	24184.45	24185.16
13	24172.82	24172.67	24185.22	24185.95
14	24172.73	24172.60	24186.02	24186.76
15	24172.66	24172.55	24186.83	24187.60
16	24172.62	24172.53	24187.68	24188.46
17	24172.60	24172.53	24188.54	24189.35
18	24172.60	24172.55	24189.43	24190.26
19	24172.63	24172.60	24190.35	24191.19
20	24172.69	24172.67	24191.29	24192.15

E.2 ^{137}BaF

$A\ \Pi\ (v = 0) \leftrightarrow X\ ^2\Sigma\ (v = 0)$

	P_1	Q_1	R_1	P_2	Q_2	R_2
N_{lower}	$1 + i$	i	i	$3 + i$	$2 + i$	$1 + i$
J_{lower}	$\frac{3}{2} + i$	$\frac{1}{2} + i$	$\frac{1}{2} + i$	$\frac{1}{2} + i$	$\frac{3}{2} + i$	$\frac{1}{2} + i$
J_{upper}	$\frac{1}{2} + i$	$\frac{1}{2} + i$	$\frac{3}{2} + i$	$\frac{3}{2} + i$	$\frac{3}{2} + i$	$\frac{3}{2} + i$

i	P_1	Q_1	R_1	P_2	Q_2	R_2
0	11630.06	11630.24	11631.26	12260.57	12262.38	12262.72
1	11629.96	11630.31	11632.02	12259.78	12262.27	12262.80
2	11629.86	11630.38	11632.76	12258.98	12262.16	12262.86
3	11629.74	11630.44	11633.51	12258.17	12262.05	12262.91
4	11629.62	11630.49	11634.24	12257.36	12261.92	12262.96
5	11629.50	11630.54	11634.97	12256.54	12261.79	12263.01
6	11629.36	11630.58	11635.69	12255.71	12261.65	12263.04
7	11629.22	11630.61	11636.40	12254.88	12261.50	12263.07
8	11629.07	11630.64	11637.11	12254.04	12261.35	12263.09
9	11628.91	11630.65	11637.81	12253.19	12261.19	12263.10
10	11628.75	11630.66	11638.50	12252.33	12261.02	12263.11
11	11628.58	11630.67	11639.18	12251.47	12260.85	12263.10
12	11628.40	11630.66	11639.86	12250.60	12260.66	12263.10
13	11628.22	11630.65	11640.53	12249.72	12260.47	12263.08
14	11628.02	11630.63	11641.19	12248.83	12260.28	12263.06
15	11627.82	11630.61	11641.85	12247.94	12260.07	12263.03
16	11627.62	11630.58	11642.50	12247.04	12259.86	12262.99
17	11627.40	11630.54	11643.14	12246.14	12259.64	12262.95
18	11627.18	11630.49	11643.77	12245.22	12259.42	12262.90
19	11626.95	11630.43	11644.40	12244.30	12259.19	12262.84
20	11626.72	11630.37	11645.02	12243.37	12258.95	12262.77

Appendix F

Copper Skimmer Fabrication Procedure

We have also fabricated our own skimmers (initially designed as baffles for stray light reduction) by electroforming copper on to a stainless steel mandrel. The procedure was devised by one of the undergraduates working in the lab, George Burkhard [65]. The procedure is [65]:

1. Make a stainless steel mandrel (figure F.1) in the form of the object you want to produce.

2. Set up the electroforming bath. We used a solution of deionized water, copper sulfate, sulfuric acid, hydrochloric acid, and Copper Gleam CLX from `http://www.thinktink.com/stack/volumes/voliii/consumbl/cplatmix.htm`. Place a sheet of copper in a ring around the inside rim of the bath and attach it to the positive terminal of the power supply; it is important that the copper sheet surround the mandrel when it is placed in the bath.

3. Hold the mandrel so that it is suspended in the bath and all parts that

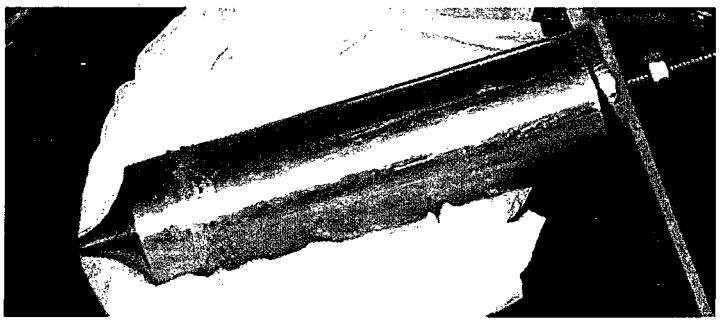

Figure F.1: Stainless steel mandrel for electroforming copper skimmer cones. The part of the mandrel to the left of the blue residue is submerged in the electroforming solution.

are to have copper deposited are submerged; connect it to the negative supply.

4. Run the power supply at about 1/3 amp (for a part the size of the skimmer; a common rule of thumb is 100 amps/meter^2 of surface to be coated. Extremely rough growth will result if the current is too high; low currents gave slow and poor growth. We found that it took about 8-12 hours to produce a sturdy, uniform copper cone.

5. Remove the mandrel from the solution and wash it off. It will have a rough surface, but should uniformly cover the mandrel.

6. Put the mandrel on the lathe and use emery paper to polish the copper surface. It is easier to handle the part while it is on the mandrel than after we remove it. A sequence of 300/600/1000 grit tends to work well. The tip of the skimmer cone can be polished using a pencil eraser.

7. Remove the part from the mandrel by heating it with a torch and dunking it in water. If the part is overheated, the surface will oxidize (but can be cleaned off with a fine emory paper after the part is removed).

Appendix G

System VI Information

Two programs are primarily used to run the system and acquire data. The *mcs_and_laser.vi* program (figure G.1) displays the time-of-flight signal from the laser-induced fluorescence measurements. The top pane, labeled time-of-flight, shows the signals recorded in the state preparation region before the magnet (blue) and the detection region after the magnet (red), averaged over the previous 10 molecular beam pulses. Most of the molecules are detected between bins 75 and 100 (750 and 1000 μs after the "start" signal sent from the Quantum Composer) in the state preparation region, and between bins 412 and 438 in the detection region. The two regions are 2.03 m apart, so this time difference corresponds to a mean velocity of 602 m/s. The pane below that, labeled "summation", shows the cumulative sum of the time-of-flight pulses. The PMT1 and PMT2 boxes below that specify the region of interest; the program sums up the total number of counts within the time window that we expect to see a signal and subtracts the background counts. The recent history of net counts are displayed on the right.

The mode control is used to change the data acquisition mode. In *Normal*

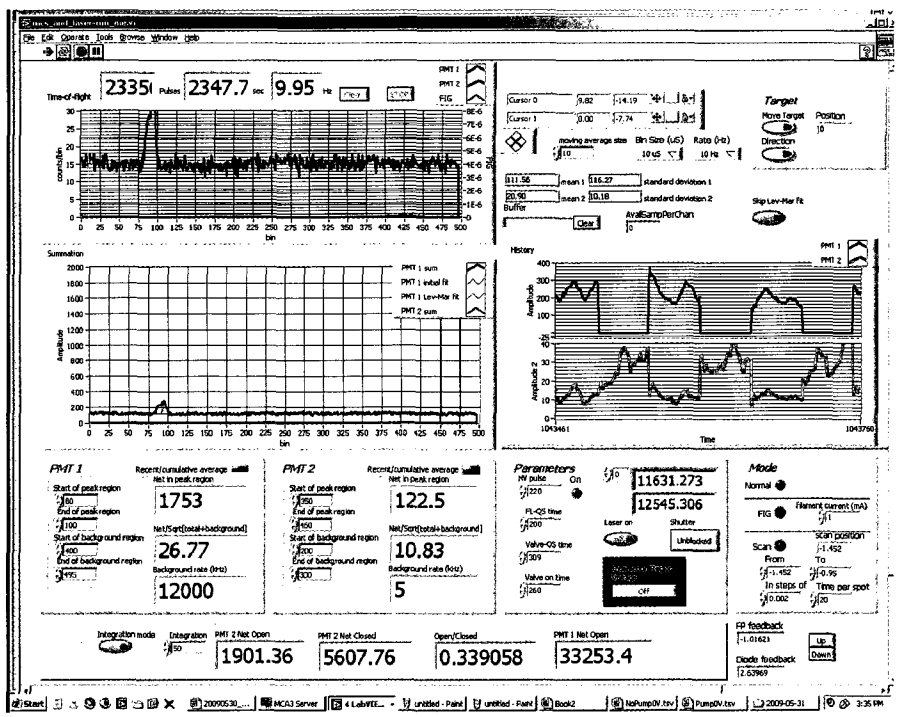

Figure G.1: Sample screenshot of the data acquisition computer running the system diagnostic program *mcs_and_laser.vi*, which is used to monitor the time-of-flight fluorescence signal and do spectroscopic and optical pumping studies.

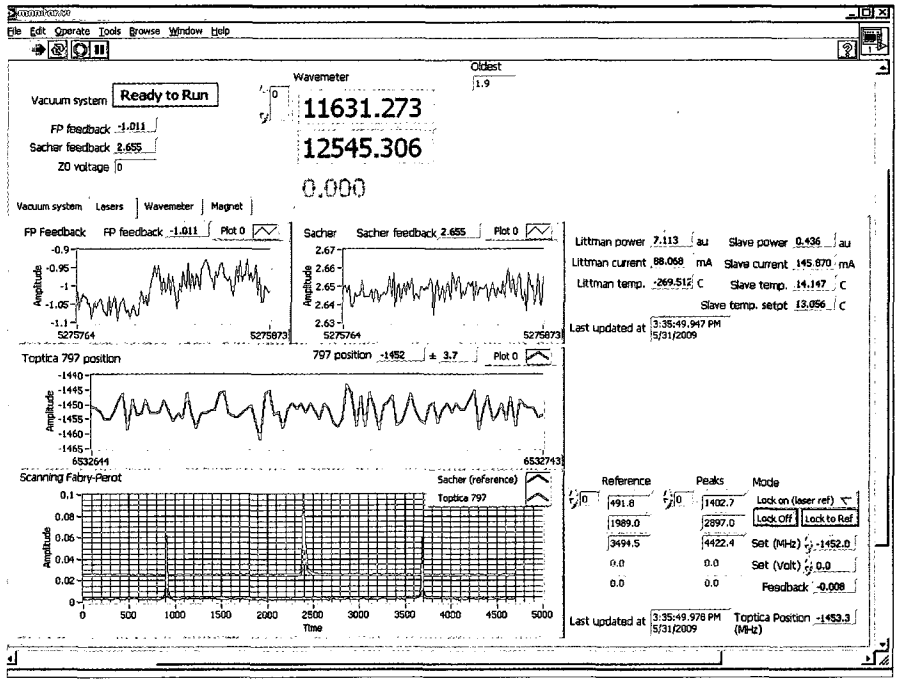

Figure G.2: Sample screenshot of the data acquisition computer running the system monitor program *monitor.vi*, which is used to monitor the status of the lasers, vacuum system, and magnet.

mode, the scan position (control value sent to the diode laser) is determined by the value in the "From" box below the *Scan* button and the signal is shown in the History pane. This mode is ideal for optimizing the molecular beam apparatus, such as by adjusting the rod, ablation laser, detection laser frequency, or pulsed valve parameters. The *FIG* mode button turns off the PMTs and turns on the fast ion gauge. This replaces the time-of-flight pane with a measurement of the gas pressure as a function of time and can be used to optimize the relative timing of the ablation laser and pulsed valve without having to rely on spectroscopic measurements. The *Scan* mode is used to acquire fluorescence spectra by scanning the controlled diode laser over a range of frequencies. Finally, the *Integration* mode (bottom pane) is used to test the optical pumping ratio (ratio of the number of counts observed in the detection region with the state preparation laser unblocked vs. blocked). Ideally, if the state preparation laser is tuned properly, the *Open/Closed* ratio would be 0 (the state preparation laser would completely depopulate the state). In practice, the optimized system reaches a ratio of about 0.18. Limitations in optical pumping will be discussed more in the section on laser-induced fluorescence spectroscopy.

The *monitor.vi* program, also shown in figure G.1, tracks the state of the apparatus and allows easy control of parameters. It communicates with the PLC to monitor the state of the vacuum system, with the wavemeter to record the absolute laser wavelengths, and the magnet computer to set the value of the magnetic field. The screen shown shows details related to the state of the diode lasers. It receives feedback information from the Pound-Drever-Hall control system to make sure that the feedback values are within range, and displays the output from the scanning Fabry-Perot interferometer. This provides a quick way to verify that all lasers are operating single-mode and properly locked, and are not modehopping.

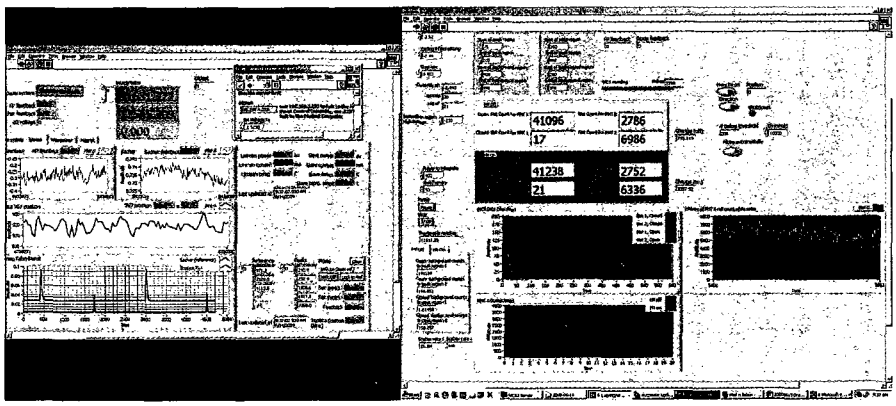

Figure G.3: Screenshot showing operation of *scanb.vi*. This program controls the measurement of the optical pumping ratio as the magnetic field is scanned through resonance. It is not intended to operate interactively, but does provide feedback on the performance of the molecular beam in case parameters need to be adjusted during a data collection run.

The data acquisition computer is connected to multiple monitors and keyboards around the room, so that the system performance can be seen while adjusting the lasers or the molecular beam source.

The other important data acquisition program is *scanb.vi*, which measures the optical pumping ratio as the magnetic field is scanned through resonance. This program is used to record the level crossing data shown in the DC Stark effect measurements in the next chapter.

Other information which is measured by *monitor.vi* includes the laser frequency (via an Agilent 86120B wavemeter), and the laser diode currents and temperatures.

Appendix H

Codes for Spectroscopic Calculations

We have used two software programs for spectroscopic calculations of BaF. The first program, provided by Prof. Steimle at Arizona State University, is not documented here. The second, MX_PNC, was provided by Mikhail Kozolv at the St. Petersburg Nuclear Physics Institute (PNPI). The latter was written for the calculation of nuclear spin-dependent parity violation effects in diatomic molecules. To this end, it calculates the rotational structure of the $^2\Sigma$ and $^2\Pi_{1/2}$ states of diatomic molecules in a magnetic field, DC Stark matrix elements, situations in which magnetic sublevels of opposite parity are degenerate, and coefficients related to the strength of parity violating effects present at these level crossings. I have prepared an extended version of this program, *mx_pnc.nb*, an adaptation in Mathematica 5.1 of the original Fortran 77 code. This version of the code adds additional terms to the Zeeman Hamiltonian, simulation of observable laser spectra, and a more flexible scheme for tracking and analyzing the results of the calculations.

Case (c) name		Related to case ($a_{\beta S}$) by		Case ($a_{\beta s}$) name
Rotational constant	B	B	B	Rotation
	R	$B/4 - \gamma/2$		
Ω-doubling	δ	$-2B + \gamma$	γ	Spin-rotation
$A_\parallel$ part of hyperfine	A_z	$b_F + \frac{2c}{3}$	b_F	Hyperfine ($\sim \lvert\Psi(0)\rvert^2$)
$A_\perp$ part of hyperfine	A_{xy}	$b_F - \frac{c}{3}$	c	Hyperfine ($\sim \left\langle \frac{3\cos^2\theta - 1}{r^3} \right\rangle$)
$G_\parallel$ part of G-factor	G_z	G_S	G_S	Electron spin G-factor
$G_\perp$ part of G-factor	G_{xy}	$G_S + G_L$	G_L	Ang. momentum G-factor
Nuclear spin g-factor	g	g	g	Nuclear spin g-factor

Table H.1: Relationship between Hund's case (c) constants (as used in MX_PNC) and Hund's case (a) constants.

H.1 Detailed Description of MX_PNC

The principles of MX_PNC are outlined in Kozlov's paper on the behavior of $^2\Sigma$ and $^2\Pi$ states of diatomic molecules in a strong magnetic field [3].

H.1.1 Constants

The code we received from Kozlov expects the parameters to take a different form:

$$\begin{aligned} A_z &= b_F + 2c/3 \\ A_{xy} &= b_F - c/3 \end{aligned} \tag{H.1}$$

Kozlov also uses different notation for the G-factors in the Zeeman Hamiltonian:

$$G_z = G_S \tag{H.2}$$

$$G_{xy} = G_S + G_L \tag{H.3}$$

H.1.2 State Preparation

Kozlov's derivations of the effective Hamiltonian are done in the Hund's case (c) basis. Nominally, we expect case (c) states (before considering nuclear spins) to be of the form

$$|\eta, J_a, J, \Omega, m_J\rangle$$

where $J_a = L + S$ is the total electronic angular momentum of the molecule. Since only Ω is a good case (c) quantum number and Λ, Σ are not, all levels with the same values of J and Ω can mix (eg. $A^2\Pi_{1/2}$, $X^2\Sigma_{1/2}$, $A'^2\Delta_{1/2}$, and $B^2\Sigma_{1/2}$ are all mixed). This means we can't easily express a conversion between case (a) and case (c) basis sets in the way we can for cases (a) and (b) (which is given in [31]). However, we are using empirical constants for doublet states derived in a case (a) or (b) framework[12]. In this case we can assume the only the given electronic state (X, A', A, B, ...) contributes, and each choice of Ω implies particular combinations of Λ and Σ (eg. $\Omega = -1/2$ for a $^2\Pi$ state implies that $\Lambda = -1$ and $\Sigma = 1/2$). This relationship between a case (c) and case (a) basis is not true for all states; for example, in a $^3\Pi$ state with $\Omega = 0$, we could have $\Lambda = 1, \Sigma = -1$ or $\Lambda = -1, \Sigma = 1$. However, our work here is restricted to $^2\Sigma$ and $^2\Pi$ states.

Kozlov's code does not require the intermediate sum J_a, and so we exclude it from the basis. We create the basis in the manner in which we would create a case (a) basis, as a list of states of the form:

$$\{\Lambda, S, \Sigma, \Omega, J, I_1, F_1, I_2, F_2, m_F\}$$

$States[S\_, \Sigma\_, \Lambda\_, Nmax\_, I1\_, I2\_, mF\_]$ generates a list of states in the basis, given

- S is the electron spin ($S = 1/2$ for a single valence electron)

- $\Sigma$is the projection of S on to the internuclear axis $\hat{n}$ ($\Sigma = 1/2$ for a doublet state)
- $\Lambda$is the projection of L on to the internuclear axis $\hat{n}$ ($\Lambda = 1$ for a Π state, $\Lambda = 0$ for a Σ state)
- $Nmax$ is the maximum value of N for which to generate the basis ($Nmax = 5$ is usually acceptable if we limit ourselves to studying the first few rotational levels)
- $I1$ is the nuclear spin of the first atom (eg. $I1 = 0$ for ^{138}Ba, $I1 = 3/2$ for ^{137}Ba)
- $I2$ is the nuclear spin of the first atom (eg. $I2 = 1/2$ for ^{19}F)
- mF is the magnetic sublevel m_F for which to generate the basis; the Hamiltonian does not mix levels with different values of m_F, so these can be generated and diagonalized separately.

The return value is

- list of $\{\Lambda, S, \Sigma, \Omega, J, I_1, F_1, I_2, F_2, m_F\}$

Before actually using this basis (but not within the *States*[] function described below), we will restrict the basis to states with $\Omega = \pm 1/2$. The code is not written to handle $\Omega = 1/2$ and $\Omega = 3/2$ in the same basis, as can occur in the $^2\Pi$ state but not the $^2\Sigma$ state. This can be done by filtering the list of states with the command `Select[States[...],(Abs[#[[4]]] == 1/2)&]`.

The Mathematica code for *States*[...] is:

```
States[S_, Σ_, Λ_, Nmax_, I1_, I2_, mF_] :=
  Flatten[Table[{Λsgn Λ, S, Σsgn Σ, Λsgn Λ + Σsgn Σ, Abs[Λsgn Λ + Σsgn Σ] + N,
      I1, F1, I2, F2, mF},
    {N, 0, Nmax},
    {Λsgn, -Sign[Λ], Sign[Λ], 2},
    {Σsgn, -Sign[Σ], Sign[Σ], 2},
    {F1, Abs[Abs[Λsgn Λ + Σsgn Σ] + N - I1], Abs[Λsgn Λ + Σsgn Σ] + N + I1},
    {F2, Max[Abs[F1 - I2], Abs[mF]], F1 + I2}], 4]
```

We also define a set of accessor functions to make it easy to access the quantum numbers of a given state:

$\Lambda_{s\_,i\_} := s[\![i,1]\!]$; $S_{s\_,i\_} := s[\![i,2]\!]$; $\Sigma_{s\_,i\_} := s[\![i,3]\!]$;

$\Omega_{s\_,i\_} := s[\![i,4]\!]$; $J_{s\_,i\_} := s[\![i,5]\!]$; $I1_{s\_,i\_} := s[\![i,6]\!]$;

$F1_{s\_,i\_} := s[\![i,7]\!]$; $I2_{s\_,i\_} := s[\![i,8]\!]$; $F2_{s\_,i\_} := s[\![i,9]\!]$;

$mF_{s\_,i\_} := s[\![i,10]\!]$;

We define some functions to compare whether two states have similar angular momenta:

$\delta[a\_, b\_] :=$ `KroneckerDelta[a, b]`

$\delta F[s\_, i\_, j\_] := \delta[mF_{s,i}, mF_{s,j}]\delta[F1_{s,i}, F1_{s,j}]\delta[F2_{s,i}, F2_{s,j}]$

And finally, we define a few functions to help clean up the notation for the addition of angular momenta:

```
ThreeJ[a_] := If[Chop[a[[2,1]] + a[[2,2]] + a[[2,3]]] == 0,
    ThreeJSymbol[{a[[1,1]], a[[2,1]]}{a[[1,2]], a[[2,2]]}, {a[[1,3]], a[[2,3]]}], 0]
SixJ[a_] := SixJSymbol[a[[1]], a[[2]]]
```

$\langle j1\_, m1\_, j2\_, m2\_ | j\_, m\_ \rangle :=$ `ClebschGordan[{j1, m1}, {j2, m2}, {j, m}]`

This lets us use natural notation like

$$\begin{pmatrix} j_1 & j_2 & j \\ m_1 & m_2 & m \end{pmatrix} = \texttt{ThreeJ[}\begin{pmatrix} j1 & j2 & j \\ m1 & m2 & m \end{pmatrix}\texttt{]}$$

and

$$\begin{Bmatrix} a & b & c \\ d & e & f \end{Bmatrix} = \texttt{SixJ[}\begin{pmatrix} a & b & c \\ d & e & f \end{pmatrix}\texttt{]}$$

in place of the nonstandard notation of the `ThreeJSymbol[]` and `SixJSymbol[]` functions.

It is also useful to turn off many of the error messages related to the calculation of angular momenta:

```
Off[ClebschGordan :: tri]; Off[ClebschGordan :: phy];
```

H.1.3 Field-Free Hamiltonian

The effective Hamiltonian used [3] has the following terms:

$$\mathcal{H} = \mathcal{H}_{rot} + \mathcal{H}_{\Omega-dbl} + \mathcal{H}_{hfs,1} + \mathcal{H}_{hfs,2} + \mathcal{H}_{quad} \tag{H.4}$$

where

- $\mathcal{H}_{rot} = B\vec{N}^2$ describes the rotational energy of the molecule
- $\mathcal{H}_{\Omega-dbl} = \gamma\vec{N}\cdot\vec{S}$ describes the spin-rotation coupling, which lifts the degeneracy between states of $\pm\Omega$
- $\mathcal{H}_{hfs} = \boldsymbol{A}\vec{I}\cdot\vec{S}$ is the hyperfine splitting, with a tensor component $\boldsymbol{A}$ that allows different effective coefficients $A_\parallel$ and $A_\perp$ for the I_zS_z and $I_\pm S_\pm$ components of the Hamiltonian

- $\mathcal{H}_{quad} = \frac{eq_0Q}{4I(2I-1)}\left(3I_z^2 - I^2\right) - \frac{eq_2Q}{8I(2I-1)}\left(I_+^2 + I_-^2\right)$ describes the interactions due to the quadrupole moment of the nucleus

The calculations in Mathematica have parameters of the form $Hrot[s, i, j, R, B]$, where

- s is the list of states in the basis, as returned from $States[\ldots]$
- i and j are the states for which to calculate the Hamiltonian $\langle i|\mathcal{H}_{rot}|j\rangle$, where i and j are given as integer indices into the list of states s
- The remaining inputs (in this case, R and B) are the effective constants related to this part of the Hamiltonian

H.1.4 Magnetic Field Hamiltonian

The magnetic field Hamiltonian is

$$\mathcal{H}_z = -\mu_B\left(G_{xy}\vec{S}\cdot\vec{B} + \left(G_z - G_{xy}\right)\left(\vec{S}\cdot\hat{n}\right)\left(\vec{B}\cdot\hat{n}\right) + g_r\vec{N}\cdot\vec{B}\right) + \mu_N\left(\vec{I}_1\cdot\vec{B} + \vec{I}_2\cdot\vec{B}\right)$$

for a $^2\Sigma$ state, with G_z defined as $g_\parallel$ and G_{xy} defined as $g_\perp$. As noted in chapter 4, the explicit expression for the matrix element derived from this can also be used for the $^2\Pi_{1/2}$ state, if suitable values are chosen for G_z and G_{xy}. A clear way to see this is through evaluation of the case (a) matrix element given in eq. 9.71 of Brown and Carrington [31].

H.1.5 Calculating Levels

The main routine to calculate the energy levels is $calc[Nmax,\ Brange,\ lvl, iso,\ mF]$.

$calc[Nmax\_,\ Brange\_,\ lvl\_,\ iso\_,\ mF\_]$ calculates the energy levels and eigenstates of the X, $A\,^2\Pi_{1/2}$, or D states of ^{137}BaF or ^{138}BaF, given

- *Nmax* chooses the largest rotational angular momentum N to include in the basis; we typically choose $N = 5$ if we are concerned only with the lowest one or two rotational states

- *Brange* is a list of magnetic field values (in Gauss) at which to calculate the eigenstates; for example, setting *Brange* to `Union[Range[0, 5000, 5], Range[4600, 4700, 1]]` will calculate the levels at 5 Gauss intervals from 0 to 5000 Gauss, and in 1 Gauss intervals from 4600 to 4700 Gauss.

- *lvl* and *iso* choose which set of molecular constants to use; for example, *lvl* can be "X", "A", or "D", while *iso* can be 137 or 138

- mF chooses which magnetic sublevel m_F to calculate; the interactions do not mix different m_F, and so we do not need to calculate all possible m_F simultaneously

The return value is $\{states, ev, es, \mathcal{H}_0, \mathcal{H}_z, \mathcal{H}_e\}$ where

- *states* is a list of the basis states used in the calculation

- *ev* is a list of the eigenenergies, at each magnetic field value, such that $ev[\![i, j]\!]=\{B_j, E_i(B_j)\}$ where $E_i(B_j)$ is the energy of the ith lowest state at the magnetic field B_j

- *es* is a list of the eigenstates, at each magnetic field value, such that $es[\![i, j]\!]=\{E_j(B_i), \{c_1, c_2 \ldots, c_{Length[states]}\}\}$ gives the state composition of the jth lowest state at the magnetic field B_i

- $\mathcal{H}_0$, $\mathcal{H}_z$, and $\mathcal{H}_e$ are the matrices representing the field-free, Zeeman, and DC Stark Hamiltonians

The routine is usually called multiple times, in order to find the structure for individual values of m_F. The routine *calcmf*[...] can be used to automatically calculate multiple values of m_F.

H.1.6 Displaying Results

The content of individual states can be shown using the function *showstate*[...] or the related functions *showdecoupledstate*[...], *showparitystate*[...], and *showNstate*[...]. A display of all the states in a range of energies at a particular magnetic field can be obtained by using *wtable*[...], *wdtable*[...], *wptable*[...], and *wntable*[...]. A plot of the level energies as a function of magnetic field is made using *DoPlot*[...].

H.2 MX_PNC Code to Calculate Rotational Structure in $^2\Sigma$, $^2\Pi_{1/2}$ States

This version of the MX_PNC code, written for Mathematica 5.1 from Wolfram Research[1], is a collection of routines for calculating rotational structure of the $^2\Sigma$ and $^2\Pi_{1/2}$ states relevant for our measurements of parity violation in BaF. The code consists of a single file, *mx_pnc.nb*. The routines required for performing the calculations are loaded as "initialization cells" when the user first evaluates an expression within the notebook. The code is divided into the following sections:

- Constants - defines the values of the molecular constants for each relevant state
- State Preparation - generates a case (a) basis set (compatible with case (c))
- Hamiltonian
  - Field-Free - calculates the field-free Hamiltonian in a case (c) basis

[1]The code has not been tested in newer versions of Mathematica. Version 6 introduced significant changes to the plotting routines, and the plotting routines would need to be revised accordingly. The routines for calculation are unlikely to be affected.

  - External Field - calculates the Zeeman Hamiltonian in a case (c) basis
  - Additional Terms - calculates $\left\langle \left(\vec{S} \times \hat{n} \right) \cdot \frac{\vec{I}}{I} \right\rangle$ as a proxy for the nuclear spin-dependent parity violating Hamiltonian matrix element
  - Dipole Moment - calculates the dipole matrix elements, DC Stark Hamiltonian, and transition moments relevant for simulating the laser spectra of the molecule

- Calculation & Display
  - Calculation - routines to calculate the rotational energy levels and state composition at a range of magnetic fields
  - Display - routines to display the composition of a given state in a choice of basis sets, or to plot the energy levels as a function of magnetic field

- Testing - comparison of the output of this code with the original Fortran-77 version of MX_PNC written by Mikhail Kozlov

For the sake of brevity, the Mathematica code required for the calculation of the rotational structure of ^{138}BaF and ^{137}BaF is available in a separate addendum.

Bibliography

[1] V. V. Flambaum and I. B. Khriplovich, "P-odd nuclear forces–a source of parity violation in atoms", Sov. Phys. JETP 52 (1980) 835-839

[2] I. B. Khriplovich, *Parity Nonconservation in Atomic Phenomena* (Gordon and Breach, Philadelphia, 1991)

[3] M. G. Kozlov, L. N. Labzovskii, and A. O. Mitrushchenkov, "Parity non-conservation in diatomic molecules in a strong constant magnetic field", Sov. Phys. JETP 73 (1991) 415-421

[4] M. G. Kozlov, L. N. Labzowsky, "Parity violation effects in diatomics (topical review)", J. Phys. B 28 (1995) 1933-1961

[5] Wu, C. S. et al., "Experimental Test of Parity Conservation in Beta Decay", Phys. Rev. 105 (1957) 1413-1415

[6] C. Y. Prescott et al., "Parity non-conservation in inelastic electron scattering", Phys. Lett. B77 (1978) 347-352

[7] C. Y. Prescott et al., "Further measurements of parity non-conservation in inelastic electron scattering", Phys. Lett. B84 (1979) 524-528

[8] E. J. Beise, M. L. Pitt, D. T. Spayde, "The SAMPLE experiment and weak nucleon structure", Prog. Part. Nucl. Phys. 54, 289-350 (2005), nucl-ex/0412054

[9] Paul Langacker, Mingxing Luo, and Alfred K. Mann, "High-precision electroweak experiments: A global search for new physics beyond the Standard Model", Rev. Mod. Phys. 64 (1992) 87-190

[10] D. M. Meekhof, P. Vetter, P. K. Majumder, S. K. Lamoreaux, and E. N. Fortson, "High-precision measurement of parity nonconserving optical rotation in atomic lead", Phys. Rev. Lett. 71 (1993), 3442-3445

[11] G. Herzberg, *Spectra of Diatomic Molecules* (Van Nostrand, Princeton, 1950)

[12] C. Effantin et al., "Studies of the electronic states of the BaF molecule Part I: Effective constants for seven states below 30 000 cm^-1", Mol. Phys. 70 (1990) 735-745; A. Bernard et al., "Studies of the electronic states of the BaF molecule Part II: The 5d(v = 0, 1, 2) states", Mol. Phys. 70 (1990) 747-755

[13] Holstein, Barry R., *Weak Interactions in Nuclei* (Princeton University Press, Princeton, 1989)

[14] A. T. Nguyen et al., "Search for parity nonconservation in atomic dysprosium", Physical Review A (1997) 3453-3463

[15] S. L. Gilbert and C. E. Wieman, "Atomic-beam measurement of parity nonconservation in cesium", Physical Review A 34 (1986) 792-803

[16] C. S. Wood et al., "Measurement of Parity Nonconservation and an Anapole Moment in Cesium", Science 275 (1997), 1759

[17] J.S.M Ginges and V. V. Flambaum, "Violations of fundamental symmetries in atoms and tests of unification theories of elementary particles", Physics Reports 397 (2004) 63-154

[18] V. V. Flambaum and D. W. Murray, "Anapole moment and nucleon weak interactions", Phys. Rev. C 56 (1997) 1641-1644

[19] R. N. Cahn and G. L. Kane, "Parity Violations in Hydrogen and the Fundamental Structure of the Weak Current", Physics Letters 71B (1977) 348-352

[20] W. J. Marciano and A. Sirlin, "Radiative corrections to atomic parity violation", Physical Review D 27 (1983) 552-556

[21] W. J. Marciano and A. Sirlin, "Some general properties of the $O(\alpha)$ corrections to parity violation in atoms", Physical Review D 29 (1984) 75-88

[22] J. J. Sakurai, *Modern Quantum Mechanics* (Addison-Wesley, Redwood City, 1985)

[23] D. DeMille et al., "Using Molecules to Measure Nuclear Spin-Dependent Parity Violation", Physical Review Letters 100 (2008) 023003

[24] L.-E. Berg et al., "Lifetime measurements of the $A^2\Pi_{1/2}$ state of BaF using laser spectroscopy", Chemical Physics Letters 287 (1998) 89-93

[25] L.-E. Berg, T. Olsson, et al., "Lifetime measurements of excited molecular states using a Ti:sapphire laser", Molecular Physics 79 (1993) 721-725

[26] B. E. Sauer, J. Wang, and E. A. Hinds, "Laser-rf double resonance spectroscopy of ^{174}YbF in the $X^2\Sigma^+$ state", J. Chem. Phys. 105 (1996) 7412

[27] M. Nayak and R. Chaudhuri, "Ab Initio calculation of P, T-odd interaction constant in BaF", J. Phys. B 39 (2006) 1231-1235

[28] T. Steimle, private communications

[29] J. M. Brown et al., "An analysis of hyperfine interactions in the electronic spectrum of AlF", Physica Scripta. 17 (1978) 55-67

[30] Ira A. Levine, *Molecular Spectroscopy* (John Wiley and Sons, New York, 1975)

[31] John Brown and Alan Carrington, *Rotational Spectroscopy of Diatomic Molecules* (Cambridge University Press, Cambridge, 2003)

[32] NIST Atomic Spectra Database, online at `http://physics.nist.gov/PhysRefData/ASD/index.html`

[33] W. E. Ernst et al., "Hyperfine structure and electric dipole moment of BaF $X^2\Sigma$", Journal of Chemical Physics 84 (1986), 4769-4773

[34] WebElements, `http://www.webelements.com`

[35] William Weltner, Jr., *Magnetic Atoms and Molecules* (Academic Editions, New York, 1983)

[36] P. R. Bunker, "The electronic isotope shift in diatomic molecules and the partial breakdown of the Born-Oppenheimer approximation", Journal of Molecular Spectroscopy 28 (1968), 422-443

[37] Stephan Sauer, "A relation between the rotational g-factor and the electric dipole moment of a diatomic molecule", Chemical Physics Letters 297 (1998), 475-483

[38] G. Coulston and K. Bergmann, "Population transfer by stimulated Raman scattering with delayed pulses: Analytical results for multilevel systems", Journal of Chemical Physics 96 (1992), 3467-3475

[39] N. V. Vitanov et al., "Laser-Induced Population Transfer by Adiabatic Passage Techniques", Annual Review of Physical Chemistry 52 (2001), 763-809

[40] J. Martin, B. W. Shore, and K. Bergmann et al, "Coherent population transfer in multilevel systems with magnetic sublevels. III. Experimental results", Physical Review A 54 (1996), 1556-1569

[41] R.M. Jordan web site, `http://www.rmjordan.com/c211-451.html`

[42] S. K. Tokunaga et al., "A supersonic beam of cold lithium hydride molecules", Journal of Chemical Physics 126 (2007), 124314; arXiv:physics/0612163v1

[43] G. Scoles, ed. *Atomic and molecular beam methods* (Oxford University Press, Oxford, 1988)

[44] J. Arnó and J. W. Bevan, "Infrared spectroscopy in supersonic free jets and molecular beams", in Jet Spectroscopy and Molecular Dynamics, Hollas and Phillips, eds. 1995, Chapman and Hall, London.

[45] G. J. Van Wylen et al., *Fundamentals of Classical Thermodynamics* (Wiley, 1994)

[46] Pauly, H. *Atom, Molecule, and Cluster Beams Volumes 1 & 2*, Springer 2000

[47] M. J. Zucrow and J. D. Hoffman, *Gas Dynamics* (Wiley, New York, 1976)

[48] R. E. Miller, in G. Scoles, *Atomic and Molecular Beam Methods, Vol. 1* (Oxford University Press, Oxford, 1988)

[49] J. B. Anderson and J. B. Fenn, "Velocity distributions in molecular beams from nozzle sources", Phys. Fluids 8 (1965) 780-787

[50] G. Tejeda et al., "Temperature and density mapping of supersonic jet expansions using linear Raman spectroscopy", Phys. Rev. Lett. 76 (1996), 34-37

[51] M. R. Tarbutt, J. J. Hudson, B. E. Sauer, E. A. Hinds, V. A. Ryzhov, V. L. Ryabov, and V. F. Ezhov, "A jet beam source of cold YbF radicals", Journal of Physics B 35 (2002) 5013-5022

[52] D. Egorov et al., "Buffer-gas cooling of atomic and molecular beams", Physical Review A 66 (2002) 043401

[53] V. L. Ryabov, V. F. Ezhov, M. A. Kartasheva, "Low-pressure inductively coupled plasma as a new source of molecular beams", Technical Physics Letters 32 (2006) 969-971

[54] D. Proch and T. Trickl, "A high-intensity multi-purpose piezoelectric pulsed molecular beam source", Review of Scientific Instruments 60 (1988) 713-716

[55] T. Steimle, private communication

[56] T. Steimle, private communication

[57] B. N. Chichkov, C. Momma, S. Nolte, F. von Alvensleben, A. Tünnermann, "Femtosecond, picosecond and nanosecond laser ablation of solids", Appl. Phys. A 63 (1996) 109-115

[58] Anatoliy Y. Vorobyev, Chunlei Guo, "Residual thermal effects in laser ablation of metals", Journal of Physics Conference Series 59 (2007) 418-423

[59] B. C. Stuart, M. D. Feit, A. M. Rubenchik, B. W. Shore, M. D. Perry, "Laser-Induced Damage in Dielectrics with Nanosecond to Subpicosecond Pulses", Phys. Rev. Lett. 74 (1995) 2248-2251

[60] Steven Chambreau, Monica L. Neuburger, Tom Ho, Brian Funk, and David Pullman, "Low cost, mechanically refrigerated diffusion pump baffle for ultrahigh vacuum chambers", J. Vac. Sci. Technol. A Volume 18, Issue 5, pp. 2581-2585 (September 2000).

[61] Saul Dushman, *Scientific Foundations of Vacuum Technique*, 2nd ed. 1962 p. 99; http://www.lesker.com/newweb/technical_info/conductance_calc.cfm

[62] Dennis Murphree, "Nuclear Spin Dependent Parity Nonconservation in Diatomic Molecules", dissertation, Yale University.

[63] http://www.chemie.fu-berlin.de/chemistry/general/constants_en.html

[64] Matt Nicholas, thesis, DeMille group summer project

[65] George Burkhard, thesis, DeMille group summer project

[66] Yeagle Tech, http://www.yeagletech.com/techinfo/molecularpath.html

[67] D. Herriott, H. Kogelnik, and R. Kompfner, "Off-axis paths in spherical interferometers", Applied Optics 3 (1964), 523-526.

[68] K. Kerner et al., "Variable Free Spectral Range Spherical Mirror Fabry-Perot Interferometer", http://budker.berkeley.edu/papers/pdfs/katie(SFPI).pdf

[69] D. Budker et al., "Obtaining frequency markers of variable separation with a spherical mirror Fabry-Perot interferometer", Review of Scientific Instruments 71 (2000) 2984-2987

[70] B. Sauer, M. Tarbutt, et al., poster presentation, ICAP 2006.

[71] Jessie Petricka, dissertation, Yale University.

[72] D. Budker, D. Kimball, D. DeMille, *Atomic Physics: an exploration through problems and solutions* (Oxford University Press, Oxford, 2004)

[73] Z. J. Jakubek and R. W. Field, "Core-Penetrating Rydberg Series of BaF: New Electronic States in the n^*=4 Region", Journal of Molecular Spectroscopy 179 (1996) 99-124

[74] Z. J. Jakubek and R. W. Field, "Core-Penetrating Rydberg Series of BaF: Single-State and Two-State Fits of New Electronic States in the $4.4 \leq n^* \leq 14.3$ Region", Journal of Molecular Spectroscopy 205 (2001) 197-220

[75] T. F. Gallagher, "Rydberg Atoms", Rep. Prog. Phys. 51 (1988) 143-188

[76] E. Wilson, J. Decius, and P. Cross, *Molecular Vibrations* (Dover Publications, New York, 1955); and `http://electron6.phys.utk.edu/qm2/modules/m1-3/molecules.htm`

[77] John Barry, private communication

[78] E. S. Shuman, J. F. Barry, D. R. Glenn, D. DeMille, "Radiative force from optical cycling on a diatomic molecule", arXiv:0909.2600 online at `http://arxiv.org/abs/0909.2600`

[79] C. Zener, "Non-adiabatic Crossing of Energy Levels", Proceedings of the Royal Society of London, Series A 137 (1932) 692-702